VDMA
Fluid Power Association

22nd ISC

International Sealing Conference

Stuttgart, Germany
October 01 - 02, 2024

Sealing Technology –
Challenges accepted!

IMA UNI STUTTGART

ISBN 978-3-8163-0768-6

Fachverband Fluidtechnik im VDMA e. V. Lyoner Str. 18
50628 Frankfurt am Main
Germany

Phone +49 69 6603-1513
E-Mail maximilian.baxmann@vdma.org
Internet www.vdma.org/fluid

Ladies and Gentlemen,

We are delighted to welcome you to the **22nd ISC on October 01 and 02, 2024** in Stuttgart. It is now the tenth time that the International Sealing Conference will take place at the University of Stuttgart, after it could not be held in 2020 due to the pandemic. This conference is again jointly organized by the VDMA and the Institute of Machine Components (IMA) at the University of Stuttgart.

Under the motto **"Sealing Technology - Challenges accepted!"** lectures will be held that convey the latest findings from research and development, as well as practical experience. The lectures will be held in English, only, with simultaneous translation into German provided.

Ingrid Hunger
Chairwoman of the Fluid Power
Sealing Group of VDMA

Frank Bauer
Head of Sealing Technology
IMA, University of Stuttgart

Peer Review at the ISC

All authors were offered the opportunity of an optional peer review of their paper. This guarantees that the examined papers meet high scientific requirements and may receive their respective appreciation for research projects or doctoral theses.

The reviewed papers are marked with the label "REVIEWED" in the conference proceedings.

A paper registered for the review process will be independently reviewed by two specialized experts (one from industry, one from academia). This scientific panel consists of the members of the programme committee as well as other experts from industry and academia.

After this initial evaluation, the authors have the opportunity, if necessary, to revise their paper with the required changes and submit it again. If the reviewers accept the changes – if necessary with the request for further minor corrections – the paper will be accepted as "REVIEWED" for the conference proceedings (see flow chart for review procedure).

This extensive review process serves the purpose of content and formal quality assurance and would not have been possible without the expert support of the scientific panel. The organizers of the ISC want to thank all reviewers for their support.

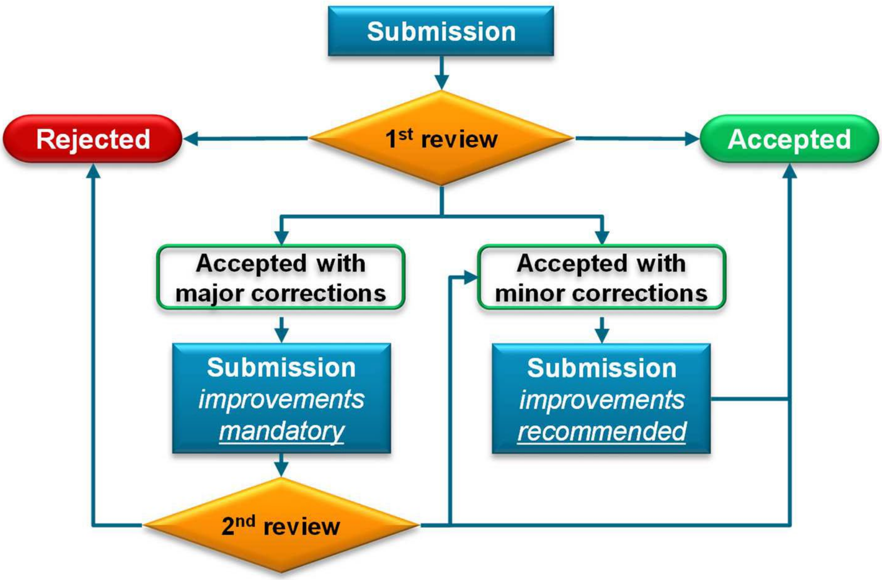

Programme Committee

Prof. Dr.-Ing. Frank Bauer	Universität Stuttgart, Institut für Maschinenelemente (IMA)
Prof. Dr. Eberhard Bock	Freudenberg FST GmbH
Stefan Brödner	Bosch Rexroth AG
Thomas Bürkle	FESTO SE & Co. KG
Dr.-Ing. Nino Dakov	Trelleborg Sealing Solutions Germany GmbH
Ozan Devlen	Kastas Sealing Technologies
Martin Goerres	Freudenberg FST GmbH
Maximilian Baxmann	Fachverband Fluidtechnik im VDMA e.V.
Andreas Hübner-Hecker	HECKER WERKE GmbH
Ingrid Hunger	Hunger DFE GmbH
Christoph Olbrich	Universität Stuttgart, Institut für Maschinenelemente (IMA)
Prof. Dr. Alexander Riedl	Fachhochschule Münster, FB Physikalische Technik
Robert Stäber	ARLANXEO Deutschland GmbH
Prof. Dr. Katharina Schmitz	RWTH Aachen, Institut für fluidtechnische Antriebe und Systeme
Jun. Prof. Dr. Stefan Thielen	Technische Universität Kaiserslautern, Lehrstuhl für Maschinenelemente und Getriebetechnik (MEGT)
Klaus G. Wagner	Herbert Hänchen GmbH & Co. KG
Prof. em. Dr. Peter Waidner	seal-ing - der dichtungsdoktor - the sealing doctor

Contents

			Page
Summaries			**13**
I - Session 1: Introduction Lectures			
I 02	S. Bond	Static Seals for Sealing Hydrogen: A Review	39
A- Session 2: Applications in practice I			
A 01	C. Olbrich J. Gerhard S. Feldmeth F. Bauer	Influence of rolling-element bearings on rotary shaft seals	61
A 02	N. Dakov M. Franz J. Baehl S. Wagoner	A high-pressure radial shaft seal with enhanced wear performance	79
A 03	A. M. Lehmann A. Dobrinsky M. Franz	A smart seal energizer from shape-memory-alloy	91
A - Session 3: Simulation I			
A 04	P. Shisode R. Willems B. van der Vorst M. Sansalone	Enabling more sustainable sealing solutions via multiscale friction modelling	107
A 05	B. Sundararajan M. Fasching M. Sansalone T. Schwarz B. van der Vorst	A new constitutive model describing the rate-, temperature- and strain- dependent behaviour of polymeric sealing materials	12
A 06	M. Hofmeister F. Fischer L. Boden K. Schmitz	Simulative Prediction of Leakage for Seat Valves and Bio-Hybrid Fuels	133
A 07	M. Wittmaack M.André S. Rakowski K. Schmitz	Influence of surface topography on stick-slip-effects – an experimental and numerical study	141

A - Session 4: Hydrogen

A 08	J. Müller	TEADIT’s sealing solutions for the electrolyser market	171
A 09	P.Hirstein S. Kofink J. Thompson	Influence of hydrogen on the material properties of non-metallic materials for sealing applications	183
A 10	M. Fasching T.Schwarz S. Schreymayer T. Hafner G. Theiler N. Cano Murillo A. Kaiser	Investigation of sealing materials with excellent cold temperature flexibility in hydrogen environments	195
A 11	Hashimoto S. Norikyo A. Aoyagi H. Tanaka T. Morita Y. Sawae J. Sugimura	Influences of hydrogen and trace moisture content on the friction of silicone rubber	211

A - Session 5: Simulation II

A 12	M. Graf T. Lankenau K. Ottink T. Ebel	Simulation of Leakage Flow in dynamic seals from 3D-printing	225
A 13	N. Bauer K. Schmitz	Pneumatic Seals: A Review of Experimental Measurement and Theoretical Modeling of Sealing Friction	237
A 14	T. Hantusch C. Schousboe Andreasen B. Ólafsson	Direct numerical simulation of mixed lubrication in elastohydrodynamic systems	251
A 15	F. Kaiser A. Gropp D. Savio D. Frölich C. Wilbs D. Möhring	Prediction of RSS Sealing Performance by Fully Coupled EHL Simulation	267

A - Session 6: Rotary Shaft Seals

A 16	M. Amro B. Wennehorst, G. Poll	Frictional characteristics of elastomeric radial lip seals at extremely low temperatures	279
A 17	Y. Lin R. Nepp M. Kröger	Stochastic analysis on tribological behavior of radial shaft seals with focus on lubricants	287
A 18	L. Marques de Castro Silva Y. Stiemcke T. Schollmayer O. Koch S. Thielen	Performance Analysis of Radial Shaft Seals in Non-Stationary Rotational Movements	299
A 19	M. Gohs L. Hörl F. Bauer	Development and Testing of Sleeve-Type Lip Seals with Stamped Back-Pumping Structures	315

A - Session 7: Materials and Surfaces II

A 20	L. Boden M. Hofmeister F. Brumand-Poor K. Schmitz	Predicting Compatibility of Sealing Material with Bio-Hybrid Fuels: Development and Comparison of Machine Learning Methods	333
A 21	J. Möschel	Poetry and truth, how does the hydrolysis-resistant structure come into the polyurethane?	349
A 22	C. Wilbs M. Adler D. Frölich A. Bellon N. Schuster J. Menzel E. Bopp	Micro-mechanical characterization of a tribological stressed elastomer surfaces with respect to Radial-Shaft-Seals	357

B - Session 2: Materials and Surfaces I

B 01	H. Tanaka A. Aoyagi H. Hashimoto Y. Sawae J. Sugimura	Friction and wear properties of several rubber materials for high pressure O-ring	369
B 02	M. Junk J. Germanus	Testing elastomeric materials in liquified gases	379

B 03	C. Tanyeri M. Unlu B. Caylak A. Kocamaz O. Devlen	Enhancing sealing element security: Quantum dot marking Solutions of NBR and TPU sealing elements	387

B - Session 3: Additive Manufacturing

B 04	T. Ebel K. Ottink	Functional testing of additively manufactured hydraulic rod seals	399
B 05	J. Gerhard L. Hörl F. Bauer	Additive Manufacturing of Sealing rings: Material Selection and Application Development	411
B 07	A. Kocamaz, O. Devlen C. Tanyeri B. Engendahl	Innovation in Seal Production: Novel Additive Manufacturing for High-Performance PU Seals	429

B - Session 4: Test procedures

B 08	A. Heinl C. Wilbs, D. Frölich M. Adler	Performance of the radial shaft sealing system under the influence of shaft lead	447
B 09	M. Engelfried M. Baumann F. Bauer	From Tactile to Optical - Advancements in Shaft Lead Analysis	461
B 10	G. Haffner M. Baumann F. Bauer	Insights into the pumping behavior of sealing counterfaces using continuous logging	479
B 11	T. Horiuchi Y. Sakai A. Aoyagi	In Situ Observation of a Grease Lubricant Film on a Radial Seal by Fluorescence Induced Microscopy	495

B - Session 5: Applications in practice II

B 12	S. Shevchenko	Study of the non-contact seals influence on the centrifugal machine's dynamic characteristics	505
B 13	T. White	Thermal Behaviour of Marine Lip Seals – A Pathway Towards Condition Monitoring	521

B 14	O. Morad V. Saikko R. Viitala	Frictional behavior of marine lip seals: Sensitivity to operational parameters	535
B 15	J. Kaleshian R. Clark H. Azibert M. Grimanis	A method of direct thermal conditioning of mechanical seal faces: CFD, empirical analysis and testing	545

B - Session 6: Reciprocating Seals

B 16	G. Barillas A. Gropp	Further Observations in Wiper design and Particle Transport Simulation in the Sealing Gap	567
B 17	F. Brumand-Poor F. Barlog N. Plückhahn M. Thebelt K. Schmitz	Advancing Lubrication Calculation: A Physics-Informed Neural Network Framework for Transient Effects and Cavitation Phenomena in Reciprocating Seals	577
B 19	A. Dobrinsky S. Betz C. Schüle B. Brodmann	Advanced characterization of counter surfaces in linear applications	595

B - Session 7: Static Seals

B 21	H. Kurz M.Hübner Hecker	Optimized rubber gasket with internal force shunt	611
B 22	F. Bartmann A. Riedl E. Moritzer	Development of an analytical calculation method for the design of thermoplastic flange systems	619

Summaries

I- Session 1: Plenary Talks I

I 02

Stephen Bond, The Flexitallic Group Research and Development, Houston, United States

Static Seals for Sealing Hydrogen: A Review

Hydrogen has a potentially large role in the future of energy, either as a fuel, as an energy storage vehicle, or both. Based on the amount of research work and government funding in this area, such as the US Government's pledge of $7 billion for hydrogen hubs, it would be a good assumption that the role of hydrogen is set to grow for the foreseeable future. This is especially the case for so called green hydrogen, where hydrogen is produced by the electrolysis of water and the electricity used in the electrolysis is from a renewable energy source (e.g., wind, solar).
Due to its inherent properties, there has been some concern about the potential for leak-age of hydrogen in this new process industry. This, of course, brings into focus the sealing of static bolted connections, i.e., bolted flange joints.
The most common leakage tests for bolted flange connections use either helium (EN13555), methane (ASME B16.20) or nitrogen (DIN 3535), but not hydrogen. There are good reasons for choosing these gasses, particularly helium, which is safe and a small molecule which can be detected and measured by standard equipment such as a mass spectrometer.
Other literature has shown that leak rate of different gases cannot be judged and predicted by molecule size alone, therefore the conversion of leak rate using a standard test and test gas cannot be easily converted to a leak rate of hydrogen. Therefore, testing of gaskets with hydrogen has been required to make engineering decisions.
This paper will review recent public domain papers on sealing tests using hydrogen, especially those comparing hydrogen sealing rates to helium sealing rates. This paper will also include some recent hydrogen sealing testing commissioned at a third party test house using spiral wound gaskets with different fillers.

A- Session 2: Applications in practice I

A 01

Christoph Olbrich, Jacqueline Gerhard, Simon Feldmeth, Frank Bauer, University of Stuttgart, Institute of Machine Components (IMA), Stuttgart, Germany

Influence of rolling-element bearings on rotary shaft seals

Rotary shaft seals are commonly used to seal rotating machine components and prevent the leakage of fluids into the environment. Failures of elastomeric rotary shaft seals are often the result of overheating in the contact area between the sealing edge and the shaft. High temperatures in this contact area occur due to high frictional power and/or inadequate heat dissipation. The surroundig of the seal has a significant impact on the temperatures occurring in the contact area. Studies by Kunstfeld [1] have already demonstrated that additional elements near the seal influence the temperature.
Especially rolling-element bearings near the seal strongly influence the contact temperature. The frictional heat generated in the bearings results in an increase in the temperature of the fluid near the seal, consequently raising the contact temperature. Tapered roller bearings pump oil [2] and, depending on the installation situation, can lead to a higher or lower fluid level next to the seal.

Tests are conducted on a High-Speed friction torque test bench [3]. This investigation involves four different bearing arrangements, as well as a reference variant without bearings. In these test runs, both the frictional torque and the temperature near the contact area are examined.In addition to the experiments on the test bench, Conjugate Heat Transfer (CHT) simu-lations are conducted with the same installation conditions. The simulated temperatures are compared with the measured temperatures. In most cases, the correlation is good. However, for one bearing arrangement, the correlation is significantly worse [4]. These differences are investigated further.

References:
[1] Kunstfeld, T.; Haas, W.: Dichtungsumfeld, Abschlussbericht
[2] Schaeffler Technologies AG & Co. KG: Wälzlagerpraxis
[3] IMA: High-Speed Universal Test Bench
[4] Hannss, J.; Grün, J.; Olbrich, C.; Feldmeth, S.; Bauer, F.: Multiphase Conjugate Heat Transfer Analyses on the Assembly Situation of Rotary Shaft Seals

A 02

Nino Dakov, Martin Franz, Jeff Baehl, Sam Wagoner, Trelleborg Sealing Solutions Germany GmbH, Stuttgart, Germany

A high-pressure radial shaft seal with enhanced wear performance

High-pressure radial shaft seals are typically used in hydraulic pumps to seal a continuously rotating shaft within a housing bore. When the seal is pressurized, the sealing lip's contact with the shaft increases, which leads to higher wear. At very high pressures, the seal's cross-section can collapse, forcing the garter spring out of its retaining groove. This issue can be mitigated by stiffening the membrane area, though this reduces the seal's ability to accommodate radial movement of the shaft. The current study presents a new approach to stabilize the seal's cross-section. Multiple pads are added on the seal above the membrane area and next to the spring. As a result, a considerably lower laydown is achieved, resulting in improved wear performance during tests. Additionally, the pads help maintain the spring's position. The theoretical considerations are supported by tests conducted under varying pressure and shaft speed conditions, demonstrating the practical benefits of this new seal design.

A 03

Anne Marie Lehmann, Anja Dobrinsky, Martin Franz, Trelleborg Sealing Solutions Germany GmbH, Research and Development, Stuttgart, Germany

A smart seal energizer from shape-memory-alloy

Harsh operating conditions can strongly reduce the seal's lifetime, potentially damaging people, and the environment. One solution to this challenge is the use of actuatable seals which are able to adapt to the operating conditions. The high operating displacement and comparably low tension force, combined with the freedom of design make a shape-memory-alloy (SMA) the perfect actuator for polymer seals. This work presents a proof of concept for a PTFE seal energized by a SMA wire. The wire is wrapped around the circumference of the seal and activated by means of induction. When the wire is activated, it constricts in length and increases the radial load of the seal. Due to the tunable radial load, the sealing function and friction properties can be tailored to the operating conditions in application.

This work presents a proof of concept for a PTFE seal energized by a SMA wire. The wire is wrapped around the circumference of the seal and activated by means of induction. When the wire is activated, it constricts in length and increases the radial load of the seal. Due to the tunable radial load, the sealing function and friction properties can be tailored to the operating conditions in application.

A- Session 3: Simulation I

A 04

Meghshyam Prabhakar Shisode, Ron Willems, Bas van der Vorst, Mickael Sansalone, SKF Seals, Global Research & Innovation, Houten, The Netherlands

Enabling more sustainable sealing solutions via multiscale friction modelling

A reliable and accurate seal friction model is paramount in optimizing sealing products towards energy-efficient and sustainable sealing systems. In seals, depending on the contact conditions, boundary and mixed lubrication regimes are as prevalent as the full-film regime due to, for example, rougher contacting surfaces, lubricant starvation, low speed, severe contact pressure, temperature, etc. Although the research on full-film lubrication regime is well matured, a reliable predictive model for rubber dry friction, contributing to boundary and mixed lubrication regimes, is still lacking, therefore hindering the friction and wear models accuracy for sealing applications.

In this work, a predictive analytical model to estimate temperature and speed dependent rubber dry friction is proposed. The model is inspired by a multiscale representation of a metallic counterface combined with a first-order analytical approximation of contact stresses and rubber deformation. The counterface is decomposed into different scales of roughness and the rubber dissipation energy is then determined on each scale. The transition between different scales is also modeled, which is important to correctly estimate the contribution from each scale. Subsequently, a cumulative frictional energy loss is estimated to predict the friction force.

The resulting model is able to predict temperature and sliding speed dependent friction coefficient and shows a good correlation with in-house experiments. The proposed dry friction model can be combined with the lubricant viscous shearing friction model to predict the overall friction more reliably in the sealing contact, thereby accelerating the design of more sustainable and energy-efficient sealing solutions.

A 05

Bharath Kumar Sundararajan, Michael Fasching, Mickael Sansalone, Thomas Schwarz, Bas van der Vorst, SKF B.V., Global Research and Innovation, SKF Seals Business Unit, Houten, The Netherlands

A new constitutive model describing the rate-, temperature- and strain- dependent behaviour of polymeric sealing materials

The continuous advancement of virtual simulation platforms is a fundamental aspect of the ongoing global digitalization megatrend. To broaden the applicability of these platforms to sealing applications, there is a need for more comprehensive material models that can describe the complex and diverse behaviour exhibited by various polymeric ma-terials used in sealing products, such as elastomers, thermoplastic polyurethanes (TPUs) and PTFE.

To address this need, a new generalized modelling framework and approach is introduced in this paper. The proposed approach allows different aspects of the model to be modified, tailoring to the material being studied. The model demonstrates a remark-able potential to accurately describe the strain rate, temperature, and strain dependent behaviour of a chosen seal material, PTFE, within the relevant conditions experimentally covered.

A 06

Marius Hofmeister, Felix Fischer, Lukas Boden, Katharina Schmitz, Institute for Fluid Power Drives and Systems - RWTH Aachen University, Aachen, Germany

Simulative Prediction of Leakage for Seat Valves and Bio-Hybrid Fuels

Seat valves play a critical role in various technical applications, such as automotive injectors. Here, predicting leakage is vital, as it can lead to poor combustion behavior or complete system failure. To address this, a simulation model originally designed for predicting leakage of air and hydrogen in ball seat valves was adapted for the use with bio-hybrid fuels.

The simulation model uses a modified flow equation based on the Hagen–Poiseuille equation and the effective medium approach to calculate leakage flow. The corresponding input parameters are calculated according the Persson's contact mechanics considering the surface roughness at the sealing zone. This method considers the elasto-plastic deformations of the surface asperities on a microscopic level, leading to a description of the contact pressure relation. This relation is used in the calculation of the elastic deformations on the macroscopic level. Good agreement between the model and experimental results was found for air and liquid water.

Since many bio-hybrid fuels differ significantly in their fluid-mechanical properties from conventional fuels and gases like air and hydrogen, the simulation model cannot be used for these liquids without any adjustments. For instance, leakage is influenced by their low viscosity, low density, and high vapor pressure of these fuels. Furthermore, deviating interfacial interactions between liquid and solid bodies within the valves is of great importance when investigating leakage. For this reason, additional experiments and simulations have been conducted for bio-hybrid fuels.

This study aims to investigate the influence of deviating fluid properties of bio-hybrid fuels on the prediction of leakage in seat valves in comparison to conventional fuels. For this reason, the relevant fluid properties are determined for selected bio-hybrid fuels and implemented in the simulation model. Subsequently, the obtained results are compared with experimental data.

A 07

Martin Wittmaack, Markus André, Sebastian Rakowski, Katharina Schmitz, University of Applied Sciences and Arts Hannover Faculty II - Mechanical and Bioprocess Engineering, Hannover, Germany

Influence of surface topography on stick-slip-effects – an experimental and numerical study

Lubricated sealing systems, such as in automotive brake master cylinders or other hydraulic systems, tend to have undesirable stick-slip-effects under certain service conditions. These stick-slip-effects are clearly driven by the complex frictional behavior in the mixed lubrication regime. A significant factor in this tribological system is the surface topography. Thus, it is necessary to investigate and describe the lubrication effects on a micromechanical level.

In the presented study, SRV-tribometer tests are performed in order to study stick-slip-effects and significant parameters, such as the surface topography. In these tests, a cylindrical EPDM specimen is moved over a ground steel surface in a sinusoidal manner. are achieved. The test results then show: If the EPDM specimen is moved perpendicular to the grinding direction of the steel sample, the stick-slip effect does not occur with any of the tested fluids. However, if the steel sample is rotated by 90°, so that the EPDM specimen is moved in the direction of grinding, it is possible to provoke a stick-slip-effect. This clearly proves that the surface topography has a strong influence on the stick-slip-effect. Corresponding numerical contact- and CFD-simulations, based on the measured surface topography are performed and consider the surface roughness on a micro-scale. These numerical studies allow to motivate the influence of

The steel surface is wetted with brake fluid, so that conditions close to a hydraulic cylinder sealing system micromechanical models is then used in a transient finite element computation of a reciprocating sealing system, considering the fluid film dynamics. the surface topography on the fluid dynamics in the lubrication gap. The data from these
Finally, these numerical investigations enable a deeper understanding of the stick-slip mechanisms in lubricated sealing contacts and point out the influence of surface topology.

A- Session 4: Hydrogen

A 08

Johannes Müller, TEADIT International Produktions HmbH, Kirchbichl, Austria

TEADIT's sealing solutions for the electrolyser market

There is a global competition to achieve a clean energy transition, and green hydrogen, generated through water electrolysis using renewable energy sources, is considered crucial for achieving net-zero emissions. As electrolyzer manufacturers continue to enhance current technologies, explore new ones, and scale up their production capacities to meet the increasing demand, there is a corresponding surge in the demand for electrolyzer components. The sealing of large electrolyzer and fuel cell stacks, which consist of hundreds of individual cells, is essential for ensuring their safe and efficient operation. According to Frank Weber, CEO of EMEA and Asia-Pacific at TEADIT, a 5 MW alkaline electrolyzer typically requires approximately 500 seals. These seals can be quite large, measuring up to 1.6 meters in diameter, and are needed in significant quantities. As future electrolyzer plants are expected to have capacities measured in gigawatts, each gigawatt of capacity could necessitate around 100,000 seals. This presents a tremendous opportunity for companies like TEADIT to contribute to the global scale-up of green hydrogen production.
PTFE (polytetrafluoroethylene) has emerged as a popular material choice for gaskets used in electrolysers due to its excellent sealing properties. While electrolysers have been used in various industries for decades, previous seals often incorporated asbestos coated with PTFE. However, in modern applications, asbestos is no longer used, and gaskets made entirely of PTFE have become the standard alternative.

A 09

Philipp Hirstein, Sandra Kofink**,** Joel Thompson, Trelleborg Sealing Solutions Germany GmbH, Stuttgart, Germany

Influence of hydrogen on the material properties of non-metallic materials for sealing applications

Hydrogen entails challengiHydrogen entails challenging conditions for all sealing materials. For metals, the effect of hydrogen embrittlement is well known. However, little attention has been paid to elastomers and plastics, which are commonly used as sealing materials. For hydrogen storage and transport, high pressures and extreme temperature situations must be covered. This paper discusses the influence of hydrogen on mechanical properties, volume and weight change as well as compression set. Additionally, the influence of extreme application temperatures on mechanical properties is presented. In general hydrogen has no harmful influence on the compounds presented in this study, which are known as polymers suitable for hydrogen use.ng conditions for all sealing materials. For metals, the effect of hydrogen embrittlement is well known. However, little attention has been paid to elastomers and plastics, which are commonly used as sealing materials. For hydrogen storage and transport, high pressures and extreme temperature situations must be covered.

This paper will discuss which material properties are relevant to describe the sealing performance and how hydrogen influences these factors

A 10

Michael Fasching, Thomas Schwarz, Silvio Schreymayer, Thomas Hafner; Geraldine Theiler, Natalia Cano Murillo, Andreas Kaiser, SKF Sealing Solutions Austria GmbH, Austria

Investigation of sealing materials with excellent cold temperature flexibility in hydrogen environments

Reliable operation is a key requirement for hydrogen technology. Operating conditions of up to 1000bar pressure and temperatures of -40°C and 85°C, which are demanded for hydrogen-powered vehicles, are challenging to be met by sealing materials such as TPEs and rubbers.

In-depth understanding of material behavior is therefore needed to meet the requirement of reliable operation. In this work, the relevant properties for hydrogen applications are studied for two polyurethane grades, one EPDM, and two NBR grades with low ACN-content.

To characterize low temperature properties, results of typical methods to characterize the glass transition of sealing materials are compared to static sealability on a component level test with a T-seal design.

To measure permeation of hydrogen through those materials, a test rig was developed that allows the measurement of hydrogen permeation at temperatures up to 75°C and pressures of up to 800 bar within research project funded by the European Union.

Samples of the mentioned sealing materials were placed in an autoclave and exposed to temperatures at the upper service temperature at a pressure of 1000bar. Mechanical properties were tested accordingly before and shortly after the exposure. The tests after exposure were repeated 48 hours after the pressurized hydrogen exposure in order to quantify the reversibility of effects such as swelling.

As another dimension to compatibility, material samples were exposed to pressurized hydrogen at room temperature and tribological properties (wear, coefficient of friction) were characterized in-situ with a linear tribometer in ball-on-plate configuration.

Results show that all selected materials meet the demand of cold-temperature flexibility and compatibility to hydrogen, however distinguish in their swelling behavior, wear resistance and permeability.

A 11

Hikaru Hashimoto, Suguru Norikyo, Ayako Aoyagi, Hiroyohshi Tanaka, Takehiro Morita, Yoshinori Sawae, Joichi Sugimura, NOK corporation, Engineering Research Department, Fujisawa city, Japan

Influences of hydrogen and trace moisture content on the friction of silicone rubber

In recent years, the utilisation of hydrogen energy has gained importance in order to achieve carbon neutrality. This utilisation requires the establishment of technologies for the safe use of hydrogen, and the role of sealing materials is essential. Examples of sealing materials used in hydrogen include piston rings used in reciprocating compressors as dynamic seals and O-rings that are subjected to repeated loads of high-pressure hydrogen as static seals. These sealing products are subjected to sliding in hydrogen when in use. Unexpected high friction causes excessive elastic deformation and possibly induces serious mechanical failure of O-rings. For this reason, research has recently been carried out to lay the foundations for frictional properties in hydrogen (1)(2).The friction coefficient of the friction test in hydrogen was higher than that in air. Futhermore, the friction coefficient of the friction test in wet hydrogen (water content = 30~300 ppm) was higher than that in relatively dry hydrogen (water content = 4~7 ppm). These results suggested that gas atmosphere and water content of gas had an influence on the friction between rubber and SUS316L. To elucidate the friction mechanism, the surfaces of the rubber and SUS316L after testing were analyzed using optical microscopy, SEM/EDS and FT-IR.

(1) Sawae Y et al. Friction and wear of PTFE composites with different filler in high purity hydrogen gas, 157 (2021) 106884.
(2) Theiler G et al. Influence of counterface and environment on the tribological behaviour of polymer materials, 93 (2021) 106912.In this study, the effect of hydrogen on the friction mechanism between silicone rubber and SUS316L was investigated. The rubber was molded in the shape of a hemisphere. Reciprocating friction tests were performed with a pin-on-disk apparatus in air, hydrogen and gases bubbled in water to vary the amount of water content at atmospheric pressure.

A- Session 5: Simulation II

A 12

Matthias Graf, Tobias Lankenau, Kathrin Ottink, Thomas Ebel, University of Applied Sciences "Hochschule Emden/Leer", Maschinenbau, Emden, Germany

Simulation of Leakage Flow in dynamic seals from 3D-printing

Additive manufacturing (AM) technologies make strong progress in these years and impact seals as well. However the surface quality of AM seals is typically lower compared to seals from conventional production. For example Fused Filament Fabrication produces parts with a regular string-like surface structure. This structure is generated from a thin moving nozzle that extrudes melted filament material to strings. The size of the surface structure is in the order of the fluid film thickness of a dynamic rod seal. A fluid-structure interaction (FSI) with fully coupled Navier-Stokes equations analyses the fluid flow between seal and rod. It shows that a periodically fragmented contact, which is generated by FFF, impacts sealing properties of the dynamic seal. A simulation-based comparison between conventional seals and those from FFF manufacturing shows e.g. consequences for leakage flow through the seal gap.

A 13

Niklas Bauer, Katharina Schmitz, RWTH Aachen University, Institute for Fluid Power Drives and Systems (ifas), Aachen, Germany

Pneumatic Seals: A Review of Experimental Measurement and Theoretical Modeling of Sealing Friction

Pneumatic components perform mechanical work by pressured air. Seals in pneumatic components enable the functionally relevant pressure build-up and are thus crucial parts of their respective component. Dynamic seals in pneumatic cylinders and valves are subject to a motion relative to their counterface, which in turn causes a friction force acting between the seal and the counterface. This friction force reduces the dynamics of the component, leads to additional losses and can negatively affect the control behavior.
In the past decades, several attempts have been made to understand the friction behavior of pneumatic seals both by experiments and simulation models. This includes measurements of the friction force for different pneumatic pressures,

velocities, grease types or grease film heights. However, even for basic questions like the velocity dependence of the friction force there is no clear consensus amongst different authors up to this day.
While some authors found an increase of the friction force with increasing velocity, others authors have described a decrease of friction force instead. Furthermore, some sources even found no relevant influence of the velocity on the friction force at all. This unclear state of research makes modeling, constructing and dimensioning pneumatic sealing systems a difficult task during the development process.

This paper aims to give a comprehensive overview of the state of research regarding pneumatic sealing friction. For that, this paper presents a literature review of friction force measurements with special regard to the influence of the parameters of the sealing system. In addition, different modeling concepts are compared regarding their capability to calculate and understand the behavior of pneumatic seals. Finally, the paper highlights the challenges in modeling pneumatic sealing friction and proposes a new simulation framework based on the findings from the presented literature.

A 14

Tim Hantusch, Casper Schousboe Andreasen, Böðvar Ólafsson, A/S Gunnar Haagensen, Engineering - R&D, Allerød, Denmark

Direct numerical simulation of mixed lubrication in elastohydrodynamic systems

In the field of hydraulics, reciprocating rod and piston seals are crucial for the performance of cylinders and actuators. With respect to energy efficiency, leakage as well as product lifetime, numerical design tools play an important role in the design process of these seals. In recent decades, various numerical models for the prediction of tribological characteristics of reciprocating seals have been proposed. However, these models are often time-consuming to set up and come with long computation times. In recent years, advances in soft- and hardware have lead to the trend to solve complex elastohydrodynamic systems undergoing mixed lubrication within a single multiphysics platform.

By coupling solid mechanics, surface mechanics and fluid mechanics using the direct method, mixed lubrication in elastohydrodynamic systems has been successfully modeled for axisymmetric O-rings. Building on this, the presented work explores a two-component sealing system using the COMSOL® Multiphysics platform, enabling comprehensive coupling of solid, surface, and fluid mechanics. The numerical model's validation involves a test rig measuring friction from reciprocating seals, 3D surface texture characterization of the sealing lip, and an application-oriented test apparatus to determine the coefficient of friction for the rod-seal contact pair. This study aims to validate the direct method for a multi-part elastohydrodynamic system, emphasizing experimental validation to assess the accuracy of mixed lubrication models.

A 15

Fabian Kaiser, A. Gropp, D. Savio, D. Frölich, C. Wilbs, D. Möhring, Freudenberg Technology Innovation SE & Co. KG, Tribology, Weinheim, Germany

Prediction of RSS Sealing Performance by Fully Coupled EHL Simulation

The pumping and leakage behavior of radial shaft seals (RSS) has challenged researchers for more than half a century. The main phenomena contributing to reverse pumping have been identified some decades ago, e.g. by Kammüller. However, there is no conclusive proof nor comprehensive model for the exact sealing mechanisms, making it impossible to derive precise guidelines for radial shaft seal design. Thus, the question how to tune and optimize RSS is still open to this day.

To change this, Freudenberg has developed its own simulation tool to gain insight in the pumping mechanism and the sealing performance of RSS: FIRS³T – Freudenberg Integrated Radial Shaft Seal Simulation Tool.

It includes all steps required to simulate the pumping rate, among which: the Finite Element Analysis of the deformation of the seal, contact mechanics calculations and EHL-modelling of the sealing contact, all the way to the circumferential deformation of the sealing lip roughness in the contact due to the frictional shear stresses.

Using this tool, the pump rate of RSS can be simulated accurately and new insights in the sealing mechanism are possible. Furthermore, it will be shown how FST uses this tool to develop new seals with unrivalled functionality

A- Session 6 : Rotary Shaft Seals

A 16

Mousa Amro, Bengt Wennehorst, Gerhard Poll, Leibniz Universität Hannover , Institut für Maschinenkonstruktion und Tribologie, Garbsen, Germany

Frictional characteristics of elastomeric radial lip seals at extremely low temperatures

A novel low-temperature radial lip seal test rig was set up, allowing for simultaneous non-contact, telemetric measurements of both radial lip seal contact temperature and seal friction torque. Extreme cooling of the sealing contact zone down to below -50 °C was achieved by continuously feeding carbon dioxide snow pellets into the bore of a hollow seal counterface adaptor. Though this setup enables a simultaneous evaluation of two identical test seals, where the inner space is filled with lubricant, in this work, the frictional characteristics of wetted, single test seals were investigated. This eliminates the churning losses of the oil-filled ring gap that, due to the drastic increase of the lubricant viscosity at low temperatures, would severely hinder the correct determination of the seal friction torque.

Experiments were conducted with plain radial lip seals made of NBR and FKM, using two polyglycol oils with different viscosity grades VG 220 and VG 46, respectively. Starting from a stationary state at 100 rpm (0.419 m/s) with contact temperatures in the range of 45 °C to 60 °C, the sealing contacts were subsequently cooled down, finally reaching steady state seal contact temperatures as low as approx. -50 °C. Thus, during cool-down of the sealing systems, both seal elastomers pass through the glass transition, and both lubricants pass through their pour points. In contrast to warm operating conditions, where speed-step dependent seal friction changes could be accurately predicted based on soft micro-elastohydrodynamic asperity lubrication theory, speed step experiments at such extremely low temperatures revealed that there was no viscous friction response, i. e. the seal friction was due to Coulomb-type friction. While showing larger fluctuations, the overall level of this Coulomb-type friction was comparable to the steady-state seal friction measured under warm operating conditions. When warming the systems up, the original lubrication mode was reestablished.

A 17

Yongzhen Lin, Ringo Nepp, Matthias Kröger, Technische Universität Freiberg, Institut für Maschinenelemente, Konstruktion und Fertigung, Freiberg, Germany

Stochastic analysis on tribological behavior of radial shaft seals with focus on lubricants

This study deals with a methodical interpretation into the complex landscape of the tribological behavior of Radial Shaft Seals (RSS) using dynamic investigations focusing on the influence factor lubricant. The RSS forms a tribological system with the shaft surface as counterpart and the applied lubricant as medium. The lubricant has been identified as one of the main drivers for the tribological behavior of RSS especially due to its chemical structure and physical viscosity. Previous research has shown that the tribological behavior of RSS, such as leakage or wear, can be observed during and after testing with different lubricants, especially with different viscosities. This study evaluates the impact of lubricants with different chemical structure but similar viscosity, which allows to gain a deeper understanding of the further properties of lubricants. More specifically, different kinds of lubricants have been analyzed on RSS with different materials and diameters. Thereby, the rotational speed has been varied in relevant ranges. Using stochastic calculus analysis, the tribological behavior of RSS with lubricants can be evaluated in more detail. Especially, the variance of the frictional moment of the seal can be analyzed and interpreted depending on the test conditions. Secondly the potential damage and the wear formation can be evaluated optically with a microscopy. These results not only contribute to the academic discourse on RSS and lubricants as well as the tribological system, but also classify the different operating combinations for real applications. A specially designed RSS test rig at the Institute for Machine Elements, Design and Manufacturing is available for the experimental investigations. The aim of the extensive investigations is to create a basis for future, more in-depth research into understanding on the tribological behavior of the RSS as well as predictions for specific classified working environment for the different RSS systems

A 18

Lenine Marques de Castro Silva, Y. Stiemcke, T. Schollmayer, O. Koch, S. Thielen, Rheinland-Pfälzische Technische Universität Kaiserslautern-Landau, Chair of Machine Elements, Gears and Tribology - MEGT, Kaiserslautern, Germany

Performance Analysis of Radial Shaft Seals in Non-Stationary Rotational Movements

The number of applications involving rotational non-stationary movements has significantly increased in the past decade. Such dynamic rotational oscillations are often found in applications such as robotic arms. These dynamic rotational oscillations correspond to high levels of acceleration along with frequent changes in the direction of rotation. However, the impact of these oscillations on radial shaft seals (RSS) remains unknown. In practical applications, mineral oil has been found in undesirable situations, and previous studies suggested a potential correlation between these non-stationary movements and the buildup of vacuum in the intermediate cavity (the cavity between the dust lip and the sealing lip of an RSS). Therefore, this study aimed to bridge this knowledge gap by investigating the performance of an RSS operating under dynamic rotational oscillation and verifying the correlation between the vacuum pressure buildup and the occurrence of leakage. To explore various operational scenarios and assess the influence of each parameter variation on sealing performance, a set of experiments was designed. These experiments were conducted using the IWD Test Bench from MEGT. The IWD Test Bench consists of two test cells directly coupled to two servomotors, which can replicate dynamic rotational oscillation. Additionally, a prick device was developed to measure the pressure in the intermediate cavity with the aid of a pressure sensor and a medical needle. The tests were realized by varying the following parameters: (i) the acceleration at the sealing contact; (ii) the angle of oscillation; (iii) the degree of greasing in the intermediate cavity; and (iv) the type of curve performing the oscillation.

The results showed the occurrence of leakage under certain circumstances, specifically with short oscillation angles, and photographs of the sealing contact indicated the occurrence of leakage concomitantly with the region of maximum negative pressure.

A 19

Marco Gohs, Lothar Hörl, Frank Bauer, IMA, Univerität Stuttgart, Dichtungsrechnik, Stuttgart, Germany

Development and Testing of Sleeve-Type Lip Seals with Stamped Back-Pumping Structures

The Back-Structured Shaft Seal (B3S) was developed to achieve an optimal balance between static and dynamic tightness, thermal and chemical resistance, as well as high reliability and durability for PTFE shaft seals. Structures on the back of the sleeve create an active pumping mechanism in the sealing contact. These structures are designed as indentations, locally influencing the stiffness of the sealing lip. During assembly, the circumferential strain causes flat channels in the contact area. The shape of these channels can be influenced by the geometry of the structures in terms of their shape, depth, and angle. When the shaft rotates, the channels create a pumping effect that actively prevents leakage. The hydrodynamic pressure in the sealing contact increases the structuring, ensuring its effectiveness even as the surface wears.

The structures were optimized for laser engraving. Due to modifications, it is now possible to also produce it by stamping. The geometry was therefore optimized to create a high-quality impression of the negative. Tests on initial variants demonstrated a similar effect to that of the laser-structured variant. During stamping, the outcome is influenced by temperature, force and duration. The stamping process caused alterations to both the material properties and surface of the seal. The identified factors were analyzed by simulation and compared to the laser engraved variant. Prototypes with varying stamping parameters were produced and underwent both static and dynamic examination on the test bench. The simulation results were validated based on the measurements of the prototypes.

Simulation and experimental investigation demonstrate that the B3S principle can be implemented in a stamped version. However, the design of the structure must take additional influencing factors into account. The stamped variant's unique features allow for further optimization of the seal. In addition, a more efficient production of the B3S can be achieved.

A- Session 7: Materials and Surfaces

A 20

Lukas Boden, Marius Hofmeister, Faras Brumand-Poor, Katharina Schmitz, Institute for Fluid Power Drives and Systems - RWTH Aachen University, Aachen, Germany

Predicting Compatibility of Sealing Material with Bio-Hybrid Fuels: Development and Comparison of Machine Learning Methods

Bio-hybrid fuels, derived from sustainable raw materials and green energies, offer a promising alternative to conventional fuels made of mineral oil. An advantage of bio-hybrid fuels over other alternative energy sources, such as fuel cells or electrical energy, is the use of existing infrastructure. If bio-hybrid fuels are used as so called “drop-in fuels” in existing combustion engines, a worldwide network of filling stations and petrochemical industry production sites can be used.
Within the cluster of excellence “The Fuel Science Center” at RWTH Aachen bio-hybrid fuels are investigated on a holistic level. Methods are developed to optimize fuel properties, which posts another benefit compared to fossil fuels. One property that is addressed is the compatibility with sealing material. Previous time-consuming experimental investigations revealed that many bio-hybrid fuels show poor material compatibility with conventional elastomer sealing materials (e.g. NBR & FKM) leading to issues such as volume expansion, hardness alteration, or chemical reactions upon immersion. These incompatibilities could result in catastrophic failures during practical applications.
Due to the high number of possible fuels, fuel-mixtures and therefore fuel/seal combinations a solely empirical approach is impractical. Consequently, machine learning methods have been chosen to predict material compatibility. Based on existing experimental data and fluid properties, an analysis of correlation is conducted to identify significant parameters influencing compatibility. Subsequently, machine learning methods suitable for this approach are selected and applied. Their results are compared and discussed critically with particular attention to the limited amount of experimental data. This method aims to assist experimental investigation by previously reducing the number of fuel/seal combinations, thereby minimizing experimental expenses.

A 21

Joachim Möschel, Konzelmann GmbH, Löchgau, Germany

Poetry and truth, how does the hydrolysis-resistant structure come into the polyurethane?

New, soft, chemical-resistant TPU for pneumatics with proportionate biogenic raw material content: Elastic sealing materials contribute significantly to the function, energy efficiency and service life of pneumatic cylinders and valves. These should be correspondingly soft, i.e. in particular smaller than 90 Shore A. Traditionally, thermoplastic polyurethanes compete with soft rubber materials, especially when it comes to meeting high-quality chemical requirements within this genre. Also to enable the important sliding properties required for energy efficiency. Rubber materials have so far been the first choice when it comes to higher temperature requirements and chemical resistance. The TPU grades available on the market are considered to be particularly susceptible to hydrolysis. Konzelmann GmbH has recently started to represent TPU materials that are tailored to pneumatic requirements. In addition to the high-quality physical property profiles, their special properties are primarily in the area of chemical resistance. These new materials are suitable for various types of pneumatic applications and can be flexibly adjusted in terms of Shore hardness. In addition to their exceptional chemical stability, these TPU materials were also certified to have outstanding cold properties. In this lecture, the targeted innovations in the TPU structure in contrast to commercially available TPU will be described and differentiated, thereby providing an explanation for this progress. The TPU grades available on the market are considered to be particularly susceptible to hydrolysis. Konzelmann GmbH has recently started to represent TPU materials that are tailored to pneumatic requirements. In addition to the high-quality physical property profiles, their special properties are primarily in the area of chemical resistance.

These new materials are suitable for various types of pneumatic applications and can be flexibly adjusted in terms of Shore hardness. In addition to their exceptional chemical stability, these TPU materials were also certified to have outstanding cold properties. In this lecture, the targeted innovations in the TPU structure in contrast to commercially available TPU will be described and differentiated, thereby providing an explanation for this progress.

A 22

Christian Wilbs, Matthias Adler, Daniel Frölich, Alisa Bellon, Nicole Schuster, Jasmin Menzel, Emely Bopp, Freudenberg FST GmbH, Mannheim, Germany

Micro-mechanical characterization of a tribological stressed elastomer surfaces with respect to Radial-Shaft-Seals

Polymers play an important role as sealing materials in refrigeration systems and heat pumps. Knowledge about the interaction of these materials with refrigerants is therefore of interest. Consequently, the compatibility testing of sealing materials is already a topic in standards for refrigeration systems and heat pumps such as ISO 14903 and ISO 21922.

The test method described in these standards covers aging in liquid refrigerant. The post-exposure test procedure includes a test in "wet" and "dry" condition. The wet state is defined as testing within 30 minutes of removal from the test chamber, while the dry condition means that the samples are degassed until the mass is constant.

As part of a project to investigate the in-situ swelling behaviour of elastomers, the performance of the materials in liquid refrigerants was investigated. The tests were carried out in a sight glass autoclave equipped with a high-resolution camera system.

In parallel to the in-situ investigations, standard aging tests were carried out in stainless steel pressure vessels. The investigation focused on how the materials behaved during and after depressurisation in the autoclave.

The data clearly indicate that "after removal from the test chamber" is not a defined state and is insufficient to ensure comparable measurements.

The time interval between depressurization and measurements, rather than the time after sample removal, is critical as the most important changes in volume and other properties occur within the first 15 minutes after the onset of depressurization.

To ensure that the compatibility tests are comparable, it is proposed to replace the wording "after removal from the test chamber" with "after the onset of depressurization". In addition, the speed of the pressure drop must be defined, as decompression phenomena can significantly change the measured values.

B- Session 2: Materials and Surfaces

B 01

Hiroyoshi Tanaka, Ayako Aoyagi, Hikaru Hashimoto, Yoshinori Sawae, Joichi Sugimura, Kyushu University, Mechanical Engineering, Fukuoka, Japan

Friction and wear properties of several rubber materials for high pressure O-ring

Friction and wear characteristics of rubber materials were investigated to look for the suitable candidates for O-ring using in hydrogen energy system for renewable energy society. In this study, reciprocating sliding test of rubbers were conducted under hydrogen environment. To understand the sealing performance and durability of rubber O-rings, friction and wear characteristics of hemispherical rubber specimens sliding against stainless steel disk were evaluated

Several rubber materials including silicone rubber, EPDM rubber, fluorinated rubber and natural rubber-based materials were selected to identify the best fit for the hydrogen facility. Each rubber material exhibited unique friction and wear performance depending on its nature (mechanical properties, chemical composition, type of filler), environment gases and operating conditions. A silicone rubber demonstrated that low wear and high and stable coefficient of friction in hydrogen. A fluorinated rubber with carbon black filler showed low coefficient of friction in hydrogen. In order to understand the wear process of each rubber, topography measurement and surface analysis were conducted after the sliding test.

B 02

Margrit Junk, Joachim Germanus, Institut für Luft- und Kältetechnik gemeinnützige Gesellschaft mbH, Applied Materials Engineering, Dresden, Germany

Testing elastomeric materials in liquified gases

Polymers play an important role as sealing materials in refrigeration systems and heat pumps. Knowledge about the interaction of these materials with refrigerants is therefore of interest. Consequently, the compatibility testing of sealing materials is already a topic in standards for refrigeration systems and heat pumps such as ISO 14903 and ISO 21922.
The test method described in these standards covers aging in liquid refrigerant. The post-exposure test procedure includes a test in “wet” and “dry” condition. The wet state is defined as testing within 30 minutes of removal from the test chamber, while the dry condition means that the samples are degassed until the mass is constant.
As part of a project to investigate the in-situ swelling behaviour of elastomers, the performance of the materials in liquid refrigerants was investigated. The tests were carried out in a sight glass autoclave equipped with a high-resolution camera system.
In parallel to the in-situ investigations, standard aging tests were carried out in stainless steel pressure vessels. The investigation focused on how the materials behaved during and after depressurisation in the autoclave. The data clearly indicate that "after removal from the test chamber" is not a defined state and is insufficient to ensure comparable measurements.
The time interval between depressurization and measurements, rather than the time after sample removal, is critical as the most important changes in volume and other properties occur within the first 15 minutes after the onset of depressurization.
To ensure that the compatibility tests are comparable, it is proposed to replace the wording "after removal from the test chamber" with "after the onset of depressurization". In addition, the speed of the pressure drop must be defined, as decompression phenomena can significantly change the measured values.

B 03

Cem Tanyeri, Mine Unlu, Baris Caylak, Alper Kocamaz, Ozan Devlen, Kastas Sealing Technologies Research and Development, Izmir, Turkey

Enhancing sealing element security: Quantum dot marking Solutions of NBR and TPU sealing elements

In response to the escalating need for integrated product security amidst the rising challenge of counterfeiting, luminescent labels have emerged as crucial tools for safeguarding original products. Leveraging nanoparticles for marking activities not only enhances product safety but also mitigates operational costs while bolstering traceability and sustainability. This study focuses on integrating quantum dot (QD) marking solutions into NBR and TPU, widely utilized in sealing elements crucial for hydraulic and pneumatic systems.
Initially, the research delves into the optical properties of elastomer materials infused with various types of QDs. Mechanical property alterations and optical readings of marked elastomers post-abrasion and aging with different media are examined in the initial phase. Subsequently, the study elucidates the benefits of incorporating QD markers into elastomers, emphasizing traceability, product safety, and sustainability.
Employing specially designed sensors and embedded smart algorithms, quantum tags crafted from the optical properties of nanoparticles facilitate optical reading, conversion of readings into electronic signals, and signal processing for sample qualification and/or verification. Product verification entails comparing obtained signals with reference data, thereby ensuring authenticity.
By showcasing the efficacy of QD marking solutions on elastomers, this research underscores the potential for bolstering sealing element security, offering a promising avenue for combatting counterfeiting and enhancing product integrity in critical industrial systems

B- Session 3: Additive Manufacturing

B 04

Thomas Ebel, Kathrin Ottink, Hochschule Emden-Leer, Faculty of Technology Mechanical Engineering, Emden, Germany

Functional testing of additively manufactured hydraulic rod seals

Hydraulic rod seals are crucial machine elements in a lot of applications. Malfunction of rod seals can cause huge economic loss by long shutdown times for repair. Especially if equipment is used in remote areas in the nature, malfunction can also cause severe environmental damage by spilled polluting hydraulic fluid. The delivery time of dynamic rod seals for hydraulic applications can last weeks or even months as these seals are often manufactured on demand. In addition, the last years have shown that also geopolitical incidences like a war or a pandemic can have a huge impact on international channels of trade.
In order to avoid, or at least minimize, machine shutdown times, it seems to be desirable to have local production solutions for rod seals by using easy to handle machinery and a single, simple raw material. A possible solution to circumvent delivery challenges can be the use of an additive manufacturing (AM) method. The research question addressed in the presented study is whether it is possible to produce functional rod seals using simple AM methods.
The results of the method screening and the preliminary investigations were presented at the 21st International Sealing Conference in Stuttgart in 2022. One of the results was the choice of Fused Filament Fabrication (FFF) as the additive manufacturing method for the study and thermoplastic polyurethane (TPU) as the material class to be used. Our latest results, the outcomes of two

series of functional tests conducted with these different filaments, will be the core of the presentation that we plan to give at this year's conference.

Parts that are produced by using the Fused Filament Fabrication method are never fully dense due to the process. Nevertheless, the functional tests conducted on a rod seal test rig showed that the research question can be answered in an affirmative way for tested pressures up to 15 MPa. Even in a long-term test the function of the additively manufactured seals met the demands.

B 05

Jacqueline Gerhard, Lothar Hörl, Frank Bauer, University of Stuttgart, Institute of Machine Components Sealing Technology, Stuttgart, Germany

Additive Manufacturing of Sealing rings: Material Selection and Application Development

The use of additive manufacturing, particularly 3D printing, for the production of sealing rings is a promising way to speed up the development cycle of new products. Complex geometries that were previously impossible or difficult to produce could now be realized. In addition, this technology allows for the rapid exploration and implementation of geometric variations in sealing profiles, enabling rapid optimization for individual applications.

However, this manufacturing process presents new challenges. In order to guarantee the required sealing function, the sealing material must meet specific requirements. These requirements cannot yet be fully met by 3D printable materials, which is why the use and success of additive manufactured seals is still limited. In addition, there are a number of geometric requirements that have to be considered when printing sealing rings.

In this study, a comprehensive analysis is performed focusing on the evaluation of various material properties to identify the most suitable materials for effective sealing functionality. Therefore, several elastic 3D printable materials and their printing settings were analyzed for material properties such as compression set, elongation at break, wear rate and chemical resistance. A liquid crystal display printer was used for all tests. Materials that showed optimal performance in these analyses were further tested for their printability. The geometric accuracy and reproducibility of the printed seals were analyzed and the printing parameters were optimized in order to print an optimum seal geometry.

Based on the material property studies, the most suitable materials were selected. The first prototypes of additive manufactured rod seals were tested on a test bench and compared to commercially available rod seals. In this way, the functionality of the printed seals and their materials was tested under real conditions and their performance validated.

B 07

Alper Kocamaz, Ozan Devlen, Cem Tanyeri, Barthel Engendahl, Kastas Sealing Technologies, Research and Development, Izmir, Turkey

Innovation in Seal Production: Novel Additive Manufacturing for High-Performance PU Seals

Our study unveils a groundbreaking additive manufacturing (AM) technology poised to redefine the standards of polyurethane seal production. By meticulously merging the precision of AM with the robustness of injection-molded TPU, this technology not only promises to bridge existing manufacturing gaps but also to set new benchmarks for seal performance and durability.

Our rigorous evaluation underscores the technology's superior design flexibility, enabling the creation of custom, high-performance seals that surpass traditional capabilities in both efficiency and environmental sustainability. The results of our comprehensive testing and validation process reveal a significant leap forward, offering not just an alternative, but a superior solution in seal manufacturing. We propose this AM technology as a transformative force, capable of revolutionizing industry standards and paving the way for innovative applications across sectors. This is not just an advancement; it's a call to reimagine what's possible in seal manufacturing.

B- Session 4: Test procedures

B 08

Adrian Heinl, Christian Wilbs, Daniel Frölich, Matthias Adler, Freudenberg FST GmbH, Weinheim, Germany

Performance of the radial shaft sealing system under the influence of shaft lead

The performance of a radial shaft sealing system depends primarily on the main components radial shaft seal (RSS), shaft surface and lubricant and how they interact with each other. The dynamic sealing mechanism of the seal depends on many influencing factors, one of which is the shaft surface topography. Therefore, the shaft surface roughness parameters must be in an acceptable range. Now, different parameters or machining processes of the shaft can generate the same surface roughness but totally different surface topographies. To ensure the performance of the sealing system, in addition to the known roughness parameters, the shaft must be free of fluid-pumping structures. Those structures are known in the sealing technology community as shaft lead. Depending on the shaft lead characteristics, the lead can create an axial pumping effect of the fluid which disturbs the sealing mechanism. The latter expresses itself either in the form of direct leakage or poor lubrication conditions and therefore to an increased wear of the sealing edge. Different lead structures can be measured and quantified with state-of-the-art measuring and analyzing methods. Using these methods, the correlation between lead parameters and leakage resp. seal wear can be shown. The insights drawn, will be applied to unpressurized and pressurized radial shaft sealing systems. Based on those results, acceptable limits for shaft lead can be set to ensure a reliable sealing system.

B 09

Maximilian Engelfried, Matthias Baumann, Frank Bauer, University of Stuttgart, Institute of Machine Components Sealing Technology, Stuttgart, Germany

From Tactile to Optical - Advancements in Shaft Lead Analysis

Tactile measuring instruments were used for a long time to measure surface characteristics of sealing counterfaces and are still state of the art today throughout the industry. The data measured are roughness profiles in the axial direction of the shaft. Rapid developments in computer hardware and software have improved optical measurement technology, advancing its application in the analysis of sealing counterfaces. The measurement data are topographies that represent partial areas of the shaft with high resolution in both the axis and circumferential direction. These characteristics are especially useful for the analysis of shaft lead.
Lead describes all types of structural features on the shaft surface that axially pump oil in sealing contact during operation. Their pumping effect influences the sealing mechanism depending on the direction of rotation of the shaft and can result in leakage.
Lead structures appear in various forms and sizes – micro and macro lead, which are superimposed on the shaft surface. Optical measurements enable the detection of the superimposed structures with a single measurement run. Specially developed segmentation algorithms can be used to sperate micro and macro lead and then identify flow channel-like structures as individual elements in surface topographies. The statistical analysis of the segmentation results offers an objective characterization of the sealing counterface.
This article presents the benefits of utilizing optical measurement techniques in conjunction with innovative structure-based analysis approaches for lead on shaft counterfaces. The outcome can improve the reliability of sealing systems and associated products.

B 10

Georg Haffner, Matthias Baumann, Frank Bauer, University of Stuttgart, Institute of Machine Components Sealing Technology, Stuttgart, Germany

Insights into the pumping behavior of sealing counterfaces using continuous logging

Surface structures of the sealing counterface are called “lead structures” when they have the capability to pump oil rotation dependent through the sealing contact of a rotary shaft seal systems. This feature is called “pumping effect”. The structures interrupt the equilibrium state of the sealing system, which may lead to dry run or leakage as failure result. Especially for higher circumferential velocities the pumping effect increases and therefore cannot be neglected.
To assess the influence of lead structures on the sealing system, one can measure the pumping rate of the sealing counterface experimentally. The higher the pumping rate of a sealing counterface, the more likely the sealing system will fail. In this paper, the development a new pumping rate evaluation method with the help of a continuously measuring scale, which allows to visualize the course of the pumping rate over time, is described. With this knowledge it is possible to determine the end of the running-in phase of the sealing ring and to determine the minimum duration of the pumping rate tests. The pumping rate evaluation method is demonstrated with different shaft counterfaces to validate the stability of the new method.

B 11

Takao Horiuchi, Yohei Sakai, Ayako Aoyagi, NOK corporation, Engineering Research , Fujisawa-shi, Japan

In Situ Observation of a Grease Lubricant Film on a Radial Seal by Fluorescence Induced Microscopy

Industrial robots are operated by servomotors and reduction gears in their joints. Grease lubrication of the reduction gears is important for the delicate movements of the robot, and radial lip seals prevent lubrication leakage. Their operational behavior and sealing mechanism were examined by various authors and therefore is comparatively well understood [1]. Y. Sato observed the lubrication film on the radial lip seal in oil using LIF. However, the lubrication film on the radial lip seal in grease has not been observed [2]. It has been known that microscopic infrared spectroscopy and fluorescence induced microscopy are effective in observing grease behavior in situ. These methods were used due to their special feasibility of observing film thickness and thickener separately [3,4]. Previous verification results suggest that thickener particles are present in the sealing gap and are influencing the performance of the sealing system [5].

In this study, the sliding surfaces of radial lip seals in grease lubrication were observed using a fluorescence induced microscope to verify the grease lubrication and sealing condition. A glass shaft was used to observe the lubrication film on the radial lip seal and the sliding surface was observed from the shaft side. Lithium soap grease was used as the lubricant. Two dyes were used in this grease to observe film thickness and thickener separately. We observed changes in oil film thickness and amount of thickener on the sliding surfaces and discussed the seal lubrication mechanism of the grease in radial lip seals.

[1]E.T.Jagger, Proceedings of the Institution of Mechanical Engineers, Vol171, Issue1, 597-616, 5.1957
[2] S.Yuki (2001) , Kyushu University
[3] Y. Hoshi et al., J. Japanese Soc. Tribol. (Toraiborojisuto), 4, 15, 201, 2020
[4] D. Kostal et al., Faculty of Mechanical Engineering, Brno University of Technology, 17, 8, 2022
[5] Sommer M. et al., Tribology International, 103, 574-583, 2016

B- Session 5: Applications in practice

B 12

Serhii Shevchenko, G.E. Pukhov Institute for Modelling in Energy Engineering, Kyiv, Ukraine

Study of the non-contact seals influence on the centrifugal machine’s dynamic characteristics

Higher parameters of centrifugal machines are constantly required, such as the pressure of the medium to be sealed and the speed of rotation of the shaft. However, as the parameters increase, it becomes more and more difficult to ensure the effectiveness of sealing. Non-contact seals, in addition to sealing, perform an equally important function – to improve the vibration state of the centrifugal machine. Design measures aimed at increasing the hydraulic resistance of seals, as a rule, increase their hydrostatic stiffness and damping and thus improve their dynamic qualities. Non-contact seals are considered as hydrostatic-dynamic bearings that can effectively dampen rotor oscillations, and as automatic control systems. Models of systems "rotor-gap seals", impulse seals, "rotor-hydraulic face" and seals-supports of a shaftless pump have been studied to assess the effect of seal systems on the

oscillatory characteristics of the rotor. Analytical dependencies are obtained for calculating the dynamic characteristics and stability limits of seals as hydromechanical systems.
The directions for improving the safety of operation of critical pumping equipment due to a targeted increase in the rigidity of non-contact seals are determined, which leads to an increase in the vibration resistance of the centrifugal machine's rotor.

A general algorithm for constructing the dynamic characteristics of non-contact seals due to their hydrodynamic properties created and the directions for purposefully changing the parameters of sealing units to improve vibration characteristics determined. Expressions are obtained for calculating the amplitude and phase frequency characteristics, as well as for assessing the dynamic stability of various sealing units. The proposed general technique makes it possible to purposefully select the design parameters of seals to adjust sealing systems to work in vibration-safe modes

B 13

Thomas White, Aalto-korkeäkoulusäätiö Department of Mechanical Engineering, Helsinki, Finland

Thermal Behaviour of Marine Lip Seals – A Pathway Towards Condition Monitoring

Marine lip seals are commonly used in a variety of marine propulsion systems. Predicting marine lip seal behaviour, however, is difficult: the harsh conditions in which the seals operate greatly increase the likelihood of malfunction, increased wear and/or failure. Moreover, published literature pertaining to the matter is exceedingly scarce. Condition monitoring provides a pathway to addressing the main shortcomings associated with the use of marine lip seals, such operational oil spillage and costly unscheduled maintenance. This paper examines the behaviour of marine thruster lip seals in a full-scale, fully flooded environment with a view to developing the basic requirements of a condition monitoring system. Lip contact temperature was identified as a suitable variable to characterise the condition of the seal. A custom test device was built to measure the sub-surface contact temperature of a commercial thruster seal package operating fully submerged. The seal package consisted of three seals of 300 mm nominal diameter. A typical tungsten carbide coated stainless steel shaft liner was used as the counterface.
The liner was drilled to accommodate thermocouples situated 0.5 mm below its surface, thus facilitating the sub-surface measurement of lip seal contact temperature. The contact temperature was measured at five points across each seal. A sub-gigahertz frequency was used to reduce attenuation when transmitting measurements through the test device. Seals were tested under conditions that simulated normal running and conditions that precipitated seal failure. The shaft rotational speed was used as the only strictly controlled experimental parameter. Shaft speed, water, bulk oil, and lubricating oil temperatures were measured. Pressure differentials across each seal were assigned, set, and measured. Results validated the viability of the proposed concept and highlighted the interdependent nature of seal behaviour in a package configuration.

B 14

Omar Morad, Vesa Saikko, Raine Viitala, Aalto University Mechanical Engineering, Espoo, Finland

Frictional behavior of marine lip seals: Sensitivity to operational parameters

Marine lip seals are a topic seldom studied in published literature compared with other types of lip seals. Marine lip seals are unique in their harder material compound and larger diameters, in addition to higher operational oil pressures. This paper explores the behavior of marine thruster lip seals with a nominal diameter of 300 mm under normal operating conditions. The counterface is a stainless-steel shaft liner coated with tungsten carbide. The lip seals and counterfaces studied are commonly used in marine applications. A test device was designed and constructed to study the effects of different parameters on the behavior of lip seals, namely the oil temperature, oil pressure, and rotational speed. For each parameter, three values were selected, which totaled 27 parameter combinations per seal, and the sample size was 3. The behavior was characterized by measuring the frictional torque and the subsurface temperature at a given test point for one hour.

The measurements for each seal were taken after an initial running in period of at least 100 hours. Air bearings were used to support the seal housing, to allow for a more accurate measurement of the frictional torque. The subsurface temperature was measured 0.5 mm beneath the contact using a wireless temperature probe embedded in the liner. The contact pressure was measured before the start of test sequence and after its completion. The results showed that the speed had the most significant effect on the subsurface temperature, which increased with increasing speed. The oil pressure had the most significant effect on the frictional torque, which increased with increasing pressure. Increasing oil temperature resulted in lower frictional torque and higher subsurface temperature. The peak contact pressure was higher for new seals compared with used seals. This paper demonstrates the sensitivity of the lip seal frictional behavior to the operational parameters.

B 15

Joseph Kaleshian, Ray Clark, Henri Azibert, Michael Grimanis, A.W. Chesterton Company Innovation Engineering, Groveland, United States

A method of direct thermal conditioning of mechanical seal faces: CFD, empirical analysis and testing

Existing API flush plans provide indirect cooling conditions for mechanical seals not only to enhance the durability of the seal but also contribute to the overall efficiency and performance of the machinery. This concept thermally conditions the mechanical seal faces by circulating cooling or heating fluid directly through a process isolated flow channel formed by a specially designed stationary seal ring and a modified seal gland. Test results under both wet and dry running conditions at low rates of coolant flow exhibited significant performance improvement. An exponential increase in dry running PV limit was experienced throughout extensive testing.

In addition, significantly lower wear measurements were consistently recorded. Results obtained from CFD modeling agreed well with both wet (water) and dry (nitrogen gas) process fluid data. An optimized direct thermal conditioning design of the stationary seal ring can be a key factor to:

- Eliminate the need to maintain circulating fluid pressure above that of the process.
- Increase sustainability with reduced environmental leakage.
- ncrease efficiency in thermal conditioning of the seal, thereby reducing energy requirements.
- Avoid compatibility requirement between the circulating and process fluids.
- Reduce life cycle operating costs.

B- Session 6 : Reciprocating Seals

B 16

Gonzalo A. Barillas, Andreas Gropp, Freudenberg Sealing Technologies GmbH, Schwalmstadt, Germany

Further Observations in Wiper design and Particle Transport Simulation in the Sealing Gap

In the last ISC results with several wiper designs with regards to dirt insert rate into a sealing system was presented. Also, the simulation of the motion of such particles in the sealing gap was shown. Material wear resistance and fluid streamlines before the lip seems to have an influence on particle's ability to pass the gap between seal and rod.

In this paper, starting from a standard wiper, lip design alterations were tested. By changing the wiper's lip design a change in the flow lines of the fluid and therefore the particle insert rate was intended. Among the lip design changes furthermore the improvement in simulation of particle flow in the wiper-rod interaction area is presented. The effects of the lip variation on the particle insert test results will be discussed and compared with simulation results.

B 17

Faras Brumand-Poor, Florian Barlog, Nils Plückhahn, Matteo Thebelt, Katharina Schmitz, RWTH Aachen University, Institute for Fluid Power Drives and Systems (ifas) Faculty of Mechanical Engineering, Aachen, Germany

Advancing Lubrication Calculation: A Physics-Informed Neural Network Framework for Transient Effects and Cavitation Phenomena in Reciprocating Seals

In numerous technical applications, gaining insights into the behavior of tribological systems is crucial for optimizing efficiency and prolonging operational lifespans. Experimental investigations of such systems require considerable costs and time investments, particularly in the field of sealing, notably reciprocating seals for fluid power systems. A more feasible method is the application of elastohydrodynamic lubrication (EHL) simulation models, such as the dynamic description of sealings (DDS) model, which compute friction of seals by the hydrodynamics within the sealing contact according to the Reynolds equation, the seal's deformation, and the contact mechanics. The main drawback of these distributed parameter simulations is the necessity of a time-intensive resolution process. Given these experimental and computational constraints, machine learning algorithms offer a promising solution.

Physics-informed machine learning (PIML) represents a noteworthy advancement in machine learning in tribology, extending traditional models with physics-based rules and enhancing accuracy in determining phenomena such as friction, wear, and lubrication. Within this field, physics-informed neural networks (PINN) emerge as a powerful class of hybrid solvers, combining data-driven and physics-based approaches to solve partial differential equations, the governing equations in EHL simulations. By integrating physical principles into the neural network's parameter optimization, PINNs provide an accurate and accelerated solution.

In this contribution, a PINN framework is applied to predict pressure build-up and cavitation in sealing contacts with housing. The capability of PINNs to determine transient and cavitation effects is thoroughly investigated and validated by the solution of the Reynolds equation obtained by the DDS. The results demonstrate the potential of PINNs for modeling tribological systems and highlight their significance in enhancing computational efficiency.

B 19

Anja Dobrinsky, Sebastian Betz, Christoph Schüle, Boris Brodmann, Trelleborg Sealing Solutions R&D, Stuttgart, Germany

Advanced characterization of counter surfaces in linear applications

Counter surfaces are an important aspect for every sealing application and have a direct influence on the sealing performance of the system. Historically, the counter surface is described with multiple roughness parameters based on 2D profile or 3D topography measurements. In addition to the standard parameters, light scattering can be used to describe the counter sur-face. Compared to the common profile roughness parameters, light scattering measures the angle distribution of a profile and is therefore more robust against external influences.

In addition, light scattering measurements are faster at characterizing a complete running surface. In this study, the effect of one rod seal geometry made from PTFE and PU materials on the surface characteristics of the rod is investigated. A deeper understanding of the tribological system is achieved by analyzing for the first time the light scattering roughness parameters of a tested rod surface in addition to the standard profile roughness parameters.

B- Session 7: Static Seals

B 21

Hariolf Kurz, Michael Hübner Hecker, Hochschule Weihenstephan Triesdorf, Agrartechnik, Weidenbach, Germany

Optimized rubber gasket with internal force shunt

With the introduction of TA Luft 2021, plant manufacturers and operators have to carry out flange connection calculations according to DIN EN 1591-1, including gasket parameters DIN EN 13555. This will lead to enhanced plant safety and less emissions, however, this also implies the development of optimized gasket materials and design.

According to the design-rule “for every functionality, implement a specific feature”, a well-known gasket principle is to put the sealing material in force shunt. This way, the load transfer element and the sealing element are in separate locations, leading to the possibility to optimize them independently. This works already very well for O-Ring seals, spiral-wound gaskets and as well, rubber gaskets with an external force shunt. Due to high manufacturing cost and high mounting effort, these solutions are not widespread in use in the field.

A solution to the discussed aspects is the design of a rubber gasket with an internal force shunt. The design implements a spiral wound metal-wire with indentations. It lies inside the rubber material and thus is enclosed, held by the rubber and is easily and efficiently to produce

The design leads to a unique sealing performance with a very high tightness (L < 10-3 mg/(sm)) even at very low gasket pressures below 2,5 MPa, no creep relaxation (PQR > 0.99) and very high load bearing capacity (Qmax > 150 MPa). This enables plant manufacturers and operators to effortlessly

- meet the tightness-requirements according to TA-Luft
- successfully carry out flange connection calculations for almost any flange type
- find suitable mounting torques for the mounting process
- minimize leakage due to mounting errors
- choose the right gasket material (according to temperature and medium specs)
- generally enhance plant safety
- and reduce overall in-situ emissions of the plant

B 22

Finn Bartmann, Alexander Riedl, Elmar Moritzer, FH Münster / University Paderborn
Center of Sealing Technologies, Steinfurt, Germany

Development of an analytical calculation method for the design of thermoplastic flange systems

In the course of environmental protection and the amendment of TA Luft, emissions from flange connections must be reduced (to L0.01). The design and calculation of steel flanges is easy to handle with the help of EN 1591-1 and EN 13555. However, these standards are not suitable in their current form for thermoplastic sealing joints, such as those used in natural gas supply. For this reason, lengthy and cost-intensive tests must currently be carried out to verify tightness and strength.

The aim of a doctoral project is to develop a time-efficient and cost-effective analytical calculation method based on the existing standards. For this purpose, the energy-elastic material parameters of the steel must be replaced by elastoplastic material parameters of the thermoplastics and the calculation algorithm adapted accordingly. The problem is to be investigated with the aid of numerical structural simulations (FEM) and experimental tests.

Group I
Session 1

Plenary Talks I

I 02

Stephen Bond, The Flexitallic Group Research and Development, Houston, United States

Static Seals for Sealing Hydrogen: A Review

Static Seals for Sealing Hydrogen: A Review

Stephen Bond, Ph.D., FRSC.

Hydrogen has a potentially large role in the future of energy, either as a fuel, as an energy storage vehicle, or both. Based on the amount of research work and government funding in this area, such as the US Government's pledge of $7 billion for hydrogen hubs, it would be a good assumption that the role of hydrogen is set to grow for the foreseeable future. This is especially the case for so called green hydrogen, where hydrogen is produced by the electrolysis of water and the electricity used in the electrolysis is from a renewable energy source (e.g., wind, solar).

Due to its inherent properties, there has been some concern about the potential for leakage of hydrogen in this new process industry. This, of course, brings into focus the sealing of static bolted connections, i.e., bolted flange joints. The most common leakage tests for bolted flange connections use either helium (EN13555), methane (ASME B16.20) or nitrogen (DIN 3535), but not hydrogen. There are good reasons for choosing these gasses, particularly helium, which is safe and a small molecule which can be detected and measured by standard equipment such as a mass spectrometer.

Other literature has shown that leak rate of different gases cannot be judged and predicted by molecule size alone, therefore the conversion of leak rate using a standard test and test gas cannot be easily converted to a leak rate of hydrogen. Therefore, testing of gaskets with hydrogen has been required to make engineering decisions.

This paper will review recent public domain papers on sealing tests using hydrogen, especially those comparing hydrogen sealing rates to helium sealing rates. This paper will also include some recent hydrogen sealing testing commissioned at a third party test house using spiral wound gaskets with different fillers.

1 Introduction

Hydrogen is well placed to be a key part of any transition towards a cleaner and more sustainable energy economy. Decarbonization of processes such as electricity generation, steel making, and other industrial processes will likely utilize hydrogen as a key part of the process.

It would not be a valuable use of time to spend a large part of this paper discussing the place of hydrogen in upcoming energy transition when there are multiple conferences and publications in this field which cover this subject in more detail. Examples would be publications and events organized by the Fuel Cell and Hydrogen Energy Association [1] and Hydrogen Europe [2].

The chemical element hydrogen is part of many everyday chemicals and materials, including fossil fuels and polymers. Therefore, there is already an established global industry that uses hydrogen or chemicals containing hydrogen. One of the most common, as will be discussed below, is the petrochemical industry. This industry contributes significantly to the more than 100 Mt/y of hydrogen produced today, often by steam methane reforming. While this industry is established, it will likely have to move beyond its current grey hydrogen production and into blue and even to green hydrogen (see Figure 1 below).

While the science of the matter is still evolving, it currently appears that hydrogen is an indirect greenhouse gas [3]. This means that it indirectly contributes to global warming by impacting chain reactions in the troposphere and stratosphere [3]. In fact, one recent report has shown that hydrogen has a Global Warming Potential (GWP) over 100 years of at least eleven times that of carbon dioxide. By way of comparison the GWP of methane is >80 times that of carbon dioxide [4].

Therefore, as hydrogen use becomes more common in decarbonization, the control of fugitive emissions of hydrogen will become more important, including controlling flange leaks.

A common concern with the use of hydrogen is the safety issues surrounding its use. While appropriate safety precautions must be taken, hydrogen is arguably no more or less difficult to use than other flammable gases [5]. However, as the gas is flammable, the fugitive emissions can also present a risk.

Table 1: Comparison of flammability limit and explosive limit properties

	Flammability Limits in Air (vol %)	Explosion Limits in air (vol %)
Hydrogen (H_2)	4.0 - 74.0	18.8 - 59.0
Methane (CH_4)	5.3 - 15.0	5.7 - 14.0

Clearly from a test laboratory perspective, helium is a more preferred test media than hydrogen. There are a few reasons for this, including helium being inert and non-flammable and easily detected using a mass spectrometer. Typically, few modifications are needed to any test laboratory in order to use helium. In contrast, testing with hydrogen or methane would require significant safety related modifications to a test environment.

2 Materials and Methods

There are a number of test methods currently used in the industry, and a number of different gasket types that can be used to seal hydrogen, based on application conditions. These will be introduced below.

2.1 Colours of Hydrogen

In the simplest explanation, hydrogen is a colorless, odorless, tasteless, non-poisonous, and non-toxic gas. Therefore, the use of colors when describing hydrogen a potential source of confusion.

	Colour	Fuel	Process	Products
	Brown/Black	Coal	Steam reforming or gasification	$H_2 + CO_2$ (released)
	White	N/A	Naturally occurring	H_2
	Grey	Natural Gas	Steam reforming	$H_2 + CO_2$ (released)
	Blue	Natural Gas	Steam reforming	$H_2 + CO_2$ (% captured and stored)
	Turquoise	Natural Gas	Pyrolysis	$H_2 + C$ (solid)
	Red	Nuclear Power	Catalytic splitting	$H_2 + O_2$
	Purple/Pink	Nuclear Power	Electrolysis	$H_2 + O_2$
	Yellow	Solar Power	Electrolysis	$H_2 + O_2$
	Green	Renewable Electricity	Electrolysis	$H_2 + O_2$

Figure 1: Illustration of the colours of hydrogen and the processes involved [6]

From a chemist's perspective and assuming equal purity, one color of hydrogen is exactly the same as another. In Sealing Technology terms, one color of hydrogen should not be more difficult to seal than another.

The colour designation is often used to indicate the method of its production. What is more important to the sealing requirements, are the process conditions, which obviously differ depending on the colour and process. For example, grey hydrogen can be produced at >400°C and relatively high pressures, whereas green hydrogen from a Polymer Electrolyte Membrane (PEM) stack or alkaline stack will be produced at <100°C, at near ambient pressure.

Grey hydrogen is by far the most common in the world today and has been for many decades. Grey hydrogen accounts for >95% of the hydrogen manufactured today and is by definition made from fossil fuels, specifically natural gas, most typically inside a refinery using steam methane reforming. One refinery will have multiple steam methane reformers and the grey hydrogen will either be consumed within the refinery or collected as a feedstock for a process elsewhere.

Blue hydrogen is essentially grey hydrogen where the carbon consumed and/or produced in manufacturing is captured and prevented from being emitted to the atmosphere. Most commonly, this is through carbon capture and storage (CCS). This would commonly be achieved in brownfield sites by adding a sequestering unit to existing equipment.

Green hydrogen is hydrogen that is (typically) manufactured by the electrolysis of water into its constituent elements (hydrogen and oxygen) using renewable energy such as wind or solar. Electrolyzer stacks are being developed that are based on multiple evolving technologies, including PEM, Alkaline and Solid Oxide (SOEC).

Stacks fall into generally two types, higher temperature (500-900°C) technologies such as SOEC and occasionally Molten Carbonate Cells (MCEC) and lower/moderate temperature (75-200°C) technologies such as PEM and Alkaline.

2.2 Gasket Types

There are several situations where hydrogen can be used and therefore would need to be sealed. Examples include its manufacture by possibly steam methane reforming or electrolysis, subsequent compression, liquefaction, or storage. This means logically that a wide range of static seal (gasket) types would be used to seal hydrogen, but exactly which type of gasket would depend on the exact application conditions, particularly the temperature and pressure.

Steam methane reforming systems have been sealed by standard semi-metallic gaskets for decades. Typically, a Spiral Wound Gasket (SWG) with austenitic stainless steel winding wire and a graphite filler can be used successfully (figure 2).

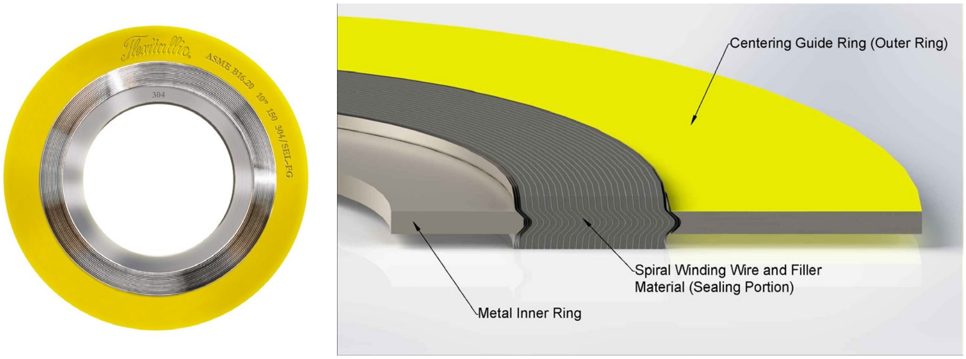

Figure 2: Illustration of a Spiral Wound Gasket. Front view (left) and cross section (right)

SWGs can be manufactured with a variety of conformable filler materials. Exfoliated graphite (also known as Flexible Graphite) is the most common filler for SWGs. However, other filler materials are used in other applications where there are different operating conditions, and these different operating conditions may be encountered in different parts of the Hydrogen industry. Some new sealing data will be presented below in Section 4.

An illustration of a Kammprofile gasket, discussed in section 3.5 below is shown in figure 3.

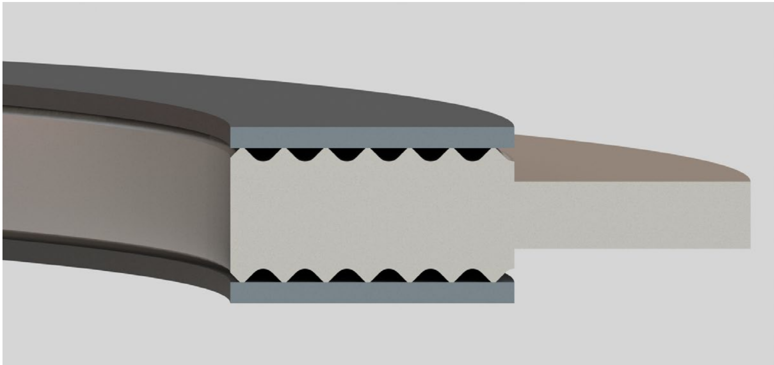

Figure 3: A cross section iillustration of a Kammprofile gasket, with a serrated metal core and outer ring, plus a soft sealing material as a facing

In electrolysis for green hydrogen using PEM or Alkaline stacks, the temperature is relatively moderate, therefore high-quality rubber and PTFE gaskets can be used. For sealing SOEC systems, which operate at temperatures between 500 and 900°C, a key issue can be the low stress available to seal due to both the temperature and the nature of the ceramic components used. This can lead to some challenging sealing situations. In SOEC systems, typical seals are either glass or vermiculite based.

2.3 Testing Methods

The most common leakage tests for gaskets in bolted flange assemblies include CEN EN13555 [7], which uses helium as the test gas, ASME B16.20 [8] (methane) and DIN3535 [9] (nitrogen). None of these tests mandate the use of hydrogen. It should also be noted that there is little mechanical similarity between these tests, and it is hard to compare results from one test with results from another.

There are good and practical reasons for choosing these gases, particularly helium, which is a safe test gas, it is nonflammable and non-toxic. Furthermore, it is the smallest molecule. It is true that hydrogen is the smallest atom, but hydrogen exists in diatomic form as H_2 which is larger than helium, which exists in the atomic form.

It has been shown from earlier papers [10] that molecule size is not the only factor which effects leakage rates, and the conversion of leakage rate from one gas to another is not universally understood.

However, the type of gas flow that leads to leakage could be laminar flow, molecular flow, or a mixed mode. Therefore, depending on the type of gas flow, the relative rates for different gases can vary and the rates themselves are different for each mode [11]. The experimental investigation of gas flow and leakage is not the purpose of this paper, but it remains an area of industry interest.

2.3.1 EN13555 Testing Methodology

This section is simply a summary of the test methodology, full details are in the standard [7]. The EN13555 sealing test is typically carried out on a Amtec Temes *fl.ai1* test machine, the test is pre-programmed into the software.

In the test, helium leakage is measured at successive gasket stresses which change according to the specification. Typically, the stress is successively raised, and drops back after each new, higher stress, with a 40 bar helium leakage test at each step. Data is presented graphically and in tabular form.

Graphically, leakage vs gasket stress is presented (for example Figure 7 below). The leakage axis is logarithmic, with horizontal lines at each decade. The black dots represent actual leakage tests. The dots are joined sequentially with the course of the test.

The software interpolates the minimum load required to reach a certain sealing class (eg a leak rate of 0.01 mg/m/s, which is designated L 0.01) and this is given in a table and shown as a yellow dot on the graph (figure 7) at each decade of leakage. The table shows data for stress required on assembly to reach a certain leakage class ($Q_{min(L)}$ or loading) and in service ($Q_{smin(L)}$ or unloading).

This $Q_{(min)L}$ term is defined in EN13555 [7] Section 3.2 as the minimum gasket surface pressure, on assembly, required at the ambient temperature in order to seat the gasket into the flange facing roughness and close the internal leakage channels so that the tightness class to the required level (L) for the internal test pressure. The term $Q_{smin(L)}$ is defined as the minimum surface pressure required for leakage rate class L after off loading.

3 Review of Published Data

In recent years several third-party test laboratories have expanded their test capabilities to include leakage testing with hydrogen [12, 13, 14]. Comparisons can only be made from the plots made available in the publications. Sometimes estimations must be made from observing the plots as exact leak rate data may not be noted on the chart (it is not normal for this information to be noted on the chart) and from the $Q_{(min)L}$ table (also typically not shown but always recorded during the test). For data gathered in house, this leak rate data is available, as is the minimum required gasket stress in assembly, $Q_{(min)L}$.

It should be noted that some of this data has previously been reviewed [15], but since the publication of that paper, further data has become available for inclusion.

3.1 Aramid Fibre/Rubber Compressed Sheet gaskets

Aramid fibre and rubber compressed sheets have been known for many years, and their predecessor formulations date back over 120 years. In 2022, Übermesser et al published some data on the sealing of these types of materials using hydrogen and helium [16]. This testing used a flange connection using the principles of

VDI2440/2200 [17]. The authors concluded that at two gasket stresses, using their test conditions, there were no significant differences between the sealing of helium and the sealing of hydrogen.

Berger [18] completed some hydrogen compatibility tests on these types of gaskets and some graphite sheet gaskets and concluded that no notable changes in gasket material properties could be observed with storage in hydrogen. Berger also completed some leakage testing of three grades of sheet material with hydrogen and nitrogen using the principles of DIN 28090-02 [19]. In all cases, the mass leak rate for nitrogen was higher than for hydrogen. Also, the order of performance for the three grades was the same for both gasses, which is still a useful conclusion.

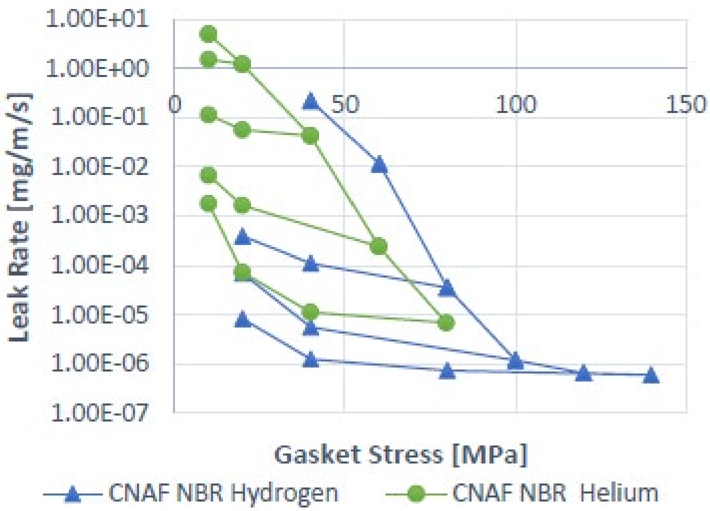

Figure 4: EN13555 sealing plot for Aramid Fiber/Rubber compressed sheet gasket

In a different publication, General and Norman [20] tested an un-named material using EN13555 testing using both hydrogen and helium. Figure 22 in this publication (figure 4 here) shows a direct comparison between leakage tests with these two gasses. Unfortunately, the data for helium is only shown to 80MPa while the data for hydrogen is shown to 160 MPa. While the leakage curves are somewhat similar, the leak rate for hydrogen appears to be consistently lower. This lower leakage rate with hydrogen is probably approximately the difference from the helium data than would be expected from normal experimental variation.

General and Norman also tested some ASME B16.21 sheet materials, specifically a FKM gasket and some ePTFE (discussed in section 3.3 below). Unfortunately, no reference was made to their source or physical properties.

In order to compare the hydrogen sealing data of FKM from Gordon and General, we completed a sealing test of a representative FKM gasket [15] and determined that (bearing in mind some assumptions) the performance was similar in hydrogen and helium.

3.2 ePTFE Gaskets

Expanded PTFE (ePTFE) is a specific form of PTFE that can be formed into a useful sheet gasket material, it is especially useful for low stress situations and aggressive chemicals. This material was developed by W. L. Gore [21], however the key patents have expired, and this type of material is now manufactured by a small number of other manufacturers.

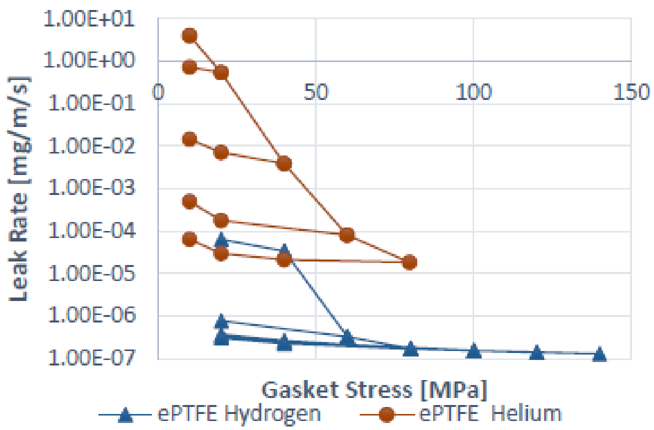

Figure 5: EN13555 sealing plot for ePTFE gaskets [20]

General and Norman [20] also included a comparison of hydrogen and helium sealing for an ePTFE sheet. Unfortunately, they provided no source information on the grade of ePTFE used. Figure 23 of their paper (figure 5 here) shows that the leakage rate for helium is as much as two orders of magnitude higher than the leakage rate with hydrogen. This is a very significant difference that is unlikely to be explained by test error or variation.

Teadit have published a product information sheet [22] showing hydrogen sealing data for their ePTFE grade 24 SH (figure 6). It was possible to compare this data to data published helium leakage data on gasketdata.org [23], shown in figure 7. Figures 6 and 7 show that sealing for hydrogen is again better than sealing of helium.

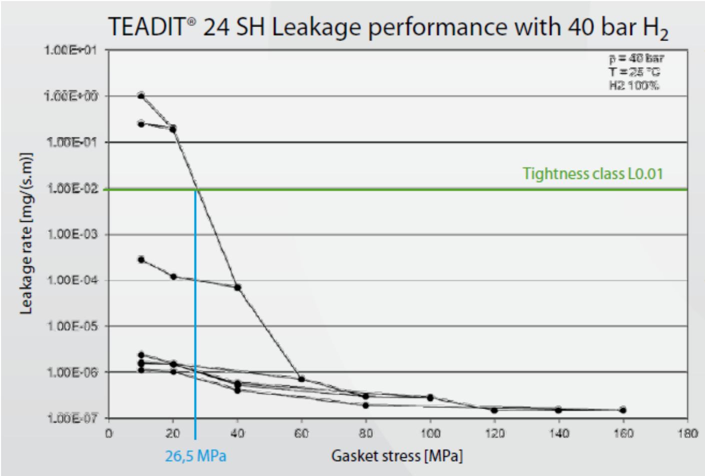

Figure 6: EN13555 Sealing plot for ePTFE [22]

The $Q_{(min)L}$ data for L 0.001 are similar, 26 MPa for hydrogen and 30 MPa for Helium, but at gasket stresses greater than 60 MPa the sealing of hydrogen is better.

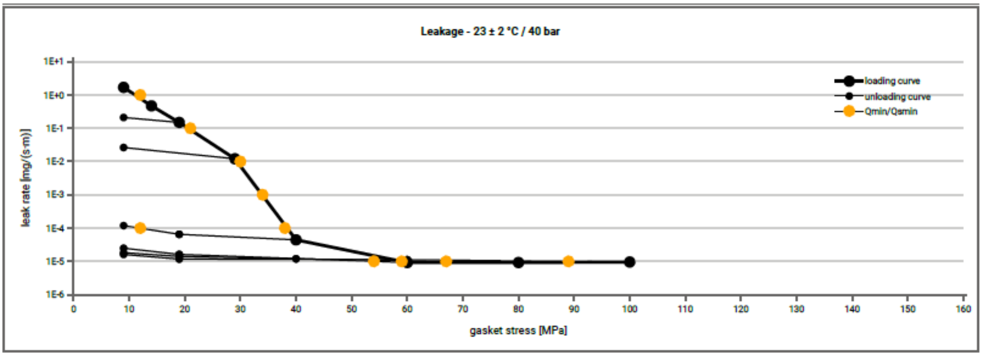

Figure 7: EN13555 Sealing plot for ePTFE [23]

At this point it is not clear why there is a difference between hydrogen and helium sealing performance with ePTFE gaskets. This difference has been shown by two independent studies.

3.3 Graphite Sheet Gaskets

Berger [18] also discussed graphite gaskets and showed that testing of graphite gaskets gave a similar pattern of results to the results for aramid fibre / rubber compressed sheet gaskets. Nitrogen mass leak rates were again higher than hydrogen leak rates. Different results were recorded for different sheets and the order was the same, as observed above.

SGL Carbon have published a comprehensive document on hydrogen stability (compatibility) and sealing for their range of graphite gasket materials [24]. They provide hydrogen sealing curves for a number of their grades of materials, including some testing at different internal pressures and a comparison of hydrogen and helium leakage curves for Sigraflex Hochdruck Pro (figure 8).

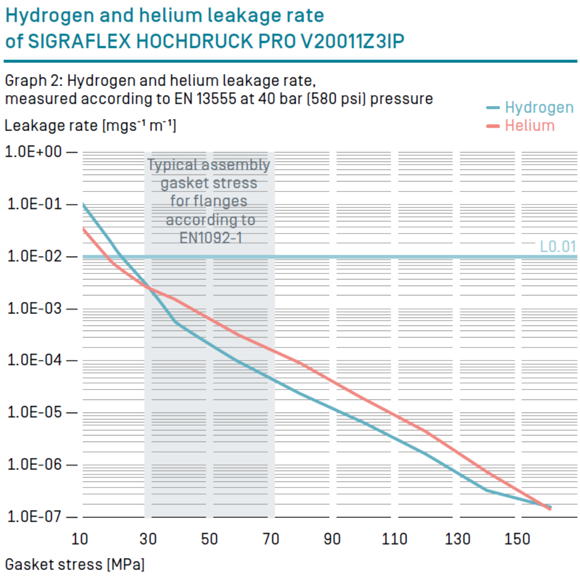

Figure 8: EN13555 Hydrogen sealing plot for a Graphite Sheet Gasket

Their conclusion is that at gasket stresses of above 40MPa the leakage of hydrogen is less than the leakage of helium. However, the difference is not large. They further conclude that helium data could be used to perform flange tightness calculations such as EN1591-1. They also provide some long-term sealing plots in accordance with DIN28090-1 and -2 [19] (using nitrogen as a test gas) and conclude that over a 10,000 hour test, graphite can provide a reliable and consistent seal.

The same publication [24] discussed chemical resistance of graphite with hydrogen. The publication states that graphite is chemically resistant in hydrogen from -269°C to 900°C. Starting at temperatures above 900°C, it is possible that the graphite can begin to degrade when the carbon atoms of the graphite can react to form methane gas.

This publication [24] also discusses hydrogen embrittlement of metals and concludes that austenitic stainless steels such as 316L and 304 are less prone to degradation and are the standard (preferred) materials in hydrogen technologies. This conclusion is also pertinent to spiral wound gaskets and kammprofile gaskets.

3.4 Kammprofile Gaskets

Kammprofile gaskets are well known gaskets and are included in standards such as ASME B16.20 [8] and EN 1092 [25]. They consist of a metallic core and a soft facing or sealing material (figure 3). The sealing material is often a similar grade of Flexible Graphite to that used in sheet gaskets and SWGs. Other facings are used when the application conditions require it.

General and Norman [20] discussed the sealing of Kammprofiles in their publication. Figure 19 in this paper (figure 9 here) is an EN13555 plot of a graphite faced Kammprofile comparing sealing hydrogen and helium and Figure 20 is a similar plot for ePTFE faced Kammprofiles.

In both cases there is no discernible difference in the sealing performance in hydrogen and helium.

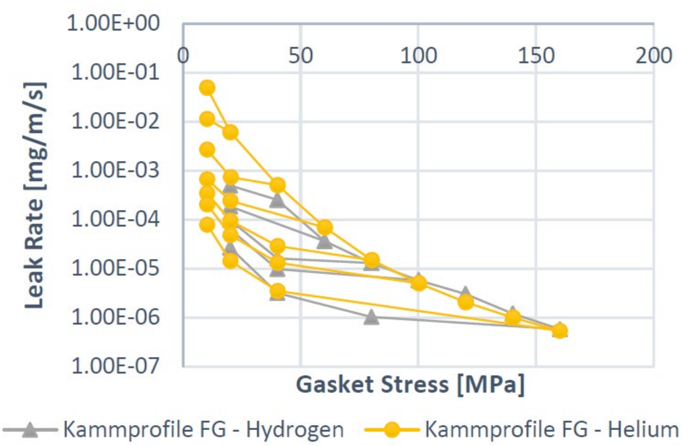

Figure 9: EN13555 Hydrogen sealing plots for graphite faced Kammprofile gaskets.

3.5 Spiral Wound Gaskets

Spiral Wound Gaskets are well known gaskets, they are included in standards such as ASME B16.20 [8] and EN1092 [25]. The sealing element comprises a profiled and wound metal, typically but not exclusively, a stainless steel, co-wound with a soft sealing material, the soft sealing material is often flexible exfoliated graphite, but other fillers can be used depending on the application conditions. These other fillers include PTFE, mica and vermiculite-based fillers.

General and Norman [20] presented sealing data for hydrogen and helium on graphite SWGs. They compared construction of gasket, Low Emission (LE) vs “Standard” constructions. While the LE gasket sealed more effectively than the standard construction, the difference between hydrogen and helium sealing was not discernible in either case.

In house manufactured SWGs were included in a previous publication [15], however, some new data has been gathered and the information will be presented in the following section.

4 Spiral Wound Gasket Sealing Data

The information published previously [15] investigated different types of filler, that data will be presented here, along with new data on a PTFE filled SWG. In all cases, the SWGs were made in our Houston facility and a stack of ten sequentially produced gaskets was used for the testing. Each gasket was wound with 316 stainless steel winding wire and fitted with a 316L stainless steel inner ring and a carbon steel outer ring.

Four different fillers were tested in total. A high quality, oxidation resistant flexible graphite, our proprietary high temperature vermiculite-based filer, our proprietary lower temperature vermiculite-based filler and a pure un-sintered PTFE filler.

Helium sealing tests were carried out in our Houston Test lab using the EN13555 sealing method, using an automated multifunctional test rig (Ametc TEMES fl.ai1). Hydrogen sealing testing was carried out at Amtec NA [26] using a similar rig but with modifications for hydrogen testing.

It should be remembered that SWGs manufacturers typically recommend a minimum gasket stress of 69MPa (converted from 10,000psi) and this should be considered when viewing EN13555 test plots, which typically start at 5 MPa gasket stress. The maximum tested gasket stress is typically 160 MPa, which is usually driven by the load available on the Amtec TEMES fl.ai1, which is 1 MN.

4.1 Graphite Filled SWGs

The previously reviewed leakage plots for graphite filled SWGs with different test gases are slightly different (Figures 3 & 6 in reference [15], the hydrogen plot is figure 10 here). The lowest leak rate is recorded at 160 MPa for helium is 3 x 10^{-5} mg/m/s and for hydrogen it is 4.3 x 10^{-6} mg/m/s. For helium the $Q_{min(L)}$ 0.001, which represents the minimum gasket stress in assembly, is 59 MPa and for hydrogen it is 54 MPa which is relatively similar, and lower than the typical minimum required stress to seal for a SWG of 69 MPa. See table 3.

This suggests similar sealing of hydrogen and helium at moderate stresses, and better sealing in hydrogen at high stresses. The unloading curves are also very similar.

4.2 Vermiculite Filled SWGs

While it is understood that the high temperature vermiculite filler was not intended for ambient temperature use, it is a worthwhile test to carry out in the context of this review. The high temperature (HT) vermiculite based SWG filler has a very similar lowest leakage rate (at 160 MPa) in both cases, the lowest leakage rate was 3.0 x 10^{-7} mg/m/s for the helium and 1.7 x 10^{-7} mg/m/s for hydrogen.

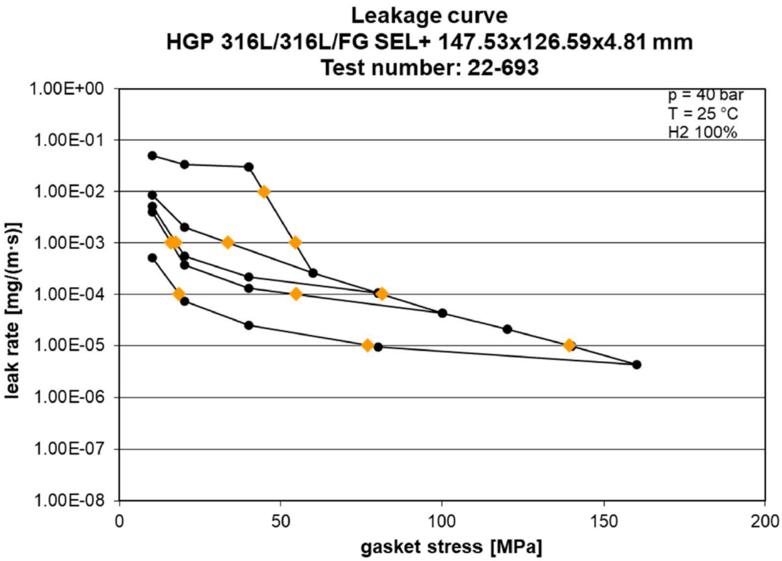

Figure 10: EN13555 Hydrogen sealing plot for the LT vermiculite (CR235) SWG

The Tightness Class L0.001 in helium was 87 (compared to 59 for graphite), in hydrogen this tightness class was achieved at 28 MPa, which is extremely low (good). In fact, a tightness class of 0.000001 was achieved at 75 MPa in Hydrogen (this level was not achieved in helium). This suggests the high temperature vermiculite has some ambient sealing advantages in hydrogen, compared to graphite.

The lower temperature (LT) rated vermiculite filler has a different proprietary formulation to the high temperature version and will not go through significant thermal changes within its operating window. The data shows it has a very attractive sealing curve, especially with hydrogen as the test gas, see Figure 11. The lowest leak rate when tested with hydrogen is 1.2 x 10^{-7} mg/m/s (compared to 2.3 x 10^{-6} mg/m/s when tested with helium), See Table 2.

The LT vermiculite filled gasket reaches high tightness levels at a stress less than the nominal minimum recommended assembly stress for both test gases. A tightness class of 0.001 was achieved at 58 MPa with helium and 60 MPa with hydrogen. A lower tightness class of 0.00001 was achieved at 83 MPa with helium and 60 MPa with hydrogen as the test gas. Both of these stress levels are around the nominal minimum load to seal for SWGs (10,000 psi / 69 MPa). See table 3.

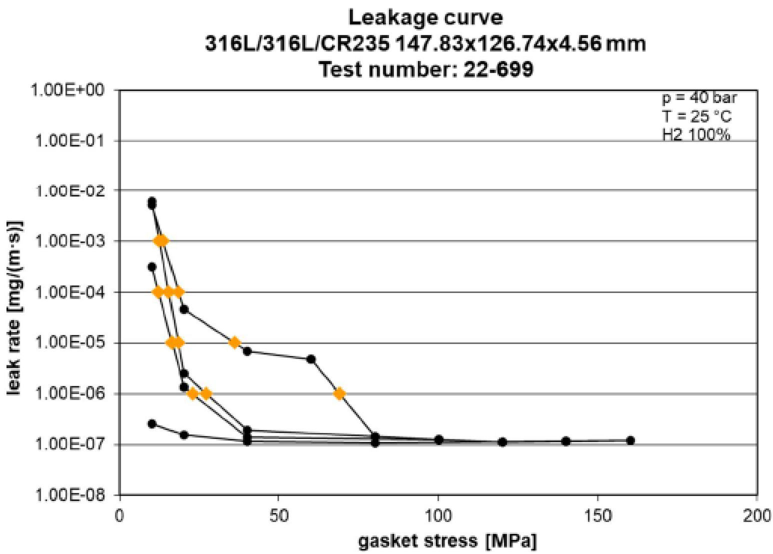

Figure 11: EN13555 Hydrogen sealing plot for the LT vermiculite (CR235) SWG

Interestingly, the LT vermiculite filler has a leak rate which is slightly lower than the high temperature vermiculite filler at 160 MPa and an order of magnitude better than graphite in these SWGs in hydrogen.

Furthermore, the unload lines from the hydrogen sealing test for the low temperature vermiculite filler are very flat until at 40MPa or below. The $Q_{smin(L)}$ in every case is below 30 MPa, which is potentially advantageous.

4.3 PTFE Filled SWGs

As with previous testing, helium leakage tests were carried out in-house and hydrogen testing was carried out at a third party (Amtec NA) [26]. Figure 11 is reproduced from the second of these reports [26]. The lowest leak rate was recorded at 160 MPa and was 6.0 x 10^{-8} mg/m/s for helium and 3.4 x 10^{-7} mg/m/s for hydrogen. This is a very low leak rate in both helium and hydrogen.

The minimum stress required to achieve a tightness class of 0.001 as reported above was achieved at below 20 MPa for hydrogen. The same low stress to seal was found with helium, see table 3.

During the unloading cycles, the leakage of the PTFE SWGs stayed very low (Figure 11) and the $Q_{smin(L)}$ in every case is very low, lower than SWGs with other fillers.

4.4 Summary of SWG Performance

Table 2 and Table 3 show a summary of the sealing properties of SWGs with different fillers, where both helium and hydrogen are used as the test gas. In Table 3

L=0.001 was chosen as it is tighter than the VDI requirements and the results for this tightness class are often close to the minimum stress to seal for a SWG.

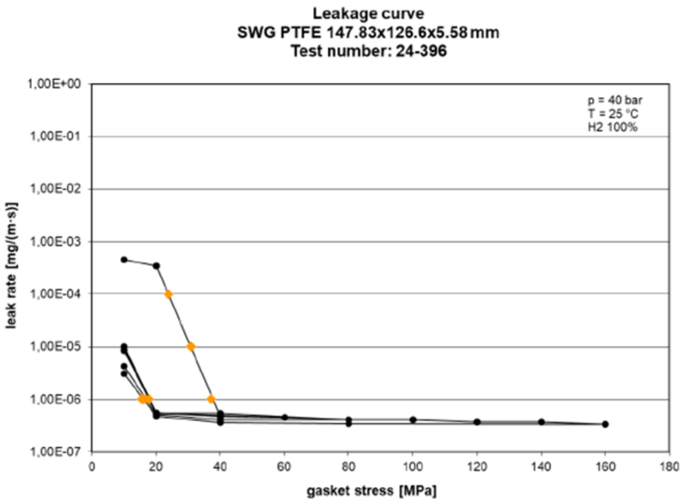

Figure 11: EN13555 Hydrogen sealing test for a PTFE filled SWG.

Table 2 shows that in terms of sealing at higher stresses (160 MPa) all of the gaskets are generally good, but the graphite filled SWG stands out as the least good in hydrogen by approximately an order of magnitude. This is true for the graphite gasket tested with helium also. Both of the Vermiculite filled SWGs perform better than graphite in both test gasses. The PTFE filled SWG is the best in helium and similar to both vermiculite filled SWGs when the test gas is hydrogen. However, as previously stated, all of these results are good. This is confirmed using different data in table 3, below.

TABLE 2: Leak rate at 160 MPa for different SWG fillers (mg/m/s)

SWG Filler	Test Gas	
	Helium	Hydrogen
Graphite	3.1×10^{-5}	4.3×10^{-6}
HT Vermiculite	3.0×10^{-7}	1.7×10^{-7}
LT Vermiculite	2.3×10^{-6}	1.2×10^{-7}
PTFE	6.0×10^{-8}	3.4×10^{-7}

In terms of minimum load to seal in the assembly condition, L = 0.001, all of the SWGs are slightly better when hydrogen was the test gas. Almost every case this tightness class was achieved at lower than the typical recommended stress to seal for a SWG.

In all cases, the unloading portion of the EN13555 leak test was good and the $Q_{smin(L)}$ values were low. In the interest of brevity these are not shown here. In each case the unload lines were flat until 40MPa or lower was reached.

TABLE 3: Stress (MPa) required to achieve tightness class L = 0.001

SWG Filler	Test Gas	
	Helium	Hydrogen
Graphite	59	54
HT Vermiculite	87	28
LT Vermiculite	58	<60
PTFE	<20	<20

One final consideration when sealing hydrogen is fire safety. One of the most common tests for gaskets is the API 6FB fire test [27]. Only a few sheet gaskets are considered fire safe, while many kammprofiles and SWGs are. PTFE SWGs are not generally considered fire safe, including in this API 6FB test. However, graphite [28] and vermiculite filled SWGs (both LT and HT) [29, 30] pass this fire test.

5 Discussion

It is clear that hydrogen will form an important part of the energy transition and of multiple industries in the upcoming decades. Therefore, it is important that the sealing of hydrogen is well understood, across a range of application conditions and for a range of gasket styles and types.

From the data collated from many sources and presented above, it can be observed that many, if not all, of the common conformable sealing materials used today are compatible with hydrogen and therefore suitable for sealing hydrogen.

It can generally be observed that the leakage rates of helium and hydrogen are relatively similar.

Previous work has shown that aramid fiber sheets, elastomeric sheets and ePTFE sheets can seal well in both hydrogen and helium.

As one would expect, very low leakage values are achieved for many types of gasket including graphite and ePTFE. Semi-metallic gaskets such as kammprofiles and SWGs also provide very good seals with hydrogen leak rates as low as 1.2 x 10-7 mg/m/s at 160 MPa for a low temperature vermiculite filled SWG. This is better than the standard graphite filled SWG.

If fire safety is a concern when sealing hydrogen, then graphite or vermiculite SWGs or kammprofiles are considered fire safe, using the API 6FB test standard.

6 Conclusion

Work reviewed here has shown that many common sealing materials can be considered resistant to hydrogen, this includes many soft sealing materials, including common sheet gaskets, and semi metallic gaskets where austenitic stainless steels are commonly used.

Based on the results reviewed, it appears that for many types of gaskets, the sealing performance is similar in hydrogen and helium. This is not the case for nitrogen or methane, as discussed in an earlier publication [15].

Therefore, while some specific applications may require hydrogen testing, the bulk of the data reviewed here suggests that most engineering decisions can safely be made helium leakage data.

7 Acknowledgements

The author would like to thank all of those at Flexitallic who have helped in this work, particularly the Research and Development Team and the New Energy Team. The author also acknowledges all the authors of work referenced in this review.

8 References

[1] www.fchea.org (online)

[2] www.hydrogeneurope.eu/ & www.hydrogeneuroperesearch.eu/ (online)

[3] Ocko and Hamburg. Climate consequences of hydrogen emissions. Atmospheric Chemistry and Physics. **22,** 9349 – 9368, 2022. https://acp.copernicus.org/articles/22/9349/2022/

[4] Control methane to slow global warming – fast. Editorial. Nature **596**, 461 (2021). https://nature.com/articles/ d41586-021-02287-y

[5] Office of Energy Efficiency and Renewable Energy (Online). www.eere.energy.gov/hydrogenandfuelcells/pdfs/h2_safety_sheet.pdf. Accessed on line January 11th 2023.

[6] Sustainable Northern Ireland. www.sustainableni.org/blog/many-colours-hydrogen. Online. Accessed 11th January 2024.

[7] BS EN13555:2019. Flanges and their joints – Gasket parameters and test procedures relevant to the design rules for gasketed circular connections. European Committee for Standardization. Brussels, Belgium.

[8] ASME B16.20-2017. Metallic Gaskets for Pipe Flanges. American Society of Mechanical Engineers, New York, NY. USA.

[9] DIN 3535-6:2011-01 Gaskets for gas supply – Part 6. Gasket Materials based on fibres, graphite or polytetrafluoroethylene (PTFE) for gas valves, gas appliances and gas mains.

[10] Cazauran, Birembaut, Hahn, Kockelmann and Moritz. Gas Leakage Correlation. PVP2009-77882. Society of Mechanical Engineers. Pressure Vessel and Piping Conference 2009.

[11] Mansfield and Wilson. The Use of Different Media in Leakage Testing. Bolting Symposium 2024. Jan 9-11 South Shore Harbor, TX.

[12] www.bam.de/Navigation/EN/Topics/Energy/energy.html Online. Accessed 1/23/2024

[13] www.cetim-engineering.com/energy/ Accessed Online 1/23/2024

[14] Amtec Newsletter, August 2022. Gasket Testing with Hydrogen.

[15] Bond. Sealing of Hydrogen: An Overview of Published Data. PVP2024-130053. American Society of Mechanical Engineers. Pressure Vessel and Piping Conference, PVP2024.

[16] Übelmesser, Mohar and Majcen. Soft Sealing Materials: leakage tests with helium and hydrogen. Industrial Fittings 3/2022.

[17] TA-Luft in accordance with VDI guideline 2440. November 2000. Emission control - mineral refineries. TA-Luft in accordance with VDI guideline 2200. June 2007. Tight bolted flange connections: selection, calculation, design and assembly of bolted flange connections.

[18] Berger. Sealing Solutions for Hydrogen Applications. 21st International Sealing Conference. Stuttgart 12-13 October 2022.

[19] DIN 28090. Static Seals for Flange Connections- Part 1: Characteristic values and test procedures. 1995. Deutsches Institut für Normung, Berlin, Germany.

[20] General and Norman. Understanding Hydrogen Leakage with Standard ASME B16.20 and ASME B16.21 Gaskets. PVP2023-105909. Society of Mechanical Engineers. Pressure Vessel and Piping Conference 2023.

[21] W.L. Gore. US Patent 3,953,566, US Patent 3,962,153, and US Patent 4,187,390

[22] Teadit publication “Hydrogen: Complete Sealing Solutions” dated March 2022 ref 127-127. Online. Accessed 12 December 2023.

[23] www.gasketdata.org. Online. Accessed 12 December 2023.

[24] SGL Carbon. Long-term safe sealing of hydrogen with SIGRIFLEX. TIS SIGRIFLEX Hydrogen.00. 06/2022.

[25] BS EN1092: 2018. Flanges and their joints – Circular flanges for pipes, valves, fittings and accessories, PN designated. Part 1: Steel flanges. European Committee for Standardization. Brussels, Belgium.

[26] Amtec NA Inc, Report Numbers A 300 303 1/- November 10th 2022 and A 300 303 2/-. April 30th 2024.

[27] API Specification for Fire Test for End Connections. API Specification 6FB. Third Edition. November 1998. Reaffirmed July 2006. American Petrochemical Institute. Washington, DC, USA.

[28] Amtec North America Inc, Fire Test API 6FB Report. Graphite Spiral Wound Gasket. Project Number A300 117. 25.07.2014

[29] Yarmouth research and Technology LLC. Fire Test Report, Thermiculite 835 Spiral Wound Gasket. Yarmouth Project Number 212098. June 25, 2012.

[30] Amtec North America Inc, Fire Test API 6FB Report. Corriculite Spiral Wound Gasket. Project Number A303 151. 21.04.2016

9 Author

The Flexitallic Group

433 Plaza Verde Drive, Suite 100, Houston, TX, USA

Stephen Bond, PhD, FRSC. sbond@flexitallic.com

https://doi.org/10.61319/BCWRTC108

Group A
Session 2

Applications in practice I

A 01

Christoph Olbrich, Jacqueline Gerhard, Simon Feldmeth, Frank Bauer, University of Stuttgart, Institute of Machine Components (IMA), Stuttgart, Germany

Influence of rolling-element bearings on rotary shaft seals

A 02

Nino Dakov, Martin Franz, Jeff Baehl, Sam Wagoner, Trelleborg Sealing Solutions Germany GmbH, Stuttgart, Germany

A high-pressure radial shaft seal with enhanced wear performance

A 03

Anne Marie Lehmann, Anja Dobrinsky, Martin Franz, Trelleborg Sealing Solutions Germany GmbH, Research and Development, Stuttgart, Germany

A smart seal energizer from shape-memory-alloy

Influence of rolling-element bearings on rotary shaft seals

Christoph Olbrich, Jacqueline Gerhard, Simon Feldmeth, Frank Bauer

Rotary shaft seals are commonly used to seal machines with rotating shafts and prevent the leakage of fluids into the environment. Failures of elastomeric rotary shaft seals are often the result of overheating in the contact area between the sealing edge and the shaft. High temperatures in this contact area occur due to high frictional power and/or inadequate heat dissipation. The surrounding of the seal has a significant impact on the temperatures occurring in the contact area. Especially rolling-element bearings near the seal strongly influence the contact temperature. The frictional heat generated in the bearings results in an increase in the temperature of the fluid near the seal, consequently raising the contact temperature. Tapered roller bearings pump oil. Depending on the installation situation, this can lead to a higher or lower fluid level next to the seal. Tests are conducted on a high-speed friction torque test bench. This investigation involves four different bearing arrangements, as well as a reference variant without bearings. In these test runs, both the frictional torque and the temperature near the contact area are examined. In addition to the experiments on the test bench, Conjugate Heat Transfer (CHT) simulations are conducted with the same installation conditions. The simulated temperatures are compared with the measured temperatures. In most cases, the correlation is good. However, for one bearing arrangement, the correlation is significantly worse. These differences are investigated further.

1 Introduction

Rotary shaft seals and rolling-element bearings are two of the most commonly used machine components. In many technical systems, rotary shaft seals are installed near rolling-element bearings. In this context, they have to seal the fluid (used for lubricating and cooling of the bearing) at the point where a shaft exits a housing [1]. Studies by Kunstfeld [2] have already demonstrated that additional elements near the seal influence the temperature. In this paper, the influence of rolling-element bearings on rotary shaft seals in relation to temperature and frictional torque is analysed further.

1.1 Rotary shaft seals

Rotary shaft seals are commonly used to seal machines with rotating shafts. In the majority of applications, these seals must contain a fluid within a designated space and prevent leakage into the surrounding environment. It is necessary that all components within the tribological system of the rotary shaft seal operate in unison to ensure this function. The tribological system extends beyond the seal ring itself and includes the corresponding counter face (the surface of the shaft), and the sealed fluid (lubricant or operational fluid). The tribological system of a typical rotary shaft seal is seen in Figure 1.

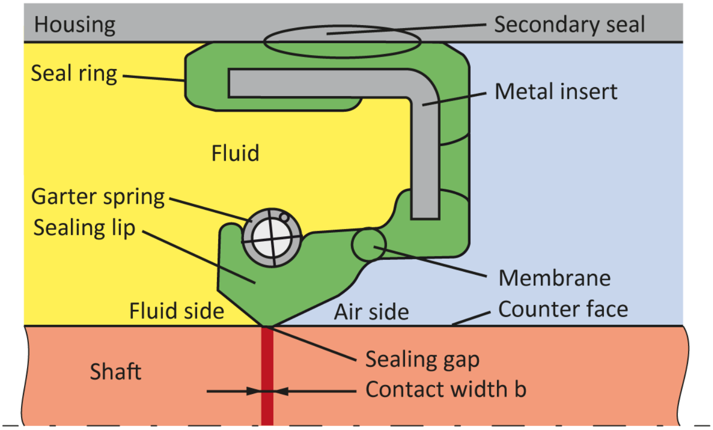

Figure 1: Sealing system of a rotary shaft seal

The structure of a rotary shaft seal is defined in ISO 6194-1 [3] and ISO 6194-2 [4]. The seal ring consists of a metal insert to which an elastomeric sealing lip is moulded.

The area, where the seal ring touches the shaft is called contact area. The contact area typically has a contact width of 0.1 to 0.2 mm. The sealing lip and the garter spring are expanded, when the seal ring is mounted on a shaft. This results in an average contact pressure of approximately 1 MPa in the contact area. When the shaft rotates, elasto-hydrodynamic processes create a thin lubricating film (<1 µm). This film lifts the sealing lip, and is commonly referred to as the sealing gap.

The rotation of the shaft in combination with the asymmetric distribution of pressure within the sealing gap creates a pumping effect from the air side towards the oil side. This pumping effect can be explained by the distortion principle and wiping edge principle. Any fluid that gets to the air side is pumped back to the fluid side retaining the fluid within the system and preventing leakage [1].

1.2 Rolling-element bearings

In most cases rolling-element bearings are used to support rotating components like shafts. These bearings are designed to facilitate smooth and efficient motion by minimizing friction between moving parts. Unlike plain bearings that rely on sliding contact, rolling-element bearings use small, rolling elements (such as balls or cylindrical rollers) that reduce friction and wear. The basic structure of a rolling-element bearing typically consists of an inner race, an outer race, and the rolling elements themselves. The inner and outer races are the ring-shaped structures that house the rolling elements. A cage ensures the proper alignment and movement of the rolling elements. The rolling elements, positioned between the races, distribute the load and enable the smooth rotation of the bearing [5].

Rolling-element bearings come in various types, each tailored to specific applications and load requirements. They can be split into two general types, ball bearings and roller bearings [6]. Three of the most common types are deep groove ball bearings, cylindrical roller bearings and tapered roller bearings. In this paper the influence of these three types on rotary shaft seals is analysed further.

1.3 Contact temperature

Overheating in the contact area between the lip of the rotary shaft seal and the shaft can lead to failures of the seal. The increased temperatures in the contact area are typically the result of high frictional power and/or inadequate heat transfer out of the contact area [7]. One of the typical failure modes of a rotary shaft seal is the hardening of the sealing lip, which is usually the result of excessive temperatures. Hardening prevents the distortion of the sealing edge and thus disables the pumping effect via the distortion principle [1]. Hardening of the sealing lip in combination with increased mechanical stress, for example by an excentric shaft, can result in the development of axial cracks. Elevated temperatures near the sealing lip can also induce fluid decomposition. This decomposition often results in oil carbon deposits in or near the contact area. The accumulated oil carbon can disturb the sealing mechanism, ultimately leading to leakage. [1, 8].

A failure of a rotary shaft seal can be both ecologically and economically significant. Information about the resulting contact temperature is crucial to avoid overheating. This awareness plays a pivotal role in preventing failures, enhancing product reliability, and prolonging the lifespan of the seal.

To choose an appropriate seal for a particular application, an understanding of the potential contact temperatures in later use is essential. An increase in temperature of about 10 K can half the anticipated service life [9]. To determine the potential contact temperature there are three different approaches: The measurement on a prototype, the simulation of the entire system or using estimation methods [10]. Measurements on a prototype and Simulations are more accurate. However, it is often necessary to quickly and easily estimate the contact temperature. In these cases it is useful to use less precise but simple estimation methods.

1.4 Frictional torque

In most applications, no special attention is paid to the frictional torque of seals. The frictional torque of a single seal of usually less than one newton meter appears very low compared to other components of a typical technical system. However, the friction in the contact area directly influences the contact temperature. Especially in combination with high rotational speeds, minimizing friction and thus frictional power is advantageous. In addition to the power losses at the seal, significant losses also occur at the rolling-element bearings. This power loss heats the oil and the shaft additionally. Some rolling-element bearings pump fluid in axial direction [11]. Hence, the bearings have a significant impact on the operating conditions of the seal. They influence not only the temperature but also the oil level and potentially the pressure of the oil near the seal. The altered operating conditions affect both the heat generation in and transfer out of the contact area.

Exposure of a rotary shaft seal to a higher pressure on the fluid side than on the air side leads to an increase in the radial load on the sealing lip. Consequently, this enlarges the contact area between the sealing lip and the shaft, leading to additional friction and increased contact temperatures and wear [12].

2 Setup

All tests are conducted on a high speed universal friction torque test bench [13]. The basic design of the test bench consists of a motor spindle and a test chamber in which the seal ring is mounted. The motor spindle enables speeds of up to 24000 rpm. The test shaft is mounted on the motor spindle through a hollow shaft taper (HSK). The test chamber is supported by an aerostatic bearing. Due to the aerostatic bearing, the chamber can rotate almost frictionless around its centre axis. The chamber is supported by a lever arm on a force sensor. The torque at the seal is transferred to the chamber and to the force sensor. The frictional torque is calculated by multiplying the length of the lever arm and the measured force. The frictional torque is recorded by the measuring computer.

Figure 2 shows the design of the high speed universal friction torque test bench.

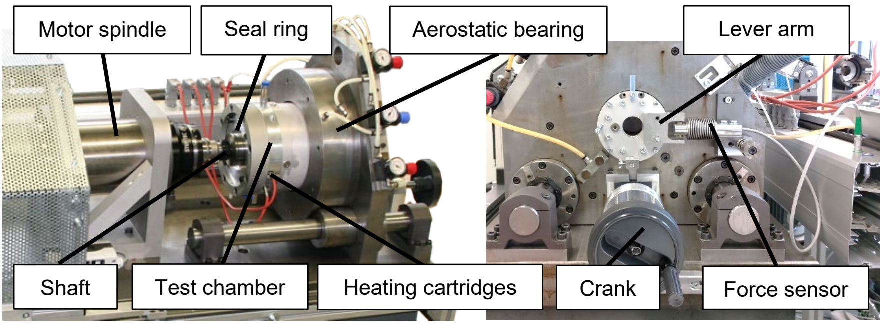

Figure 2: Setup high speed universal friction torque test bench [13, 14]

Before the experiment, the test chamber is filled (with the fluid to be examined) up to the centre of the shaft and then closed with a vent for ventilation. Temperature control is achieved through heating cartridges and a temperature sensor, which are installed in the chamber. They are controlled and evaluated by the control software. The test chamber can be moved along linear guides using a crank. This way different positions of the sealing lip can be set on the shaft.

2.1 Tested components

For all experiments, rotary shaft seals according to ISO 6194 [3] with dimensions of 100x80x10 are used. The seal rings are made out of fluoro rubber.

Four different rolling-element bearing arrangements are investigated. The bearing next to the seal is varied between a ball bearing, a cylindrical roller bearing, a tapered roller bearing in an X arrangement, and a tapered roller bearing in an O arrangement. An overview of the used bearings is provided in Table 1.

Table 1: Used rolling-element bearings.

	Rolling-element bearing		
Type	Cylindrical roller bearing	Ball bearing	Tapered roller bearing
Cross section	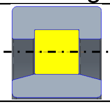	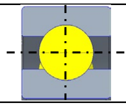	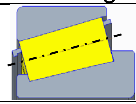
Inner diameter d [mm]	85	85	85
Outer diameter D [mm]	130	130	130
Width B [mm]	22	22	29
Max speed in test [rpm]	6.300	6.300	3.200

To mount the rolling-element bearings in the test chamber, a new mounting structure was designed and manufactured. The adapted test chamber is seen in Figure 3.

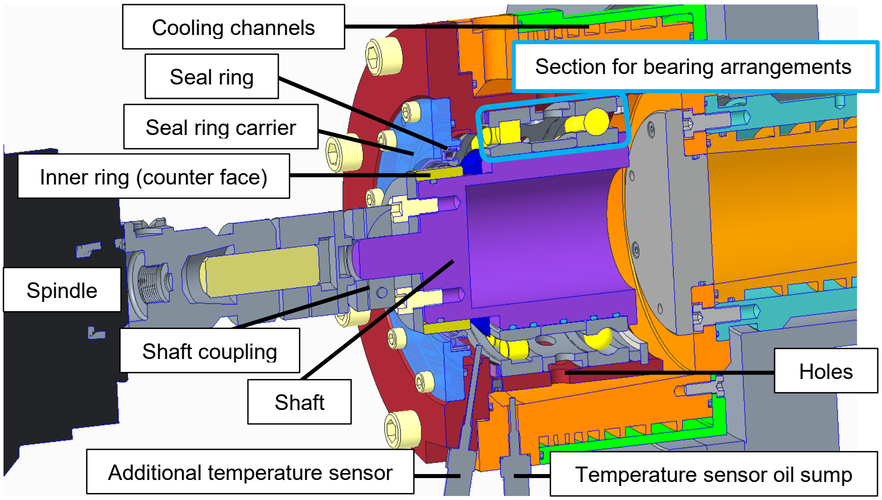

Figure 3: Adapted test chamber to mount rolling-element bearings

The bearings can be installed in to the adapted test chamber. A corresponding shaft body allows for the installation of the bearing inner rings on the shaft. 24 holes with a diameter of 10 mm allow for the circulation of the oil between the bearings.

The shaft counter face of the seal is realized with a plunge gound inner ring of a needle bearing. A seal ring carrier made out of transparent PMMA enables the visual observation of the oil flow near the seal. An additional temperature sensor is installed in the gap between the bearing and the seal. This sensor measures the oil temperature near the seal. In the case of the bearing variants, the shaft body is supported by the bearings installed in the test chamber. For these variants, a coupling is used on the air side to prevent the bearings from binding (misalignment to the motor spindle). The coupling can compensate for any misalignment that may occur. The four different rolling-element bearing arrangements, as well as a reference Variant without bearings are shown in Table 2.

Table 2: Tested arrangements.

Abbreviation	**Meaning / Explanation**	**Picture**
Ref-SV	Reference variant for surrounding variation: Variant without bearings as a reference to investigate a single seal.	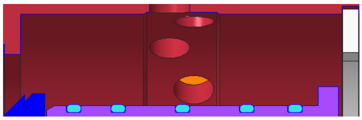
Ba	Ball bearing: Deep groove ball bearing next to the seal (Bearing: 6017)	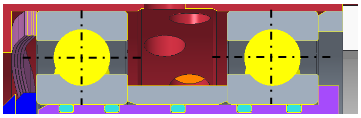
Cyl	Cylindrical roller bearing: Cylindrical roller bearing next to the seal (Bearing: NU1017-XL-M1 + 6017)	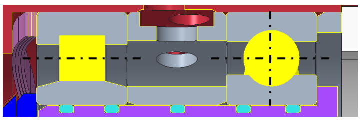
O	O arrangement Tapered roller bearing in an O arrangement next to the seal (Bearing: 32017 X)	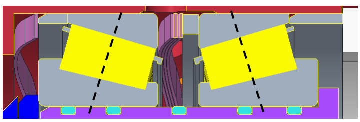
X	X arrangement Tapered roller bearing in an X arrangement next to the seal (Bearing: 32017 X)	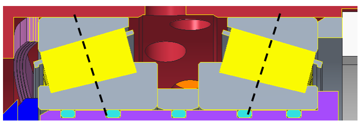

2.2 Testing procedure

All tests are conducted with a new seal ring and counter face. Before the tests, the chamber is filled with oil up to the centre of the shaft. This is a deviation from the typical setup for bearing tests as described in ISO 15312, where the oil level only reaches the centre of the rolling element in the lowest position [15]. The oil sump temperature is set to 80°C. Due to the frictional power loss in the bearings all bearing variants were tested with an actively cooled test chamber. The tests follow a specific load collective [16], which consists of two phases. The first phase is a preconditioning phase during which the shaft rotates with a speed of 1000 rpm. This phase ends after twelve hours. After the preconditioning phase the second phase starts. During this phase all the measurements are conducted. The rotational speed is varied in this phase. Each speed is held for thirty minutes and increased by about twenty percent after each speed, starting at 500 rpm and ending at 6300 rpm. Figure 4 shows the load collective. The variants with tapered roller bearings (O and X) are only run up to 3200 rpm due to speed limitations of the bearings.

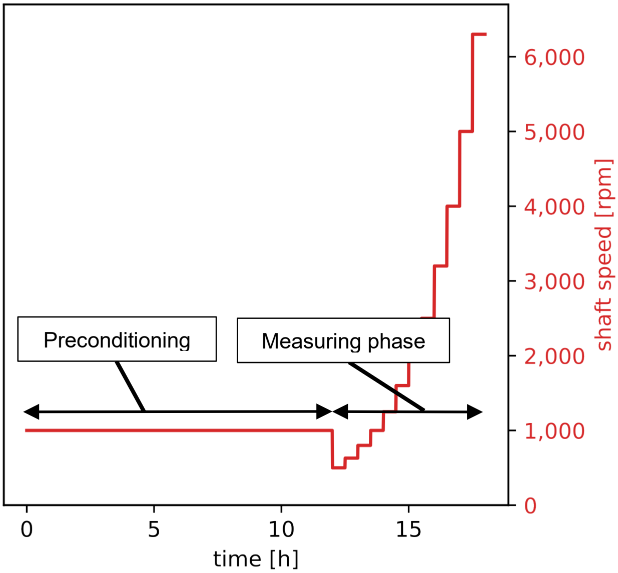

Figure 4: Load collective

During the whole test the frictional torque is measured and documented by the test bench. At the end of each speed interval the Temperature at the airside near the sealing contact is measured with a thermal imager (Fluke Ti480-Pro; accuracy: ±2 °C or ±2 % [17]; emissivity = 0.95, transmission = 100 %). For the sake of simplicity, this temperature is referred to as the contact temperature in the following, even if the temperature in the direct contact area between the sealing lip and the shaft can't be measured.

3 Results

Figure 5 shows the measured frictional torque of all variants over the rotational speed. For each variant at least two individual test runs are conducted. The scatter bars show the maximum and minimum frictional torques of the individual test runs at the respective shaft speeds for each variant.

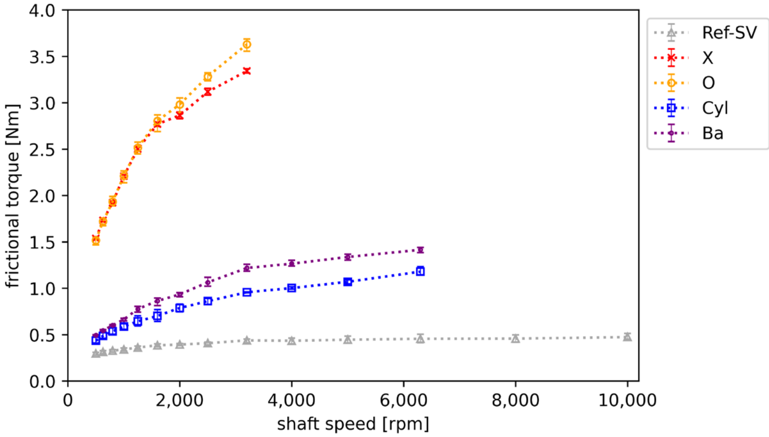

Figure 5: Torque over shaft speed

The reference variant (Ref-SV) shows the lowest frictional torque. The bearing variants show a trend of increasing frictional torques with speed, which flattens with higher speeds. Of the variants with bearings the cylindrical roller bearings (Cyl) has the lowest frictional torque. Slightly higher frictional torques are measured with the deep groove ball bearings (Ba). The largest frictional torques occur with the tapered roller bearings. In this case, the X arrangement (X) shows a slightly flatter trend at higher speeds compared to the O arrangement (O). As expected the tapered roller bearings show a strong pumping behaviour from the side of the smaller diameter to the side of the larger diameter, significantly influencing the oil fill level near the seal. Figure 6 shows the resulting oil levels at the lowest speed of 500 rpm for the X and O arrangements.

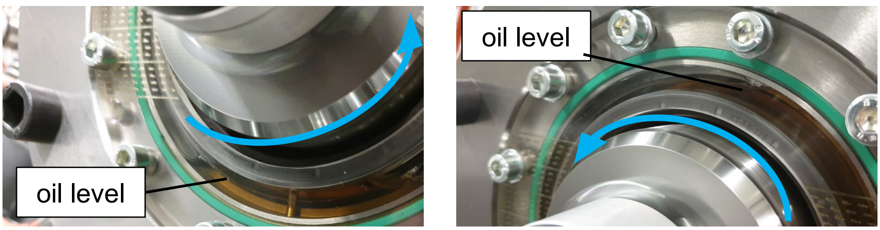

Figure 6: Oil levels 500 rpm for the X (left) and O (right) arrangement [18]

Already at the lowest speed of 500 rpm, the X arrangement shows a fill level below the lowest point of the sealing edge. In the O arrangement, the space between the bearing and the seal is almost completely filled with oil. This becomes even more apparent with increasing speeds. The other two bearing arrangements, as well as the reference variant of the surroundings variation (Ref-SV), show no pumping effect. Figure 7 shows the Temperature at the sealing edge over the shaft speed.

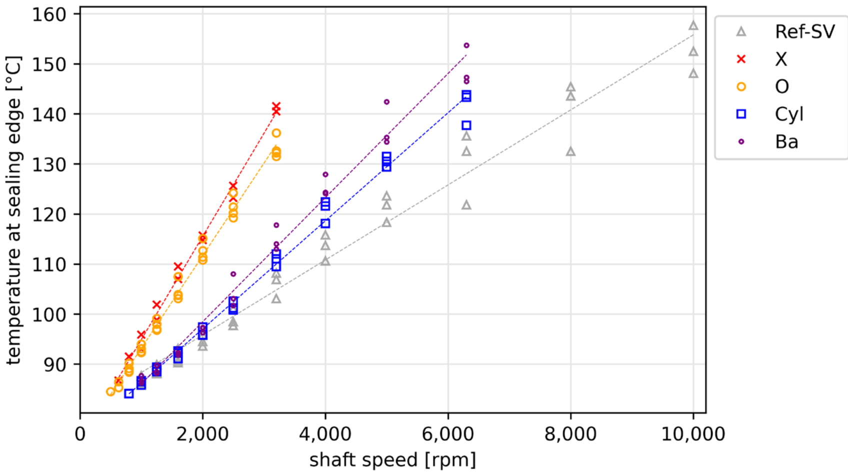

Figure 7: Temperature at the sealing edge over shaft speed

The highest temperatures occur at the X arrangement closely followed by the O arrangement. The variants with the cylindrical roller bearing (Cyl) and the deep groove ball bearings (Ba) show lower temperatures. The lowest temperatures occur without bearings (Ref-SV).

The temperature of the oil near the seal is relevant for the heat transfer out of the contact area. The temperature difference between the oil near the seal (additional sensor, see Figure 3) and the oil sump at 80 °C is shown in Figure 8. For all variants the temperature difference increases nearly linear with the shaft speed. The variants with bearings show higher temperatures of the oil near the seal than the reference variant. the O arrangement (highest torque) has the highest temperature difference.

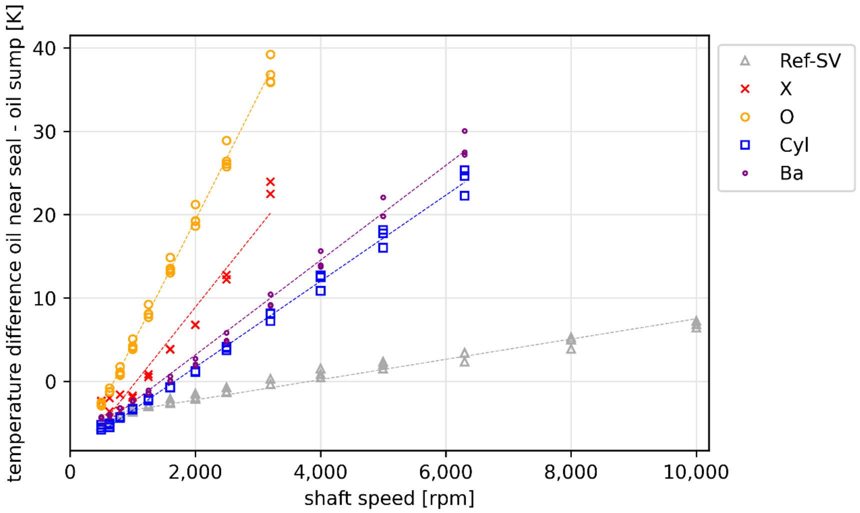

Figure 8: Temperature difference between the oil near the seal and the oil sump over shaft speed

In Figure 9 the temperature difference between the sealing edge and the oil near the seal is plotted over the shaft speed.

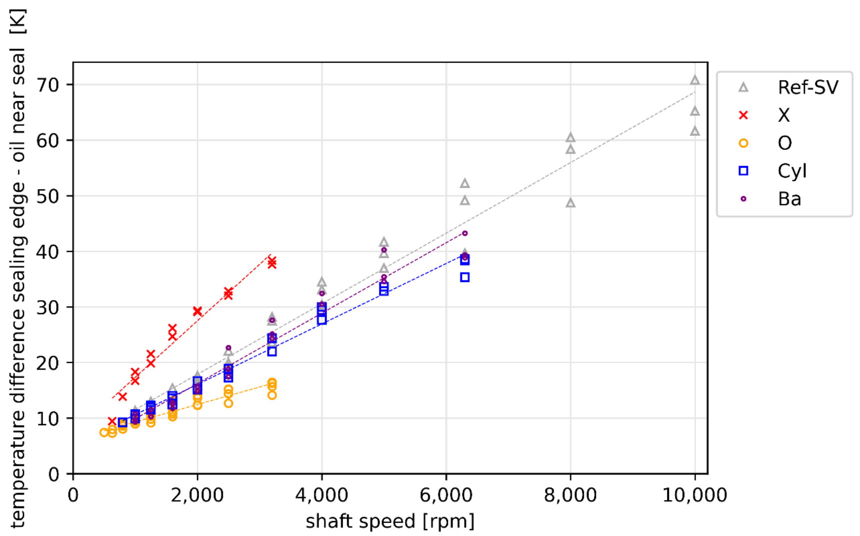

Figure 9: Temperature difference between the sealing edge and the oil near the seal over shaft speed

The highest temperature differences between the sealing edge and the oil near the seal occur in the X arrangement (X). Due to the low oil level near the seal, the heat generated in the contact area cannot be transferred out of the contact area effectively, leading to particularly high temperature differences and the highest contact temperatures. The O arrangement (O) has the second highest contact temperatures, however the lowest temperature differences to the oil near the seal occur at this variant. Due to the high oil level near the seal, the heat generated in the contact area can be transferred out of the contact area more effectively, resulting in lower temperature differences between the sealing edge and the oil near the seal. The variants with no pumping effect (Ref-SV, Cyl and Ba) show very similar temperature trends with respect to speed. The temperature differences are slightly lower for the cylindrical roller bearing (Cyl) compared to the deep groove ball bearing (Ba) and the reference variant (Ref-SV).

4 Simulation of the contact temperature

In addition to the experiments on the test bench, the different rolling-element bearing variants were simulated [19]. The numerical fluid flow simulations were conducted in Ansys CFX 2021 R2. Due to the heat exchange between solid and liquid domains in the model, the Conjugate Heat Transfer (CHT) method was used. This method allows the calculation of temperature distributions in both the solid and fluid domains. Due to the interaction of oil and air in the oil chamber, a multiphase flow approach was chosen for this area. The simulation closely matches the results from the temperature measurements (difference < 5 K) at the test bench except for the O arrangement (max. difference of 26 K). It is suspected that the higher temperatures of the measurements in comparison to the simulation is due to a pressure build up in the area between the bearing and the seal. This would lead to increased contact pressure in the sealing contact and higher frictional torque at the seal, explaining the difference to the simulation without increased torque.

5 Additional Measurements

In order to further investigate the pressure build up in the area between the bearing and the seal of the O arrangement additional tests are conducted. Instead of the second temperature sensor the space between the bearing and the seal is connected to a vertical tube. Using the principle of a liquid column manometer the pressure is determined by the difference in oil level in the tube. The setup is shown in Figure 10.

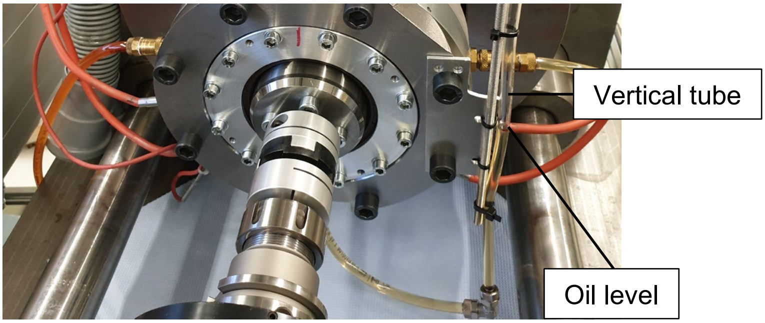

Figure 10: Setup for pressure measurement

The pressure was measured in two test runs. The pressures at different shaft speeds can be seen in Figure 11.

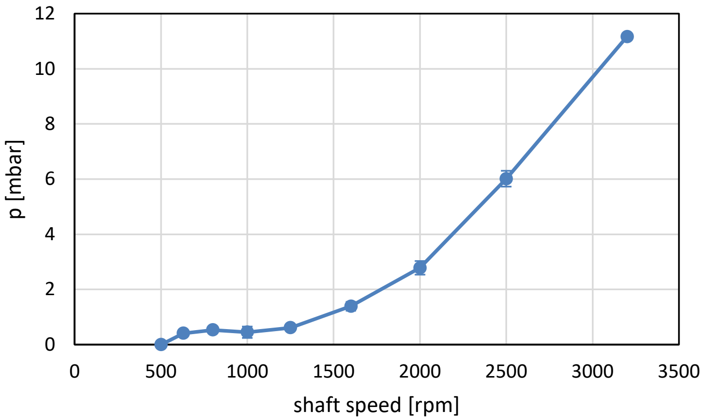

Figure 11: Pressure in area between seal and bearing over shaft speed

The pressure increases with the shaft speed. For speeds over 1500 rpm there is a significant increase in pressure. The radial load of a seal ring increases with pressure. For the tested ring the radial load increases by about 0,08 N per mbar [20]. For the tested seal ring the radial load should increase by about 0,9 N for the highest shaft speed of 6300 rpm. The radial load of a seal at 80 °C (oil sump temperature) is about 28 N. Therefore the radial load increases by about 3 %.

In order to get a better understanding of the frictional torque of the seal under the pressurized condition, additional tests are conducted. In these tests the reference configuration is used and the oil chamber is pressurized. The pressure is set according to the measurements (see Figure 11). The frictional torque of the pressurized and unpressurized test runs is shown in Figure 12.

The pressurized seal (Ref+p) shows higher frictional torque than the unpressurized seal (Ref). For the slower shaft speeds the pressure is very low, thus the frictional torque is similar for these speeds. For the highest shaft speed of 6300 rpm the frictional torque increases by about 4 % compared to the unpressurised variant. The increase in frictional torque (4 %) is very similar to the increase in radial load (3 %)

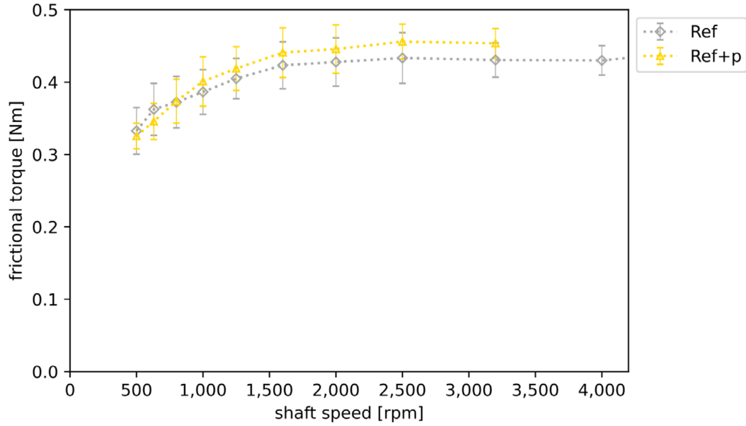

Figure 12: Seal torque over shaft speed with and without pressure

6 Simulation of the O arrangement with measured torque

The simulation of the O arrangement of chapter 4 is updated with the measured torque at the seal. In this simulation the frictional power is calculated with the frictional torque at the respective shaft speed and is applied directly in the contact area instead of the previously used frictional power model (standard seal, no pressure). Figure 13 compares the measurements with the updated simulation results.

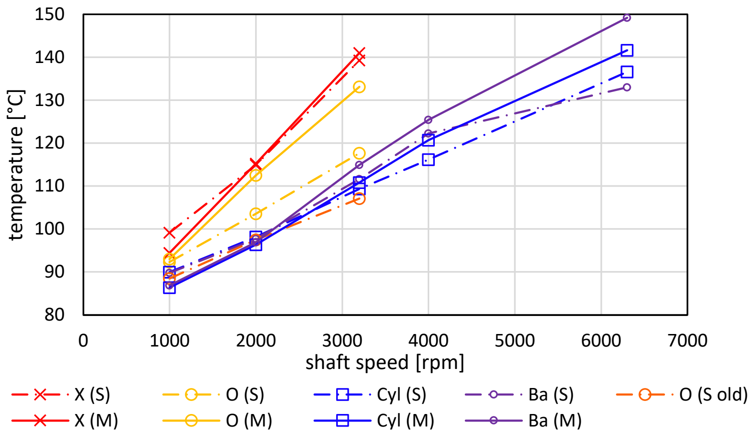

Figure 13: Maximum temperature at the airside of the sealing lip: simulation results (dashed) compared to the measured temperatures (full colored).

In order to get a comparable result from the simulations the maximum temperature at the airside of the sealing lip is compared with the measurements. These simulated results are marked with an (S). The results from the measurements are marked with an (M). The simulation closely matches the results from the temperature measurements at the test bench. The O arrangement O (S) still produces colder simulation results with a maximum deviation of 15 K, however this is still an improvement compared to the deviation of 26 K of the previous simulation O (S old). The frictional torque of the seal ring during the tests with the O arrangement was likely higher. A potential cause for this could be the higher temperature of the oil next to the seal in comparison to the tests with a pressurized single seal (Figure 12) and the different oil levels at the seal (centerline for single seal and flooded for O arrangement).

The simulations depend on the frictional torque of the seal and the bearings. Therefore, measurements on a test bench are still necessary.

7 Conclusion

Rolling-element bearings near the seal strongly influence the contact temperature. The heat generated in the bearings due to friction results in an increase in the temperature of the fluid near the seal, and consequently, an increase in the contact temperature. Tapered roller bearings have the highest torque compared to the other variants and pump oil. Depending on the installation situation the pumping leads to a higher or lower fluid level near the seal. The X arrangement significantly lowers the fluid level in the area near the seal, causing the highest contact temperatures. The O arrangement significantly increases the fluid level and has the highest overall torque (including the bearings and the seal). For higher shaft speeds the O arrangement increases the pressure at the seal leading to higher frictional power at the sealing edge. However, the O arrangement has a lower contact temperature than the X arrangement due to better cooling. The variants with no pumping effect (Ref-SV, Cyl and Ba) show very similar temperature differences to the oil next to the seal, which increase with speed. Since the temperature in the contact area cannot be measured directly, simulations can be used to get an understanding of the temperature in the contact area.

8 Acknowledgements

The IGF project 21587 N/1 of the Forschungskuratorium Maschinenbau e.V. (FKM) was funded by the AiF as a support of the Industrielle Gemeinschaftsforschung (IGF, Industrial Collective Research) by the Federal Ministry for Economic Affairs and Climate Action (BMWK) on the basis of a decision by the German Bundestag.

Supported by:

Federal Ministry for Economic Affairs and Climate Action

on the basis of a decision by the German Bundestag

FKM Forschung im VDMA

9 References

[1] **Bauer, F.:** *Federvorgespannte-Elastomer-Radial-Wellendichtungen. Grundlagen der Tribologie & Dichtungstechnik, Funktion und Schadensanalyse*, Wiesbaden, Heidelberg: Springer Vieweg, 2021, Springer Fachmedien Wiesbaden, - ISBN 978-3-658-32922-8.

[2] **Kunstfeld, T.; Haas, W.:** *Dichtungsumfeld. Einfluss des bespritzungs- und luftseitigen Umfeldes auf die Dichtwirkung von Radial-Wellendichtungen*. Abschlussbericht FKM Vorhaben Nr. 236, Frankfurt am Main: FKM, 2001, Forschungskuratorium Maschinenbau e.V. (FKM).

[3] **International Organization for Standardization:** ISO 6194-1: *Rotary shaft lip-type seals incorporating elastomeric sealing elements - Part 1: Nominal dimensions and tolerances.* 15.09.2007.

[4] **International Organization for Standardization:** ISO 6194-2: *Rotary shaft lip-type seals incorporating elastomeric sealing elements - Part 2: Vocabulary.* 2009.

[5] **Ahmed Abdelbary; Li Chang:** *10 - Practical applications of tribology.* published in: *Principles of Engineering Tribology*, Ahmed Abdelbary; Li Chang: Academic Press, 2023 - ISBN 978-0-323-99115-5.

[6] **Schaeffler Technologies AG & Co. KG:** *A Brief Introduction to Rolling Bearings,* URL: https://www.schaeffler.com/remotemedien/media/_shared_media/08_media_library/01_publications/schaeffler_2/brochure/downloads_1/bwk_de_en.pdf. [accessed on 06.12.2023].

[7] **Feldmeth, S.; Olbrich, C.; Bauer, F.:** *Influence of Lubricants on the Thermal Behaviour of Rotary Shaft Seals.* 21th International Sealing Conference (ISC), Stuttgart, 12.-13. Oktober 2022; Fluidtechnik; Frankfurt am Main: Fachverband Fluidtechnik im VDMA e.V, 2022, S. 147–161.

[8] **Marchetti, K.:** *Schäden an Dichtungen durch Alterung - Erfahrungen aus der Praxis.* VDI Fachkonferenz Dichtungstechnik 2017, Schweinfurt, 27. / 28.06.2017, 2017, Vortrag 19.

[9] **Trelleborg Sealing Solutions:** *Rotary Seals,* URL: https://www.trelleborg.com/seals/-/media/tss-media-repository/tss_website/pdf-and-other-literature/catalogs/rotary_gb_en.pdf?rev=-1. [accessed on 25.04.2024].

[10] **Feldmeth, S.; Bekgulyan, S.; Bauer, F.:** *Estimating the contact temperature and the pumping rate of rotary shaft seals*. JAHRBUCH 2024. 2023 , S. 129–146. ISGATEC GmbH Mannheim.

[11] **Schaeffler Technologies AG & Co. KG:** *Ball and Roller Bearings. Handbook on the design and calculation of rolling bearing arrangements*: Vereinigte Fachverlage GmbH, 2022, - ISBN 978-3-7830-0423-6.

[12] **SKF Group:** *Industrial shaft seals,* URL: https://cdn.skfmediahub.skf.com/api/public/09433a92e9164581/pdf_preview_medium/09433a92e9164581_pdf_preview_medium.pdf. [accessed on 17.11.2023].

[13] **Institute of Machine Components (IMA):** *High-Speed Universal Test Bench. IMA-TechSheet #101040 V1,* URL: https://www.ima.uni-stuttgart.de/dokumente/forschung/dichtungstechnik/einrichtungen/en/101040en.pdf. [accessed on 05.12.2023].

[14] **Zepf, D.:** *Experimental Investigation of the Influence of Lubricants, Shaft Coatings and Shaft Sleeves on the Thermal Behaviour of Rotary Shaft Seals*. Master's thesis [in German], 2022, University of Stuttgart, Institute of Machine Components, Stuttgart.

[15] **International Organization for Standardization:** ISO 15312: *Rolling bearings — Thermal speed rating — Calculation.* 02.2018.

[16] **Olbrich, C.; Feldmeth, S.; Hannss, J.; Grün, J.; Bauer, F.:** *Temperaturberechnung – Erweitertes Berechnungstool für die Kontakttemperatur bei Radial-Wellendichtungen*. Heft 349, Forschungskuratoriums Maschinenbau e.V., Abschlussbericht, Vorhaben 919, Frankfurt am Main, 2023.

[17] **Fluke Deutschland GmbH:** *Thermal Imagers Fluke Ti480 PRO,* URL: https://dam-assets.fluke.com/s3fs-public/ti480proum-eng0300.pdf?jVqXM47s982AOMYiRVWm3gh2LI7DWz5j. [accessed on 13.05.2024].

[18] **Wollschläger, F.:** *Experimental analysis of the influence of the sealing environment on the thermal behavior of rotary shaft sealsWellendichtungen*. Thesis project [in German], 2022, University of Stuttgart, Institute of Machine Components, Stuttgart.

[19] **Hannss, J.; Grün, J.; Olbrich, C.; Feldmeth, S.; Bauer, F.:** *Multiphase Conjugate Heat Transfer Analyses on the Assembly Situation of Rotary Shaft Seals*. Applied Sciences. 2023, 13 (19).

[20] **Hengstler, P.; Ji, Y.; Seiler, S.; Weng, D.:** *Analyse des Anlageverhaltens von Radial-Wellendichtring und Welle mittels FEM-Simulation*. project report [in German], 2015, University of Stuttgart, Institute of Machine Components, Stuttgart.

10 Authors

University of Stuttgart, Institute of Machine Components (IMA)

Pfaffenwaldring 9, 70569 Stuttgart, Germany:

Christoph Olbrich, M. Sc., ORCID 0000-0002-6978-921X,

christoph.olbrich@ima.uni-stuttgart.de

Jacqueline Gerhard, M. Sc., ORCID 0000-0002-4879-5653,

jacqueline.gerhard@ima.uni-stuttgart.de

Dipl.-Ing. Simon Feldmeth, ORCID 0000-0003-0018-0710,

simon.feldmeth@ima.uni-stuttgart.de

Prof. Dr.-Ing. Frank Bauer, ORCID 0000-0001-7799-7628,

frank.bauer@ima.uni-stuttgart.de

https://doi.org/10.61319/R1WJDXWC

A high-pressure radial shaft seal with enhanced wear resistance

Nino Dakov, Martin Franz, Jeff Baehl, Sam Wagoner

High-pressure radial shaft seals are typically used in hydraulic pumps to seal a continuously rotating shaft within a housing bore. When the seal is pressurized, the sealing lip's contact with the shaft increases, which leads to higher wear. At very high pressures, the seal's cross-section can collapse, forcing the garter spring out of its retaining groove. This issue can be mitigated by stiffening the membrane area, though this reduces the seal's ability to accommodate radial movement of the shaft. The current study presents a new approach to stabilize the seal's cross-section. Multiple pads are added on the seal above the membrane area and next to the spring. As a result, a considerably lower laydown is achieved, resulting in improved wear performance during tests. Additionally, the pads help maintain the spring's position. The theoretical considerations are supported by tests conducted under varying pressure and shaft speed conditions, demonstrating the practical benefits of this new seal design.

1 Introduction

Radial shaft seals (RSS), also known as radial oil seals (ROS), are used to seal continuously rotating shafts within housing bores, as depicted in Figure 1. These rubber-to-metal seals typically separate an air side from an oil side. The elastomer-covered metal insert ensures a proper static seal at the outer diameter, adding stability to the sealing profile. The sealing lip features a sharp sealing edge, which is connected to the metal insert by a flexible membrane. The sealing edge is pressed against the shaft and energized by a garter spring [1-2].

The contact force, also referred to as radial force or radial load, between the seal and the shaft results from both a garter spring as well as the elastic deformation of

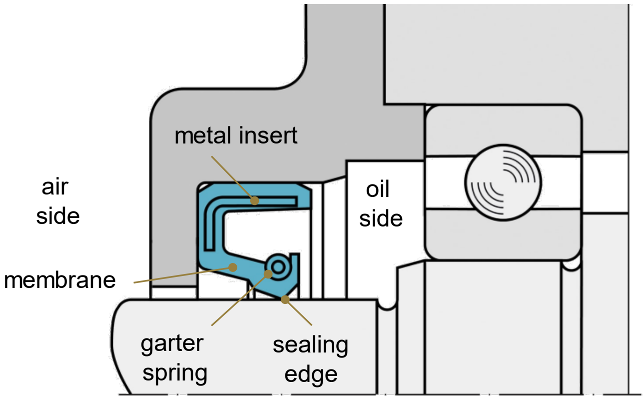

Figure 1: Schematic of a radial shaft seal

the seal due to the overlap with the shaft. The sealing edge is further characterized by an air side contact angle to the shaft that is smaller than the oil side contact angle, creating an asymmetric contact pressure distribution. The asymmetry in contact pressure is essential for reliable dynamic sealing [1].

The membrane adds flexibility to the sealing edge, allowing it to accommodate the misalignment-induced oscillations of the shaft during operation. By design, the RSS is capable of sealing against pressure from the oil side. When the seal is pressurized, both the membrane and the sealing edge are pressed firmly onto the shaft. The pressure activation of the lip ensures leak-tight sealing under high pressure on the oil side. However, increased pressure also enlarges the contact area, leading to higher friction, elevated contact temperatures, and ultimately, accelerated wear of the seal [2].

1.1 High-pressure radial shaft seals

High-pressure radial shaft seals are typically used in gearboxes, hydraulic pumps and motors, speed reducers and robotic applications. To endure the additional load on the lip from pressure activation, these seals feature special lip designs. For high pressure environments, designs are optimized to reduce the laydown of the sealing lip on the shaft typically by either shortening or thickening the membrane, thereby increasing the membrane's stiffness [1], Figure 2. Additionally, the use of a harder elastomer grade can further enhance performance. The metal insert is overmolded with a thicker elastomer layer and reinforced with an axial support, ensuring the spring remains in place even when the sealing lip is strongly deformed.

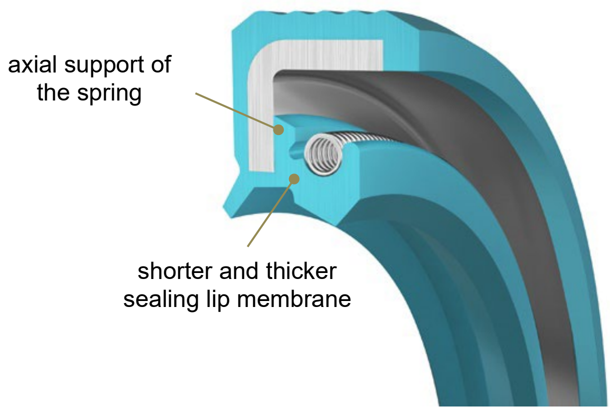

Figure 2: Design aspects of high-pressure radial shaft seals

However, there is an upper limit to how much the membrane area can be stiffened. Some flexibility of the sealing lip is essential for the RSS to compensate for shaft runout. Additionally, as the membrane becomes stiffer, the radial load increases.

Excessive radial load leads to unwarranted friction and wear, potentially causing premature thermal failure of the sealing system.

1.2 Performance criteria

To assess the dynamic properties of a high-pressure RSS, different performance criteria are considered:

- Leak-tightness
- Friction torque and contact temperature
- Wear resistance

Indication as to how well the criteria are met, can be drawn from analytical and numerical calculations. Actual tests are then carried out to measure performance criteria and validate the design.

2 Materials and methods

Finite element analysis (FEA) was used to evaluate the deformation and stress state of the seal. Subsequently, a dynamic test was conducted to validate the design's wear performance, as well as other general factors such as friction torque and contact temperature.

2.1 Simulation approach

A 3D-FEA model is utilized to analyze the deformation and stress state of the seal, focusing on a circumferential segment spanning 60 degrees. The mechanical properties of the 75 ShA fluoroelastomer (FKM) material were characterized using a hyper-elastic material model. The actual 3D geometry of the spring was included in the FEA to study the interaction between the spring and the spring groove. The metal insert was excluded, with nodes contacting the metal fixed in all possible degrees of freedom. The assembly of the seal into the housing, and consequently the effect of the static sealing at the outer diameter, were omitted from the analysis.

The FEA consisted of four analysis steps:

1. Assembling the garter spring into the spring groove.
2. Mounting the radial shaft seal onto the shaft.
3. Increasing the temperature to the fluid's operating temperature of 70 °C, accounting for thermal expansion and softening of the elastomer.
4. Pressurizing the seal to 10 bar.

In the numerical model, the contact stress between the seal and the shaft under higher pressure were examined in detail. The contact stress is crucial for understanding the seal's leak-tightness and wear behavior during operation. Furthermore, the friction torque and contact temperature were estimated using the radial load of the seal and the contact area between the seal and the shaft.

2.2 Test equipment and procedure

Validation tests are performed to assess the performance of the RSS design. The test rig, shown in Figure 3, consists of a shaft positioned inside the test chamber, with a RSS installed at each end. The shaft is supported by two bearings within the chamber. During testing, a continuous oil flow of 1 liter/min simulates real-world conditions akin to a hydraulic pump or motor. The chamber is fully flooded with oil and the oil temperature is kept constant at 60 °C.

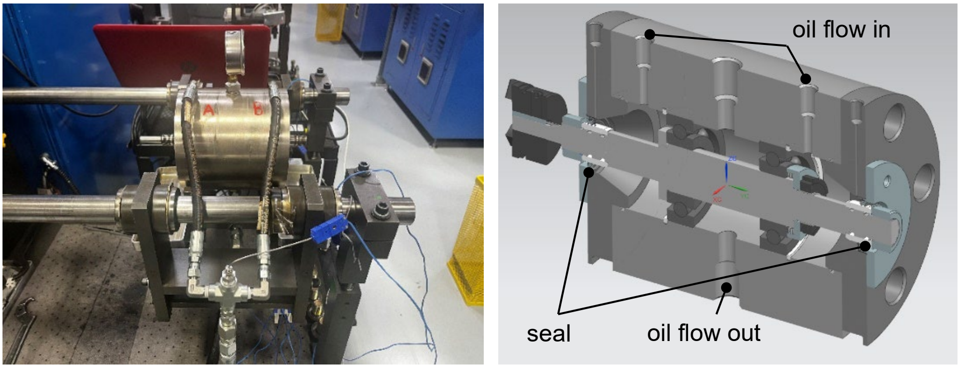

Figure 3: Rotary test rig

The validation tests are carried out at a steady pressure-velocity-value (pv-value) of 10 bar·m/s over a 48-hour period. The following pressure and velocity combinations are examined:

- 3.5 bar x 2.86 m/s
- 5.0 bar x 2.00 m/s

In the test, dynamic leak-tightness is continuously monitored. Any leakage is collected in a beaker and measured. Additionally, friction torque is recorded via a load cell. After the test, the wear of the seal on the shaft is analyzed through light imaging laser profile sensor measurements [3].

The shaft sleeves used are plunge-ground and hardened at ≥ 55 HRC. The surface roughness values, Ra and Rz, range from 0.2 to 0.5 µm and 1.2 to 3.0 µm, respectively. The bearing ratio is maintained between Rmr = 50 to 70 % at a cutting depth of c = 0.25 x Rz.

3 New design for high-pressure radial shaft seals

To prevent the cross-sectionsl collapse under high pressures, pads are incorporated into the radial shaft seal between the garter spring and the shaft, Figure 4. The pads act as an axial stop for the spring. The deformation of the free end of the spring retaining groove is limited locally which results in stabilizing the sealing lip at higher pressure. The example in Figure 4 features a radial shaft seal measuring 28 x 40 x 6 mm with a total of six equally spaced pads along the circumference.

From a manufacturing feasibility standpoint, these pad features are a highly cost-effective performance enhancement, as they can be easily integrated into the tooling process and produced using standard manufacturing techniques.

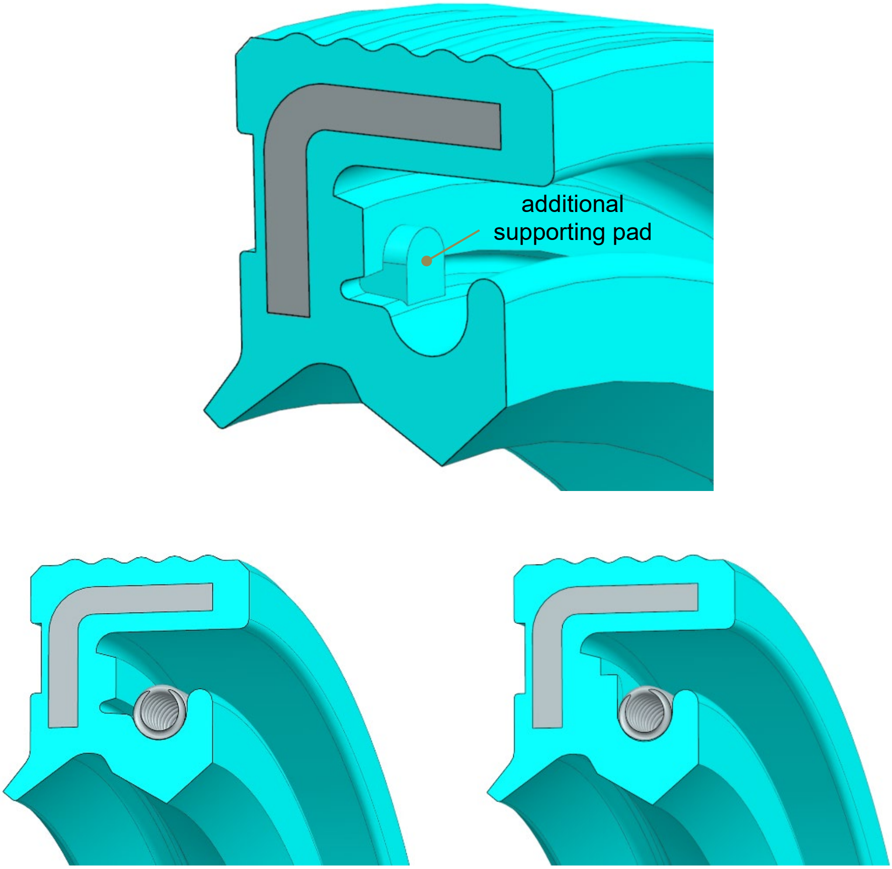

Figure 4: Radial shaft seal design for a pv-value of 10 bar·m/s of size 28 x 40 x 6 mm with six supporting pads (top), section view outside pad (bottom left) and at/near pad (bottom right)

4 Results and discussion

The presented design was analyzed numerically and validated experimentally. The results are summarized and discussed in the following two sections.

4.1 FEA results

The focus of the FEA is on the deformation of the seal under high pressure. The complex interaction between the spring, groove and pad is illustrated using a detailed 3D model of the actual spring in its groove. Figure 5 shows the effect of the pad on the deformation of the seal's cross-section at an overpressure of 10 bar. At the pad's location, the cross-section tilts 27 degrees relative to the radial direction, while outside the pad area, the tilting increases to 34 degrees which is 25 % greater. At the pad, the garter spring provides additional support, acting like a stiff inlay, which stabilizes the lip and reduces deformation at higher pressures. Consequently, the pad locally reduces the laydown of the sealing lip on the shaft.

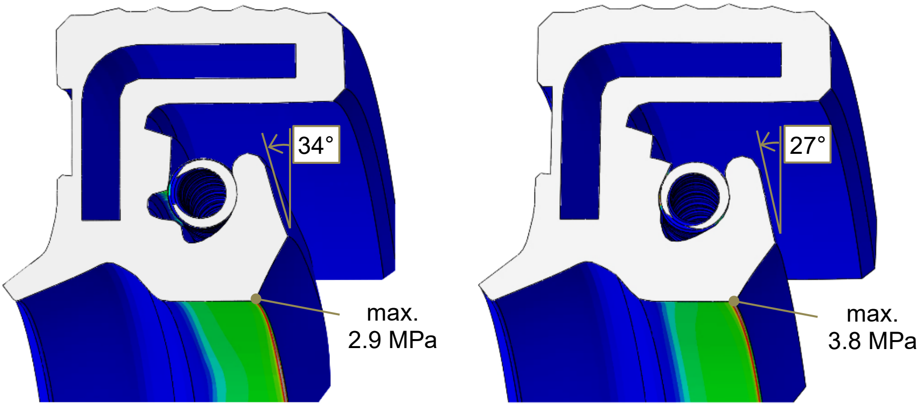

Figure 5: Seal at 10 bar pressure, cross-section at a position without pad (left) and at position of pad (right)

The question arises regarding the effect of the pad at different pressure levels. Figure 6 shows polar plots of the contact band width along the circumference at different pressure values. Starting at 3.5 bar, an undulation of the contact band is visible. The maximum contact width aligns with that of a seal design without supporting pads. At the pad locations, the contact width is reduced, forming a daisy pattern along the seal's circumference. The greatest reduction in contact band width, approximately 15%, occurs at 3.5 and 5 bar. At 7.5 bar, the contact width reduction decreases to about 9 %. Thus, for the given pad design, the optimal reduction in contact area is achieved between 3.5 and 5 bar. Moreover, the pad design can be modified to better achieve a lower contact area within a specific pressure range.

The reduced contact width leads to a lower friction torque and less wear on the seal. Additionally, the undulation in the sealing contact can enhance lubrication underneath the sealing lip, prolonging the lifetime of the seal. Up to an overpressure of approximately 5 bar, the undulation amplitude is proportional to the pressure level, indicating a self-intensifying effect. Above 5 bar, the positive effect stabilizes at an absolute contact band width reduction of about 0.15 mm.

Another aspect that favors improved lubrication is the variation in the maximum contact pressure along the circumference. Figure 5 shows that the contact stress between two pads is 2.9 MPa. At the pad location, the maximum contact stress increases to 3.8 MPa, representing a 30 % increase at the investigated pressure level of 10 bar. This means the contact band width is minimal at the pad, while the contact stress is maximal. These 3D contact area and pressure distributions are deemed favorable for forming a stable lubrication film between the seal and the shaft.

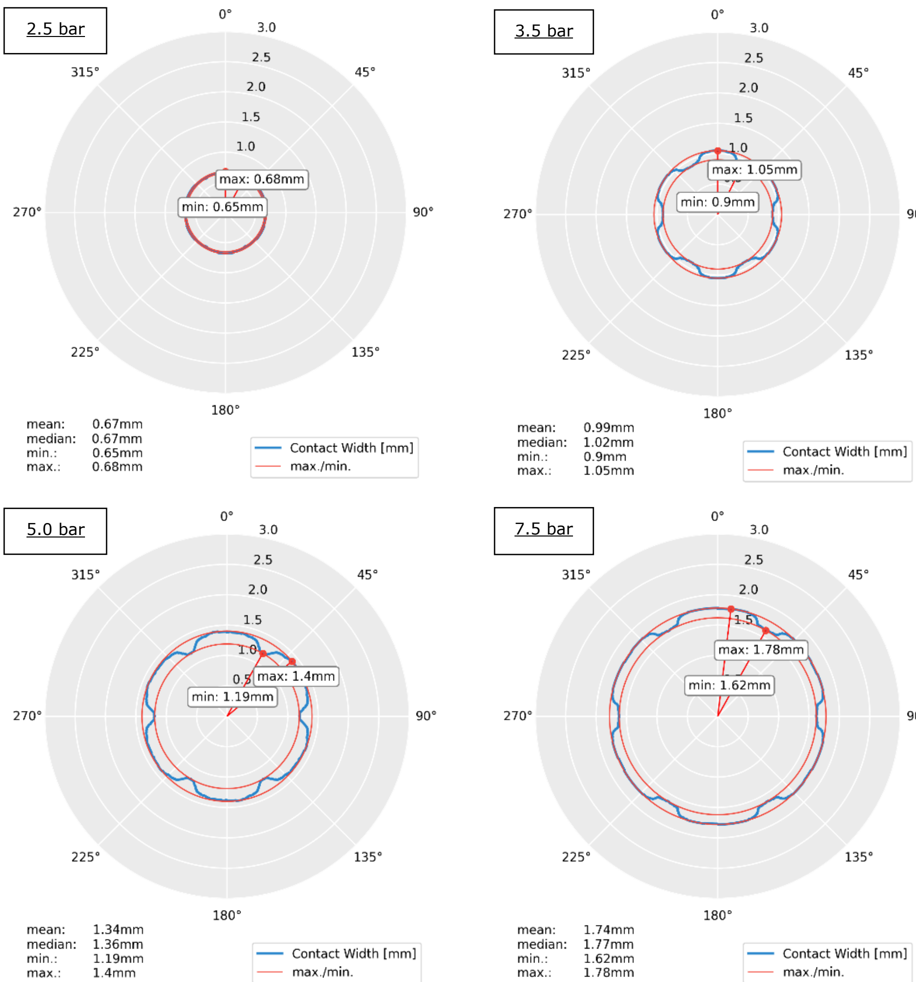

Figure 6: FEA contact band width along circumference at different pressure levels

4.2 Test results

The new seal design concept underwent testing as outlined in Section 2.2, using a standard high-pressure RSS design without supporting pads as a benchmark. All tests were completed without any leakage. The wear results for both pressure and velocity combinations are shown in Figures 7 and 8.

Figures 7 a-b) and 8 a-b) depict light images of the wear tracks in the seals' running areas. Except for the new seal design at 3.5 bar x 2.86 m/s in Figure 7 a), all seals exhibit circumferential grooves and a wear band width (WBW) ranging from 1 to 1.6 mm. The benchmark seals show a significantly wider WBW compared to the padded seals. Furthermore, it can be inferred that at the same pv-value, higher pressure results in a broader WBW. However, visual analysis reveals that the WBW of the new seal design varies along the circumference, making precise quantitative comparison impossible based on a single-spot WBW measurements for each seal.

For a more detailed analysis, the wear track was measured off-shaft over 360° using laser profilometry [2]. A total of 10,000 profiles were recorded along the circumference and assembled into a pseudo 3D plot of the seal's surface, as shown in Figures 7 c-d) and 8 c-d). The left and right borders of the running area, highlighted in green, were identified using a lower and upper limit for the gradient of the profiles in axial direction. From these profiles, it is evident that, in the addition to a greater width, the benchmark seal has a considerably higher maximum depth in the wear track. The circumferential grooves in the benchmark seals' wear track are also visible in the 3D pseudo-topography, indicating more severe damage compared to the padded design.

The WBW was evaluated as the distance between the left and right ends of the wear track, as shown in Figures 7 c-d) and 8 c-d). Quantitative WBW comparisons are displayed as polar plots in Figures 7 e-f) and 8 e-f). Both at 3.5 bar x 2.86 m/s and 5 bar x 2 m/s, the padded seal design exhibits a regular daisy pattern in the WBW. Consistent with the FEA results, the minimum WBW aligns with the location of the pad. At 3.5 bar x 2.86 m/s, the average WBW of the new design is 1.22 mm, which is 20 % less than the benchmark seal's mean width of the wear track of 1.52 mm. At 5 bar x 2 m/s, the average reduction in the wear band due to the stabilizing effect of the pads is 16 %, a similarly substantial decrease.

The reduced contact area of the padded design directly impacts the maximal frictional power loss and contact overtemperature, shown in Figure 9. Contact overtemperature refers to the difference between the contact area's temperature, measured using thermography imaging, and the oil sump temperature in the test. Both seal designs exhibit higher fictional power loss and contact temperature at 3.5 bar and 2.86 m/s compared to 5 bar and 2 m/s. In terms of maximal frictional power loss, a 13 % reduction is achieved at 3.5 bar and 2.86 m/s. Regarding maximal overtemperature, both tests show a significant reduction with the padded design compared to the benchmark. At 3.5 bar and 2.86 m/s, the padded design's contact area

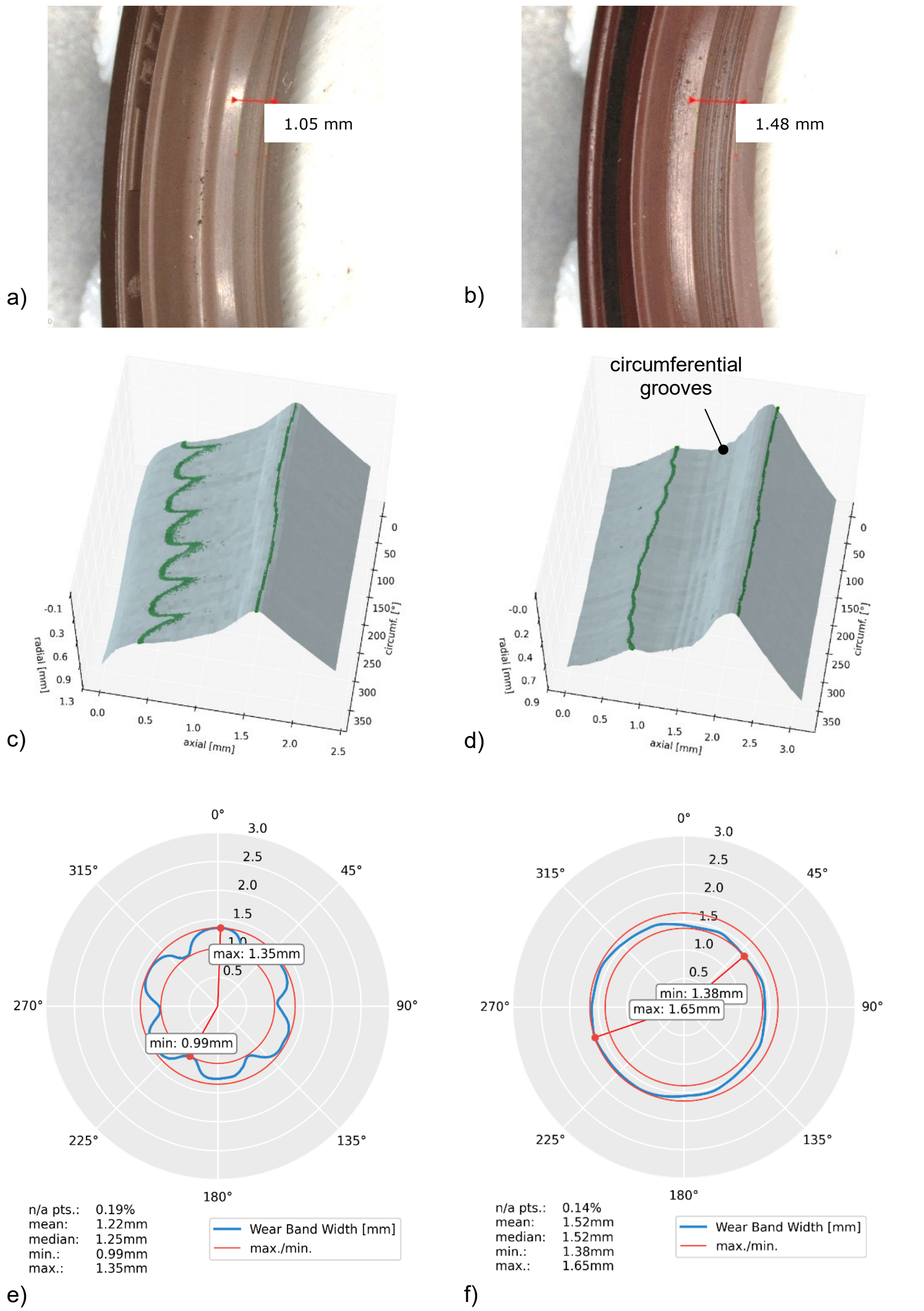

Figure 7: 3.5 bar x 2.86 m/s test, padded design (left) vs benchmark (right): a-b) light image of wear area; c-d) 360° of laser profile measurements; e-f) wear band width

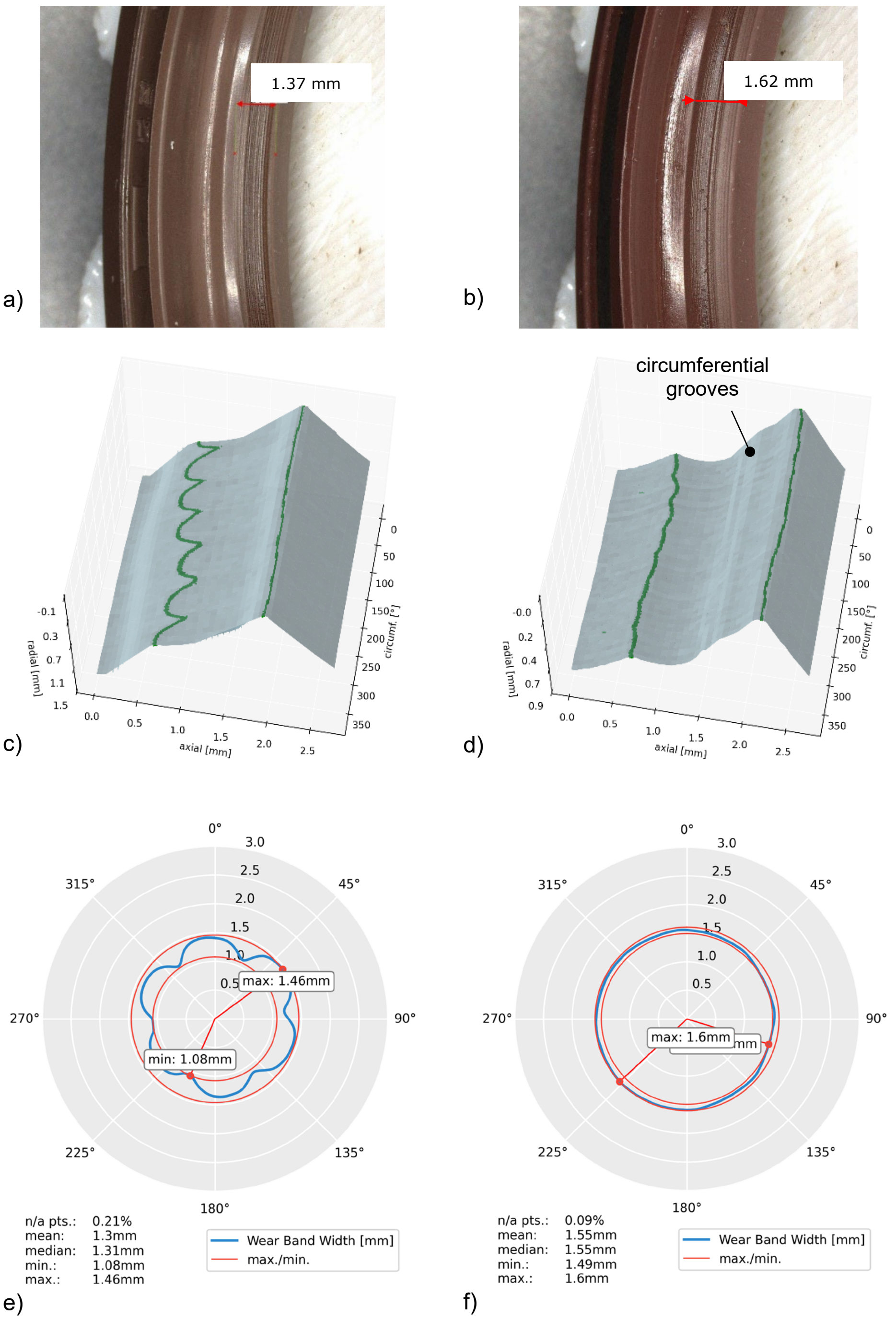

Figure 8: 5 bar x 2 m/s test, padded design (left) vs benchmark (right): a-b) light image of wear area; c-d) 360° of laser profile measurements; e-f) wear band width

is 7 K cooler, while at 5 bar and 2 m/s, the pads provide an advantage of approximately 3 K. Notably, in accordance with the Arrhenius equation [4-5] a 10 K reduction in the temperature can substantially increase service life by nearly halving the speed at which aging effects, such as compression set, occur in the elastomer material.

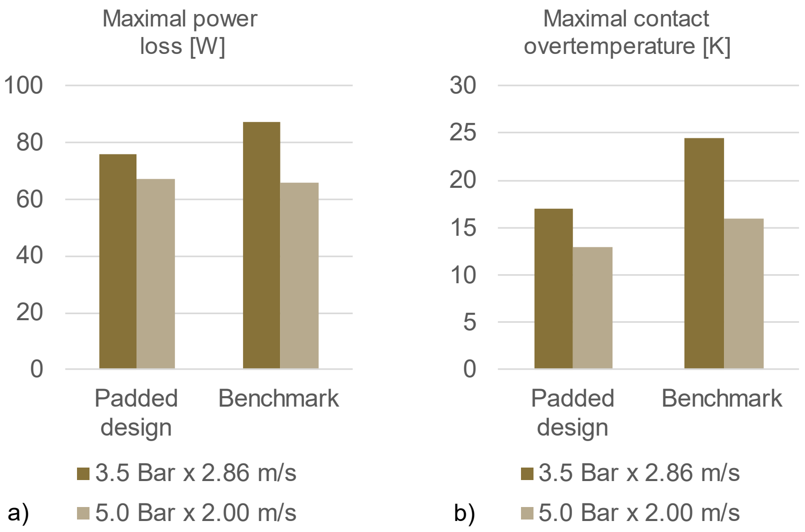

Figure 9: Summary of the measured a) maximal power loss and b) maximal contact overtemperature

5 Summary and conclusion

High-pressure radial shaft seals are essential for various applications, including gearboxes, hydraulic pumps and motors, speed reducers and robotics. To withstand high pressure, these specialized radial shaft seals feature a shorter and thicker sealing lip membrane. In this study, we introduced a new design for a 10 bar·m/s radial shaft seal, incorporating additional pads along the seal's circumference. Under high pressure, the pads stabilize the cross-section by minimizing the laydown of the sealing lip.

A detailed 3D FEA model was used to thoroughly analyze the new design. The results indicated a significant decrease in the contact width at the pad locations for a pressure range from 3.5 to 5 bar. Performance benchmarks were conducted at 3.5 bar x 2.86 m/s and 5 bar x 2 m/s, comparing the padded seal design to a conventional high-pressure seal. The innovative padded design demonstrated considerably improved wear performance, exhibiting a distinct daisy-shaped wear bandwidth pattern consistent with the contact width pattern predicted by FEA.

Moreover, the reduced wear of the new design concept led to lower friction power loss and a decrease in maximal contact temperature during testing. These findings highlight the overall performance enhancement achieved through the innovative pad feature.

6 References

[1] Müller, H. K., Nau., B. S.: *Fluid sealing technology*, Marcel Dekker, New York, 1998, ISBN 978-0-8247-9969-4.

[2] Horve, L.: *Shaft seals for dynamic applications*. CRC Press, 1996. ISBN 978-0-8247-9716-4.

[3] Baumann, M., & Bauer, F. *Moderne visuelle Untersuchungsmethoden für die Verschleißanalyse am Beispiel Radial-Wellendichtring*, 20th International Sealing Conference 2018, Stuttgart, Germany, 2018.

[4] Gillen, K. T., Bernstein, R., Celina, M.: *Challenges of accelerated aging techniques for elastomer lifetime predictions.* In: *Rubber Chemistry and Technology*, *88*(1), 1-27, 2015.

[5] Wehmann, C., Kulkarni, A., Durn, F., Gulcur, M.: *Modeling the compression set of elastomers to predict the lifetime of sealing systems by finite element analysis*, 21st International Sealing Conference 2022, Stuttgart, Germany, 2022.

7 Authors

Trelleborg Sealing Solutions Germany

Schockenriedstr. 1, 70565 Stuttgart, Germany:

Dr. Nino Dakov

ORCID 0000-0002-0989-9943, nino.dakov@trelleborg.com

Martin Franz

ORCID 0009-0008-0457-9116, martin.franz@trelleborg.com

Trelleborg Sealing Solutions Americas

2531 Bremer Rd, Fort Wayne, IN 46803, USA:

Jeff Baehl

ORCID 0009-0003-6939-1943, jeff.baehl@trelleborg.com

Sam Wagoner

ORCID 0009-0001-5957-0265, sam.wagoner@trelleborg.com

https://doi.org/10.61319/HHAECYDA

A smart seal energizer from shape-memory-alloy

Anne Marie Lehmann, Anja Dobrinsky, Martin Franz

Harsh operating conditions can significantly shorten a seal's lifetime, potentially harming people and the environment. One effective solution to this challenge is the adoption of actuatable seals that can adapt to varying operating conditions. Shape-memory-alloys (SMA) serve as ideal actuators for polymer seals, thanks to their high operating displacement, relatively low tension load and flexible design capabilities. This work presents a proof of concept for a polytetrafluoroethylene (PTFE) rod seal energized by a SMA wire. The wire is coiled around the seal's outer circumference and activated through induction. Upon activation, the wire contracts, thereby increasing the seal's radial load. The adjustable radial load allows the sealing function and friction properties to be precisely tailored to the specific operating conditions in application.

1 Introduction

Global changes, such as Industry 4.0 [1], climate change and increasing individualization, demand flexibility and adaptation. In modern technical systems, harsh operating conditions already challenge the longevity of seals . A crucial factor for a seal's lifespan in dynamic application is the optimal distribution of contact pressure. Typically, sealing solutions employ energizers like metal springs or elastomer O-Rings to ensure and maintain adequate contact pressure. There are primarily two conventional approaches for energizers in dynamic sealing systems: the inherent elasticity of sealing materials and the additional use of steel springs.

Some sealing solutions can adapt passively to varying operating conditions through mechanisms such as thermal expansion [2] and centripetal forces that cause displacement and deformation [3]. Nevertheless, the lifetime of sealing systems is finite always subject to improvement. Actively adapting a sealing system using smart materials represents a promising third approach to optimally adjust contact pressure and extend a seal's lifetime.

SMAs are well-known smart materials and have exceptional displacement and restoring properties [4]. This paper explores how a SMA can be utilized to regulate the contact pressure of a sealing profile, potentially enhancing the overall performance and durability of sealing systems.

2 Theoretical background

2.1 Dynamic Seals

Dynamic seals are essential components in various mechanical systems, ensuring the containment of fluids or gases while permitting relative motion between parts.

Unlike static seals, which remain stationary, dynamic seals must accommodate movement without compromising integrity.

As depicted in Figure 1, a basic dynamic seal comprises a movable seal body (SB) and a surface in motion (MS) that moves relative to the seal body. The primary sealing interface (P) is formed between the mating seal faces. The gap at this interface, known as the "seal gap" or "film thickness," is extremely narrow, typically measured in micrometers (µm).

The secondary sealing interface (S) prevents leakage between the seal body and the housing (H). This is achieved by applying a closing force (F), which reduces clearance at both the primary and secondary sealing interfaces. Additionally, a retention device (R) prevents the seal body from slipping due to friction with the moving surface. In more complex sealing systems, a second sealing body often forms an additional secondary sealing interface (S) [2].

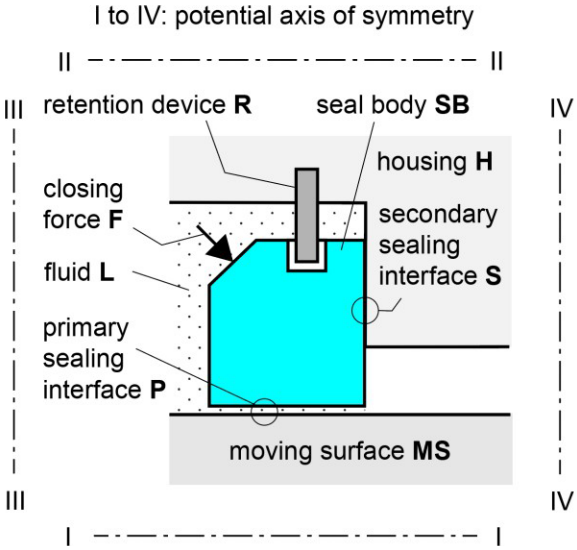

Figure 1: Schematic of a dynamic seal (adapted from [2]).

Maintaining the closing force between the counter surface and the sealing body is crucial for effective sealing. This is achieved by ensuring the total specific load (closing force minus the sealing interface area) exceeds the pressure of the sealed fluid. Figure 1 illustrates these closing forces as a combined closing force (F). Additional closing forces can be implemented, as demonstrated in Figure 2**Fehler! Verweisquelle konnte nicht gefunden werden.**. Mechanical seals utilize compression springs (a) or bellows, which act as springs. Elastomeric seals can be preloaded through dimensional interference and elastic deformation of the seal itself (b). Soft packing rings are axially precompressed, creating a closing force at the sealing interface (c) [2].

Ideally, the closing force should compensate for wear and adapt to dynamic conditions. Some sealing solutions can adapt passively, due to different operational conditions linked to thermal expansion [2] and centripetal forces, which cause displacement and deformation [3]. Active adaptation is not yet available for conventional sealing technologies. This paper focuses on an active, adaptable contact force based on

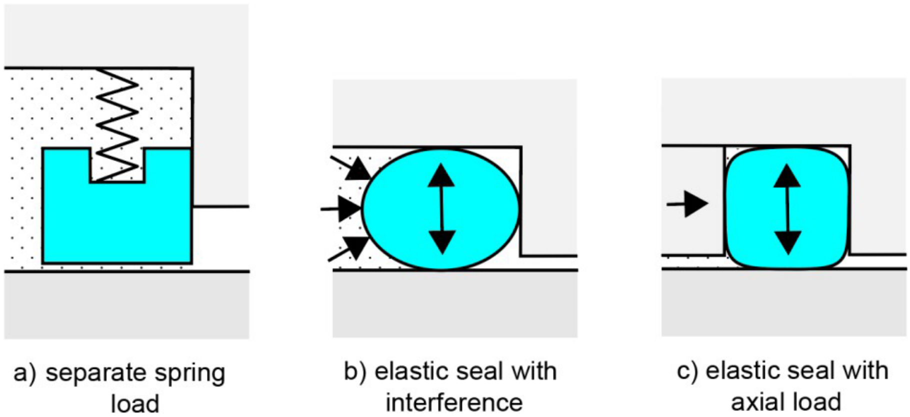

Figure 2: Examples of conventional preloading concepts (adapted from [2]).

the concept of separate spring loading as shown in Figure 2a.

2.2 Shape-memory alloys (SMAs)

SMAs are a type of thermo-mechanical-transformation materials that are known for unique ability to switch between different atomic structures based on temperature. The most common compositions are copper-aluminium-nickel (CuAlNi) and nickel-titanium (NiTi), although they can also be synthesized using other elements like zinc, copper, gold and iron. While commercially available iron-based and copper-based SMAs (such as Fe-Mn-Si, Cu-Zn-Al, and Cu-Al-Ni) are more affordable, NiTi-based SMAs are preferred in most applications due to their stability and practicality [5] [6] [7].

The remarkable effects of SMAs arise from their ability to transition between the martensite and austinite phases. Martensite has a face-centered cubic structure with an atomic packing factor (APF) of 68 %, while austinite has a body-cantered cubic structure with an APF of 74 %, as shown in Figure 3. This phase transition causes a volume shift, with specific temperatures marking the start and finish of the transitions (M_s, M_f, A_s, A_f).

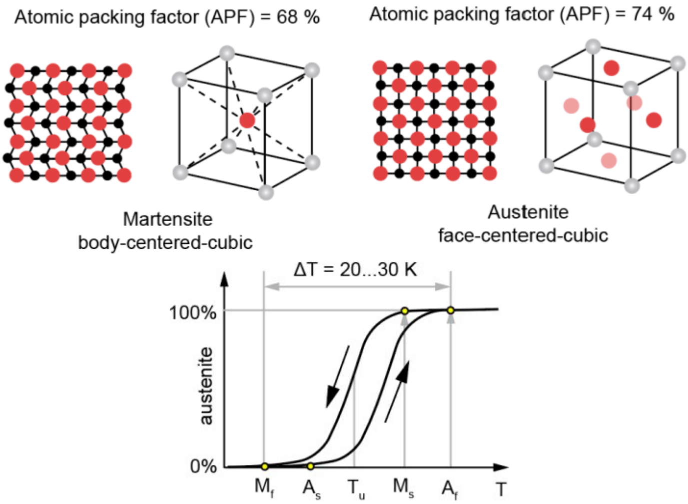

Figure 3: Transition from martensite to austenite (adapted from [4]).

In addition to temperature-induced effects, the martensite exhibits pseudo-plasticity, which is explained through a stress-strain-diagram and crystallography as shown in Figure 4. Initially, martensite exists in a twinned crystal structure (State A). Applying tension leads to elastic deformation, and at a specific tension (Point B), detwinning occurs. Heating the SMA above A_s and then cooling it reverses the deformation, re-twinning the martensite (pseudo-plasticity).

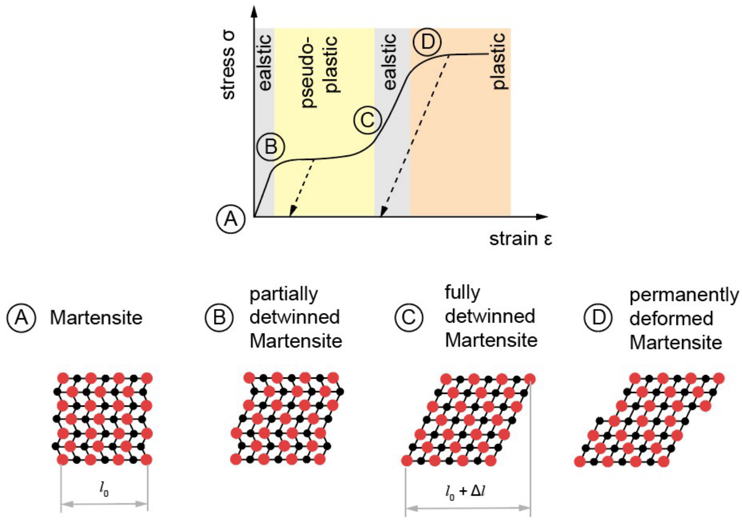

Figure 4: Pressure effects in the martensite structure (adapted from [4]).

Figure 5 shows how the combination of pseudo-plasticity and phase change can be used for the one-way effect. The material is pseudo-plastically deformed (A to C) and responds to a temperature shift with actuation (C to D). To repeat the actuation, the SMA must be cooled (D to A) and deformed again (A to C), with the material only memorizing the high-temperature austinite state. As to see in the diagram, a temperature increase from state A to D causes only a small change of deformation.

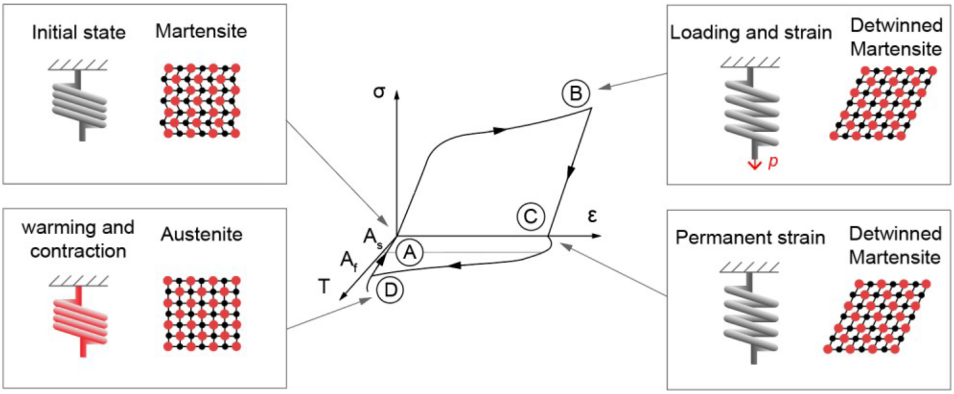

Figure 5: One-way effect (adapted from [4]).

For significant deformation between different temperatures, the two-way effect is necessary. This effect is achieved by training the SMA's microstructure through tension. The intrinsic material effect is shown in Figure 6, where the SMA cycles between detwinned martensite and austenite states. This effect can be enhanced under tension, known as the extrinsic two-way effect.

To increase pressure in the SMA, force can be applied, either by a constant force , or by an antagonist spring (Figure 7).

In this paper, the extrinsic two-way effect is used, in which the SMA is acting against a spring.

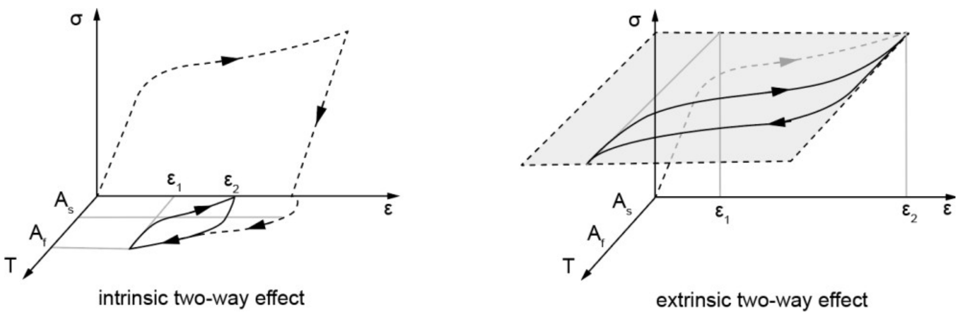

Figure 6: Two-way effect (adapted from [4]).

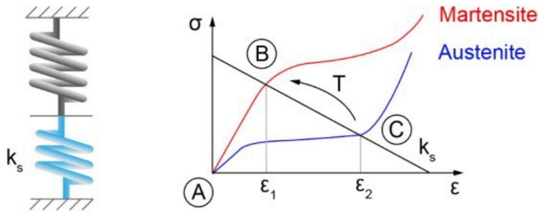

Figure 7: Two-way effect under variable force (adapted from [4]).

3 Test Set-up

The utilization of SMAs to adapt contact pressure was investigated through an experimental set-up. This process required several key steps:

- Selecting the appropriate SMA
- Developing an adaptable sealing concept
- Activating the smart energized seal
- Collecting data
- Establishing test procedures.

3.1 Selecting the appropriate SMA

The primary function of the SMA is to adjust the contact pressure of the chosen seal. It must be flexible and adaptable to various geometries. Key requirements for the SMA included shape-shifting at safe handling temperatures above ambient, availability in multiple sizes and a material that offers maximum design flexibility. A NiTiNol wire alloyed with NiTiCu was chosen, featuring an austinite finishing temperature of 60 °C (+/-5) and a thickness of 0.25mm and 0.5 mm.

3.2 Developing an adaptable sealing concept

The SMA serves as a smart energizer to adjust the radial load of a linear seal made from a bronze-filled PTFE compound. The seal's cross section is designed in a rectangular shape, as illustrated in Figure 8. The wire is positioned in a groove along the outer diameter of the rectangular ring. The wire ends are joined with a reef knot. Two different SMA wire thicknesses are chosen for placement in the groove:

- 0.25 mm
- 0.5 mm.

Figure 8: Design of the SMA actuated PTFE ring. a) CAD-PTFE ring with a groove, b) PTFE ring with SMA wire in the groove, c) reef knot of the SMA.

3.3 Activating the smart energized seal

The chosen SMA wire has a high nickel content, which gives it a relatively high magnetic permeability. This property makes it ideal for contactless, inductive heating, allowing for precise heating of the SMA wire compared to other heating methods.

The smart energized seal is primarily powered by a conventional laboratory power supply. The direct current from the power supply is converted into high frequency alternating current via an induction converter. This alternating current is then applied to a copper coil, which heats the SMA wire through induction.

3.4 Collecting data

The radial force of the smart energized seal is measured using a radial force measurement device in accordance with DIN 3761-9. Instead of employing a rod, the seal is mounted on two mandrels – one stationary and the other moveable, connected to a load cell. As the radial force of the seal increases, the gap between the mandrels decreases, causing deformation in the load cell. This load cell acts as a force-sensing resistor, which can be monitored using a voltage divider. The voltage signal is then amplified, recorded by a computer and displayed as a live graph. Figure 9 shows the test setup.

3.5 Establishing test procedures

For all experiments, the test setup shown in Figure 10 was used to examine the influence of the SMA wire on radial contact force. The success of these measurements hinged on two factors: observing significant thermal effects and ensuring the safety of personnel and equipment. To this end, only the necessary voltage was applied to the power supply for each measurement.

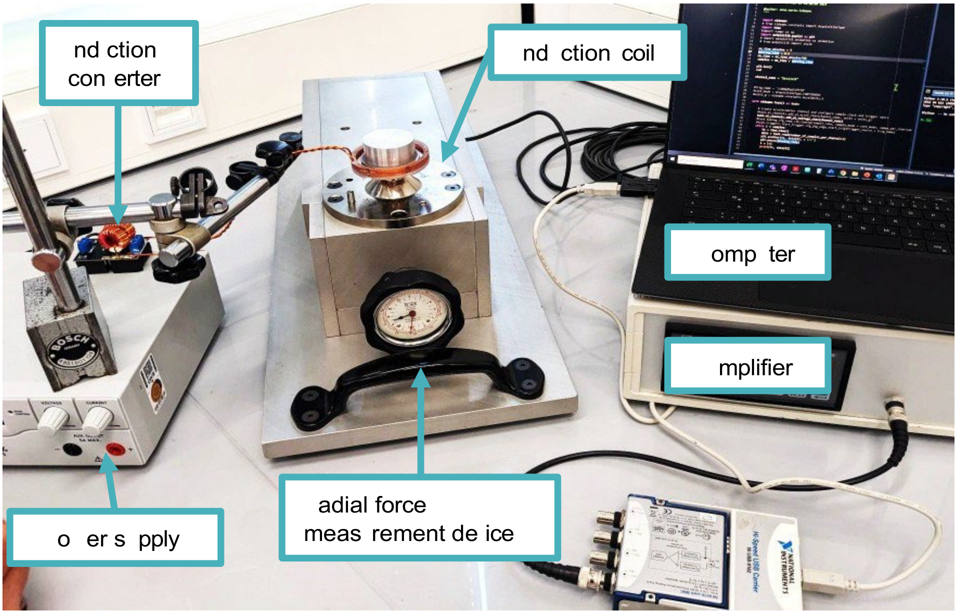

Figure 9: Test set-up for actuation and measuring the PTFE-SMA ring.

A human-in-the-loop approach was adopted, where an operator monitored the live graph, detected any unusual heat and adjusted the rotary knob of the power supply to balance safety requirements and data validity. The procedure involved switching on the power supply and observing the live graph until a notable change was detected. Two different wire sizes (0.25 mm and 0.5 mm) were tested and the tests were named accordingly:

- 0.25 actuated test
- 0.5 actuated test.

The second experiment aimed to determine whether the SMA wire could maintain a specific contact force. Here, the control loop was managed by a human operator, who monitored the live graph and adjusted the power supply accordingly. This experiment was conducted with the 0.5 mm-SMA wire and is referred to as the maintaining-force test. Results and Discussion

3.6 Results

Figure 10 shows the 0.25 actuated test and Figure 11 presents the results of the 0.5 actuated tests. Both tests begin with a measurement without activation. In the 0.25 actuated test, the radial force decreases with heating and increases again once the heating is stopped, allowing the set-up to cool passively by the environment. During the heating process from 20 to 53 s the graph shows a step-function.

Conversely, the result of the 0.5 actuated test shows an increase in contact pressure at the onset of heating and a decrease once the heating stops. The graph is smooth and reaches a similar level of radial force in the unactuated state after 7 s of passive cooling.

Figure 12 shows the maintaining-force test, which begins in an activated state. Similar to the 0.5 actuated test, stopping the heating after 17 s decreases the radial forces, which restarting it increases them. Stopping the heating again results in a rapid decrease in radial force to a level comparable to the last non-heated phase. It was possible to maintain a contact force of approximately 60 N for about 100 seconds, albeit with some noise.

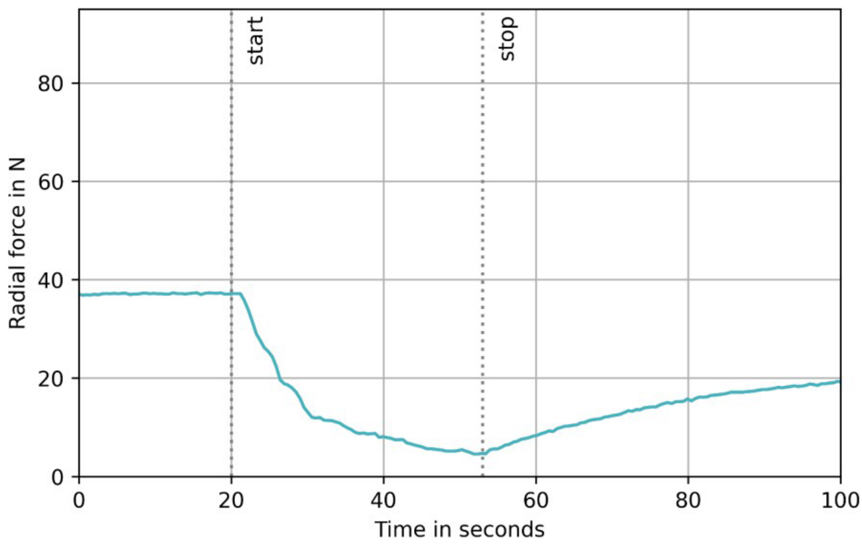

Figure 10: Radial force during heating a 0.25 mm SMA wire.

Figure 12 shows the maintaining-force test, which begins in an activated state. Similar to the 0.5 actuated test, stopping the heating after 17 s decreases the radial forces, which restarting it increases them. Stopping the heating again results in a rapid decrease in radial force to a level comparable to the last non-heated phase. It was possible to maintain a contact force of approximately 60 N for about 100 seconds, albeit with some noise.

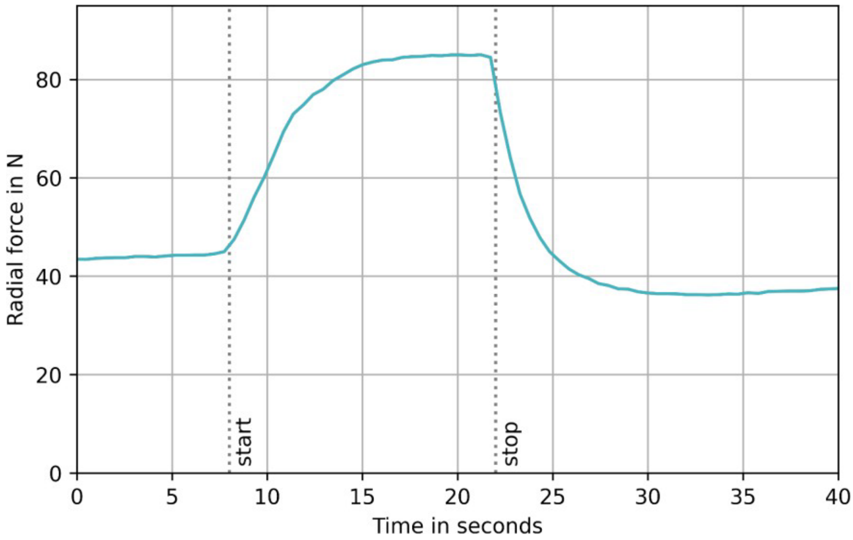

Figure 11: Radial force during heating a 0.5 mm SMA wire.

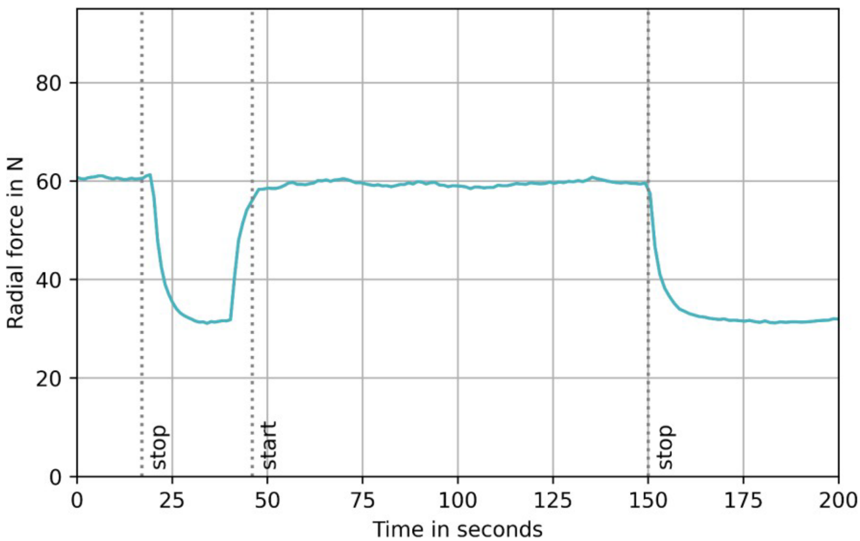

Figure 12: Test for maintaining contact pressure with 0.5 mm SMA wire.

3.7 Discussion

The test using a 0.5 mm SMA wire demonstrated an increase in radial force upon activation, while the 0.25 mm SMA wire showed a decrease. Maintaining a consistent contact pressure was possible in the activated state. Deactivating the 0.5 mm SMA wire led to a rapid return to the inactivated radial force level.

As illustrated in Figure **10**s 10-11, the thickness of the SMA wire significantly influences the qualitative effect on contact force. This is explained by the thermal behavior and the equilibrium of forces under thermal influence.

The displacement $u(r)$ of an annular ring disk, such as a PTFE ring, under a temperature shift ΔT and a relocatable outer boundary is given in Equation (1) and depends on the thermal expansion coefficients α_t.

Materials such as thermosets and steels typically have positive thermal expansion coefficient α_t, with steels generally expanding less then thermoplastics under heat. The thermal expansion of the mandrel or rod is therefore neglected in the analysis.

$$u(r) = \alpha_t \Delta T\, r \tag{1}$$

Notably, SMA's do not behave according to Equation (1) during their phase shift temperature; instead, they exhibit shrinkage as shown Chapter 2.1.

Assuming a linear time-invariant system and heating conditions within the SMA shift temperature range, the final radial force is a cumulation of forces, as shown in Figure 13. The expansion force of the PTFE opposes the shrinkage force of the SMA wire.

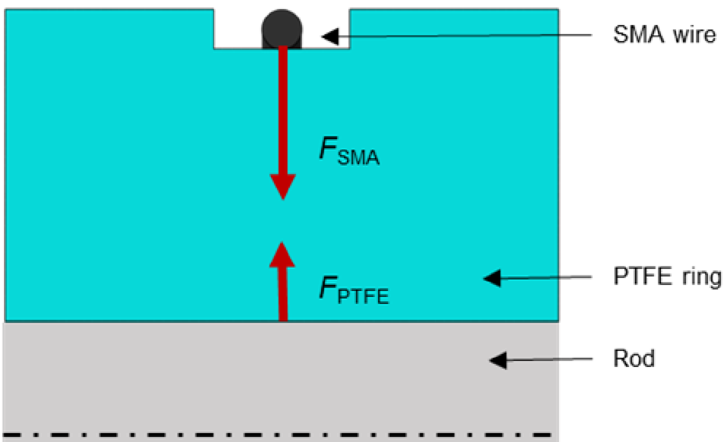

Figure 13: Direction of forces under heating.

The actuating volume of the SMA wire is strongly dependent on its diameter. Doubling the diameter results in a volume four times larger. Consequently, the force of the 0.5 mm SMA wire is therefore assumed to be four times stronger than that of the 0.25 mm SMA wire. This suggests that in the 0.25 actuated test, the SMA wire was not thick enough to counteract the thermal expansion of the PTFE ring; unlike the 0.5 mm wire, which increased the radial force upon activation.

Some artifacts of the human-in-the-loop control are evident in the graphs. During the 0.25 actuated test, the power was incrementally regulated. When the temperature exceeded the austinite finishing temperature of 60 °C, activation was halted. The 0.5 actuated test was regulated by gradually increasing the power output, resulting in smoother heating and cooling phases. During the force-maintaining test, the radial force was regulated to a specific level, this led to some noise generation.

There was a slight difference in radial force before and after stopping activation. Functions with high gradients are very sensitive to changes. Both SMAs and elastomers are known for their non-linear effects. Figure 7 simplistically shows how resulting deformations are set by the equilibrium of forces. Any slight change that might have occurred could alter the deformation states accordingly. Reasons for changes in the measured deformation might include the loosening of the reef knot, non-linear effects of SMA and PTFE, load cell drift, different cooling curves of the SMA wire and PTFE ring or insufficient recording time to reach a stationary unactuated cooling temperature.

4 Summary and Conclusion

For the first time, a test featuring a rectangular sealing ring and SMA was performed. Two different SMA wire thicknesses were evaluated. An induction coil setup was developed to facilitate the testing. Key findings revealed the importance of the sealing ring's thermal expansion and the necessity for the wire thickness to be suitable for the ring's cross-sectional dimensions. By manually controlling the input voltage, a consistent radial holding force was maintained. Performance parameters crucial to functionality, such as friction force and leakage – both dependent on radial force – can be utilized as signals to calculate adjustments for the SMA wire.

Sealing applications entail numerous requirements, the most critical being a compact installation space and ease of system assembly. For practical use, it is essential to thoroughly examine a system configuration that integrates feedback signals and meets these specific requirements.

5 Nomenclature

Variable	*Description*	*Unit*
A_f	austenite finishing temperature	[°C]
A_s	austenite starting temperature	[°C]
F	force	[N]

k	PTFE-spring stiffness	[N/m]
M_f	martensite finishing temperature	[°C]
M_s	martensite starting temperature	[°C]
$u(r)$	displacement under temperature shift	[m]
α_t	thermal expansion coefficient	[mm^{-1} K^{-1}]
ΔT	temperature shift	[K]
r	radius	[m]
ε	strain	[%]
σ	stress	[Pa]
NiTi	nickel-titanium	
NiTiCu	nickel-titanium-copper	
PTFE	polytetrafluoroethylene	
SMA	shape memory alloy	

6 References

[1] Winkler, H., Berger, U., Mieke C., Schenk, M.: *Flexibilisierung der Fabrik im Kontext von Industrie 4.0*, Logos Verlag Berlin GmbH, 2017.

[2] Müller, H., Nau, B.: *Fluid Sealing Technology: Principles and Applications*, Dekker, 1998.

[3] Schüle, C., Franz, M., Wehmann C., Amorim, S.: *Axial seal for high-rpm application and poor lubrication*. 21st International Sealing Conference 2022, Stuttgart, Germany, 2022.

[4] Sinapius, J. M.: *Adaptronik*, Springer Vieweg, Berlin, 2018.

[5] Cederström J., Van Humbeeck J.: *Relationship Between Shape Memory Material Properties and Applications*, In: *Journal de Physique IV,* 1995.

[6] Hodgson, D. E., Wu, M. H., B. R. J.: *Shape Memory Alloys, Properties and Selection: Nonferrous Alloys and Special-Purpose Materials,* 1990.

[7] Wilkes K. E., Liaw, P. K.: *The fatigue behavior of shape-memory alloys*, Springer, 2000.

[8] Kang, G., Yu, C., Kan, Q.: *Thermo-Mechanically Coupled Cyclic Deformation and Fatigue Failure of NiTi Shape Memory Alloys*, , Springer Singapore, 2023.

[9] Kang, G., Kan, Q., Qian L., Liu, Y.: *Ratcheting deformation of super-elastic and shape-memory NiTi alloys*, *Mechanics of Materials* 41.2: 139-153, 2009.

[10] Chaudhari, R., Vora, J. J., Parikh, D. M.: *A Review on Applications of Nitinol Shape Memory Alloy*, In: Recent Advances in Mechanical Infrastructure: Proceedings of ICRAM 2020 (2021): 123-132.

[11] Kang, G., Kan, Q., Yu, C., Liu, Y.: *Whole-life transformation ratchetting and fatigue of super-elastic NiTi alloy under uniaxial stress-controlled cyclic loading*, In: Materials Science and Engineering: A, 535, 228-234.

7 Authors

Trelleborg Sealing Solutions Germany

Schockenriedstraße 1, 70565 Stuttgart, Germany

Anne Marie Lehmann

ORCID 0009-0001-4299-6307, anne.marie.lehmann@trelleborg.com

Anja Dobrinsky

ORCID 0009-0002-0300-0535, anja.dobrinsky@trelleborg.com

Martin Franz

ORCID 0009-0008-0457-9116, martin.franz@trelleborg.com

https://doi.org/10.61319/D19MQHL2

Group A
Session 3

Simulation I

A 04

Meghshyam Prabhakar Shisode, Ron Willems, Bas van der Vorst, Mickael Sansalone, SKF Seals, Global Research & Innovation, Houten, The Netherlands

Enabling more sustainable sealing solutions via multiscale friction modelling

A 05

Bharath Kumar Sundararajan, Michael Fasching, Mickael Sansalone, Thomas Schwarz, Bas van der Vorst, SKF B.V., Global Research and Innovation, SKF Seals Business Unit, Houten, The Netherlands

A new constitutive model describing the rate-, temperature- and strain- dependent behaviour of polymeric sealing materials

A 06

Marius Hofmeister, Felix Fischer, Lukas Boden, Katharina Schmitz, Institute for Fluid Power Drives and Systems - RWTH Aachen University, Aachen, Germany

Simulative Prediction of Leakage for Seat Valves and Bio-Hybrid Fuels

A 07

Martin Wittmaack, Markus André, Sebastian Rakowski, Katharina Schmitz, University of Applied Sciences and Arts Hannover Faculty II - Mechanical and Bioprocess Engineering, Hannover, Germany

Influence of surface topography on stick-slip-effects – an experimental and numerical study

Enabling more sustainable sealing solutions via multi-scale friction modelling

Dr. Meghshyam Shisode, Dr. Ron Willems, Dr. Bas van der Vorst, Dr. Mickael Sansalone

A reliable and accurate seal friction model is paramount in optimizing sealing products towards energy-efficient and sustainable sealing systems. In seals, depending on the contact conditions, boundary and mixed lubrication regimes are as prevalent as the full-film regime due to, for example, counterface roughness, lubricant starvation, low speed, severe contact pressure, temperature, etc. Although the research on full-film lubrication regime is well matured, a reliable predictive model for rubber dry friction, contributing to boundary and mixed lubrication regimes, is still lacking, therefore hindering the friction and wear models accuracy for sealing applications.

In this work, a predictive analytical model to estimate temperature and speed dependent rubber dry friction is proposed. The model is inspired by a multi-scale representation of a metallic counterface combined with a first-order analytical approximation of contact stresses and rubber deformation. The counterface is decomposed into different scales of roughness and the rubber dissipation energy is then determined on each scale. The transition between different scales is also modeled, which is important to correctly estimate the contribution from each scale. Subsequently, a cumulative frictional energy loss is estimated to predict the friction force.

The resulting model is able to predict temperature and sliding speed dependent friction coefficient and shows a good correlation with in-house experiments. The proposed dry friction model can be combined with the lubricant viscous shearing friction model to predict the overall friction more reliably in the sealing contact, thereby accelerating the design of more sustainable and energy-efficient sealing solutions.

1 Introduction

Currently, there is significant momentum in both the industrial and automotive sectors to reduce seal friction while simultaneously enhancing seal wear resistance and longevity. One of the key customer requirements is to minimize the rotating shaft seal friction torque, which improves system efficiency, reduces energy consumption, and lowers overall carbon emissions. Given stricter CO_2 regulations, the challenge lies in designing optimal sealing solutions with reduced friction. To address this, new predictive tools are being developed to estimate seal friction, thereby streamlining the testing process and accelerating time to market.

In sealing contacts, total friction arises from two main sources: material friction due to direct asperity contact and friction resulting from lubricant viscous shearing. The specific contributions of material friction and lubricant viscous shearing depend on various factors such as material properties, speed, surface topography, contact load, counterface wetting and temperature. While models have matured significantly in estimating friction due to lubricant viscous shearing, research is still evolving regarding the modeling of rubber material friction resulting from direct asperity contact. The objective of our research initiative is hence to develop a physics-based, simplified and reliable approach for predicting rubber dry friction in sealing applications, with the aim to provide rapid solutions for end-users.

Rubber dry friction is a complex phenomenon fundamentally related to the viscoelastic nature of the material. In dry conditions, the interface conditions become significant, as adhesion effects are generally activated and may contribute to viscoelastic friction. Under lubricated conditions, the effect of adhesion is expected to substantially reduce due to the presence of a lubricant layer that inhibits direct intermolecular bonding between the rubber and metal counterface. However, viscoelastic friction still predominantly exists in boundary and mixed lubrication regimes. Therefore, this study focuses on modeling the viscoelastic friction, in alignment with its relevance for sealing applications.

Grosch [1] conducted the first experimental study on dry friction in rubber. In this research, rubber pads were slid across glass, steel, and abrasive plates, resulting in viscoelastic deformation within the rubber material. The study revealed that rubber friction reached a maximum at a specific speed, declining at higher speeds. Interestingly, the speed at which this maximum friction occurred shifts with temperature as described by the Williams–Landel–Ferry (WLF) equation [2]. This equation is based on measurements of rubber viscoelastic properties. Grosch's observations led to the conclusion that near-surface viscoelastic deformation plays a crucial role in dry rubber friction.

In the literature, two main theories of rubber dry friction have been published. One theory, proposed by Klüppel and Heinrich [3], and another by Persson [4], both focus heavily on the multi-scale nature of counterface and their fractal roughness. Persson et al. [4] developed condensed but mathematically complex equations to predict rubber friction. However, these models rely on strong assumption of truncating the fractal surface spectrum to a chosen wavevector (q_1), which makes them less robust as the viscoelastic loss significantly depends on the choice of truncation wavevector (q_1).

In 2000, Wassink et al. [5] proposed a physical model for seal viscoelastic friction. Wassink used a multi-scale description of surface roughness. They decomposed the counterface into 16 different scales. When a seal slides over a rough shaft, the seal material must deform to move past the asperities on the shaft surface. Since the seal material is viscoelastic, the deformation and recovery processes result in energy loss, contributing to total friction. By determining the energy loss per roughness scale, the overall viscoelastic friction is estimated. The results from Wassink's model show a good qualitative correlation with experimental data. However, the model requires specification of multiple fitting parameters, which limits its versatility.

This paper proposes a different approach to address the challenges encountered with existing models. Rather than considering a continuous spectrum of frequencies used in [3] [4], a discrete set of scales is proposed to describe the counterface topography. This model is based on the concept of determining energy loss due to viscoelastic material behavior of rubber interacting at various roughness scales on the contacting metallic surface, similar to the approach described by Wassink et al. [5]. However, unlike the Wassink model, the model proposed in this paper requires only a single model parameter.

2 Multi-scale dry friction model

This section introduces a first-order model for rubber friction. The model is built upon a multi-scale representation of the counterface and utilizes analytical equations to calculate stresses and deformations in rubber. The predictions highlight the significance of multi-scale surface roughness effects and their relationship with rubber material properties in dry friction. Key parameters governing rubber friction include contact temperature and speed. For example, the coefficient of friction can vary between 0.1 and 2, depending on the speed and temperature combination.

2.1 Multi-scale decomposition of surface roughness

While standard steel-to-steel friction models employ a single-scale representation of surface roughness, predicting rubber friction necessitates a multi-scale description of the counterface. In fact, such an approach is required to account for all dissipative phenomena generated during sliding. The method proposed in this paper considers a discrete number of scales. For simplicity, each scale is represented as a sinusoidal function. Moreover, to avoid superposition of dissipative effects, these scales must be distinct from each other. Consequently, a maximum of five scales is utilized in the proposed approach to cover the frequency range developed onto the surface. The counterface is first measured using confocal microscopy, and 2D profiles in the sliding direction are extracted. By discretizing each profile using Fourier transform and then applying inverse Fourier transform, five distinct roughness scales are determined for each of the original 2D profiles. For each scale of 2D profile obtained, parameters such as roughness R_a, wavelength λ, and mean asperity radius R (Equation (1)) can be determined. Figure 1 illustrates the example of a measured 2D profile and its corresponding five different roughness scales, while Table *1* provides details of roughness parameters for each scale.

$$R = \frac{\lambda^2}{2\pi R_a} \tag{1}$$

Table 1: Roughness parameters for different scales

Scale	1	2	3	4	5
Wavenumber domain (m^{-1})	<11359	11359 - 31552	31552 - 88346	88346 - 239797	239797 - 646190
Ra (um)	0.15	0.10	0.06	0.05	0.03
Wavelength (um)	162.5	29.7	11.5	4.9	2.2

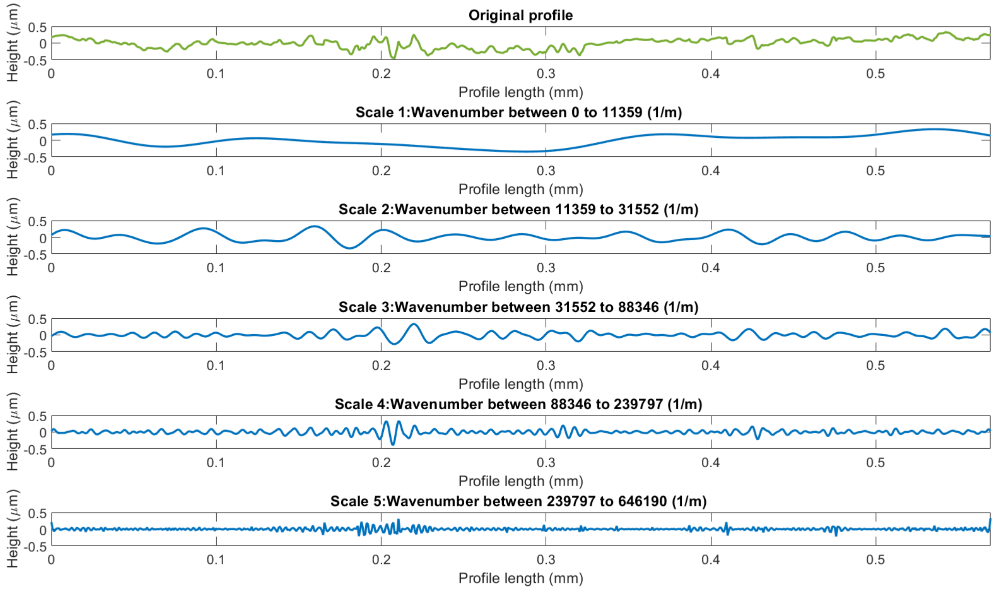

Figure 1: Measured profile of a counterface ($R_a = 0.45\mu m$) and its decomposition into 5 roughness scales

2.2 Dry friction model for viscoelastic dissipation

A simple analytical model is proposed to predict the friction resulting from the bulk deformation of rubber at each discretized scale of the counterface. The model assumes that the deformation and release of rubber at each scale lead to energy dissipation due to its viscoelastic nature. The resulting friction is derived by summing up all the dissipative effects generated at different scales. Additionally, the model assumes that only the rubber surface deforms, while the metallic counterface asperities remain rigid. When metallic asperities slide on a rubber surface, the total strain energy due to bulk rubber deformation can be expressed as follows:

$$\Delta E_T = \iint_{Volume,time} \sigma_{ij} \frac{d\varepsilon_{ij}}{dt} dt dV \tag{2}$$

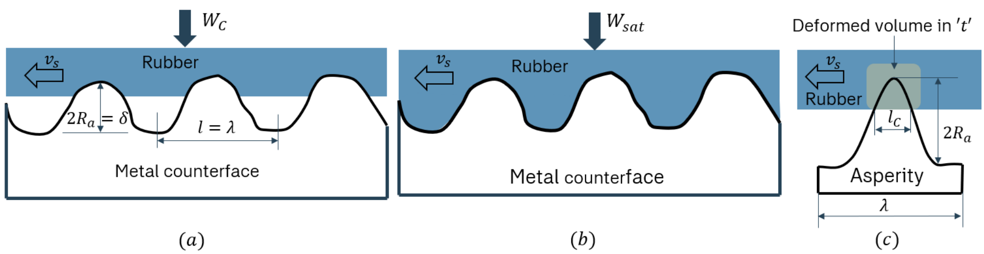

Figure 2: Sliding of rubber on metal counterface (a) in unsaturated contact condition (b) in saturated contact condition (c) single asperity contact

where σ_{ij} and ε_{ij} are the stress and strain components respectively. Since the roughness scale of the metallic counterface is described as a sinusoidal function, stresses and deformations are also assumed to respond in the same manner in time and space. This allows for the energy dissipation to be approximated as:

$$\Delta E = -\varepsilon_C \sigma_C \frac{G"(\omega_C)}{G^*(\omega_C)} V_{def} \tag{3}$$

where V_{def} is the considered deformed volume of rubber (Figure 2c) and ω_C the frequency of deformation. G^* is the combined shear modulus and $G"$ is the loss shear modulus. Considering v_s to be the sliding speed and l_C, the contact length at asperity in the sliding direction, the frequency ω at which rubber is excited at this scale, and the deformed volume during time $t,$ can be expressed as:

$$\omega = \frac{v_s}{\lambda}, \qquad V_{def} = S_{def}\, v_s t \tag{4}$$

where S_{def} is the deformed section in the plane perpendicular to the sliding direction. Finally, assuming the behavior of rubber to be linear elastic, the energy dissipated can be written as:

$$\Delta E \approx -G"(\omega_C) \frac{\sigma_C^2}{3G^*(\omega_C)^2} S_{def} v_s t \tag{5}$$

The total dissipated energy and the frictional force F_{fric} can be calculated as follows:

$$\Delta E \approx \sum_{i=1}^{n_{scale}} -n_{a_i} G"(\omega_i) \frac{\sigma_i^2}{3G^*(\omega_i)^2} S_{def,i} v_s t \tag{6}$$

$$F_{fric} \approx k_f \sum_{i=1}^{n_{scale}} n_{a_i} G"(\omega_i) \frac{\sigma_i^2}{3G^*(\omega_i)^2} S_{def,i} \tag{7}$$

where n_{a_i} is the number of asperities at scale i and k_f is the model parameter determined by reducing the error in model results and experiments. The parameter k_f is introduced to account for complex phenomena that are not adequately captured by the proposed first-order model. The coefficient of friction resulting from viscoelastic losses is then estimated as follows:

$$\mu_{dry} = \frac{F_{fric}}{W_C} = \frac{F_{fric}}{A_C P_C} \tag{8}$$

where W_C, P_C and A_C are normal contact load, mean contact pressure and apparent contact area respectively. Finally, the coefficient of friction estimated for each 2D profile is averaged to determine the overall dry friction coefficient.

2.2.1 Geometry and stresses for a single asperity

The asperity level calculations of stress and deformations are based on the Hertzian theory and on Johnson developments [6] for elastic contacts of sinusoidal surfaces. The number of asperities n_{a_i} and load on each asperity W_i at scale i can be determined as:

$$n_{a_i} = \frac{A_C}{\lambda_i^2}, \quad W_i = \frac{W_C}{n_{a_i}} \tag{9}$$

According to the Hertzian theory, the contact area is defined by the following diameter of contact l_i:

$$l_i = 2\left(\frac{3}{16}\frac{W_i R_i}{G^*(\omega_i)}\right)^{1/3} \tag{10}$$

where R_i is the mean radius of asperity (Equation (1)) and ω_i is the frequency at scale i (Equation (4)). The mean contact stress can thus be expressed as:

$$\sigma_i = \frac{4W_i}{\pi l_i^2} \tag{11}$$

These equations are valid when the penetration of an asperity into the rubber is relatively small. However, as the load increases, saturation occurs, and the rubber fully penetrates the contacting surface asperities (see Figure 2b). Under such situation a different equation is required. Johnson [6] showed that the stress at which saturation occurs can be calculated as:

$$\sigma_{sat,i} = \frac{8\pi R_{a_i} G^*(\omega_i)}{\lambda_i} \tag{12}$$

When the saturation stress ($\sigma_{sat,i}$) is reached, $\sigma_i = \sigma_{sat,i} = P_C$, $l_i = \lambda_i$, $\delta_i = 2R_{a_i}$ and since the stress varies between 0 and $\sigma_{sat,i}$, a following relation is assumed between contact stress σ_i and penetration depth δ_i:

$$\delta_i = 4R_{a_i}\left(\frac{\sigma_i}{\sigma_i + \sigma_{sat,i}}\right) \tag{13}$$

From these relations, the deformed section of rubber can be estimated as:

$$S_{def,i} = l_i \delta_i \tag{14}$$

Finally using Equation (7), the friction force at each asperity scale can be calculated.

2.2.2 Roughness scale interaction

Up until now, dissipative effects have been estimated independently at each scale and then aggregated to determine the overall frictional energy loss. However, this approach ignores the interaction and effects of roughness scale at subsequent scales. An important parameter influenced by scale interaction is indeed the apparent area available at the subsequent scale.

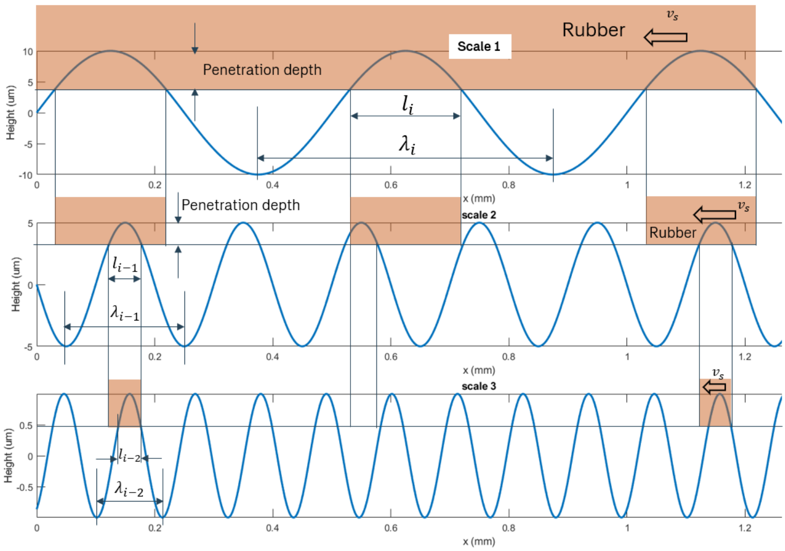

Figure 3: Illustration of subsequent roughness scales interaction

As illustrated in Figure 3, if the apparent area available at scale i is A_C then at scale $(i+1)$, the total available apparent contact is $A_{corrected} = A_{f_{i+1}} * A_C = \frac{l_i}{\lambda_i} A_C$ where $A_{f_{i+1}}$ is the area correction factor. Similarly, for scale $(i+2)$, $A_{corrected} = A_{f_{i+2}} * A_C = \frac{l_{i-1}}{\lambda_{i-1}} * \frac{l_i}{\lambda_i} A_C$. Therefore, at scale $i = 1, A_{corrected} = A_C$ and for all subsequent scales $i > 1, A_{corrected} = A_{f_i} * A_C$. Accordingly, the number of asperities n_{a_i} and load on asperity W_i (Equation (9)) at scale i are updated to account for the roughness scale interaction.

2.2.3 Viscoelastic friction computation

The detailed flow used to compute the viscoelastic dry rubber friction can then be described as illustrated in Figure 4 below:

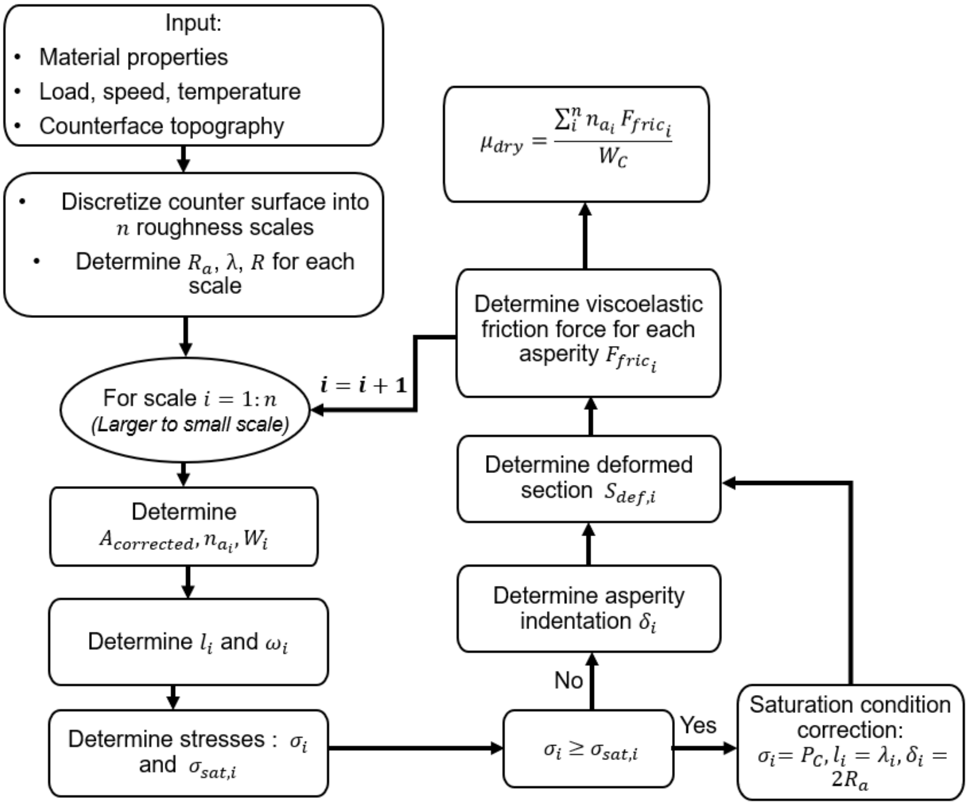

Figure 4: Flow chart: rubber viscoelastic friction computation in dry contact condition

3 Experiments and model validation

Rubber friction highly depends on the operational conditions. Under dry conditions, the coefficient of friction can vary between 0.1 and 2, depending on the speed and temperature. Therefore, it is necessary to characterize rubber friction across various temperatures and sliding speeds. To achieve this, an in-house CETR universal tribometer is used to measure the dry friction coefficient using a rubber ring on a steel disk configuration and across a range of relevant temperatures and sliding speeds.

3.1 Tribometer set-up and friction measurement

The setup principle is illustrated in Figure 5. A stationary ring made of elastomer material, applies load against a rotating steel disk. A 3D load sensor measures the resulting frictional torque. The ring, along with its support and the load sensor, can be vertically displaced to load and unload the sample. To ensure alignment between the ring and disk surfaces, the ring is mounted on a ball joint. The tribometer features an insulated chamber, allowing tests at temperatures ranging from -20°C to +150°C under stable conditions. The ring's inner diameter is 32mm, and the outer diameter is 40mm. An electrical motor drives the steel disk at a predefined rotational speed. To minimize self-heating during contact, the maximum rotational speed range is limited to 0.01 to 50 RPM, which corresponds to a linear sliding speed range of 0.02 to 95mm/s. Experiments are conducted at different temperatures (25°C to 85°C) and with a normal load, resulting in a nominal contact pressure of 0.1 - 0.2 MPa. For a given temperature and normal load, speed sweeps from 0.02 to 95 mm/s are repeated at least twice. The coefficient of friction is then determined based on the stable part of the friction torque curve obtained for each speed. Ultimately, the average coefficient of friction is calculated across repetitions for a specific speed, temperature, and normal load combination.

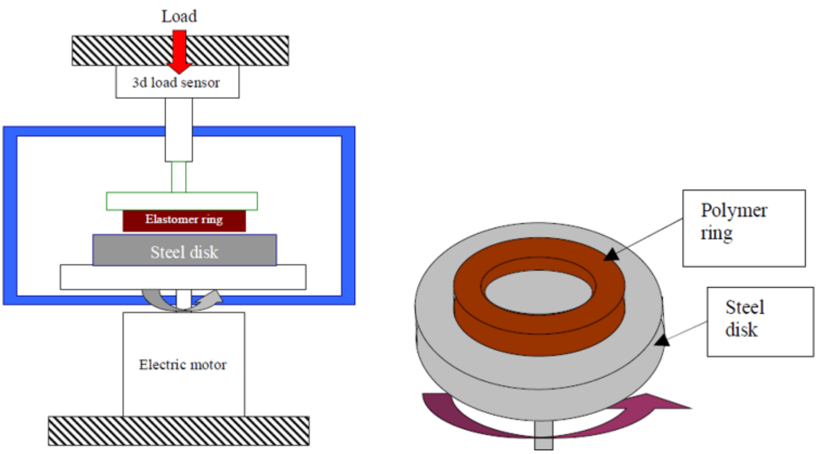

Figure 5: Tribometer setup

3.2 Samples

Several proprietary fluoro-elastomers (FKM1, FKM2, FKM3 and FKM4) are used for this study. The required material properties are thus procured from a proprietary sealing material' database. The counterface used is a steel disk of 54mm diameter and a surface roughness of $R_a = 0.5\mu m$. The surface is purposefully plunge ground resulting in a roughness pattern oriented in the sliding (circumferential) direction, as shown in Figure 6.

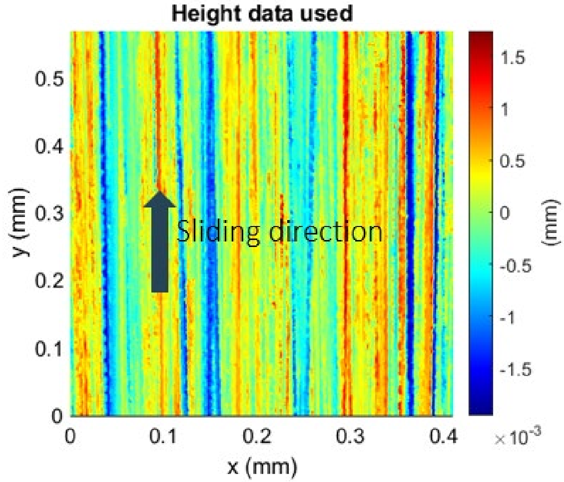

Figure 6: Surface topography of steel counterface

3.3 Results: model vs. experiments

The experimental results and their comparison with the model for four different FKM materials are shown in Figure 7 to 10. It should be noted that, the unique model parameter k_f is derived by minimizing the difference between experiments and the model prediction for FKM1, FKM2, and FKM3 materials. Subsequently, this derived parameter is applied to validate the model for FKM4 material. The comparison reveals a strong qualitative and quantitative correlation between the model predictions and experimental data across the whole range of speed and temperature considered.

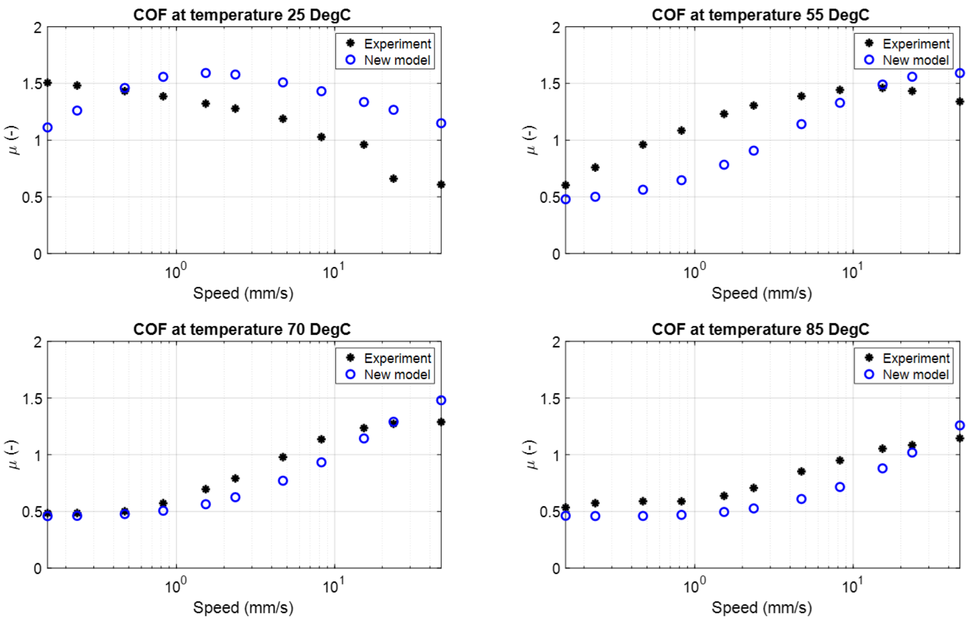

Figure 7: Coefficient of friction (COF) comparison for FKM1; model vs. experiments

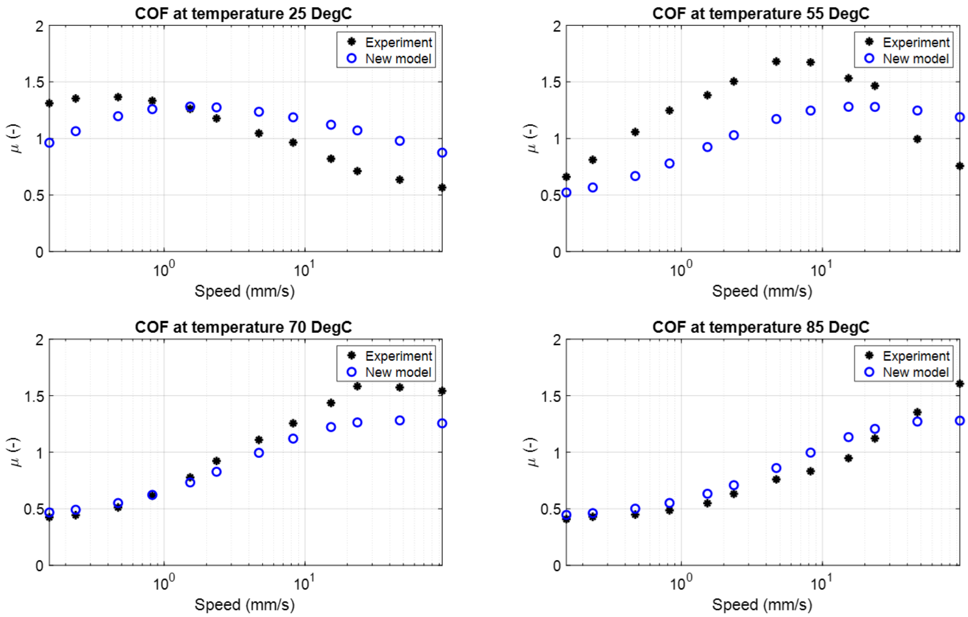

Figure 8: Coefficient of friction (COF) comparison for FKM2; model vs. experiments

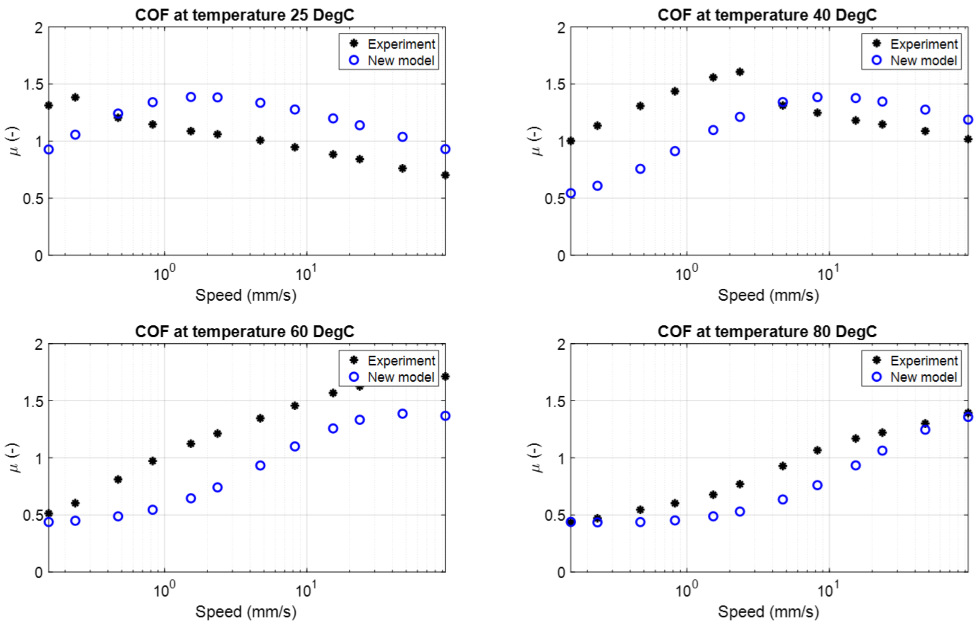

Figure 9: Coefficient of friction (COF) comparison for FKM3; model vs. experiments

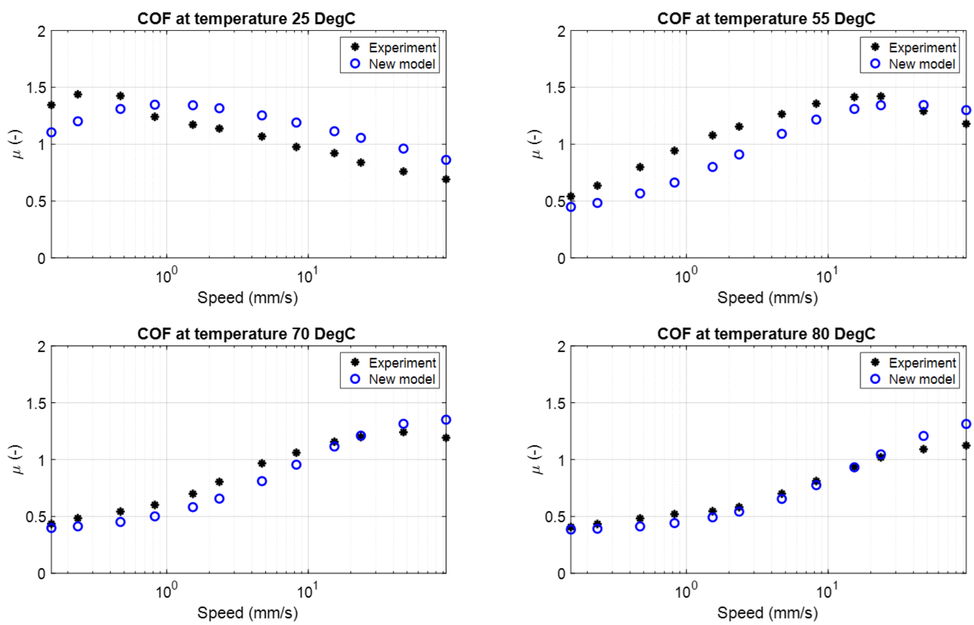

Figure 10: Coefficient of friction (COF) comparison for FKM4; model vs. experiments

4 Seal material optimization for sustainability

The urgent need to address climate change has led to a growing focus on sustainability. It is crucial to engage all stakeholders across the entire value chain, including suppliers, manufacturers, and customers, in discussions about the environmental impact of our products. As part of SKF's commitment to sustainability, web-based calculation tools are developed, such as the CO_2 emissions estimator, to assess the impact of our products.

Seals are sustainable by nature, as their main function consists of preventing spillage of lubricant into the environment and protecting rotating equipment from external contamination, thereby enabling extension of machine service life. However, to ensure this main function seals also play a significant role in the friction of rotating equipment, accounting for up to 60% of the total friction torque in some applications. Reducing seal friction is a key customer requirement to enhance system efficiency, lower energy consumption, and minimize overall carbon emissions. With stricter CO_2 regulations, designing optimal sealing solutions that balance low friction with effective sealing performance remains a challenge. Accurate prediction of seal transient dynamics and friction, aided by simulation tools, is essential for accelerating product development and achieving customer-defined friction targets.

In lubricated contact conditions, adhesion effects are significantly reduced and friction originates predominantly from two main sources: viscous shearing of the lubricant in the contact and direct asperity contacts (viscoelastic friction). The contribution from these components depends on various parameters, with the lubrication regime being a critical factor. Material friction can be significant in boundary and mixed lubrication regimes when surfaces are not fully separated by a lubricant film. Conversely, in the full-film lubrication regime, lubricant viscous shearing dominates. Sealing applications can experience all these lubrication regimes during operation. Combining the results of dry (material) friction estimated from the proposed model with viscous shearing effects allows us to determine the overall seal friction. Therefore, this new model serves as a valuable tool for optimizing new sealing solutions towards reduced friction. For example, to minimize material friction, different seal materials can be ranked based on the dry friction coefficient estimated virtually within the relevant range of application conditions.

To illustrate such virtual material selection process, Figure 11 shows the estimated dry friction coefficient for three different proprietary NBR (nitrile butadiene rubber) compounds at a nominal contact pressure of 0.2MPa and temperature and speed range of 25 to 60^{0}C and 10 to 100mm/s respectively. Figure 11 and Table 2 clearly show that there can be substantial difference in dry friction depending on the rubber compound. Assuming that all three compounds satisfy other seal design requirements, then choosing NBR2 over NBR1 enables to reduce the contribution of material dry friction by **~55%** on average. However, the overall seal friction will not be reduced by 55% due to the unaccounted lubricant viscous friction contribution. Nevertheless, it can be safely assumed that at least 30% of the overall friction torque will be caused by material dry friction. In that case, selecting the right material leads to a net reduction in overall friction torque by 0.55*0.3**~16.5%.**

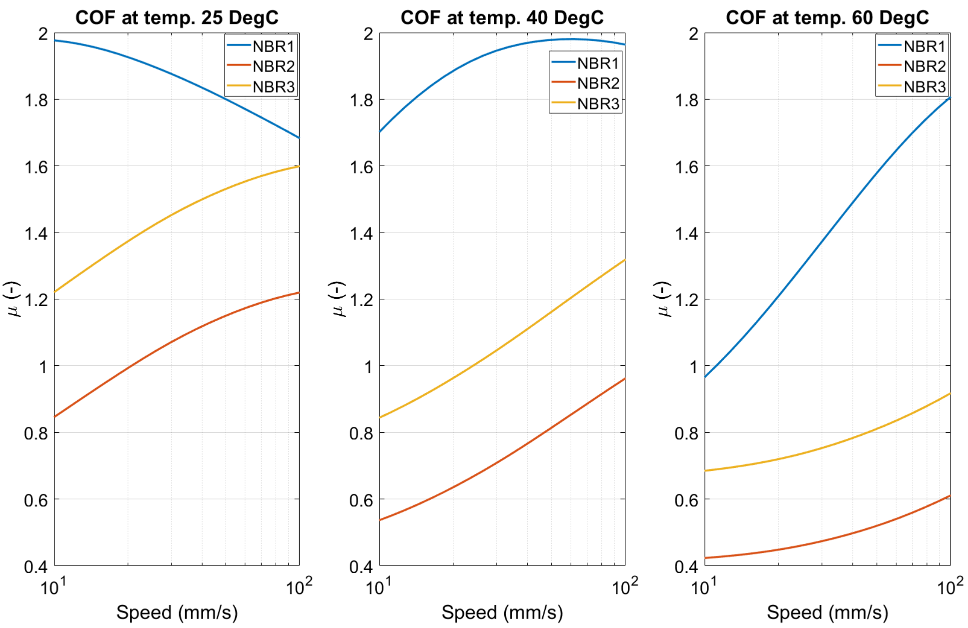

Figure 11: Estimated coefficient of friction (COF) comparison for three different NBR compounds in the temperature and speed range of 25-60°C and 10-100mm/s respectively

Table 2: Estimated COF comparison for different NBR compounds

Material	Average COF (Temperature: 25-60°C Speed: 10-100mm/s)
NBR1	1.72
NBR2	0.76
NBR3	1.09

To demonstrate the potential of sustainable seal design, an example of railway wheel bearing unit system is considered which is gaining an increased attention to reduce friction. Assuming 6 wagons per train, 2 bogies per wagon and 4 bearings per bogie leads to total of 48 bearing units. Each bearing unit has 2 seals and furthermore assuming a realistic reference torque of 0.8Nm per seal based on the test data results in a total seal frictional torque of 1.6Nm per bearing unit system. Therefore the reduced seal frictional torque for optimized seal material (NBR2) is expected to be 1.37Nm per bearing unit (16.5% less). Based on this estimate and using aforementioned SKFs CO2 emissions estimator, the net reduction in CO2 emission using NBR2 sealing material (scenario # 2) over NBR1 sealing material (scenario # 1) for total wheel bearing units (48x) on yearly basis can be estimated as depicted in Figure 12. The CO_2

emissions due to estimated frictional losses are calculated based on the regional CO_2 emissions per kWh for the chosen geographical location. In this example, the chosen region is European union for which the CO_2 conversion factors are used from the Greenhouse Gas Protocol [7].

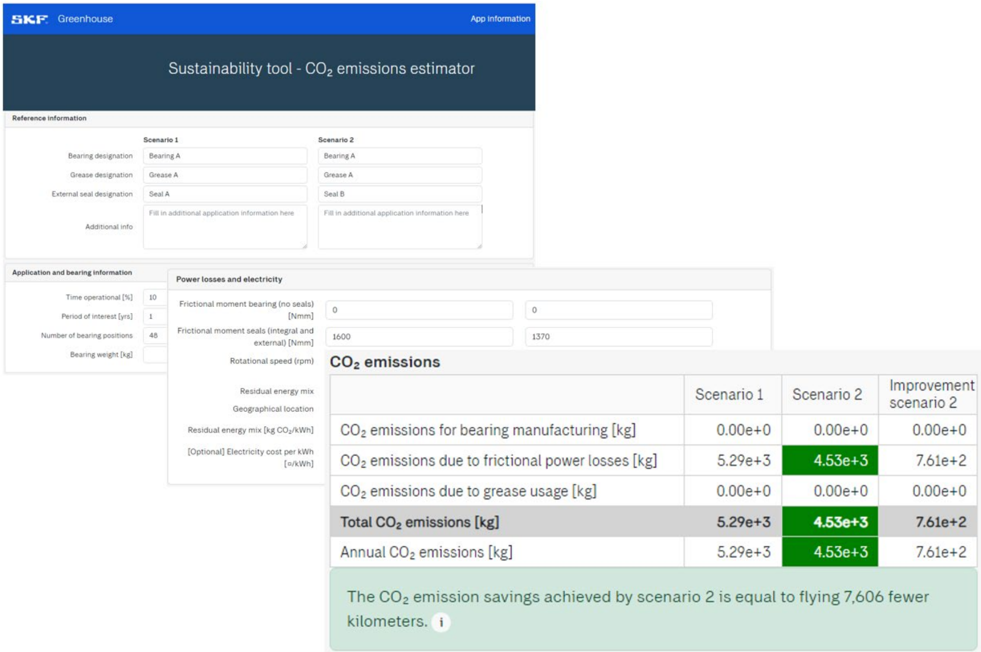

Figure 12: CO_2 emission - estimation using SKFs CO_2 estimator

5 Summary and conclusions

Rubber friction is a complex phenomenon, which is fundamentally related to the viscoelastic nature of the material in question and the multi-scale character of the counterface. Three physical phenomena are involved in rubber friction: lubricant shearing, viscoelastic losses due to the deformation of rubber by the counterface roughness and intermolecular interactions (adhesion) between the two surfaces. In this paper, an enhanced 1st order approach based on viscoelastic energy dissipation at different counterface roughness scales has been developed. This approach allows for rapid prediction of rubber dry friction. The method is applicable for seals and can be coupled with friction due to lubricant viscous shearing to estimate the overall seal friction. The model does not yet take into account the adhesion contribution, although the fitting parameter k_f indirectly accounts for its effect.

The predictions emphasize the importance of the multi-scale surface effects and the relation between rubber material properties and rubber friction under dry condition. Comparison with experiments showed the validity of this approach developed to model rubber dry friction. Finally, this simple yet effective model can be used to compare the dry friction characteristics of different sealing compounds and thereby assisting seal designers in selecting the optimal compound for sustainable and efficient sealing solutions.

6 References

[1] K. A. Grosch, "The Relation Between the Friction and Visco-Elastic Properties of Rubber," *Proc. R. Soc. London, Ser. A, 274,* p. 21–39, 1963.

[2] M. L. Williams, R. F. Landel and J. D. Ferry, "The temperature dependence of relaxation mechanisms in amorphous polymers and other glass-forming liquids.," *Journal of the American Chemical society 77, no. 14,* pp. 3701-3707, 1955.

[3] M. Klüppel and G. Heinrich, *Rubber Chem. Technol.,* pp. 73,578–606, 2000.

[4] B. Persson, "Theory of rubber friction and contact mechanics," *J. Chem. Phys.,* pp. 115, 3840–3861, 2001.

[5] D. B. Wassink, V. G. Lenss, J. A. Levitt and K. C. Ludema, "Physically Based Modeling of Reciprocating Lip Seal Friction," *J. Trib., 123(2),* pp. 404-412, 2001.

[6] K. L. Johnson, Contact mechanics, Cambridge university press., 1987.

[7] "Greenhouse gas protocol," [Online]. Available: https://ghgprotocol.org/tools-resources.

7 Authors

SKF Seals Global Research & Innovation

Meidoornkade 14, 3992 AE Houten, The Netherlands

Dr. Meghshyam Shisode, meghshyam.shisode@skf.com

Dr. Ron Willems, ron.willems@skf.com

Dr. Bas van der Vorst, bas.van.der.vorst@skf.com

Dr. Mickael Sansalone, mickael.sansalone@skf.com

https://doi.org/10.61319/UQVN37SQ

A new constitutive model describing the rate-, temperature- and strain-dependent behaviour of polymeric sealing materials

Dr. Bharath Kumar Sundararajan, Dr. Michael Fasching,
Dr. Mickael Sansalone, Dr. Thomas Schwarz, Dr. Bas van der Vorst

The continuous advancement of virtual simulation platforms is a fundamental aspect of the ongoing global digitalization megatrend. To broaden the applicability of these platforms to sealing applications, there is a need for more comprehensive material models that can describe the complex and diverse behaviour exhibited by various polymeric materials used in sealing products, such as elastomers, thermoplastic polyurethanes (TPUs) and PTFE. To address this need, a new generalized modelling framework and approach is introduced in this paper. The proposed approach allows different aspects of the model to be modified, tailoring to the material being studied. The model demonstrates a remarkable potential to accurately describe the strain rate, temperature, and strain dependent behaviour of a chosen seal material, PTFE, within the relevant conditions experimentally covered.

1 Introduction

In recent years, virtual simulation platforms have become indispensable in the design and development of sealing solutions. Within these platforms, the usage of material models serve as foundational elements that accurately captures the seal's behaviour under various operating conditions. The challenge here lies in the diverse range of polymeric materials used in sealing products, displaying a spectrum of behaviours ranging from simple linear viscoelasticity to more complex and non-linear elastoviscoplasticity. Consequently, the stress levels experienced by these materials in application are significantly influenced by various factors such as deformation level, deformation rate, and operating temperature.

Over the past decades, numerous models have been proposed to predict the complex behaviour exhibited by different polymer materials, and the approach generally tailored to specific applications. These models often employ networks of springs and dashpots, such as Maxwell or Kelvin Voigt units, to establish constitutive equations that determine the material's stress response as a function of strain. However, there remains a need for a more generic and universal modelling framework, that allows for adapting the model to the material under study by selectively activating and deactivating its different components.

Therefore, this paper seeks to address the existing gap by proposing a new constitutive modelling approach, validated using Polytetrafluoroethylene (PTFE) as the material system. PTFE exhibits a complex, non-linear elastoviscoplastic behaviour compared to their rubber counterparts and hence, serves as an ideal candidate for demonstrating the complete capabilities of the proposed approach. Uniaxial tensile experiments are conducted on unfilled PTFE material at different strain rates and temperatures. The yield and post-yield kinetics are then carefully analysed to gain insights into the underlying phenomenology and a suitable law is proposed to describe the observed behaviour. Finally, the output from the proposed model is compared against the experimental data to demonstrate its predictive capabilities.

2 Phenomenology and constitutive modelling of PTFE

Polytetrafluoroethylene (PTFE), also commonly known as Teflon, has some remarkable and unique properties that makes it suitable for sealing applications. Notably, PTFE has the ability to withstand extremely high and low temperatures, demonstrates excellent chemical resistance and a low coefficient of friction [1] resulting in enhanced wear resistance and reduced energy consumption compared to elastomers. Therefore, despite the ongoing PFAS discussions, PTFE is still being used in a wide array of applications.

Given its diverse usage, there exists a pressing need to understand its mechanical behaviour under anticipated operating conditions. However, being a semicrystalline thermoplastic polymer, PTFE exhibits a complex behaviour that is dependent on several factors including processing conditions, operating temperature, deformation rate, load and deformation levels, among others.

Figure 1 provides a schematic illustration of a typical stress-strain curve observed with PTFE materials when subjected to an uniform deformation rate. Initially, at very small strains, PTFE exhibits fairly linear viscoelastic response, which progressively transitions to a non-linear response until reaching a yield point. The Young's modulus and yield point are strongly dependent on the applied deformation rate, $\dot{\varepsilon}$ and temperature, T. Post-yield, at large deformations, stress levels continue to increase exhibiting a strain hardening behaviour due to the orientation of polymer chains along the loading direction [2].

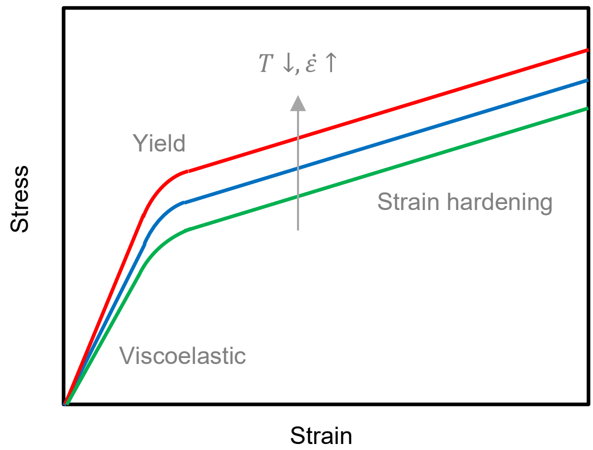

***Figure 1**: Schematic representation of a typical stress-strain response of PTFE*

The new constitutive model proposed in this study is a phenomenological model, following the notable work of Haward and Thackray [3]. The model can account for the stress contributions arising from diverse interactions within polymer over the entire deformation range. Consequently, the total stress (σ) is decomposed into two components: a driving stress (σ_d) and a hardening stress (σ_h) contribution as depicted in equation (1).

$$\sigma = \sigma_d + \sigma_h \tag{1}$$

The hardening stress is typically characterized by the elastic response of the entanglement network at large deformations and can be represented by a linear elastic spring. The driving stress, on the other hand, is primarily governed by the intermolecular interactions and helps in characterizing the viscoelastic response of the polymer up to and including yield. This is typically represented by an elastic spring connected in series with a dashpot. The well renowned Eyring equation [4], which has been shown to effectively capture the rate and temperature dependent yield kinetics of several polymers [5-7], is used for representing the dashpot. The yield kinetics can then be expressed as shown in Equation (2).

$$\sigma_y = \frac{kT}{V^*} * \sinh^{-1}\left(\frac{\dot{\varepsilon}}{\dot{\varepsilon}_0}\exp\left(\frac{\Delta U}{RT}\right)\right) \tag{2}$$

where $\dot{\varepsilon}_0$ is a thermodynamic constant, ΔU is the activation energy, V^* is the activation volume, k and R are Boltzmann and universal gas constant respectively. Furthermore, in order to accurately represent the behaviour of polymers across a wide range of temperatures and strain rates, the use of just a single spring-dashpot network is found to be rather insufficient. Hence, it is a common practice to include multiple branches in parallel, which is representative of a spectrum of relaxation times that is associated with the polymer.

Additionally, it is known that certain polymers also exhibit a thermorheologically complex behaviour. As a result, the driving stress contribution could potentially arise from more than one molecular process. In case of a semicrystalline thermoplastic polymer like PTFE, driving stress originates from the mobility of the main chain of the amorphous phase (α-relaxation) as well as transitions associated with the crystalline phase (β-transition) [8].

From a modelling perspective, this is easily addressed by adding multiple spring-dashpot networks in parallel, each representative of the relevant molecular process under consideration. The yield kinetics are then described using the Ree-Eyring modification to the Eyring equation [9], as shown in equation (3), where the different molecular processes are considered to act simultaneously and their stress contributions being additive in nature.

$$\sigma_y = \sum_{i=1}^{n} \frac{kT}{V_i^*} \sinh^{-1}\left(\frac{\dot{\varepsilon}}{\dot{\varepsilon}_{0,i}}\exp\left(\frac{\Delta U_i}{RT}\right)\right) \tag{3}$$

Incorporating multiple relaxation times and accounting for contributions from molecular processes having different origins are essential for effectively capturing the different transitions occurring within the material, in the range of conditions that is relevant to real-world applications.

Additionally, in the subsequent section (refer Figure 8 (b)), it will be demonstrated that the mere implementation of the conventional Ree-Eyring equation for the dashpot is rather insufficient to fully describe the complex behaviour exhibited by PTFE. In addition to the strain rate and temperature dependence, PTFE also exhibits a strong dependency on the strain level. Therefore, to address this, a new strain modified Eyring equation is proposed in this study, as expressed in equation (4).

$$\dot{\varepsilon} = \dot{\varepsilon}_0(\varepsilon) * \sinh\left(\frac{qV^*(\varepsilon)}{kT}\right) \exp\left(\frac{\Delta U(\varepsilon)}{R}\left(\frac{1}{T} - \frac{1}{T_{\mathrm{ref}}}\right)\right) \tag{4}$$

$$V^*(\varepsilon) = f(V^*_{\mathrm{initial}}, V^*_{\mathrm{final}}, \varepsilon, \varepsilon_0) \tag{5}$$

$$\Delta U(\varepsilon) = f(\Delta U_{\mathrm{initial}}, \Delta U_{\mathrm{final}}, \varepsilon, \varepsilon_0) \tag{6}$$

$$\dot{\varepsilon}_0(\varepsilon) = f(\dot{\varepsilon}_{0,\mathrm{initial}}, \dot{\varepsilon}_{0,\mathrm{final}}, \varepsilon, \varepsilon_0) \tag{7}$$

Where ε is the strain accumulated in the material. $\dot{\varepsilon}_0(\varepsilon)$, $V^*(\varepsilon)$ and $\Delta U(\varepsilon)$ are the strain modified rate constant, activation volume and activation energy parameters. These parameters are defined as a function of the strain level and ε_0, a strain based numerical constant, in such manner that they change from an initial to final value as indicated in equations (5-7).

Considering all essential aspects discussed above to describe the behaviour of PTFE, the mechanical analogue of the proposed model is constructed and illustrated in Figure 2. The model incorporates stress contributions from both α and β processes, connected in parallel. Each process has multiple branches that corresponds to the multiple relaxation times associated with them. The dashpot is modelled using the strain-modified Eyring equation, resulting in a fully non-linear elastoviscoplastic model. The final equilibrium branch, represented by a standalone elastic spring, captures the elastic strain hardening component of PTFE.

It is worth noting that, having such a modular and versatile modelling approach helps in selectively choosing the level of complexity based on the material under consideration. For instance, when applying the model to a material exhibiting predominantly linear viscoelastic behaviour, the approach can be simplified by deactivating the strain dependency in the Eyring dashpot or even using a linear Newtonian dashpot if proven sufficient. Furthermore, if the material demonstrates a thermorheologically simple response across temperatures and strain rates, a single-process version of the model may suffice. Therefore, this approach presents a universal sealing material modelling framework that can be tailored to any polymeric sealing product and application.

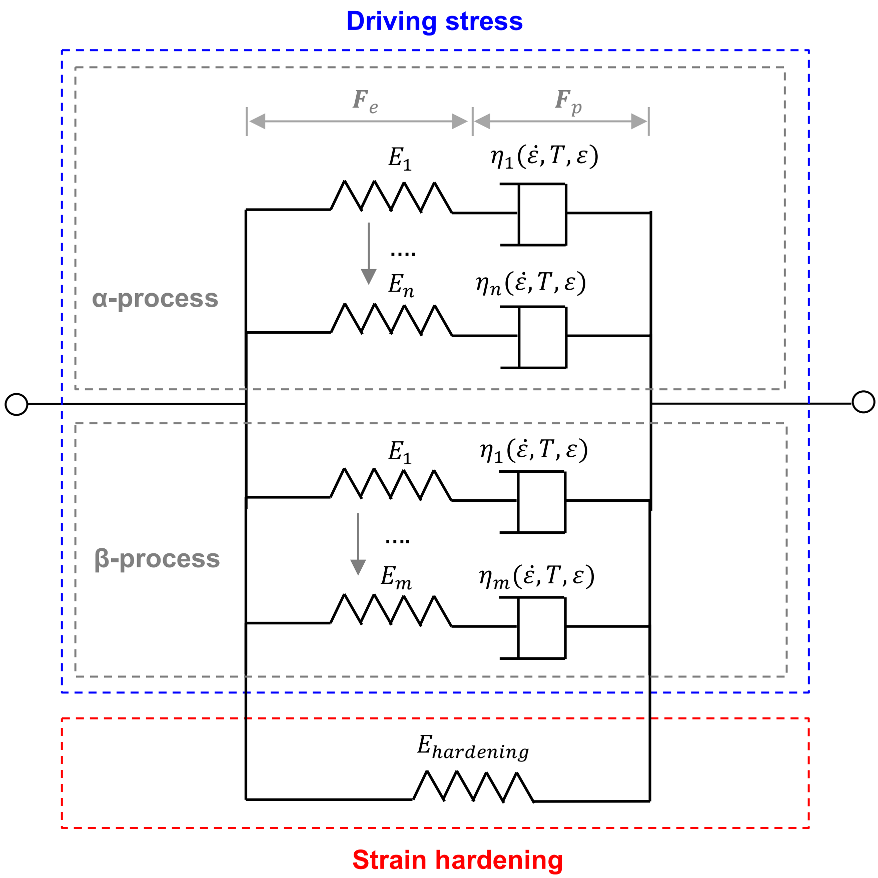

***Figure 2**: Mechanical analogue of a two process model for PTFE, with each process having multiple relaxation times. The modified Eyring dashpot takes into consideration the influence of strain rate, temperature as well as the strain levels.*

2.1 Implementation using ABAQUS Parallel Rheological Framework

In order to implement the proposed model for PTFE, the parallel rheological framework (PRF) of ABAQUS, a finite element software package, is utilized. The complete description and formulation of PRF can be found in the work of Dalrymple *et al.* [10]. Though the constitutive equations can be found there, it is important to emphasize that, for a finite deformation, the deformation gradient ($\boldsymbol{F_i}$) in each branch is multiplicatively decomposed into an elastic ($\boldsymbol{F}_{e,i}$) and plastic part ($\boldsymbol{F}_{p,i}$) as depicted in equation (7).

$$\boldsymbol{F}_i = \boldsymbol{F}_{e,i}.\boldsymbol{F}_{p,i} \tag{8}$$

Meanwhile, the total stresses are determined as a summation of the stress contributions from each individual branch. Furthermore, PRF only allows the use of a single hyperelastic model for all the springs used in the model. Therefore, In order to get a simple linear elastic response, the neo-Hookean hyperelastic model available in ABAQUS is utilized. On the other hand, although PRF has several built-in functions for describing the viscosity evolution in the dashpot, they are not representative of the strain modified Eyring equation that is necessary to describe the behaviour of PTFE. Therefore, the subroutine UCREEPNETWORK of the PRF is utilized to implement equation (4). In the following section, the experimental methodology adopted for testing the unfilled PTFE material is discussed, followed by the experimental results and a comparison of the model output against it in order to showcase its capabilities.

3 Experimental method

The material used for model development and validation as mentioned above is virgin PTFE. Experiments are conducted using a universal testing machine equipped with a 0.5 kN load cell, employing uniaxial tension. The testing procedure consists of two phases. In the initial *loading* phase, samples undergo loading at a constant crosshead displacement rate until reaching a predefined strain level. Subsequently, in the *relaxation* phase, the sample is maintained at the predefined strain level for one hour, during which the decay of stress over time is recorded. This testing protocol is designed to replicate real-world scenarios (Figure 3), such as when a seal is assembled on to a shaft (loading phase) and subjected to operational conditions where radial forces gradually diminish over time post-installation (transient relaxation phase).

During the loading phase, strain rates of 0.1 s^{-1} and 0.02 s^{-1} controlled by the crosshead displacement are chosen to understand the strain rate sensitivity of PTFE. In order to analyse the influence of temperature, tests are conducted at room temperature, 50°C, 80°C and 120°C. In the relaxation phase, the influence of strain on the relaxation rate is analysed by stopping the loading phase at three different strain levels, at each strain rate and temperature tested. The overall test matrix listing all the test conditions are presented in Table 1. Two samples are tested per test condition to ensure repeatability of the test results presented.

Table 1: Test matrix with Virgin PTFE

Temperature [°C]	Strain rate [s^{-1}]	Strain level [%]
23	0.1	5, 16, 25
	0.02	5, 16, 26
50	0.1	6, 16, 28
	0.02	6, 16, 28
80	0.1	6, 18, 28
	0.02	6, 17, 28
120	0.1	5, 17,28
	0.02	6, 17, 28

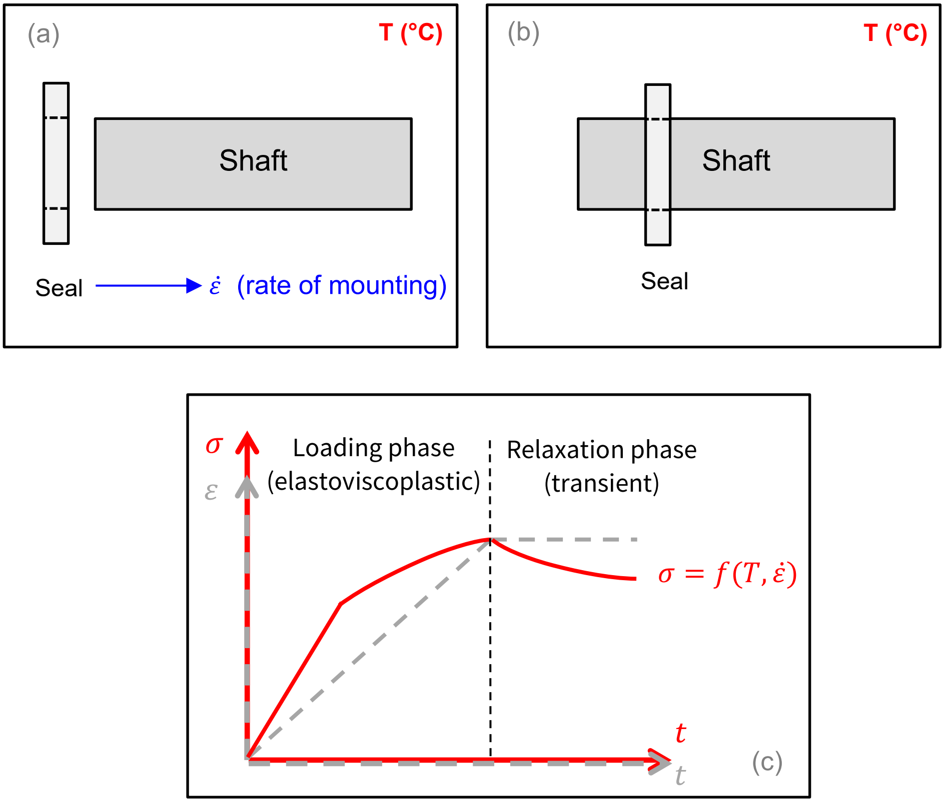

***Figure 3**: (a) Loading phase: Seal is assembled on to a shaft inducing strain in the material. (b) Relaxation phase: After the seal is assembled, the strain in the material is fixed while the stresses that developed during the loading phase decays over time. (c) Schematic representation of the stress and strain as a function of time during both loading and relaxation phase.*

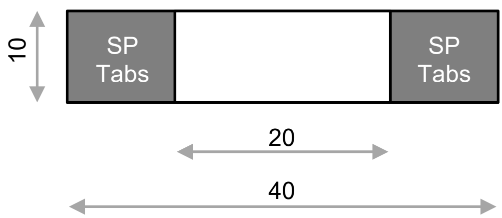

***Figure 4**: Schematic representation of tensile test samples. All dimensions in mm.*

Tensile test samples were prepared in a stripe geometry, as depicted in Figure 4, with dimensions of 40 mm * 10 mm * 2 mm. A gauge length of 20 mm and a gripping length of 10 mm on either side of the gauge section were employed. To prevent slipping during testing, sandpaper (SP) tabs were used in the gripping region. Additionally, a clamping pressure of 7 bar was used with the help of pneumatic clamps while performing the experiments.

Digital Image Correlation (DIC) technique was employed for a precise measurement of the engineering strain values. Spray pattern was applied on the specimen in the gauge section. Considering the homogeneous deformation state of the specimen, the line strains of the middle part of the specimen is considered as the region of interest, with a gauge length of 10 mm. After the completion of an experiment, the engineering strains are calculated, which are then converted to true strain and true stress following the expression in equation (9).

$$\varepsilon_t = \ln(1+\varepsilon) \; ; \; \sigma_t = \sigma(1+\varepsilon) \tag{9}$$

where ε_t is the true strain, σ_t is the true stress, ε is the engineering strain and σ is the engineering stress. Furthermore, since the strains are calculated after the experiment, it is important to note that reaching the same precise true strain as intended is not feasible with each experiment.

4 Results and discussion

4.1 Uniaxial tensile test results

In general, the experimental methodology adopted in this study produces highly repeatable results and is demonstrated in Figure 12 for some of the results in Appendix 1. Therefore, in order to ensure clarity in visualizing the data in the following sections, only one set of data is presented in the figures.

In Figure 5 (a), the quasi-static data obtained during the loading phase illustrates the material's response to different strain rates and temperatures. It becomes evident that stress levels within the material are strongly influenced by these factors due to the time dependent behaviour exhibited by PTFE, with higher strain rates or lower temperatures resulting in increased stresses for a given strain level, and vice versa.

However, identification of a distinct yield point proves challenging from the true stress strain curves presented in Figure 5 (a). Instead, the yield point is determined by considering the intersection between the initial slope within the viscoelastic region and the hardening slope observed at larger strains. Subsequently, the yield kinetics of PTFE is depicted in Figure 5 (b), where the experimental markers are fit using Equation (3) and the parameters listed in Table 2. The data reveals two distinct regions: Region I having a higher rate dependence at lower temperatures, and Region II with a lower rate dependence at higher temperatures. As discussed in the previous section, this observation is attributed to the contributions of multiple molecular processes within PTFE, stemming from its amorphous (α-process) and crystalline (β-process) phases.

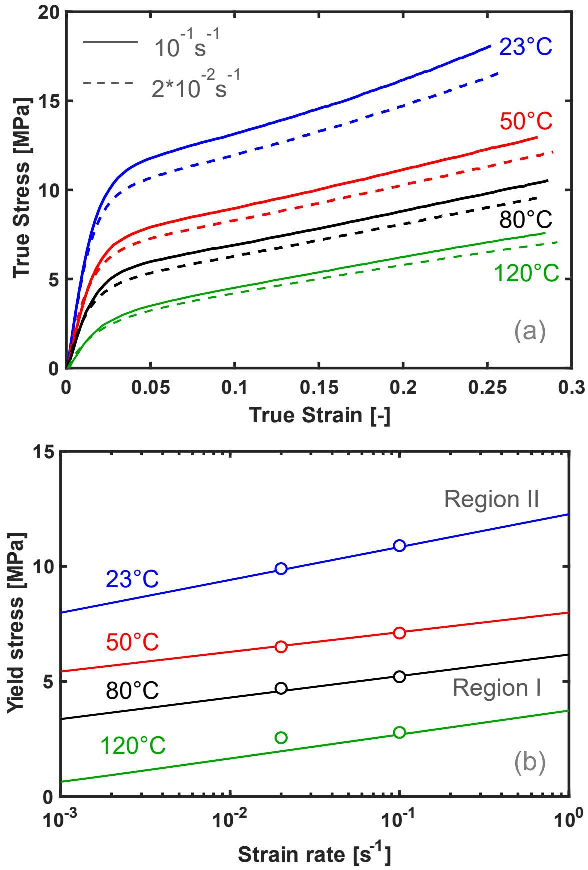

***Figure 5**: (a)True stress-strain plots at four different temperatures and two strain rates. (b) Yield stress dependence on strain rate and temperature visualized on a semi-log scale. Solid lines are fit using Equation (3) and parameters listed in Table 2.*

Table 2: Eyring parameters needed to fit the yield kinetics of PTFE

Process	V^* **[nm³]**	$\dot{\varepsilon}_0$ **[s⁻¹]**	ΔU **[KJmol⁻¹]**
α-process	12	$2*10^{23}$	205
β-process	14.7	$6*10^{164}$	950

Dynamic Mechanical Analysis (DMA) data obtained internally (Figure 6), along with other literature findings [8], provide substantial support for this observation. The β-transition associated with the crystalline phase occurs between 20°C and 30°C, and the α-relaxation related to the amorphous phase, occurs at 120°C. As a result, in Region I, only the α-process is active, whereas in Region II, both α and β processes are active, resulting in increased rate dependence. Consequently, at 120°C, where α-relaxation occurs, the strain rate dependence becomes almost negligible, and therefore depicts a deviation from the Ree-Eyring description as observed in Figure 5 (b).

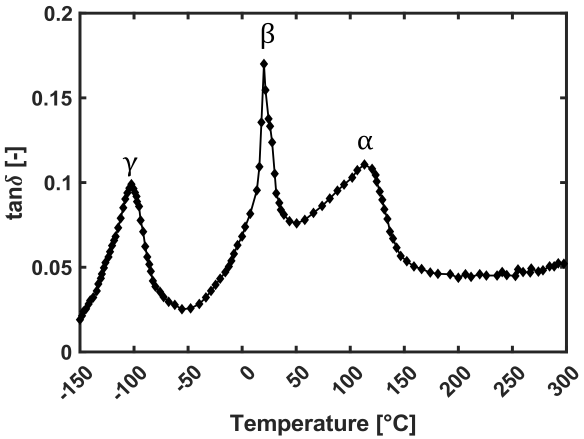

Figure 6*: Tan delta versus temperature plot from DMA analysis showing the different relaxation processes occurring in PTFE.*

Moreover, the quasi-static data presented in Figure 5 (a) indicates a strain hardening response that is not purely elastic, but rather dependent on both the loading rate and temperature. Specifically, the strain hardening component appears to be more pronounced at lower temperatures and higher strain rates. This observation has been shown for other polymers such as polycarbonate [11] and may be attributed to an additional viscous contribution arising from the entanglement network within the material.

Figure 7 illustrates the data in the subsequent stress relaxation phase [1], for a loading rate of 0.02 s^{-1}. The stresses in Figure 7 are normalized to highlight the differences in the relaxation behaviour as the strain level and temperature varies in the experiment. The data clearly suggests a strong dependence of the relaxation behaviour on the predefined strain level at which the relaxation phase begins and the testing temperature. This observation further highlights the need for the implementing the full non-linear elastoviscoplastic model proposed in this study. The following section will detail on the procedure adopted to obtain all the necessary parameters required for the model.

[1] Please note that the data for a loading rate of 0.1 s^{-1} is presented in Appendix 2, Figure 13

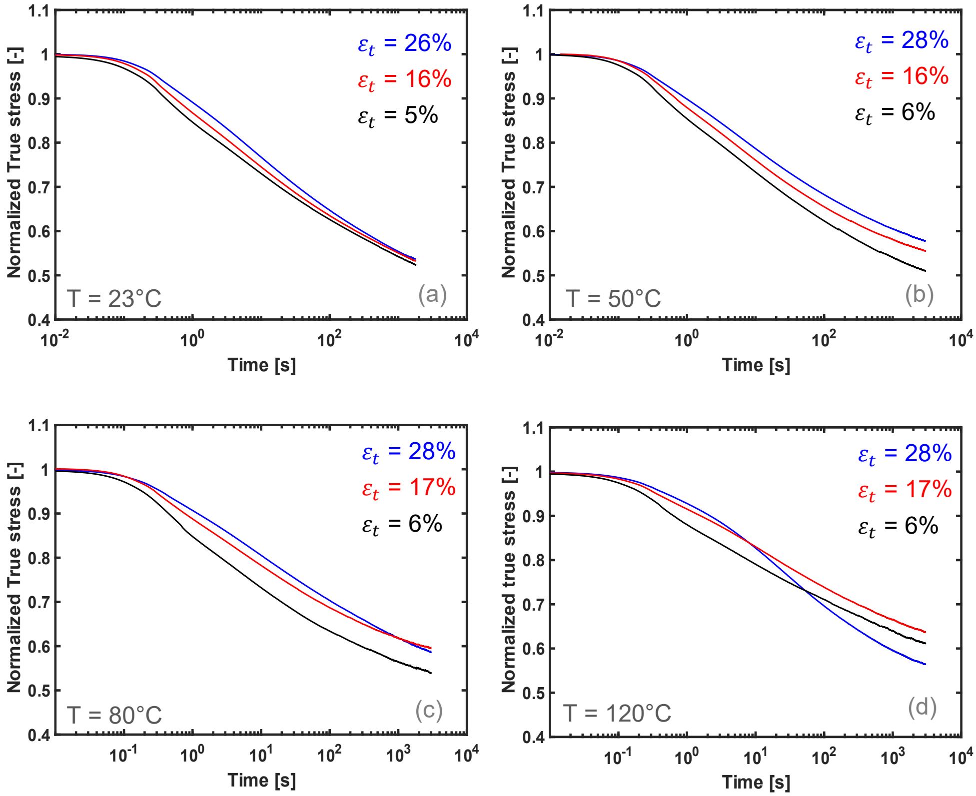

***Figure 7**: Stress relaxation behaviour of PTFE at three different strain levels under a strain rate of $2*10^{-2}\ s^{-1}$ and four different temperatures.*

4.2 Parameter determination for the PTFE model

As briefly described in section 2.1, the PRF framework of ABAQUS is utilized to implement the model. Since the quasi-static data suggests the contribution of two molecular processes towards the yield kinetics of PTFE, a two-process model as depicted in Figure 2 is used. The initial Eyring parameters for both the processes are taken from Table 2.

The methodology presented in the work of Kadin and Schaake [12] is utilized to determine the C10 modulus of the neo-Hookean hyperelastic spring and the initial Eyring parameters of the dashpot in each branch of α-process. The true stress-strain curve at 50°C and a strain rate of $0.1s^{-1}$ is used for this purpose, as at this condition only the α-process is active (refer DMA data presented in Figure 6). To achieve an accurate fit of PTFE's initial non-linear viscoelastic response up to the yield point, 14 branches for the α-process are required, as shown in Figure 8(a). It has to be noted that the strain hardening parameter is not yet included in the model and hence, once the yield point is reached, there is no additional stress contribution from the model.

The final Eyring parameters of α-process are determined by fitting the post-yield data at 50°C and 80°C under a strain rate of 0.1 $s^{-1}$and the model fit is presented in Figure 8 (b) (solid lines). The figure also shows the output from the standard Eyring model (dash-dotted lines) without strain dependency. While the standard Eyring model matches the data well up to the yield point, they deviate significantly at higher strain levels. In contrast, the new model, which includes strain dependency, aligns closely with the experimental data. This observation once again reiterates the importance of implementing the strain dependent Eyring equation proposed in this study to accurately describe the mechanical behaviour exhibited by PTFE. It is worth noting that in these simulations, the strain hardening parameter was included to showcase the differences highlighted.

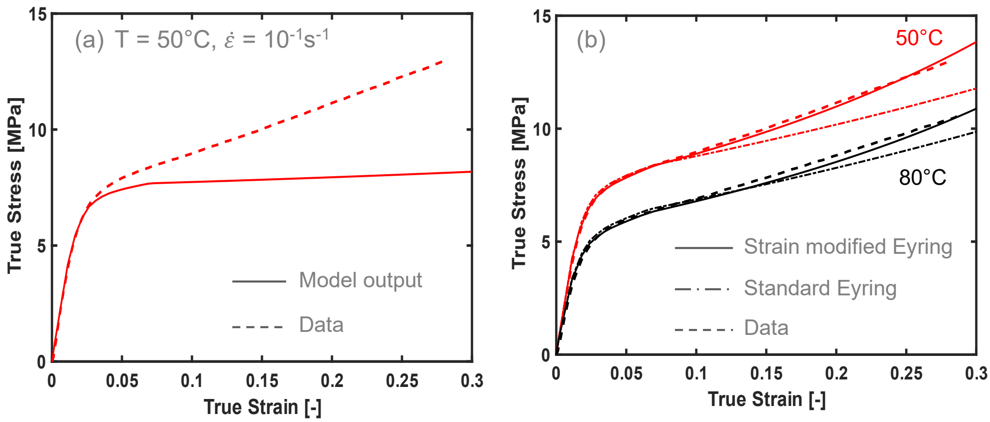

***Figure 8**: (a) Model fit (solid line) to tensile data obtained at 50°C under a strain rate of 0.1 s^{-1}, to determine the initial Eyring parameters for all the branches of α-process using the methodology proposed in [12]. (b) Model output compared against the experimental data. Dashed-dotted lines are output from the standard Eyring model, whereas solid lines are output from the strain modified Eyring model proposed in this study. Dashed line in both figures represent experimental data.*

Subsequently, the initial and final Eyring parameters for the β -process is obtained through the best fit of the data at room temperature under a strain rate of 0.1 s^{-1}. This is illustrated in Figure 9, where the model fit is represented by blue solid line. The figure also highlights the importance of having a two process model for PTFE by displaying the model output (grey solid line) when only the contribution from the α-process is considered. Clearly, in this case, there is a substantial difference in the modulus and the stress levels predicted by the model when compared to the experimental data. Therefore, the decision to include multiple processes, supported by the DMA data, is also verified through the simulation results. It is worth noting that, since the β-process is active only at room temperature among the tested temperatures, a single branch is sufficient to achieve a good fit, as observed in Figure 9.

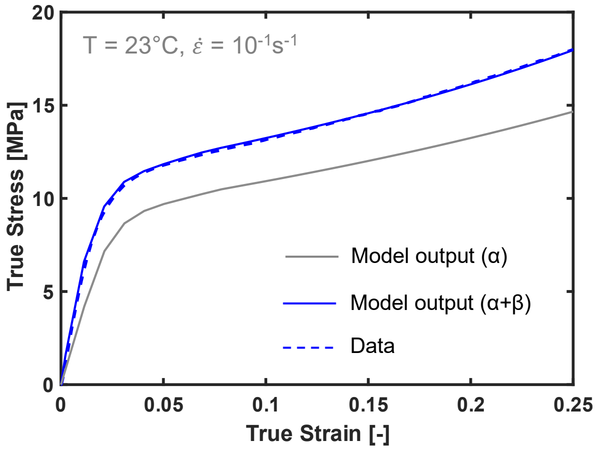

***Figure 9**: (a) Model fit to tensile data obtained at 23°C under a strain rate of 0.1 s^{-1}, to determine the initial and final Eyring parameters for β-process. Blue solid line is the model output when both α and β processes are included in the model. Grey solid line is the model output when only α process is included in the model.*

Furthermore, based on the best fit of the data presented in both Figure 8 (b) and Figure 9, it is found that it is necessary to implement the strain dependency for the activation volume of both the processes. The activation energy parameter is made strain dependent for the α-process, whereas, it is strain independent for the β -process. The thermodynamic constant, $\dot{\varepsilon}_0$, is kept constant for both the processes. Importantly, it should also be noted that all the model parameters are determined based on the *short-term* quasi-static data obtained during the loading phase. Therefore, the model output for the *long-term* stress relaxation behaviour in the subsequent phase can be considered to be predictive.

4.3 Model predictions

After acquiring all the necessary parameters as discussed in the preceding section, simulations are run in ABAQUS using a single element, 2-D axisymmetric model, considering the isotropic nature of virgin PTFE, and replicating the conditions of uniaxial tensile testing outlined in section 3.

Figure 10 illustrates the comparison between the output from these simulations, represented by solid lines, and the experimental data obtained during the loading phase, represented by dashed lines. Given that the model parameters are derived through fitting data at temperatures of 23°C, 50°C and 80°C under a strain rate of 0.1 s^{-1}, it is anticipated that the model would exhibit good agreement with these data. However, it is quite remarkable to observe that the predictions at other conditions also closely align with the data. The strain rate and temperature dependencies are aptly captured, following the Eyring equation. Importantly, the model demonstrates a remarkable potential in capturing the strain rate- and temperature-dependent hardening behaviour, due to the addition of strain dependency in the Eyring equation.

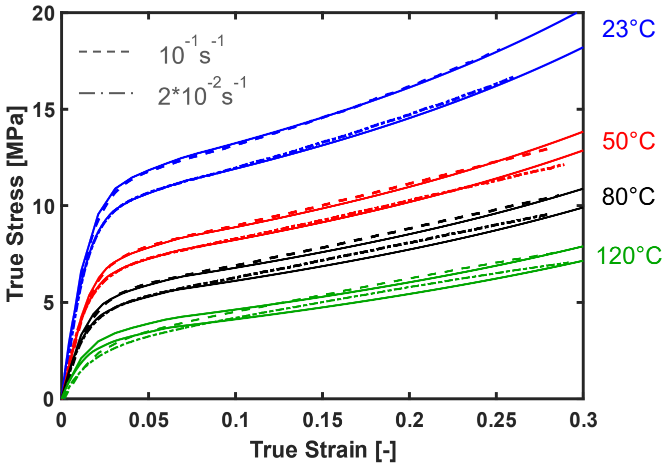

Figure 10*: Model predictions, represented by solid lines, compared against the experimental data obtained at four different temperatures and two strain rates during the loading phase.*

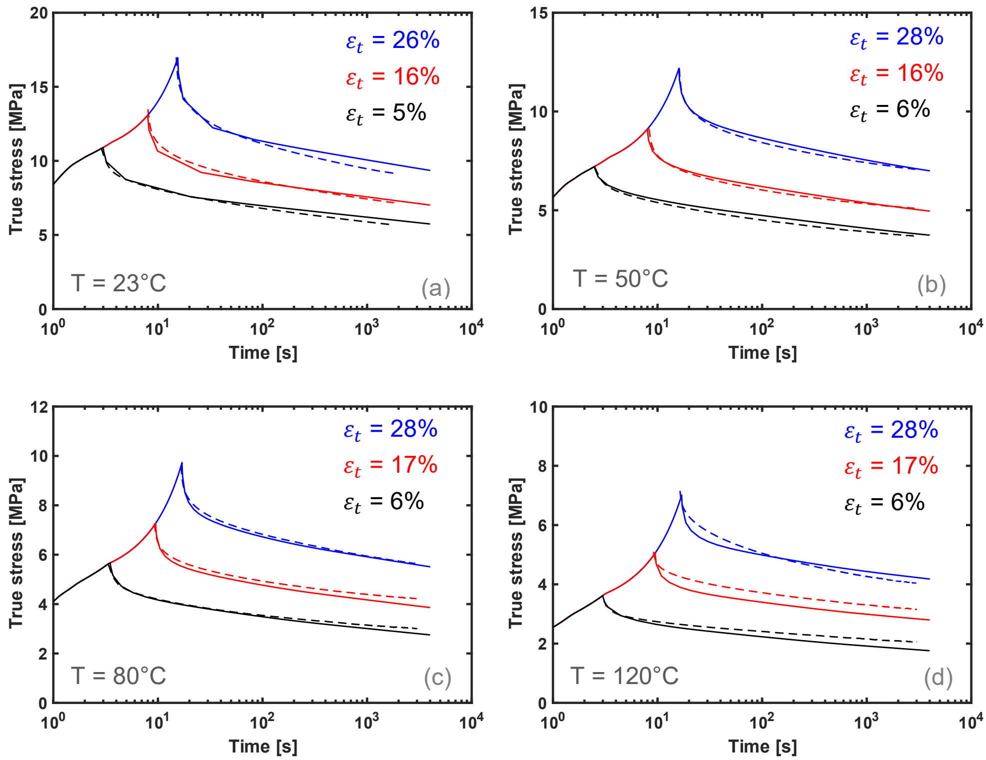

Figure 11*: Stress relaxation behaviour of virgin PTFE under a strain rate of 0.02 s^{-1}. Solid lines represent model predictions and dashed lines are experimental data in all figures.*

Following this, the model's capability to predict the stress relaxation behaviour is assessed. Figure 11 reveals an excellent agreement between the data and model predictions across all strain levels and temperatures tested [2], under a strain rate of 0.02 s^{-1}. Similar to the observation in the loading phase, the figures strongly suggest that the strain rate, temperature and strain dependency exhibited by PTFE in the relaxation phase are also captured remarkably well. Additionally, the model is able to capture the transient relaxation response based only on quasi-static short-term stress-strain data obtained at different temperatures and strain rates during the loading phase. This clearly depicts the consistency of the model in terms of strain rate, temperature and strain level influence across different solicitations and response mechanisms (loading versus relaxation).

5 Conclusion

A novel modelling approach is proposed in this study which is found to be very effective in describing the non-linear elastoviscoplastic behaviour exhibited by virgin PTFE under uniaxial tensile loading conditions. By incorporating the newly proposed strain-modified Eyring equation, the model accurately predicts both quasi-static and transient relaxation phenomena, while taking into account the influence of strain rate, temperature and strain levels. Consequently, the model also holds the potential to predict seal behaviour under anticipated operating conditions.

Furthermore, given the versatility of the proposed approach, it is possible to tailor it to other polymeric materials such as elastomers and thermoplastic polyurethanes (TPUs), thereby enabling a universal modelling framework for materials used in sealing applications.

6 Acknowledgements

The authors would like to express their sincere appreciation to Polymer Competence Centre Leoben GmbH for their invaluable collaboration. All the uniaxial tensile experimental data presented in this paper were performed at their state-of-the-art research facility.

7 References

[1] E. Dhanumalayan and G. M. Joshi, 'Performance properties and applications of polytetrafluoroethylene (PTFE)—a review', *Adv Compos Hybrid Mater*, vol. 1, no. 2, pp. 247–268, Jun. 2018, doi: 10.1007/s42114-018-0023-8.

[2] I. M. Ward and J. Sweeney, Mechanical Properties of Solid Polymers: Third Edition, 1st ed. Wiley, 2012. doi: 10.1002/9781119967125.

[2] Comparison between data and model predictions for a strain rate of 0.1 s^{-1} is presented in Figure 13 under Appendix 2

[3] R. N. Haward and G. Thackray, "The use of a mathematical model to describe isothermal stress-strain curves in glassy thermoplastics," Proc. R. Soc. Lond. A, vol. 302, no. 1471, pp. 453–472, Jan. 1968, doi: 10.1098/rspa.1968.0029.

[4] H. Eyring, "Viscosity, Plasticity, and Diffusion as Examples of Absolute Reaction Rates," The Journal of Chemical Physics, vol. 4, no. 4, pp. 283–291, Apr. 1936, doi: 10.1063/1.1749836.

[5] C. Bauwens-Crowet, J. C. Bauwens, and G. Homès, "Tensile yield-stress behavior of glassy polymers," J. Polym. Sci. A-2 Polym. Phys., vol. 7, no. 4, pp. 735–742, Apr. 1969, doi: 10.1002/pol.1969.160070411.

[6] J. A. Roetling, "Yield stress behaviour of polymethylmethacrylate," Polymer, vol. 6, no. 6, pp. 311–317, Jun. 1965, doi: 10.1016/0032-3861(65)90081-9.

[7] J. A. Roetling, "Yield stress behaviour of isotactic polypropylene," Polymer, vol. 7, no. 7, pp. 303–306, Jul. 1966, doi: 10.1016/0032-3861(66)90025-5.

[8] G. Calleja, A. Jourdan, B. Ameduri, and J.-P. Habas, "Where is the glass transition temperature of poly(tetrafluoroethylene)? A new approach by dynamic rheometry and mechanical tests," European Polymer Journal, vol. 49, no. 8, pp. 2214–2222, Aug. 2013, doi: 10.1016/j.eurpolymj.2013.04.028.

[9] T. Ree and H. Eyring, "Theory of Non-Newtonian Flow. I. Solid Plastic System," Journal of Applied Physics, vol. 26, no. 7, pp. 793–800, Jul. 1955, doi: 10.1063/1.1722098.

[10] T. Dalrymple, J. Hurtado, I. Lapczyk, and H. Ahmadi, "Parallel rheological framework to model the amplitude dependence of the dynamic stiffness in carbon-black-filled rubber," *Constitutive Models for Rubber IX*, no. September, pp. 189–196, 2015. DOI:10.1201/b18701-35.

[11] D. J. A. Senden, S. Krop, J. A. W. Van Dommelen, and L. E. Govaert, 'Rate- and temperature-dependent strain hardening of polycarbonate', *J Polym Sci B Polym Phys*, vol. 50, no. 24, pp. 1680–1693, Dec. 2012, doi: 10.1002/polb.23165.

[12] Y. Kadin and R. Schaake, "Modeling viscoelasticity and cyclic creep of PEEK by parallel rheological framework (PRF)," *European Journal of Mechanics - A/Solids*, vol. 104, p. 105216, Mar. 2024, doi: 10.1016/j.euromechsol.2023.105216.

8 Authors

SKF Seals Global Research & Innovation
Meidoornkade 14, 3992 AE Houten, The Netherlands

Dr. Bharath Kumar Sundararajan, bharath.kumar.sundararajan@skf.com
Dr. Bas van der Vorst, bas.van.der.vorst@skf.com
Dr. Mickael Sansalone, mickael.sansalone@skf.com

SKF Sealing Solutions Austria GmbH
Gabelhoferstraße 25, 8750 Judenburg, Austria

Dr. Michael Fasching, michael.fasching@skf.com
Dr. Thomas Schwarz, thomas.schwarz@skf.com

9 Additional data and simulation output

Appendix 1: Repeatability of the uniaxial tensile test data

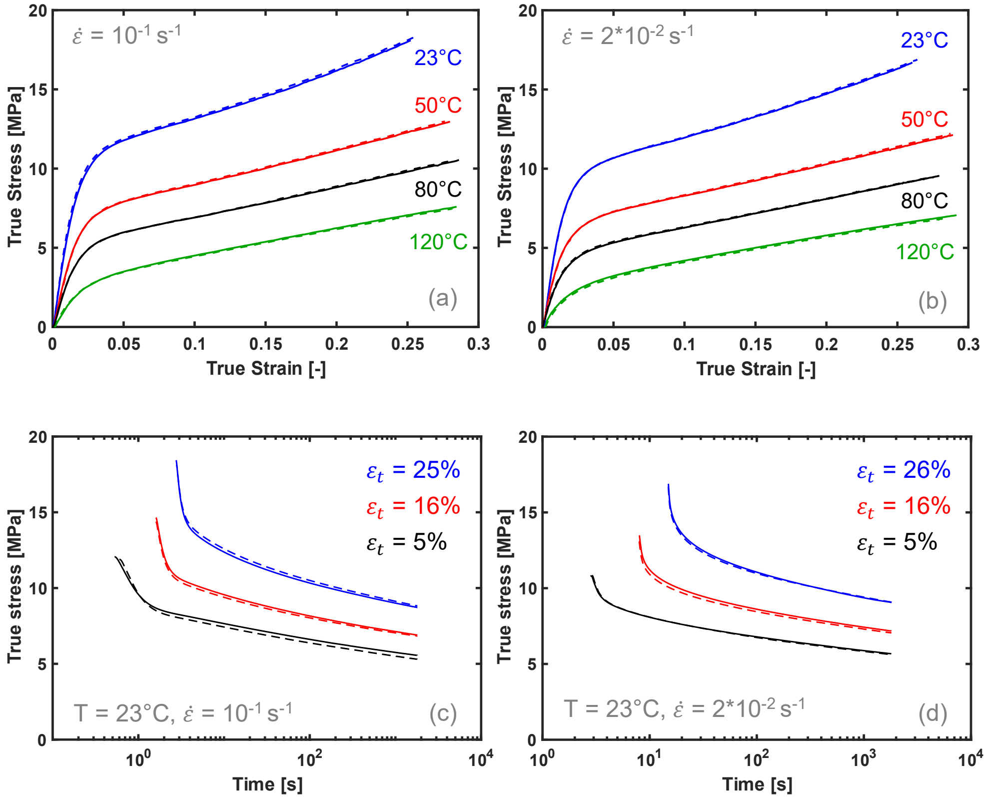

***Figure 12**: Quasi-static and stress relaxation data for Virgin PTFE. For stress relaxation, only the data at room temperature is presented as an example. Dashed lines indicates test that is repeated. The data at each test condition lies exactly on top of each other, indicating excellent repeatability of the methodology adopted.*

Appendix 2: Stress relaxation behaviour of virgin PTFE obtained at a strain rate of 0.1 s^{-1} and compared against model predictions

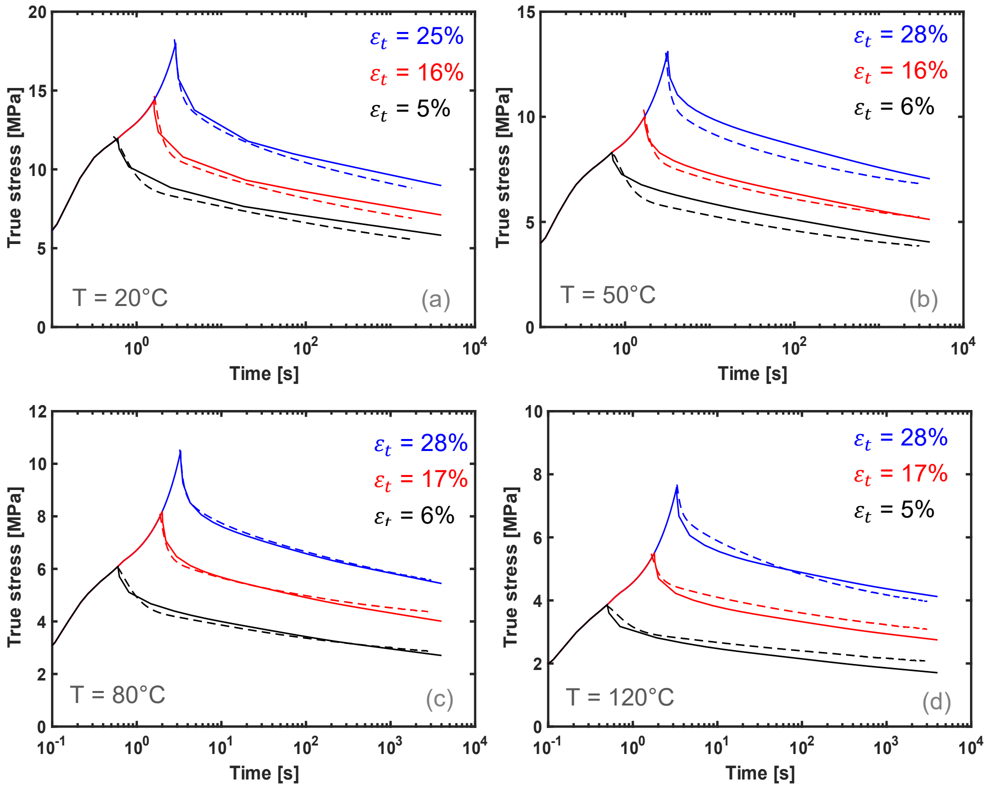

Figure 13*: Stress relaxation behaviour of virgin PTFE at three different strain levels at a strain rate of 0.1 s^{-1} and four different temperatures, namely 23°C, 50°C, 80°C and 120°C. Solid lines represent model predictions and dashed lines are experimental data.*

https://doi.org/10.61319/1HKY1OJS

Simulative Prediction of Leakage for Seat Valves and Bio-Hybrid Fuels

Marius Hofmeister, Felix Fischer, Lukas Boden, Katharina Schmitz

Seat valves play a critical role in various technical applications, such as automotive injectors. Here, predicting leakage is vital, as it can lead to poor combustion behaviour or complete system failure. To address this, a simulation model originally designed for predicting leakage of air in ball seat valves was adapted for the use with bio-hybrid fuels. Since many bio-hybrid fuels differ significantly in their fluid-mechanical properties from conventional fuels and gases like air, the simulation model cannot be used for these liquids without any adjustments. For this reason, additional experiments and simulations have been conducted for various bio-hybrid fuels. The corresponding results are compared and discussed in this study.

1 Introduction

Bio-hybrid fuels are produced based on renewable energy and non-fossil carbon sources. This way a closed carbon loop and CO2 neutral combustion is feasible. Therefore, bio-hybrid fuels are a promising alternative to other green energy carriers such as electric batteries and hydrogen. Within the excellence cluster “The fuel science center”, bio-hybrid fuels are investigated at a holistic level, with the aim of developing methods that can predict the properties of a fuel based solely on its molecular structure. This includes the prediction of combustion related properties like ignition delay, spray propagation and soot formation. Ultimately, these methods can be used to perfectly design a fuel to meet specific technical, economic, and ecological boundary conditions.

By using bio-hybrid fuels as drop-in fuels, existing vehicles and an extensive network of refineries and filling stations can be used, which is a further advantage over other alternative energy sources. To benefit from the mentioned advantages and to ensure safe operation, the compatibility with automotive components is a mandatory prerequisite. However, previous investigation revealed intolerable rates of swelling of elastomer sealing materials, bad lubrication and deviating fluid mechanical properties affecting spray propagation [1–7].

For safe operation especially the functionality of the injection system is of great importance, since unwanted leakage leads to poor combustion affecting engine efficiency and soot formation. In the worst case, leakage can result in damage to components or failure of the entire system. Since many bio-hybrid fuels differ significantly from conventional fuels in terms of their fluid-mechanical properties, it is necessary to check whether conventional injection systems can be used for these fuels or how they need to be modified. To address this, a simulation model originally designed for predicting leakage of air and hydrogen in metallic ball seat valves was adapted for the use with bio-hybrid fuels [8–14]. The aim of this study is to investigate the extent to which the deviating properties of bio-hybrid fuels influence poppet valves.

In the first part of this contribution the used simulation model is described.

Subsequently, the experimental setup for the validation of the simulation model is presented. Here, particular attention is paid to the measurement problems arising from the high vapor pressures of the liquids under investigation. Furthermore, the measurement methods for the determination of the fluid mechanical properties and the surface parameters needed for the simulation model are described. Afterward, the results obtained by means of the simulation model and the experimental results are discussed.

2 Simulation model

The simulation model used in this work is based on the contact mechanics model developed by Persson [15, 16] and a leakage model based on the Hagen–Poiseuille equation. The simulation method has been described comprehensively in previous works [10, 14]. This method can be separated into two distinct steps: a macroscopic simulation and a microscopic simulation. A schematic diagram of the simulation model can be seen in Figure 1. The constituent parts of the simulation are further described in the following subsections.

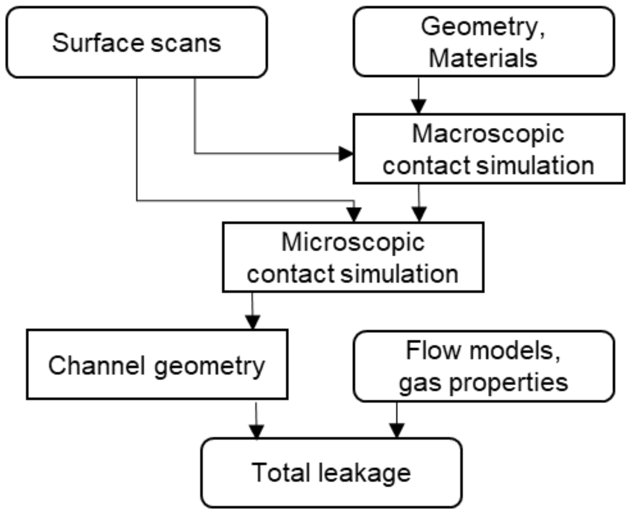

Figure 1 Scheme of the leakage simulation model

2.1 Macroscopic model

The macroscopic simulation model aims to calculate the contact pressure distribution at the sealing surface between the ball and the conical seat. The contact pressure distribution is calculated using an analytical description of the geometry of the ball and the seat at the contact area as well as the elastic material properties of both bodies.

It is important to incorporate the effects of surface roughness into this calculation. The nonzero roughness of all physical bodies leads to a smoothening of the calculated contact pressure distribution; it increases the contact area and reduces the maximal contact pressure. These effects can be included in analytical or numerical models like the finite element method (FEM) by calculating a relation between the distance of the surfaces and the contact pressure; this relation is called the contact–pressure relation.

There are multiple methods to calculate the contact–pressure relation; the most well-known being the Greenwood–Williamson method. This work uses the contact mechanics model developed by Persson two decades ago [16]. The Persson method is based on the spectral decomposition of the rough surfaces and can thus incorporate roughness of multiple length scales. This theory is also fit to describe the effects of the plastic deformation of the surface asperities leading to an increased leak-tightness compared to the purely elastic case.

The calculated contact pressure distributions of the rough surfaces in contact are in the next step used as input parameters of the microscopic simulation model.

2.2 Microscopic model

The microscopic model aims to predict the geometry of the microscopic slit (or more accurately the geometry of the systems of microscopic channels through the apparent contact area) causing the leakage through the valve, as well as calculating the resulting leakage.

The length of the leakage slit can be estimated by defining a contact width based on the contact pressure distribution determined in the previous simulation step. Meanwhile, the height of the channels at the determined contact pressure can be calculated by using a method developed by Persson based on his previously mentioned method [15]. This theory predicts the height of the microscopic net of channels using a percolation-based method. The percolation theory is a mathematical theory predicting the fraction of real contact area and contactless area, at which a free path is formed through a 2D porous medium, in this case, the contact area. The width and length of this critical path, as well as the macroscopic circumference of the contact area, are used to describe the geometry of the leakage slit.

Finally, the leakage through this microscopic slit is calculated using the Hagen–Poiseuille equation for the flow of viscous liquids through a thin rectangular slit.

3 Experimental setup

In the following the experimental setup used in this study is presented. This includes a test rig for the validation of the simulation results, measurements methods for the determination of the fluid mechanical properties needed for the execution of the simulation model, and the optical measurement methods for the evaluation of the surface parameters of the ball seat valve.

3.1 Leakage test rig

For the validation of the simulation the test setup shown in **Figure 2** was build up. The test rig mainly consists of a ball placed on a metallic seat. Due to a piston supplied by pneumatic pressure $p_{\mathrm{pneumatic}}$, the contact force between seat and ball is adjusted. At the inlet the test rig housing is connected to the pressurized sample liquid. From there the sample liquid flows through the sealing seat and the outlet. When leaving the outlet drops form, which are collected in a measuring cylinder. For the determination of the flow rate at the outlet of the test rig, two different methods are used in parallel. The first method is counting the number of droplets passing through the outlet. The determination of the droplet volume will be explained in more detail later. The second approach is measuring the volume flow directly with a measuring cylinder. Additionally, the flow rate is determined with help of a scale. The first method is suitable for low leakage rates, while the second method can be used for high leakage. Depending on the expected flow rate, three different measurement cylinders can be placed into the tube shown in Figure 2. The nominal and actual volume as well as the resolution and the standard deviation indicated by the manufacturer are listed in **Table 1** for each measurement cylinder.

Table 1: Volume and measuring resolution of the used measurement cylinders

Measurement cylinder	Nominal volume	Mean volume	Measuring resolution
1	10 ml	10,01 ± 0,01 ml	0,1 ml
2	25 ml	24,90 ± 0,02 ml	0,5 ml
3	50 ml	50,09 ± 0,06 ml	1,0 ml

The Accuracy of the described measurement principle depends highly on a constant and time-independent droplet size. However, due to the high vapor pressure of some investigated fuel, an evaporation rate can be expected, which is high compared to the measured leakage flow and avoids precise evaluation of flow rate. For this reason, the described setup was adjusted for the use of low-boiling liquids. To avoid evaporation during the measurement process, an additional tube is mounted at the outlet of the test rig, which is sealed to the atmosphere (Figure 2). Inside of the tube a measuring cylinder is placed. Before each measurement series, the measuring cylinder is filled with corresponding sample liquid. Now the sample liquid starts to evaporate, whereupon the level in the measuring cylinder lowers. When the liquid level inside the measuring cylinder doesn’t change anymore, the thermodynamic equilibrium is reached, and no more evaporation occurs during the actual measuring process.

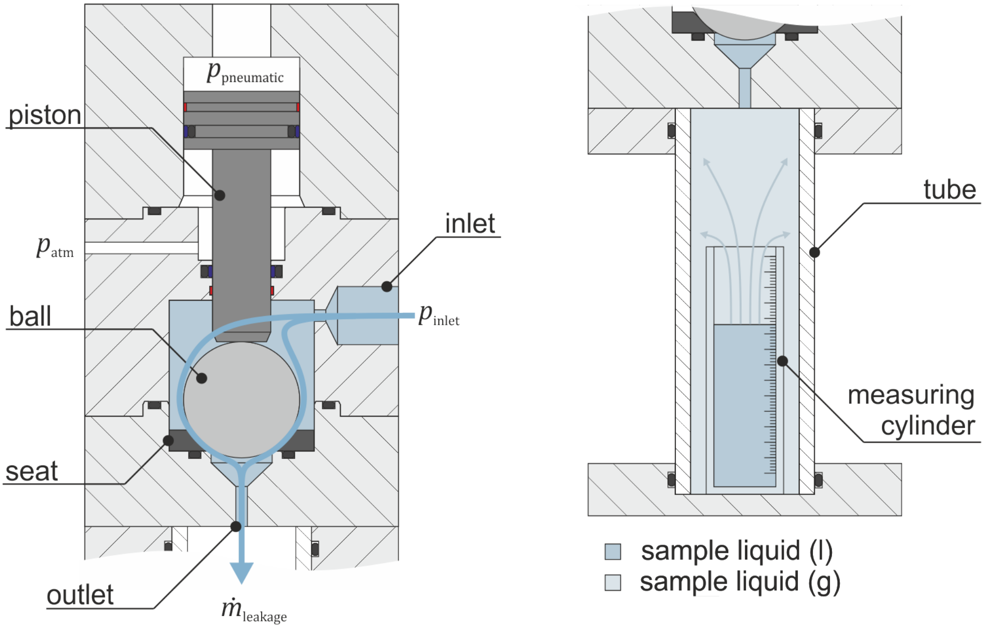

Figure 2 Test rig for the determination of leakage flow rate

Since leakage strongly depends on the viscosity and density and therefore on the liquid temperature, the temperature in the laboratory is measured for each test process. Afterwards, the measured temperature is used to calculate the fluid mechanical properties based on the measurement results presented in section 4.1. The corrected fluid mechanical properties are used as input parameters for the simulation model.

3.2 Determination of droplet volume

To measure the leakage for small flow rates precisely, the droplet volume for the different sample liquids must be estimated with sufficient accuracy. To check the plausibility of the measured droplet volume, the size of the droplets is also estimated by evaluating the surface and gravitational forces acting at the outlet (**Figure 3**).

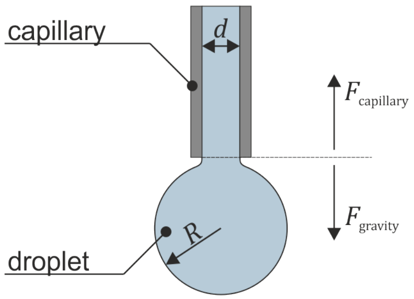

Figure 3 Equilibrium of forces at outlet capillary

The equilibrium of surface and gravitational forces is shown in equation (1). The capillary force $F_{\text{capillary}}$ is the product of the liquid surface tension σ and the capillary diameter d_c multiplied by π. The gravitational force F_{gravity} acts against the capillary force and depends on the droplet volume V_{D} and the liquid density ρ.

$$\sum_{i=1}^{n} F_i = \underbrace{\sigma d_{\text{c}} \pi}_{F_{\text{capillary}}} - \underbrace{V_{\text{D}} \rho \text{g}}_{F_{\text{gravity}}} \tag{1}$$

If both forces are in equilibrium, the droplet volume reaches its maximum and can be calculated with (2).

$$V_{\text{D}} = \frac{\sigma d_{\text{c}} \pi}{\rho \text{g}} \tag{2}$$

In this study a capillary made of stainless steel with an inner diameter d_c of 0.6 mm and an outer diameter of 0.8 mm was used.

3.3 Determination of fluid mechanical properties

For the calculation of leakage and the estimation of droplet volume, the fluid mechanical properties viscosity, density and surface tension are necessary. In the following the measurement methods used for the determination of these values are presented.

Kinematic viscosity

The kinematic viscosity of the different fuels is determined by means of an Ubbelohde viscometer according to DIN 55660 [17]. For tempering the sample liquid during the measurement, a temperature control unit with an accuracy of 0.01 K is used. At the beginning of the experiment, the Ubbelohde viscometer is filled with sample liquid and is placed into the temperature control unit. To ensure a constant temperature level of the liquid, the actual measurement starts 30 minutes after the viscometer were placed into the temperature control unit. An overall number of 7 sub measurements is conducted for each temperature step, whereby the first two measurements are meant to flush the capillary of the viscometer and are not considered for the evaluation of viscosity. The mean value is calculated from the remaining 5 measurements. For all measurements, care was taken to ensure that the measurement time was not less than 100 s.

Density

The liquid density is measured by help of the Archimedean principle [2, 18]. In total 10 sub measurements are carried out from which the mean value is calculated. For the temperature control of the liquid the same system is used as for the determination of kinematic viscosity.

Surface tension

The surface tension of the sample liquids was determined by the du Noüy ring method in accordance with DIN EN 14370 [19]. The used tension scale has a measurement resolution of 0.1 mg. In total 10 measurements are conducted for each fuel and each temperature step. The temperature of the sample liquid is controlled by a temperature control unit with a temperature accuracy of 0.02 K.

4 Results and discussion

In the following the results obtained in this study will be shown. First, the results for the fluid mechanical properties viscosity, density and surface tension are shown. Afterwards, the measured and the simulated leakage rates are presented.

4.1 Fluid mechanical properties

In **Figure 4** the results for the viscosity measurements described in 3.3 are shown for EN 590, Ethanol and Acetone for a temperature range between 10 and 30 °C. Overall a low standard deviation less than 0.5 % could be achieved for each liquid and temperature step. The highest values for viscosity are obtained for EN 590 with 3.898 mm²/s at 20 °C. The viscosity of ethanol and acetone is significantly lower than for diesel EN 590 (1.5 mm²/s, 0.317 mm²/s).

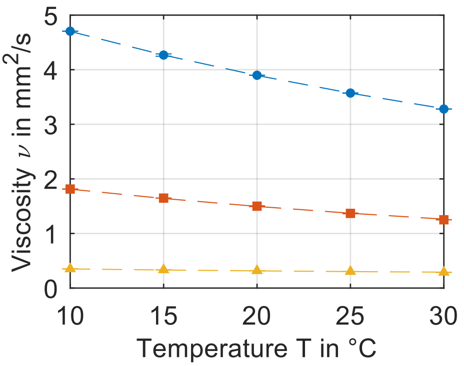

Liquid	A	B	C
EN 590	0.123	0.079	0.183
Ethanol	670.2	480.5	33.11
Acetone	173.7	143.4	40.64

Figure 4 Results for kinematic viscosity and corresponding Arrhenius coefficients

To correct the viscosity values for the simulation model, based on the measurement data and the Arrhenius equation visible in (3) a regression analysis was performed.

$$\nu(T) = A \cdot \exp\left(\frac{B}{C+T}\right) \tag{3}$$

With help of (3) and the calculated Arrhenius coefficients listed in Figure 4 the viscosity can be calculated for varying liquid temperatures during the leakage experiment.

The results for the density measurements and the coefficients of the linear regression analysis are shown in **Figure 5**. The standard deviation for each measuring point is less than 1 %.

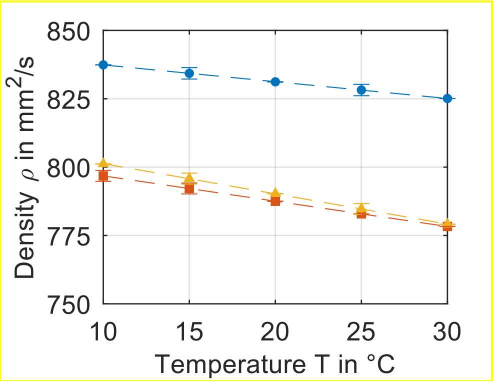

	Liquid	A	B
●	EN 590	843.5	-0.614
■	Ethanol	806.1	-0.926
▲	Acetone	812.3	-1.106

Figure 5 Results for density and corresponding linear coefficients

In **Figure 6** Results for surface tension and corresponding linear coefficients the results for the surface tension measurements conducted with the du Noüy ring method are shown. Just as with the density results, a linear regression analysis was performed. The corresponding coefficients of the analysis are shown in Figure 6.

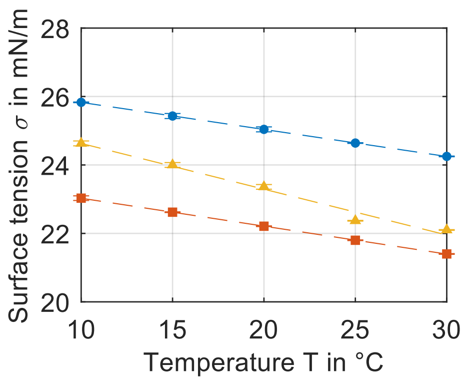

	Liquid	A	B
●	EN 590	26.62	-0.079
■	Ethanol	23.84	-0.082
▲	Acetone	25.97	-0.134

Figure 6 Results for surface tension and corresponding linear coefficients

4.2 Droplet size

Depending on the fluid mechanical properties determined in 4.1 the droplet size was calculated according to the simplified approach described in (2). The results for temperatures in a range between 10 and 30 °C are shown in **Figure 7**.

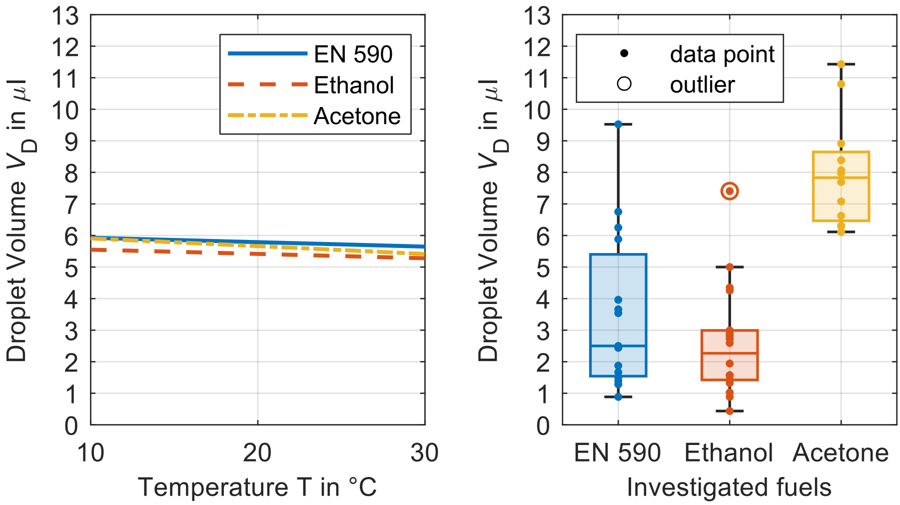

Figure 7 Estimated droplet volume V_D and measured droplet size deviation

Due to the high surface tension the droplet volume of EN 590 is the highest in the considered temperature range. The values for Ethanol and Acetone are slightly lower but in the same order of magnitude.

The results show that the droplet volume in the relevant temperature range depends insignificantly on the temperature. The target temperature during the leakage tests is 20 °C. Assuming a maximum temperature deviation of 2 °C during or between individual experiments, the maximum deviation of the drop volume is only 0.48 % for EN 590. For ethanol and acetone, the maximum deviation is 0.50 and 0.87 %.

The estimated droplet volume was also used to check the plausibility of the measured droplet sizes. On the right-hand side in Figure 7 one can see the results for the droplet volume obtained with the methods described in 3.2. As can be seen the results are in the same order of magnitude for the calculated and measured values. However, for each fuel a high deviation in droplet size is obtained. In case of EN 590 and Ethanol the measured mean value is below the calculated drop size. For Acetone the simplified underestimates the measured mean value.

4.3 Leakage

The leakage measurements described in 3.1 were carried out for two different seats differing in surface properties. In **Figure 8** the results for the flow rate measurements are shown for the investigated liquids and seat 1. For all fuels and seats a pneumatic piston pressure and a fluid pressure of 3 bar was applied. Although all measurements were carried out under similar boundary conditions, there are large deviations within the individual measurement series. This is most evident for the diesel measurement. Here, the averaged flow rate for measurement 2 is 27 µl/s and therefore one order of magnitude higher than for measurement 1 and 3 (2.3 µl /s and 1.8 µl/s).

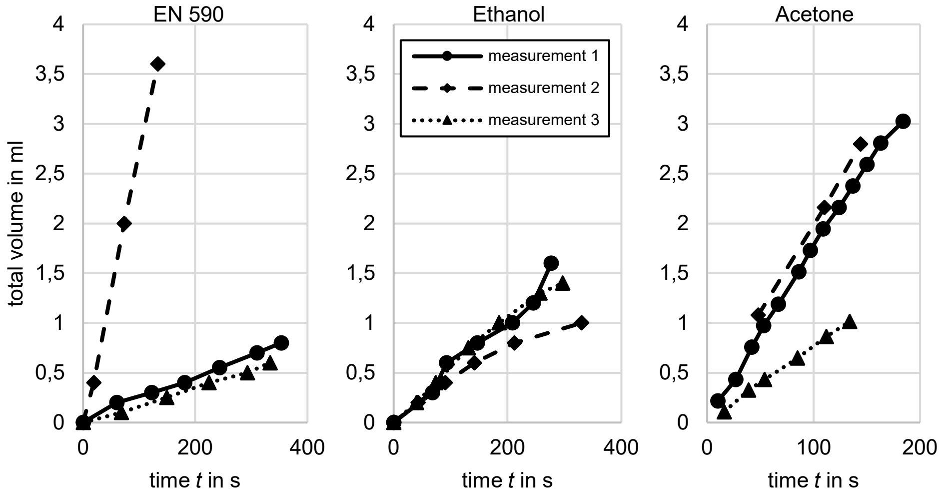

Figure 8 Flowrate measurements for seat 1

For ethanol and acetone, the results are more reproducible than for EN 590, although they still differ greatly from each other. Furthermore, the results show that the volume flow decreases after a certain time. This phenomenon can be seen most clearly for ethanol and the sub measurements 2 and 3. While the average flow rate at the beginning of the measurement between the first two increments is 4.65 µl/s (measurement 2) and 5.00 µl/s, it decreases significantly over time. At the end of each measurement series, the flow rate for measurement 2 is 1.69 µl/s and for measurement 3 2.50 µl/s. Here it was assumed that during the measurement, particles increasingly accumulate in the contact between the ball and the seat, which gradually close the gap and reduce the flow rate.

Similar behavior is already known from measurements with distilled water. Here it was assumed that during the measurement, particles increasingly accumulate in the contact between the ball and the seat, which gradually close the gap and reduce the flow rate. For measurements performed with nitrogen as sample fluid, this behavior could not be observed. For this reason, it is assumed that particles are also responsible for the phenomena shown in this case [12, 13].

The averaged results for the measured leakage flow rate and for the simulated flow rate are listed in **Table 2**. As already indicated in Figure 8, the repeatability of the leakage measurements is poor, which is reflected in a high standard deviation for all seats and liquids examined. In the case of diesel and seat 2, the standard deviation is even greater than the calculated mean value.

It can also be seen that the measured leakage is very high compared to the simulated values. For most measured values are one order of magnitude higher than calculated.

Table 2: Measured and simulated leakage flow rate for different seats

		Seat 1		Seat 2	
		S_Q = 2.53	γ = 0.75	S_Q = 1.9	γ = 0.35
		Leakage in µl/s		Leakage in µl/s	
Sample liquid	Viscosity in mm²/s	measured	simulated	measured	simulated
Acetone	0.317	66 ± 17	5.1	17 ± 6	2.6
EN 590	3.898	12 ± 6	0.47	10 ± 12	0.25
Ethanol	1.500	55 ± 20	1.3	5.1 ± 1.4	

The investigated seats differ from each other regarding their surface properties indicated by the mean squared roughness value S_Q and the Peklenik number γ. In this context an infinite Peklenik number corresponds to a surface with grooves in parallel to the flow direction. An Peklenik number equal to zero is related to grooves aligned orthogonally to the direction of flow. Consequently, the surface of seat 1 is rougher, and the surface peaks are more aligned in flow direction than for seat 2. Both factors promote leakage flow. This trend can be seen both in the measurement results and in the results of the simulation.

5 Summary and Conclusion

In this paper, a simulation model for the investigation of leakage in ball seat valves and corresponding methods for the experimental validation of the leakage flow were presented. A particular focus was placed on the challenges arising from the low viscosity and high vapor pressure of many bio-hybrid fuels.

Subsequently, the experimental results and the results of the simulation were presented. It was found that the results for leakage vary greatly. This is especially true for EN 590. A probable reason for the large deviations could be the contamination of the test liquids by particles.

It was also found that the simulation underestimates the leakage by an order of magnitude, which can also be explained by particles that prevent the valve from closing completely.

Overall, the high standard deviations of the measurement results make a meaningful comparison with the simulation results difficult. For this reason, future investigations will focus on the improvement of reproducibility. This primarily involves the systematic investigation of the particle load of the test liquids used and a finer pre-filtering of the liquids. The tests are then repeated using the filtered liquids with a defined particle load.

At the same time, the results also show that the qualitative trends like the influence of surface parameters and viscosity on the leakage can already be correctly captured by the simulation.

6 Acknowledgements

Funded by the Deutsche Forschungsgemeinschaft (DFG, German Research Foundation) under Germany´s Excellence Strategy – Exzellenzcluster 2186 „The Fuel Science Center".

7 Nomenclature

Variable	***Description***	***Unit***
A B C	Coefficients for regression analysis of fluid mechanical properties	
d_c	Capillary diameter	[mm]
$F_{\text{capillary}}$	Capillary force	[N]
F_{gravity}	Gravitational force	[N]
g	Gravitational constant	[m/s^2]
$\dot{m}_{\text{leakage}}$	Leakage mass flow	[kg/s]
p_{atm}	Atmospheric pressure	[bar]
p_{inlet}	Inlet pressure	[bar]
$p_{\text{pneumatic}}$	Pneumatic pressure	[bar]
R	Droplet radius	[mm]
S_Q	Mean square roughness	[µm]
T	Temperature	[°C]
V_{D}	Droplet volume	[ml]
γ	Peklenik number	[-]
σ	Surface tension	[mN/m]
ρ	Liquid density	[kg/m^3]
ν	Kinematic viscosity	[mm^2/s]

8 References

[1] HOFMEISTER, Marius; Boden, Lukas; Schmitz, Katharina: *Challenges in the Use of Bio-hybrid Fuels as Drop-in Fuel*. In: *ASME 2024 - 18th International Conference on Energy Sustainability* (2024)

[2] HOFMEISTER, Marius, et al.: Tribological properties of PTFE sealing materials with regard to bio-hybrid fuels. In: *Sealing technology - old school and cutting edge* : *International Sealing Conference : 21st ISC, Stuttgart, Germany, October 12-13, 2022*. Frankfurt am Main : Fachverband Fluidtechnik im VDMA e.V, 2022, S. 89–104

[3] HOFMEISTER, Marius, et al.: *Neue Herausforderungen an Dichtungswerkstoffe im Hinblick auf bio-hybride Kraftstoffe*. In: *Mobility* 7 (2022), RWTH-2022-09721. URL https://publications.rwth-aachen.de/record/854697

[4] HOFMEISTER, Marius, et al.: Optimization of Bio-hybrid Fuel Blends regarding Material Compatibility with Elastomer Seals. In: *11th FSC* : *Fuel Science - From Production to Propulsion*, 2023

[5] VÖLKER, Simon, et al.: The drop-in potential of hydroformylated Fischer-Tropsch fuels from CO2. In: *11th FSC* : *Fuel Science - From Production to Propulsion*, 2023

[6] VÖLKER, Simon, et al.: Towards sustainable transport with hydroformylated Fischer-Tropsch fuels as drop-in fuels employing drop-in technology. In: *11th FSC* : *Fuel Science - From Production to Propulsion*, 2023

[7] GRÜTERING, Carolin; Honecker, C.: *Methyl ketones: a comprehensive study of the last biofuel* (2023)

[8] FISCHER, Felix J., et al.: Finite Element Analysis of the Hard-Hard Contact in Seat Valves. In: *Global Fluid Power Society PhD Symposium*.

[9] FISCHER, Felix J.; Bady, Dariush; Schmitz, Katharina: *Leakage of Metallic Ball Seat Valves with Anisotropic Surfaces*. In: *Chemical Engineering & Technology* 46 (2023), Nr. 1, S. 102–109

[10] FISCHER, Felix J.; Murrenhoff, Hubertus; Schmitz, Katharina: *Influence of normal force in metallic sealing*. In: *Engineering Reports* 3 (2021), Nr. 10

[11] PENG, Chao, et al.: *Comparative analysis of leakage calculations for metallic seals of ball-seat valves using the multi-asperity model and the magnification-based model*. In: *Tribology International* 163 (2021), S. 107130

[12] FISCHER, Felix J.; Peng, Chao; Schmitz, Katharina: Research on Leakage Characteristics of Metallic Seals Based on Soft/Hard Contact Theories. In: *10. International Conference on Fluid Power Hangzhou*.

[13] FISCHER, Felix J., et al.: *Geometry of Ball Seat Valves*. In: *International Journal of Fluid Power* (2021)

[14] FISCHER, Felix. J., et al.: *Fluid Leakage in Metallic Seals*. In: *Tribology Letters* 68 (2020), Nr. 4

[15] PERSSON, B. N. J.: *Fluid dynamics at the interface between contacting elastic solids with randomly rough surfaces*. In: *Journal of physics. Condensed matter : an Institute of Physics journal* 22 (2010), Nr. 26, S. 265004

[16] PERSSON, B. N. J.: *Theory of rubber friction and contact mechanics*. In: *The Journal of Chemical Physics* 115 (2001), Nr. 8, S. 3840–3861

[17] 1976. *DIN 55660:1976-02*

[18] GRÜTERING, Carolin, et al.: *Methyl ketones: a comprehensive study of a novel biofuel*. In: *Sustainable Energy & Fuels* 8 (2024), Nr. 9, S. 2059–2072

[19] 2004. *DIN EN 14370:2004-11*

9 Authors

RWTH Aachen - Institut für fluidtechnische Antriebe und Systeme (ifas),

Campus-Boulevard 30, 52074 Aachen, Germany:

Marius Hofmeister, M. Sc., ORCID 0000-0002-6672-5800,
marius.hofmeister@ifas.rwth-aachen.de

Felix Fischer, M. Sc., ORCID 0000-0003-2081-1823,
f.fischer@ifas.rwth-aachen.de

Lukas Boden, M. Sc., ORCID 0009-0003-1282-8032,
lukas.boden@ifas.rwth-aachen.de

Univ.-Prof. Dr.-Ing. Katharina Schmitz, ORCID 0000-0002-1454-8267,
katharina.schmitz@ifas.rwth-aachen.de

https://doi.org/10.61319/HTXAF9PX

Influence of surface topography on stick-slip-effects – an experimental and numerical study

Martin Wittmaack, Markus André, Sebastian Rakowski, Katharina Schmitz

Lubricated sealing systems tend to have undesirable stick-slip-effects under certain service conditions. This paper presents a tribometer test to analyze the influence of the surface topography on the stick-slip effect. In this test, it is possible to provoke or avoid the stick-slip effect by rotating the surface structure by 90°. Corresponding numerical contact- and CFD-simulations, based on the measured surface topography show clearly the influence of the surface structure on the flow in the lubrication gap. These numerical studies show the influence of the surface topography on the fluid dynamics in the lubrication gap of translational seals and enable a deeper understanding of the stick-slip mechanisms in lubricated sealing contacts.

1 Introduction

Lubricated sealing systems, such as in automotive brake master cylinders or other hydraulic systems, tend to have undesirable stick-slip-effects under certain service conditions. These stick-slip-effects are clearly driven by the complex frictional behavior in the mixed lubrication regime [1]. A significant factor in this tribological system is the surface topography. Thus, it is necessary to investigate and describe the lubrication effects on a micromechanical level. The systematic structuring of the surface topography can enhance the load carrying capacity of the lubricating film while simultaneously reducing friction [2, 3]. Furthermore, this targeted change in hydrodynamic lubrication allows minimizing the stick-slip tendency in pin on disk tribometer tests [4, 5].

In this paper, a tribometer test is presented and used to investigate the influence of surface structure on the stick-slip effect. Finally, numerical contact and CFD simulations are carried out based on measured surfaces, which show the influence of the surface topography on the flow in the lubrication gap and thus provide some conclusions on the complex friction behavior.

2 Tribometer test

The standard DIN 51834-5 [6], which is currently in the draft status, was recently published for the investigation of the stick-slip tendency of brake fluids in EPDM (ethylene propylene diene monomer rubber)-steel contacts. In this standard tribometer test, a roller bearing steel ball rubs on a roughened EPDM surface (point contact). This test procedure allows to successfully quantify the stick-slip tendency of brake fluids [7]. For a better tribological description of lubricated sealing systems, this standard test is modified so that an EPDM cord slides on a steel surface (line contact).

2.1 Experimental setup

In this test the tribometer presses a cylindrical $70\ \mathrm{ShA}$ EPDM specimen (Figure 1 - Item 2) (diameter: $5\ \mathrm{mm}$, length: $5\ \mathrm{mm}$) onto a ground C45 steel surface (Figure 1 - Item 4) with a defined normal force $F_N = 10, 20, 30\ \mathrm{N}$. The tribometer performs an oscillating motion $u(t)$ with the frequency $f = 1, \dots, 6\ \mathrm{Hz}$ and an amplitude $a = 1.5\ mm$ according to

$$u(t) = a \cdot sin\,(2 \cdot \pi \cdot f \cdot t). \tag{1}$$

The specimen holder is connected to the tribometer with two flat springs with a thickness of $0.5\ \mathrm{mm}$. The resulting stiffness per spring is $315\ \mathrm{N/mm}$. The stiffness of the adapter can be adjusted using the flat springs. The fluid (Figure 1 - Item 3) to be tested covers the steel specimen. In this work, a brake fluid with a viscosity of $\eta = 11.5 \cdot 10^{-3}\ \mathrm{Pa \cdot s}$ and ethanol with a viscosity of $\eta = 1.2 \cdot 10^{-3}\ \mathrm{Pa \cdot s}$ are examined.

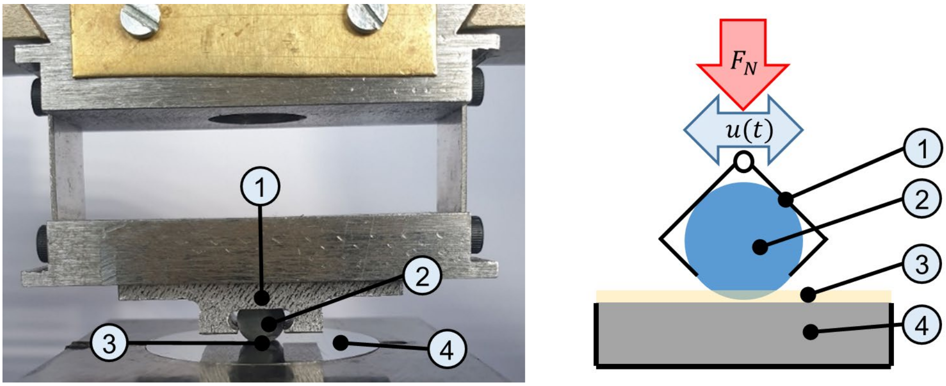

Figure 1: Experimental setup: 1) specimen holder; 2) cylindrical EPDM specimen; 3) fluid; 4) steel specimen

2.2 Investigated surfaces

The size of the analyzed surface section is $99.58 \times 99.58\ \mathrm{\mu m}^2$ and is measured with a confocal laser-scanning microscope (Keyence VK-100) with a resolution of $\Delta x = \Delta y = 0.341\ \mathrm{\mu m}$. This results in a surface resolution of 293×293 pixels. After the measurement, the curvature and the inclination of the measured surface are corrected using a second order polynomial. Furthermore, the measured data is smoothed with a 3x3 Gaussian matrix filter. Figure 2 shows the undeformed surfaces $r_{1,0}(x, y)$ and $r_{2,0}(x, y)$. As well, the visualization of the steel surface in Figure 2 as the roughness parameter in Table 1 and Table 2 show the clear anisotropic roughness of the steel surface due to grinding. The line roughness parameters are calculated for seven equidistant lines with an evaluation length of $89.349\ \mathrm{\mu m}$. The average values (Avg.) and the standard deviations (SD) of the multiple lines are listed in Table 1. Table 2 shows the surface roughness values for both surfaces.

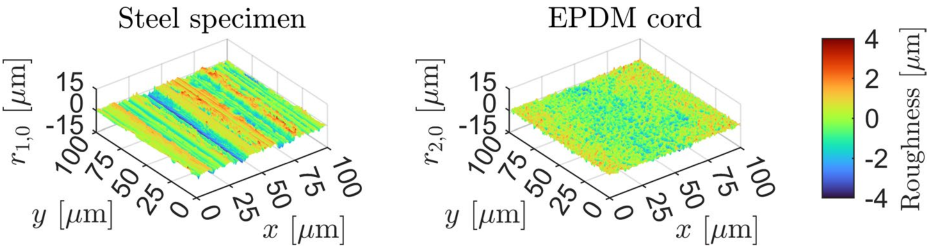

Figure 2: Examined surfaces

Table 1: Line roughness parameters of the examined surfaces

Surface	Direction		R_a [µm]	R_{pk} [µm]	R_k [µm]	R_{vk} [µm]	R_z [µm]
Steel	x	Avg.	0.964	0.911	2.748	1.522	6.605
		SD	0.038	0.314	0.195	0.191	0.509
Steel	y	Avg.	0.548	0.431	1.484	0.784	2.925
		SD	0.190	0.202	0.659	0.799	1.084
EPDM	x	Avg.	0.593	0.542	1.766	0.943	4.110
		SD	0.050	0.134	0.230	0.252	0.491
EPDM	y	Avg.	0.512	0.592	1.408	0.914	3.838
		SD	0.032	0.121	0.131	0.236	0.323

Table 2 Surface roughness parameters of the examined surfaces

Surface	S_a [µm]	S_{pk} [µm]	S_k [µm]	S_{vk} [µm]	S_{td} [°]	S_{tr} [−]
Steel	0.923	0.962	2.58	1.583	91.2	0.082
EPDM	0.649	0.671	1.972	1.081	82.8	0.132

2.3 Test results

Figure 3 shows the ratio of the friction force F_R to normal force F_N depending on the harmonic motion $u(t)$ for two orientations of the steel sample. In the load case shown, the normal force is $F_N = 20\ \mathrm{N}$ and the frequency $f = 4\ \mathrm{Hz}$. On the left side, the EPDM sample slides perpendicular ($\perp$) to the grinding direction. It can be seen, that no stick-slip effect occurs. The maximum ratio F_R/F_N occurs when the EPDM changes from sticking to sliding ($u \approx 1\ \mathrm{mm}, u \approx -1.2\ \mathrm{mm}$). Afterwards the friction force decreases and increases again as the sample slows down. However, if the steel sample is rotated by 90° so that the EPDM sample slides in the direction of grinding (right diagram (||)), the stick-slip effect occurs. In this case, the maximum ratio F_R/F_N during the change from sticking to sliding is nearly constant. The stick-slip effect is not only visible in the friction force signal, but is also clearly audible through squeaking noises.

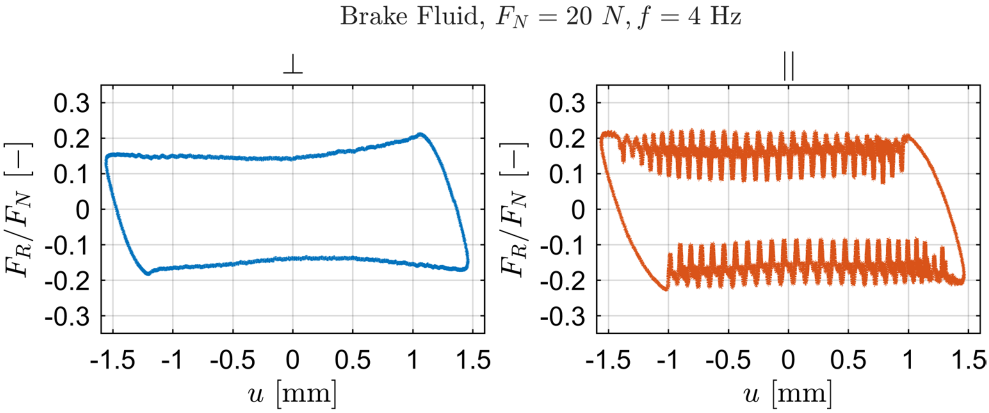

Figure 3: Measured ratio of friction force to normal force for two orientations of the steel sample for the brake fluid

For the quantification of the stick-slip tendency of a brake fluid to the standard DIN 51834-5 defines the stick-slip index σ. This index corresponds to the standard deviation of the oscillating force during stick-slip movement. Details on the calculation of the stick-slip index σ can be found in [6, 8].

Figure 4 shows the stick-slip index σ for the test program of the brake fluid. It is clearly visible, that no stick-slip occurs while the EPDM cord is rubbing perpendicular $\perp$ to the grinding direction. If the surface structure is orientated parallel to the moving direction, it can be seen that the stick-slip effect occurs with the exception of the frequency $f = 1$ Hz. The diagram shows also that the stick-slip index has a maximum at a frequency of $f = 4$ Hz and decreases again with higher excitation frequencies and the resulting higher sliding velocities.

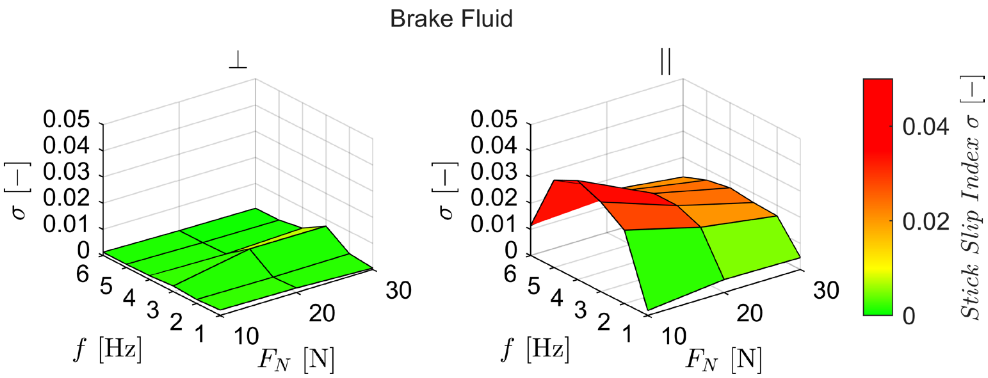

Figure 4: Stick-Slip Index force for two orientations of the steel sample for the brake fluid

Figure 5 shows the ratio of the friction force F_R to normal force F_N for the fluid Ethanol. Just as in the tests with brake fluid, the stick-slip effect occurs when sliding in the grinding direction (||) and does not occur when the EPDM cord is rubbing perpendicular (⊥) to the surface structure. Furthermore the friction force is higher compared to the brake fluid due to the lower lubricating effect of the ethanol.

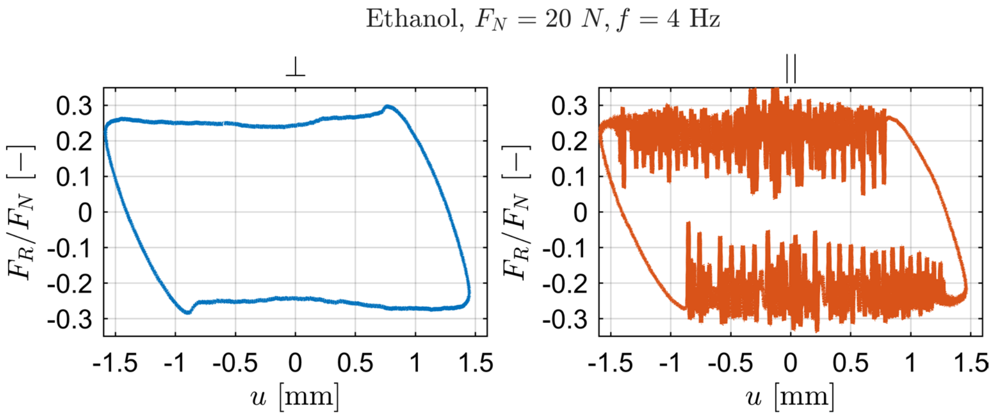

Figure 5: Measured ratio of friction force to normal force for two orientations of the steel sample for the fluid Ethanol

The stick-slip index for ethanol (Figure 6) also shows the dependence on the orientation of the surface structure. For movement perpendicular ⊥ to the grinding direction, there is no stick-slip effect. Similar to the brake fluid, no stick-slip occurs at a frequency of $f = 1\,\mathrm{Hz}$. According to the ratio F_R/F_N, the stick slip indexes σ are greater than for brake fluid due to the larger amplitudes. In addition, compared to the brake fluid, there is no drop in the index with increasing frequencies.

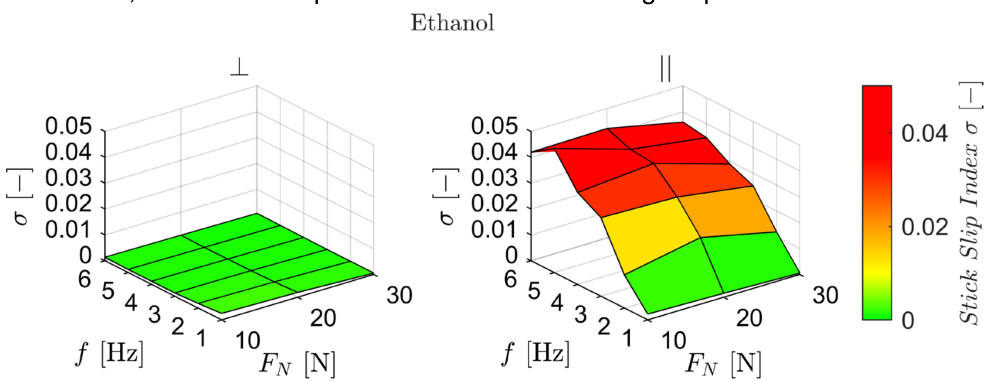

Figure 6: Stick-Slip Index force for two orientations of the steel sample for the fluid Ethanol

3 Numerical Study

For a deeper understanding of the test results, a numerical analysis of the tribological system is carried out below. For this purpose, the solid contact between the EPDM cord and the steel surface is first simulated on a microscopic scale. Subsequently, flow simulations between the deformed surfaces show the influence on the lubricating film.

3.1 Contact simulation on micro scale

Figure 7 shows the effective gap height $h(x,y)$, which is calculated from the difference between the z-coordinates of the deformed surfaces 1 and 2 to

$$h(x,y) = z_1(x,y) - z_2(x,y). \tag{2}$$

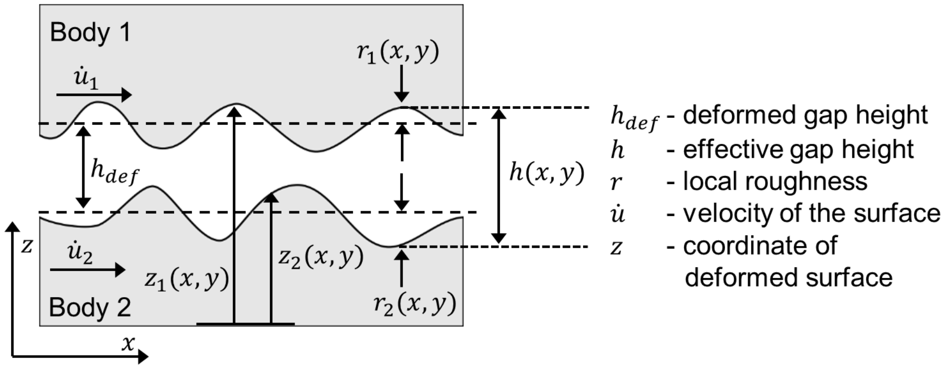

Figure 7: Definition of the gap height

In macroscopic component simulations, the surfaces of the parts are usually modelled as ideally smooth surfaces. This ideally smooth surface can be interpreted as the average plane of roughness. In this sense, the deformed gap height h_{def} takes into account the mechanical deformations caused by the local contact of the two surfaces. It is calculated by averaging over the examined surface section Ω as follows

$$h_{def} = \frac{1}{\Omega} \int_{(\Omega)} h(x,y)\, d\Omega. \tag{3}$$

To describe the elastic deformations in the solid contact and the normal force as a function of the distance between the two rough surfaces, a contact simulation of real measured surfaces (Figure 2) is carried out on a microscopic scale. An elastic half-space model is used for this purpose, by solving the Boussinesq equation according to Bartel [9].

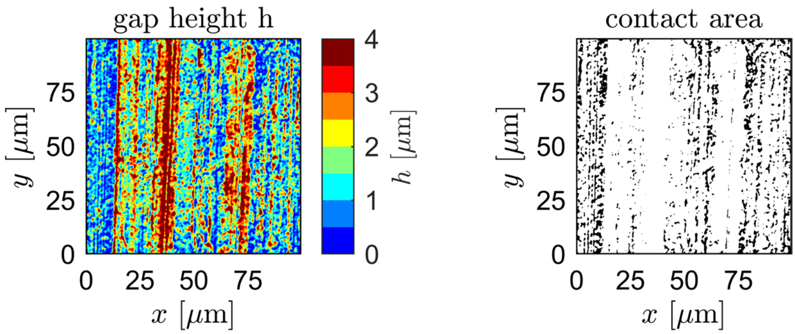

Figure 8: Gap height $h(x, y)$ and the real contact area at $h_{def} = 2.06\ \mu m$

Figure 8 shows on the left side an example of the effective gap height $h(x, y)$ at the deformed gap height $h_{def} = 2.06$ µm. The structure of the steel surface is still clearly visible. In addition to the effective gap height $h(x, y)$, Figure 8 shows the real contact area. It can be seen that contact only occurs at the roughness peaks of the steel surface.

3.2 Flow simulation

The common approach to describe the lubricant film is the Reynolds equation. Assuming an incompressible Newtonian fluid (density $\rho = \text{const.}$, viscosity $\eta = \text{const.}$), this equation depends on the gap height h, the pressure gradients $\partial p/\partial x$ and $\partial p/\partial y$, the tangential velocities $\dot{u}$ and $\dot{v}$ of the moving surfaces 1 and 2

$$\frac{\partial}{\partial x}\left(\frac{h^3}{12\eta}\frac{\partial p}{\partial x}\right) + \frac{\partial}{\partial y}\left(\frac{h^3}{12\eta}\frac{\partial p}{\partial y}\right) = \frac{\dot{u}_1 + \dot{u}_2}{2}\frac{\partial h}{\partial x} + \frac{\dot{v}_1 + \dot{v}_2}{2}\frac{\partial h}{\partial y}. \quad (4)$$

The components of the specific volume flows q for the x- and y-direction are computed as follow

$$q_x = \frac{h^3}{12 \cdot \eta}\frac{\partial p}{\partial x} - \frac{\dot{u}_1 + \dot{u}_2}{2} h$$

and (5)

$$q_y = \frac{h^3}{12 \cdot \eta}\frac{\partial p}{\partial y} - \frac{\dot{v}_1 + \dot{v}_2}{2} h.$$

The specific volume flow can be determined from the directional components (Equation (4))

$$q = \sqrt{q_x^2 + q_y^2}. \quad (6)$$

To perform a computational fluid dynamic (CFD) simulation of the lubrication film, the Reynolds equation (4) is used and is solved by applying the finite difference method (FDM). The FDM uses a central difference scheme according to Equation (7). The derivations in the y-direction are computed accordingly. This FDM scheme is implemented in the mathematics program MATLAB.

$$\left(\frac{\partial p}{\partial x}\right)_{j,i} = \frac{p_{j,i+1} - p_{j,i-1}}{2 \cdot \Delta x}$$
$$\left(\frac{\partial^2 p}{\partial x^2}\right)_{j,i} = \frac{p_{j,i+1} - 2 \cdot p_{j,i} + p_{j,i-1}}{\Delta x^2} \tag{7}$$

The previously performed contact simulation using a half-space model provides the deformed gap geometries $h(x,y)$ for several deformed gap heights h_{def}. These deformed gap geometries are now used to perform both pressure and shear flow simulations for the brake fluid ($\eta = 11.5 \cdot 10^{-3}$ Pa · s). In order to obtain a more accurate solution the mesh is refined using a cubic spline. In the pressure flow simulation, 10 additional points are generated between the individual pixels. For the shear flow simulation 20 additional points are generated between the individual pixels.

3.2.1 Results of the flow simulation

To carry out the pressure flow simulation, a fluid pressure of $p_{in} = 0.2$ MPa is specified on the inlet side $(x = 0)$ and a fluid pressure of $p_{out} = 0.1$ MPa on the outlet side($x = 99.58$ µm). The surface velocities are assumed to be zero ($\dot{u}_1 = \dot{u}_2 = \dot{v}_1 = \dot{v}_2 = 0$). The flow of the fluid is prevented by specifying a pressure gradient ($\partial p/\partial y$) equal to zero on the sides($y = 0, y = 99.58$ µm). Figure 9 shows the specific volume flow for the pressure flow simulation at a deformed gap height of $h_{def} = 2.06$ µm. If the fluid flows perpendicular (⊥) to the grinding direction, the roughness impedes the fluid. The fluid therefore flows through branched channels. If the fluid flows in grinding direction (||), the surface topography supports the fluid flow, which results in a higher specific volume flow.

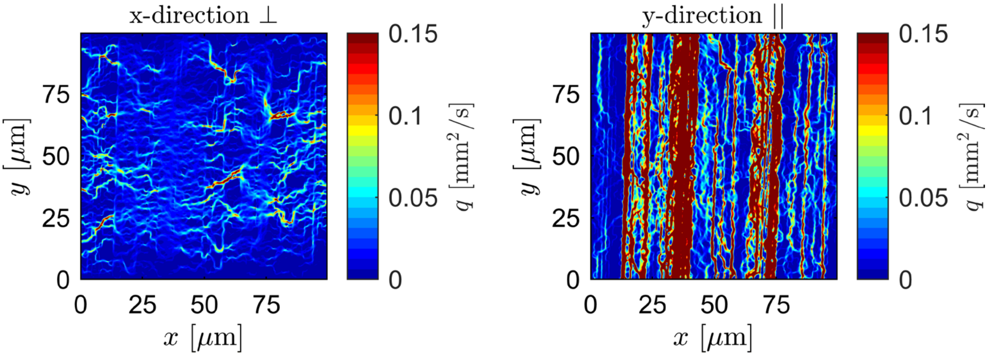

Figure 9: Specific volume flow for the pressure flow simulation at $h_{def} = 2.06\ \mu m$

For the shear flow simulation, the same pressure is defined on the inlet and outlet side $p_{in} = p_{out}$. The velocities of the surfaces are specified in opposite directions to each other in the direction of flow ($\dot{u}_1 = -\dot{u}_2 = 100$ mm/s). Similar to the pressure flow simulation, a pressure gradient equal to zero prevents the fluid from flowing out over the sides. Figure 10 shows the specific volume flow for this load case at a deformed gap height $h_{def} = 2.06$ µm. If the surfaces move perpendicular (⊥) to the grinding direction, the roughness valleys transport more fluid than if they move parallel (||) to the surface structure.

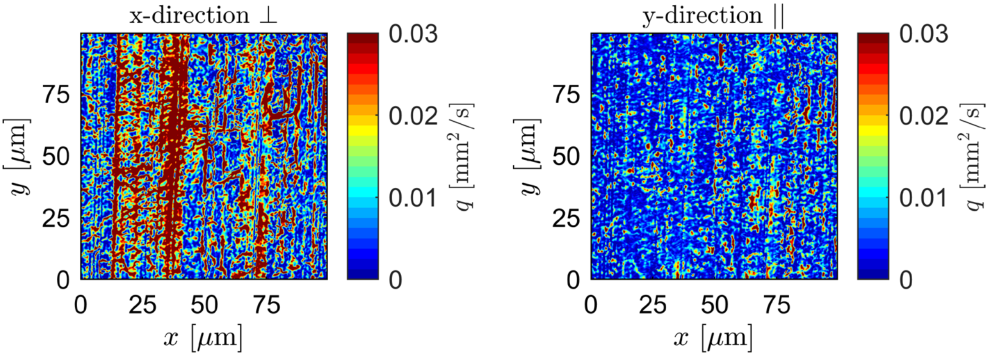

Figure 10: Specific volume flow for the shear flow simulation at $h_{def} = 2.06\ \mu m$

If the EPDM cord rubs perpendicular to the grinding direction, the surface topography hinders the fluid so it enters the lubrication gap. At the same time, the surface topography in the lubrication gap impedes the volume flow and thus supports the build-up of fluid pressure. If the EPDM cord now switches between sticking and slipping, a lubricating film builds up. Once this has built up, the surface topography prevents the fluid from flowing out, resulting in a stable lubricating film. However, if the EPDM cord rubs in the direction of grinding (||), the cord partially pushes the fluid in front of it. Within the lubrication gap, the surface topography supports the volume flow. When alternating between sliding and sticking, a smaller lubricating film builds up compared to the perpendicular movement. Furthermore, the surface structure allows the fluid to flow off again quickly. This is why the contact quickly switches back from slipping to sticking.

3.2.2 Flow Factors

Usually the Reynolds equation (4) above describes the fluid film dynamics for smooth surfaces. The direct depiction of surface roughness in component simulation would be associated with a large computational effort due to the differences in scale (component simulation $[\mathrm{mm}]$ – surface topography $[\mu\mathrm{m}]$). Therefore, the method of flow factors by Patir and Cheng [10, 11] is often used to describe the influence of roughness on the flow in the lubrication gap. For further illustration of this roughness influence, the flow factors are calculated below based on the previous flow simulations.

The flow factor method extends the Reynolds equation (4) by the pressure flow factor Φ^{p} and the shear flow factor Φ^{s}. The pressure flow factor Φ^{p} scales the Poiseuille term of the Reynolds equation and describes the influence of the surface roughness on the fluid film. Additional Couette terms containing the shear flow factors Φ^{s} describe the additional fluid transport through the surface roughness. By adding the flow factors, the Reynolds equation is obtained as follows

$$\frac{\partial}{\partial x}\left(\Phi_x^p \cdot \frac{h^3}{12\cdot\eta}\frac{\partial p}{\partial x}\right)+\frac{\partial}{\partial y}\left(\Phi_y^p \cdot \frac{h^3}{12\cdot\eta}\frac{\partial p}{\partial y}\right)=$$

$$\frac{\partial}{\partial x}\left(\frac{\dot{u}_1+\dot{u}_2}{2}h+\frac{\dot{u}_1-\dot{u}_2}{2}\Phi_x^s\right)+\frac{\partial}{\partial y}\left(\frac{\dot{v}_1+\dot{v}_2}{2}h+\frac{\dot{v}_1-\dot{v}_2}{2}\Phi_y^s\right). \tag{8}$$

The pressure flow factor Φ^{p} (Equation (9)) indicates the ratio of the average specific volume flows of the pressure flow in the rough gap $\bar{q}_{rough}$ and the pressure flow in the ideally smooth gap $\bar{q}_{smooth}$. The average volume flow is calculated from the integration over the examined surface section Ω.

$$\Phi_x^{\mathrm{p}}=\frac{\bar{q}_{rough,x}}{\bar{q}_{smooth,y}}=\frac{1}{h_{def}^3\cdot\frac{p_{in}-p_{out}}{L_x}}\cdot\left(\frac{1}{\Omega}\int_{(A)}\frac{h^3}{12\cdot\eta}\frac{\partial p}{\partial x}\,d\Omega\right) \tag{9}$$

Based on the shear flow simulation carried out above, the shear flow factor Φ^{s} is calculated from the average specific volume flow and velocities of the surfaces as follows

$$\Phi^{\mathrm{s}}=\frac{2}{\dot{u}_1-\dot{u}_2}\cdot\left(\frac{1}{\Omega}\int_{(A)}\frac{h^3}{12\cdot\eta}\frac{\partial p}{\partial x}\,d\Omega\right). \tag{10}$$

Figure 11 shows the pressure and shear flow factors depending on the sliding direction. A dashed line marks the deformed gap height h_{def} of the pressure flow simulation in Figure 9. In the pressure flow simulation perpendicular ($\perp$) to the surface structure, the specific volume flow is smaller than for a flow between two smooth surfaces, which results in $\Phi^p < 1$. At the marked deformed gap height $h_{def} = 2.06\ \mu m$, flow is barley possible because there is almost solid contact at the peaks of the roughness, which can also be seen from the contact area shown in Figure 8. The pressure flow simulation parallel (||) to the roughness results in $\Phi^p > 1$, because the surface topography favors the fluid. It is noticeable here that Φ^p drops again for small gap widths. The reason for this is that the individual flow channels are blocked by the solid contact as the gap becomes smaller. This behavior correlates very well with the specific volume flows of the pressure flow simulation, shown in Figure 9.

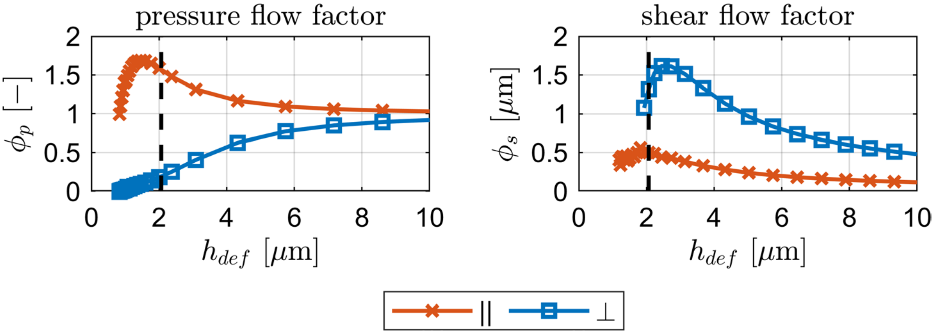

Figure 11: Flow factors for the flow parallel || and perpendicular ⊥ to grinding direction

The comparison of the shear flow factors Φ^s shows that more fluid is transported in the flow perpendicular to the surface structure. The shear flow factor reaches its maximum for the flow perpendicular to the roughness at $h_{def} = 3\ \mu\mathrm{m}$ and then declines again due to the increasing solid contacts.

4 Summary and Conclusion

To investigate the influence of surface topography on stick-slip effects, a standard tribometer test was improved in order to better represent the tribological system of a lubricated dynamic seal. In addition to quantifying the stick-slip tendency of individual fluids, this test also enables the investigation of the influence of the surface structure on stick-slip effects. By rotating the surface structure, it is possible to provoke and prevent the stick-slip effect.

Furthermore, contact and CFD simulations based on measured surfaces are carried out to check the plausibility of the results. These simulations clearly show the influence of the surface topography on the lubricating film. If the EPDM cord slides perpendicular to the grinding direction, the flow is prevented through the surface structure, which favors the buildup of a stable fluid film, which results in no stick-slip effect. If the EPDM cord slides parallel to the grinding direction, the surface structure favors the flow, so that the fluid can quickly flow out again during sticking and the lubricating film that has formed collapses, which supports the occurrence of stick-slip effects.

By combining experiment and simulation, this work contributes to a deeper understanding of stick-slip effects and the influence of surface structuring on them.

5 Acknowledgements

We thank FREUDENBERG Sealing Technologies for providing the EPDM cords.

6 Nomenclature

Variable	***Description***	***Unit***
a	Amplitude	[mm]
f	Frequency of the tribometer	[Hz]
F_N	Normal Force	[N]
F_R	Friction Force	[N]
h	Effective Gap Height	[µm]
h_{def}	Deformed Gap Height	[µm]
p	Pressure	[MPa]
q	Specific Volume Flow	[mm²/s]

$\bar{q}$	Average Specific Volume Flow	[mm²/s]
r	Local Roughness	[µm]
u	Displacement in x –direction	[mm]
$\dot{u}$	Velocity in x –direction	[mm/s]
$\dot{v}$	Velocity in y –direction	[mm/s]
x	Coordinate	[mm]
y	Coordinate	[mm]
z	Coordinate	[mm]
η	Viscosity	[Pa·s]
Φ^p	Pressure Flow Factor	[-]
Φ^s	Shear Flow Factor	[µm]
ρ	Density	[g/cm³]
σ	Stick-Slip Index	[-]
Ω	Surface section	[mm²]

7 References

[1] Ibrahim, R. A.: *Friction-Induced Vibration, Chatter, Squeal, and Chaos—Part I: Mechanics of Contact and Friction*, In: Applied Mechanics Reviews, Vol. 47-7/1994, pp. 209-226,1994, https://doi.org/10.1115/1.3111079

[2] Etison, I., Burstein, L.: A Model for Mechanical Seals with Regular Microsurface Structure, In: Tribology Transactions, Vol 39-3/1996, pp. 677-683, 1996, https://doi.org/10.1080/10402009608983582

[3] Keller, D., Jacobs, G., Neumann, S.: *Development of a Low-Friction Radial Shaft Seal: Using CFD Simulations to Optimise the Microstructured Sealing Lip*, In: Lubricants, Vol 8-4/2020, 41, 2020, https://doi.org/10.3390/lubricants8040041

[4] Wang, H., Xie, X., Hua, X., Yin, B., Du, H., Xu, S., Qiu, B. J.: *The effect of laser surface texturing to inhibit stick-slip phenomenon in sliding contact*, In: Advances in Mechanical Engineering, Vol. 11-9/2019, pp. 1-10, 2019, https://doi.org/10.1177/1687814019874635

[5] He, Y., Yang, J., Wang, H., Gu, Z., Fu, Y.: *Micro-dimple and micro-bulge textures:Influence of surface topography types on stick–slip behavior under starved lubrication*, In: Applied Surface Science, Vol. 585, 2022, https://doi.org/10.1016/j.apsusc.2022.152501

[6] E DIN 51834-5:2022-10: *Prüfung von Schmierstoffen - Tribologische Prüfung im translatorischen Oszillations-Prüfgerät - Teil 5: Quantifizierung der reibungsbedingten Geräuschentwicklung von Bremsflüssigkeiten in EPDM-Stahl-Kontakten*, Beuth-Verlag, Berlin, 2022

[7] Wittmaack, M, André, M., Schmitz, K.: *Dynamic Friction Model for the Investigation of Stick-Slip Oscillations*, In: Chemical Engineering and Technology, Vol. 46-1/2023, pp. 28-36, 2023, https://doi.org/10.1002/ceat.202200416

[8] Wittmaack, M., André, M., Molter, J.: *Analyse von Einflussparametern auf den Stick-Slip Effekt mittels Tribometerversuchen und FE-Simulation.* In: Tribologie und Schmierungstechnik, Vol 69-1/2022, pp. 5-14; 2022, https://doi.org/10.24053/TuS-2022-0002

[9] Bartel, D.: *Simulation von Tribosystemen. Grundlagen und Anwendungen*, Vieweg + Teubner, Wiesbaden, 2010

[10] Patir, N., Cheng, H. S.: *An Average Flow Model for Determining Effects of Three-Dimensional Roughness on Partial Hydrodynamic Lubrication*, In: Journal of Lubrication Technology, Vol 100-1/1978, pp. 12-17, 1978, https://doi.org/10.1115/1.3453103

[11] Patir, N. u. Cheng, H. S.: *Application of Average Flow Model to Lubrication Between Rough Sliding Surfaces*, In: Journal of Lubrication Technology, Vol 101-2/1979, pp. 220-229, 1979, https://doi.org/10.1115/1.3453329

8 Authors

Hochschule Hannover, University of Applied Sciences and Arts Hannover, Faculty II – Mechanical and Bioprocess Engineering

Ricklinger Stadtweg 120, 30459 Hannover, Germany:

Martin Wittmaack, M. Eng., ORCID 0000-0003-3879-0274, Martin.Wittmaack@hs-hannover.de

Prof. Dr.-Ing. Markus André, Markus.Andre@hs-hannover.de

Prof. Dr.-Ing. Sebastian Rakowski, ORCID 0009-0004-5197-4398, Sebastian.Rakowski@hs-hannover.de

RWTH Aachen University, Institute for Fluid Power Drives and Systems (ifas)

Campus-Boulevard 30, 52074 Aachen, Germany:

Univ.-Prof. Dr.-Ing. Katharina Schmitz, ORCID 0000-0002-1454-8267, Katharina.Schmitz@ifas.rwth-aachen.de

https://doi.org/10.61319/YPUC46M7

Group A
Session 4

Hydrogen

A 08

Johannes Müller, TEADIT International Produktions HmbH, Kirchbichl, Austria

TEADIT's sealing solutions for the electrolyser market

A 09

Philipp Hirstein, Sandra Kofink, Joel Thompson, Trelleborg Sealing Solutions Germany GmbH, Stuttgart, Germany

Influence of hydrogen on the material properties of non-metallic materials for sealing applications

---

A 10

Michael Fasching, Thomas Schwarz, Silvio Schreymayer, Thomas Hafner; Geraldine Theiler, Natalia Cano Murillo, Andreas Kaiser, SKF Sealing Solutions Austria GmbH, Austria

Investigation of sealing materials with excellent cold temperature flexibility in hydrogen environments

---

A 11

Hikaru Hashimoto, Suguru Norikyo, Ayako Aoyagi, Hiroyohshi Tanaka, Takehiro Morita, Yoshinori Sawae, Joichi Sugimura, NOK corporation, Engineering Research Department, Fujisawa city, Japan

Influences of hydrogen and trace moisture content on the friction of silicone rubber

TEADIT’s sealing solutions for the electrolyser market

PhD Johannes Müller, TEADIT International Produktions GmbH

1 Importance of hydrogen as an energy source of the future

Due to its wide range of applications and its potential role in the decarbonization of various sectors, hydrogen is considered a promising energy carrier of the future. The competitiveness of hydrogen to generate the much-mentioned hydrogen ramp-up is the immediate focus here. On the one hand, this includes the ability of this form of energy to compete with other energy sources and technologies in terms of cost, efficiency, availability and applicability. As hydrogen is seen as a promising energy carrier of the future, its competitiveness is crucial for its widespread adoption and adoption. The following topics are particularly important to consider. The costs of hydrogen production, storage, distribution and use are crucial. Hydrogen from renewable energy sources such as electrolysis can be competitive, especially if the cost of renewable energy continues to fall. The efficiency of hydrogen production and use is important to ensure that the efficiency is high enough compared to other forms of energy to be economical and environmentally friendly. The availability of sufficient infrastructure for hydrogen production, storage, distribution and use is crucial to enable widespread adoption and application. Support measures such as government subsidies, tax breaks and subsidy programs can increase the competitiveness of hydrogen and increase its economic attractiveness. International cooperation between countries and companies can help scale hydrogen production and use, thus reducing costs. The relevance of such a hydrogen ramp-up is also underlined by the National Hydrogen Strategies (NWS). Germany, for example, published its first decision of the NWS in June 2020. This was expanded and expanded in July 2023 and represents an even more detailed solution and implementation of the above points. In addition, three hydrogen flagship projects were presented, including the sub-areas H2-Mare, H2-Giga and TransHyDE. These flagship projects are a key contribution of the Federal Ministry of Education and Research (BMBF) to the implementation of the National Hydrogen Strategy to advance the production of green hydrogen.

1: The BMBF's flagship projects on behalf of Project Management Jülich (from left): H2-Mare, H2-Giga and TransHyDE.

In addition, the Kopernikus projects were adopted, which support partners from science, business and civil society in ensuring that Germany is to be largely climate-neutral by 2050. The Kopernikus projects are one of the largest research initiatives of the German government on the topic of the energy transition. Together, they want to enable a secure, climate-neutral and affordable energy supply for Germany. They are divided into the ENSURE project, which is responsible for the development of the power grid of the future, as follows. The P2X project investigates the conversion of renewably generated electricity into gases, fuels, chemicals and plastics. The third project, SynErgie, investigates how energy-intensive industrial processes can be made more flexible and thus adapted to the availability of renewable energies. The last project, called ARIADNE, analyses political measures that can be used to successfully implement the energy transition – and includes the results of its sister projects in its analysis. [1]

Furthermore, a standardization roadmap "Hydrogen Technologies" is intended to support the market ramp-up and is scheduled to run until the end of 2025. Hydrogen is a central building block for the transformation to a fossil free economy as an energy carrier, storage and element of sector coupling. The joint project "Standardization Roadmap for Hydrogen Technologies", funded by the German Federal Ministry for Economic Affairs and Climate Action (BMWK), actively supports the hydrogen market ramp-up and helps to establish a corresponding quality infrastructure for hydrogen technologies. Norms and standards define terminology, interfaces, safety, system and quality requirements, as well as testing and certification principles, thus creating a uniform understanding across disciplines and enabling the scaling of this technology. Technical regulation also supports legally secure action and forms the basis for resilient economic investments. As part of the joint project, which started in January, a strategic roadmap is being developed together with experts from business, politics, science and civil society for a rapid and targeted expansion and adaptation of the technical regulations in the field of hydrogen technologies. The standardisation roadmap for hydrogen technologies is being developed in the five working groups (AK) Generation, Infrastructure, Application, Quality Infrastructure and Training, Safety, Certification. Each of the working groups consists of thematically in-depth sub-working groups (UAK) and subordinate working groups (AGs). The content work is carried out in the working groups, in which all interested parties can participate (Fig. 2). [2]

Fig. 2: Committee structure of the working groups Standardization Roadmap "Hydrogen Technologies".

2 TEADIT's manufacturing process of ePTFE

The general-purpose single-expanded PTFE sealing products (Fig. 3, left) are manufactured from 100% pure PTFE (polytetrafluoroethylene). A special thermo-mechanical stretching process results in a microporous fiber structure that adds high tensile strength and deformability to the overall advantages of PTFE, while the negative properties such as cold flow and creep are almost eliminated. Due to the excellent deformability of expanded PTFE, sealing products easily adapt to individual installation structures required in electrolyser production, for example. The manufacturing process of monoaxially expanded PTFE strips further improves the cold flow properties and deformation properties of the expanded PTFE material. In addition, the complex stretching process has been further developed to result in a multidirectional fiber structure that ensures uniform tensile strength in all directions (Fig. 3, center). As a result, the new material has excellent dimensional stability and shows significantly superior creep resistance. All this has been realized without losing the excellent sealing properties of pure PTFE. For this reason, ePTFE products are predestined for use in H2 applications. The latest addition to the ePTFE sealing products is supported by TF tapes. A unique manufacturing process results in a highly fibrillated PTFE structure of the sealing tapes, which - together with the carefully selected filling materials - results in very high mechanical strength of the tapes to improve handling. The filling materials are selected according to the different applications that occur in all types of industrial applications (Fig. 3, right).

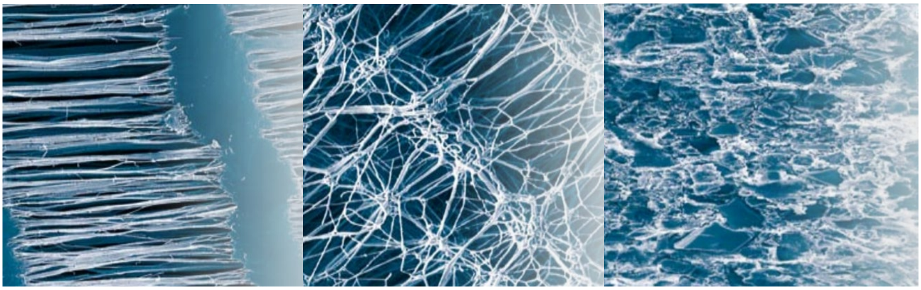

Fig. 3: Overview of the three different types of our PTFE products. From left to right: single-directional PTFE, multi-directional PTFE and structured PTFE.

3 Electrolysers – the key technology in H_2 production

The world is in a race to achieve a clean energy transition. Green hydrogen, which is produced by water electrolysis with renewable energy, is considered a central building block for achieving net zero emissions. As electrolyser manufacturers improve existing technologies, develop new ones, and increase their production capacity to meet increasing demand, the demand for electrolyser components is also increasing. Large electrolyser and fuel cell systems can consist of several hundred individual cells that must be properly sealed to ensure safe and efficient operation. The opportunity for companies to accelerate the upscaling of green hydrogen production worldwide is immense. Due to its excellent sealing properties, PTFE has become a commonly used material for seals in electrolysers. In the past, gaskets were often made of asbestos and coated with PTFE. However, nowadays asbestos is no longer used, so gaskets made of expanded or textured PTFE have become a standard alternative. In the coming years, the cumulative capacity of electrolysers is expected to reach over 200 GW by 2030 (see Fig. 4, right). The majority (48%) of hydrogen is produced by the conversion of natural gas and refinery gas (grey H_2), as a by-product of chemical production (30%, white H_2) and by coal gasification (18%, brown H_2).

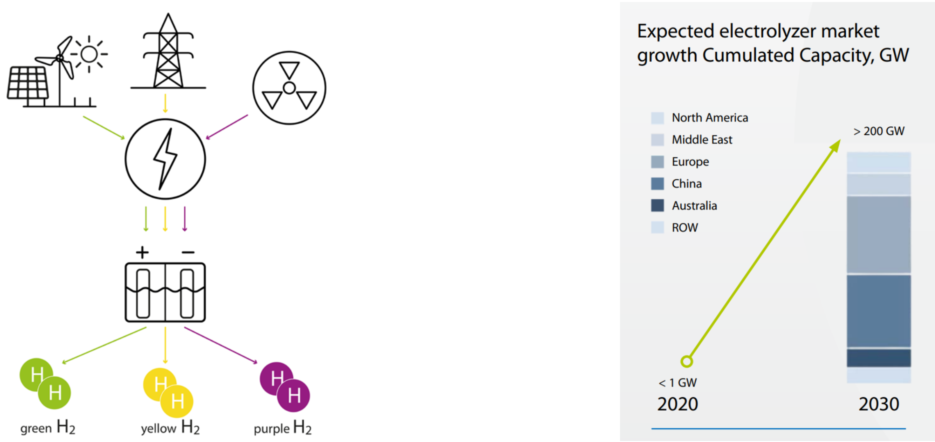

Fig. 4: Overview of the color palette: selected production possibilities of hydrogen from electrolysis.

Only about 4% of global hydrogen production comes from electrolysis. When looking at electricity allocation as an intermediate step in H_2 production, there are even more color variants of H_2. For example, purple H_2 is produced from nuclear power plants, and yellow H_2 comes from a mixture of renewable and fossil fuels. However, achieving climate-neutral H_2 production, the electricity used for water electrolysis must be green and therefore come exclusively from renewable energies such as solar energy (PV) and wind energy or from hydropower turbines. This is one of the most proven options for low-carbon hydrogen and today plays a key role in mobility, industry or energy storage. An overview of the color palette of the H_2 is shown in Fig. 4. Electrolysis plays an important role in the global energy transition. These electrolysers can be scaled according to the different input and output areas, ranging from small industrial plants in shipping containers to large-scale centralized production plants that can deliver the hydrogen by truck or be connected to pipelines. There are three main types of electrolysers: proton exchange membrane (PEM), alkaline and solid oxide electrolysers. These different electrolysers work slightly differently depending on the electrolyte materials used. Both alkaline and PEM electrolysers can deliver hydrogen on-site and on-demand, pressurize hydrogen without a compressor, and produce 99.999% pure, dry, and carbon-free hydrogen.

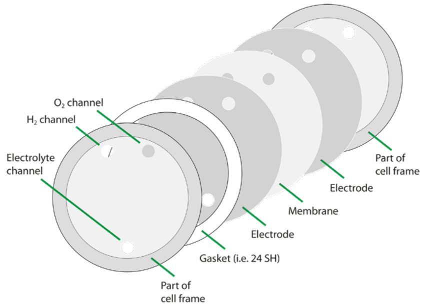

Fig. 5: left: Showcase project for the application of ePTFE seals in alkaline electrolyzers (MPreis, Völs). Right: Schematic exploded drawing of the composition of an electrolysis cell with the 24SH seal from TEADIT©.

In the electrolyser shown (Fig. 5, left), TEADIT©'s sealing solution has been co-designed, using one of our products. This single stack is located in Völs near Innsbruck and is the largest of its kind in Europe. Well-known partners were involved in the project development, implementation and testing (e.g. Sunfire). The pressurized alkaline electrolyser delivers 3.2 MW and has an operating pressure of up to 30 bar. [3]

The most interesting point for a gasket manufacturer, however, is the structure of the components that are assembled to form a cell, as well as the structure of the stack. A schematic cell composition is shown in Fig. 5 shown on the right. The stack structure (later electrolyser structure) then inevitably affects the design of the seal. This is a very important point, because due to this fact there is no general and uniform sealing solution. A new sealing solution must therefore be developed for each requirement, which appears with a new design and new dimensions. TEADIT© should be involved in project planning as early as possible to generate an optimal sealing solution. An open exchange on the status quo, ideas and thoughts are basis for a further development of the sealing solution. We take this task very seriously by incorporating our know-how into customer expertise, sharing experience and helping with the installation of the "finished" seal. TEADIT© develops seals for the energy transition strictly according to its company motto: Seals for a safer and greener future.

4 H_2 Application: Use of ePTFE seals in electrolyzers

Alkaline Electrolyser (AEL)

Alkaline electrolysers are used on an industrial scale worldwide because they are considered the best tested, work with comparatively inexpensive materials and are characterized by high long-term stability. These electrolysers use a potassium hydroxide solution (KOH) as an electrolyte with a concentration of 20 to 40%. By applying a direct voltage of at least 1.5 volts, hydrogen is produced at the cathode (positively charged) and oxygen at the anode (negatively charged). Nickel-based electrodes and titanium electrodes coated with ruthenium oxide or iridium oxide serve as electrodes. In AEL electrolysis, efficiency is limited: the anode and cathode are separated from each other by a porous, semi-permeable membrane in alkaline electrolysers. This membrane can only withstand limited pressure and can only be operated at low current densities (maximum 600 milliamperes per square centimeter of membrane area). Therefore, the hydrogen in AEL electrolysis must then be compressed at high energy consumption to be able to store it and transport it further.

Proton Exchange Membrane (PEM) Electrolysers

Instead of a liquid electrolyte, a solid polymer electrolyte is used in the PEM electrolyser for hydrogen production. This is also known as the "proton exchange membrane" (PEM). The membrane is surrounded by distilled water or drinking water. PEM electrolysis places high demands on the materials due to the aggressive, acidic environment. For this reason, the polymer membrane is equipped with a porous, platinum-coated carbon electrode on the cathode side. On the anode side, it usually has a ruthenium or iridium oxide coating. PEM electrolysis is characterized by high efficiency: With 2,000 milliamperes per square centimeter of membrane area, the solid, semi-permeable polymer membrane of PEM electrolysis enables a current density three times higher than the zirfon membrane in AEL plants. Depending on the area of application, PEM electrolysis achieves an efficiency of 60 to 70%. It can also withstand greater load fluctuations. Since PEM electrolysers can operate under high pressure, the energy required for subsequent hydrogen compression for storage and transport is reduced. The higher efficiency makes it possible to produce the same amount of hydrogen with smaller electrolysers as with larger AEL units. By replacing the expensive catalyst platinum with molybdenum sulphite, the investment costs in production can also be reduced. In addition, the comparatively new PEM electrolysis still has considerable potential for technical developments.

Anion Exchange Membrane (AEM) Electrolyzers

By integrating a membrane (DURAION)® into an AEM electrolyser, the cost of investment and operation in hydrogen production can be reduced compared to the current benchmark, PEM water electrolysis. AEM electrolysis takes place under slightly alkaline conditions, which allows precious metal-free catalysts to be used for the electrodes and low-cost materials for the cells. In contrast to AEL, AEM electrolysis can be operated at higher current densities and dynamically started and shut down, resulting in a high degree of flexibility. In this way, AEM electrolysis combines the advantages of PEM and AEL technology.

5 Test, Certification and Approval – Tigthness to H_2

The aim of the investigation is to determine the sealing parameters in accordance with the European test standard DIN EN 13555. This standard is required for the calculation according to DIN EN 1591-1 and necessary for the approval of sealing solutions for the sealing of hydrogen. The conditions that must be met under this standard are a minimum surface pressure in the assembled state Qmin(L) (40 bar) and a minimum surface pressure in the operating state Qs, min(L) (40 bar). In deviation from the test standard, the leak tests were carried out with the test medium hydrogen (H2). In the leak test, the seal is loaded and relieved in several stages, whereby the leak rate is determined for each surface pressure level. The leakage measurement is carried out up to a surface pressure level of 160 MPa. Not only the load curve is recorded, but also several relief curves based on the surface pressure levels of 20 MPa, 40 MPa, 60 MPa, 80 MPa, 100 MPa, 120 MPa and 160 MPa. The minimum surface pressure level is 10 MPa. The seal tests were carried out on TEMESfl.ai1 test equipment in amtec's test laboratories (Fig. 6). For several decades, amtec has been testing the properties of seals, calculating strength and measuring bolt forces.

Fig. 6: Presentation of the test equipment: Leak tests are carried out on the test stand of the company "amtec" (TEMESfl.ai1).

The test medium for these leak tests is hydrogen 5.0. The leakage curve can be used to calculate the required minimum surface pressure Q_{min} (L) for the different tightness classes L during assembly and the required minimum surface pressure $Q_{s,min}$ (L) during operation, depending on the previously applied initial surface pressure Q_A. The tightness class L0.01 was achieved in the test with 40 bar and a surface pressure of 26 –27 MPa. If the PTFE flat gasket 24 SH is further loaded up to 160 MPa, the leakage rate decreases. The lowest leakage rate was measured at the surface pressure level of 160 MPa with 1.5*10-7 mg/s/m. The required minimum surface pressure $Q_{s,min}$ (L) in the operating state for tightness class L0.01 with an initial surface pressure QA = 60 MPa is $Q_{s,min}$ (0.01) = 10 MPa. The results are shown in the following graph (Fig. 7).

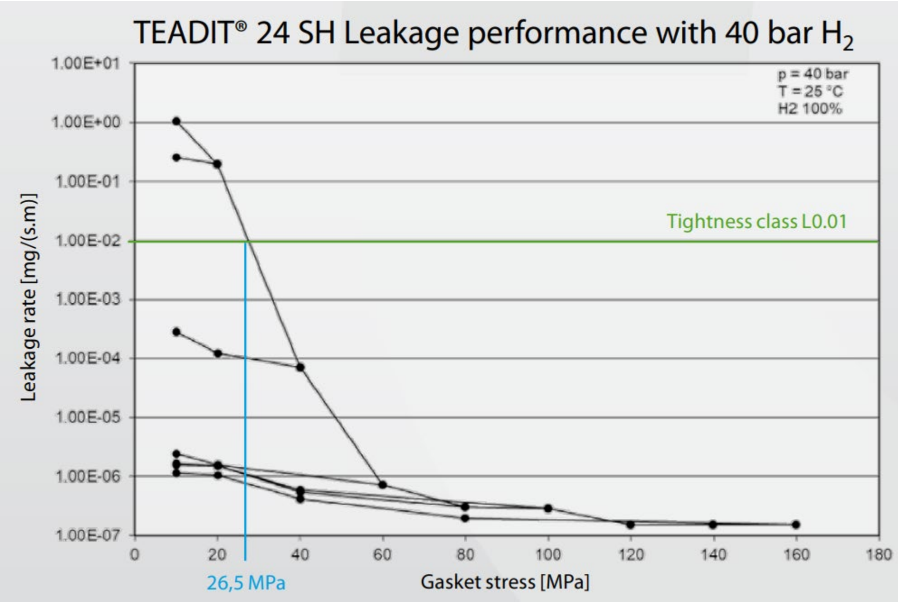

7: Presentation of the seal load test of an ePTFE gasket (24 SH) with 40 bar H2 pressure at room temperature. The green line represents the tightness class L0.01 (TA-Luft), the blue line shows the surface pressure at the required tightness level.

One of the most interesting questions in electrolysis is the technical requirements for the seals themselves. The PTFE solutions can be used universally for various electrolyser applications. They are suitable for all types of flanges, almost all media, a wide temperature range and for applications with the highest purity requirements. They are naturally clean and non-toxic. In addition, they have a high tightness (sealing ability) with low installation loads, even when the smallest molecules (H_2) are used. Since our PTFE gaskets are used in electrolyser stacks, they need to be electrically non-conductive to isolate the anode from the cathode. The PTFE fluoropolymer offers remarkable dielectric strength, high resistance and mechanical stability against creep stress. In addition, a wide range of ePTFE sealing products have been designed and manufactured to meet a wide range of industrial needs.

6 Technical requirements of seals for use in electrolysers

Understandably, the seals used must have an extraordinary tightness due to the small molecular size of the hydrogen molecule. The ePTFE boards from TEADIT can be used universally for all applications. They are suitable for all types of flanges, almost all (liquid and gas) media, a wide temperature range and for applications with the highest purity requirements. In addition, our product is typically clean and non-toxic. With its products, TEADIT has created a way to seal the smallest natural chemical element – namely hydrogen – in the best possible way (see section 5).

Furthermore, it is possible to isolate the anode and cathode from each other as well as from the electrodes or the bipolar plates, as PTFE is an electrically non-conductive fluoropolymer. In this respect, PTFE differs significantly from other insulation materials. Its remarkable electrical stability over a wide frequency range and against ambient conditions are requirements that the components of electrolyzers must inevitably meet. The dielectric strength of pure PTFE is 24 kV/mm.

In terms of mechanical stability, it can be said that our ePTFE and TF products are among the PTFE with the highest creep relaxation. This point of view results in a sealing material that has a long service life. This property in turn has to be seen from the point of view of low maintenance costs in connection with the running times of electrolysers (normally planned: 10 – 15 years). The long service life (no aging) of PTFE gaskets are further advantages in this context.

A noteworthy property is the high chemical resistance to potassium hydroxide solution (KOH, any concentration), which is particularly evident in the application in alkaline electrolysis. In the following, it can be said that TEADIT PTFE is inert against all acids and bases (pH 0 – 14).

7 Conclusion and Outlook

The demand for hydrogen is growing enormously worldwide, and at the same time the market ramp-up is starting, focusing on the production, use and integration of hydrogen. In order to be able to produce the required quantities of hydrogen, a large number of electrolysers is required. Increasing activities towards series production are becoming more and more apparent. Due to this dynamic, the demand for H_2-compatible sealing solutions will continue to grow in the coming years. TEADIT© has already become willing to offer high-quality PTFE products. Therefore, TEADIT© can serve with a portfolio of PTFE products suitable for use in electrolysers. By striving for the optimal sealing solution, TEADIT© is doing its part to create a greener, greener and safer future.

8 References

[1] https://www.wasserstoff-leitprojekte.de/startseite

[2] https://www.din.de/de/forschung-und-innovation/themen/wasserstoff/normungsroad-map-wassersoff

[3] https://www.mpreis.at/wasserstoff

Abb. 1: Die Leitprojekte des BMBF im Auftrag an den Projektträger Jülich (von links): H_2-Mare, H_2-Giga und TransHyDE. 171

Abb. 2: Gremienstruktur der Arbeitskreise Normungsroadmap „Wasserstofftechnologien". 173

Abb. 3: Überblick der drei verschiedenen Typen unserer PTFE Produkte. Von links nach rechts: einfach-direktionales PTFE, multi-direktionales PTFE und strukturiertes PTFE. 174

Abb. 4: Übersicht der Farbpalette: ausgewählte Produktionsmöglichkeiten von Wasserstoff aus Elektrolyse. 175

Abb. 5: links: Vorzeigeprojekt der Anwendung von ePTFE-Dichtungen im alkalischen Elektrolyseur (MPreis, Völs). Rechts: Schematische Explosionszeichung der Zusammensetzung einer Elektrolysezelle mit der 24SH Dichtung von TEADIT©. 176

Abb. 6: Darstellung der Testausrüstung: Dichtheitstest werden auf dem gezeigten Teststand der Firma „amtec" (TEMESfl.ai1) durchgeführt. 178

Abb. 7: Darstellung des Dichtungsbelastungstests einer ePTFE-Dichtung (24 SH) mit 40 bar H_2-Druck bei Raumtemperatur. Die grüne Linie repräsentiert die Dichtheitsklasse L0.01 (TA-Luft), die blaue Linie zeigt den Flächendruck auf dem erforderlichen Dichtheitsniveau. 179

https://doi.org/10.61319/B8QAK6DC

Influence of hydrogen on the material properties of non-metallic materials for sealing applications

Philipp Hirstein, Sandra Kofink, Joel Thompson

Hydrogen entails challenging conditions for all sealing materials. For metals, the effect of hydrogen embrittlement is well known. However, little attention has been paid to elastomers and plastics, which are commonly used as sealing materials. For hydrogen storage and transport, high pressures and extreme temperature situations must be covered. This paper discusses the influence of hydrogen on mechanical properties, volume and weight change as well as compression set. Additionally, the influence of extreme application temperatures on mechanical properties is presented. In general hydrogen has no harmful influence on the compounds presented in this study, which are known as polymers suitable for hydrogen use.

1 Introduction

The hydrogen market is experiencing rapid growth due to various factors such as the need for low-emission mobility, political support and funding [1], as well as technological advancements. It is estimated that the hydrogen market's turnover could reach 840 billion euros by 2050, potentially creating 5.4 million jobs [2]. In addition, the share of hydrogen in global final energy consumption is projected to increase to 19 percent by 2070, which would translate to an annual hydrogen production of 1,084 million tons [3].

However, the use of hydrogen poses certain technical challenges, especially in terms of sealing technology, as different requirements are imposed on seals and materials throughout the entire hydrogen value chain, including production, storage, transportation, and end applications such as fuel cells or combustion [4].

The development of hydrogen seals faces a significant hurdle due to the absence of meaningful global industry standards. The hydrogen industry sometimes utilizes specifications that are intended for high-pressure gases in the oil and gas sector, such as Norsok M-710. However, these standards do not accurately represent the actual conditions of hydrogen applications. A comprehensive analysis of the standards landscape found that only a limited number of specifications are geared towards elastomers and plastics, which are commonly classified as non-metallic materials. The tests that are typically cited include:

- Oxygen ageing (according to ASTM D572)
- Ozone ageing (according to ISO 1431)
- Hydrogen compatibility

However, the fundamental question of how hydrogen impacts the material properties of sealing materials is still not answered. Hydrogen is not an aggressive gas, but it diffuses easily into non-metallic materials such as elastomers and plastics. It is therefore crucial to understand how sealing materials are affected by the absorbed hydrogen molecules. This will help to determine if a component is “hydrogen ready”. If components and systems need to be redesigned to make them fit for hydrogen, it can cause significant costs in some cases.

2 Material Properties Relevant for Hydrogen Sealing

For metals the effect of hydrogen embrittlement is well-known and is the subject of many studies. This phenomenon can significantly reduce the ductility and load-bearing capacity, causing cracking and catastrophic brittle failures at stresses below the yield stress [5]. A frequently asked question from designers who are used to working with metal is how much sealing materials will embrittle or change under the influence of high-pressure hydrogen. Especially in the field of hydrogen storage and transport, seals must be able to withstand extreme temperatures and pressures.

When exposed to certain fluids or gases such as hydrogen, elastomers and thermoplastic materials may undergo changes in their physical and chemical properties, consequently affecting their performance and durability. Therefore, it is important to test the compatibility of the sealing material against hydrogen when it is planned to use them in a hydrogen-related application.

First, it is important to know which material properties can be affected by hydrogen. Secondly, there is a need to understand which of these properties are relevant to ensure a good sealing function. This study will investigate how the most relevant parameters change under the influence of hydrogen.

2.1 Mechanical properties

Material behavior is typically characterized by mechanical properties such as tensile strength, stiffness modulus and elongation at break. These universal characteristics need to be investigated for both elastomers and plastics.

Another important parameter which is relevant for a reliable sealing function is the change in weight and volume. Due to the small size of hydrogen molecules, diffusion into the polymer matrix is inevitable and will cause swell. In real applications, this can become critical if the sealing groove is overfilled, leading to damage of the sealing material or the surrounding hardware. However, shrinkage can be more concerning as it can easily cause leakage in sealing applications. Since hydrogen diffuses easily into the polymer matrix, it will also escape after pressure releases. Therefore, it is vital to differentiate between reversible swell, which is important for the design of a sealing system, and permanent volume change, which indicates changes in the polymer.

If weight loss is present, it means part of the polymer was extracted and is now floating in the hydrogen gas, indicating that material properties are most likely changed. Additionally, this could result in damaging sensitive downstream systems like fuel cells.

Furthermore, for elastomer sealing the change of hardness and compression set are crucial to understand if hydrogen affects the sealing properties of a compound. For plastics this is not relevant, because the plastic seals are typically activated by pressure, metal springs or elastomer energizers. Compression set describes the loss of elasticity, meaning the permanent deformation that remains after a seal has been compressed over a longer period of time. When selecting a sealing material, it is important to ensure that compression set is still in an acceptable range considering the influence of the surrounding media.

2.2 Temperature-related material properties

Especially for elastomers, the temperature limits are very important to consider when selecting a compound. At very low temperatures the elastomer will not only shrink, but also lose its elasticity, resulting in leakage. The lower temperature limit is determined by the glass transition temperature T_G and by the T_{R10} value. The latter describes the temperature at which an elastomer has 10 percent of its elasticity, which is the minimum requirement for a good sealing function. In combination with high pressures, these limits will increase, commonly known as T_G-shift. For most elastomers the T_G-shift lies in the range of two to three Kelvin per 10 MPa pressure increase. Since this phenomenon is independent of the media and not specific for hydrogen only, it will not be considered in this study.

The upper temperature limit of plastics and elastomers is largely determined by the base material. At higher temperatures, mechanical properties decrease, and degradation is accelerated. Materials for sealing applications should be selected below their upper temperature limit. Therefore in this study the change of temperature limits is not considered, but rather the influence of extreme application temperatures on the mechanical properties of sealing materials.

3 Materials and Methods

In this study we investigate four ethylene propylene diene monomer rubbers (EPDM), one fluoroelastomer (FKM) and one thermoplastic polyurethane (TPU) as elastomer sealing materials. For the plastics side one ultra-high molecular weight polyethylene (UHMW PE) and six high-performance plastics with a PTFE-matrix as listed in Table 1 are tested. The compounds are selected according to common industrial practice and hydrogen market experience.

3.1 Compatibility testing

A very established method for testing media compatibility is ISO 1817. This standard specifies a procedure for determining the resistance of vulcanized and thermoplastic rubbers to the effects of liquids or vapors in accordance with specified conditions. The method involves immersing test specimens of elastomers in a test liquid or exposing them to a test vapor for a specified duration and temperature, and then measuring the changes in their mass, volume, hardness, tensile strength and elongation at break.

Table 1: Materials used in this study

Material Family	Compound Name	Hardness	Temperature Range
EPDM	E7T30	70 Shore A	-45 °C to +150 °C
	E8T31	80 Shore A	-45 °C to +150 °C
	E8T24	80 Shore A	-50 °C to +150 °C
	EBT25	86 Shore A	-50 °C to +150 °C
FKM	V9T82	90 Shore A	-45 °C to +200 °C
TPU	ZLT	93 Shore A	-60 °C to +110 °C
Turcon® PTFE	T01	22 Ball Ind.H.	-200 °C to +260 °C
	T05	24 Ball Ind.H.	-200 °C to +260 °C
	MF2	22 Ball Ind.H.	-200 °C to +260 °C
	MF6	32 Ball Ind.H.	-200 °C to +260 °C
	MF8	55 Shore D	-200 °C to +260 °C
UHMW PE	Z80	29 Ball Ind.H.	-200 °C to +80 °C

The test method was enhanced to mirror hydrogen specific challenges to the materials. The samples were immersed for 168 hours at nominal working pressure (NWP, typically 70 MPa) and then pressure was released to ambient conditions within less than one second [6]. This approach is based on the toughest requirements for RGD-testing, namely ISO 17268 and SAE J2600.

Test samples of each material were loaded into a pressure vessel to be filled with gaseous hydrogen. Once pressurized, the vessel was placed into a temperature chamber. A typical pressure vessel is shown in Figure 1. After 168 hrs, the final pressure was recorded before depressurizing to verify that the gas did not leak during the test.

Figure 1: Compatibility test pressure chamber

The change in mass and volume was measured after one hour for the first interval and a second time after 24 hours. In contrast, tensile testing was only carried out after 24 hours as the change of mechanical properties was to be detected without the influence of remaining swelling due to hydrogen.

3.2 Compression set testing

For elastomeric sealing materials, the compression set is one of the most important values. It is a method to evaluate the ability of the material to recover to its original shape after being compressed for a period of time. Usually, the value is measured after ageing in air at a temperature dependent on the actual application temperature. The surrounding media can improve or impair the compression set of a material depending on the interaction between material and media. Tests were carried out in a hydrogen atmosphere to determine the influence of this gas on the compression set of elastomers. All tests were performed according to ISO 815-1A in which the material is compressed between two metal plates. Compression rate depends in this case on the hardness of the material as described in the standard.

Sample materials were 13 x 6 mm buttons clamped between two stainless steel plates. The fixture and compressed samples were loaded into a pressure chamber to be filled with hydrogen. A vacuum was pulled on the chamber to remove ambient air prior to pressurizing with gaseous hydrogen to 0.01 MPa. The filled gas chambers were then placed into a temperature-controlled chamber at the specified conditions for 72 hrs. Post-test material properties were measured upon test completion.

4 Results

Given the distinct nature of elastomers and plastics which results also in different test results to be investigated, the results presented in this chapter are separated by material type. Results of mechanical properties are obtained from S2 dog bone samples. Results for volume and weight change are measured on O-Ring samples, typically one hour after pressure release.

4.1 Elastomers

4.1.1 Room temperature tests

When immersed at room temperature, the samples show small changes of volume and weight (see Figure 2). Weight change is close to zero and therefore negligible. Volume increases for all elastomers, whereas the TPU material, ZLT and the FKM material, V9T82, show very small swell of much less than one percent. The EPDM materials with 80 Shore A show higher swell of around 1.5 percent. Compared to compatibility tests in other fluids, this is however still very low.

Looking at the changes of tensile strength and elongation at break, it can be stated that hydrogen does not cause embrittlement of the elastomers. The change of IRHD hardness shown in Figure 3 further confirms this. Four out of the six materials displayed show changes of less than five percent, which is negligible in the elastomer world. The TPU material, ZLT, had an 11 percent change in tensile strength and elongation values when compared to pre-test results. The absorbed hydrogen seems to cause a slight softening of the material.

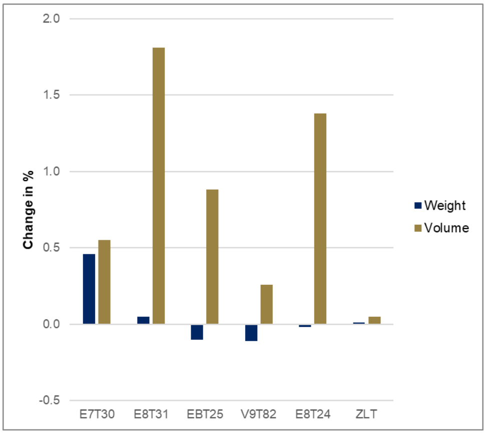

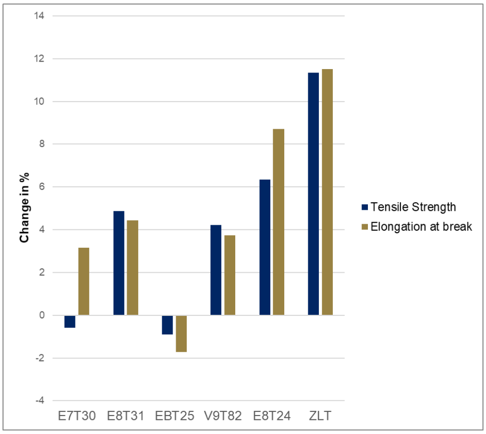

Figure 2: Change of volume, weight, tensile strength and elongation at break of different compounds after immersion in H2 for 168 h at +23 °C and 70 MPa

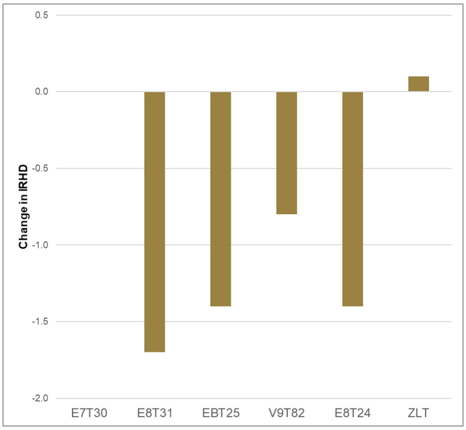

Figure 3: Change of IRHD hardness of different compounds after immersion in H2 for 168 h at +23 °C and 70 MPa

Mechanical properties are normally measured on dog bone specimens, whereas in real applications the seal is molded into a shape e.g. an O-Ring. Comparing the volume change of these two specimen types produces interesting results, see Figure 4. All materials show a much greater volume change when tested as an S2 sample; E8T31 swells three times more, EBT25 eight times more and ZLT even 10 times more. The reason for this phenomenon lies in the manufacturing method of the samples. When produced as an O-Ring, the material experiences a greater amount of shear stress in the molding tool and the polymer network is more dense than in a test sheet. Therefore, the hydrogen molecules are able to more easily enter a specimen cut from a test sheet. Thus, if a material passes a certification test based on results from a dog bone sample, the final seal will likely swell less in a real application. This phenomenon should be considered in design and certification processes.

The volume change considered here is measured one hour after taking the material out of the hydrogen atmosphere. If you compare the swell 24 hours later, it becomes obvious that the volume change is not permanent. This indicates that the hydrogen gas likely did not have any adverse effects on the polymer. The volume increase of V9T82 shown in Figure 4 is small and still within the measurement error.

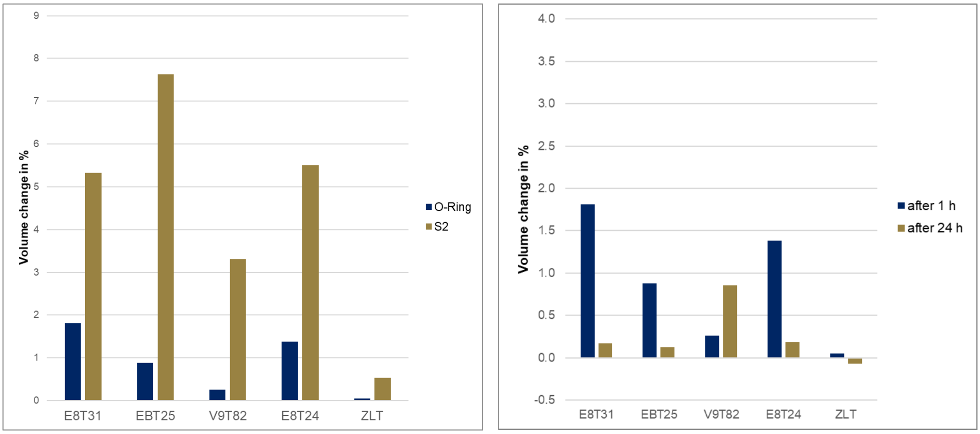

Figure 4: Volume change depending on specimens (left, 1 hour) and time of measuring (right) after immersion in H2 for 168 h at +23 °C and 70 MPa

4.1.2 Influence of the temperature

Hydrogen seals need to cover a large temperature window from typically -40 °C to +85 °C. Results for volume change at room temperature and at the temperature limits are shown in Figure 5. E8T31 shows higher swell at elevated temperature but stays overall in a small percentage range.

Figure 6 shows the change of tensile strength and elongation under the influence of temperature. Typically, elongation tends to increase at +85 °C and decrease at -40 °C. However, V9T82, E7T30, E8T24 and EBT25 show almost no change in elongation at break at elevated temperature compared to prior hydrogen immersion. A reason could lie in the higher mobility of the polymer chains which allows entrapped hydrogen molecules to escape faster. The tensile tests were done at room temperature 24 hours after pressure relief. For tensile strength there is similarly no clear trend visible. Only E8T31 shows a slight increase in tensile strength over temperature. For ZLT, the previously described slight softening is reduced at higher temperatures. After exposure to -40 °C hydrogen, the polymer shows a small embrittlement. However, it should be investigated if this effect persists after a longer period. Due to the very dense structure of this polymer, some hydrogen molecules could still be trapped in the matrix after 24 hours.

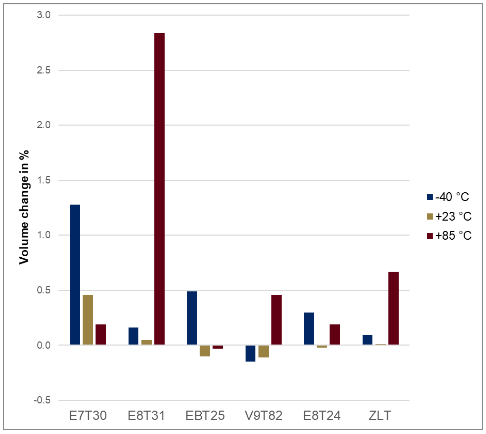

Figure 5: Volume change after immersion in H2 for 168 h at different temperatures and 70 MPa

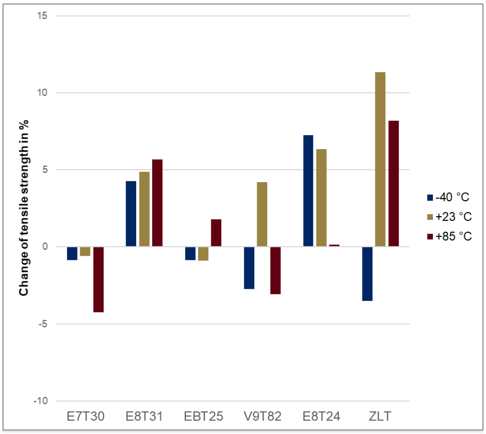

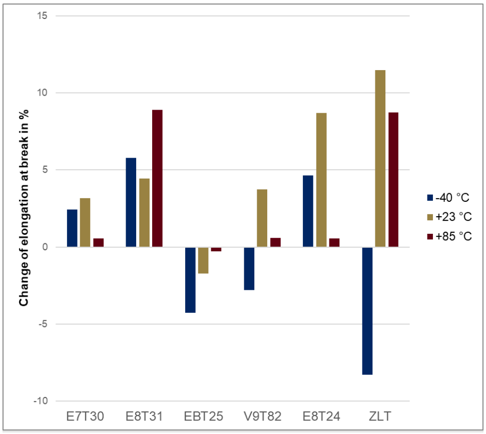

Figure 6: Change of tensile strength and elongation at break after immersion in H2 for 168 h at different temperatures and 70 MPa

In essence, the results show that there is no critical influence on the mechanical properties of the tested elastomers. Compared to immersion tests in some fluids, the changes observed here are relatively very small.

4.1.3 Compression set

When elastomer seals lose their elasticity over lifetime, leakage can occur easily. It is therefore vital to understand if the compression set changes under the influence of hydrogen. The results of five elastomers are shown in Figure 7. Except for E8T24, hydrogen has no or even a positive impact which comes most likely from the absence of oxygen. Ageing elastomers in air allows oxygen to attack the polymer chains, which is why a hydrogen atmosphere helps to reduce this effect. Small differences like in the case of V9T82 can also originate from the higher swell due to hydrogen, which could compensate the actual compression set. The reason for E8T24 showing higher compression set in hydrogen needs to be studied further.

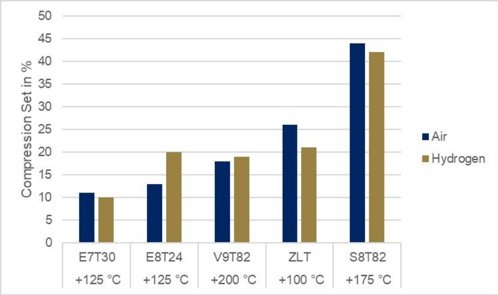

Figure 7: Compression set after immersion in H_2 and air for 72 h according to ISO 815-1A

4.2 Thermoplastic polymers

In the initial testing phase for thermoplastic polymers, the goal was to investigate the effect of hydrogen on the volume and mechanical properties of the seal material. In Figure 8, the PTFE-based compounds show a small noticeable swell independently of the filler content. This is due to the sintered structure of PTFE materials. When it comes to mechanical properties, only MF2 and T05 show an increase in strength and elongation, whereas the other PTFE compounds show a small embrittlement of less than five percent, which is normally not a reason for concern.

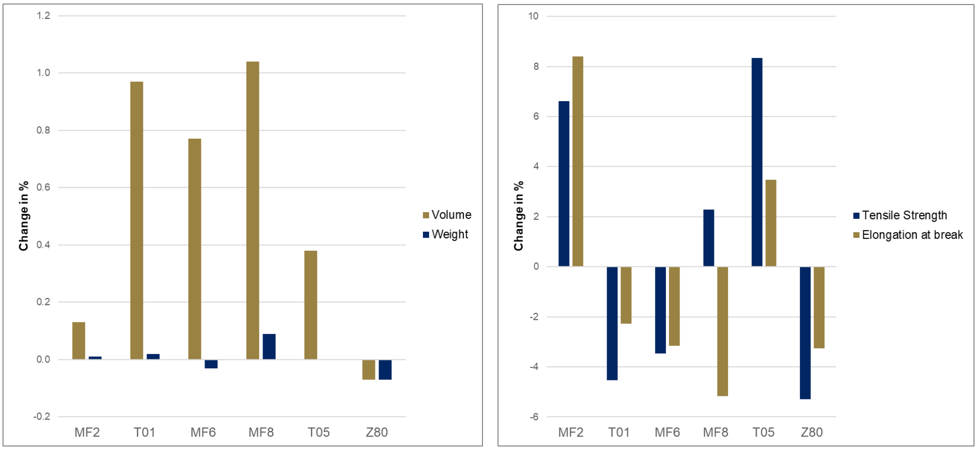

Figure 8: Change of volume, weight, tensile strength, and elongation at break of different compounds after immersion in H_2 for 168 h at +23 °C and 70 MPa

Z80 is a UHMW polyethylene with a solid thermoplastic matrix, which is why there is almost no weight or volume change, since the amount of hydrogen molecules absorbed must be very small. The mechanical properties also show a slight embrittlement below five percent.

Thermoplastic sealing materials are preferably used when the application temperature exceeds the limits of elastomers. With high temperatures, volume increases a bit more, but still below two percent as shown in Figure 9. The increase is slightly smaller in unfilled PTFE, which is T01, due to less diffusion paths for hydrogen along the fillers.

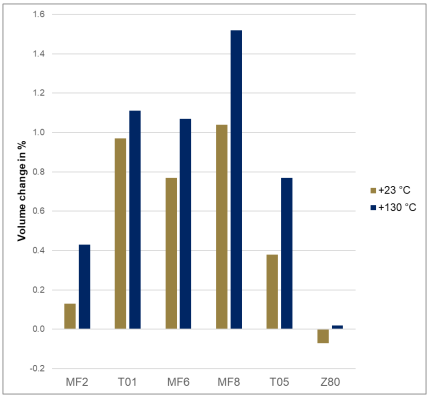

Figure 9: Volume change of thermoplastic compounds after immersion in H_2 for 168 h at +23 °C and 70 MPa

Figure 10 compares the mechanical properties at room temperature and +130 °C. Z80 is not shown, because its upper temperature limit is +80 °C. Overall higher temperatures tend to make the materials slightly more brittle. This can be observed in MF2, MF6, MF8 and T05 with low percentages. The amount of change however is

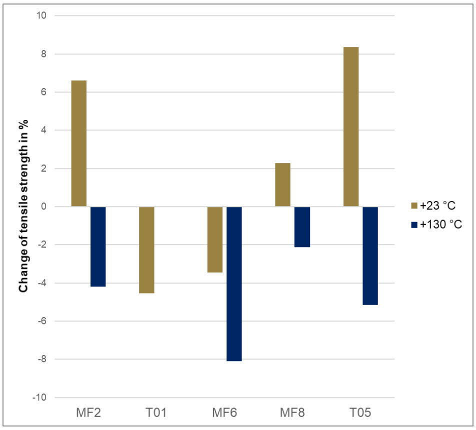

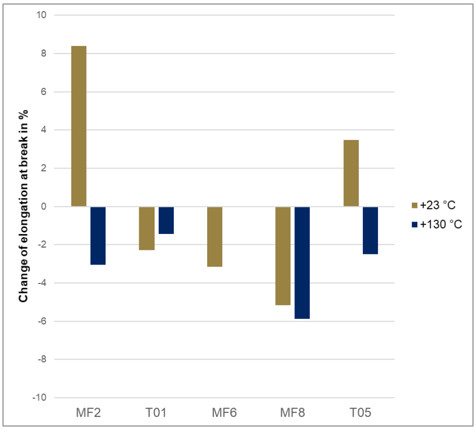

Figure 10: Change of tensile strength and elongation at break after immersion in H2 for 168 h at different temperatures and 70 MPa

still not at a worrying level. More research is needed to differentiate temperature aging effects from the influence of hydrogen at elevated temperatures.

5 Summary and Conclusion

In this study, the influence of hydrogen on non-metallic sealing materials, namely elastomer and plastics, is investigated. Focus lies on the change of mechanical properties, as well as volume, weight and hardness after hydrogen exposure at high pressure. Compression set under hydrogen atmosphere is also studied for elastomers, because it is highly relevant for the sealing performance.

The results show no embrittlement of the elastomers tested. Only in the case of one TPU material could a slight softening be observed. Also, extreme application temperatures of -40 °C and +85 °C show no critical influence on the mechanical properties of tested elastomers. The volume change is below two percent and is largely temporary. However, the results of volume change are highly dependent on the shape and production method of the samples. O-Ring samples show less change after hydrogen immersion. This phenomenon should be considered in design and certification processes. Compression set under hydrogen atmosphere shows no significant deterioration except for one compound, which needs to be studied further.

The swell of plastic materials under hydrogen atmosphere in this study is around one percent and does not depend on the filler level. The change of mechanical properties depends on the specific compound. Some improve and some decrease, but not more than five percent, which is usually not a concern. The influence of hydrogen at high temperature tends to show a slight embrittlement of the polymers investigated. More research is needed to differentiate temperature aging effects from the influence of hydrogen at elevated temperatures.

It is concluded that hydrogen has no significant influence on the compounds investigated in this study, which are known to be polymers suitable for hydrogen use. The findings should therefore not be generalized for all compounds of their material families. Specific testing may be needed to ensure a safe use in hydrogen applications.

6 References

[1] Bundesministerium für Wirtschaft und Energie: *Die Nationale Wasserstoffstrategie*, June 2020

[2] European Commission: *A Hydrogen Strategy for a Climate-Neutral Europe*, Brussels, June 2020

[3] IEA: *The Future of Hydrogen. Seizing Today's Opportunities*, 2019

[4] Trelleborg Sealing Solutions: https://www.trelleborg.com/de-de/seals/your-industry/hydrogen-sealing, visited on April 30, 2024.

[5] Barrera, O., Bombac, D., Chen, Y. et al.: *Understanding and mitigating hydrogen embrittlement of steels: a review of experimental, modelling and design progress from atomistic to continuum*. J Mater Sci 53, 6251–6290, 2018.

[6] DIN EN ISO 17268:2017-03: *Gasförmiger Wasserstoff - Anschlussvorrichtungen für die Betankung von Landfahrzeugen*, S.18

7 Authors

Trelleborg Sealing Solutions Germany

Schockenriedstr. 1, 70565 Stuttgart, Germany

Philipp Hirstein, M. Sc., Philipp.Hirstein@trelleborg.com

Sandra Kofink, M. Sc., Sandra.Kofink@trelleborg.com

Trelleborg Sealing Solutions Americas

2509 Bremer Rd, Fort Wayne, IN 46803, United States

Joel Thompson, M. Sc., Joel.Thompson@trelleborg.com

https://doi.org/10.61319/4IQN23QS

Investigation of sealing materials with excellent cold temperature flexibility in hydrogen environments

Michael Fasching, Thomas Schwarz, Silvio Schreymayer, Thomas Hafner, Geraldine Theiler, Natalia Cano Murillo, Andreas Kaiser

This work investigates various polymeric materials as sealing materials in hydrogen applications. Materials made of TPU, EPDM and NBR were investigated in relation to minimum service temperature, their permeability depending on pressure and temperature, compatibility to hydrogen, and tribological behaviour in hydrogen atmosphere. Results show that all selected materials meet the demand of cold-temperature flexibility and compatibility to hydrogen, however distinguish in their swelling behavior, wear resistance and permeability.

1 Introduction

Reliable operation is a key requirement for hydrogen technology. Operating conditions of up to 1000bar pressure and temperatures of -40°C and 85°C, which are demanded for hydrogen-powered vehicles, are challenging to be met by sealing materials such as TPEs and rubbers.

In-depth understanding of material behavior is therefore needed to meet the requirement of reliable operation. First, cold temperature flexibility of a sealing material determines the minimum service temperature under which a sealed system can be pressurized, in combination with compression and roughness of countersurface. Second, permeability of a sealing material influences the leakage rate of a sealing application. Literature [1,2] indicates that permeation is strongly dependent on temperature, but limited data is available for sealing materials at high pressure to date. Third, sealing materials are continuously exposed to high pressure hydrogen gas, which may affect their tribological behaviour and mechanical properties in general.

This paper addresses in detail all of the above topics for candidate materials, two polyurethane grades, one EPDM, and two NBR grades with low ACN content. To study the minimum service temperature per material, a cold-temperature test rig was adapted to achieve temperatures as low as -70°C with nitrogen gas. A test rig to measure permeation of hydrogen was developed that allows the measurement at conditions of up to 800 bar pressure and 75°C. To investigate the mechanical properties of sealing materials under the influence of hydrogen, material samples were placed in an autoclave and exposed to temperatures at the upper service temperature at a pressure of 1000bar. Mechanical properties were tested accordingly before and shortly after the exposure. Finally, material samples were exposed to pressurized hydrogen at room temperature and tribological properties (wear, coefficient of friction) were characterized in-situ with a linear tribometer in ball-on-plate configuration.

In this work, the relevant properties for hydrogen applications are studied for two polyurethane grades, one EPDM, and two NBR grades with low ACN-content.

2 Theoretical background

2.1 Cold temperature flexibility

Self-sealing materials such as rubbers or thermoplastic elastomers show elastic behaviour in their service temperature range, which is responsible for their sealing behaviour. When cooling such materials to the region of glass-transition and below, these materials gradually loose their elasticity and eventually their sealing functionality. In general, properties that characterize the glass transition temperature are corresponding to the minimum service temperature of a sealing material. Typical values are the E'', max of a DMA analysis, Tg obtained via DSC, or the TR-10 value. However, the real minimum service temperature of a sealing material is also significantly influenced by application details, such as (1) roughness of counter-surface, (2) interference of sealing material and housing, and (3) potential interaction of media to be sealed with sealing material (media that cause swelling of the sealing material may act as plasticisers, with a positive influence on minimum service temperature).

2.2 Permeation

Mass diffusion generally occurs between sites with different chemical potentials, in case of sealing applications caused by different gas pressures on both sides of the sealing material [1,2]. The higher upstream pressure p1 and the lower downstream pressure p2, at either side of a sample membrane, causes the gas molecules to permeate through the sample membrane to compensate for the pressure difference [3-5]. It can be assumed that the Henry sorption model and the Fick model for concentration-independent diffusion describe the sorption-desorption of gas molecules on the membrane surfaces and the diffusion of the gas molecules in the membrane, respectively, when the permeate is a gas with small molecules such as hydrogen (H2) and the sample membranes consist of elastomers or thermoplastic elastomers tested at temperatures above glass transition temperature [3, 6]. Since most membranes have a much smaller thickness compared to their lateral dimensions, the mathematical problem of permeation through the membrane can be considered to be one-dimensional. A detailed description of the theoretical background to evaluating permeation properties from permeation measurements is given by [7].

3 Experimental

3.1 Materials

A range of candidate materials with minimum service temperatures suitable for typical hydrogen applications (below -40°C) was selected, both commercially available and development grades. Table 1 gives an overview over the investigated materials.

Table 1: Materials investigated for their suitability in hydrogen applications

Material designation	Polymer	Hardness (Shore A)	Nominal service temperature range (°C)
TPU 1	TPE-U	95	-50 to 110
TPU 2	TPE-U	95	-50 to 110
EPDM 1	EPDM	90	-50 to 150
NBR 1	NBR	85	-45 to 100
NBR 2	NBR	85	-50 to 100

While the thermoplastic Polyurethanes are unfilled, all rubbers were reinforced with carbon black as main filler. Both NBRs were selected as grades with low ACN-content, and NBR 2 was additionally modified with a plasticizer to investigate the effects on compatibility in hydrogen environment. TPU 1 and TPU 2 were supplied by SKF Sealing Solutions Austria GmbH, whereas the EPDM and NBR grades were supplied by Arlanxeo Deutschland GmbH as experimental grades.

3.2 Cold temperature flexibility

In order to characterize the minimum service temperature of sealing materials in gaseous media, a test rig originally developed for seal tests according to the oil and gas test standard API 6A Annex F [8] was modified to evaluate the minimum service temperature, under which a sealing material can be activated in nitrogen gas.

Figure 1 gives a schematic overview over both test rig and sealing design. The seal design consists of a T-seal type design of the active sealing material, supported by back-up rings made of a PEEK material on both sides to prevent static extrusion. The cross-section of the active sealing material was varied in order to investigate the effect interference on the minimum temperature where the test assembly can be pressurized, which is also the minimum service temperature.

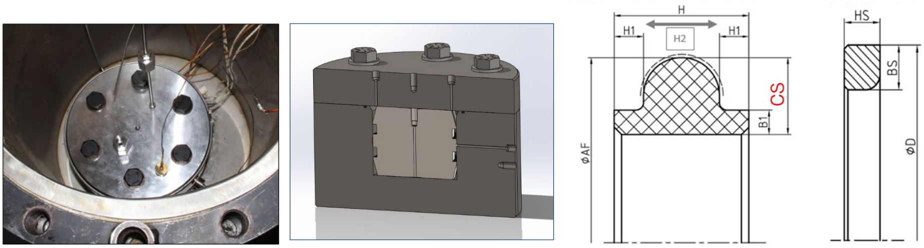

Figure 1: High pressure – low temperature test fixture and corresponding sealing design and backu-up ring

Table 2 introduces the test parameters. The approach was selected as follows: First, the test rig was cooled down to -40°C and pressurized for at least 5 minutes. In subsequent steps, the temperature was then lowered in 5°C steps, until no further activation was possible. Next, temperature was raised again in 1°C steps until the minimum temperature, where the sealing assembly could be activated, was found.

Table 2: Test parameters in high pressure- low temperature test fixture

Gas	Nitrogen
Temperature	-40°C to -70°C (theoretical minimum temperature of test rig)
Pressure	875 bar
Extrusion gap	0.17mm
Test seals	Machined T-seals, variation of cross-section

3.3 Permeation

To measure permeation of hydrogen through the investigated materials, a test rig was developed that allows the measurement of hydrogen permeation at temperatures up to 85°C and pressures of up to 1000bar. This test rig was developed within the COMET-module “Polymers4Hydrogen” at the HyCentA (Graz, Austria), with contributions from the Polymer Competence Center Leoben GmbH (Leoben, Austria) and SKF Sealing Solutions Austria GmbH.

Figure 2 shows an overview of the permeation test-set-up. On the upstream side, high pressure hydrogen is supplied to the material sample, whereas on the downstream side, nitrogen purges the permeated hydrogen as carrier gas to the hydrogen detection sensor, which is established via thermal conductivity.

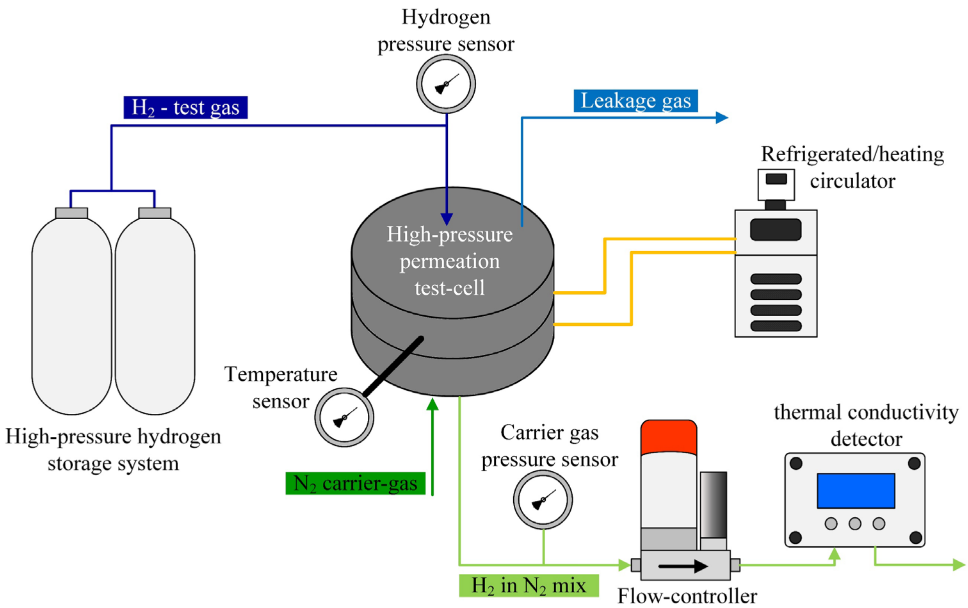

Figure 2: Permeation-system test set-up [7]

Figure 3 shows a detailed view of the permeation test cell. The material sample is supported by a sinter filter, which support the sealing materials so that a test pressure of up to 1000bar can be applied. SKF developed a sealing system that prevents leakage of the pressurized hydrogen. A leakage bore and leakage detection system was installed additionally for safety reasons. The effective sample diameter (diameter of the supporting sinter-disc) for the permeation measurement is 80mm.

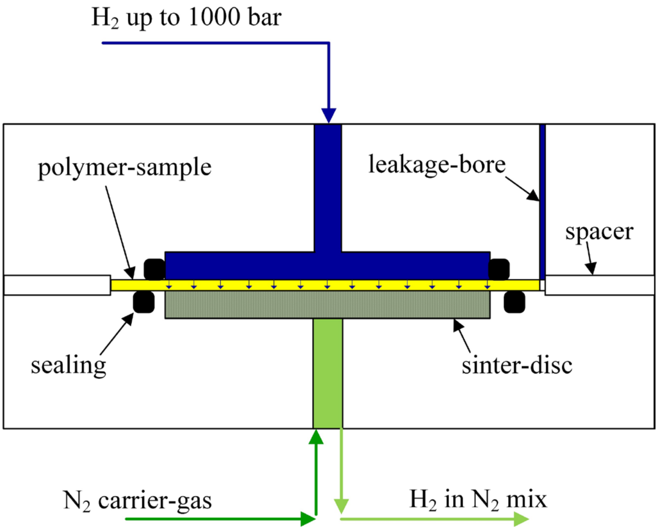

Figure 3: Schematic view of high-pressure permeation test-cell [7]

Table 3 shows the test parameters for the various candidate materials to investigate their permeation depending on pressure and temperature.

Table 3: Test program for determination of permeation of candidate materials

Material	Temperature (°C)	Pressure (bar)
TPUs	0, RT, 50, 75°C	50, 400, 800
EPDM	RT, 75°C	50, 400, 800
NBR 1	0, RT, 50, 75	50, 400, 800
NBR 2	RT, 75°C	50, 400, 800

3.4 Material compatibility tests to hydrogen including Tribology

The topic of material compatibility to hydrogen gas was investigated in various ways. First, material samples were exposed to hydrogen 85°C and 1000bar pressure for 168 hours. Mechanical properties of the materials were investigated both before and after the hydrogen exposure.

In addition, an insitu-tribometer was developed by Bundesanstalt für Material-forschung und -prüfung (BAM, Berlin, Germany), which allows the measurement of friction and wear under hydrogen atmosphere under a pressure of up to 100 bar. Pressurized tribo-experiments do allow the characterization of properties in pres-ence of swelling, which was previously found to be critical for sealing materials [9,10].

[11] gives a detailed description of the tribometer. It is designed as an insert in an autoclave made of stainless steel. Normal and frictional forces are measured using strain gauges that are attached to deformation bodies in a bridge circuit. Figure 4 gives and overview of the test set-up. It uses a ball-on-disc configuration, where the ball is made of 316L stainless steel with a diameter of 6.0mm. The disk are respective samles of the sealing materials. A normal load of 5N, frequency of 10Hz and stroke of 2mm was found to be most suitable for stable operation for characterization of material fretting. A total of 20000 cycles was conducted per material, where the tests were performed in both reference environment (ambient air, moisture range 40-50%), and in gaseous hydrogen (H2O content <500ppm), at both 1 bar and 100 bar pressure level. In order to investigate potential ageing effects of preceding hydrogen exposure on tribological behaviour, an additional tribological test setting was executed for the rubber samples. These were tribo-tested after being pre-exposed to 1000bar hydrogen for 168h at 85°C.

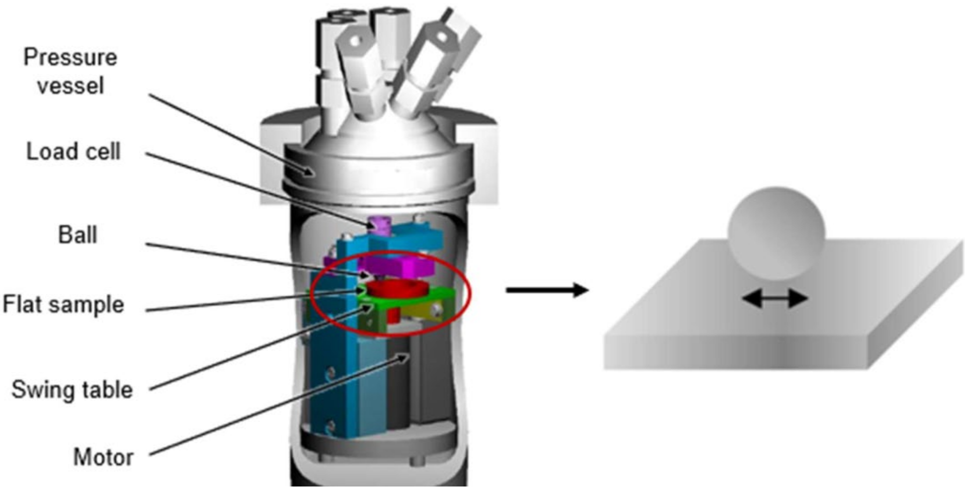

Figure 4: Permeation-system test set-up [11]

The following main results were evaluated for each material: average coefficient of friction for each condition, and wear volume, based on a 3D profile obtained with a 3D profilometer (nanofocus, Oberhausen, Germany).

4 Results and discussion

4.1 Cold temperature flexibility

Table 4 shows the results for the minimum temperature where pressure could be built-up in the cold temperature test rig for the example of TPU 1. This material shows glass transition temperature of -46.8°C, obtained with DSC, and a E' onset temperature of -54.1 °C, obtained with dynamic mechanical analysis. It can be seen that activation is possible even below the E' onset temperature which typically the lower end where a seal can be activated in static sealing applications. In addition, the level of compression applied on the seal does affect the minimum activation temperature as expected, where an increased compression reduces the minimum activation temperature.

Table 4: Minimum temperature for sealing activation depending on compression of cross-section on the example of TPU 1, nitrogen as medium, criteria: absence of leakage at a pressure of 875 bar for a minimum time of 5 minutes

Compression (%)	Minimum temperature for pressure build-up (°C)
8.5	-55.3
12.3	-57.3
15.9	-63.3

4.2 Permeation results

This subchapter shows the results for permeation through sealing materials. Due to the fact that testing effort of these tests is high (roughly 24h for on data point) and the limitation that particularly rubbers could not be tested at the combination of highest pressure and highest temperature, a selection of pressure, temperature and material was made and tested that is considered to representatively cover the material behaviour.

Figure 5 (50 bar hydrogen test pressure) and Figure 6 (400 bar hydrogen test pressure) show the temperature dependency of the hydrogen permeation, which is shown in (cm^3 x cm / (cm^2 x s x bar)). All tested materials share an almost Arrhenius-type dependency on temperature, which means that permeation at 75°C is roughly 6 to 7 times as high compared to permeation at room temperature. Furthermore, a ranking for permeation through various materials can be done. While TPU 2 shows slightly higher hydrogen permeation compared to TPU 1, both polyurethanes show the lowest permeability, followed by NBR and EPDM. The plasticizer content of NBR 2 does not seem to significantly influence the permeability, compared to NBR 1.

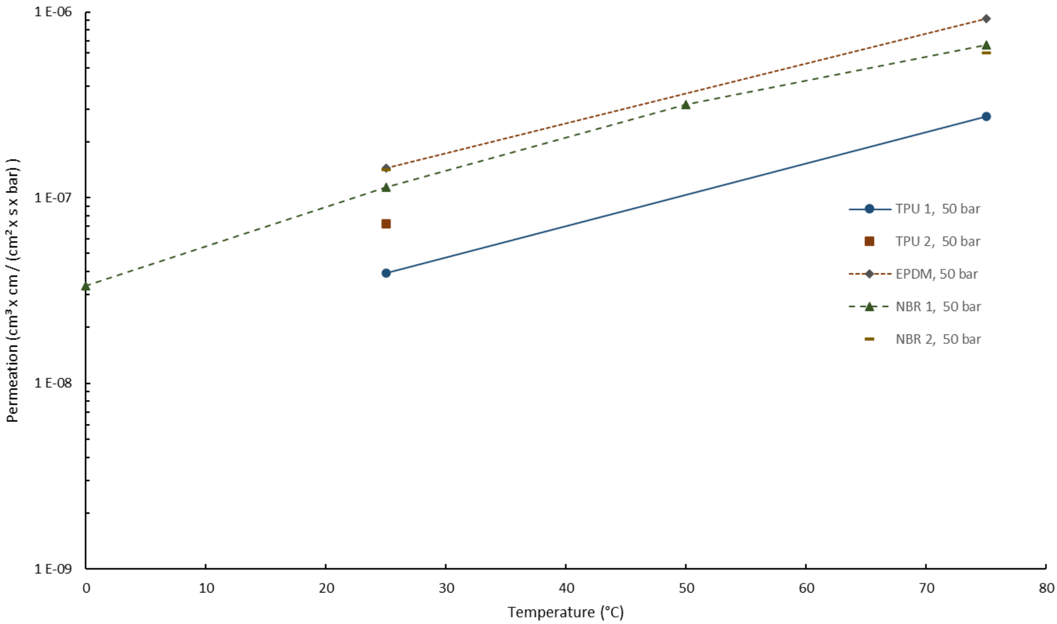

Figure 5: Hydrogen permeation results for different materials, obtained at 50 bar

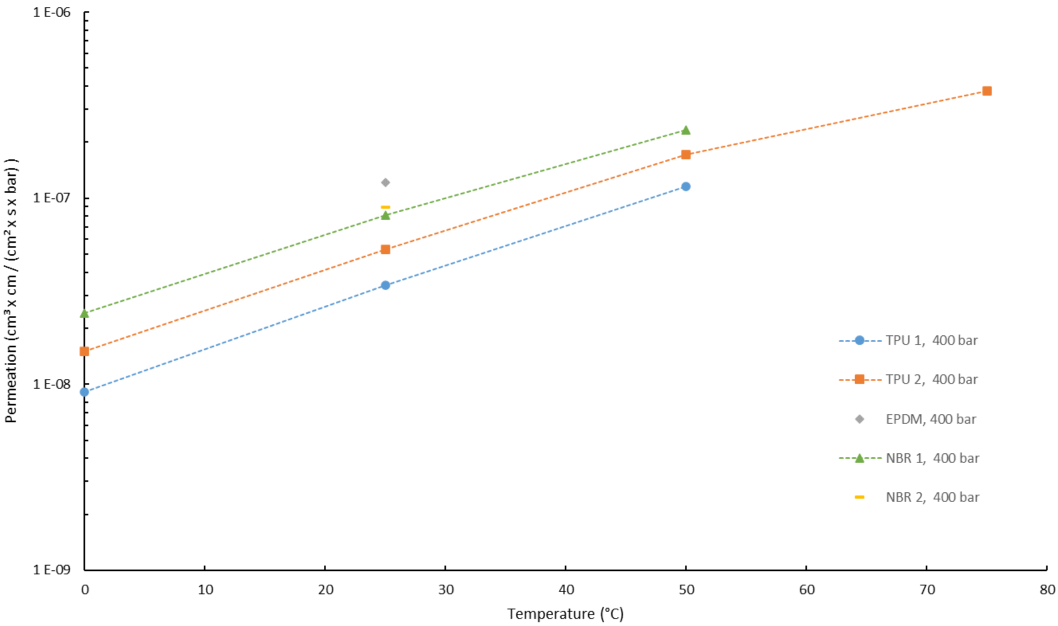

Figure 6: Hydrogen permeation results for different materials, obtained at 400 bar

Figure 7 shows the influence of pressure for the NBR materials, which are representative for all investigated polymers. The pressure level was varied in the range of 50 bar to 800 bar. It can be seen that rising pressure level reduces the permeability of the tested materials, however the effect is less pronounced than the temperature influence. A pressure increase of 750bar at room temperature roughly reduces the permeability by 50%.

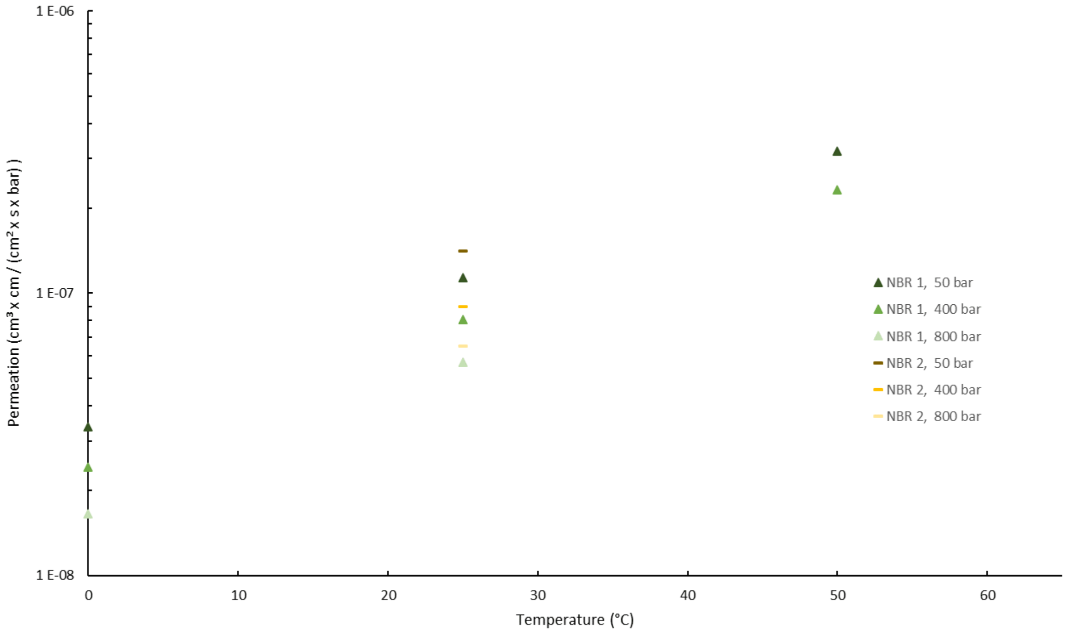

Figure 7: Influence of pressure on hydrogen permeation on the example of NBR

4.3 Compatibility

Table 5 and Table 6 show the change in properties of the investigated materials after storage in pressurized hydrogen, 2h after immersion and 48h after immersion. This was done to distinguish between physical effects such as reduction of density as consequence of hydrogen diffusion into the sealing material, and chemical ageing effects (e.g. hardening of rubbers). Comparing the hardness changes of both NBR and the EPDM rubber 2h after immersion and 48h after immersion, it can be seen that the initial decrease, which is correspondingly reflected in reduced density, is a fully reversible phenomenon and no longer measurable 48h after the exposure. It can therefore be assumed that the changes initially observed after the exposure are of physical nature and no chemical ageing phenomena could be observed. This is supported by the tensile properties, which show minor changes only. With the Polyurethanes TPU1 and TPU2, the effects of reduced hardness and density shortly after immersion could not be observed. While the amount of physical interaction (e.g. volume increase) under pressure is unknown as the autoclave in use had no window to assess volume changes in-situ, it is still an indication that the physical effects of pressurized hydrogen on TPU is lower compared to EPDM and NBR rubbers. Like with the rubbers, both TPUs did not show any signs of chemical ageing, as property changes 48h after end of immersion were small and almost within measurement scattering.

Table 5: Change of material properties measured 2h after exposure to Hydrogen at 1000bar, 85°C for 168h

	EPDM	NBR1	NBR2	TPU1	TPU2
Shore A Hardness	-13	-8	-8	+0	-1
Density	-19.6 %	-27.7 %	-9.2 %	-2.8 %	-0.5 %
Tensile strength	+11.1 %	-4.4 %	4.0 %	-0.7 %	-0.7 %
Elongation at break	-14.6 %	-3.0 %	-1.0 %	1.9 %	12.2 %

Table 6: Change of material properties measured 48h after exposure to Hydrogen at 1000bar, 85°C for 168h

	EPDM	NBR1	NBR2	TPU1	TPU2
Shore A Hardness	+0	+1	+0	+0	-1
Density	-	+0.47 %	+0.07 %	-0.01 %	-0.01 %
Tensile strength	+9.8 %	+13.0 %	-10.0 %	+1.2 %	-0.7 %
Elongation at break	-12.7 %	+4.0 %	-16.7 %	+1.9 %	+12.2 %

4.4 Tribology

This subchapter addresses the tribological fretting behaviour of the sealing materials in hydrogen atmosphere. Figure 8 shows the coefficient of friction obtained in the tribological experiment. It can bee seen that neither the pressure level, under which the tests are performed (1 bar and 100bar), nor the pre-exposure to pressurized hydrogen at elevated temperature, as was done for EPDM and the NBRs, has a significant negative impact on the obtained coefficient of friction. While EPDM shows a slight increase in friction with hydrogen atmosphere, NBRs and TPUs show a slight reduction compared to the reference measurement in ambient air.

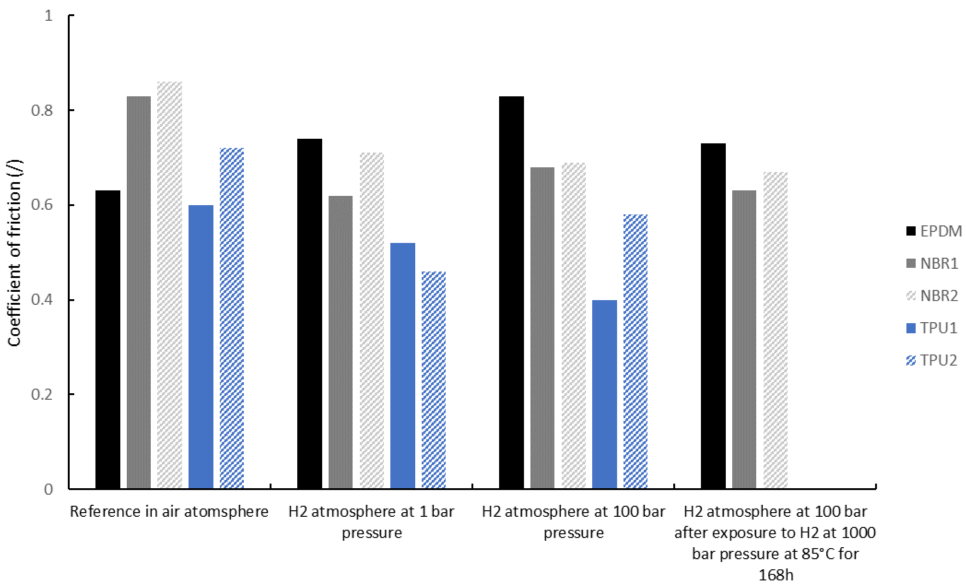

Figure 8: Coefficient of friction obtained in tribological experiments under different media and pressures

Figure 9 shows the wear volume resulting of the respective tribological experiments. For this result, no negative impact of the hydrogen atmosphere could be found on any of the materials: All wear results obtained under hydrogen were either equal or lower compared to the reference measurement in ambient air, but always in the same range. The main finding was the strong influence of the material polymer: As expected, both polyurethanes show their well-known superior wear resistance, and particularly under hydrogen atmosphere, showed wear results an order of magnitude below the next best material. Like with the other results shown in this paper, NBR 2 containing a plasticizer showed comparable results to its corresponding NBR 1 counterpart without plasticizer. Both NBRs showed wear still on a low level, particularly when compared to EPDM, for which the highest wear level was obtained by far, independent of hydrogen pressure or pre-exposure. Still, this is not an interaction caused by the hydrogen, as the reference test in air atmosphere showed very comparable results.

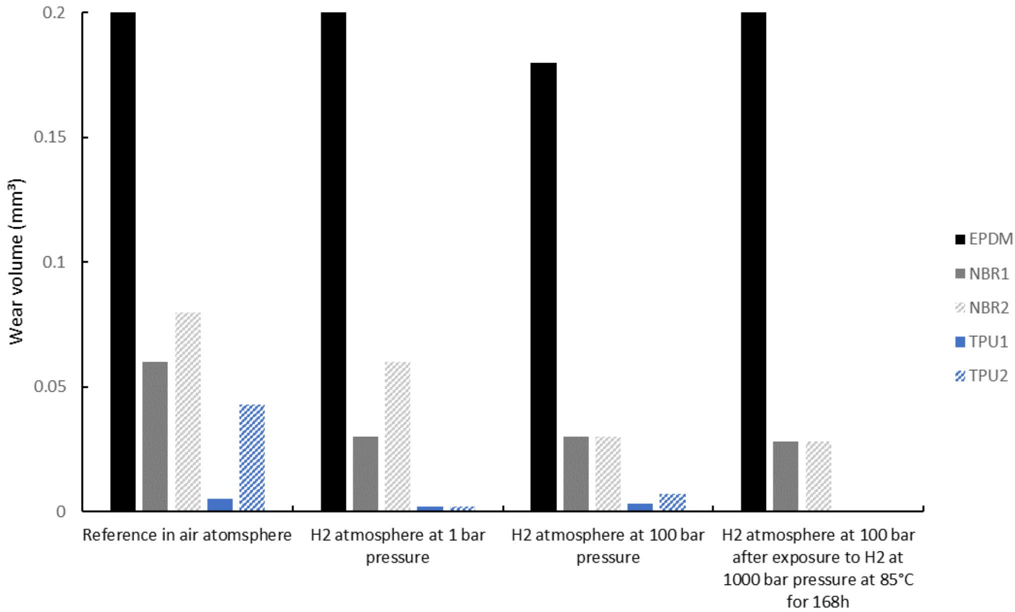

Figure 9: Wear volume obtained in tribological experiments under different media and pressures

5 Summary and Conclusion

The experiments to determine the minimum temperature where a seal can be activated show that the glass-transition temperature is a good indicator for an estimation of this temperature. However, the variation of cross-sectional compression showed that in this temperature range, tolerances are of significant importance and need to be considered for reliable functionality of a seal.

The measurements of permeability showed that permeation decreases with rising pressure level and increases with rising temperature level. Thereby, the effect of temperature is much more pronounced: an increase in temperature from room temperature to 75°C leads to a roughly 7 times increase in permeation, whereas an increase of pressure by 750bar only reduced the permeation by about 50%. It could be clearly observed that material-wise, the applied polymer has the main influence. TPU 1 and TPU 2 showed to lowest permeability, followed by NBR and EPDM. While NBR 2 containing 10phr of plasticizer did show a minor increase in permeation compared to NBR 1, the effect was comparably small and likely irrelevant for any application.

Immersion tests where material samples were exposed to 1000 bar hydrogen at 85°C for 168h revealed that none of materials showed signs of chemical ageing. Both NBR and EPDM showed significant reduction in hardness and density when being tested 2 hours after the immersion, which is likely caused by physical interaction of the hydrogen diffusing into the rubber materials. Tests 48h after the immersion confirmed that these changes in hardness and density were fully reversible. While a small reduction in density was also measurable with the TPUs 2h after immersion, the effect was significantly smaller compared to the rubbers.

The tribological experiments showed that hydrogen atmosphere, at both 1 bar pressure and 100 bar pressure, did not have a negative impact on any of the 5 tested materials and resulting coefficients of friction as well as wear volume were in the range of the reference experiment in ambient air. However, EPDM by far showed the highest wear volume, whereas both TPU grades could demonstrate their outstanding wear resistance. Like observed with other properties, the plasticizer in NBR 2 did only show a marginal effect on the tribological behaviour, which is much smaller than the effect of the polymer itself.

To summarize, all 5 tested material grades are generally suitable for hydrogen applications. While none of the materials showed chemical ageing in hydrogen atmosphere, EPDM showed higher permeation, loss of hardness caused by hydrogen diffusion, and wear volume compared to the other materials. Both TPUs showed excellent performance in all investigations and are therefore considered to be an excellent choice for sealing applications in pressurized hydrogen.

6 Acknowledgement

Parts of this research work were performed within the COMET-module “Polymers4Hydrogen” at the Polymer Competence Center Leoben GmbH (PCCL), the HyCentA Research GmbH, and the Bundesanstalt für Materialforschung und -prüfung (BAM), within the framework of the COMET-program of the Federal Ministry for Transport, Innovation and Technology and the Federal Ministry for Digital and Economic Affairs. The COMET-module is funded by the Austrian Government and the State Government of Styria.

7 References

[1] Smith, D.B., Anovitz, L.M.: Lifecycle Verification of Tank Liner Polymers, Oak Ridge National Laboratory ORNL/TM-2014/48, March 2014

[2] Klopffer, M.-H., Berne, P., Espuche, É.: Development of Innovating Materials for Distributing Mixtures of Hydrogen and Natural Gas, In: Oil & Gas Science and Technology, Rev. IFP 70(2), pp. 305-315, 2015

[3] Klopffer, M.-H., Flaconneche, B.: Transport Properties of Gases in Polymers, In: Oil & Gas Science and Technology, Rev. IFP 56 (3), pp. 223-244, 2001

[4] Fujiwara, H., Ono, H., Onoue, K., Nishimura, S.: High-pressure gaseous hydrogen permeation test method – property of polymeric materials for high-pressure hydrogen devices (1), In: International Journal of Hydrogen Energy, 45(53), pp 29082-29094, 2020

[5] Naito, Y., Kamiya, Y., Terada, K., Mizoguchi, K., Wang, J.-S.: Pressure dependence of gas permeability in a rubbery polymer, In: Journal of Applied Polymer Science, 61(6), pp. 945-950, 1996

[6] Frisch, H.-L.: Sorption and transport in glassy polymers – a review, In: Polymer Engineering and Science, 20(1), pp. 2-13, 1980

[7] Hafner, T., Macher, J., Brandstätter, S., Trattner, A.: Advancing Hydrogen Storage: Development and Verification of a High-Pressure Permeation Test Setup for Polymeric Barrier Materials, submitted to be published In: International Journal of Hydrogen Energy, 2024

[8] N.N.: Specification for Wellhead and Tree Equipment, API Specification 6A, 21st edition, 2018

[9] Nishimura, S.: Rubbers and elastomers for high-pressure hydrogen, In: Kobunshi, 64(6), pp. 356-357, 2015

[10] Yamabe, J., Nishimura, S.: Influence of fillers on hydrogen penetration properties and blister fracture of rubber composites for O-ring exposed to high-pressure hydrogen gas, In: International Journal of Hydrogen Energy, 34(4), pp. 1977-1989, 2009

[11] Theiler, G., Cano Murillo, N., Hausberger, A.: Effect of Hydrogen Pressure on the Fretting Behavior of Rubber Materials, to be published In: Lubricants, 2024

8 Authors

SKF Sealing Solutions Austria GmbH

Gabelhoferstrasse 25, 8750 Judenburg, Austria:

Dipl.-Ing. Dr. Michael Fasching, michael.fasching@skf.com

Dipl.-Ing. Dr. Thomas Schwarz

Ing. Silvio Schrymayer, M.A.

HyCentA Research GmbH

Inffeldgasse 15, 8010 Graz, Austria:

Dipl.-Ing. Thomas Hafner

Bundesanstalt für Materialforschung und -prüfung (BAM)

Unter den Eichen 87, 12205 Berlin, Germany:

Dr.-Ing. Geraldine Theiler

Dr.-Ing. Natalia Cano Murillo

ARLANXEO Deutschland GmbH

Hans-Imhoff-Strasse 6, 50679 Cologne, Germany:

Dr.-Ing. Andreas Kaiser

https://doi.org/10.61319/Z3OH8VXW

Influence of hydrogen environment on friction properties of silicone rubber

Hikaru Hashimoto, Suguru Norikyo, Ayako Aoyagi, Hiroyoshi Tanaka, Takehiro Morita, Yoshinori Sawae, Joichi Sugimura

To elucidate the effect of hydrogen on the friction properties of silicone rubber, sliding tests were conducted in hydrogen and air with various moisture contents. The friction coefficient in hydrogen was higher than that in air. Regarding moisture content in hydrogen, the rubber surface after sliding test in humid hydrogen showed severe wear compared to that in dry hydrogen. These results suggested that gas atmosphere and moisture content of gas had influences on the friction between silicone rubber and austenitic stainless steel and the wear of silicone rubber. The surfaces of silicone rubber and austenitic stainless steel after sliding tests were analysed using optical microscopy, confocal laser scanning microscopy, FT-IR microscopy and SEM/EDS to explore the influence of hydrogen on the wear process.

1 Introduction

In recent years, the utilisation of hydrogen energy has gained importance in order to achieve carbon neutrality. Safe utilisation of hydrogen energy requires establishment of new technologies for ensuring reliability and durability of machine elements used in hydrogen networks, and the role of sealing materials is essential in achieving this goal. Examples of sealing elements used in high-pressure hydrogen gas applications include piston rings for reciprocating compressors and rubber O-rings for flanges, couplings and pressure vessels. Although O-rings are used as static seals for preventing gas leakage, they are subject to repeated micro-movements within the groove during compression-decompression cycles. Consequently, these O-rings experienced sliding against the metal groove surface in hydrogen gas. Especially, unexpected high friction of the O-ring causes excessive elastic deformation and possibly induces serious mechanical failure [1-12]. For these reasons, researches have intensively been conducted to understand frictional properties of rubber [13-17] and thermoplastics [18-21] in hydrogen.

In this study, the effect of hydrogen on friction between silicone rubber and stainless steel was investigated. Reciprocating sliding tests were performed with a pin-on-disk apparatus in air and hydrogen.

2 Experimental Methods

2.1 Material

Silicone rubber and austenitic stainless steel (AISI 316L steel) were selected as a representative material for O-rings and their metal sliding counterface, respectively, in high-pressure hydrogen gas applications. The silicone rubber pin specimen had a hemispherical shape with a diameter of 5 mm. The surfaces of the stainless steel disks were polished using 3 µm diamond slurry to have a surface roughness of 0.02 µm Ra. After that, the disks were cleaned ultrasonically using a mixture of acetone and hexane for three minutes.

2.2 Sliding test

Friction and wear of the silicone rubber-on-stainless steel sliding pair was evaluated by using a pin-on-disk apparatus installed in the vacuum chamber (*Figure 1 (a)*). The vacuum chamber was evacuated with a scroll and turbomolecular vacuum pumps. Then, the gas was introduced to raise the chamber to ambient pressure. The gas continued to flow in and out of the chamber during the sliding tests. Gas leaving the chamber was directed to a moisture sensor (HUMICAP®HM70, VAISALA). The gases were continued to flow during the sliding tests. Subsequently, load to press the rubber pin against the stainless steel disk was applied by dead weights through the loading lever. The applied load and friction force were measured using a biaxial load cell. Friction coefficients were calculated by friction force divided by load. Figure 1(b) shows the speed of stainless steel disk and the relative displacement of rubber pin to stainless steel disk during sliding test. The stainless steel disk rotated at a constant speed in a certain direction and quickly switched back to the other direction.

The purity of hydrogen was 99.999%. The vacuum chamber was equipped with a precision moisture controller which was developed by Fukuda [22] and used to adjust the trace moisture content of hydrogen gas environment. Several sliding tests were performed in hydrogen, which was moisturized by using this moisture controller. All sliding tests were performed for 10000 seconds. All experimental conditions are summarized in Table 1.

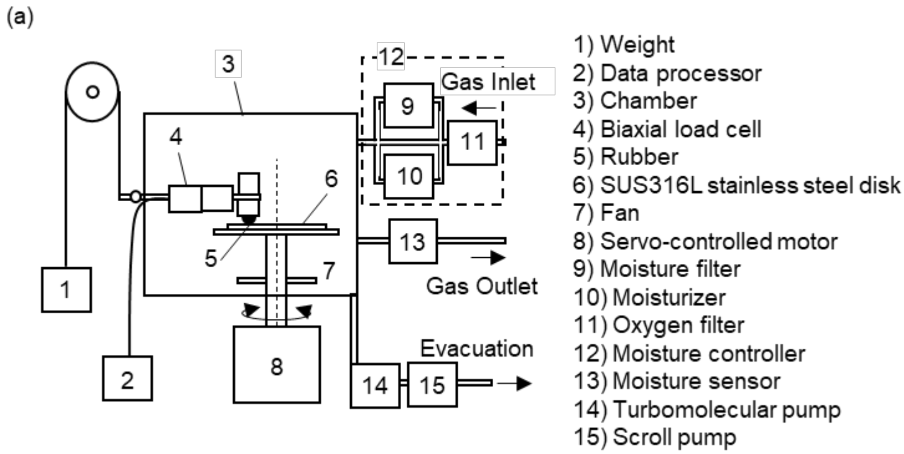

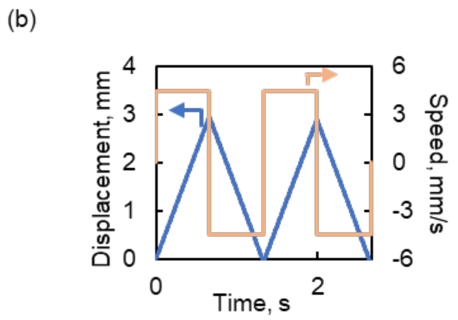

Figure 1: (a) Schematic diagram of pin-on-disk tribometer equipped with advanced atmosphere control system, (b) Motion of servo-controlled motor

Table 1: Conditions of sliding tests

Motion	Reciprocating sliding
Environment	Air, hydrogen
Load	5 N
Sliding speed	4.5 mm/s
Sliding distance	3 mm
Temperature	25 °C
Pressure	0.1 MPa

2.3 Surface analysis

2.3.1 Optical Microscopy and confocal laser microscopy

The worn surfaces of rubber specimens were observed by using optical microscope (VH7000, KENYENCE) at a magnification of 50. In addition to that, the specimens were observed by using a confocal laser microscope (VK-X1000, KENYENCE) at magnification of 10 to obtain 3D topography, arithmetic average roughness (Ra) and maximum roughness (Rz). The roughness parameters were measured on five positions near the top of rubber surface.

2.3.2 IR spectroscopy

Infrared (IR) spectroscopy (FT/IR 4X, IRT-7100, JASCO) was performed to collect spectra from silicone rubber and stainless steel. The IR spectra of silicone rubber confirming the wave number range of 400 to 4000 cm^{-1} were obtained by using attenuated total reflection (ATR) method with a diamond prism. The spectra from stainless steel surfaces were obtained by reflection method. The aperture size was 50 × 50 µm and the number of scans was 16.

2.3.3 SEM/EDS

Scanning electron microscopy and energy dispersive X-ray spectrometry (SEM/EDS) (SEM SU3500 Oxford EDS EMAX Evolution, Hitachi) was performed to observe the surface of specimen and to collect EDS spectra from silicone rubber and stainless steel. The accelerating voltage was 15kV, and operating pressure was 30Pa.

3 Results

3.1 Friction in various environments

3.1.1 Measurement of friction coefficient

Figure 2 (a)~(c) shows the transition of friction coefficient (COF) of silicone rubber in dry air and hydrogen together with the moisture content. *Figure 2 (d)~(l)* shows enlarged views of (a), (b) and (c), expressing the shape of the friction curves. Moisture contents in hydrogen ranged from 0.4 to 0.9 ppm (hereinafter called dry hydrogen) and from 83 to 110 ppm (humid hydrogen), while that in air (dry air) was from 1.4 to 2.0 ppm.

Comparing the results among the gases which have similar moisture content, the friction coefficients after 2000 seconds in dry hydrogen were higher than those in dry air. Furthermore, the friction coefficients after 2000 seconds in dry hydrogen was higher than those in humid hydrogen.

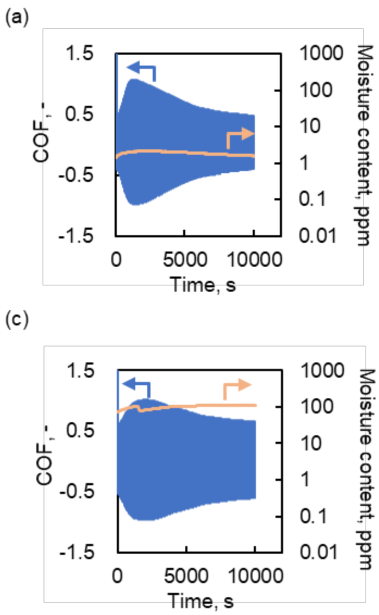

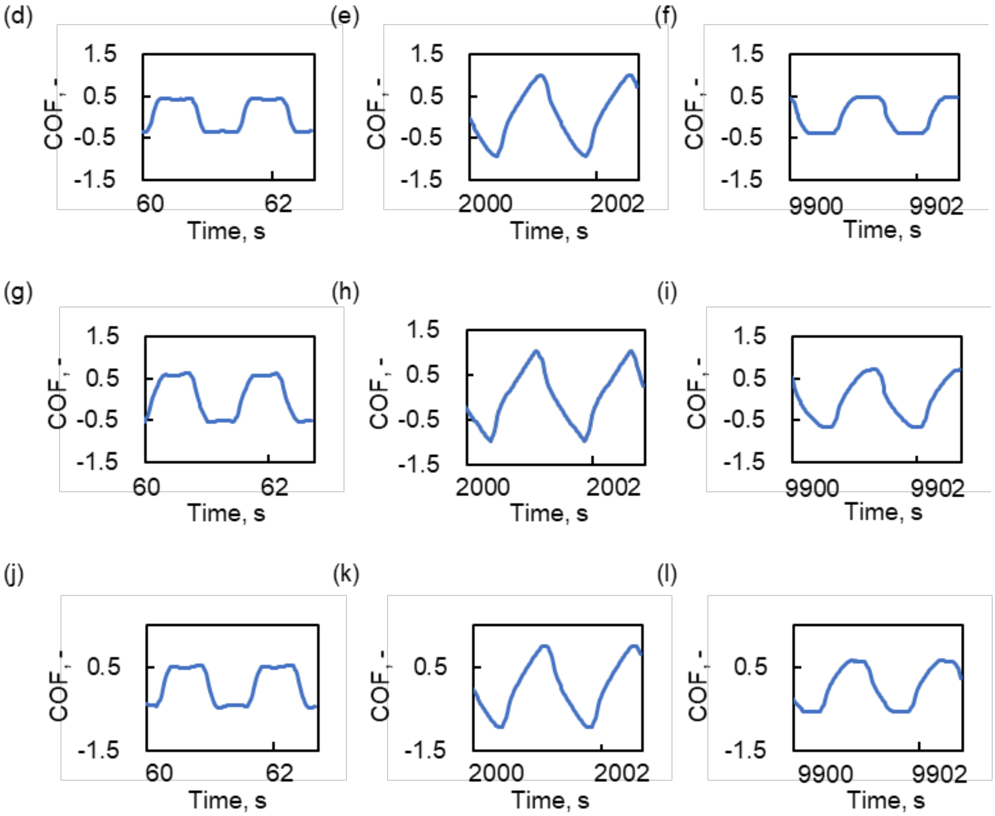

Figure 2: Transition of friction coefficient (a) in dry air, (b) in dry hydrogen, (c) in humid hydrogen, (d)(e)(f) Enlarged view of the result in dry air, (g)(h)(i) Enlarged view of the result in dry hydrogen, (j)(k)(l) Enlarged view of the result in humid hydrogen

The shape of the friction curve also depended on the environment (*Figure 2 (d)~(l)*). After 60 seconds from measurement start, the shape of friction curves was similar among all gases. The shape has plateau region, indicating that the silicone rubber slipped on the surface of stainless steel. The shape changed to a triangular shape after 2000 seconds, which suggests that silicone rubber sticked to stainless steel and did not slip on it. After 9900 seconds, the duration on the plateau region in the friction curve in dry hydrogen was shorter than that in dry air. In addition to that, that in dry hydrogen was shorter than that in humid hydrogen.

3.2 Surface analysis after sliding test

3.2.1 Morphology measurement

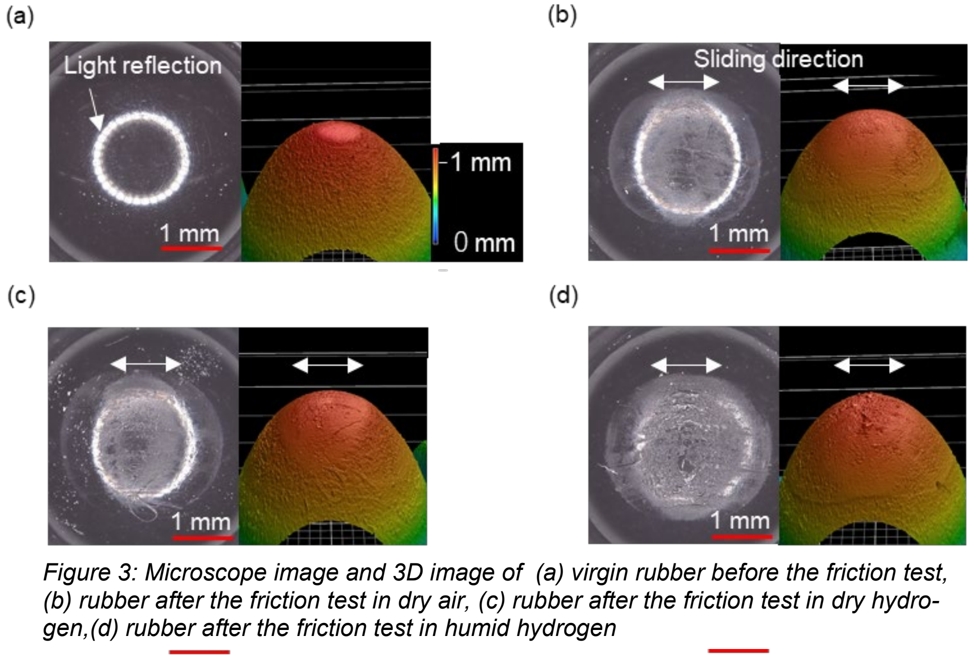

Figure 3: Microscope image and 3D image of (a) virgin rubber before the friction test, (b) rubber after the friction test in dry air, (c) rubber after the friction test in dry hydrogen,(d) rubber after the friction test in humid hydrogen

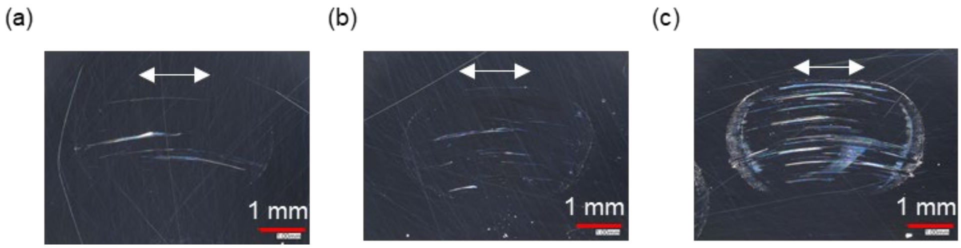

Figure 4: Microscope image of stainless steel after the friction test (a) in dry air (b) in dry hydrogen (c) in humid hydrogen

The microscope images and 3D shape obtained using confocal laser scanning microscopy are shown in *Figure 3*. The rubber surface after the sliding test in humid hydrogen (*d*) showed severe wear compared to that in dry air (*b*) and that in dry hydrogen (*c*). There was no clear difference between the rubber surface after sliding test in dry hydrogen and that in dry air. As shown in *Figure 4*, the stainless steel after sliding test in humid hydrogen exhibited a clear wear track, in addition to the severe wear on the rubber surface.

3.2.2 Investigation of chemical composition change

IR spectra of rubber surface were measured in order to analyse chemical composition changes. The spectra were shown in *Figure 5*. The peaks were observed at 787, 1006, 1258 and 2962 cm^{-1} for silicone polymer and 452 and 1068 cm^{-1} for silica filler. The observed peaks were reasonable because silicone rubber was composed of silicone polymer and silica filler. The IR spectra were normalized at 787 cm^{-1}, which was assigned to Si-C bonds of silicone polymer. The peak intensity at 452 cm^{-1} and at 1068 cm^{-1} increased after sliding tests compared to the spectrum of silicone rubber before sliding test. It suggested that the amount of silicone polymer decreased compared to that of silica filler after sliding test. The amount of silica filler on rubber surface after sliding test in humid hydrogen was greater than that in dry hydrogen. The amount of silica filler on rubber surface after sliding test in dry hydrogen was greater than that in dry air.

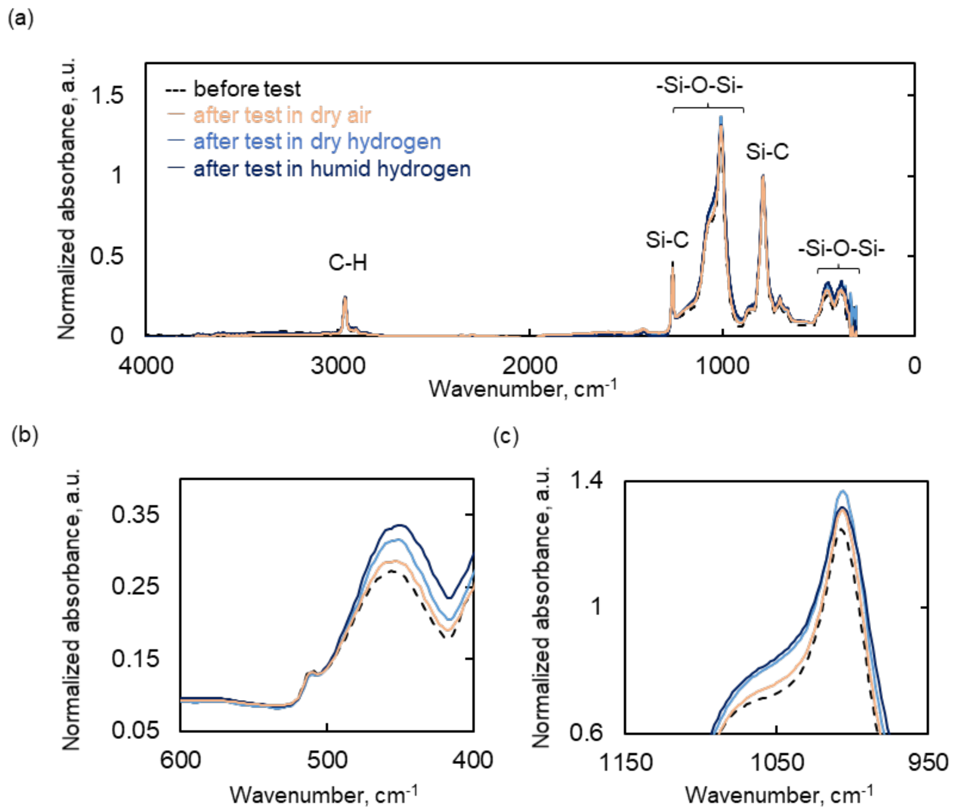

Figure 5: IR spectra of rubber surface normalized at 787 cm^{-1}

Although the observed wear appearance and wear debris were different in degree among the three conditions, the results in FTIR and SEM/EDS were similar.

Therefore, the analysis results for humid hydrogen were particularly shown in *Figure 6*. As shown in *Figure 6(b)*, the IR spectra at the edge of the friction tracks have peaks at 1100, 1258 and 2962 cm^{-1}. The peaks at 1258 and 2962 cm^{-1} were assigned to Si-C and C-H bonds of silicone polymer. The peak at 1100 cm^{-1} was assigned to Si-O-Si bonds of silicone polymer and silica filler. The EDS mapping of silicon also indicated that the particles includes silicon atoms (*Figure 6(c) and (d)*). Thus, debris of silicone rubber were transferred on the stainless steel surface. On the other hand, grooves directed to sliding direction were observed at the centre of the stainless steel (*Figure 6(e)*).

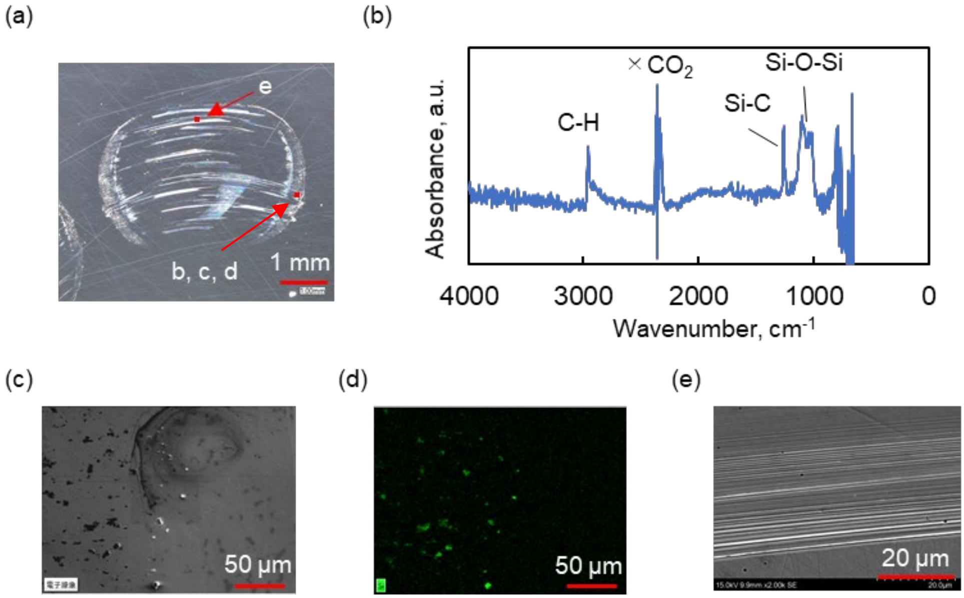

Figure 6: The analysis of countersurface after sliding test in humid hydrogen (a) Microscope image of stainless steel surface after sliding test, (b) IR spectrum obtained from the edge of wear track, (c) SEM image at the edge of wear track, (d) EDS elemental distribution map of silicon atom, (e) SEM image at the centre of wear track

4 Discussion

All the results described above suggest influences of the hydrogen environment and moisture content on the friction behaviour of silicone rubber.

As for the influence of hydrogen, friction coefficients in hydrogen after reaching its peak were higher than that in air at a similar moisture content. After sliding test in dry hydrogen, the amount of silica filler on the rubber surface increased compared to that in dry air. These phenomena may have been caused by the absence of oxidative reaction in hydrogen. When oxidative reaction occurred on rubber surface in dry air, the hardness of rubber surface increase, resulting in lower friction coefficients and reduced exposure of silica filler. However, there are other possibilities, such as the influence of hydrogen to silicone rubber. Further study will be necessary to understand the respective aspects.

Tribological characteristics of the silicone rubber were also sensitive to moisture content. Friction coefficient in dry hydrogen after reaching its peak is higher than that in humid hydrogen. After sliding test in humid hydrogen, the amount of silica filler on the rubber surface increased compared to dry hydrogen. These results may have been caused by hydrolysis reaction of silicone polymer. Similar change in IR spectrum was reported by Nagasawa [23]. Hydrolysis of silicone polymer may enhance the degradation of silicone polymer, resulting in low friction coefficients and increased exposure of silica filler. In another possibility, lower friction coefficients and increased exposure of silica filler in humid hydrogen may have been caused by the time difference in rubber slipping on stainless steel. Further study will be necessary as well.

Deep grooves were observed on the stainless steel after the sliding test in humid hydrogen. These grooves appear to have have been caused by the wear resulting from the exposed silica on the rubber surface.

5 Conclusions

In order to clarify the features of friction in hydrogen, influences of gas and moisture content to friction and wear were investigated.

As for the influence of hydrogen, friction coefficients in hydrogen were higher than those in air at a similar moisture content. Moisture content also influenced friction coefficients. The friction coefficients in the dry condition were higher than those in high humidity conditions. As moisture content increases, silicone polymer was selectively removed from the rubber surface during sliding test. As a result, the silica fillers were exposed on the rubber surface and the groove may have been generated on the stainless steel.

6 Acknowledgements

This research work was performed within the framework of the strategic international collaborative research program (SICORP, grant number: JPMJSC2121), which was supported by Japan Science and Technology Agency (JST), and the joint research project “SusSeal4H2” (funding code: 01DR23001), which was co-funded by German Federal Ministry of Education and Research.

Friction tests were performed at HYDROGENIUS (the Research Center for Hvdrogen Industrial Use and storage) in the Kyushu University.

The authors are grateful to the Bundesanstalt für Materialforschung und -prüfung (BAM), namely Dr. Theiler and Dr. Murillo, to Freudenberg Technology Innovation

SE & Co. KG corporate R&D, namely Dr. Dobbelaar, Dr. Schauber and Mr. Müller for informative discussion.

7 References

[1] Yamabe, J., Nishimura, S.; *Influence of fillers on hydrogen penetration properties and blister fracture of rubber composites for O-ring exposed to high-pressure hydrogen gas,* International Journal of Hydrogen Energy, 2009, https://doi.org/10.1016/j.ijhydene.2008.11.105

[2] Yamabe, J., Nishimura, S., Koga, A.; *A study on sealing behavior of rubber O-ring in high pressure hydrogen gas*, SAE International Journal of Materials and Manufacturing, 2009, https://doi.org/10.4271/2009-01-0999

[3] Yamabe, J., Fujiwara, H., Nishimura, S.; *Fracture analysis of rubber sealing material for high pressure hydrogen vessel*, Journal of Environment and Engineering, 2011, https://doi.org/10.1299/jee.6.53

[4] Fujiwara, H., Yamabe, J., Nishimura, S.*; Evaluation of the change in chemical structure of acrylonitrile butadiene rubber after high-pressure hydrogen exposure,* International Journal of Hydrogen Energy, 2012, https://doi.org/10.1016/j.ijhydene.2012.02.084

[5] Yamabe, J., Koga*,* A., Nishimura, S.; *Failure behavior of rubber O-ring under cyclic exposure to high-pressure hydrogen gas,* Engineering Failure Analysis, 2013, https://doi.org/10.1016/j.engfailanal.2013.01.034

[6] Fujiwara, H., Ono, H., Nishimura, S.; Degradation behavior of acrylonitrile butadiene rubber after cyclic high-pressure hydrogen exposure, International Journal of Hydrogen Energy, 2015, http://dx.doi.org/10.1016/j.ijhydene.2014.11.106

[7] Ono, H., Fujiwara, H., Onoue, K., Nishimura, S.; *Influence of repetitions of the high-pressure hydrogen gas exposure on the internal damage quantity of high-density polyethylene evaluated by transmitted light digital image,* International Journal of Hydrogen Energy, 2019, https://doi.org/10.1016/j.ijhydene.2019.07.035

[8] Fujiwara, H., Ono, H., Onoue, K., Nishimura, S.; *High-pressure gaseous hydrogen permeation test method -property of polymeric materials for high-pressure hydrogen devices (1)-,* International Journal of Hydrogen Energy, 2020, https://doi.org/10.1016/j.ijhydene.2020.07.215

[9] Fujiwara, H., Ono, H., Ohyama, K., Kasai, M., Kaneko, F., Nishimura, S.; *Hydrogen permeation under high pressure conditions and the destruction of exposed polyethylene-property of polymeric materials for high-pressure hydrogen devices (2)-*, International Journal of Hydrogen Energy, 2021, https://doi.org/10.1016/j.ijhydene.2020.12.223

[10] Castagnet, S., Ono, H., Benoit, G., Fujiwara, H., Nishimura, S.; *Swelling measurement during sorption and decompression in a NBR exposed to high-pressure hydrogen*, International Journal of Hydrogen Energy, 2017, https://doi.org/10.1016/j.ijhydene.2017.06.138

[11] Simmons, K.L., Kuang, W., Burton, S.D., Arey, B.W., Shin, Y., Menon, N.C., Smith, D.B., H-Mat; *Hydrogen compatibility of polymers and elastomers,* International Journal of Hydrogen Energy, 2021, https://doi.org/10.1016/j.ijhydene.2020.06.218

[12] Zhou, C., Zheng, J., Gu, C., Zhao, Y., Liu, P.; *Sealing performance analysis of rubber O-ring in high-pressure gaseous hydrogen based on finite element method,* International Journal of Hydrogen Energy, 2017, https://doi.org/10.1016/j.ijhydene.2017.03.039

[13] Zhou, C., Zheng, Y., Liu, X.; *Fretting characteristics of rubber X-ring exposed to high-pressure gaseous hydrogen*, energies, 2022, https://doi.org/10.1016/j.ijhydene.2019.02.224

[14] Zhou, C., Chen, G., Xiao, S., Hua, Z., Gu, C.; *Study on fretting behavior of rubber O-ring seal in high-pressure gaseous hydrogen*, International Journal of Hydrogen Energy, 2019, https://doi.org/10.3390/en15197112

[15] Duranty, E. R., Roosendaal, T. J., Pitman, S. G., Tucker, J. C., Owsley, Jr. S. L., Suter, J. D., Alvine, K. J.: *An in situ tribometer for measuring friction and wear of polymers in a high pressure hydrogen environment*, Review of Scientific Instruments, 2017, https://doi.org/10.1063/1.5001836

[16] Kuang, W., Bennett, W. D., Roosendaal, T. J., Arey, B. W., Dohnalkova, A., Petrossian, G., Simmons, K. L.: *In situ friction and wear behavior of rubber materials incorporating various fillers and/or a plasticizer in high-pressure hydrogen,* Tribology International, 2020, https://doi.org/10.1016/j.triboint.2020.106627

[17] Furusho, K., Tanaka, H., Yagi, K., Sawae, Y., Honda, S.: *9th International Tribology Conference, Fukuoka 2023*, https://confit.atlas.jp/guide/event/itc2023/top, visited on September 30, 2023

[18] Sawae, Y., Morita, T., Takeda, K., Onitsuka, S., Kaneuti, J., Yamaguchi, T., Sugimura, J.: *Friction and wear of PTFE composites with different filler in high purity hydrogen gas,* Tribology International, 2021, https://doi.org/10.1016/j.triboint.2021.106884

[19] Theiler, G., Gradt, T.: *Tribological characteristics of polyimide composites in hydrogen environment,* Tribology International, 2015, https://doi.org/10.1016/j.triboint.2015.06.001

[20] Theiler, G., Gradt, T.: *Environmental effects on the sliding behaviour of PEEK composites,* Wear, 2016, https://doi.org/10.1016/j.wear.2016.09.019

[21] Theiler, G., Gradt, T.: *Influence of counterface and environment on the tribological behaviour of polymer materials*, Polymer Testing, 2021, https://doi.org/10.1016/j.polymertesting.2020.106912

[22] Fukuda, K, Sugimura, J.: *Influences of trace water in a hydrogen environment on the tribological properties of pure iron,* Tribology Online, 2013, https://doi.org/10.2474/trol.8.22

[23] Nagasawa, S., Nishina, H., Arase, N., Nakada, M.: *Simulation test method for deterioration of engine crankshaft oil seals*, SAE International, 1990, https://doi.org/10.4271/902123

8 Authors

NOK corporation

4-3-1 Tsujidoshinmachi Fujisawa-shi, Kanagawa-ken, 251-0042 Japan:

Hikaru Hashimoto, M. Sc., hashimoto.18.hikaru@jp.nokgrp.com

Suguru Norikyo, M. Sc., norikyo.21.suguru@jp.nokgrp.com

Dr.-Eng. Ayako Aoyagi, aoyagi.07.ayako@jp.nokgrp.com

Kyushu University, Faculty of Engineering, Department of Mechanical Engineering

744 Motooka Nishi-ku, Fukuoka-ken, 819-0395 Japan:

Univ.-Asst. Prof. Dr.-Eng. Hiroyoshi Tanaka, ORCID 0000-0002-2392-4789,

tanaka.hiroyoshi.315@m.kyushu-u.ac.jp

Takehiro Morita, M. Sc.,

morita.takehiro.871@m.kyushu-u.ac.jp

Univ.-Prof. Dr.-Eng. Yoshinori Sawae, ORCID 0000-0001-9255-5297,

sawae.yoshinori.134@m.kyushu-u.ac.jp

Dr.-Eng. Joichi Sugimura, ORCID 0000-0003-1926-2169,

sugimura.joichi.666@m.kyushu-u.ac.jp

https://doi.org/10.61319/O2Y6V8UJ

Group A
Session 5

Simulation II

A 12

Matthias Grafe, Tobias Lankenau, Kathrin Ottink, Thomas Ebel, University of Applied Sciences "Hochschule Emden/Leer", Maschinenbau, Emden, Germany

Simulation of Leakage Flow in dynamic seals from 3D-printing

A 13

Niklas Bauer, Katharina Schmitz, RWTH Aachen University, Institute for Fluid Power Drives and Systems (ifas), Aachen, Germany

Pneumatic Seals: A Review of Experimental Measurement and Theoretical Modeling of Sealing Friction

A 14

Tim Hantusch, Casper Schousboe Andreasen, Böðvar Ólafsson, A/S Gunnar Haagensen, Engineering - R&D, Allerød, Denmark

Direct numerical simulation of mixed lubrication in elastohydrodynamic systems

A 15

Fabian Kaiser, A. Gropp, D. Savio, D. Frölich, C. Wilbs, D. Möhring, Freudenberg Technology Innovation SE & Co. KG, Tribology, Weinheim, Germany

Prediction of RSS Sealing Performance by Fully Coupled EHL Simulation

Simulation of Leakage Flow in dynamic seals from 3D-printing

Matthias Graf, Tobias Lankenau, Kathrin Ottink, Thomas Ebel

Additive Manufacturing (AM) technologies are advancing rapidly, even within the realm of seal production. However, the surface quality of AM seals typically falls short when compared to seals manufactured conventionally. For instance, Fused Filament Fabrication (FFF) yields components with a characteristic string-like surface texture. The dimensions of this texture align with the fluid film thickness of a dynamic rod seal. Through a fluid-structure interaction (FSI) simulation employing coupled Navier-Stokes equations, the fluid flow between the seal and rod can be analyzed. This simulation demonstrates that periodically fragmented contact has a significant impact on the sealing properties of the dynamic seal. A comparison between traditional seals and those produced via FFF manufacturing reveals notable implications, such as alterations in the reverse feed rate through the seal gap.

1 Introduction

Additive Manufacturing has made significant strides in recent years and presents itself as a viable alternative for seal production. Seals, being components subjected to wear due to tribological factors, require periodic replacement. The availability of spare parts can be improved through fast and on-demand additive manufacturing. Fused Filament Fabrication (FFF) emerges as a promising production method, particularly for TPU-based dynamic rod seals [1]. Experimental studies have indicated that careful selection of printing parameters and materials results in seals boasting impressive sealing properties [2]. Although the lifespan of FFF seals may be shorter compared to their conventionally manufactured counterparts, they serve as a quick and interim solution to prevent costly machine downtime.

However, the manufacturing process yields seals with slightly different surface structures than those from conventional methods. In FFF production, a thermoplastic filament is extruded through a heated nozzle and deposited in a viscous state. As the nozzle moves over a build platform, a structure is gradually formed, with the molten filament cooling at ambient temperature. Figure 1 illustrates a cross-section of a seal produced using this method. The notable differences in material distribution, compared to seals from conventional production, include:

1. Porosity between individual printing strands.

2. Surface topography characterized by a series of arcs rather than smoothness.

While the presence of pores (porosity) is not the primary focus of this research, as they are isolated and non-connected, the non-smooth surface topography exhibits a periodic structure at a length scale deemed relevant for sealing properties, particularly in fluid transport during the in- and outstroke. This periodic surface structure operates at a scale of a few hundred micrometers, contrasting with the significant role played by the design of the seal lip geometry, a fundamental aspect of dynamic seal design [3]. The provided source offers fundamental equations for analytical fluid flow calculations during the in- and outstroke phases.

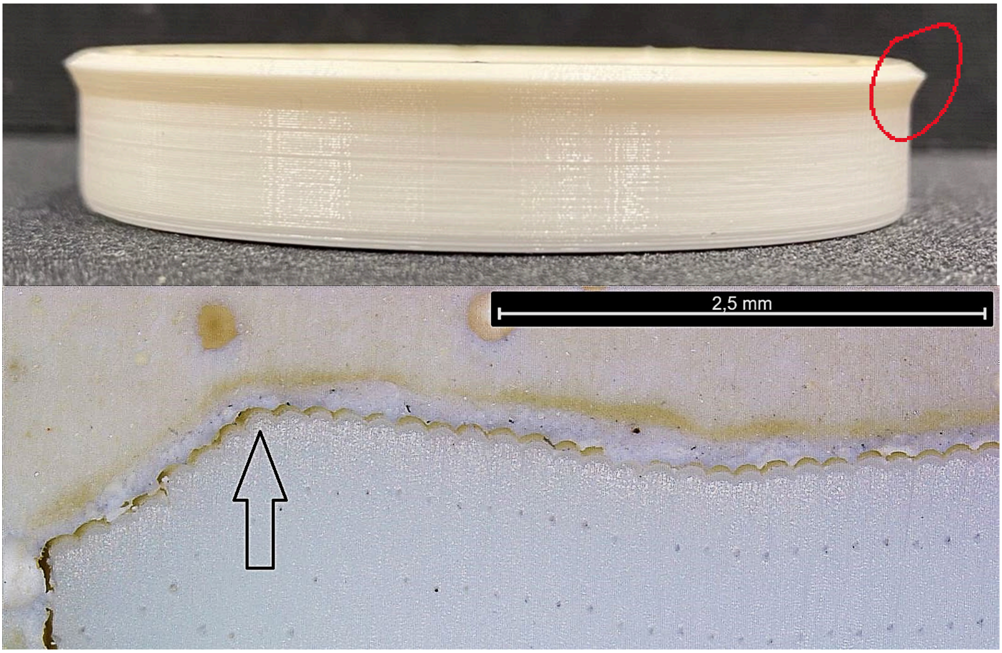

Figure 1: Surface structure and crossection of one dynamic rod seal manufactured by FFF. Arrow marks the seal lip.

A seal is typically considered tight when the reverse fluid flow through the seal is equal to or higher than the leakage flow during the outstroke. Therefore, this study focuses on assessing the capability of seal geometry to facilitate reverse fluid flow during the instroke.

2 Short state of the art

The simulation of fluid motion within a seal gap can only be analytically solved for a limited number of cases. One of the initial solutions was presented by Blok, referred to as the "inverse Theory" [4]. Generally, the flexibility of the seal introduces fluid-structure interaction (FSI). Early numerical solutions with slightly varied approaches were presented by Öngün [5] and Salant [6].

Currently, FSI simulations conducted through commercial software represent the state of the art. These software tools typically resolve the Reynolds equation for thin film flow and leverage the rotational symmetry of the system. Lankenau [7] demonstrated an instance where the Navier-Stokes equations were solved instead of the Reynolds equation for a seal application.

The sources mentioned above primarily focused on situations with microscopically smooth contact. Microscopic roughness of the seal was considered by [8]. However, the roughness examined in that study does not align with the typical surface structure produced by FFF. The FFF-generated surface structure is notably periodic, characterized by arcs arranged in rows with tip-to-tip distances of a few hundred micrometers. Studies on fluid flow simulations for the instroke motion of 3D printed seals are not yet publicly available.

3 Model definition

3.1 Physical modelling: Geometry, Parameters, Domains, Boundaries

The model system parameters are detailed in Table 1, and the geometry is illustrated in Figure 2. The intersections of geometry between the seal, rod, and groove indicate that the seal is statically energized to ensure sealing functionality.

Table 1: Parameter list for the simulation.

Variable	Name	Numerical value and Unit
v	rod velocity	$0 \ldots 2.0\ \frac{m}{s}$
$p_{ambient}$	ambient pressure	$0\ bar$
$p_{cylinder}$	cylinder pressure	$1.5\ bar$
d_{Rod}	rod diameter	$50\ mm$
η_{Oil}	dynamic oil viscosity	$0.2\ Pa \cdot s$
ρ_{Oil}	oil density	$850\ \frac{kg}{m^3}$
Δs	contact offset in seal gap	$2\ \mu m$
C_1	Neo-Hooke stiffness parameter for seal	$8\ MPa$

Two geometry cases are currently under investigation: the "reference" geometry, which represents the seal from conventional manufacturing without microscopic surface structure, and the "FFF" geometry, which is identical to the reference geometry except for the presence of surface structure at the seal lip (Figure 2). In the FFF geometry, the surface is depicted by a series of arcs. It was ensured that the outermost tip point of both geometries was identical to maintain the same macroscopic pretension in contact with the rod and groove.

The cylinder fluid pressure was set to $1.5\ bar$, and the rod was operated from standstill to a sliding velocity of $2\ m/s$ for the instroke (upward motion in Figure 2). The entire free space around the seal was filled with hydraulic oil. During instroke motion, this represents the scenario that demonstrates the maximum inward fluid transportation capability of the system. In practical terms, only the amount of fluid available on the rod surface can be transported into the cylinder.

The fluid is modeled using the Navier-Stokes equations without compressibility. Laminar flow behavior is ensured due to small Reynolds numbers. Cavitation effects are not anticipated to be dominant and are therefore neglected. The in- and outflow of the cavity where pressure is applied are subjected to Dirichlet boundary conditions. The solid seal, modeled as hyperelastic and incompressible, follows a Neo-Hook material model. Solid friction is not taken into account in the model.

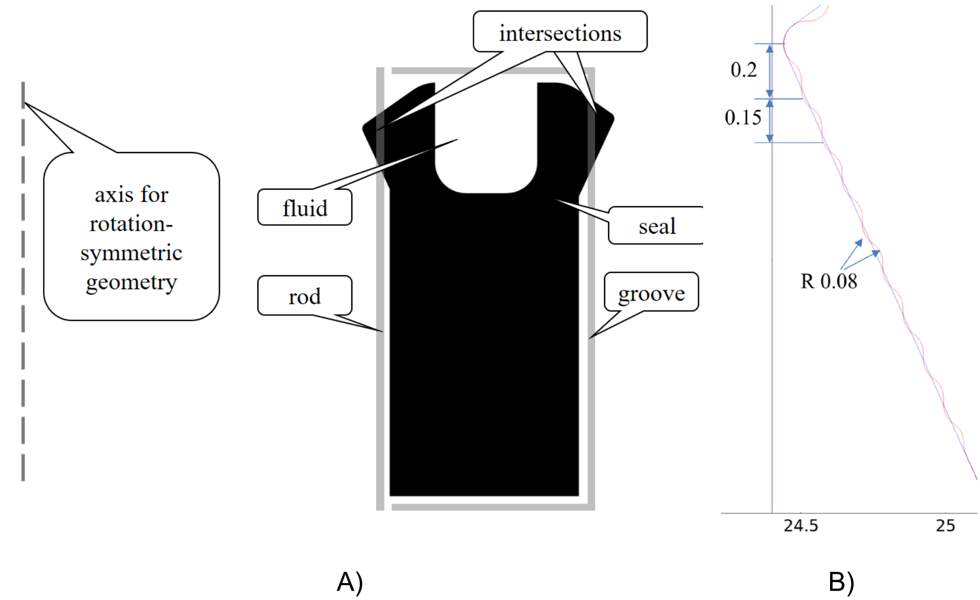

Figure 2: A) Geometry of the simulated seal in unloaded case. Position of the axis for rotation symmetry only for indication, not to scale. Upper side is cylinder side. Lower side is ambient side. B) Blue: Smooth reference surface geometry. Red: FFF surface geometry. Length in Millimetres.

The free interface between the fluid and solid is described by fully coupling the balance of forces, mass conservation, and continuity. No-slip conditions are applied to all rigid interfaces (groove, rod) or solid interfaces (seal).

3.2 Numerical solution: Solver, Elements, Steps, Contacts

The coupled FSI problem is formulated using Arbitrary Lagrangian Eulerian (ALE) coordinates. For practical modeling and numerical solution, the software tool "COMSOL Multiphysics" is utilized. The solvers employed are "MUMPS" and "PARDISO," which compute a quasistatic solution. The simulation is conducted in two steps.

- Initially, for the pretensioned seal, the fluid is not included. A "too-small" rod and a "too-big" groove are initially modeled. With the assistance of rigid body motion, the geometry is corrected, and the seal is pretensioned (see Figure 3A). The contact between the seal and rod is incorporated using a Lagrange contact condition with a permanent offset $\Delta s = 2\ \mu m$. This method, proposed by v. Wahl [9], ensures that a minimum fluid gap between the seal and rod is always maintained. The seal is modeled using linear triangle elements, with element side lengths ranging between $0.00268\ mm$ and $0.188\ mm$.

- Following the pretension buildup, the fluid is included in the simulation. The triangular fluid elements operate using quadratic shape functions, with element side lengths defined up to $0.5\ \mu m$. These elements are inserted into the gap with a smallest discretization of 13 elements for the seal gap height (see Figure 3B). In the simulation, the velocity of the rod is increased from standstill to $2\ m/s$.

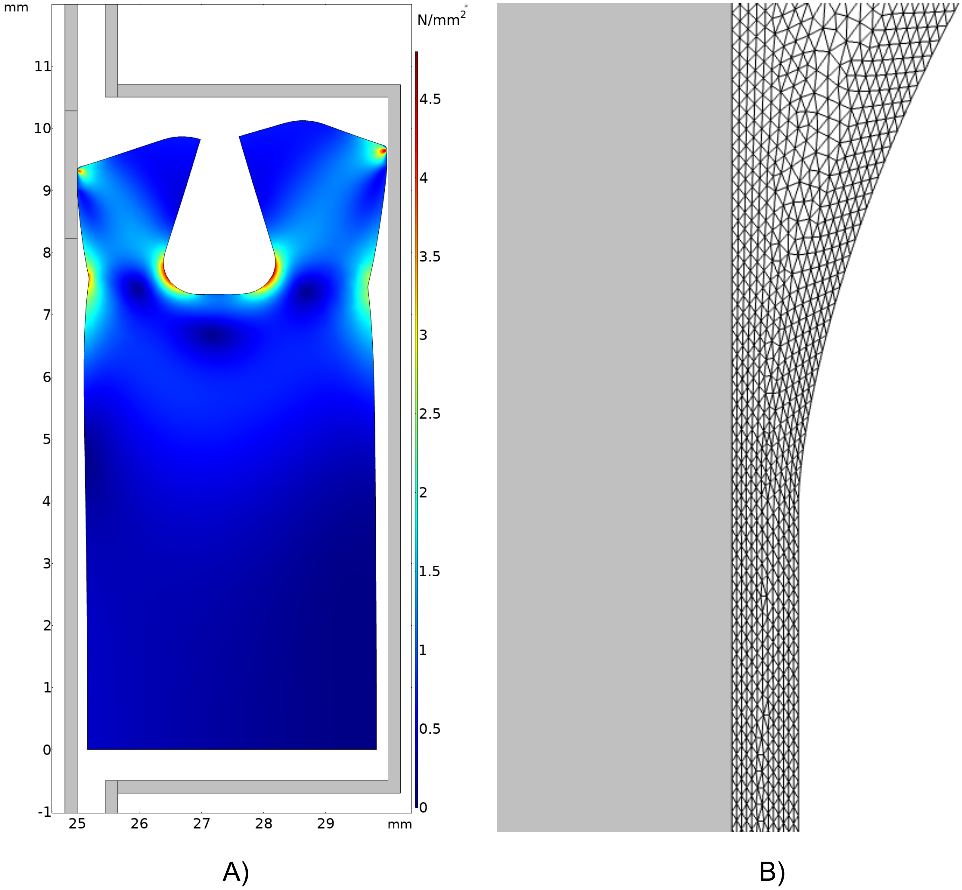

Figure 3: A) Configuration of pretensioned seal in contact with grove and rod. Color code: Von Mises equivalent stress. B) Element size for the fluid mesh in the seal gap.

The entire simulation time on a conventional workstation lasted approximately 3 hours. The analysis of results focused on fluid pressure and surface load on the seal.

4 Simulation Results and Discussion

4.1 Smooth reference geometry

Initially, the simulation focuses on the smooth reference surface geometry. Upon applying the fluid pressure in the cylinder ($1.5\ bar$), the rod undergoes acceleration for upward instroke motion. Consequently, it tends to transport hydraulic fluid from the ambient low-pressure side into the pressurized cylinder, resulting in an acting pressure difference in the cylinder. Figure 4 illustrates the increase of the elastohydrodynamic pressure peak in the converging gap. With increasing sliding velocity, the pressure peak opens the seal gap.

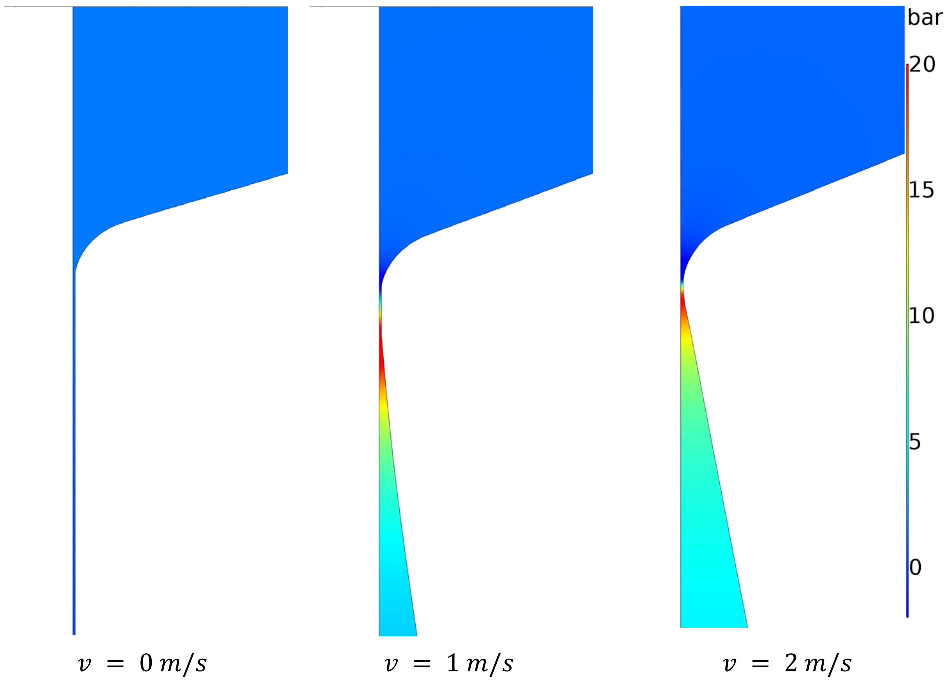

Figure 4: Fluid pressure distribution in the seal gap at different rod velocities for the smooth reference seal.

The seal lip experiences loading from two pressures: one resulting from the solid body contact with the rod and the other from the hydrodynamic fluid. Both are depicted in Figure 5. At lower sliding velocities, the solid body pressure predominates, while at higher velocities, the hydrodynamic pressure becomes dominant. It's evident that the fluid pressure acts on a significantly larger contact area compared to the contact force, resulting in a less pronounced local stress peak in the seal material. To obtain the total force on the seal lip, the stress has been surface integrated. Figure 6 illustrates how increasing rod velocity continuously converts contact force into fluid force.

For sliding velocities lower than approximately $1.86\ m/s$, a residual solid body contact is retained, with the minimum distance between the rod and seal at $\Delta s = 2\ \mu m$. However, at a sliding velocity of $1.86\ m/s$, solid body contact is lost, and only fluid forces remain. At this velocity, the minimum distance between the seal and rod increases to $2.6\ \mu m$.

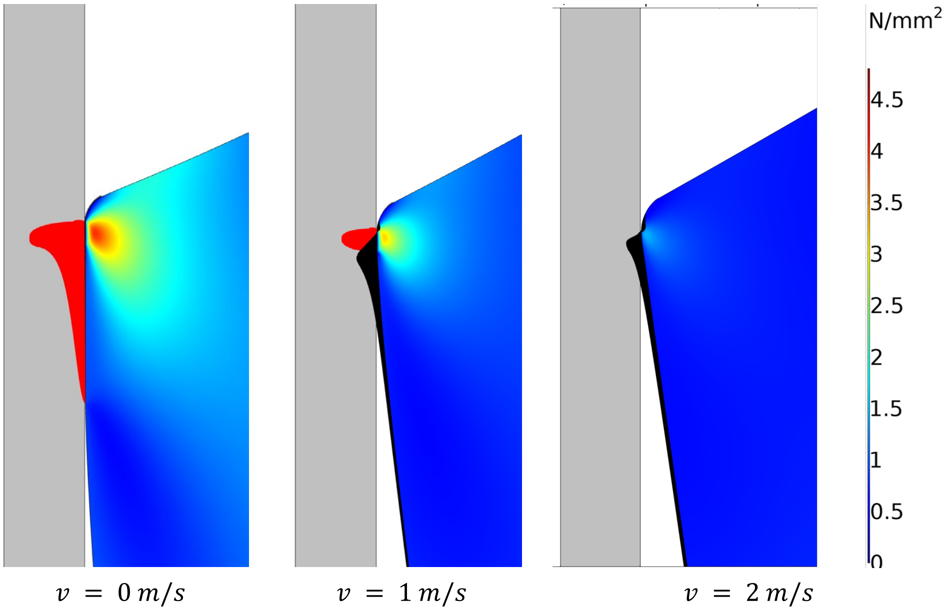

Figure 5: Contact pressure on the seal with smooth reference geometry. Red: Load from solid body contact between seal and rod. Black: Hydrodynamic load from the fluid.

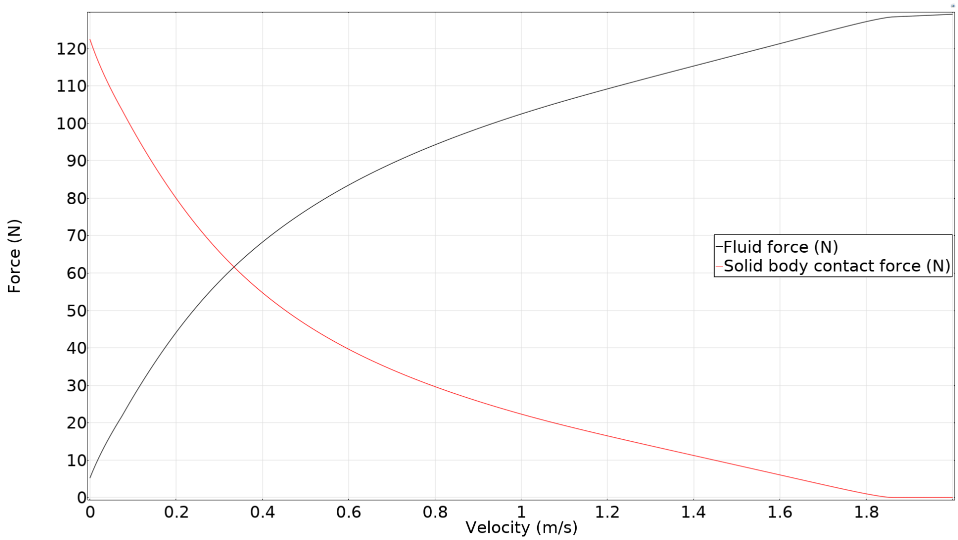

Figure 6: Velocity dependency of the load for the smooth reference geometry.

4.2 Fused Filament Fabrication (FFF) geometry

The same simulation was conducted again, this time utilizing the FFF surface geometry. Upon pressing in, three of the seal lip surface strings make contact with the rod surface. Consequently, FFF manufacturing results in a surface contact that is fragmented into several contact regions. These individual contact regions exhibit a locally nearly Hertz-like pressure distribution, as depicted in Figure 7. As the sliding velocity increases, the fluid pressure peak develops in front of the first contact between the string and rod (the lowermost in Figure 7), which the fluid must pass through. The pressure continues to grow until the contact opens. Subsequently, the pressure peak "jumps" to the next closed contact. Once again, the peak grows until the contact opens. This process of continuous opening observed in the smooth reference seal (Figure 5) is thus replaced by a stepwise opening phenomenon.

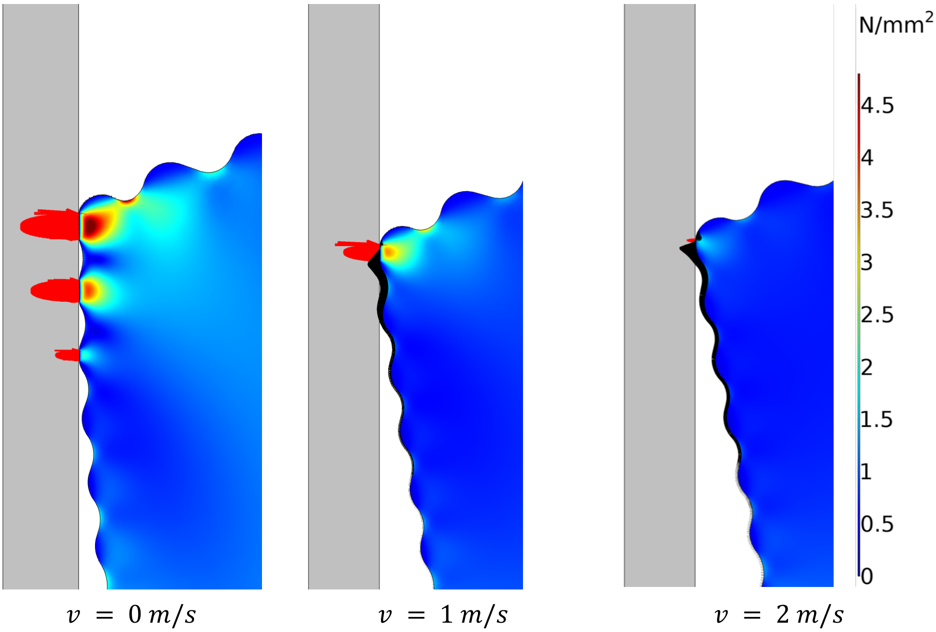

Figure 7: Contact pressure on the seal with FFF geometry. Red: Load from solid body contact between seal and rod. Black: Hydrodynamic load from the fluid.

A small region of solid body contact persists up to the maximum sliding velocity of $2\,m/s$, as illustrated in Figure 8. It becomes apparent that the transition of load from solid body contact to the fluid is no longer continuous but rather step-like. This corresponds to the locally discrete loss of contact for individual strings. This phenomenon occurs because the local converging rate at the seal gap differs between the smooth reference surface and the FFF surface generated by multiple strings.

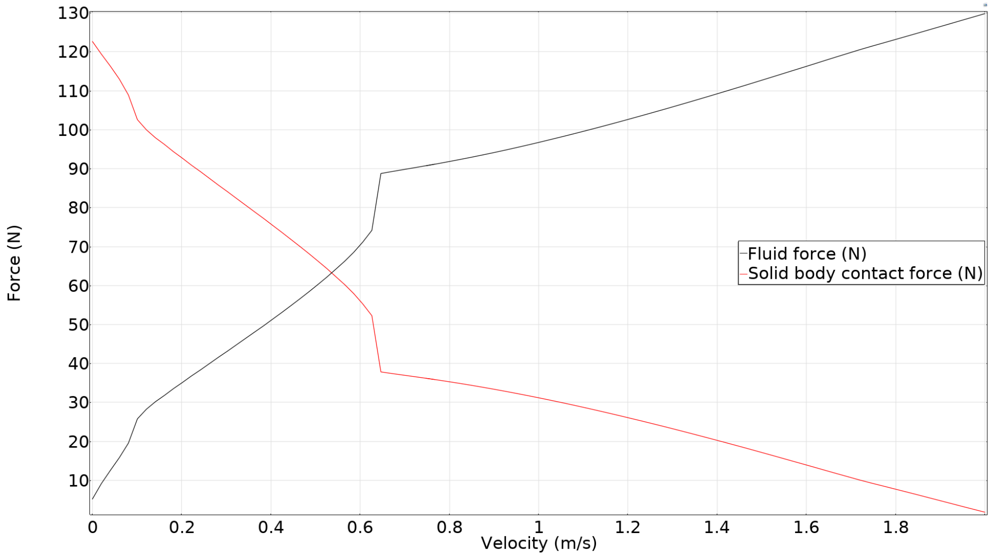

Figure 8: Velocity dependency of the load for the FFF geometry.

4.3 Consequences for fluid flow

In the fluid transport through the seal gap, drag flow predominantly occurs, which is carried with the moving rod through the seal gap against a pressure difference of $1.5\ bar$. To examine fluid transfer through the seal gap, the velocity field is integrated over the cross-section of the annular gap. Figure 9 illustrates the velocity-dependent mass flow. For velocities significantly lower than $1.86\ m/s$, the expected linear relationship between velocity and volumetric flow rate is observed. The linear behavior is nearly identical for both surface structures since the model assumes that the minimum distance between the rod and seal is identical: $2.0\ \mu m$. Smaller differences between both curves arise from the discrete loss of contact for individual strings and are not anticipated to be relevant in practical applications.

At higher sliding velocities, differences in the volumetric flow rate emerge: the smooth reference surface permits a higher volumetric flow rate compared to the FFF structure. The reason for this is that the smooth reference surface, with its continuously converging gap, loses solid body contact at significantly lower sliding velocities compared to the FFF structure. The dimples between individual strings reduce the gap's capability for continuous pressure buildup, as depicted in Figure 10. Consequently, solid body contact persists at sliding velocities higher than $1.86\ m/s$. Since at $2\ m/s$ the smallest seal gap is smaller for the FFF case ($2.0\ \mu m$) compared to the smooth reference case ($2.6\ \mu m$), the capability for fluid transport is higher in the smooth reference case.

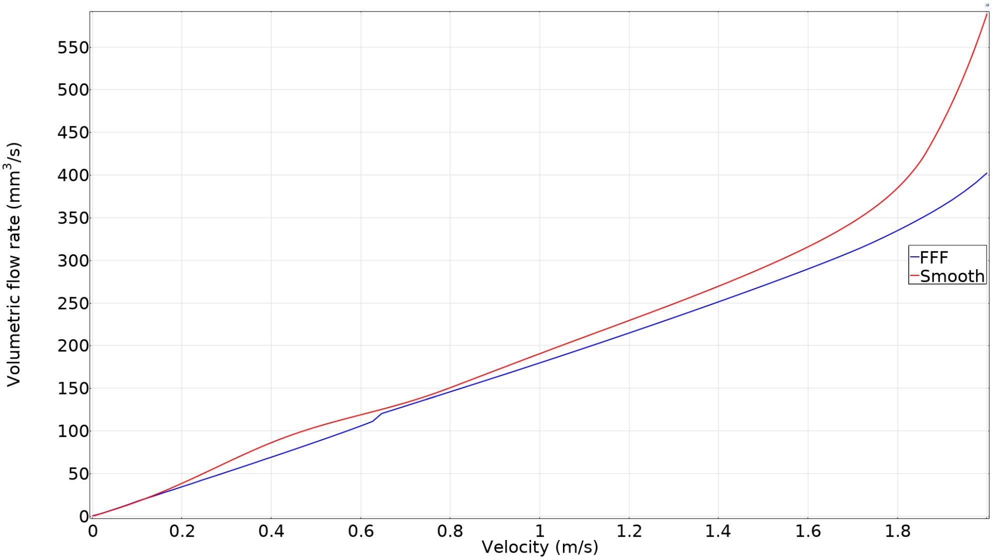

Figure 9: Maximum volumetric flow rate depending on rod velocity.

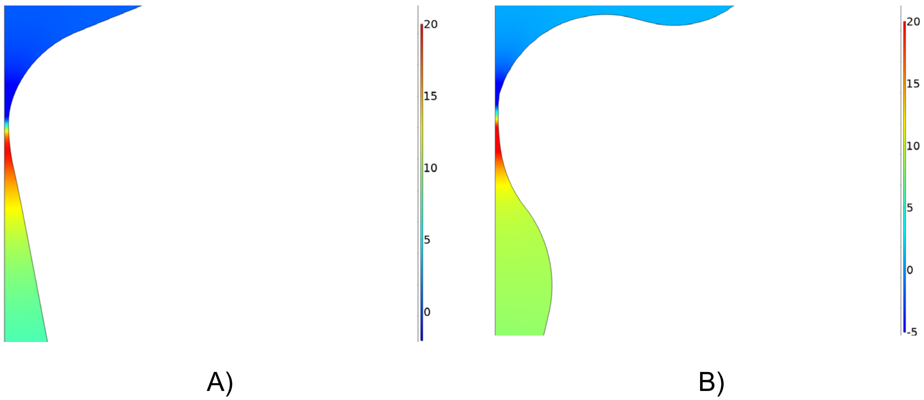

Figure 10: Comparison of fluid pressure distribution and seal gap height at $2\ m/s$. A) For smooth reference seal structure and. B) for FFF seal structure.

5 Summary and Conclusion

This numerical study employs FSI simulation to compare the fluid transport capability of dynamic rod seals during instroke back into the cylinder, against a background cylinder pressure of $1.5\ bar$. The primary transport mechanism is drag flow induced by translational motion. Two geometries are compared, differing in their local micro-structure on the seal lip: a conventional smooth reference and one inspired by the string structure of an FFF additive manufacturing process.

Key findings include:

- The FFF structure results in periodically fragmented contact with local pressure distributions similar to Hertz-type.
- Both structures exhibit very similar transport capabilities as long as they maintain solid body contact between the outermost seal tip and the rod.
- The continuously converging gap of the smooth reference surface enables the loss of solid body contact at lower velocities compared to the FFF structure. In the latter, the dimples between individual strings reduce the ability to establish a pressure peak, thereby preserving solid body contact to higher sliding velocities.
- Consequently, for higher rod velocities, the transport capability of the smooth reference seal is significantly higher compared to the FFF structure.

The model utilized in this study fully couples a fluid domain represented by the Navier-Stokes equation with a solid body domain. No free fluid surface for the ambient space was included. In practical applications, the volumetric flow during instroke is limited by the film thickness on the rod. Therefore, the computed volume flow in this study does not precisely represent the actual volumetric flow but rather provides the maximum possible transport rate that a dynamic rod seal allows.

These results suggest that seals with an FFF structure can be expected to exhibit similar transport capability compared to their smooth reference counterparts as long as they are not operated under conditions of full hydrodynamic lubrication, i.e., on the right side of the Stribeck curve.

6 Acknowledgements

This research has been partially funded by the Deutsche Forschungsgemeinschaft (DFG), project number 447009134. The authors would like to express their gratitude to the "Deutsches Institut für Kautschuktechnologie e.V." for their valuable discussions.

7 References

[1] Graf, M., Ebel, T., Lankenau, T. Ottink, K.: *Towards additively manufactured dynamic rod seals*, in: 21st International Sealing Conference Stuttgart 2022, Stuttgart, Germany, pp. 47-62, October 12-13, 2022

[2] Ebel, T., Lankenau, T., Sundermann, L., et al.: *Functional Testing of entirely additively manufactured two-component hydraulic rod seals made of TPU and NBR*, Discover Mechanical Engineering, Vol. 3, article number 4, 2024, https://doi.org/10.1007/s44245-024-00034-x

[3] Müller, H. K.; Nau, B. S.: www.fachwissen-dichtungstechnik.de *Kapitel 5 Hydraulikdichtungen*, accessed 27-02-2024

[4] Blok, H.*: Inverse problems in hydrodynamic lubrication and design directives for lubricated flexible surfaces*, Symp. Lub. and Wear, Houston, 1963

[5] Öngün, Y., André, M., Bartel, D, Deters, L.: *An axisymmetric hydrodynamicinterface element for finite-element computation of mixed lubrication in rubber seals*, Proceedings of the Institution of Mechanical Engineers, Part J: Journal of Engineering Tribology, 222, p. 471-481, 2008, https://doi.org/10.1243/13506501JET393

[6] Salant, R. F., Maser, N., Yang, B.: *Numerical Model of a Reciprocating Hydraulic Rod Seal*, Journal of Tribology 129-1, p. 91-97, 2007, https://doi.org/10.1115/1.2401222

[7] Lankenau, T., Graf, M., Ottink, K. Ebel, T.: *Simulation Strategy for Fluid-Structure Interaction of a Pre-tensioned Dynamic seal*, Proceedings in Applied Mathematics and Mechanics, Vol. 22, Issue 1, 2023, https://doi.org/10.1002/pamm.202200046

[8] Wennehorst, B., Poll, G.: *Soft micro-elastohydrodynamic lubrication and friction at rough conformal contacts*, Proceedings of the Institution of Mechanical Engineers, Part J, 231:3, pp. 302-315, https://doi.org/10.1177/1350650114558322

[9] v. Wahl*, H., Richter, T., Frei, S., Hagemeier, T.: Falling balls in viscous fluid with contact: Comparing numerical simulations with experimental data*, Physics of Fluids, 33, 03304, 2021, https://doi.org/10.1063/5.0037971

8 Authors

University of Applied Sciences Hochschule Emden/Leer

Constantiaplatz 4, 26723 Emden, Germany:

Matthias Graf, Prof. Dr.-Ing., ORCID 0000-0001-9999-7768, matthias.graf@hs-emden-leer.de

Tobias Lankenau, M. Eng., ORCID 0000-0001-8105-0082, tobias.lankenau@hs-emden-leer.de

Kathrin Ottink, Prof. Dr.-Ing., ORCID 0000-0002-5977-5316, kathrin.ottink@hs-emden-leer.de

Thomas Ebel, Dr.-Ing., ORCID 0000-0003-2099-763X, thomas.ebel@hs-emden-leer.de

https://doi.org/10.61319/IBIZNW2S

Pneumatic Seals: A Review of Experimental Measurement and Theoretical Modeling of Sealing Friction

Niklas Bauer, Katharina Schmitz

Research on friction behavior in pneumatic sealing contacts has been ongoing since the late twentieth century, predominantly through experimental characterization of friction forces for different relative velocities and operating pressures. Simulative modeling of these contacts has utilized both lumped and distributed parameter models. This paper presents an overview of the most important findings in research and discusses consensus and discrepancies among various studies in the field of reciprocating pneumatic sealing friction. It was found that there are a lot of contradictions in the experimental results especially about the influence of the relative velocity on the friction force, which can possibly be attributed to different grease film heights.

1 Introduction

The correct functioning of seals in pneumatic components is essential for safe operation. Pneumatic seals prevent the leakage of compressed air or the ingress of unwanted particles into the pneumatic system. Leakage in particular can lead to a sharp drop in the efficiency of pneumatic systems or undesired behavior. Due to the low viscosity of air, even the smallest gaps lead to high leakages. O-rings and other elastomer components or even adhesives are used for static sealing. Dynamic seals are usually reciprocating and are used as piston or rod seals in cylinders or pneumatic valves [1].

While reciprocating seals are also used in hydraulic systems, the requirements for reciprocating seals in pneumatics differ significantly. In addition to the lower operating pressures, there is a significant difference in the type of lubrication as considerably lower quantities of lubricant are used in pneumatics compared to hydraulics. In pneumatic systems, there is often an initial lubrication that is not renewed during the service life of the component. This results not only in the requirement for better dry-running behavior of pneumatic seals, but also in particular the requirement for a lower wiping effect of the seal. As a result, the geometries of pneumatic seals are less sharp-edged than hydraulic seals in the contact area and have a flatter design [2].

A typical reciprocating pneumatic sealing system consists of the actual seal, an installation groove, the counter surface and the lubricating grease in the sealing contact. During operation, there is a relative movement between the counter surface and the installation groove. Typically, the seal is made of soft material like an elastomer. The strong focus on soft seals in industrial applications is also reflected in the available literature. In recent years, far more publications have appeared that deal with the behavior of conventional soft-sealed pneumatic contacts than with alternative concepts like using air bearings [3–5], air-lubricated seals [6] or ultrasonic friction reduction [7]. Therefore, these special concepts are not discussed in this publication.

Studies on the friction behavior of pneumatic sealing contacts have been conducted since the end of the twentieth century. A large part of this work is concerned with the purely experimental characterization and measurement of friction forces. Usually, the main focus of the research lies on influence of the relative velocity and the operating pressure and less frequently also on the manufacturing tolerances or the materials. There are also some studies that deal with the simulative modeling of pneumatic sealing contacts. Both distributed and concentrated parametric simulation models have been used for that.

The aim of this paper is to give an overview of the state of research of experiments and theory of the friction in reciprocating pneumatic sealing contacts. For that, the most important results of selected literature sources from the past 30 years are briefly summarized compared. Both consistent conclusions and contradictions between the results of different authors are discussed.

2 Experimental characterization of pneumatic sealing contacts

The aim of most experimental investigations is to measure the friction force in sealing contacts. The sealing systems under consideration are usually cylinders or spool valves. Although the two components fulfil different purposes and consist of different materials, the sealing systems are nevertheless comparable in terms of operating pressures and ambient media.

A common comparison criterion for tribological systems is the coefficient of friction (COF) μ, i.e. the ratio of friction force to normal force. However, the COF is not provided in most publications on pneumatic seals, as the normal force in the sealing contact is usually unknown. The normal force in most tests is caused by compression of the sealing material due to an interference fit and/or the applied operating pressures. Since therefore the COF cannot be calculated in most publications, it cannot be used as a criterion for comparing the literature sources. As the pneumatic systems differ in type and also in size and number of seals, a comparison of the measured values for the friction forces also appears to be difficult to compare. Instead, the focus in this section is placed on the qualitative influence of individual parameters such as applied pressure difference, lubricating grease and velocity. The qualitative parameter influences measured in the literature are compared below.

2.1 Influence of pressure

Many sources do not clearly state which pressures are acting on the sides of the seal. Instead, usually only the operating pressure of the pneumatic system is given, so that an exact quantitative comparison is often not possible.

When measuring the friction force of the piston seal of a pneumatic cylinder, Qian et al [8] observed that for lip seals mounted in pairs on the piston, only the total pressure in both chambers, but not the differential pressure between the chambers, influences the friction force of the seal pair. However, if O-rings are used as piston seals instead of lip seals, the friction depends on both the total pressure and the differential pressure.

Azzi et al [9] measured the friction of piston and rod seals of pneumatic cylinders at different velocities and pressures for an O-ring, a U-ring and an X-ring piston seal. For all three seals, the friction force increases with increasing operating pressure. However, the friction force of the U-ring seal increases more steeply than that of the other two seals investigated. Whether this behavior can be attributed to the investigated geometries cannot be concluded from the investigations, as all three investigated geometries were manufactured from different materials.

The investigations by Papatheodorou [10] also show an increase in friction force with increasing operating pressure. The experiments by Tadic et al [11] investigated how the friction force changes when the chamber on the piston rod side is pressurized with ambient pressure while there is a pressure below ambient in the chamber on the piston side. Likewise, Belforte et al [12] found that an increased pressure difference at the seal also leads to an increased friction force.

Most of the sources mentioned thus show that the seal friction increases with increasing differential pressure across the seal.

2.2 Grease

Papatheodorou [10] determined the friction force of selected rod and piston seals for 15 different greases in new condition and after an unspecified “short endurance test”. The friction force for certain operating points and sealing materials differed between the grease with the highest and the lowest friction force by more than a factor two.

Further studies on the influence of the lubricating grease were carried out by Heipl [13], who selected three different greases with different thickeners and base oils. The friction when using the greases was compared for an O-ring seal and a lip seal as well as two accelerations. When using the softer grease, the friction force for an acceleration of $40\ \mu\mathrm{m/s^2}$ was up to $200\ \%$ higher than when using the other greases. For a higher acceleration of $100\ \mathrm{mm/s^2}$ and higher velocities, the friction force of the harder greases remained largely constant. The friction force of the softer grease, on the other hand, dropped significantly at high accelerations and velocities and approached the friction force of the other greases. At higher acceleration, however, the friction force for the lip ring differed significantly for all three greases tested. In particular, the two harder greases showed an increase in friction force with increasing velocity by a factor of more than 1.5. The friction force when using the softer grease was up to a factor 3 below the friction force of the other two greases from a velocity of around $30\ \mathrm{mm/}s$ and higher.

The results discussed by Heipl [13] thus show that the friction that occurs when using a lubricating grease depends massively on acceleration, velocity and seal geometry. The influence of different greases on the friction force can therefore only be compared with precise knowledge of all relevant boundary conditions. In addition, the comparison of greases is also hindered by the fact that it was not investigated whether and under which operating conditions how much lubricant was removed. Therefore, it cannot be concluded with absolute certainty whether the observed phenomena are solely related to the behavior of the lubricant in sealing contact. It is also possible that the lubricant film height was set to different levels in different test arrangements. A comprehensive comparison of the operating conditions would also have to include the lubricant film height.

2.3 Grease film height

Overall, there are only a few publications that systematically take into account the influence of film height on friction force in pneumatic sealing contacts. This is probably due to the fact that the film height can only be measured or specifically adjusted with great effort. One of the few publications that deals with the measurement of film height is by Pichon et al [14]. They determined the lubricating film height for an O-ring of a pneumatic valve in its initial state and after friction force measurements had been carried out. To determine the film height, they weighed the running surface with a precision balance. For one test, the lubricating film height was measured after each stroke. Already within the first five strokes, there was a significant decrease in the lubricant film height from about $1.2\ \mu m$ to approx.$0.2\ \mu m$.

In addition, Pichon et al [14] found in their experiments that increasing the initial lubricant film height at the start of the measurements lead to a higher resulting film height after the measurements. When increasing the initial film height beyond values of $0.6\ \mu m$ and higher, only negligible changes in the resulting film height occured after the friction force measurements. With sufficiently high initial lubrication, the resulting lubricating film was up to $0.4\ \mu m$ for tests without pressure load on the seal. In tests with a pressure load of $0.8\ MPa$ on the seal, film heights of up to $0.2\ \mu m$ were measured.

When comparing the friction force for the unlubricated and lubricated condition, Pichon et al [14] found that the friction force in the unlubricated condition is up to a factor of 10 higher than in the lubricated condition. These results are consistent with the investigations by Heipl [13], in which the friction force can also be reduced by a factor of 5 to 20 by lubrication.

Overall, a strong influence of the lubricant film height on the friction force can therefore be observed. With decreasing lubricant film height above a certain limit value, the measured friction force drops only slightly. There is no source that specifies both the roughness of the contact partners and the measured film heights.

2.4 Velocity

In contrast to the influence of pressure already discussed, where the experimental observations agree that an increase in the applied pressure causes an increase in the friction force, there are qualitatively very different measurement results for the influence of velocity.

For example, Raparelli et al [15] observed that friction increases with velocity. In a simple tribometer test, the coefficient of friction was first examined for three different lubrication conditions (dry, boundary lubrication and fluid lubrication) for velocities in a range of 20 to $250\,\mathrm{mm}/s$. A degressive increase in the coefficient of friction with velocity was found for all three lubrication states. Nevertheless, these tests clearly show that there is an increase in friction force with increasing velocity for the NBR samples tested. This was also determined by Papatheodorou [10] for 14 of the 15 lubricating greases investigated. There, the friction force also increased with the velocity in the investigated velocity range between 5 and $100\,\mathrm{mm}/s$. For one of the greases tested, however, the friction force decreased with increasing velocity. These two observations were made both in the new state and after the aforementioned unspecified “short endurance test”. The grease for which the friction force decreased with increasing velocity had the lowest base oil viscosity.

This contrasts with the results of Pichon et al [14]. They only considered the two velocities $10\,\mathrm{mm}/s$ and $100\,\mathrm{mm}/s$, but found no significant influence of velocity on the friction force.

Another deviating observation comes from Tadic et al [11], who found that the friction force initially increases with an increase in velocity from 0 to $9.3\,\mathrm{mm}/s$. For higher velocities up to the investigated maximum velocity of $236\,\mathrm{mm}/s$, however, the friction force decreases continuously.

In addition, the work of Belforte et al [12] should be mentioned, in whose investigations classical Stribeck behavior was observed. An initial decrease in friction for velocities up to $100\,\mathrm{mm}/s$ is followed by an increase in friction, which persists up to the maximum velocity of $600\,\mathrm{mm}/s$ investigated. This corresponds qualitatively with the results of Nepp and Kröger [16], who also determined Stribeck behavior for two rod seals made of FKM or NBR with a transition from mixed to fluid friction (lift-off velocity) at about $10\,\mathrm{mm}/s$. The investigations by Heipl [13] also show Stribeck behavior with a degressive increase in friction after the lift-off speed. The lift-off was typically at velocities of around $5\,\mathrm{mm}/s$ in the unpressurized state. For one of the seal geometries examined, the lift-off velocity in the unpressurized state was up to $30\,\mathrm{mm}/s$. At an operating pressure of $6\,\mathrm{bar}$, the lift-off shifted to higher velocities. Up to the maximum investigated velocity of $100\,\mathrm{mm}/s$, no clear lift-off could be identified for one of the seals investigated. The lift-off velocity therefore depends heavily on the seal geometry used and the operating pressure present. The gradient of the friction after lift-off also depends heavily on the operating pressure and seal geometry. The experimental results from Wangenheim [17] also show Stribeck behavior for the friction force.

Consequently, it can be stated that no clear tendency regarding the influence of velocity on friction can be identified from the experimental observations. Assuming that all experiments were carried out and recorded correctly, it can therefore be assumed that complex interactions between the parameters of material, geometry or lubricant are responsible for the velocity dependence of the friction force, which cannot be clearly classified according to the current state of the art.

Further work by Belforte et al [18] provides an indication of a relevant influencing factor on the velocity dependency. In the studies mentioned, it was observed that the friction force depends strongly on whether lubricated or dry conditions are present. On the one hand, this affects the amount of friction force, which is reduced by up to a quarter, and on the other hand the velocity dependency. The friction forces of the investigated seals in dry running increased by more than $100\ \%$ with an increase in velocity from 0 to $100\ \mathrm{mm/s}$, whereas the increase in friction force at the same velocity range for seals with lubrication is less than $20\ \%$.

The results presented in [18] therefore suggest that the influence of the velocity is not only quantitatively but also qualitatively significantly influenced by the lubrication condition. A comparison of the various literature data is therefore not very meaningful without precise knowledge of the lubrication condition. However, very few sources provide precise information on the lubricant used. In addition, most sources did not record the thickness of the lubricant film applied. Furthermore, no information was given as to how it was ensured that an even and comparable lubricant film was applied for all tests. The comparability of different test series and thus of different sources, especially from different authors, is therefore severely limited. However, the sparse documentation of the lubrication conditions provides a further explanation for the different velocity dependence of the friction force. If different lubrication conditions were present in different publications, this provides an explanation for the deviations in the observed behavior.

2.5 Other investigations

For the sake of completeness, studies investigating other effects than the those discussed in the sections above shall also be mentioned here. For reasons of space, however, they will not be discussed in detail here. These other studies include the investigation of geometric tolerances [19], the development of new sealing geometries [12, 18, 20, 21] and the measurement of the contact pressure distribution in the sealing contact by a film sensor [22–24] or a force sensor [25]. Investigations of causes of failure were conducted by Chen et al [26].

2.6 Conclusion on the experimental characterization

From the comparison of the studies presented, it is clear that there is not yet a comprehensive understanding of the mechanisms of pneumatic seal friction. There is a broad consensus that the friction force increases when the pressure in the sealing contact is increased, no matter whether the pressure increase is caused by higher pressures or tighter fits. In contrast, no clear statement can be derived from the experiments conducted regarding the influence of velocity. However, the investigations carried out by Belforte et al [18] suggest that the influence of velocity depends massively on the lubricant film height.

The influence of the surface structure of the seal and counter surface has not yet been systematically investigated. Furthermore, although the friction forces were measured with different lubricants, the lubricants were not comprehensively characterized in terms of their material properties. Consequently, it is not possible to deduce from the results which lubricant properties influence the friction behavior of pneumatic sealing contacts.

The research results presented show that most investigations carried out in the past have so far only dealt with the measurement of the friction force in steady states. A characterization of transient phenomena was presented in Bauer et al [27] and for the measurement of breakaway friction, as for example by Pham and Twiefel [7].

3 Theoretical modelling of pneumatic sealing contacts

After the experimental studies on pneumatic sealing friction were discussed in the previous section, a brief overview of all the methods used to date for modeling pneumatic sealing contacts is provided here. The section is divided into the groups of lumped and distributed parameter simulation models.

3.1 Lumped parameter models

All simulation and calculation models that describe the friction in pneumatic components exclusively with the aid of algebraic equations and ordinary differential equations are to be subsumed under lumped parameter modeling. These models offer the advantage of a comparatively short calculation time, but often use empirical parameters that cannot be determined directly from geometric and material properties. The calculation of friction is often only one part of a larger simulation model that describes an entire component or system, for example. It is possible to model the friction of each individual sealing contact separately, as well as to describe the combined friction force of several friction contacts of a component simultaneously.

One of the most frequently used models in literature is the LuGre model by Canudas de Wit et al [28] and Olsson [29], which models friction using elastic bristles in order to determine the friction force not only in the steady state but also before the start of steady-state sliding (“presliding displacement”). Accordingly, the friction force is defined as a function of the deformation of the bristles and the relative velocity. The parameters of the model cannot be determined directly from geometry, material or lubricant properties, but are usually fitted with the help of measured friction forces. The parameterization of the LuGre model for a pneumatic cylinder was investigated by Carneiro and de Almeida [30], among others, who compared two methods for determining the static parameters for the friction force of a pneumatic cylinder.

However, due to the abstracted modelling of the contact by bristles, the LuGre model is not or only to a very limited extent possible to optimize or redesign sealing systems. As the model is more descriptive than explanatory, it is suitable for describing the behavior of existing friction contacts as part of a larger system model. For example, a modified version of the LuGre model by Valdiero et al [31] was used to model a pneumatic servo cylinder.

Another example of the use of a lumped parameter model for a pneumatic servo cylinder comes from Soleymani et al [32]. They used a modified version of the generalized Maxwell slip model to model the friction of a pneumatic servo cylinder. They used this modeling for the position control of the servo cylinder.

Mazza and Belforte [33] took a different approach to the friction models described so far. They developed a friction model for pneumatic lip seals that is not based on the abstracted description of the contact, but instead describes an abstracted form of the macroscopic geometry. For this purpose, the sealing lip is modeled as a rigid body supported by a torsion spring, which is pressed onto the seal mating surface by the applied pneumatic pressure. In this case, the friction in the contact is modeled by a constant coefficient of friction. Unlike the friction models presented so far, this model makes it possible in principle to estimate the friction force of modified or newly developed lip seals or to investigate the influence of the operating pressure.

In contrast to the aforementioned lumped parameter approaches, the approach used by Wangenheim [17] to model pneumatic sealing friction is based on the surface topography. The approach is based on the hysteresis friction model proposed by Lindner [34], where the coefficient of friction is calculated using a spring damper element which slides over a line scan of the rigid counter surface. With his calculations, Wangenheim was able to show that less than 1 % of the dissipated energy dissipated due to friction in a pneumatic rod seal goes into the seal itself, which means that the temperature change of the seal can be neglected for friction modeling of typical pneumatic sealing systems. The temperature calculations were validated using a thermal camera. Furthermore, since his model considers the surface topography, he was able to predict and optimize the friction behavior of a pneumatic sealing contact by changing the surface topography.

3.2 Distributed parameter models

In contrast to the lumped-parameter models considered in the previous section, distributed parameter models are based on partial differential equations. As a result, these models can also take into account input parameters such as the geometries of the seal and counter surface. A disadvantage of these models is that their solution is significantly more time-consuming and computationally expensive than the solution of lumped parameter systems.

For pneumatic sealing contacts, by far the most common approach to distributed parameter modeling is structural simulation using commercial finite element programs (FEM programs) such as Abaqus/Standard or Ansys Mechanical.

To calculate friction, contact pressure and/or wear, a model of the seal geometry has to be created first. Hyperelastic material models such as the Mooney-Rivlin model are often used as material models, for example in the work of Debler [35], Belforte et al [12, 18] or Zhang et al [36]. Following the meshing and parameterization of the material model, various loads and boundary conditions are imposed on the model, such as pressures or the installation situation.

A decisive point in the modeling of friction is the choice of contact model. In addition to the Coulomb friction model, many commercial FEM programs also offer the option of implementing their own friction models. Nevertheless, the Coulomb friction model has been used most frequently in the past in distributed parametric modelling due to its simple parameterization. For friction contacts in pneumatic sealing systems, values of 0.3 up to 0.6 for dry contacts and values of 0.05 up to 0.2 for lubricated contacts were usually selected [12, 18, 21–24].

In addition to selecting a constant coefficient of friction, it is also possible to specify a function for the coefficient of friction that defines it e.g. as a function of the velocity. For example, Raparelli et al [37] used a velocity dependent coefficient of friction determined experimentally on a tribometer. They determined the coefficient of friction for three lubrication conditions, which they described as dry, boundary lubrication and fluid friction. The values of the coefficient increased degressively with velocity in the considered velocity range of 20 to $250\ \mathrm{mm/s}$, in the dry state from 0.55 to 0.75 and in boundary lubrication from 0.2 up to 0.35. For fluid lubrication, the coefficient of friction was below 0.05 for all speeds. Raparelli et al carried out simulations with all three lubrication conditions. He showed that the test results best matched the simulation results with boundary lubrication.

Regardless of the material or friction model, distributed parameter simulations can be used for various applications. Since the modelling is dependent on material and geometry parameters, existing geometries can be analyzed and optimized. For example, Calvert et al [20] used an FEM model with a constant coefficient of friction to calculate the force required to move an X-ring seal in a spool valve. The analysis of the calculated deformation of the seal predicted a loss of the sealing effect in certain operating conditions. This assumption was confirmed experimentally. Based on the simulation results, the seal cross-section was optimized so that no more leaks occurred in the simulation. Subsequent experiments with the optimized geometry confirmed that the problem had been solved.

Further optimizations of the geometry of the seal and seal seat were carried out by Conte et al [12, 18, 21–23]. In these studies, the simulation model was not validated using the calculated friction forces but using the contact pressure distribution. There was good agreement between the calculated and measured contact pressure distribution. The aim of the optimizations was to ensure the highest possible maximum contact pressure with a simultaneously low normal force in order to achieve the highest possible sealing effect with a low friction force.

In addition to geometry optimization, distributed parameter simulations can also be used to investigate the influence of assembly and manufacturing tolerances. These investigations were carried out by Belforte et al [18] for the diameter of the counter surface of a valve seal. Lin et al [19] investigated at the influence of straightness and roundness of the running surface on the friction force of the piston seal of a pneumatic cylinder.

Debler [35] dealt with the calculation of wear for a pneumatic lip seal, the wear of which he calculated mathematically using an FEM model. The local amount of wear was assumed to be proportional to the local pressure. The local pressure was calculated as the weighted sum of the pressures for different load cases. A comparison of measurement and simulation shows that the measured wear profile could be predicted very well using the FEM-based wear model.

3.3 Conclusion on computational modelling

In summary, all of the presented lumped parameter models use strong abstractions. The models can be used well for descriptive modeling or control of systems, as shown for example by Valdiero et al [31] or Soleymani et al [32]. However, it is not possible to increase the understanding of the mechanisms of pneumatic sealing contacts with these models, as measured data of the friction force or empirical knowledge must be used for parameterization.

In order to gain a better understanding of the processes in the modelled sealing contact and to make optimizations, distributed parameter models are more suitable than lumped parameter models. The potential for the analysis and optimization of sealing contacts was shown, for example, in the investigations by Calvert et al [20]. Using an FEM calculation, they succeeded in correctly predicting the leakage of a specific sealing ring geometry and developing an optimized concept, the performance of which they subsequently confirmed experimentally.

Most optimizations based on distributed parameter models are mainly based on a consideration of stresses in the material or the contact pressure. Friction in the contact, which is determined, for example, by the material pairing, the surface structure and the properties and film height of the lubricant, has not yet been taken into account by the optimization. What all the sources mentioned have in common is that no detailed modeling of the coefficient of friction has been carried out. Instead, the friction was modeled using Coulomb friction with a constant coefficient of friction or with an experimentally measured characteristic diagram. Thus, no understanding of the processes in the actual contact zone can be gained. Consequently, the theoretical potential of distribution parametric simulations to evaluate and optimize different designs before carrying out experiments cannot be fully exploited.

4 Conclusion and outlook

The research into the state of the art shows that a large number of experimental studies have been carried out in recent decades. However, the results of the experimental investigations reveal some significantly different outcomes, even for basic qualitative relations such as the velocity dependence of friction. These differences can presumably be explained by the fact that many publications only provide incomplete information on the boundary conditions of the tests presented, such as material behavior, the nature of the surfaces and, in particular, the type and quantity of lubricant used. Consequently, the results are difficult to compare with each other and it is difficult to derive general findings or gain an understanding of the mechanisms in pneumatic sealing contacts. Accordingly, there is little literature on the theoretical modeling of friction in pneumatic sealing contacts. Most of the literature sources listed in these publications are more focused on empirically based description than on increasing the understanding of the mechanisms in pneumatic sealing contacts.

According to the presented literature review, the next steps for research on pneumatic sealing friction should focus on the grease. Both the relevant properties of the grease as well as the resulting grease film heights during operation need to be better understood before further research into other influencing factors is conducted. With precise experimental investigation and theoretical modelling, new system models and design paradigms for pneumatic sealing contacts to reduce friction and increase lifetime can be derived.

5 References

[1] Schmitz K. Fluidtechnik - Systeme und Komponenten. Umdruck zur Vorlesung. Reihe Fluidtechnik. Düren: Shaker; 2022

[2] Flitney RK. Seals and sealing handbook. 5th ed. Amsterdam, Heidelberg: Butterworth-Heinemann; 2008

[3] Kim DS, Bae SK, Choi BO. Experiments and Characteristic Analysis of a Sealless Pneumatic Cylinder. KEM 2006; 326-328: 1279–1282. doi:10.4028/www.scientific.net/KEM.326-328.1279

[4] Yao YS, Zhang KR, Yu Z, et al. Research on a New Frictionless Air Cylinder. AMR 2011; 308-310: 859–863. doi:10.4028/www.scientific.net/AMR.308-310.859

[5] Belforte G, Raparelli T, Mazza L, et al. Analysis, Design, and Comparison of Different Types of Pistons for Sealless Pneumatic Cylinders and Valves. Tribology Transactions 2005; 48: 377–388. doi:10.1080/05698190591008577

[6] Belforte G, Mazza L, Visconte C. Design methodology for an air-lubricated seal. Tribology International 2014; 75: 104–110. doi:10.1016/j.triboint.2014.03.017

[7] Pham TM, Twiefel J. Ultrasonic Friction Reduction in Elastomer – Metal Contacts and Application to Pneumatic Actuators. Proceedings of the 2015 Icu International Congress on Ultrasonics 2015; 70: 55–58. doi:10.1016/j.phpro.2015.08.040

[8] Qian P, Pu C, Liu L, et al. Development of a new high-precision friction test platform and experimental study of friction characteristics for pneumatic cylinders. Meas. Sci. Technol. 2022; 33: 65001. doi:10.1088/1361-6501/ac51a6

[9] Azzi A, Maoui A, Fatu A, et al. Experimental study of friction in pneumatic seals. Tribology International 2019; 135: 432–443. doi:10.1016/j.triboint.2019.03.018

[10] Papatheodorou T. Einfluss des Schmierstoffs auf das Betriebsverhalten (Reibung, Leckage und Verschleiß) von Pneumatikdichtungen. Proceedings of the 14th International Sealing Conference, Stuttgart 2006: 373–387

[11] Tadic B, Zivkovic M, Simunovic G, et al. The Influence of Vacuum Level on the Friction Force Acting on the Pneumatic Cylinder Sealing Ring. Teh. Vjesn. 2019; 26: 970–976. doi:10.17559/TV-20180227172122

[12] Belforte G, Manuello A, Mazza L. Optimization of the Cross Section of an Elastomeric Seal for Pneumatic Cylinders. Journal of Tribology 2006; 128: 406–413. doi:10.1115/1.2162915

[13] Heipl OP. Experimentelle und numerische Modellbildung zur Bestimmung der Reibkraft translatorischer Dichtungen [Zugl.: Aachen, Techn. Hochsch., Diss., 2013]. Bd. 72. Reihe Fluidtechnik D. Aachen: Shaker; 2013

[14] PICHON V, BOUCHAYER P, GODET M. Lubricating of O-Ring seals in pneumatic applications with ultra thin grease films. Thin Films in Tribology 1993; 25: 593–610. doi:10.1016/S0167-8922(08)70413-9

[15] Raparelli T, Bertetto AM, Mazza L. Experimental Study of Pneumatic Seal Extrusion. Tribology Transactions 1997; 40: 715–719. doi:10.1080/10402009708983713

[16] Nepp R, Kröger M. Einfluss von Losbrechkräften auf das dynamische Verhalten von O-Ring-Dichtungen. Proc. Appl. Math. Mech. 2010; 10: 751–752. doi:10.1002/pamm.201010355

[17] Wangenheim M. Untersuchungen zu Reibmechanismen an Pneumatikdichtungen. Hannover : Gottfried Wilhelm Leibniz Universität Hannover; 2012. doi:10.15488/11850

[18] Belforte G, Conte M, Manuello A, et al. Performance and Behavior of Seals for Pneumatic Spool Valves. Tribology Transactions 2011; 54: 237–246. doi:10.1080/10402004.2010.538488

[19] Lin A, Wu J, Li H, et al. Effect of Geometric Error on Friction Behavior of Cylinder Seals. Polymers 2021; 13. doi:10.3390/polym13193438

[20] Calvert C, Tirovic M, Stolarski T. Design and development of an elastomer-based pneumatic seal using finite element analysis. Proceedings of the Institution of Mechanical Engineers, Part J: Journal of Engineering Tribology 2002; 216: 127–138. doi:10.1243/1350650021543951

[21] Belforte G, Conte M, Mazza L. Low friction multi-lobed seal for pneumatic actuators. Wear 2014; 320: 7–15. doi:10.1016/j.wear.2014.08.008

[22] Conte M, Manuello A, Mazza L, et al. Measurement of Contact Pressure in Pneumatic Actuator Seals. International Conference on Tribology 20-22 September 2006, Parma, Italy 2006

[23] Conte M, Belforte G, Mazza L. Study on pneumatic cylinder piston seals behaviour (2008). Online: https://www.researchgate.net/publication/262342622_Study_on_pneumatic_cylinder_piston_seals_behaviour; accessed: Februar 6, 2023

[24] Belforte G, Conte M, Bertetto AM, et al. Experimental and numerical evaluation of contact pressure in pneumatic seals. Tribology International 2009; 42: 169–175. doi:10.1016/j.triboint.2008.04.010

[25] Belforte G, Conte M, Manuello Bertetto A, et al. Indirect contact pressure evaluation on pneumatic rod seals. Tribology International 2018; 118: 240–245. doi:10.1016/j.triboint.2017.10.002

[26] Chen J, Zio E, Li J, et al. Accelerated Life Test for Reliability Evaluation of Pneumatic Cylinders. IEEE Access 2018; 6: 75062–75075. doi:10.1109/ACCESS.2018.2882767

[27] Bauer N, Bekgulyan S, Feldmeth S, Bauer F, Schmitz K. Experimental determination and EHL simulation of transient friction of pneumatic seals in spool valves. In: Proceedings of the 21st International Sealing Conference (ISC), Stuttgart, Germany; 2022
[28] Canudas de Wit C, Olsson H, Astrom KJ, et al. A new model for control of systems with friction. IEEE Trans. Automat. Contr. 1995; 40: 419–425. doi:10.1109/9.376053
[29] Olsson H. Control Systems with Friction. Institutionen för reglerteknik, Lunds tekniska högskola. Department of Automatic Control, Lund Inst. of Technology; 1996
[30] Carneiro JF, Almeida FG de. LuGre Friction Model: Application to a Pneumatic Actuated System. Controlo'2014 - Proceedings of the 11th Portuguese Conference on Automatic Control 2015; 321: 459–468. doi:10.1007/978-3-319-10380-8_44
[31] Valdiero AC, Ritter CS, Rios CF, et al. Nonlinear Mathematical Modeling in Pneumatic Servo Position Applications. Math. Probl. Eng. 2011; 2011: 1–16. doi:10.1155/2011/472903
[32] Soleymani F, Rezaei SM, Sharifi S, et al. Position control of a servo-pneumatic actuator using generalized Maxwell-Slip friction model. 2016 4th Rsi International Conference on Robotics and Mechatronics (Icrom) 2016: 246–251. doi:10.1109/ICRoM.2016.7886854
[33] Mazza L, Belforte G. Analytical/Experimental Study of the Contribution of Individual Seals to Friction Force in Pneumatic Actuators. Journal of Tribology 2017; 139. doi:10.1115/1.4033365
[34] Lindner M. Experimentelle und theoretische Untersuchungen zur Gummireibung an Profilklötzen und Dichtungen. Hannover : Gottfried Wilhelm Leibniz Universität Hannover; 2006. doi:10.15488/6740
[35] Debler C. Bestimmung und Vorhersage des Verschleißes für die Auslegung von Dichtungen. Dissertation; 2005
[36] Zhang RH, Shi JX, Hu JW. Finite Element Mechanical Analysis of Cushion Seals in High Speed Pneumatic Cylinder. AMM 2013; 275-277: 44–50. doi:10.4028/www.scientific.net/AMM.275-277.44
[37] Raparelli T, Manuello Bertetto A, Mazza L. Experimental and numerical study of friction in an elastomeric seal for pneumatic cylinders. Tribology International 1997; 30: 547–552. doi:10.1016/S0301-679X(97)00015-7

6 Authors

RWTH Aachen University – Institute for Fluid Power Drives and Systems (ifas)

Campus-Boulevard 30, 52074 Aachen, Germany:

Niklas Bauer, M. Sc., ORCID 0000-0002-5520-0611,
niklas.bauer@ifas.rwth-aachen.de

Univ.-Prof. Dr.-Ing. Katharina Schmitz, ORCID 0000-0002-1454-8267,
katharina.schmitz@ifas.rwth-aachen.de

https://doi.org/10.61319/1H3THQXY

Direct numerical simulation of mixed lubrication in elastohydrodynamic systems

Tim Hantusch, Böðvar Ólafsson, Casper Schousboe Andreasen

The present work proposes a direct numerical model for reciprocating sealing systems which are subject to mixed lubrication. A model is developed to predict tribological characteristics such as friction and leakage in mixed lubrication. The direct implementation allows a seamless coupling between macro-, micro-, and fluid mechanics and ensures full accountability for the highly non-linear material properties. The experimental validation of the model was performed on a newly developed test rig for reciprocating seals where the friction force was measured and compared to the friction force obtained by numerical analysis. The model can be used for the simulation of rod as well as piston seals.

1 Introduction

In the field of hydraulics, reciprocating rod and piston seals are crucial for the performance of cylinders and actuators. With respect to energy efficiency, leakage as well as product lifetime, numerical design tools play an important role in the design process of these seals. Early studies of the elastohydrodynamic lubrication (EHL) theory date back to the 1970's [1], [2] with later application for line contacts [3], [4] and reciprocating seals [5]. Contact mechanics models as the ones proposed by [6] and [7] along with technological progress in computing made it possible to couple solid, micro, and fluid mechanics and hence to build numerical models for mixed lubrication regimes. The obtained coupled equations can be solved both inverse and direct. The inverse method requires that the hydrodynamic pressure distribution is known to calculate the film thickness. Common models for mixed lubrication that use the inverse method use commercial FEA software to compute the static contact pressure and export an influence coefficient matrix to find the transient equilibrium in a custom offline program [8], [9], [10]. Direct methods on the other hand solve the Reynolds equation by discretizing the domain, forming a system of algebraic equations, and directly solving these to obtain the pressure distribution. Hence, direct methods require less initial knowledge about the fluid pressure distribution and include deformation of the sealing lip due to deviations between static and hydrodynamic pressure. The direct method has been used to solve mixed elastohydrodynamic lubrication for axisymmetric O-rings by [11] and [12] . Based on this work and inspired by [13], a 2-component sealing system was studied in the presented work. The model was exclusively implemented within the COMSOL® Multiphysics platform and hence allows a full coupling between macro-, micro- as well as fluid mechanics.

The validation of the numerical model is done using a test rig for friction caused by reciprocating seals. The surface of the sealing lip is characterized by 3D surface texture measurement. Finally, the coefficient of friction for the rod-seal contact pair is determined using an application-oriented test apparatus. The purpose of this work is to apply and validate the direct method for a multi-part elastohydrodynamic system. Focus is put on a profound experimental study which, along with the numerical results, provides insights into the accuracy of directly solved mixed lubrication models.

2 Numerical model

A sealing system consisting of an O-ring and a PTFE (Polytetrafluorethylene) lip seal is investigated. This specific sealing system was numerically studied by [14] and [15] using the inverse method. The system is shown in Figure 1. The rod is considered smooth whereas the surface roughness of the seal needs to be taken in to account. The simulation is carried out using 2D-axisymmetry conditions.

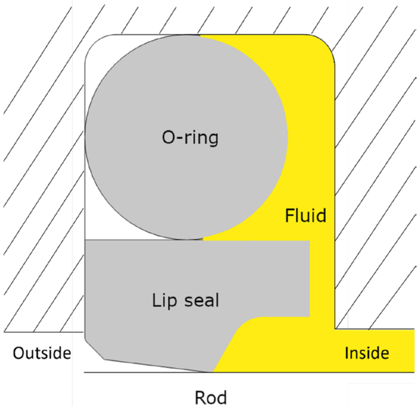

Figure 1: Sealing system

To predict the mechanical response of the O-ring, the hyperelastic Mooney-Rivlin model [16] is utilized. This model describes the strain-energy density as a linear combination of two invariants and two coefficients as seen in (1). The last term in this model describes the volumetric response of the material and can be neglected when assuming incompressibility of the material.

$$W = C_{10}(I_1 - 3) + C_{01}(I_2 - 3) + D_1(J - 1)^2 \tag{1}$$

The material used is bronze-filled PTFE which is modelled using a non-linear elastic material model calibrated with compression test data according to ISO 604 [17].

To solve the fluid mechanics in the gap between rod and seal, the Reynolds equation is used. Side leakage is neglected as axisymmetric conditions apply. Moreover, the fluid is assumed to be Newtonian and incompressible. Under these assumptions the Reynolds equation for the investigated problem takes the form:

$$\frac{\partial}{\partial x}\left(\frac{h^3}{\eta}\frac{\partial p_f}{\partial x}\right) = 12\overline{u}\frac{\partial h}{\partial x} \tag{2}$$

With respect to the finite-element implementation, the Reynolds equation is stated in its weak form:

$$\int_{\Omega}\left[\nabla\delta p_f\cdot\left(\frac{h^3}{12\eta}\nabla p_f\right)+\delta p_f\nabla(\overline{u}h)\right]d\Omega = 0 \tag{3}$$

The above equation requires the implementation of boundary conditions. In this case, Dirichlet boundary conditions are chosen and yield:

$$p_f(x = x_0) = p_{system}\ ;\ p_f(x = x_{max}) = p_{atm} \tag{4}$$

As the total load consists of a hydrodynamic and an asperity component, the friction force is the sum of the hydrodynamic shear force and the shear force caused by interacting asperities over the contact area and hence can be written as:

$$F_{f,tot} = \int_{A_{con}}\left(\tau_{asp}+\tau_f\right)dA \tag{5}$$

In terms of finite-element implementation, the total friction force takes the following form:

$$F_{f,tot} = \sum_{i=1}^{N}\int_{\Omega_i}\left(\mu p_{asp}+\frac{2\eta\overline{u}}{h}\right)d\Omega \tag{6}$$

To determine the coefficient of friction caused by the asperities a statistical model is used. The coefficient of friction for a single asperity is defined as the ratio between shear stress and pressure and is given in (7).

$$\mu_i = \frac{\tau_{asp,i}}{p_{asp,i}} \tag{7}$$

[6] proposed a widely used model to determine the asperity contact pressure, p_{asp}, in which they considered a nominally flat surface which is covered with asperities of identical radius β. The asperity height on the other hand varies randomly. Using a reference plane in the rough surface, [6] describe the probability that a particular asperity has a height between z and $z+dz$ as $\phi(z)dz$. Hence, the probability that an asperity has a height greater than the separation h can be written as shown in (8).

$$prob(\mathrm{z} > h) = \int_{h}^{\infty}\phi\,(z)dz \tag{8}$$

Thus, the total area of contact is defined as stated in (9).

$$A = \pi N\beta \int_{h}^{\infty} (z - h)\, \phi(z) dz \tag{9}$$

Finally, the total load is given in (10).

$$P = \frac{4}{3} N E' \beta^{1/2} \int_{h}^{\infty} (z - h)^{3/2}\, \phi(z) dz \tag{10}$$

Assuming that the distribution of asperity heights is Gaussian, (11) can be used for the probability function.

$$\phi * (s) = \frac{1}{\sqrt{2\pi}} e^{-\frac{s^2}{2}} \tag{11}$$

Combining (9), (10) and (11) the following expression for the asperity contact pressure is obtained:

$$p_{asp} = \frac{4}{3} E' n \beta^{1/2} \sigma^{3/2} \frac{1}{\sqrt{2\pi}} \int_{h_n}^{\infty} (s - h_n)^{3/2}\, e^{-\frac{s^2}{2}} ds \tag{12}$$

A solution for the elastohydrodynamic problem with mixed lubrication must therefore satisfy the equilibrium shown in (13).

$$p_c = p_f + p_{asp} \tag{13}$$

For the direct numerical model presented in this paper, the static FEA model of the sealing system was extended by (3) as a weak form boundary PDE. Since (12) is a statistical expression, it could not be assigned into a weak form. Hence, the surface mechanics model was added as an analytical expression. The statistical character of the Greenwood-Williamson model makes it difficult to solve for as FEA deals with deterministic problems where explicit boundary conditions can be stated. [18] has therefore suggested to perform a curve fit to obtain an analytically invertible expression for the film thickness. In this work, it was found that the statistical expression as suggested by [6] could be solved within a reasonable amount of time assuming proper scaling of variables as well as fine-tuned solver settings. The mesh size at the lip-rod interface is set to $2\mu m$ with a curvature factor of 0.01 to ensure accurate results. For the same reason, the contact model at this interface, which includes friction, is of augmented Lagrangian type. The shape functions used for both solid and fluid mechanics in this model are quadratic Lagrangian.

The scheme of the model is illustrated in Figure 2. The provided input data includes geometric properties of the sealing system, surface parameters, structural and tribological material properties as well as the application parameters. The proposed model follows the loading sequence which the sealing system would undergo under real conditions. First, the seal is mounted. Next, pressure is applied while the system remains static. In further progress of the simulation, the static contact pressure is calculated using the surface mechanics model. Finally, motion is applied to the rod and the transient system consisting of structural mechanics, surface mechanics and fluid mechanics is directly solved. The output includes the transient asperity pressure, the transient fluid pressure, the friction force, and the leakage.

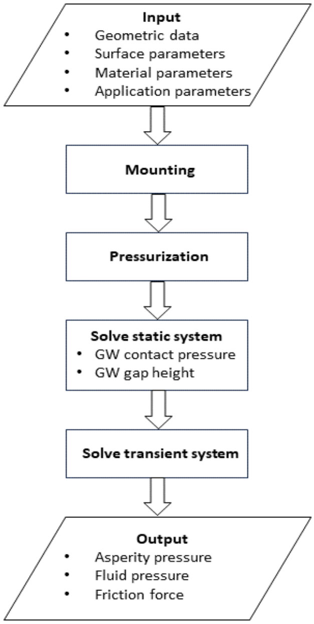

Figure 2: Multi-step numerical model

3 Identification of material parameters

As this work aims to validate the proposed numerical model by experimental investigation, an accurate determination of material parameters used in the equations presented in chapter 2 is required.

To start with, the Greenwood-Williamson surface model requires a profound investigation of the surface texture to determine the parameters σ, β and n. For this project a 3D surface texture measurement is performed using a high-resolution optical instrument. Both the values for cut-off length and magnification can be found in Table 1. The profile is evaluated in the transverse direction, i.e. in the direction of the tool during manufacturing. Moreover, the profile is levelled before extraction of surface parameters.

(6) contains the dry coefficient of friction (dry COF) for the contact between sealing lip and piston rod. As the asperity friction force is proportional to the dry COF, it is

important to determine this parameter highly accurate. To do so, a test apparatus as shown in Figure 3 was built for this project. The dry COF is measured from specimens that are cut from the investigated seal and mounted on a load sledge that slides on two parallel piston rods similar to the one mounted in the test rig.

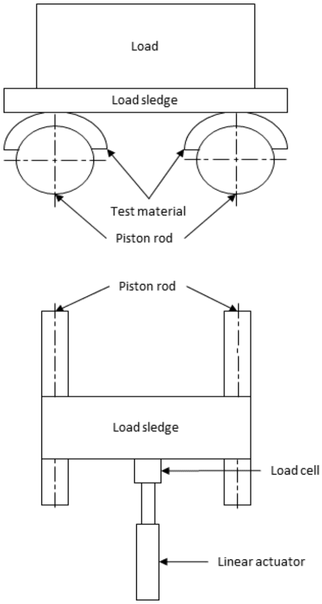

Figure 3: Test setup for the determination of the dry COF

Several studies have shown that the dry COF depends on both the normal load and the sliding velocity [19], [20], [21]. For the determination of the dry COF in this work, a fixed normal load is chosen. The value of this load can be found in Table 1 and is chosen so that approximately half of the area under the contact pressure curve for 100bar in Figure 4 lie below the dry COF test pressure.

Table 1: Material and processing parameters

Parameter	Unit	Value
β	mm	3×10^{-3}
λ_c	mm	25×10^{-3}
μ	$-$	0.085
σ	mm	2×10^{-3}
M	$-$	20
n	$\frac{1}{mm^2}$	1×10^5
p_{cof}	MPa	20

4 Numerical results

Here, the results for the operating conditions defined in Table 2 are presented. The static pressure distributions for the investigated pressures are given in Figure 4. The coordinate, which is to be found on the x-axis of the plot, refers to the spatial coordinate of the nodes. The oil is located at the lower coordinate values outside the contact area. This applies for all the figures in this chapter.

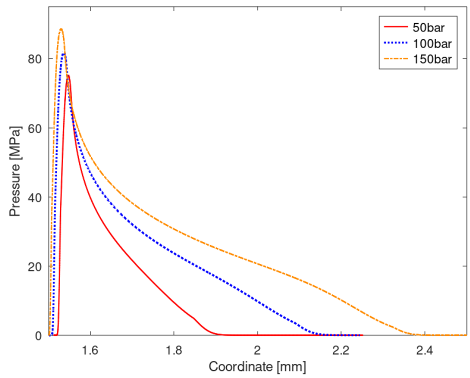

Figure 4: Static contact pressure distribution

Next, the pressure distributions for the outstroke can be seen in Figure 5. Due to the relative motion between rod and seal, the static contact pressure is split up into asperity pressure and fluid pressure fractions.

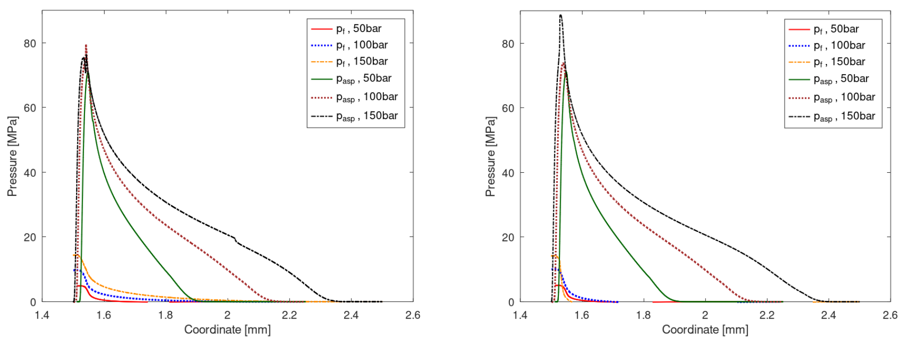

Figure 5: Pressure distributions for 50mm/s (left) and 150mm/s (right), outstroke

For the investigated system, the asperity pressure is significantly higher than the fluid pressure. Towards the air side, the fluid pressure drops to zero. Both investigated velocities show similar pressure distributions. However, the fluid pressure extends further towards the air side for 50 mm/s than for 150 mm/s. For instroke, it is to be noted that the simulation assumes a sufficient amount of oil on the rod in order to properly lubricate the contact zone. Looking at the results in Figure 6, the asperity pressure is found to carry the major share of the total load. At lower pressures up to 100 bar, the pressure distributions are close to the ones obtained for outstroke. For 150bar, the fluid pressure extends significantly longer towards the air side. This applies to both 50 mm/s and 150 mm/s rod velocity.

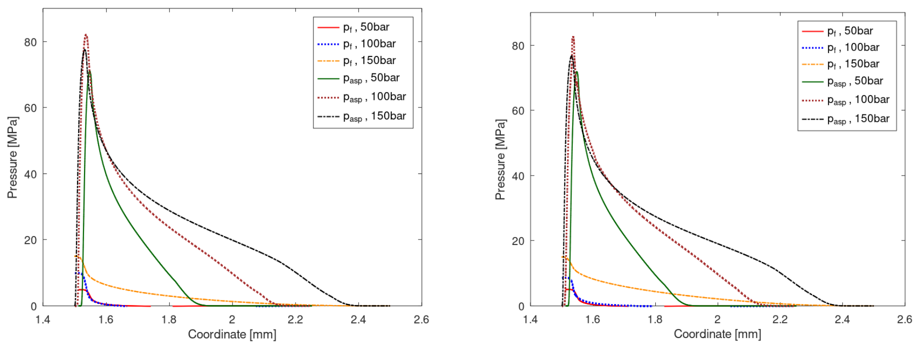

Figure 6: Pressure distributions for 50mm/s (left) and 150mm/s (right), instroke

Figure 7 shows the film thickness for both the static condition as well as instroke and outstroke at 50bar and 100bar respectively. The corresponding film thickness at 150bar is given in Figure 8. For better visualization, the plot contains a zoom-in of the region between maximum and minimum contact pressure gradient.

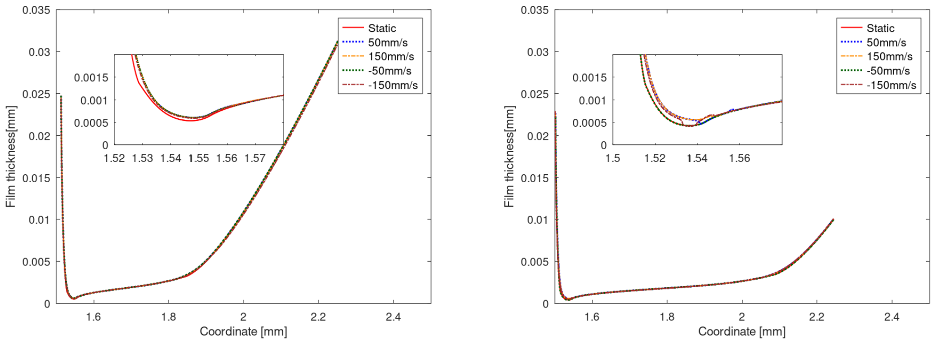

Figure 7: Film thickness for 50bar (left) and 100bar (right)

The deviation between the static and transient film thickness is due to the fluid film pressure and thus dependent on the rod velocity (see chapter 2). Within the analysed velocity range, this dependency cannot be clearly observed for 50bar pressure.

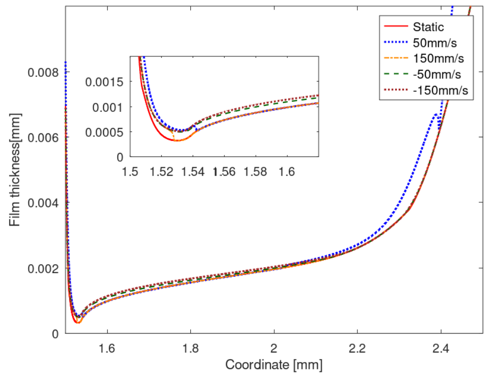

Figure 8: Film thickness at 150bar

5 Experimental setup

To validate the proposed numerical model, a hydraulic test rig for reciprocating seals was developed at *Haagensen A/S*. The test rig is capable of friction and leakage measurement for both rod and piston seals. Figure 9 shows a simplified sketch of the test rig which consists of a test and a load cylinder, a hydraulic pump station as well as a sensor and control system. The seal to be investigated is mounted in the test cylinder where all other friction sources are eliminated. Both pressure and temperature are constantly measured in the test cylinder. The force transmitted between test and load cylinder is measured by a force transducer and compared to the force acting on either rod or piston in the test cylinder.

Table 2: Test parameters

Parameter	Unit	Value
Rod diameter	mm	40
Fluid	–	Hydraulic oil ISO VG 46
Stroke length	mm	800
Evaluation length	mm	500
Pressure	MPa	50, 100, 150
Rod velocity	$\frac{mm}{s}$	-150, -50, 50, 150
Ambient temperature	°C	23

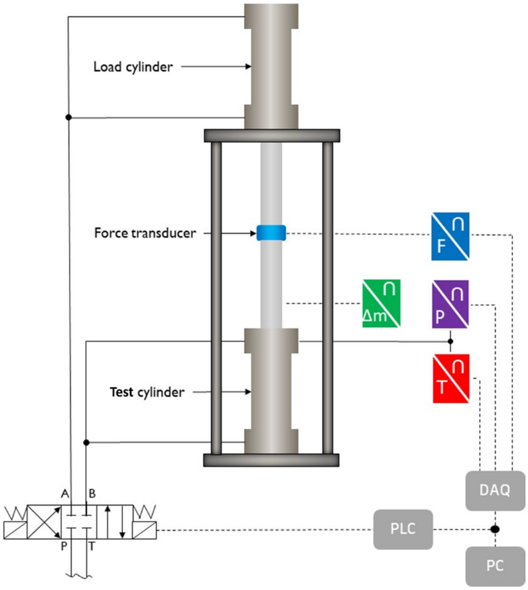

Figure 9: Reciprocating test rig

Test rigs for reciprocating seals can follow different design principles. One commonly used principle uses a symmetric pressurized housing where the piston rod sticks out on both sides of the housing. The advantage of this principle is that the net force on the rod is zero. However, as the housing is symmetric, two seals are needed where always one seal operates on instroke while the other seal is on outstroke. Examples of this test rig can be seen in [22] and [10] . Another principle is the one used in the presented work, where two hydraulic cylinders work against each other. The forces in the cylinder are higher, which requires an accurate measurement of both the cylinder pressure and the transmitted force. Through careful alignment of piston rods of the test and load cylinder, the developed test rig can temporarily run without additional guide rings or bushings, ensuring that the investigated seal is the only source of friction during the test.

6 Comparison between numerical and experimental results

To validate the proposed numerical model, the friction forces obtained by both simulation and experiment are compared. The results are given in Figure 10. The results for the experimental friction force plotted in this figure are obtained by averaging the friction force over the evaluation length of the stroke, which is defined as the part of the cycle where the rod velocity is at steady state. For each operation point, a total of 7 strokes are evaluated. The results for each evaluated stroke are included in Figure 10, which also contains the simulation results for 10, 20, 30, 40 and 75bar.

The experimental results for instroke match closely with the simulations. At 50bar and 50mm/s, the experiments show a maximum deviation of -5.8% compared to the numerical results. This deviation increases towards higher velocities, resulting in a maximum deviation of +15% for 50bar at 150mm/s. For 150bar, the experiments show a maximum deviation of -13.6% to the numerical results at 50mm/s and a maximum deviation of -11.5% at 150bar.

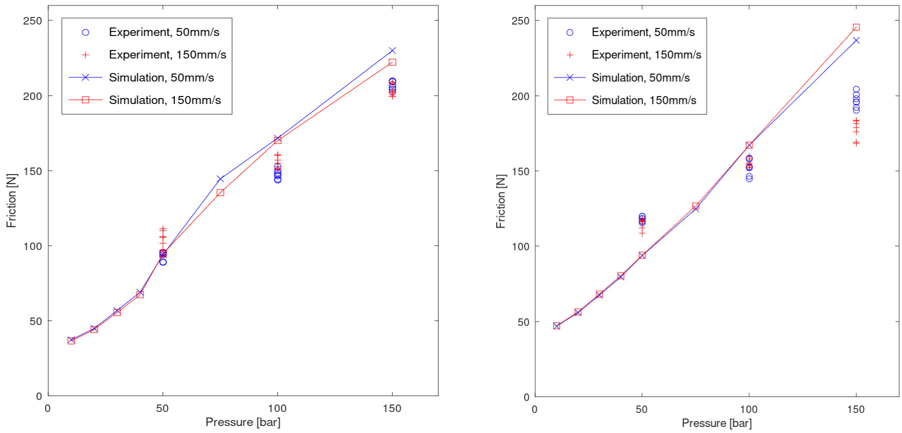

Figure 10: Instroke(left) and outstroke (right) friction force

The deviations for outstroke are in general slightly higher than the ones seen for instroke. At 50bar and 50mm/s, the experiments show a maximum deviation of +27.5% compared to the numerical results. At 150bar and 150mm/s, this maximum deviation is found to be -31%.

Although there is a good overall agreement between experiments and simulations, the simulations tend to underestimate the friction force for low pressures. This is concluded based on the results obtained at 50bar pressure for both test velocities on in- and outstroke. At higher pressures, the simulations overestimate the friction force for both test velocities on in- and outstroke. A possible explanation for the increasing overestimation of the friction force towards higher pressures could be found in chapter 3, where it is stated that the friction coefficient for PTFE is load dependent and decreases with increasing load [19], [20], [21] .

7 Conclusion

The presented work introduces a direct numerical model for reciprocating sealing systems which are subject to mixed lubrication. The implementation of the model is done exclusively within the COMSOL® Multiphysics platform. The numerical model covers solid mechanics, surface mechanics as well as fluid mechanics by manual implementation of the Reynolds equation as a weak boundary PDE and the Greenwood-Williamson surface model as an analytical expression. The full coupling between macro-, micro- and fluid mechanics allows for a continuous adjustment of non-linear material properties and a deviation between static and dynamic contact pressure. The model is characterized by a high robustness as well as a short set-up time. Provided a profound analysis of the seal's surface texture and an application-oriented determination of the friction coefficient, the model shows good agreement with experimentally obtained data for the friction force for both instroke and outstroke motion of the rod. For instroke, the accuracy of simulation results is closer to the experimental values than for outstroke.

The results presented in this paper show that complex tribological models can be implemented within a single multiphysics platform while reaching a high agreement with experimentally obtained data. This way, set-up and computation time can be reduced significantly. Using correct values for the friction coefficient and the surface texture parameters is crucial for an accurate determination of the fluid film thickness and friction force in mixed lubrication.

8 Nomenclature

Variable	***Description***	***Unit***
Ω	Domain indicator	$[-]$
β	Radius of asperities	$[mm]$
δ	Laplace operator	$[-]$
η	Dynamic viscosity	$[MPas]$
λ_c	Cut-off length	$[mm]$
μ	Friction coefficient	$[-]$
σ	Standard deviation of peak heights	$[mm]$
τ_{asp}	Asperity shear stress	$[MPa]$
τ_{f}	Viscous shear stress	$[MPa]$
∇	Gradient operator	$[-]$
A_{con}	Contact area	$[mm^2]$
C_{ij}	Material model parameter(s)	$[MPa]$
D_i	Volumetric response parameter(s)	$[MPa]$
E'	Effective Young's modulus	$[MPa]$
$F_{f,tot}$	Total friction force	$[N]$
I_i	Matrix invariant(s)	$[-]$
J	Determinant of deformation gradient	$[-]$
M	Magnification factor	$[-]$
N	Number of asperities	$[-]$
W	Strain energy density	$[MPa]$
$\overline{u}$	Mean velocity, $\frac{u_a+u_b}{2}$	$[\frac{mm}{s}]$

h	Film thickness	$[mm]$
h_n	Standardized film thickness, $\frac{h}{\sigma}$	$[-]$
n	Asperity density	$[\frac{1}{mm^2}]$
p_{asp}	Asperity pressure	$[MPa]$
p_{cof}	Pressure for determination of μ	$[MPa]$
p_c	Contact pressure	$[MPa]$
p_f	Fluid pressure	$[MPa]$
x	Coordinate variable	$[mm]$

9 References

[1] B. J. Hamrock and D. Dowson, “Isothermal Elastohydrodynamic Lubrication of Point Contacts: Part II—Ellipticity Parameter Results,” *Journal of Lubrication Technology*, vol. 98, no. 3, pp. 375–381, Jul. 1976, doi: 10.1115/1.3452861.

[2] B. J. Hamrock and D. Dowson, “Isothermal Elastohydrodynamic Lubrication of Point Contacts: Part 1—Theoretical Formulation,” *Journal of Lubrication Technology*, vol. 98, no. 2, pp. 223–228, Apr. 1976, doi: 10.1115/1.3452801.

[3] B. J. Hamrock and J. H. Tripp, “Numerical methods and computers used in elastohydrodynamic lubrication,” in *Developments in Numerical and Experimental Methods Applied to Tribology*, Elsevier, 1984, pp. 11–19. doi: 10.1016/B978-0-408-22164-1.50005-3.

[4] M. K. Ghosh and B. J. Hamrock, “Thermal Elastohydrodynamic Lubrication of Line Contacts,” *A S L E Transactions*, vol. 28, no. 2, pp. 159–171, Jan. 1985, doi: 10.1080/05698198508981608.

[5] A. F. C. Kanters, “Paper XIII (i) On the Elastohydrodynamic Lubrication of Reciprocating Elastomeric Seals: The Influence of the Surface Roughness,” 1991, pp. 357–364. doi: 10.1016/S0167-8922(08)70152-4.

[6] J. A. Greenwood and J. B. P. Williamson, “Contact of Nominally Flat Surfaces,” 1966. [Online]. Available: https://about.jstor.org/terms

[7] A. W. Bush, R. D. Gibson, and T. R. Thomas, “The elastic contact of a rough surface,” *Wear*, vol. 35, no. 1, pp. 87–111, Nov. 1975, doi: 10.1016/0043-1648(75)90145-3.

[8] R. F. Salant, N. Maser, and B. Yang, “Numerical model of a reciprocating hydraulic rod seal,” *J Tribol*, vol. 129, no. 1, pp. 91–97, Jan. 2007, doi: 10.1115/1.2401222.

[9] A. K. Bullock, D. G. Tilley, D. N. Johnston, C. R. Bowen, and P. S. Keogh, “Non-linear friction in reciprocating hydraulic rod seals: Simulation and measurement,” in *Journal of Physics: Conference Series*, Institute of Physics Publishing, 2009. doi: 10.1088/1742-6596/181/1/012009.

[10] C. Xiang, Z. Wang, X. Jia, and F. Guo, “Numerical simulation model of a reciprocating seal based on the mixed-lubrication theory,” *The Journal of Engineering*, vol. 2019, no. 13, pp. 49–53, Jan. 2019, doi: 10.1049/joe.2018.8948.

[11] T. Schmidt, M. André, and G. Poll, “A transient 2D-finite-element approach for the simulation of mixed lubrication effects of reciprocating hydraulic rod seals,” *Tribol Int*, vol. 43, no. 10, pp. 1775–1785, Oct. 2010, doi: 10.1016/j.triboint.2009.11.012.

[12] S. Stupkiewicz, “Finite element treatment of soft elastohydrodynamic lubrication problems in the finite deformation regime.”

[13] T. Lohner, A.Ziegltrum, J. P. Stemplinger, and K. Stahl, “Engineering Software Solution for Thermal Elastohydrodynamic Lubrication Using Multiphysics Software,” *Advances in Tribology*, vol. 2016, 2016, doi: 10.1155/2016/6507203.

[14] H. Ran, S. Wang, and D. Liu, “A multiscale wear model for reciprocating rod stepseal under mixed lubricating conditions based on linear elasticity,” *Proceedings of the Institution of Mechanical Engineers, Part J: Journal of Engineering Tribology*, vol. 235, no. 1, pp. 161–180, Jan. 2021, doi: 10.1177/1350650120902602.

[15] R. F. Salant, B. Yang, and G. W. Woodruff, “NUMERICAL MODELING OF RECIPROCATING FLUID POWER SEALS,” 2008.

[16] “Large elastic deformations of isotropic materials. I. Fundamental concepts,” *Philosophical Transactions of the Royal Society of London. Series A, Mathematical and Physical Sciences*, vol. 240, no. 822, pp. 459–490, Jan. 1948, doi: 10.1098/rsta.1948.0002.

[17] ISO, “ISO 604:2002; Plastics - determination of compressive properties,” 2002.

[18] J. L. Streator and G. W. Woodruff, “A Model of Mixed Lubrication with Capillary Effects.”

[19] T. T. Tevruz¨, “Tribological behaviours of bronze-filled polytetrafluoroethylene dry journal bearings,” 1999.

[20] M. A. Chowdhury *et al.*, “Frictional Behavior of Polymers Sliding Against Smooth and Rough Mild Steel Counter Faces,” *Middle-East Journal of Scientific Research*, vol. 21, no. 3, pp. 477–486, 2014, doi: 10.5829/idosi.mejsr.2014.21.03.21161.

[21] H. Unal, “Tribological Studies of Bronze Filled PTFE Polymer.”

[22] O. Heipl and H. Murrenhoff, “Friction of hydraulic rod seals at high velocities,” *Tribol Int*, vol. 85, pp. 66–73, 2015, doi: 10.1016/j.triboint.2015.01.002.

10 Authors

Haagensen A/S, Hejrevang 6, 3450 Allerød, Denmark:
Tim Hantusch, R&D Engineer, M.Sc., tih@haagensenseals.com

Technical University of Denmark (DTU), Department of Civil and Mechanical Engineering, Section of Solid Mechanics
Koppels Allé, Building 404, 2800 Kongens Lyngby, Denmark
Böðvar Ólafsson, Mechanical Engineer, M.Sc.

Technical University of Denmark (DTU), Department of Civil and Mechanical Engineering, Section of Solid Mechanics
Koppels Allé, Building 404, 2800 Kongens Lyngby, Denmark
Casper Schousboe Andreasen, Associate Professor, PhD, csan@dtu.dk

https://doi.org/10.61319/NPEWSCWX

Prediction of RSS Sealing Performance by Fully Coupled EHL Simulation

Fabian Kaiser, Andreas Gropp, Daniele Savio, Daniel Frölich, Christian Wilbs and Dirk Möhring

The pumping and leakage behavior of radial shaft seals (RSS) has challenged researchers for more than half a century. While the main phenomena contributing to reverse pumping have been identified some decades ago, to this day there is no conclusive proof nor a comprehensive model for the exact sealing mechanisms, making it impossible to derive precise guidelines for radial shaft seal design. Therefore, Freudenberg has developed its own simulation tool based on elasto-hydrodynamic lubrication (EHL) to gain insight in the pumping mechanism and the sealing performance of RSS. It includes all steps required to simulate the pumping rate, from Finite Element Analysis to the EHL-modelling of the sealing contact, including the circumferential deformation of the sealing lip roughness. Using this tool, the pump rate of RSS can be simulated accurately and new insights in the sealing mechanism are possible.

1 Introduction

Radial shaft seals are mostly made of elastomer since synthetic nitrile rubber, compatible with mineral oils, became available in the 1930s. Through decades of ongoing research and improvements in materials and design of these seals, some fundamental principles to ensure tightness were established:

- The sealing lip must have an asymmetric shape with a significantly larger oil side angle α than air side angle β (Fig. 1).
- The region of the sealing lip in contact with the shaft requires a certain roughness that must persists even when the seal wears. This is determined by the exact rubber compound.
- The shaft should be hardened to minimize wear, and plunge-ground to remove surface features that might transport oil to the air side.

If these conditions are met, the seal will actively pump fluid from the air side to the oil side, creating an active dynamic sealing mechanism [1]. Several models have been proposed to explain this mechanism, the most popular of which being the asperity deformation model by Kammüller [2]: After installation, an asymmetric contact pressure distribution between the shaft and the seal is formed due to the difference between the angles α and β with the maximum being closer to the oil side. When the shaft is rotated, the elastomer surface is deformed in circumferential direction due to the frictional shear stress with the maximum deformation in the same location as the contact pressure peak. The stretched micro-asperities in the contact create a pumping effect towards the location of maximum pressure. As most of the asperities are located on the air side, a net reverse pumping flow ensues, see Figure 1.

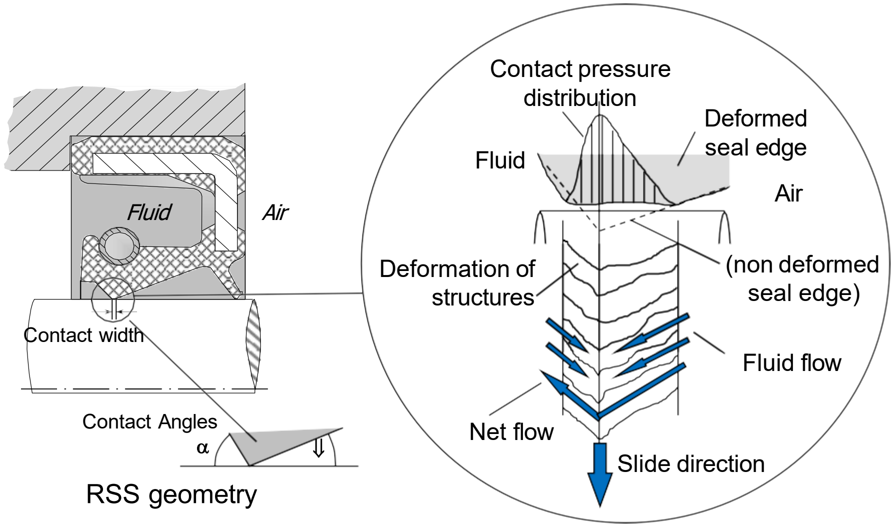

Figure 1: Radial shaft seal and explanation of pumping mechanism according to Kammüller

2 Current State of Research

The asperity deformation model of Kammüller has been verified experimentally to some degree, but local asperity behavior is not fully understood yet. Experimental studies with hollow, transparent shafts were conducted [6] and the pumping effect was demonstrated using e.g., fluorescent particles in the oil. However, the fine details at asperity level are hardly accessible due to the confined space and optical resolution. Additionally, changing the shaft from ground steel to optically smooth glass or sapphire will influence the pumping rate.

Typically, numerical simulation can provide new insights on the underlying effects. For instance, it is standard practice to calculate the contact pressure distribution of a radial shaft seal using finite element methods, but up to now it is impossible to measure contact pressures with µm-resolution.

Still, a comprehensive reverse pumping simulation requires the coupling of several numerical models: 3D elasto-hydrodynamic (EHL) film thickness and flow calculations including cavitation, simulation of the circumferential deformation due to the shear stresses and the contact mechanics between the asperities and the shaft. One of the first to present a full model was Salant [3]. More recently, Thielen developed a model that includes thermal effects and can simulate the friction torque of radial shaft seals accurately [4]. These two models, however, lack an accurate representation of the seal surface roughness, as asperities are assumed to be sinusoidal.

The latest attempt to simulate the pump rate of shaft seals was published by Grün et al. [5]: They use a high-resolution FEA simulation of the deformed surface asperities as input for a transient multiphase computational fluid dynamics (CFD) model.

Thus film thickness and asperity deformation are not coupled to the flow, but calculated from empirical formulas. It is shown that the pump-rate can vary along the circumference of a seal, even leading to local leakage, the average value agreeing well with experiments. This provides new clues as to how a seal can stay well lubricated without leaking.

In summary, no fully coupled model that takes all effects into account exists today. Nevertheless, the existing methods provide very useful insights into the function of radial shaft seals.

3 Materials and Methods

3.1 Seals and Shafts

In this study, standard radial shaft seals with 80 mm shaft diameter were used, made by Freudenberg Sealing Technologies (FST) from a FKM and a NBR material, both having 75 Shore A hardness. The shafts were made from hardened 90MnCrV8 steel (1.2842) and plunge ground to a roughness of Rz 1.5 µm. Figure 2 shows exemplary roughness measurement results of the sealing lip after the tests and the shaft, obtained using confocal microscopy and white light interferometry (WLI) respectively. As expected, the sealing lip is significantly rougher than the shaft surface.

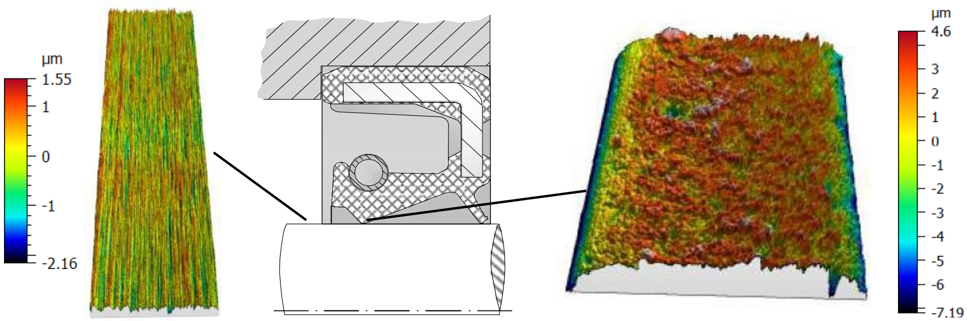

Figure 2: Roughness of ground shaft and sealing edge (shape removed)

The oil used was a commercial mineral oil with 220 mm²/s as nominal kinematic viscosity at 40 °C. At the operating conditions of 60 °C, the dynamic viscosity is 0.069 Pa s.

3.2 Simulation Model

The model presented here aims to couple all relevant effects in a single model.

At first, the contact pressure distribution and deformed geometry of the radial shaft seal is calculated using a FEA method. The rubber material is modelled as hyperelastic at an operating temperature of 60 °C. The resulting pressures and deformed geometries for the two variants can be seen in Figure 3. The NBR seal has the narrower sealing contact compared to the FKM.

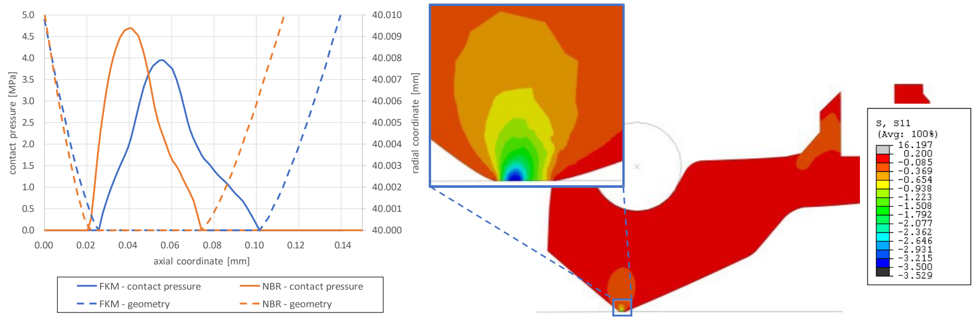

Figure 3: Deformed geometry and contact pressure distributions of analyzed seals.

In order to obtain the local film thicknesses and fluid pressures, the 2D Reynolds equation is solved iteratively, including mass conserving cavitation [10]. For the elastic deformation calculation of the sealing lip asperities, a computationally efficient FFT algorithm is used [11]. From the results, the shear stress acting on the seal can be calculated, being then used as input to compute the circumferential deformation. Following this step, the film thickness is updated, and the process is iteratively repeated until convergence is achieved. For computational reasons, the number of nodes is currently limited to 16,384 (e.g., 128x128). For a contact width of 0.1 mm, this would be equal to a resolution of 0.7 µm, but for other seal types like pressure seals with wider contact bands up to 1 mm, the resolution could be restricted to 8 µm.

Two additional methods are employed to correctly account for asperity contact and fluid flow at scales smaller than the aforementioned resolution limit. First, the contact mechanics theory by Persson and coworkers was used to calculate the asperity load and average separation of the surfaces as a function of the nominal contact pressure [7].

In a similar way, flow factors account for the effect of the roughness on the flow between two surfaces based on Almquist's homogenization method [9]. As stated above, the deformation according to shear stresses is a very important factor in the contact of radial shaft seals. This means that the roughness structures are distorted by a certain angle. Therefore, the existing flow factor calculation is extended to also be a function of this distortion angle, allowing an efficient implementation in the EHL model.

Finally, the 2D-Reynolds equations for steady state condition reads:

$$\nabla\left(-\underline{\underline{A}}_h \nabla p_{fl} - \underline{\underline{B}}_h(\underline{v}_a - \underline{v}_b) + \frac{h_{fl}}{2}(\underline{v}_a + \underline{v}_b)\right) = 0 \qquad (1)$$

$\underline{\underline{A}}_h$ and $\underline{\underline{B}}_h$ are the flow factor matrices that are a function of the local distortion angle γ; $\underline{v}_a$ and $\underline{v}_b$ are the velocities of shaft and seal surface.

For the results presented in here, all surface features with a wavelength bigger than 20 µm were fully discretized using the EHL model, while accounting for the smaller features using flow factors and contact mechanics.

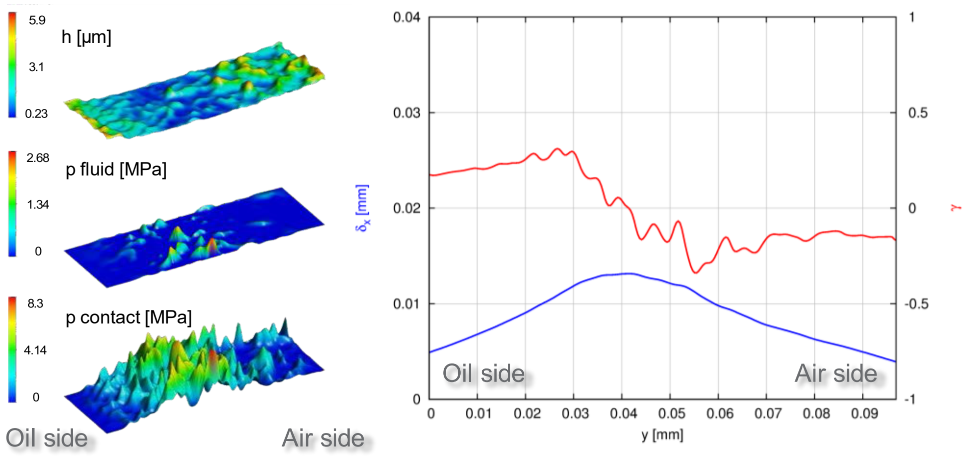

Figure 4: Simulation results for 2 m/s shaft speed: Film thickness distribution h, fluid pressure, contact pressure, circumferential deformation δ_x and distortion angle γ

Figure 4 shows typical results of a pump rate calculation: At a shaft speed of 2 m/s, the tangential deformation is maximal at the location of the contact pressure maximum with a value of 0.012 mm, in line with [source]. The fluid pressure graphs show that despite the full lubrication, most or the load is still supported by asperity contact. The simulated pump rate for this segment is 2.1 ml/h towards the oil side.

Currently, thermal heating of the contact and the changes in viscosity and elastomer stiffness are not considered, as well as starved lubrication, i.e., dry air side. However, the model is built with these extensions in mind, they will be added in the near future.

3.3 Pump Rate Experiments

To validate the simulation results, pump rate experiments were done at different speeds. The pump rate was measured by installing the seal invertedly (oil on air side) and collecting the leakage over 48 hours. The results are shown in Figure 5. The measured pump rates represent the averages of four tests, each test was rotated in clockwise direction and counter-clockwise.

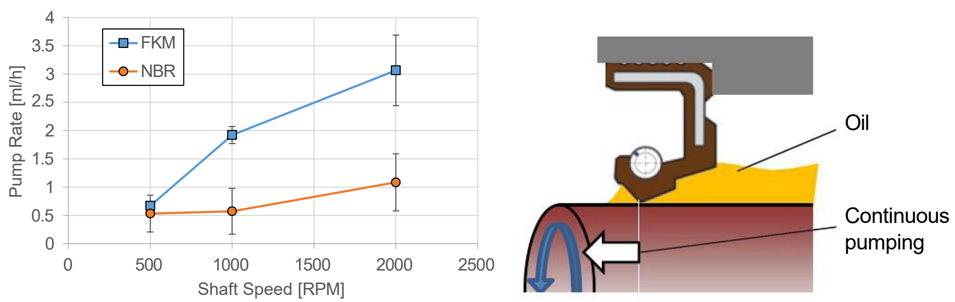

Figure 5: Configuration for pump rate measurement [8] and results

4 Discussion

The simulation of multiple segments of radial shaft seals quickly shows similar results as Grün et al. found [5]: Individual surface patches vary significantly regarding their pumping rate with some even showing leakage. With many surfaces, the average value shows good back-pumping behavior (negative pump rate, Figure 6), in good qualitative agreement with the experiments. It is observed that the pump rate of a segment can change from pumping to leaking depending on the shaft speed.

The discrepancy regarding the absolute values of the pump rate can be explained with the oil viscosity in the sealing gap: Currently, the sump temperature of 60 °C is used to calculate the viscosity for the simulation, but as Remppis has shown [12], the temperature in the contact can be more than 20 °C above the sump temperature. Such an increase would approx. halve the viscosity of the oil used here, reducing the pump rate significantly. This will be considered in a future version of the simulation model. An additional parameter which could explain the discrepancy is the elastomer-steel boundary friction coefficient – currently set to $\mu_{boundary} = 0.2$ as obtained from tribological experiments. Although we consider this a good estimation, the actual value could vary in the radial shaft seal due to the complex contact conditions.

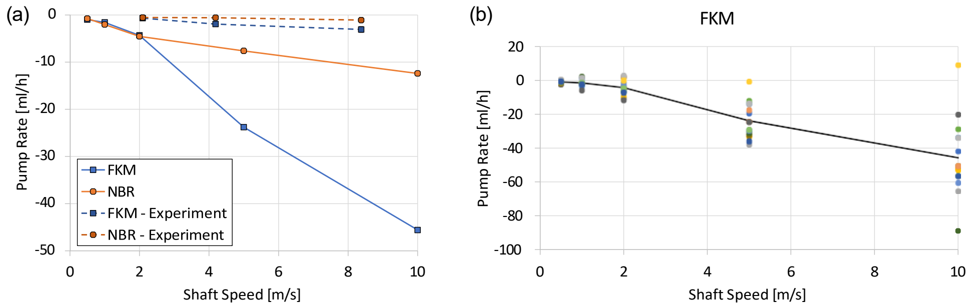

Figure 6: Simulated pump rate vs. measurement: a) Comparison of mean values for simulation and experiment; b) Mean simulated pump rate and values of individual surfaces

The simulations allow a detailed analysis of the flow in the sealing contact. The flow patterns and, crucial for the sealing function, the movement of a virtual particle from the air side to the oil side can be analyzed, see Figure 7. It is apparent, that the main movement of the fluid is in the direction of rotation, with a smaller component perpendicular to it. It is, however, very difficult to identify features on the seal surface that cause the pumping. On average, it takes about 20 mm of circumferential travel to traverse the 0.08 mm wide sealing contact (FKM). Note that these 20 mm are not across several patches but, due to the symmetry boundary condition used in the model, around 200 times across the same patch, entering a bit further towards one side from crossing to crossing due to the pumping. Following a particle across many segments would be very interesting but is computationally unfeasible.

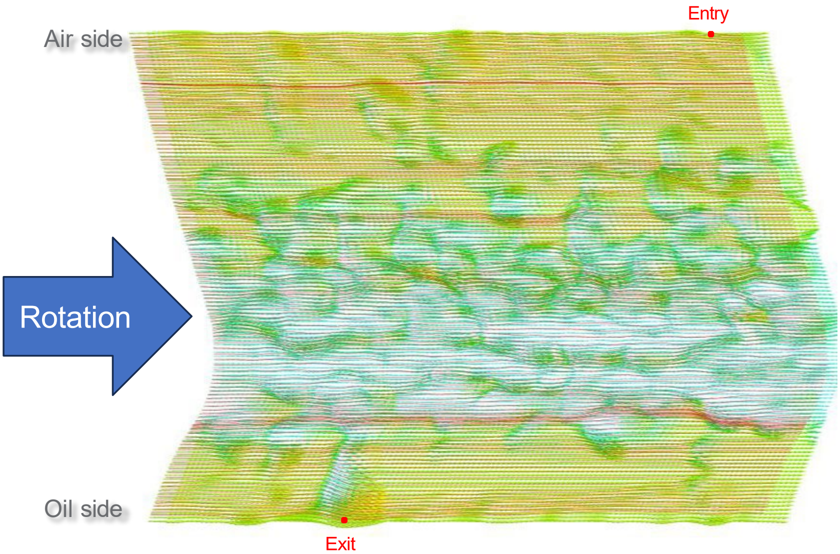

Figure 7: Transversal of virtual particle through the sealing contact

From the findings using the present model and [5], the lubrication and sealing balance of rotary seals needs to be re-thought: Instead of a fixed pumping rate, varying only from part to part, one single seal seems to have many different local pump rates along its circumference, i.e., the seal pump rate variability SPRV. Understanding and being able to control these variations will create opportunities to improve the performance of radial shaft seals: The SPRV may need to be big enough to ensure proper lubrication even at high speeds while still being small enough to avoid leakage.

5 Summary and Conclusion

The model presented here can calculate the film thickness and pump rate of radial shaft seals with good agreement to experimental results and literature. As such, it is one of the first models to comprehensively consider all relevant parameters in a fully coupled way, at least in its planned final configuration. Already now, the findings are leading towards new research aspects to improve the performance of rotary seals, particularly in challenging conditions.

This is very important for Freudenberg to remain a leading manufacturer of high performance products and to offer the best products possible to its customers.

6 Acknowledgements

The authors thank Dr.-Ing. Gerhard Stelzer, MTS, RPTU Kaiserslautern-Landau for providing seal surface measurement data.

7 Nomenclature

Variable	*Description*	*Unit*
p_{fl}	Fluid Pressure	[MPa]
p_{sol}	Solid Body Pressure	[MPa]
h_{fl}	Fluid Film Thickness	[µm]
v	Velocity	[m/s]
A_h, B_h	Influence Coefficient Matrices	[-]
γ	Distortion Angle	[rad]

8 References

[1] Müller, H. K., Nau, B. S.: *Fluid Sealing Technology*, Marcel Dekker, New York, 1998, ISBN 978-0-8247-9969-4

[2] Kammüller, M.: *Zur Abdichtwirkung von Radial-Wellendichtringen*, Dissertation, Stuttgart, Institut für Maschinenelemente, 1986

[3] Salant, R. F.: *Modelling Rotary Lip Seals*, In: Wear, 1997, https://doi.org/10.1016/S0043-1648(96)07463-7

[4] Thielen, S.: *Entwicklung eines TEHD-Tribosimulationsmodells für Radialwellendichtringe*, Dissertation, Kaiserslautern, Lehrstuhl für Maschinenelemente, Getriebe und Tribologie, 2019

[5] Grün, J., Feldmeth, S., Bauer, F.: *Multiphase Computational Fluid Dynamics of Rotary Shaft Seals*, In: Lubricants, 2022, https://doi.org/10.3390/lubricants10120347

[6] Mizuta, H., Furuyama, H., Sato, Y.: *Measurement Method of Pumping Ability of Radial Lip Seals for Small Shaft Diameters*, SAE Technical Paper 2007-01-1521, 2007, https://doi.org/10.4271/2007-01-1521

[7] Yang, C., Persson, B.N.J.: *Contact mechanics: contact area and interfacial separation from small contact to full contact*, J. Phys.: Condens. Matter, 2008 (20)

[8] Remppis, M.: *Untersuchungen zum Förderverhalten von Dichtsystemen mit Radial-Wellendichtringen aus Elastomer*, Dissertation, Stuttgart, Institut für Maschinenelemente, 2016

[9] Almqvist, A.: *On the effects of surface roughness in lubrication*, PhD-Thesis, Luleå University of Technology, 2006

[10] Elrod, H. G.: *A Cavitation Algorithm*, J. of Lubrication Tech. Jul 1981, 103(3): 350-354, https://doi.org/10.1115/1.3251669

[11] Wang, Q. J., Sun, L., Zhang, X., Liu, S., Zhu, D.: *FFT-Based Methods for Computational Contact Mechanics*, Front. Mech. Eng., 2020, https://doi.org/10.3389/fmech.2020.00061

[12] Remppis, M.: *Untersuchungen zum Förderverhalten von Dichtsystemen mit Radial-Wellendichtringen aus Elastomer*, Dissertation, Stuttgart, Institut für Maschinenelemente, 2016

9 Authors

Freudenberg Technology Innovation SE & Co. KG

Höhnerweg 2-4, 69469 Weinheim, Germany:

Dr.-Ing. Fabian Kaiser, ORCID 0009-0003-7525-7062, fabian.kaiser@freudenberg.com

Dipl.-Ing. Andreas Gropp, andreas.gropp@freudenberg.com

Dr.-Ing. Daniele Savio, ORCID 0000-0003-1908-2379, daniele.savio@freudenberg.com

Freudenberg FST GmbH

Höhnerweg 2-4, 69469 Weinheim, Germany:

Dr.-Ing. Daniel Frölich, ORCID 0000-0002-2707-948X, daniel.froelich@fst.com

Christian Wilbs, M.Sc., christian.wilbs@fst.com

Dipl.-Ing. (FH) Dirk Möhring, dirk.moehring@fst.com

https://doi.org/10.61319/2OAHH0DH

Group A
Session 6

Rotary Shaft Seals

A 16

Mousa Amro, Bengt Wennehorst, Gerhard Poll, Leibniz Universität Hannover , Institut für Maschinenkonstruktion und Tribologie, Garbsen, Germany

Frictional characteristics of elastomeric radial lip seals at extremely low temperatures

A 17

Yongzhen Lin, Ringo Nepp, Matthias Kröger, Technische Universität Freiberg, Institut für Maschinenelemente, Konstruktion und Fertigung, Freiberg, Germany

Stochastic analysis on tribological behavior of radial shaft seals with focus on lubricants

A 18

Lenine Marques de Castro Silva, Y. Stiemcke, T. Schollmayer, O. Koch, S. Thielen, Rheinland-Pfälzische Technische Universität Kaiserslautern-Landau, Chair of Machine Elements, Gears and Tribology - MEGT, Kaiserslautern, Germany

Performance Analysis of Radial Shaft Seals in Non-Stationary Rotational Movements

A 19

Marco Gohs, Lothar Hörl, Frank Bauer, IMA, Univerität Stuttgart, Dichtungsrechnik, Stuttgart, Germany

Development and Testing of Sleeve-Type Lip Seals with Stamped Back-Pumping Structures

Frictional characteristics of elastomeric radial lip seals at extremely low temperatures

Mousa Amro, Bengt Wennehorst, Gerhard Poll

A novel, low-temperature radial lip seal test rig was set up, allowing for simultaneous non-contact, telemetric measurements of both radial lip seal contact temperature and seal friction torque. Extreme cooling of the sealing contact zone down to below -50 °C was achieved by continuously feeding carbon dioxide snow pellets into the bore of a hollow seal counterface adaptor. In this work, the frictional characteristics of single test seals that were wetted were investigated.

Experiments were conducted with plain radial lip seals made of NBR and FKM, respectively, using two polyglycol oils with different viscosity grades of VG 220 and VG 46, respectively. Starting from a stationary state at 200 rpm (0.84 m/s) with contact temperatures in the range of 45 °C to 60 °C, the sealing contacts were cooled down, finally reaching steady state seal contact temperatures as low as approx. -50 °C. Thus, during cool-down of the sealing systems, both seal elastomers pass through the glass transition, and both lubricants pass through their pour points. In contrast to warm operating conditions, where speed-step dependent seal friction changes could be accurately predicted based on soft micro-elastohydrodynamic asperity lubrication theory, speed step experiments at such extremely low temperatures revealed that there was no viscous friction response, i.e., the seal friction was due to Coulomb-type friction. While showing larger fluctuations, the overall level of this Coulomb-type friction was comparable to the steady-state seal friction measured under warm operating conditions. When warming the systems up, the original lubrication mode was reestablished.

1 Introduction

Although elastomeric radial lip seals are used at extremely low temperatures, their behaviour under these conditions has not been sufficiently explored. Especially during operation at temperatures below the glass transition point (T_g) of the elastomer as well as the pour point of the lubricant, the properties of the sealing system (e.g., the seal's elastic modulus or lubricant's viscosity) change drastically, preventing the prediction of the seal's behaviour.

The aim of this study, which was originally presented in [1], is to introduce a method for the characterization of the friction losses of cooled down elastomeric seals and to discuss the behaviour of different combinations of elastomers and lubricants.

2 Experimental setup

This section describes the experimental equipment and tested materials in this study.

2.1 Low-temperature test rig

To investigate the functional behaviour of radial lip seals with regard to friction torque and contact temperature, a novel low-temperature functional test rig was developed and built, see Figure 1.

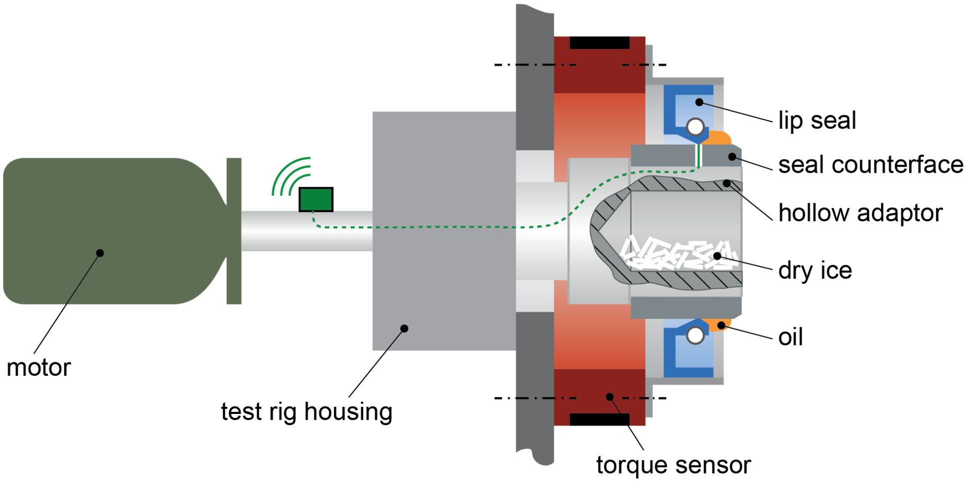

Figure 1: schematic illustration of the low-temperature test rig

In this work, a single test seal was mounted on the seal counterface in such a way that the sealing edge was placed on a miniature thermocouple cemented into and ground along with the counterface. This thermocouple, which had a diameter of approximately 0.4 mm, enables a direct measurement of the temperature inside the contact zone of the seal. A similar approach to measure the contact temperature is also described in [2], see Figure 2. The temperature signal is then transmitted telemetrically to the data acquisition system. To cool the sealing contact area, dry ice pellets approximately the size of a grain of rice were continuously fed into the hollow adaptor of the counterface by means of a feeding device consisting of a funnel and a covering disc, as seen in Figure 3. The contact zone in this design is cooled directly via the counterface so that, depending on the sliding speed, extreme contact temperatures of below -50 °C could be achieved. To lubricate the sealing system, oil was applied manually to the oil side using a syringe. The seal itself was mounted in an adaptor that was connected to a torque measuring flange. By measuring frictional torque using this technique rather than at the drive shaft, systematic errors resulting from additional friction in the test rig bearings are eliminated.

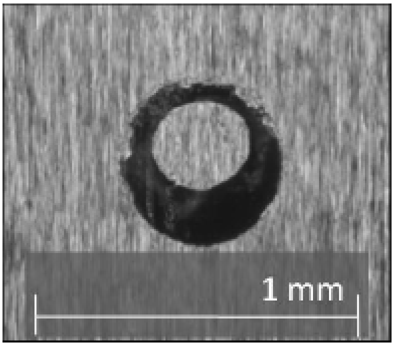

Figure 2: Miniature thermocouple ground along with the counterface, [2]

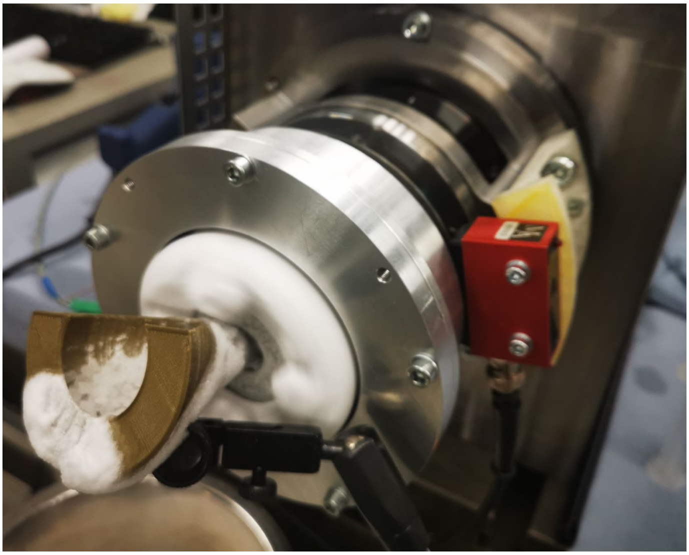

Figure 3: Low-temperature test rig during an experiment

Although two identical test seals with an oil-filled inner gap in between may be evaluated in this setup, an arrangement with only one seal was studied in this work. By using this method, the oil-filled ring gap is avoided, the churning losses of which – caused by the oil's increasing viscosity as temperature drops – would significantly impede the measurement of the seal friction. As a result, the measured friction torque can be directly associated with the friction occurring in the seal lip.

2.2 Investigated elastomers and lubricants

The experiments were conducted with plain radial lip seals with a nominal diameter of 80 mm made of NBR and FKM, respectively, using two polyglycol (PG) oils with different viscosity grades of VG 220 and VG 46, respectively.

In order to understand the characteristic behaviour of the sealing system, it is necessary to have information on the behaviour of its components. The temperature-dependent dynamic properties complex shear modulus (G^*) and loss factor ($\tan(\delta)$) of both elastomers were obtained by means of dynamic mechanical analysis at the Deutsches Institut für Kautschuktechnologie e.V. (DIK, Hannover). This analysis revealed a glass transition temperature (T_g) of -28 °C for NBR and -12 °C for FKM at a frequency of strain oscillation of 0.1 Hz. At this temperature, $\tan(\delta)$ reached its peak value, indicating a viscoelastic behaviour of the elastomer.

According to the datasheet of the lubricants, the pour points of PG ISO-VG 46 and PG ISO-VG 220 are -40 and -35 °C, respectively. At these temperatures, the oils lose their viscous behaviour.

3 Experimental results

Without yet cooling the sealing contact, the manually performed tests began at 200 rpm rotating speed (approx. 0.84 m/s). After the contact zone reached a steady-state temperature, dry ice was continuously fed into the hollow counterface adaptor. Once the contact temperature stabilised, the speed was gradually reduced to 2 rpm. Thereafter, the speed was gradually increased back up to the initial speed again, depending on the observed sealing contact behaviour. Finally, the cooling of the sealing contact was terminated so that a steady-state condition at 200 rpm was re-established at the end of the test. By comparing the corresponding temperatures and seal friction torques with the initial steady-state, conclusions can be drawn about wear effects as well as damage to the sealing systems.

3.1 Friction torque at very low temperatures

In each of the experiments, cooling down the system at first resulted in an increase of the frictional losses in the sealing system, which can be explained by the increased viscous friction due to the increasing lubricant viscosity. After reaching a maximum value, the frictional losses start to decrease until they reach a level similar to that observed at the end of the uncooled run-in period, as seen in Figure 4 for an experiment with an NBR-seal and PG ISO-VG 220 as a lubricant.

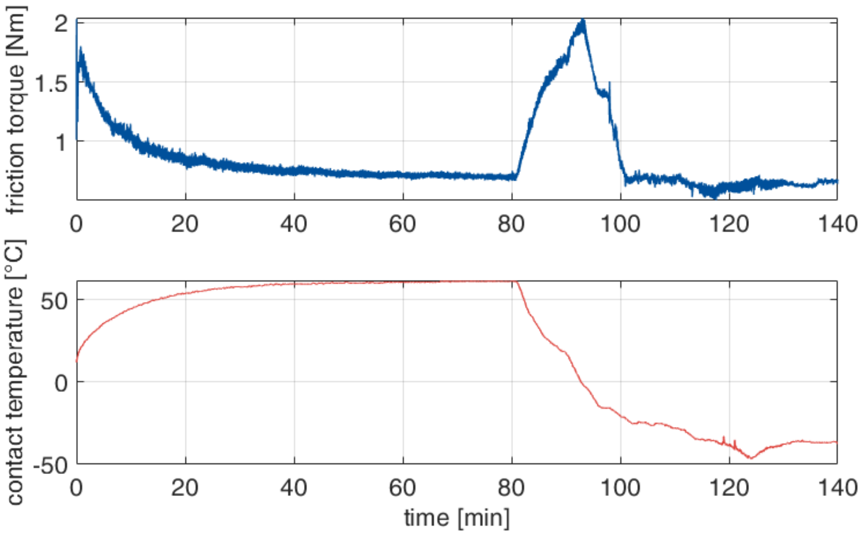

Figure 4: Trend of friction torque during the cool-down phase; NBR, PG ISO-VG 220

The decrease in the friction torque can be explained by the strongly increasing oil viscosity and the loss factor of the elastomer. As cooling continues, the increasing viscosity of the lubricant, combined with the pumping mechanism of the sealing contact, prevents the lubricant from wetting the seal's contact zone, which reduces the viscous friction. Furthermore, once the temperature is lowered below the glass transition temperature, there is a drop in the loss factor, i.e., a decrease in the viscoelastic losses in the elastomer. Both effects result in the observed steep drop of the friction torque after cooling the contact zone down below 0 °C. It is worth noting that the poor lubrication of the sealing contact may cause deeper counterface wear tracks and increased seal lip wear, as observed in long-term tests carried out on a different test rig where the lubricating oil was cooled down to -15 °C [1].

Under the conditions described above, the viscous friction in the contact zone declines and we may therefore attribute the observed friction to largely Coulomb-type boundary friction. This is supported by Figure 5, which shows that, when the rotation speed is altered, the friction does not change, as would be the case when assuming a viscous lubricant behaviour.

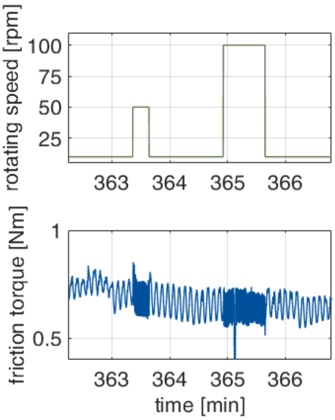

Figure 5: Friction torque in speed step experiment, contact temperature: approx. -40 °C

Despite the frictional torque maintaining a consistent level, it shows increased fluctuations and instabilities compared to the uncooled state. Notably at extremely low speeds below 20 rpm and contact temperatures ranging from -50 to -40 °C, intense vibrations and noise emissions were detected. Interestingly, under these conditions, the frictional torque decreased by more than 50 % compared to the levels observed when no vibrations were present. This effect stopped once the shaft was accelerated to 200 rpm.

3.2 Ice build-up and influence of condensate on the lubrication condition

In the course of each experiment, ice formed on the test rig, as shown in Figure 6. At the end of an experiment, while the test rig was heating up again, and soon after this ice started to melt, the friction torque suddenly dropped to a considerably lower level. After a certain period, it returned to its original level. An example for this phenomenon is shown in Figure 7.

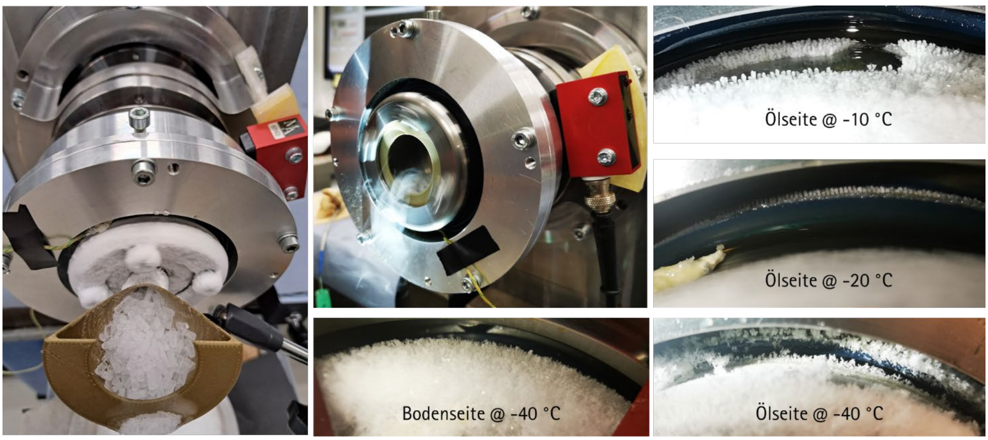

Figure 6: Ice build-up during the experiments

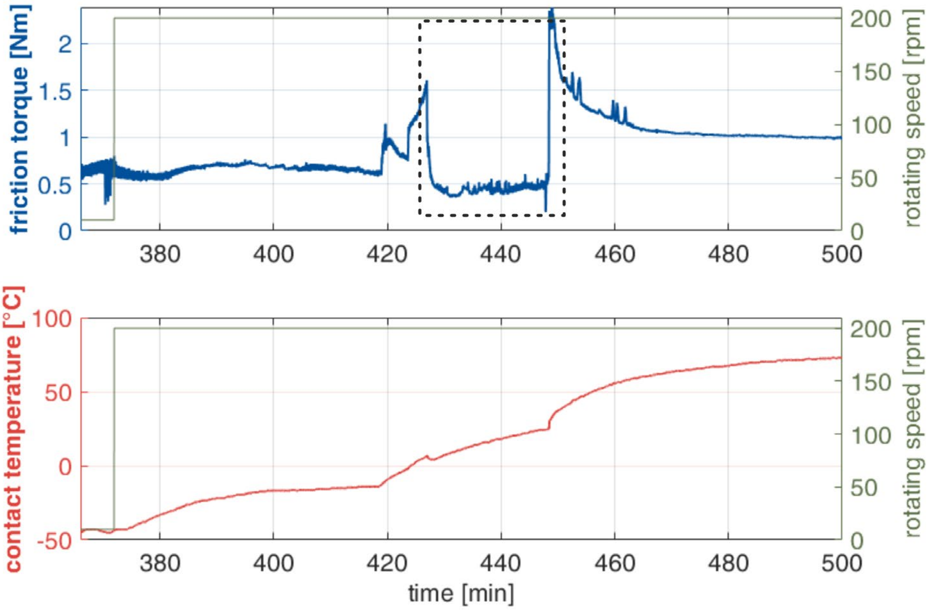

Figure 7: drop in the friction torque during the heat-up phase; NBR, PG ISO-VG 220

This behaviour indicates that water entered into the air side of the sealing contact and mixed with the lubricant within the contact zone, thus lowering its viscosity. After the water was pumped onto the oil side by the seal, the friction torque returned to its initial level and the initial lubricating state was restored.

It deserves attention that this effect was exclusively observed in NBR seals. In contrast, FKM seals did not exhibit a similar behaviour on their own, but the effect could be induced by actively injecting water into the air side of the sealing contact. This effect might, therefore, be related to a different wettability of FKM and NBR seals.

3.3 Influence of extremely low temperatures on the seal

At the end of each experiment, the cooling was stopped, allowing the systems to stabilize and return to their initial thermal steady-state conditions. In this state, all experiments showed similar friction torque and contact temperature levels as initially recorded before cooling down the sealing contacts. This indicates that, although having been subject to impaired or even starved lubrication when operated at extremely low temperatures, the lip seals were not damaged during the tests.

4 Conclusion

Using a novel low-temperature radial lip seal test rig, the behaviour of radial lip seals made out of NBR and FKM was studied at contact temperatures as low as approx. -50 °C.

It was observed that, following an initial increase during the cooling phase due to the lubricant's increasing viscosity, the friction torque at low contact temperatures finally reached levels comparable to those observed during uncooled steady-state operation, and that the friction of the sealing system evidently transitioned from viscous lubricant friction to Coulomb-type boundary friction.

In addition to this observation, it was seen, that under specific conditions, condensate could enter into the sealing contact and alter the lubrication mode. The impact of water within the sealing contact zone on the lip seals' behaviour will be explored in future research.

5 Acknowledgements

The authors gratefully acknowledge the support of the Research Association for Drive Technologies (FVA) who funded this research.

6 References

[1] Mohaupt, M., Amro, M., Schollmayer, T., Wennehorst, B. Dr., Poll, G. Prof. u. Thielen, S. Prof.: Tieftemperaturverhalten von Radialwellendichtringen. Forschungsvorhaben Nr. 895 der FVA / Forschungsvereinigung Antriebstechnik e.V. Frankfurt a.M. 2024

[2] Engelke, T.: Einfluss der Elastomer-Schmierstoff-Kombination auf das Betriebsverhalten von Radialwellendichtringen. Dissertation. Gottfried Wilhelm Leibniz Universität Hannover 2011

7 Authors

Leibniz University Hannover, Institute of Machine Design and Tribology (IMKT)

An der Universität 1, 30823 Garbsen, Germany

Mousa Amro, M. Sc., amro@imkt.uni-hannover.de

Dr.-Ing. Bengt Wennehorst, wennehorst@imkt.uni-hannover.de

Prof. Dr.-Ing. Gerhard Poll, poll@imkt.uni-hannover.de

https://doi.org/10.61319/GZ9WGC2O

Stochastic analysis on tribological behaviour of radial shaft seals with focus on lubricants

Yongzhen Lin, Ringo Nepp, Matthias Kröger, Stefanie Haupt

This study deals with a methodical interpretation into the complex landscape of the tribological behaviour of Radial Shaft Seals (RSS) using dynamic investigations focusing on the influence factor lubricant. The lubricant has been identified as one of the main drivers for the tribological behaviour of RSS, especially due to its chemical structure and physical properties such as viscosity. This study evaluates the impact of lubricants with different chemical structure but similar viscosity on the tribological behaviour of RSS, which allows to gain a deeper understanding of the further physical properties of lubricants. More specifically, the tribological performance of different types of lubricants have been examined on different RSS materials. Thereby, the rotational speed has been varied in relevant ranges. Using stochastic calculus analysis, the tribological behaviour of RSS with lubricants can be evaluated in more detail. The aim of the extensive investigations is to provide a basis for future, more in-depth research into understanding on the tribological behaviour of RSS as well as predictions for specific classified working environments such as minimal lubricant condition, high temperature, etc., for the different RSS systems.

1 Introduction

In the modern industry the application of the combination of Radial Shaft Seal (RSS) with minimal lubrications, such as grease and oil, has been widely developed and utilized, as well as widely researched in the scientific field [1] [2]. The RSS, the shaft as well as the counter surface and the applied lubricant form a specific tribological system [3]. The functional task of the simplified RSS is to avoid fluid leakage [3]. A utilized combination of the RSS and the correctly selected lubricant should help to avoid the irregular wear and extend the service lifetime of the RSS. This work is about to gain a better understanding of the tribological behaviour on different possible combinations of RSS and lubricants, especially how the lubricants with similar physical properties such as viscosities reflect on the tribological behaviours of RSS. In addition, the physical properties of lubricants with similar viscosities are about to be evaluated and discussed using stochastic analysis.

2 Test Procedure and Test Material

In this chapter, the test procedure, or more precisely the test rig and the applied test materials will be introduced. A specially designed RSS test rig is available at the Institute for Machine Elements, Design and Manufacturing for the experimental investigations based on the minimal lubrication principle. Other than that, specifically applied test materials such as the RSS parts and the lubricants are studied according to the minimal lubrication principle. The selection of determinant factors on RSS and lubricants is introduced.

2.1 Test Setup for Tribological Measurement

The tribological measurement in this study has been investigated on a self-developed test rig at the institute, which has been used for many previous friction performance measurements [1] [2]. Specifically, the friction performance parameters of a RSS system such as torque and temperature can be measured with different operating conditions. The test rig includes the fundamental components is described in Figure 1. This test rig was used to collect the significant measurement data for this work.

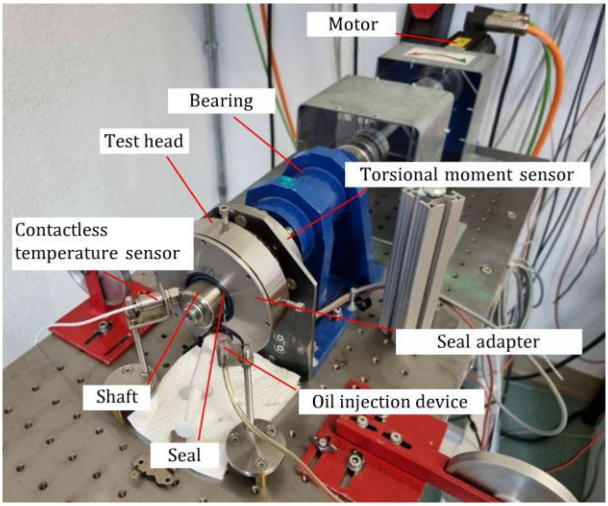

Figure 1: Test rig with sufficient components.

As shown in Figure 1, the main components of the test rig are the motor, bearing, test head including the torsional moment sensor, and the counter face. The RSS is mounted with a seal adapter. The oil injection device and a contactless temperature sensor are placed on the sides with defined distance onto the contact area. During the tests, the oil injection device provides continuously certain amount of lubricants into the contact area.

2.2 Test Material

This chapter is about to introduce the applied materials, more specifically the RSS, the shaft surface and the lubricant.

2.2.1 Radial Shaft Seals and Shaft Counter Surfaces

A specific RSS with a helical spring but without the dust lip from Freudenberg (in Simmerring® BAUM form) has been investigated in this work. This typical RSS is manufactured according to the German standard DIN 3760 [4]. The RSS elements in this work vary in two different materials: seal A is fluoro rubber (FKM) and seal B is nitrile butadiene rubber (NBR), as well as in two different dimensions: 45x75x7 and 38x52x7 ($d \times D \times B$ $[mm]$). Though the comparison between different dimensions is not focused in this work, which has been analysed in previous works [5] [6].

The shaft part in this tribological system serves as the counterface. In this work two different counter faces have been applied. One is a plunge ground shaft made of bearing steel 42CrMo4 specifically for RSS with dimension 45x75x7, while the other is C45R specifically for RSS with dimension 38x52x7. There is no focusing on the comparison of the potential difference caused by different counter faces in this work. This influence factor has been deeply analysed in different aspects in other researches [7] [8].

2.2.2 Lubricants

As it has been researched in the recent years, lubricants have a significant influence on the tribological behaviours of RSS under minimal lubrication environment [1]. In the modern industry, the variations of lubricants are basically classified into nature mineral oil and synthetic oil. More and more synthetic oils have been developed with sustainable and environment friendly considerations. In order to improve the synthetic oil development meeting industrial operation demands, the functional aspects of lubricants need to be examined for stabile tribological behaviours. Based on the applications, synthetic oil should perform stable in higher temperature range such as above 90 °C. In this study mineral oils and synthetic oils with similar physical properties are applied for the specific tribological behaviour analyzing.

The applied lubricants are listed in Table 1. Basically, there are two types of mineral oils and 5 different synthetic oils. The important relevant parameters are shown in Table 1. The synthetic oils share one ISO VG class, while the mineral oils have a higher ISO VG class. The ISO VG class describes the relative temperature dependence of lubricants, which significantly affects the tribological behaviour of RSS.

Table 1: Physical properties of the applied oils with short labels.

Label	Description	Kinematic viscosity [mm²/s]		ISO VG	Density (by 20°C) [g/cm³]
		40°C	100°C		
M1	Mineral oil	320	24	320	0.9
M2	Mineral oil	345	25	320	0.9
PAO1	Poly-alpha olefin oil	234	30	220	0.85
PAO2	Poly-alpha olefin oil	234	22	220	0.85
PG1	Polyglycol oil	220	41	220	1.06
PG2	Polyglycol oil	220	41	220	1.06
PG3	Polyglycol oil	220	41	220	1.06

From the table, it’s significant to realize that the oils in each group (M_i, PAO_i or PG_i) share similar physical properties such as kinematic viscosities or densities. Slight differences between the oils in each group are caused by production processes and potentially different proportions of additives, etc., which lead to the hypothesis of this work if the potential different tribological performances are recognisable.

2.3 Measuring Procedure

In this work, the operational variations in the investigations are partially located on different rotational speed profiles. Investigations with different approach profiles have been analysed in a previous study and provided significant results under simple variable method [5]. The specifically applied rotational speed profiles for this work under two or multi variables are listed in Table 2. The measurement results after operating with different rotational speed profiles show significant difference among the individual RSS and lubricant combinations. The different combinations show different tribological performances after operation, which will be analysed in next section.

Table 2: Applied different approach profiles with short labels.

Label	Description	Diagram
E1	Run in profile	2 hours constant high rotation speed
Testing	Short testing profile	Added up rotation speed from minimal to defined maximal n_{max} with short time stepping rate
V_i	Long added up profile	Added up rotation speed from minimal to limit n_{lim} with long time stepping rate

As it's shown in Table 2, the applied approaches can be generally sorted into three groups: run in, short testing and long added up profiles. Approach E1 is performed in 2 hours constantly with the highest rotational speed, which services as running-in process of each new RSS part.

In order to generate the following different rotation speed profiles V_i, one particular testing profile has been introduced to define the maximum and the limit rotation speed. In the testing approach, the rotation speed is added up after each short time period, starting at from minimum to a defined maximal n_{max}. In each step, the rotation speed remains constant in order to observe short time tribological performance and to observe the difference after rotation speed change.

Approaches V_i are all added up profiles from minimum to a defined limit rotation speed n_{lim} with different relative stepping rates. With help of these different approaches in this working, it is possible to identify the different tribological performances of RSS.

3 Results and Discussion

3.1 Measurement Analysis

In the very beginning, approach testing has been used to set a limit rotation speed n_{lim} for further research. Figure 2 shows the measurement results from possible variable combinations among RSS and lubricants. In the diagram the torque developments varied very much from one combination to another. Especially the absolute values differ from each other strongly. This could be explained by the particular tribological behaviour of the combinations of RSS and lubricants. But the tendency of the torque development in the whole testing phase is quite similar. The most significant change in tendency occurs between t_i and t_j, while in one particular combination it occurs earlier between t_h and t_i. One the other hand, the temperature developments varied only slightly from each other till t_h. However, after t_i the tendency of the temperature development varies from each other very strongly.

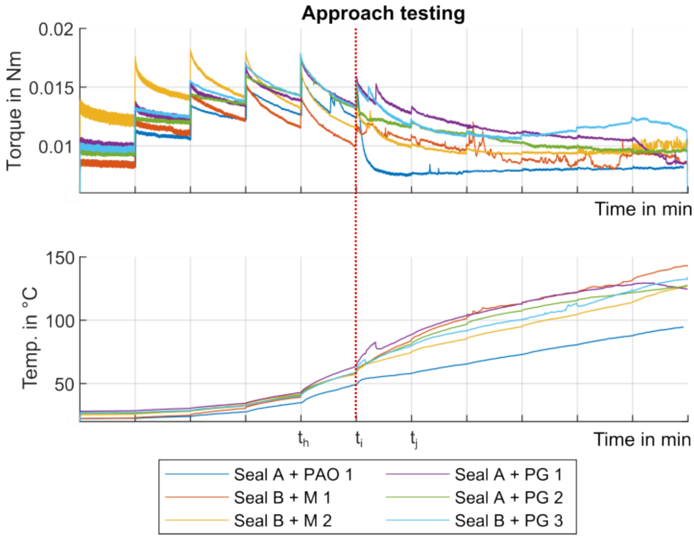

Figure 2: Determination of a limit rotation speed n_{lim}, Seal A – FKM, Seal B – NBR .

To keep the further research, more specifically the investigation process effective in short time, a limit rotation speed n_{lim} has been set for this study to observe the significant different tribological performances among different RSS and lubricant combinations.

After extensive investigations with different measurement setups, the measurement data could be analysed in various ways. In general, similar but in detail different developments on the tribological performance will be discussed in this following section. Figure 3 first shows the measurement results on two RSS rings applied with one specified operating condition (V_i) and with one particular lubricant.

As it's shown in Figure 3, with one particular rotation speed profile, two RSS parts with different materials displayed similar tribological performance. In this particular rotation speed profile, the rotation speed increases with defined ranges after one hour constantly running. In each testing, the developments of torque and temperature have been measured. In each constant rotation speed phase, the development of torque and temperature is significant recognizable, especially after each rotation speed change.

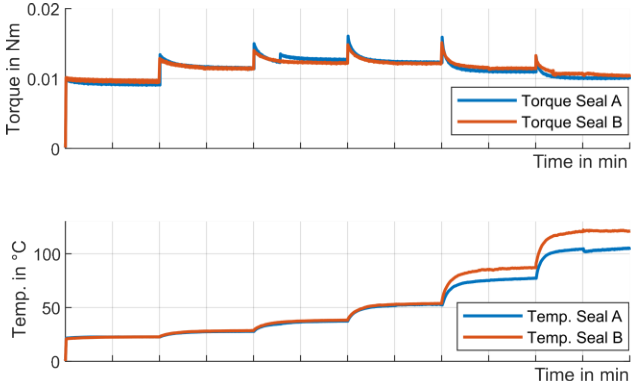

Figure 3: Friction performances from two different RSS, Seal A – FKM, Seal B – NBR, with lubricant PAO1.

On one hand, the development of torque increased immediately due to the break-away friction between the RSS and the shaft. The increasing of rotation speed causes momentary interaction onto the contact area. Along the time, rotation speed in one phase keeps constant. As a result, after the short time break-away, torque decreases to a steady state. This phenomenon in torque development will be changed till next rotation speed change.

On the other hand, the development of temperature presents firstly a climbing due to the increasing relative movement between the RSS and the shaft. Along the time, rotation speed in one phase keeps constant. As a result, the growth rate of temperature tends to be constant. Other than some minimal difference between two different RSS materials, the tribological performances are basically similar according to one rotation speed profile as input.

In Figure 3, some irregular peaks can be observed in torque and temperature development. Especially there is one peak in torque by seal A – FKM, meanwhile no effect on the temperature. On the opposite, friction oscillating can be observed by both different seals in the last time phase with correlated temperature oscillating. The correlation between torque and temperature development need to be further studied. [9]

In another case, the difference among different approaches has been analyzed with the help of Figure 4. The measurement results from seal A - FKM and PAO1 are shown with approach V1 in red, V2 in blue and V3 in black curves. The developments of temperature in three different approaches represents the changing in rotation speed inputs. The climbing in each phase is correlated with the adding up of rotation speed. On the opposite, the developments of torque are not correlated with the rotation speed inputs. Especially the development of torque from V1, has the lowest peak points in the first half time period compared with V2 and V3, but the highest peak points in the second half time period.

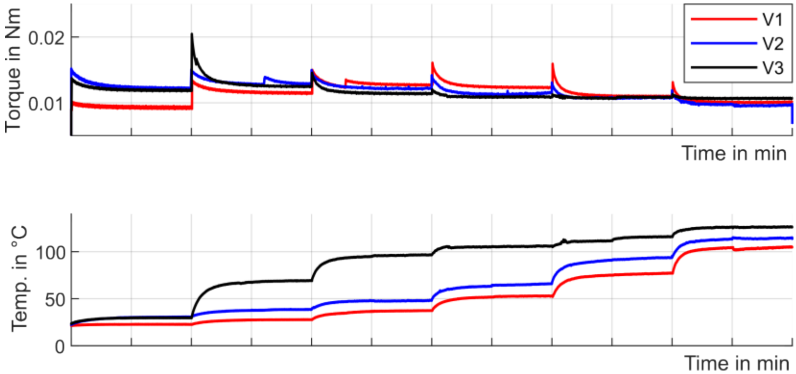

Figure 4: Friction performances from three different approaches V_i and with lubricant PAO1, Seal A – FKM. V1 = blue curve in Figure 3.

This phenomenon could not only be found by analysing on different seal materials, but also could be found by analyzing on different lubricants. In some particular cases, the tribological performance can not be correlated with influence factors such as different lubricants or different approaches. To find out the correlations more deeply in details, large number of investigations need to be implemented with diligent design of experiments.

3.2 Stochastic Analysis

In order to understand the tribological performance of RSS in more details with limited measurement signals, the measurement data will be analysed under aspects such as mean values, variance, tendency and distribution based on a stochastic analyse principle.

Figure 5 shows the distribution of torque and temperature on Seal A - FKM with one particular rotation speed profile and one particular lubricant. It is displayed for both systematic variables in the different time phases, or the constant rotation speed phases. As it is observed from the distributions of torque and temperature, it is clear to conclude that the torque distribution in each constant rotation speed phase stays mostly normal distributed. On the other hand, the temperature distribution shows a continuously increasing trend in the whole process as well as in each time phase.

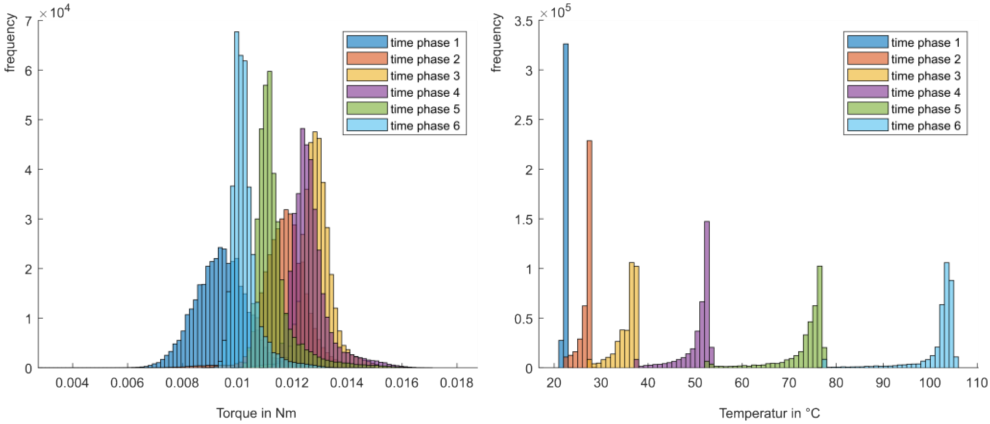

Figure 5: stochastic analyze from one approach with seal A - FKM, with lubricant PAO1 and rotation speed profile V1.

In both diagrams the y-axis represents the frequency of the measured value in torque or temperature. This could be used as a criteria of the stability of this tribological system. In the torque distribution, it could be observed that the frequency of the mean value (as well as the highest frequency in each time phase) of each time phase is higher one after another. On the other hand, the frequency of temperature is increasing in each time phase. However, the highest frequency of each time phase is decreasing, while the interval length in x-axis in each time phase is increasing. This could be interpreted as the slower temperature increasing in the whole time phases, even with smaller temperature changes. While the temperature changing in the final phases is mostly with quicker climbing and greater value changes.

In Figure 6 it’s shown the distribution of torque and temperature on seal B - NBR with the same rotation speed profile and the same lubricant. It could be observed that the distribution in torque and temperature from different seal materials has similar tribological developments and distributions. A slight difference can be observed in the absolute frequency value in torque distribution, especially in the last time phase. Also the trend in temperature distribution differs from the other seal material in Figure 5.

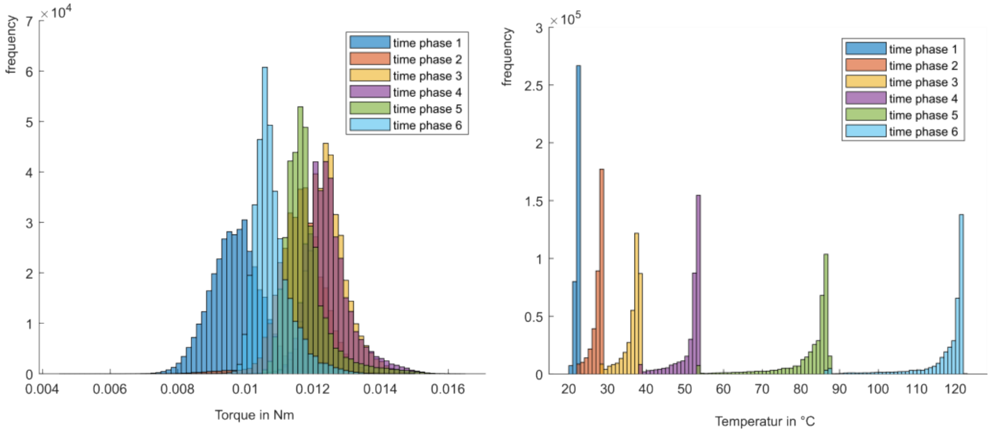

Figure 6: Stochastic analyze from one approach with Seal B - NBR, with lubricant PAO1 and rotation speed profile V1.

Another example in the stochastic analysis in comparison with different lubricants and with repeated runs is shown in Figure 7. Both diagrams show significant analyze results in different ways. In the left diagram, the comparison between different lubricants is presented in sub-figures in each time phase. From one particular rotation speed profile, the torque development as well as the distribution in the first two time phases are similar from one oil to another. But the torque development and distribution varies strongly in the next time phases. In the first two time phases, with lower temperature environment, the two PAO lubricants with similar physical properties present as well similar tribological performance on one particular RSS.

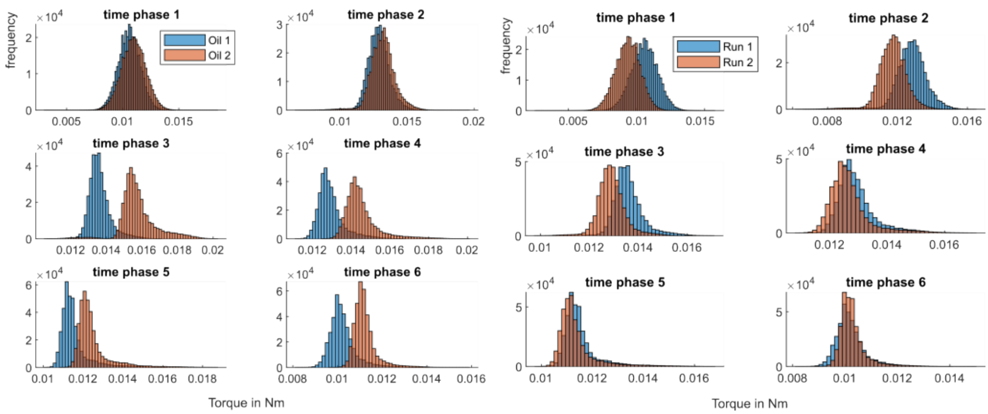

Figure 7: Stochastic analyze in comparison: Left 6 sub-figures: Seal A – FKM with PAO1 and PAO2. Right: Seal A – FKM with PAO1 with repeated runs.

In the right diagram, the comparison between repeated runs is presented as well in sub-figures in each time phase. As each testing set up is manually adjusted, there is a slight difference in the first half time phases. Since in these two repeated runs the set ups are identical, the torque development and distribution approaches from one to another. This could be interpreted as local minor difference in a generally similar situation.

4 Summary and Conclusion

In this work investigations with different combinations of RSS and various operating conditions have been carried out and the results have been analysed in different aspects, with the goal of deeper understanding on this particular tribological system, especially with the focus on lubricants. Among all the lubricants used in this works, which could be classified in 3 essential groups. In each group, the selected lubricants share similar physical properties. This work aims to figure out whether they present similar tribological performance as well. After a large number of investigations with different combinations, the measurement data were first analysed according to the testing process over time. Afterwards, the data has been analysed with different stochastic approaches.

In the end, it shows that different combinations of RSS and lubricants even if the lubricants have similar physical properties, can lead to different tribological performance on RSS. This phenomenon needs to be further studied to gain more in-depth knowledge about the tribological behaviour of RSS with different combinations of lubricants, as well as the potential predictions for special classified operating conditions to extend the potential lifetime.

5 Nomenclature

Variable	***Description***	***Unit***
B	Seal width	[mm]
d	Seal normal diameter	[mm]
D	Seal outer diameter	[mm]
M_d	Torque	[Nm]
n	Shaft rotation speed	[rpm]
n_{max}	Defined maximum shaft rotation speed	[rpm]
n_{lim}	Defined limit shaft rotation speed	[rpm]
T	Temperature	[K]
t	Time	[min]
v	Velocity	[m/s]
ρ	Density	[g/cm^3]
ν	Kinematic viscosity	[mm^2/s]
η	Dynamic viscosity	[Pas]

Abbrev.	*Description*	
E_i; V_i	Approach label	
FKM	Fluoro rubber	
NBR	Nitrile butadiene rubber	
M_i	Mineral oil label	
PAO_i	Poly-alpha olefin oil label	
PG_i	Polyglycol oil label	
RSS	Radial shaft seal	
t_h, t_i, t_j	Time variables	[min]

6 References

[1] C. Berndt, Tribologie von Radial-Wellendichtungen, BoD–Books on Demand, 2019.

[2] R. J. Teichert, Tribologie von fettgeschmierten Radialwellendichtungen, 2022.

[3] W. Tietze, Handbuch Dichtungspraxis. 3.Aufl., Essen: Vulkan-Verl., 2003.

[4] Deutsches Institut für Normung e.V. (Hrsg.), *DIN 3760:1996-09: Radial-Wellendichtringe,* Berlin: Beuth, 1996.

[5] Y. Lin, R. Nepp, J. Gerschler and M. Kröger, "Radial shaft seal with different relative velocities and on a 3D printed counter surface," *Industrial Lubrication and Tribology,* pp. 758-764, 75(7) 2023.

[6] M. Kröger, R. Teichert and Y. Lin, "Scaling of radial seals - Safely go into series production," in *JAHRBUCH Dichten. Kleben. Polymer.*, ISGATEC, 2024, pp. 80-90.

[7] M. Schulz, F. Bauer and W. Haas, "Einfluss supergefinishter Dichtungsgegenlaufflächen auf die Funktion von Radial-Wellendichtungen," in *19th ISC*, Stuttgart, 2016.

[8] M. Baumann, Abdichtung drallbehafteter Dichtungsgegenlaufflächen-Messung, Analyse, Bewertung und Grenzen, Stuttgart: Institut für Maschinenelemente, 2017.

[9] M. Kröger, Y. Lin, R. Nepp und S. Haupt, „Observation of local tribology of shaft seals," in *Arnold Tross Colloquium*, Hamburg, 2024.

7 Authors

TU Bergakademie Freiberg, Institute for Machine Elements, Design and Manufacturing (IMKF)

Agricolastraße 1, 09599 Freiberg, Germany:

Yongzhen Lin, M. Sc., ORCID 0000-0002-0700-0914, Yongzhen.Lin@imkf.tu-frei berg.de

Dr.-Ing. Ringo Nepp, ORCID 0009-0001-7837-258X, Ringo.Nepp@imkf.tu-freiberg.de

Univ.-Prof. Dr.-Ing. Matthias Kröger, ORCID 0000-0002-4132-8323, Kroeger@imkf.tu-freiberg.de

Stefanie Haupt, M. Sc., ORCID 0009-0006-3015-4619; Stefanie.Haupt@klueber. Com

https://doi.org/10.61319/4SNT0D7B

Performance Analysis of Radial Shaft Seals in Non-Stationary Rotational Movements

Lenine M. de C. Silva, Yvo Stiemcke, Tim Schollmayer, Oliver Koch, Stefan Thielen

This work aimed to investigate the impact of non-stationary rotational movements on radial shaft seals (RSS). To explore various operational scenarios, a set of experiments was designed, and conducted using the MEGT High Acceleration Test Bench. The tests were realized analysing the development of negative pressure in the intermediate cavity between main and dust lip and observing the influence of the variation of several parameters in this negative pressure appearance. The results showed the occurrence of oil leakage under short oscillation angles and concluded that the negative pressure build-up might change the sealing geometry as well as the followability of the RSS to the movement leading to failure of the sealing lip.

1 Introduction

The number of applications involving rotational non-stationary movements has significantly increased in the past decade. Such dynamic rotational oscillations are often found in applications such as robotic arms. These dynamic rotational oscillations correspond to high levels of acceleration along with frequent changes in the direction of rotation. However, the impact of these oscillations on radial shaft seals (RSS) remains unknown [1] [2] [3] [4]. In practical applications, mineral oil has been found in undesirable situations such as in groceries [5] [6] [7] [8] [9] [10] [11]. Machines from the food production chain for instance work under critical operating conditions being frequently washed with hot water jets. The avoidance of leakage in such situations is primordial and the usage of RSS with dust lip to protect the sealing lip might be recommendable.

A initial study about non-stationary rotational movements has tested several work conditions such as RSS with and without dust lip, RSS with and without garter spring, RSS with and without grease in intermediate cavity, casing completely filled up and up to the middle of the shaft of oil, rolled and ground shafts, and four different types of curves, which the motors should perform during the test, in order to reproduce the non-stationary rotational movements. The study concluded that the use of a contacting, non-vented dust lip is essential for the occurrence of leakage [12] [13]. Although, the role of the dust lip during the non-stationary rotational movements remained unknown.

A later work proposed then an investigation about the role played by a contacting dust lip of an RSS in the non-stationary rotational movements. The study developed a mechanism capable to carry out reproducible pressure measurements directly from the intermediate cavity. These measurements were realized with the aid of pressure sensor and a medical needle, which could be always positioned in the middle of the dust lip to prick and have access to the intermediate cavity of the RSS

(C.f.Figure 2). The work observed that a negative pressure is build-up in the intermediate cavity during the non-stationary rotational movements and that this negative pres- sure deforms the intermediate cavity as well as change the angles formed between the sealing lip and the dust lip with the shaft [14]. The results of this work represented a substantial advancement in the explanation of the reasons why the RSS without dust lip or with a vented dust lip do not present any sign of leakage, and in some cases RSS with a non-vented dust lip produced leakage. However, the non-station- ary rotational movements involve several dynamic variables as well as variables in- herent to the application of an RSS in a mechanical system, whose influence on this negative pressure appearance remain unknown. Such analysis of several parame- ters in various levels of intensity has been described by [15] and might be suitable for practical applications as in the sealing technology.

This current work merges the conclusions drawn by the prior studies carrying out a series of experiments, which vary systematically the work parameters along with the realization of pressure measurements during the tests. The main objective of this work is to point out the influence of the working parameters at different levels in the formation of negative pressure in the intermediate cavity of RSS with contacting dust lip as well as in the occurrence of leakage during non-stationary rotational movements.

2 Materials and methods

To investigate different operational conditions and evaluate the impact of parameter changes on sealing performance during the non-stationary rotational movements, a series of tests was structured. These tests were executed on the High Acceleration Test Bench at MEGT, which features dual test cells directly coupled to two servomotors, enabling dynamic rotational oscillation. In addition, a device was designed to measure the pressure in the intermediate cavity using a pressure sensor and a medical needle. The experiments varied the following parameters: (*i*) the acceleration at the sealing contact; (*ii*) the oscillation angle; (*iii*) the greasing level in the intermediate cavity; and (*iv*) the curve type used in the oscillation.

2.1 The High Acceleration Test Bench

The operating condition of non-stationary rotational movements were executed by the MEGT's High Acceleration Test Bench. This test bench consists of two test cells to which two servo motors are coupled. Each test cell consists of a metallic housing with a driving shaft that is supported by two bearings in an O-arrangement and is lubricated in an oil sump. Each test cell is then sealed with one test shaft and one RSS per side (see Figure 1).

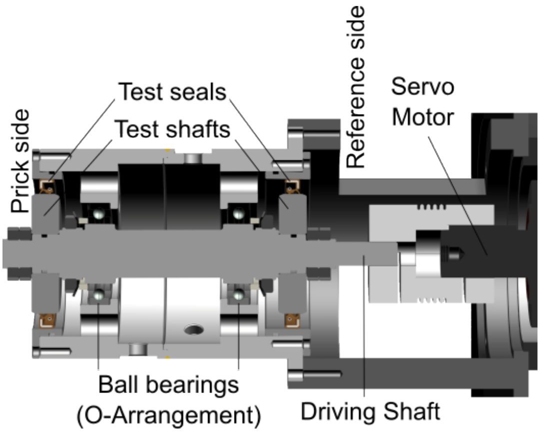

Figure 1: Section view of a test cell

2.1.1 Pressure Measuring Device

In addition to the High Acceleration Test Bench, a pressure measuring device was developed with the aim of measuring the negative pressure, which is formed in intermediate cavity during the non-stationary rotational movements. This device consists of two aluminium profiles for adjusting the vertical position, hand screws in the horizontal position to adjust the angle of the sensor with the horizontal line and a pressure sensor connected with a medical needle that has a diameter of Ø 0.4 mm (see Figure 2). Once the medical needle is positioned in the middle of the dust lip, a linear spindle needs to be rotated by hand to prick the dust lip and connect the pressure sensor with the intermediate cavity of the RSS.

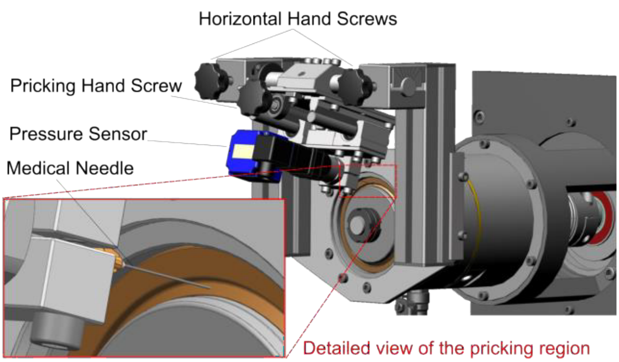

Figure 2: Pressure Measuring Device

After the prick, the puncture area needs to be sealed with silicone sealant, to avoid pressure equalization during the tests. The sealant fully dries after 24 hours, and then the High Acceleration Test Bench is ready for tempering the test cells. The pressure data were recorded during the tests.

2.1.2 Tempering System

Besides the pressure measuring device, the test bench is equipped with a tempering system, whose purpose is to ensure that the oil sump works with the operating temperature of 60°C. Each cell was equipped with a tempering sleeve, which can temper the housing uniformly minimizing the risk of local overheating. In addition, the cells are equipped with a safety system that switches off the entire test bench if a cell temperature reaches 120°C.

2.2 Work Method

The work executed 18 experiments with the High Acceleration Test Bench, each lasting up to 400 hours. The experiments varied several working parameters systematically, to determine the influence of each parameter on the sealing performance. The selected working parameters were: (*i.*) the cycle type, which is the curve that has to be followed by the motor in order to reproduce the non-stationary movements (see Figure 3); (*ii.*) the linear acceleration-maximum between the sealing ring and the shaft (i.e. at the sealing contact); (*iii.*) the angle of amplitude in which the shaft oscillates; and (*iv.*) the degree of greasing, which determines the proportion of grease in the intermediate cavity.

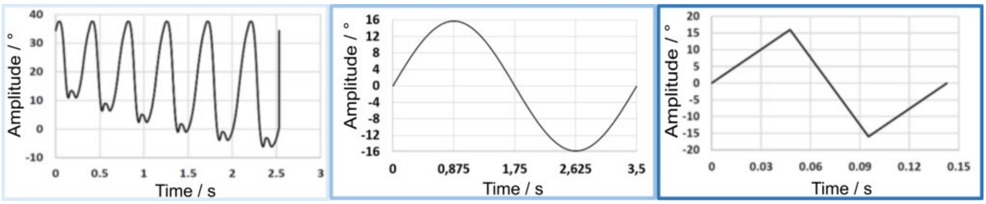

Figure 3: Representation of the cycles used to reproduce the non-stationary rotational movements. From left to right: industrial curve, sine curve, triangular curve.

In addition, the values of each parameter variation were planned according to the results obtained by [12] [13], and each parameter was varied at three levels (light, medium and heavy) to cover the most various situations in non-stationary rotational movements (see Table 1).

Table 1: Parameters with their 3 levels of values variation.

Parameters	Settings		
RSS Model	RSS without garter spring, with dust lip, material 75 FKM 585		
Counter surface	Rolled		
Oil Sump	Volume=1000 ml; full filled test cell; Temperature=60°C		
Cycle type	Industrial curve	Sine curve	Triangular curve
Acceleration / m/s²	80	160	240
Angle of Amplitude / °	5	10	15
Degree of Greasing / %	30	50	70

The complete variation of 4 factors in 3 levels would lead to 81 different combinations of tests. Considering that each test could last up to 400 hours, the realization of 81 tests would be a time-consuming process. Therefore, some combinations were chosen in order to cover the most challenging situations with some variations. The detailed test plan can be found in Table 2.

Table 2: Test plan for parameter variations test with non-stationary rotational movements

Test	Cycle	Amplitude/ °	Acceleration / m/s²	Greasing / vol%	Test	Cycle	Amplitude/ °	Acceleration / m/s²	Greasing / vol%
T1	Indus.	5	160	30%	T10	Sine	20	160	30%
T2	Triang.	15	240	30%	T11	Sine	10	160	50%
T3	Triang.	15	240	70%	T12	Sine	5	160	50%
T4	Triang.	15	240	50%	T13	Triang.	10	160	50%
T5	Triang.	10	240	70%	T14	Sine	5	240	70%
T6	Triang.	5	240	70%	T15	Indus.	10	160	50%
T7	Triang.	15	160	70%	T16	Indus.	5	80	70%
T8	Triang.	15	80	70%	T17	Sine	15	160	50%
T9	Sine	20	160	70%	T18	Sine	10	80	50%

Each test lasted up to 400 hours, and the measurement of the pressure in the intermediate cavity was conducted during the tests as well as the monitoring of leakage in both sides of the test cells.

Considering the factorial design method presented by [15] to analyse different variables ranging from different levels of intensity, the test plan presented in Table 2 would be classified as fractioned factorial design 3^4. A fractioned factorial design 3^4 has 4 factors varying in 3 different levels of intensity and its analysis is conducted assuming values of -1, 0 and 1 for the lowest level, the intermediate and the highest level of intensity of each factor respectively to analyse the main effect of each factor. The Table 3 considers also the parameters cycle, angle of amplitude, acceleration and greasing in the intermediate cavity as the factors I, II, III and IV respectively. In order to analyse de interaction effect between two factors, the product of the notation -1, 0 and 1 of the parameters' levels within the combinations should be considered.

Table 3: Fractional factorial design 3^4 for the non-stationary rotational movements' tests.

Test	I	II	III	IV	IxII	IxIII	IxIV	IIxIII	IIxIV	IIIxIV
T1	-1	-1	0	-1	1	0	1	0	1	0
T2	1	1	1	-1	1	1	-1	1	-1	-1
T3	1	1	1	1	1	1	1	1	1	1
T4	1	1	1	0	1	1	0	1	0	0
T5	1	0	1	1	0	1	1	0	0	1
T6	1	-1	1	1	-1	1	1	-1	-1	1
T7	1	1	0	1	1	0	1	0	1	0
T8	1	1	-1	1	1	-1	1	-1	1	-1
T9	0	1	0	1	0	0	0	0	1	0
T10	0	1	0	-1	0	0	0	0	-1	0
T11	0	0	0	0	0	0	0	0	0	0
T12	0	-1	0	0	0	0	0	0	0	0
T13	1	0	0	0	0	0	0	0	0	0
T14	0	-1	1	1	0	0	0	-1	-1	1
T15	-1	0	0	0	0	0	0	0	0	0
T16	-1	-1	-1	1	1	1	-1	1	-1	-1
T17	0	1	0	0	0	0	0	0	0	0
T18	0	0	-1	0	0	0	0	0	0	0

The calculation of the main effect and the interaction effect shall be conducted as follows:

$E = \overline{y_+} - \overline{y_-}$ (1)

which,

E: the effect, and

$\bar{y}_{+\,or-}$: the mean of the response variable for the negative or positive variation

3 Results

The results confirmed the expectation of a negative pressure buildup in the intermediate cavity during the non-stationary rotational movement tests (e.g. see Figure 4). Moreover, the results showed different responses according to the variations applied on the parameters. Table 4 summarizes the tests carried out presenting the following information:

1. the maximum negative pressure during the test,
2. the time required to reach the maximum negative pressure during the test,
3. the highest net flow rate during the test,
4. the time required to reach the highest net flow rate during the test,
5. whether there was leakage on the pricking side or on the reference side.

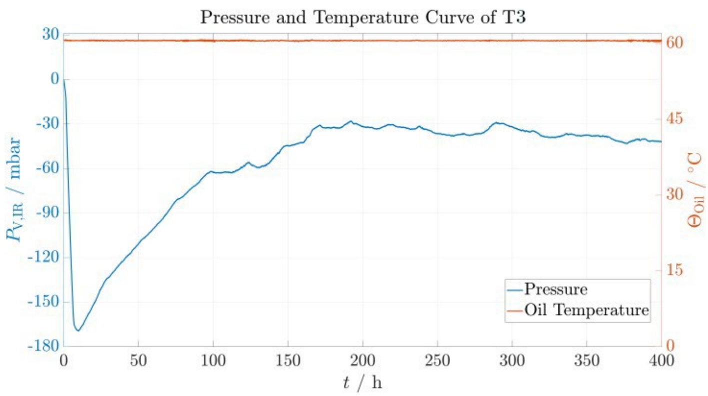

Figure 4: Pressure curve of T3

The net flow rate mentioned in point 3 is the volume of air per unit of time that was aspirated out of the intermediate cavity during a test. It was determined based on the theoretical amount of air that must be aspirated to create the measured pressure change [14]. Suctioning this volume of air creates a negative pressure in the intermediate cavity.

Table 4: Parameters and results from the non-stationary rotational movements' tests

Test	Cycle	Amplit. / °	Accelerat. / m/s²	Greasing / vol%	Pressure		Net Flow Rate		Leakage	Side
					Max. / mbar	Time / h	Max. / m³/h	Time / h		
T1	Indus.	5	160	30%	-15	321	3	45	-	-
T2	Triang.	15	240	30%	-41	137	18	1	-	-
T3	Triang.	15	240	70%	-169	12	47	4	Grease	Prick
T4	Triang.	15	240	50%	-21	17	5	1	-	-
T5	Triang.	10	240	70%	-73	66	6	4	Grease	Ref.
T6	Triang.	5	240	70%	-47	102	6	287	Oil	Both
T7	Triang.	15	160	70%	-98	25	16	2	-	-
T8	Triang.	15	80	70%	-54	124	4	109	Grease	Ref.
T9	Sine	20	160	70%	-177	24	24	0	-	-
T10	Sine	20	160	30%	-76	192	10	54	-	-
T11	Sine	10	160	50%	0	89	0	89	-	-
T12	Sine	5	160	50%	-44	28	7	1	Oil	Ref.
T13	Triang.	10	160	50%	-57	48	7	1	-	-
T14	Sine	5	240	70%	-67	37	6	6	-	-
T15	Indus.	10	160	50%	-39	164	7	0	-	-
T16	Indus.	5	80	70%	-115	90	8	315	-	-
T17	Sine	15	160	50%	-16	186	5	157	-	-
T18	Sine	10	80	50%	-43	335	6	1	Grease	Both

3.1 The Most Negative Pressures: T3, T9 and T16

Considering that the negative pressure in the intermediate cavity is an important variable to be analysed, since it changes the geometry of the intermediate cavity as well as the angles from the dust and the sealing lip [14], the T3, T9 and T16 were the tests, which presented the most negative pressures and so should be highlighted among the other tests. The Table 5 exhibit the mentioned tests with their applied parameters along with their respective results in terms of negative pressure, net flow rate and leakage.

Table 5: Parameters and results from T3, T9 and T16

Test	Cycle	Amplitude / °	Acceleration / m/s²	Greasing / vol%	Pressure		Net Flow Rate		Leakage	Side
					Maximum / mbar	Time / h	Maximum / mm³/h	Time / h		
T3	Triang.	15	240	70%	-169	12	47	4	Grease	Prick
T9	Sine	20	160	70%	-177	24	24	0	-	-
T16	Indus.	5	80	70%	-115	90	8	315	-	-

The comparison between the applied parameters on T3, T9 and T16 shows that:

1. each test used a different cycle from the other two tests,
2. T9 applied the greatest angle of amplitude, as T16 used the smallest angle of amplitude among the others,
3. T3 applied the highest acceleration at the sealing contact, as T16 applied the lowest acceleration among the others, and
4. all three tests applied the highest level of greasing in the intermediate cav- ity.

The comparison between the results obtained on T3, T9 and T16 shows that:

1. T9 presented the greatest negative pressure among the others test, which is 8 mbar greater than T3 and 62 mbar greater than T16,
2. the time of achievement in T3 (12 hours) is two times shorter than T9 and 7,5 times shorter than T16, and
3. the net flow rate values are inversely proportional to time of achievement.

3.2 The Oil Leakage Cases: T6 and T12

A similar analysis has been made considering the leakage cases, i.e. T6 and T12. Table 6 displays the specified tests along with the parameters used and their corresponding outcomes, including negative pressure, net flow rate, and leakage occurrences.

Table 6: Parameters and results from T6 and T12.

Test	Cycle	Amplitude / °	Acceleration / m/s²	Greasing / vol%	Pressure		Net Flow Rate		Leakage	Side
					Maximum / mbar	Time / h	Maximum / mm³/h	Time / h		
T6	Triang.	5	240	70%	-47	102	6	287	Oil	Both
T12	Sine	5	160	50%	-44	28	7	1	Oil	Ref.

The comparison between the applied parameters on T6 and T12 shows that:

1. both tests applied the same angle of amplitude, and,
2. theoretically, T6 applied in parameters cycle, acceleration and greasing one level more critical than the parameters applied on T12.

The comparison between the results obtained on T6 and T12 shows that:

1. the difference of maximal negative pressure developed by both tests is 3 mbar and both tests presented similar pressure curves,
2. the difference of maximal net flow rate achieved by both tests is 1 mm³/h, and
3. T6 produced oil leakage in both sides of the test cell, as T12 produced oil leakage at reference side of the test cell.

3.3 The Factorial Design Analysis of the Results

In order to calculate the main effects and the interaction effects the Table 3 was filled with the results obtained with the realized tests. The correlation between fac- tors, interactions and results can be visualized in Table 7. The application of the Equation (1) for the main effects of each factor and for the interactions' effects be- tween fac- tors can be visualised in Table 8 and Table 9 respectively.

Table 7: Fractional factorial design 3^4 for the non-stationary rotational movements' tests and their results.

Test	I	II	III	IV	Ix II	Ix III	Ix IV	IIx III	IIx IV	IIIx IV	P	t_p	N	t_N
T1	-1	-1	0	-1	1	0	1	0	1	0	-15	321	3	45
T2	1	1	1	-1	1	1	-1	1	-1	-1	-41	137	18	1
T3	1	1	1	1	1	1	1	1	1	1	-169	12	47	4
T4	1	1	1	0	1	1	0	1	0	0	-21	17	5	1
T5	1	0	1	1	0	1	1	0	0	1	-73	66	6	4
T6	1	-1	1	1	-1	1	1	-1	-1	1	-47	102	6	287
T7	1	1	0	1	1	0	1	0	1	0	-98	25	16	2
T8	1	1	-1	1	1	-1	1	-1	1	-1	-54	124	4	109
T9	0	1	0	1	0	0	0	0	1	0	-177	24	24	0
T10	0	1	0	-1	0	0	0	0	-1	0	-76	192	10	54
T11	0	0	0	0	0	0	0	0	0	0	0	89	0	89
T12	0	-1	0	0	0	0	0	0	0	0	-44	28	7	1
T13	1	0	0	0	0	0	0	0	0	0	-57	48	7	1
T14	0	-1	1	1	0	0	0	-1	-1	1	-67	37	6	6
T15	-1	0	0	0	0	0	0	0	0	0	-39	164	7	0
T16	-1	-1	-1	1	1	1	-1	1	-1	-1	-115	90	8	315
T17	0	1	0	0	0	0	0	0	0	0	-16	186	5	157
T18	0	0	-1	0	0	0	0	0	0	0	-43	335	6	1

Table 8: Main effects of the factors on the response variables.

Main Effects	P / mbar	t_P / h	N / mm³/h	t_N/ h
Cycle	-13,67	-127,3	7,62	-68,87
Ampli.	-23,9	-25,97	10,125	-89,8
Accel.	1	-121,17	8,67	-91,17
Greas.	-56	-156,67	4,29	57,54

Table 9: Interactions' effects between the factors and their impact on the response variables.

Interact. Effects	P / mbar	t_P / h	N / mm³/h	t_N / h
Cycle + Amp.	-26,28	1,71	8,4286	-218,86
Cycle + Accel.	-23,67	-53,33	11	-7
Cycle + Greas.	2	-5,17	0,67	-82,83
Amp. + Accel.	-30,5	-23,67	14,17	-53,75
Amp. + Greas.	-33,4	-10,4	9,2	-100,6
Accel. + Greas.	-19	-62,75	6,25	-66,41

4 Conclusions

This work carried out successfully a series of experimental tests varying systematically several working conditions in order to reproduce the non-stationary rotational movements and monitored the impact of the variation of these parameters on RSS and their sealing effectiveness. The results showed that:

- The grease volume in the intermediate cavity has the major effect on the negative pressure induction.
    - The negative pressure is on average increased in -56 mbar, when the greasing level is raised from a lower level to a directly upper level.
    - The effect of the greasing on the formation of the negative pres- sure can be visualized by taking T3, T4 and T16 into account, which had just the greasing level as a common parameter in the same level.
- The amplitude has second greatest effect on the negative pressure induc- tion and the greatest effect on the net flow rate.
    - T9 applied a greater amplitude than T3 and T16 and, although, T9 had applied lower levels of cycle and acceleration than T3, T9 pro- duced the highest negative pressure among all tests.
    - The amplitude has the major effect on the net flow rate induction, and this can also be visualized in the interaction effects involving the amplitude and the other parameters.
- The amplitude might have a major effect in the cases of leakage of oil.
    - T6 and T12 just had the level of the amplitude as a common parameter, which was the smallest angle tested.
    - The effect of small oscillations angles on the followability of the dust lip of RSS must be considered for further studies.
- The acceleration shows a small influence on the negative pressure formation as main effect, but its interactions' effects with parameters are considerable.

5 Nomenclature

P: Maximal pressure in intermediate cavity,

t_P: Time of achievement of the maximal pressure in intermediate cavity,

N: Maximal net flow rate, and

t_N: Time of achievement of the maximal net flow rate.

6 Acknowledgements

The IGF project 22032 N of the Research Association for Drive Technology e. V. (FVA project 784 I) was funded by the Federal Ministry for Economic Affairs and Energy via the AiF/DLR as part of the program for the promotion of Industrial Collec- tive Research (IGF) based on a resolution of the German Bundestag.

7 References

[1] P. Waidner, „Auswirkung von drehzahlgeregelten Antrieben für Pumpen auf das Betriebsverhalten von Gleitringdichtungen - eine Herausforderung für die Zukunft,“ *19th International Sealing Conference (ISC),* 2016.

[2] F. B. u. W. H. A. Eipper, „Einfluss von Drehzahlwechseln in Lastkollektiven auf das System Radial-Wellendichtring,“ *9th International Sealing Conference (ISC),* 2016.

[3] B. u. M. Kröger, „Radial-Wellendichtringe bei instationären Betriebsbedingungen,“ *19th International Sealing Conference (ISC),* 2016.

[4] C. B. u. A. R. M. Kröger, „Untersuchung von Drehzahlsprüngen an Radialwellendichtringen,“ *55. Tribologie Fachtagung,* 2014.

[5] Foodwatch, „Säuglingsmilch mit Mineralöl belastet,“ *Foodwatch Test,* 2019.

[6] Bundesamt für Risikobewertung, „Fragen und Antworten zu Mineralölbestandtei,“ *Bundesamt für Risikobewertung,* 2020.

[7] EFSA Panel on Contaminants in the Food Chain (CONTAM), „Scientific Opinion on Mineral Oil,“ *EFSA Journal,* p. 185, 2012.

[8] Foodwatch, „Mineralöle in Lebensmitteln - Ergebnisse des foodwatch-Tests,“ *Foodwatch Test,* 2015.

[9] Foodwatch, „Mineralöl in Schokoladen-Osterhasen,“ Foodwatch Test, 2016.

[10] N. Kwasniewski, „Labors finden Mineralölrückstände in Milchpulver für Säuglinge,“ Spiegel.de, 2020.

[11] Foodwatch, „Staatliche Labore finden Mineralöl in Babymilch,“ *Foodwatch Test,* 2020.

[12] S. Thielen, A. Aghdasi und B. Sauer, „Gegenmaßnahmen bei Leckageauftritt von Radialwellendichtringen im instationären Betrieb,“ *Konstruktion,* 2020.

[13] S. Thielen, „Reibverhalten und Dichtfunktion von Radialwellendichtringen bei instationärer Wellendrehzahl . Forschungsvorhaben 784 I,“ Forschungsvereinigung Antriebstechnik e.V. (FVA), IGF-Nr.: 18870 N, Abschlussbericht, FVA-Heft Nr. 1355,“ 2019.

[14] Y. Stiemcke, S. Thielen, T. Schollmayer, O. Koch and , “Investigation of the Effect of Underpressure Between Main and Dust Lip on the Performance of Radial Shaft Seals Under Instationary Shaft Movements,” *Journal of Tribology,* pp. 064401_1-064401_9, June 2024.

[15] D. C. Montgomery and , Design and Analysis of Experiments, Willey, 2017.

[16] C. Burkhart, K. Peter, S. Thielen and B. Sauer, “Online determination of reverse pumping values of radial shaft seals and their tribologically equivalent system.,” in *International Colloquium Tribology: Industrial and Automotive Lubrication, Technische Akademie Esslingen (TAE)*, Esslingen, 2020.

8 Authors

University of Kaiserslautern-Landau, Chair for Machine Elements, Gears and Tribology (MEGT)

Gottlieb-Daimler Straße, 67663 Kaiserslautern, Germany:

Lenine M. de C. Silva, M. Sc., ORCID 0000-0003-1272-0171, lenine.silva@rptu.de
Yvo Stiemcke, Dipl.-Ing., yvo.stiemcke@rptu.de

Tim Schollmayer, Dipl.-Ing., tim.schollmayer@rptu.de

Prof. Dr.-Ing. Oliver Koch, ORCID 0000-0001-5967-0242, oliver.koch@rptu.de

Jun. Prof. Dr. -Ing. Stefan Thielen, ORCID 0000-0003-3310-7659, stefan.thielen@rptu.de

https://doi.org/10.61319/96K3VQ2C

Development and testing of sleeve-type lip seals with stamped back-pumping structures

Marco Gohs, Lothar Hörl, Frank Bauer

The Back-Structured Shaft Seal (B3S) [1] was developed to achieve an optimal balance between static and dynamic tightness, thermal and chemical resistance, as well as high reliability and durability for PTFE shaft seals. Structures on the back of the sleeve create an active pumping mechanism in the sealing contact. This paper sums up the results of a stamped version in comparison to the laser engraved version. The stamping process causes significant alterations to the material properties of the seal. All prototypes underwent both static and dynamic tests which demonstrate that the B3S principle can be successfully implemented in a stamped version. However, the design of the structures must take additional influencing factors into account.

1 Introduction

In mechanical engineering, a multitude of diverse seals are employed to seal rotating shafts [2]. To guarantee a dependable, leakage-free seal, a back-pumping effect is indispensable. Consequently, shaft seals function as miniature pumps, actively pumping fluid back so that it does not occur as leakage. In the case of rotary shaft seals made of elastomer, a self-induced back-pumping effect is created by the geometry of the sealing edge and the surface roughness in contact with the shaft [3]. Therefore, no additional sealing aids are necessary [4].

In the event of high thermal or chemical loads, the use of elastomers is often no longer an option, necessitating the use of higher-grade materials such as PTFE compounds. Sleeve-type lip seals made of PTFE do not exhibit a self-induced back-pumping effect [5]. However, in order to achieve a back-pumping effect spiral grooves or other sealing aids in the sealing contact are used [6-7]. The back-structured shaft seal was developed at the Institute of Machine Components (IMA) for this purpose, representing an optimal combination of the positive properties of different shaft seal types. It ensures good static and dynamic tightness with high thermal and chemical resistance. The back-pumping effect is caused indirectly by structures on the backside of the sleeve, ensuring high reliability and a long service life [8].

This novel seal design was subjected to extensive testing and optimization with prototypes on test benches. The prototypes for this were produced by laser engraving. In order to facilitate more efficient production with reduced emissions, particularly in view of possible restrictions in the use of per- and polyfluoroalkyl substances (PFAS), stamping has now been tested as an alternative production process. Compared to laser engraving, stamping results in additional alterations to the material properties and thus a change in the sealing properties. The same geometry as a pumping structure exhibits different properties in stamped form than in laser engraved form. This paper therefore compares the functional behavior of stamped back-structured shaft seals to that of the laser engraved reference variant. The advantages and special features of the stamped variant are demonstrated on the basis of experimental investigations, thereby illustrating the suitability of stamping as an alternative manufacturing process for back-structured shaft seals.

2 Sleeve type lip seals made of PTFE

PTFE is utilized in the production of sleeve type lip seals, which is compounded with fillers to reduce wear and creep tendency while maintaining high chemical and thermal resistance and optimum dry-running properties [9]. Flat disks are typically employed, which are clamped in sheet metal rings. Due to the inner diameter being smaller than the shaft diameter, the sleeve lies flat on the shaft surface after the installation, as illustrated in Figure 1. Due to the surface roughness and the lack of a back-pumping effect, it is inevitable that leakage will occur during operation.

Spiral grooves (Figure 1, middle) or stamped structures in the sealing contact (Figure 1, right) are used to enhance dynamic tightness. However, the continuous spiral reduces static tightness and only one direction of rotation is possible [7]. Stamped structures in the sealing contact can also be utilized for shafts rotating in both directions, but are subject to heavy wear and are therefore not durable [6,10]. Bidirectional hydrodynamic seals where first mentioned in [11].

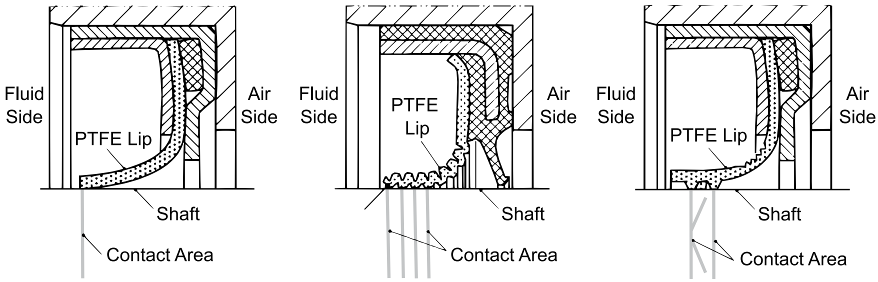

Figure 1: PTFE Lip Seals without and with Sealing Aids [8]

2.1 Back Structured Shaft Seal

The indirect structuring of the B3S combines the advantages of the three aforementioned variants. As the structures are not in the sealing contact, the static tightness remains at a similarly high level as with the unstructured sleeve type lip seal. The structures are applied as indentations on the side facing away from the shaft. As a result of the widening of the inner diameter during assembly, flat, very active pumping channels result in the contact area, as illustrated in Figure 2. The geometry of the structuring allows for the creation of channels with a wide range of shapes, enabling the realization of both unidirectional and bidirectional structures [12]. The active pumping channels in the sealing contact are a consequence of the structuring on the backside and remain effective even in the presence of wear, as they are also activated in dynamic operation by drag pressure due to the locally lower stiffness of the material.

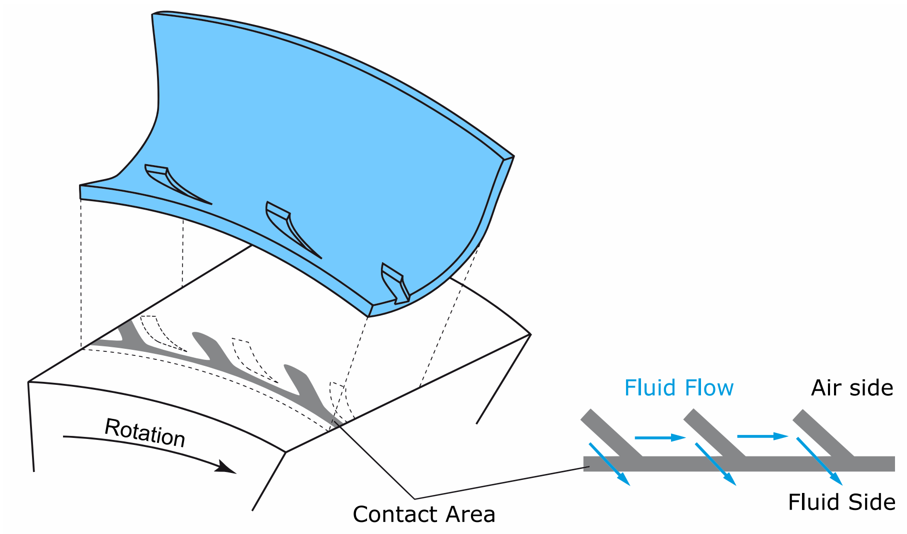

Figure 2: Working Principle of the Back Structured Shaft Seal [12]

A comprehensive account of the B3S's functionality and testing on laser engraved variants has been previously published by STOLL and DAKOV [8,12]. Optimal geometries were developed and tested for various applications using different geometry variants. The sickle-shaped geometry implemented here was found to be the most robust variant. In particular, the position, number, and depth of the structures can be varied within certain limits without a significant impact on the function. This allows for a seamless transition to a stamping die.

3 Manufacturing of the Prototypes

The raw material utilized in the production of the sheet material is a PTFE compound filled with glass spheres [13]. The base material in this case is expanded PTFE, which exhibits compressibility and provides optimal conditions for the stamping process. The same raw material was employed in the experiments before with the laser engraved variant, ensuring direct comparability with previous investigations.

3.1 The Stamping Process

For the production of stamped back-structured shaft seals, the geometry was first adapted to the requirements of a stamping die. Prototypes were then produced and the influence of the stamping parameters, namely pressure, duration and temperature during stamping, was investigated.

3.2 Adaptation of the geometry

A subtractive manufacturing process, such as laser engraving, allows for the creation of structures with no restrictions on distance, geometry, or depth. This enables the structuring to be designed with great freedom, with the goal of achieving the optimal pumping effect. However, material deposition during stamping is necessary, and there must be sufficient distance between structures to ensure clean impression accuracy. Additionally, it is essential to ensure that the metal stamping die, which is to be produced as a negative of the stamped geometry, can be manufactured. The optimized geometry of the laser engraved version (Figure 3, left) was therefore adapted (Figure 3, right). In order to achieve a greater distance between the structures, the number of structures was reduced and the shape slightly adjusted.

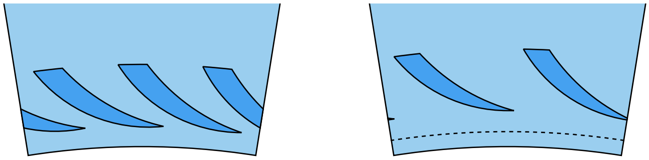

Figure 3: Reference Geometry and for Stamping optimized Version

The inner diameter was chosen slightly smaller to allow cutting to obtain an optimal edge. This is done by removing the burr caused by the gap of the die. The dotted line marks the position where the cut is made.

3.3 The Stamping Process

The prototypes were produced on a stamping press with heatable plates, as illustrated in Figure 4. For this purpose, the disk of raw material is placed between a milled stamping die, which has the shape of the structuring as a negative on the surface, and a counter mold. The heatable plates at the top and bottom can heat the stamping die and the disk up to 270°C. The stamping process is realized via a pressure-controlled hydraulic cylinder. It can be subjected to a pressure of up to 25MPa, which corresponds to a force of up to 200kN. The PTFE disks have an inner diameter of 65mm and an outer diameter of 100mm.

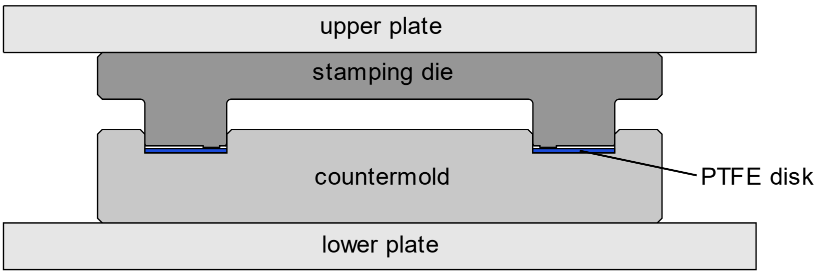

Figure 4: Scheme of the Stamping Process

The stamping process can be divided into four steps. First, the disk is placed in the die. Second, the die is heated for approximately 10 minutes between the preheated plates of the press. After heating, pressure is applied and maintained for a predetermined time. For all the variants in this paper the pressure was applied for one minute. Finally, the stamped disk is removed and allowed to cool down. The stamping die used for the prototypes is shown in Figure 5.

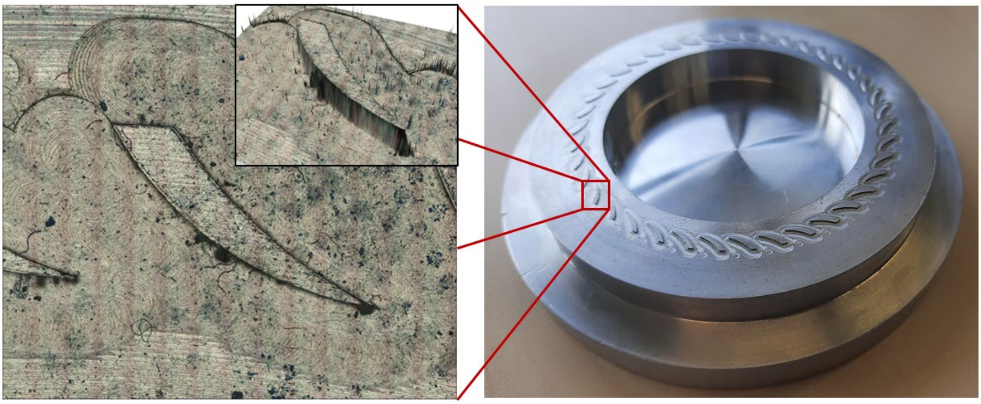

Figure 5: Stamping Die

The structures of the die have an average height of approximately 0.32 mm.

3.4 Evaluation of the structures

Different stamping parameters result in variations in the replication of the stamping die in the material to be stamped. They also cause shallow indentations on the opposing sleeve surface. The variants enumerated in Table 1 were created with the objective of identifying the relationships between the stamping parameters and the resulting stamped geometry. The mean contact pressure in table 1 is the mean pressure applied on the whole disk surface during the stamping process.

Table 1: Stamping Parameters of the Analyzed Variants

Stamping Pressure		20 MPa	10 MPa	5 MPa	2.5 MPa
Mean Contact Pressure		35.3 MPa	17.6 MPa	8.8 MPa	4.4 MPa
Stamping Temperature	20°C	G001	G002	G003	G004
	200°C	G005	G006	G007	G008

Figure 6 illustrates the three variants G001, G004 and G005. The differences in characteristics between the structures with varying stamping parameters are clearly evident.

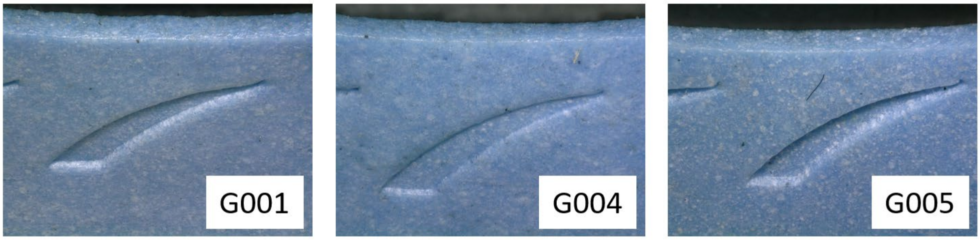

Figure 6: Examples of Stamped Structures with different Stamping Parameters

The depth of the structures and the depth of the indentations in the contact area were measured and evaluated. The surface measurements were conducted on a laser scanning microscope (Keyence VK9700 Gen. II). An illustrative example of a measurement of the top and bottom sides is presented in Figure 7.

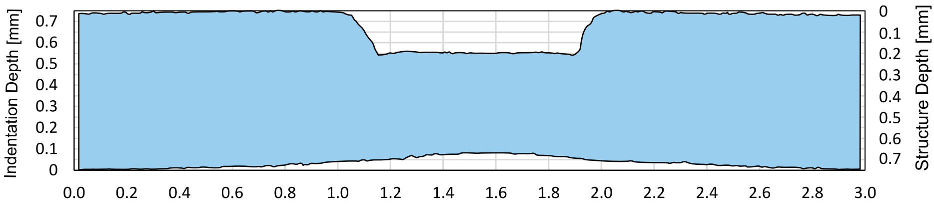

Figure 7: Example of a Measurement of the Top and Bottom Side

3.4.1 Structures on the back

Figure 8 presents the measured depths of the various variants.

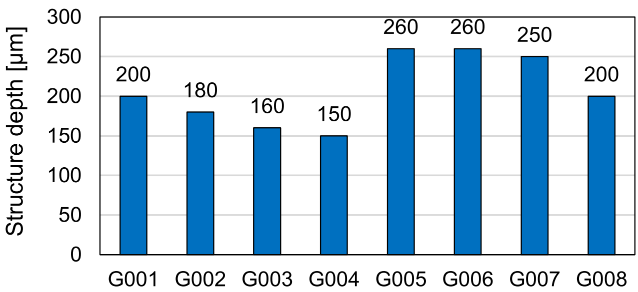

Figure 8: Depth of the Stamped Structures

The structures of the variants stamped at 200°C are significantly deeper than those of the variants stamped at 20°C. This behavior can be explained by the fact that the PTFE flows more strongly at higher temperatures and already deforms plastically at lower strains. The structure depth decreases with lower stamping pressure. In the variant stamped at 200°C, no discernible differences in depth are observed between 10 and 20MPa stamping pressure. Therefore, 10MPa at 200°C is sufficient for achieving the maximum depth of the structure.

The stamping temperature also has a significant effect on the shape of the stamped structure. Figure 9 shows the cross-sectional geometry of a structure stamped at 20°C (left) and one stamped at 200°C (right). Note that the structures stamped at higher temperature have significantly sharper edges. The structures stamped at 20°C show a curvature of the bottom surface in addition to the strongly rounded top edges.

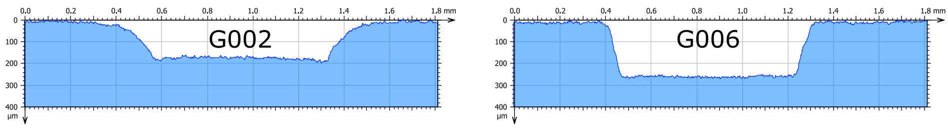

Figure 9: Profiles of the Stamped Structures at different Temperatures

3.4.2 Structures in the contact area

The indentations that have been formed on the opposite surface are approximately 50 µm deep at the deepest point in the variant stamped at 200°C. In the variant stamped at 20°C, they are slightly deeper at approximately 80 µm. The results from the contact analysis, which follow in section 4.2.2, also confirm this.

In conclusion, it can be stated that a higher stamping temperature results in deeper structures on the back side and a more accurate geometry of the structures. Conversely, a higher stamping temperature results in shallower indentations on the contact side.

4 Experimental tests of the functionality

In order to demonstrate the effect of the stamped structures and to compare them with the laser engraved version, a series of static and dynamic tests were carried out on prototypes.

4.1 Manufacturing and selection of variants

Prototypes were produced with the following stamping parameters for the purpose of experimental investigation of the stamped variant:

- **S01**: 1 minute at 200°C and 20MPa stamping pressure
- **S02**: 1 minute at 20°C and 20MPa stamping pressure

In addition to a variant without pumping structures, two reference variants were produced with laser engraving to permit a direct comparison under identical test conditions:

- **WS**: Smooth lip without pumping structures
- **L01**: Reference geometry with 60 structures, 0,4mm deep
- **L02**: Geometry of the stamped variant with 40 structures, 0,25mm deep

A series of four identical seals of each variant were tested in order to ascertain the impact of the stamping process. The reference variant, L01, corresponds to the unchanged original laser engraved variant. The variant L02 was equipped with the geometry adapted for the stamping die. A depth of 0.25 mm was selected, as this corresponds to the measured structure depth of the stamped variants. L02 therefore represents the geometrically identical equivalent to the stamped variants. Due to the laser engraving process, this variant does not exhibit the material-related changes caused by the stamping process. Consequently, it is possible to differentiate the properties caused by the structure from those caused by the stamping process.

4.2 Preliminary and follow-up studies

The radial load was quantified on all manufactured variants both before and after the tests. Furthermore, the contact area was evaluated, and the sealing edges were visually inspected.

4.2.1 Radial load

In the case of seals, the radial load is the load with which the sealing edge is pressed against the shaft. The measurements were conducted on a radial load measuring device using the split shaft method and Automatic Diameter Control [14]. The sealing rings were mounted on a shaft and stored for one hour prior to the first measurement. The second measurement was conducted after the static test. This corresponds to a total time of approximately 240 hours mounted on the shaft at 20°C. The third measurement was conducted after the subsequent endurance test. The seals were therefore mounted on the shaft for a total of approximately 480 hours and exposed to an oil temperature of 20°C for half the time and 120°C for the other half. The measured values are presented in Figure 10. For each variant, all the seals were measured at four points, with each point offset by 90°. Consequently, each bar is averaged over a total of 16 values.

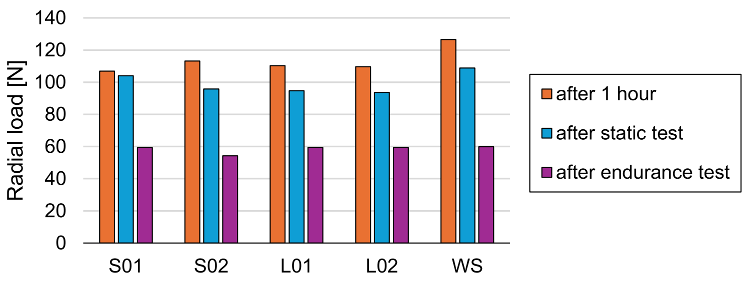

Figure 10: Radial Loads

It is clear that the stamping process of version S01 and S02 has an effect on the radial load compared to the smooth lip WS. The smooth lip WS also represents the values of the disk before the stamping process as it is not possible to measure the radial load before and after the stamping process on the same seal due to plastic deformations while mounting. The radial load after 1 hour is slightly lower for the variant S01 than for the variant S02. However, with increasing storage time on the shaft, the radial loads of the variant S01 remain almost constant, while the radial load of the variants S02 decreases significantly. The behavior of the stamped variants S01 and S02 is very similar to the behavior of the laser engraved variants L01 and L02. After 240 hours of continuous running at 120°C, the radial loads are almost identical for all variants. However, they remain significantly lower than before the endurance test.

4.2.2 Contact analysis

During contact analysis, the seals are mounted on a hollow glass shaft that is illuminated from the front surface. This type of illumination makes the areas that touch the shaft appear bright, which allows for the visualization of the very flat structures in the sealing contact. The images were taken with a Sealobserver, which enables the observation of the sealing edge radially from the inside to the outside through the glass shaft onto the sealing edge [15]. Selected images of the different variants before the tests are shown in Figure 11.

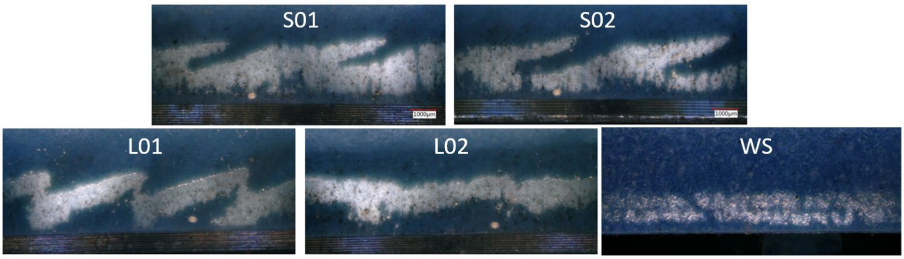

Figure 11: Contact Areas before the Endurance Test

It is evident that both stamped variants exhibit a continuous pressure line on the fluid side in the circumferential direction. This renders the stamped variant more advantageous in this regard than the reference variant L01. The laser engraved variant L02 clearly demonstrates that, in the absence of the additional effects resulting from the stamping process, the structuring merely creates a relatively weak pumping structure in the form of a wavy pressure line and lacks any ridges in the pressure distribution.

The contact analysis after the endurance test at 120°C in Figure 12 shows that the laser engraved structures have become less pronounced. In the stamped variants, there is a clear difference between the variants S01 and S02 visible. In variant S01, the channels have even become slightly more pronounced, while in variant S02, the geometry of the channels has changed significantly. This again illustrates the influence of the stamping parameters on the back-pumping structures.

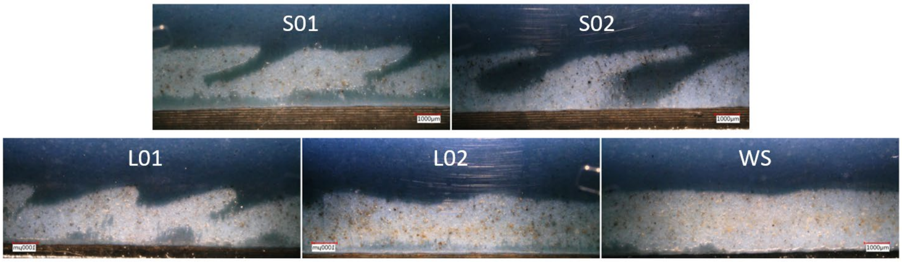

Figure 12: Contact Areas after the Endurance Test

4.3 Static tightness

In the process of testing the static tightness, the seal is completely flooded on the fluid side and the extent of the leakage at the sealing edge is evaluated visually. This evaluation is carried out at specified intervals. The leakage is qualitatively divided into six classes, which are illustrated in Figure 13. The classes range from P6, which indicates that no leakage is visible, to P1, which signifies that the leakage has already reached the housing. The classes in between are used for finer gradation. The ratings of the five variants are presented in Figure 13.

Duration	Variant				
	S01	S02	WS	L01	L02
0 min	P6	P6	P6	P6	P6
5 min	P6	P6	P6	P6	P6
30 min	P6	P5	P6	P6	P6
1 h	P6	P5	P6	P6	P6
3 h	P6	P5	P6	P5	P6
6 h	P6	P4	P6	P5	P6
12 h	P5	P3	P6	P4	P6
24 h	P5	P2	P6	P4	P6
48 h	P5	P2	P6	P3	P5
72 h	P5	P1	P5	P2	P5
96 h	P4	P1	P5	P2	P5
168 h	P4	P1	P5	P1	P5
192 h	P3	P1	P4	P1	P4

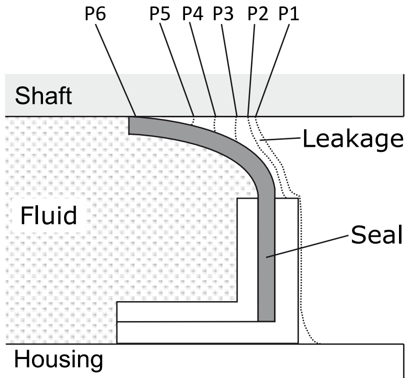

Figure 13: Static Leakage and Measurement Method [7]

As anticipated, the variant WS without any structuring (WS) exhibited the best performance. The variant L02 with the laser engraved equivalent structures exhibited slightly inferior performance, but within a similar order of magnitude. The at 200°C stamped variants (S01) exhibited particularly favorable results, demonstrating significantly enhanced static tightness compared to the reference structure (L01) despite the channels that are clearly visible in the contact analysis. This evidence demonstrates the significance of the closed pressure line on the fluid side, which is absent in the laser engraved reference variant (L01) and consequently results in inferior static tightness.

4.4 Pumping rates

To test the pumping rate, the seals are mounted on the test bench in reverse. Fluid is now present on the air side and the pumping action pumps fluid from the air side to the fluid side of the seal. With the fluid side now facing outward, the amount of pumped fluid escapes and can be measured. Pumping rate measurements were taken both before and after the endurance test on two samples of each version to evaluate the change in pumping efficiency over time. Figure 14 shows the measured pumping rates before the endurance test and Figure 15 shows the values after the endurance test.

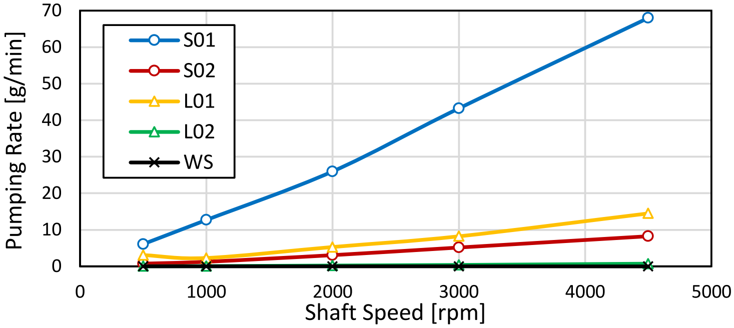

Figure 14: Pumping Rates before the Endurance Test

As expected, the seals without pumping structures (WS) also show no pumping effect. The laser engraved reference variant L01 has a pumping rate of about 15 g/min at 4500 rpm. The two stamped variants S01 and S02 differ significantly. The variant S01 had more than four times the pumping rate of the laser engraved reference variant L01. However, variant S02 had a lower pumping rate than the reference variant L01. Variant L02 clearly shows that the structuring of the stamped versions alone, without the influence of the stamping process, has a very low pumping rate. It can be concluded that the very good pumping effect is mainly caused by the changes that occur during the stamping process, in particular the significantly reinforced structures in the sealing contact.

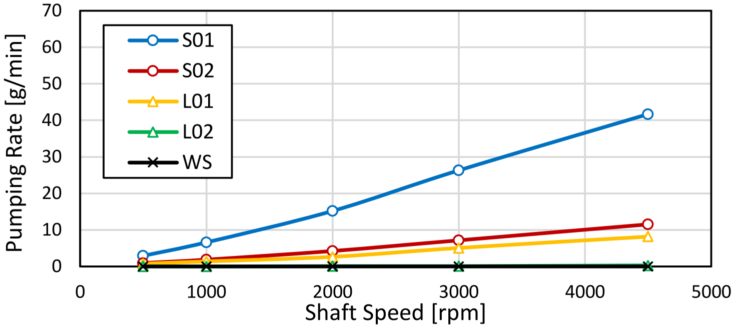

Figure 15: Pumping Rates after the Endurance Test

As a result of the endurance test, the pumping effect of the laser engraved variants L01 and L02 and the stamped variant S01 is reduced by more than 30%. The stamped variant LS02 shows a slight improvement in the pumping effect, which means that both stamped variants now have a higher pumping effect than the laser engraved variants. It is positive to emphasize that all back-structured variants show a clear pumping effect even after the endurance test, thus demonstrating the durability of the structuring.

4.5 Endurance test

Endurance tests were performed to verify the function over a longer period of use. The test conditions and a section of the used test rig are shown in Figure 16.

Shaft Diameter	80 mm
Shaft Material	100Cr6
Surface	Plunge Ground
Oil	0W 30
Oil Temperature	120 °C
Oil Level	Shaft Centre
Speed	4,500 rpm
Duration	240 h

Figure 16: Test Rig and Operation Conditions

None of the stamped variants showed any leakage over the entire test period. The exceptions were individual failures that were due to other causes and therefore could not be included in the evaluation of the stamped structure.

5 Influence on the material behavior through the stamping process

The PTFE compound used is compressible, which alters the mechanical properties as a consequence of the stamping process. To ascertain the influence of this phenomenon, tensile tests were conducted on compressed raw material at 20°C and 120°C. The raw material was therefore pressed at 20°C and 200°C. The tensile specimens were then punched out of the prepared material and the thickness was measured, (Figure 17 left). The material compressed at 20°C exhibited a compression of approximately 13%, while the material compressed at 200°C showed a compression of around 46%.

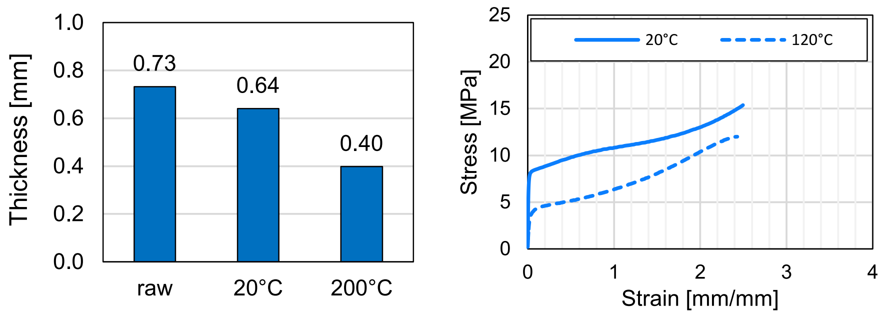

Figure 17: Measured Specimen Thickness and Stress-Strain Curve of the Raw Material

Figure 17 on the right shows the stress-strain curves of the raw material measured at 20°C and 120°C. The stress is reduced by about 50% due to the increased ambient temperature whereas the elongation at break remains nearly the same at about 2.5 mm/mm.

The stress-strain curves of the compressed PTFE sheets are shown in Figure 18. The plot on the left shows measurements on specimens compressed at 20°C for one and ten minutes and the plot on the right shows the measurements on specimens compressed at 200°C for one minute.

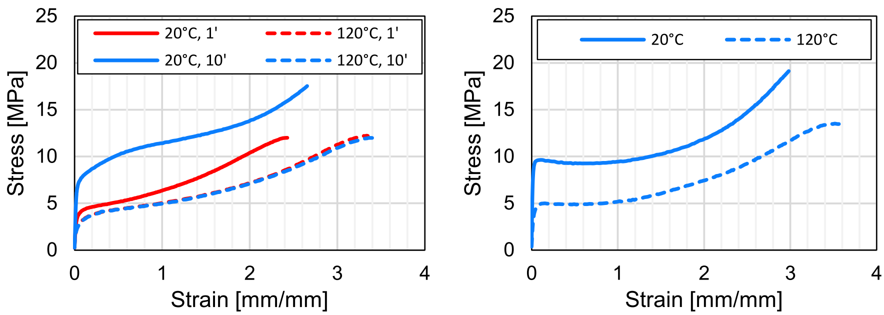

Figure 18: Stress-Strain Curves of the Compressed Material at 20°C and 200°C

At 20°C it is evident that the length of time the material has been compressed has a significant influence on the stress-strain behavior. The material compressed for 10 minutes almost reaches the values of the raw material, while the material compressed for one minute shows significantly lower stresses. This difference is not visible in the tensile tests at 120°C. It can therefore be concluded that the residual stresses generated by the pressing process are relieved either by heating or longer compression times when not heated. The material shows a discernible shift in its physical properties upon compression at 200°C. Initially, the material exhibits a nearly linear response, followed by the onset of viscous flow under a consistent stress level.

6 Summary and Conclusion

Seals made of elastomer are often unsuitable for sealing rotating shafts in thermally or chemically challenging conditions. In contrast, sleeve type lip seals are employed in this area of application. Unlike rotary shaft seals made of elastomer, sleeve type lip seals do not form a self-induced back-pumping effect that enables continuous operation without leakage. In order to achieve an optimum combination of chemical and thermal resistance, as well as static and dynamic tightness, a sleeve type lip seal with special back-pumping structures, designated the B3S, was developed at the IMA. To test the functional principle, the prototypes have so far been produced using laser engraving. However, this process is very time-consuming and involves problematic emissions during production. The studies presented in this paper have demonstrated that stamping is an optimal manufacturing process for back-structured shaft seals. This implies that a simpler, more efficient manufacturing process is now available that is associated with fewer harmful emissions. Stamping creates additional active back-pumping structures on the contact side, thus resulting in an enhanced back-pumping effect compared to the variant produced by laser engraving. The back-pumping effect can be significantly influenced by the stamping pressure and temperature.

7 Outlook

The data obtained from the material analysis now permits the precise design of the stamped structures through the use of simulative optimization. The effects of the stamping process can now be incorporated into the design. Furthermore, the test results can be used to optimize the pumping effect and to develop a B3S with optimized stamped bidirectional pumping structures.

8 References

[1] Patent EP 3555503 B1, Device for Sealing an Object, 2021

[2] Müller, H. K.; Nau B. S.: *Fluid Sealing Technology : Principles and Applications*. New York : Dekker, 1998

[3] Nakamura, K.; Kawahara, Y.: *An Investigation of Sealing Properties of Lip Seals through Observation of Sealing Surfaces under Dynamic Conditions*. 10th International Conference on Fluid Sealing, BHRA The Fluid Engineering Centre, Cranfield, Bedford, England, 1984

[4] Bauer, F.: *Federvorgespannte-Elastomer-Radial-Wellendichtungen. Grundlagen der Tribologie & Dichtungstechnik, Funktion und Schadensanalyse*. Springer Vieweg, Wiesbaden, 2021, ISBN 978-3-658-32921-1

[5] Schmitt, W.: *Radial Shaft Seal with PTFE Sealing Lips*. SAE Technical Paper 852347, 1985

[6] Gölz, J.: *Manschettendichtringe aus PTFE-Compounds – Funktionsmechanismus von PTFE-Manschettendichtungen und Entwicklung von Rückförderstrukturen für beidseitig drehende Wellen*. Dissertation, University of Stuttgart, 2017

[7] Bauer, F.: *PTFE-Manschettendichtungen mit Spiralrille – Analyse, Funktionsweise und Erweiterung der Einsatzgrenzen*. Dissertation, University of Stuttgart, 2008

[8] Stoll, M.; Dakov, N.; Hörl, L.; Bauer, F.: *A New Innovative Design for Shaft Seals*. 24th International Conference on Fluid Sealing, BHR Group, Manchester, 2018, P. 119-131, ISBN: 978-1-85598-1638

[9] Chiad, M.; Fatu, A.; Hajjam, M.: *Experimental study of PTFE lip seals with spiral grooves*. 21st International Conference on Fluid Sealing, BHR Group, Milton Keynes, UK, 2011

[10] Hoffmann, C.: *Untersuchungen an PTFE-Wellendichtungen*. Dissertation, University of Stuttgart, 1995

[11] Patent EP 0128645 A2, *Bi-directional hydrodynamic seal*. 1984

[12] Stoll, M.: *Entwicklung und Funktionsanalyse rückenstrukturierter Manschettendichtringe aus PTFE-Compound*. Dissertation, University of Stuttgart, 2019, ISBN 978-3-936100-93-8

[13] Garlock GmbH: *Garlock_GSK_3-1_Gasketing_Technical_Manual*. 03.2017

[14] Feldmeth, S.; Stoll, M.; Bauer, F.: *How to measure the radial load of radial lip seals*. Tribologie + Schmierungstechnik, 68. Jahrgang 3-4/2021

[15] Institut für Maschinenelemente: *TechSheet #102070 – Sealobserver*. University of Stuttgart, 2019

9 Authors

University of Stuttgart, Institute of Machine Components (IMA)
Pfaffenwaldring 9, 70569 Stuttgart, Germany:

Marco Gohs, M. Sc., ORCID 0000-0003-4747-6738,
marco.gohs@ima.uni-stuttgart.de

Dipl. Ing. Lothar Hörl, ORCID 0000-0002-2851-3364,
lothar.hoerl@ima.uni-stuttgart.de

Prof. Dr.-Ing. Frank Bauer, ORCID 0000-0001-7799-7628,
frank.bauer@ima.uni-stuttgart.de

https://doi.org/10.61319/EFNFS9KB

Group A
Session 7

Materials and Surfaces II

A 20

Lukas Boden, Marius Hofmeister, Faras Brumand-Poor, Katharina Schmitz, Institute for Fluid Power Drives and Systems - RWTH Aachen University, Aachen, Germany

Predicting Compatibility of Sealing Material with Bio-Hybrid Fuels: Development and Comparison of Machine Learning Methods

A 21

Joachim Möschel, Konzelmann GmbH, Löchgau, Germany

Poetry and truth, how does the hydrolysis-resistant structure come into the polyurethane?

A 22

Christian Wilbs, Matthias Adler, Daniel Frölich, Alisa Bellon, Nicole Schuster, Jasmin Menzel, Emely Bopp, Freudenberg FST GmbH, Mannheim, Germany

Micro-mechanical characterization of a tribological stressed elastomer surfaces with respect to Radial-Shaft-Seals

Predicting Compatibility of Sealing Material with Bio-Hybrid Fuels: Development and Comparison of Machine Learning Methods

Lukas Boden, Marius Hofmeister, Faras Brumand-Poor, Linda Pleninger, Katharina Schmitz

Bio-hybrid fuels, derived from sustainable raw materials and green energies, offer a promising alternative to conventional fuels made of mineral oil. Within the cluster of excellence “The Fuel Science Center (FSC)” at RWTH Aachen bio-hybrid fuels are investigated on a holistic level, including an examination of their compatibility with sealing materials. Previous time-consuming experiments revealed that many bio-hybrid fuels show poor material compatibility with elastomer sealing materials (e.g. NBR & FKM) leading to issues such as volume expansion, hardness alteration, or chemical reactions upon immersion. These incompatibilities could result in catastrophic failures during practical applications. Due to the high number of possible fuels, fuel-mixtures and therefore fuel/seal combinations a solely empirical approach is impractical. Consequently, this work presents a hands-on framework of machine learning (ML) regression models that predicts material compatibility based on experimental results and selected fluid properties, thereby enabling the preselection of possible fuel/seal combinations for subsequent immersion tests.

1 Motivation and Introduction

In terms of global climate change, CO_2-neutral forms of energy from sources other than fossil feedstock are of immense importance to all of society. One possibility for providing climate-neutral energy for automotive applications is the use of bio-hybrid fuels, which are produced either based on biological resources or with the use of other carbon sources and renewable energy. In order to select fuels from the almost infinite number of possible molecules that meet environmental, economical, and technical requirements, the Cluster of Excellence "The Fuel Science Center (FSC)" is developing methods to identify optimal fuel candidates.

One advantage of bio-hybrid fuels over other alternative energy sources, such as fuel cells or electrical energy, is the use of existing infrastructure. If bio-hybrid fuels are used as so-called "drop-in fuels" in existing combustion engines, a worldwide network of filling stations and production facilities in the fuel industry can be utilized.

A mandatory prerequisite for the unrestricted use of “drop-in fuels” developed in the FSC is material compatibility with all system components. Static and dynamic seals are particularly at risk. Failure of seals can have far-reaching consequences as has been shown in the past with test bench failures caused by damaged seals. Previous studies and immersion tests have shown that many bio-hybrid fuels have poor material compatibility with conventional elastomer sealing materials, leading to an increase in elastomer volume of more than 200 % [1, 2]. Such large amounts of swelling lead to immediate failure in real technical applications. In addition to swelling, other wear mechanisms such as changes in hardness or chemical reactions were observed [1, 2]. Based on these findings, material compatibility has become a important design parameter for bio-hybrid fuels within the FSC and therefore is addressed in this study.

Given the vast array of fuel candidates and blends, along with corresponding fuel/seal combinations, conducting manual immersion tests becomes impractical. In addressing this challenge, an automated test rig was developed, facilitating the simultaneous execution of 90 immersion tests. However, despite this advancement, achieving a comprehensive examination of all potential fuel/seal combinations remains unfeasible. Thus, there arises the necessity for a strategic selection of combinations to investigate further.

Machine learning (ML) has proven to be successful in the area of fluid power applications, like fault detection [3] and data-based condition monitoring [4]. Furthermore, several studies have been conducted on the discovery of new materials and prediction of fuel properties with ML algorithms [5, 6]. The ability of ML algorithms to discover patterns and trends in a vast amount of data represents a powerful tool for the identification of material compatibility and the prediction of compatibility of untested combinations, resulting in a narrowed-down fuel/seal configuration. Hereby, a pairing is valid if the hardness change and sealing material volume after the immersion test are close to the values of immersion tests with conventional fuels, such as diesel or gasoline. The configurations are not further considered if the values deviate too much.

In the following study, the process of conducting immersion tests, selecting suitable parameters, and preprocessing the resulting dataset is presented. Furthermore, the setup of the ML framework, model training, and evaluation and subsequently the comparison of different regression models are shown.

2 Methodology

In the following section the investigated bio-hybrid fuels and regression methods are introduced.

2.1 Investigated bio hybrid fuels

Different promising drop-in fuel candidates have emerged out of the FSC. Six of them are included in this work. Additionally, diesel in accordance with DIN EN 590 and gasoline according to DIN EN 228 are used as reference fuels [7, 8]. In the following, the composition of the bio-hybrid fuels is shortly introduced.

The first representative for bio-hybrid diesel fuels is OME 3-5. OME 3-5 is a mixture of polyoxymethylene dimethyl ethers with chain lengths between 3 and 5 carbon atoms. It is intended to be produced based on methanol and formaldehyde by using low carbon electricity [9]. The two HyFit fuels can be produced using Fischer Tropsch synthesis and consist of different shares of n-alcohols and n-alkanes. HyFit1 and HyFit2 differ primarily in their accumulated alcohol content of 15 and 40 %

respectively [10]. The third bio-hybrid diesel fuel is a mixture of different methyl ketones which is derived from a microbiological process [2]. Representatives of bio-hybrid Otto fuels are KEAA and EBCC blends which are mixtures of different ketones, esters, alcohols, and alkanes [11].

Most of the fuel candidates mentioned above are mixtures of pure liquids. Some pure liquids have already been tested by the FSC for their material compatibility and are therefore included in this study [2, 12]. This has two advantages. Firstly, the experimental database is expanded, making predictions by ML regression models more significant. Secondly, the foundation is provided to further investigate the material compatibility of mixtures or fuel blends and to understand the underlying patterns.

2.2 Regression models

The field of machine learning focuses on finding patterns in data using computer algorithms. Its main purpose is to utilize these patterns to perform various tasks, such as data classification or estimation of continuous values based on the given data [13]. Since the aim of this study is to predict numerical values based on a dataset that consists of both input and their corresponding target (output) variables, a supervised learning (SL) approach is selected. In the case of SL, the output is the true value, called a label, and the model should be tuned in such a way that it predicts the particular label for the provided input set. The inputs of the ML models are the fuel properties, which are listed in Table 1. Their selection process is elaborated further in section 3.2. The provided labels are the volume amount and hardness change of the elastomer specimen. This setup represents a multi-output regression problem, which can be solved by a variety of SL algorithms, listed in Table 2. This work aims to implement a framework, which integrates these algorithms and could be extended and validated with currently available and further collected data.

Table 1: Overview of selected describing parameters

Descriptor:	**Source:**	**Reference:**	**Data type and unit:**
Density	Measured and from literature	[23, 24]	Numerical value $\mathrm{kg/m^3}$
Molar mass	From literature	[23, 24]	Numerical value $\mathrm{g/mol}$
Molar volume	Engineered from density and molar mass	-	Numerical value $\mathrm{m^3/mol}$
Boiling point	From literature	[23, 24]	Numerical value $\mathrm{°C}$
Enthalpy of vaporization	From literature (at standard conditions)	[23, 24]	Numerical value $\mathrm{kJ/mol}$

Vapor pressure	From literature (at 20°C)	[23, 24]	Numerical value kPa
Oxygen content	Calculated from molar structure	[23, 24]	Numerical value %
Ring structure	From molecular structure	[23, 24]	Either 1 or 0 -
logP_{ow}	From literature	[25]	Numerical value -

Table 2: Comparison of the investigated regression models [14]

Regression model:		**Working principle:**
Linear Model	Linear Regression (polynomial Regression)	Fits a linear (polynomial) function to the data by minimizing the difference between the true and predicted values, adjusting coefficients to find the best-fitting line (or curve)
	Lasso Regression	Additional to linear regression, the absolute size of coefficients is penalized using L1 regularization
	Stochastic gradient decent	Minimizes the loss function iteratively by randomly selecting mini batches of data and updating model parameters in the direction opposite to the computed gradient
Nonlinear Models	Multi-layer Perceptron	Data is propagated through (multiple) layers of neurons, with each layer performing transformations on the input, ultimately predicting the output by minimizing the loss function
	SVR	Aims to find the hyperplane that best fits the data by maximizing the margin between the data points and the hyperplane and minimizing the loss function
	Decision Tree Regressor	Constructs a tree-like structure where data is split into feature subsets, optimizing splits to minimize the variance of predicted values within each subset, resulting in a piecewise constant approximation of the output variable

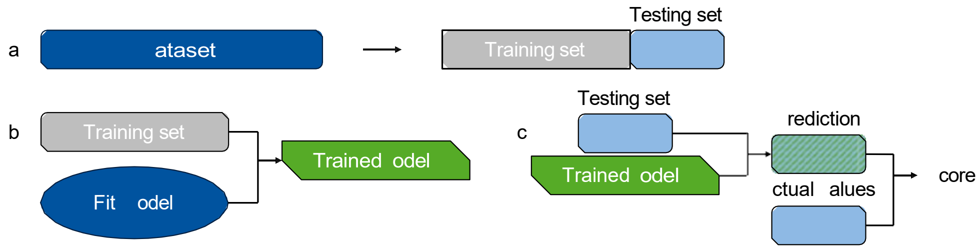

Figure 1: General process of regression tasks

The general process for solving regression tasks consists of three steps that are denoted from a) to c) in Figure 1. The first step is splitting up the dataset (a). In a second step, the model is trained (b) and lastly, the performance of the model is evaluated (c).

Splitting the dataset into a training and a test subset ensures that the subsequent training of the model is not performed on the entire dataset. The withheld test dataset is later used to evaluate the performance of the model. This also allows to assess the model's ability to generalize, which is defined as the ability to perform well on previously unseen data.

Subsequently only the training subset is considered for the fitting of the model. Based on the training input and output values, underlying patterns in the relationship between input and output are learned by the model. During this process different parameters of the models, such as weights and biases, are adjusted iteratively. If the model describes the training data well enough or if a maximum number of iterations is reached, the training process is finished, and the model can be applied to the unseen testing subset to evaluate its performance.

Based only on the testing input data, the trained model applies the learned patterns and predicts new output data. To evaluate the accuracy of this predictions, the actual testing output data are compared to the predicted values. A score is calculated using metrics, which allows the model's performance to be compared. Two commonly used metrics are introduced in Equation (2) and (3). For calculating the mean squared error (MSE), first the difference between an actual output value Y and the predicted output value Y_{pred} is computed. The difference is then squared and averaged over all n samples. A better performance is represented by a lower MSE. The coefficient of determination R^2 provides a measure of how well the regression model fits the actual data. It quantifies the proportion of the variance in the predicted values to a scale from 0 to 1, with larger values representing a better model fit.

The main benefit of observing training and testing performance is the detection of overfitting and underfitting. The former is a common weakness of SL models, where parameters are customized too specifically to a particular problem rather than learning the underlying patterns. The latter occurs when a model is insufficiently trained, often due to a lack of quality or quantity of data.

$$MSE = \frac{1}{n}\sum_{i=1}^{n}(Y_i - Y_{pred,i})^2 \quad (2)$$

$$R^2 = 1 - \frac{\sum_{i=1}^{n}(Y_i - Y_{pred,i})^2}{\sum_{i=1}^{n}(Y_i - Y_{mean})^2} = 1 - \frac{\mathrm{MSE}}{\mathrm{var(Y)}} \quad (3)$$

3 Structure and Approach

In the following section, the underlying experimental investigation as well as the pre-selection process of suitable parameters and machine learning methods are presented.

3.1 Immersion tests

The application of machine learning methods for predicting material compatibility in this study is founded upon experimental immersion tests conducted in accordance with ISO 1817 [15]. Standard reference elastomers (SRE) according to DIN ISO 13226 (SRE-NBR 28/SX and SRE-FKM/2X) were used as sealing materials and immersed into the fuels [16]. The size of the specimen is 25x25x2 mm^3. It was ensured that the specimen was always covered with sufficient fuel in the vessels during investigation.

The specimens are removed from the vessels filled with the investigated fuel after defined intervals to evaluate the change of seal properties. The time intervals for evaluation were chosen in accordance with standard DIN 53521 [17]. For this study, only the measurements of the specimen volume and hardness at the final time interval after 672 h in relation to its initial state are considered. In the work of Hofmeister et al. the measurement techniques and devices are presented in detail. It was especially paid attention to the fact, that most investigated liquids have a high vapor pressure at standard conditions and therefore significant evaporation rates are present. [1]

In the following, the focus solely is on SRE-NBR 28/SX, since in comparison to FKM a higher number of fluids are investigated. The composition of SRE-NBR 28/SX is shown in Table 3. Figure 2 lists the change of volume and hardness of SRE-NBR for all investigated fuels and fluids.

Table 3: Composition of SRE-NBR 28/SX according to ISO 13226

Formulation of the rubber mixture	Parts by mass
NBR with 28 % by mass of acrylonitrile (Perbunan NT 2845)	100,0
Antidegradant TMQ (Vulkanox HS)	2,0
Zinc oxide (Zinkoxyd aktiv)	5,0
Stearic acid	1,0

Carbon black N 550 (Corax N 550)	65,0
Accelerator TBzTD	2,5
Accelerator CBS (Vulkacit CZ)	1,5
Sulphur	0,2

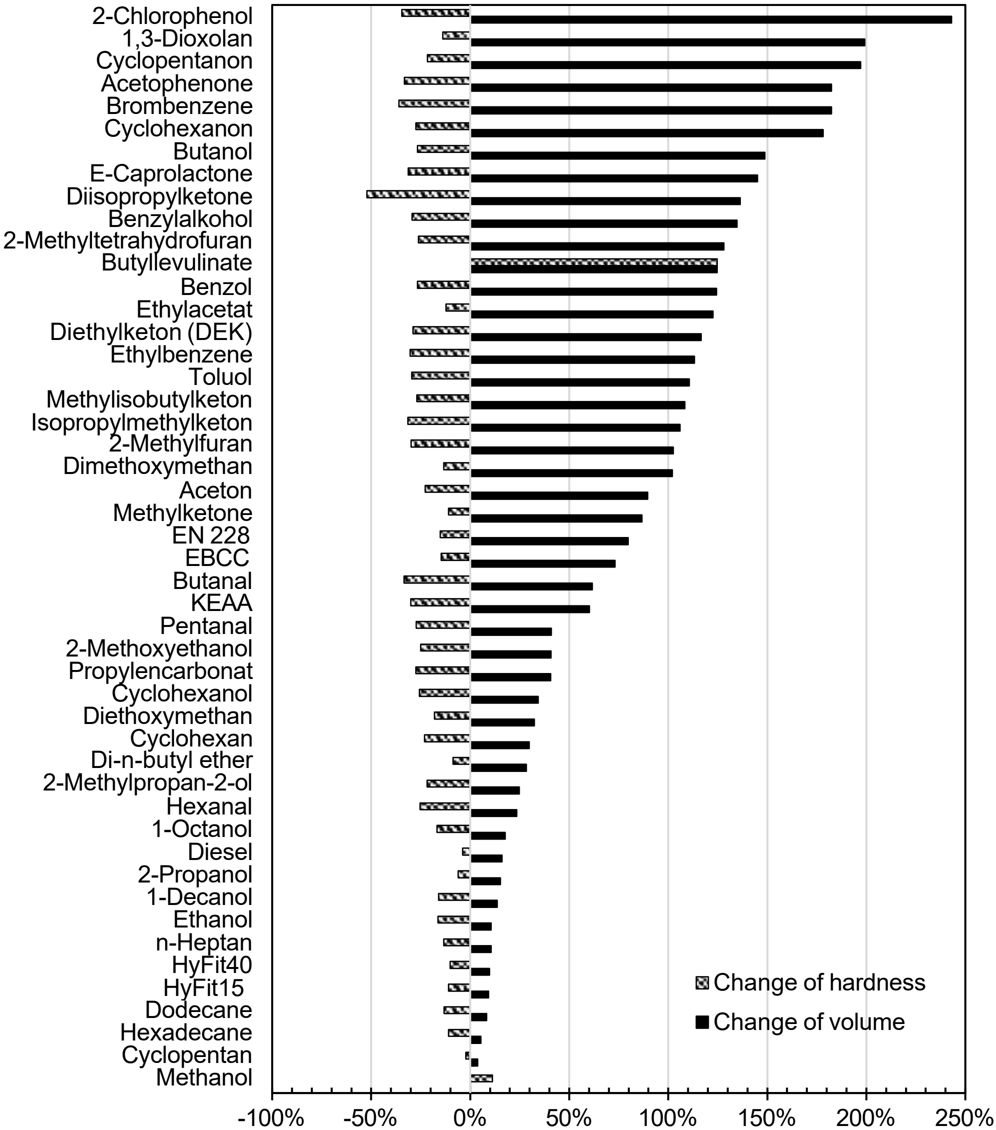

Figure 2: Results of immersion tests for SRE-NBR 28/SX

3.2 Choosing relevant parameters

The tendency of a fluid to cause polymer swelling depends largely on two factors: the polarity of the fluid and the elastomer as well as the size of the fluid molecules. According to the chemical principle “like dissolves like”, polar fluid molecules prefer to penetrate polar elastomers while nonpolar fluid molecules lead to an increased swelling of nonpolar elastomers. In terms of the steric requirement of the fluid molecules, larger molecules are more hindered to penetrate the elastomer crosslinked network. Besides fluid properties, properties of the elastomer such as the degree of crosslinking, the bulk modulus or the type and amount of additives play an important role when investigation property changes of the elastomer. Since standard reference elastomers are considered in this work, the influence of these parameters is not considered. Elastomer properties might be included as parameters in further investigations regarding technical seals.

The quantification of the polarity of molecules is the subject of numerous research projects. Kier suggests the use of a structure-based numerical index to quantify polarity [18]. Palomar et al. introduce a quantum chemical parameter for this application [19]. Furthermore, the polarity of molecules is considered in the Hansen solubility parameters to predict compatibility between different compounds [20]. Having said that, those theoretical descriptors are not commonly available and can be complex to determine especially for compound mixtures. Additionally, the weaknesses of such parameters have already been demonstrated in various studies. For example, the work of Heitzig et al. concludes that the Hansen parameters are not suitable to predict polymer swelling. One reason for this is the copolymer structure of widely used sealing materials like NBR, whose solubility would presumably have to be quantified using more than one Hansen sphere. Additionally chemical reactions, that might occur during immersion, are not considered in the theory of Hansen. [12]

For this reason, the approach presented here uses familiar physical and chemical parameters that can be found in common databases and handbooks for a wide variety of compounds. The aim was to find parameters that are both easily accessible as well as a good representation of the polarity and/or the steric requirement of the fluid-molecule. Eventually, a set of nine parameters was defined, which are presented in Table 1. The values of these parameters were taken from several open access databases and the own database of the FSC. For reasons of complexity, the focus is initially placed on the properties of the fluids while the polarity and properties of the elastomer is not taken into consideration.

The molar volume of a compound, being the ratio of the molar mass and the density, is an indicator of the steric requirement of the fluid molecule. The reason for that becomes apparent when comparing molar volumes of different C_6 organic compounds. Comparing the molar volumes of cyclohexane to hexane demonstrates the lower steric requirement of cyclic compounds compared to linear and branched molecules. Likewise, the comparison of cyclohexane to benzene shows the lower steric requirements of aromatic compounds due to their inherent planarity. This is important since compounds with a lower steric requirement show lower activation energies for diffusion and thus show a higher tendency to penetrate the elastomer network [21].

The boiling point, the molar enthalpy of vaporization, and the vapor pressure represent the magnitude of the occurring intermolecular interactions [22]. This is closely related to the polarity of the molecule due to the ability of polar substances to form stronger intermolecular interactions such as hydrogen bonds and π-π interactions in comparison to nonpolar substances.

Oxygen content can be easily determined using molecular formula and can be an indicator for bond polarization due to the strong electronegativity of oxygen. Whether the compound is cyclic derives from the molecular structure and indicates a lower steric hindrance compared to the acyclic analogue.

The decadic logarithm of the partition coefficient in octanol/water $\log P_{OW}$ is a measure of the hydrophobicity of a substance. Since hydrophilicity correlates to a certain extent with the polarity of a substance, this parameter also provides an indication of polarity.

3.3 Application of Regression Models

The general process of application is stated above in Section 2.2. In this section, the focus is set on preprocessing the data and the framework in which the different ML models are set up, tuned, and subsequently evaluated. As mentioned before the aim of this work is to implement a framework with all necessary modules for further validation land investigation.

The framework consists of several components in order to tackle common drawbacks in data-driven algorithms. Starting with the feature scaling of the input data. This results in an equalization of the features in a common band, resolving the issue of different units and magnitudes in the input data. The scaling can be done by applying min-max normalization, converting all input data to the range 0 to 1. Another method for scaling input data is by using a standard scaler, which normalizes each feature by subtracting its mean and dividing by its standard deviation. This transformation ensures that each feature has a mean of 0 and a standard deviation of 1. [14]

In a first step, a general baseline for the prediction performance is obtained by considering all nine features introduced in the previous section. One main enhancement to ML algorithms is the reduction of the input vector to the most crucial features, resulting in faster computation and less data requirement. This is achieved by comparing correlation scores between features and only considering uncorrelated features for further use (features with a correlation score lower than a set limit). Principal component analysis (PCA) further facilitates this process by transforming the original features into a new set of orthogonal (uncorrelated) variables, thereby enabling effective dimensionality reduction. [14]

Finding the best parameter of a given model requires hyperparameter tuning, since for example the optimal parameters of a neural network can be suboptimal if the network is not deep/wide enough. This hyperparameter tuning is labor-intensive and therefore is achieved by automated/heuristic/model-based algorithms. These ensure that not only the best parameter, furthermore the best hyperparameter are used.

The framework combines the above-mentioned steps to investigate the elastomer specimen volume change for a given liquid/seal combination. For an exemplary regression model and a scaled dataset, the framework is visualized in Figure 3. Since the number of samples in the entire dataset of this work is small ($n = 48$), statistical uncertainties are introduced during evaluation, making it difficult to compare different models. For this reason, the training and testing process is repeated on different randomly selected subsets, which is known as k-fold cross-validation [14]. This approach is visualized in section (a) in Figure 3. In this case, the dataset is divided into $k = 3$ separate subsets that do not overlap. For each fold the best performing model is determined using hyperparameter tuning (see (b)) in Figure 3. For this the HalvingGridSearchCV module is employed [14]. Given the best model and the testing set the model is then evaluated by applying the MSE and R^2 metric (see (c)). This is repeated for every fold and average scores are calculated for each model, enabling comparison between models.

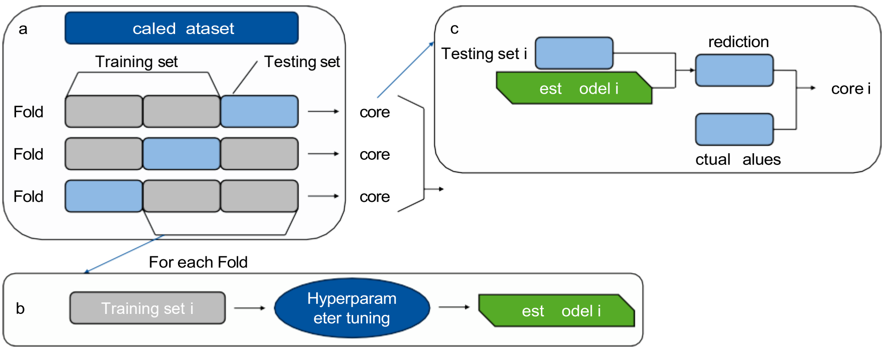

Figure 3: 3-fold cross validation and hyperparameter tuning. Redrawn from [26]

4 Results

In this section, the presented framework is evaluated by applying the MSE and R^2 score to the predictions made by the investigated models. As the data set contains only 48 samples, no statement is made about the actual performance of the investigated models. The focus of the results is on validating the hands-on approach of the framework itself. It must be noted that with each addition of new samples, the database expands, leading to more significant results.

The baseline score is obtained by utilising 5-fold cross-validation, hyperparameter tuning by HalvingGridSearchCV and normalizing all nine input parameters using the min-max scaler of the scikit learn toolbox [14]. The averaged baseline scores for the investigated models are shown in Table 4. It becomes apparent that for all models, the MSE of the training process is always lower than the prediction (testing) process. The discrepancy in R^2 values between the training and testing phases, coupled with the overall low or even negative testing R^2 values, leads to the conclusion that the models exhibit a high degree of overfitting, failing to adequately represent the underlying patterns.

Table 4: Baseline results of normalized data using all input parameters

Model	MSE		R^2	
	Training	Testing	Training	Testing
linear	0.17	0.48	58.52%	-23.13%
poly	0.00	220.01	100.00%	-52886.43%
lasso	0.31	0.36	23.97%	7.54%
mlp	0.24	0.33	39.24%	13.11%
svr	0.13	0.32	66.71%	13.57%
tree	0.13	0.35	68.90%	13.80%

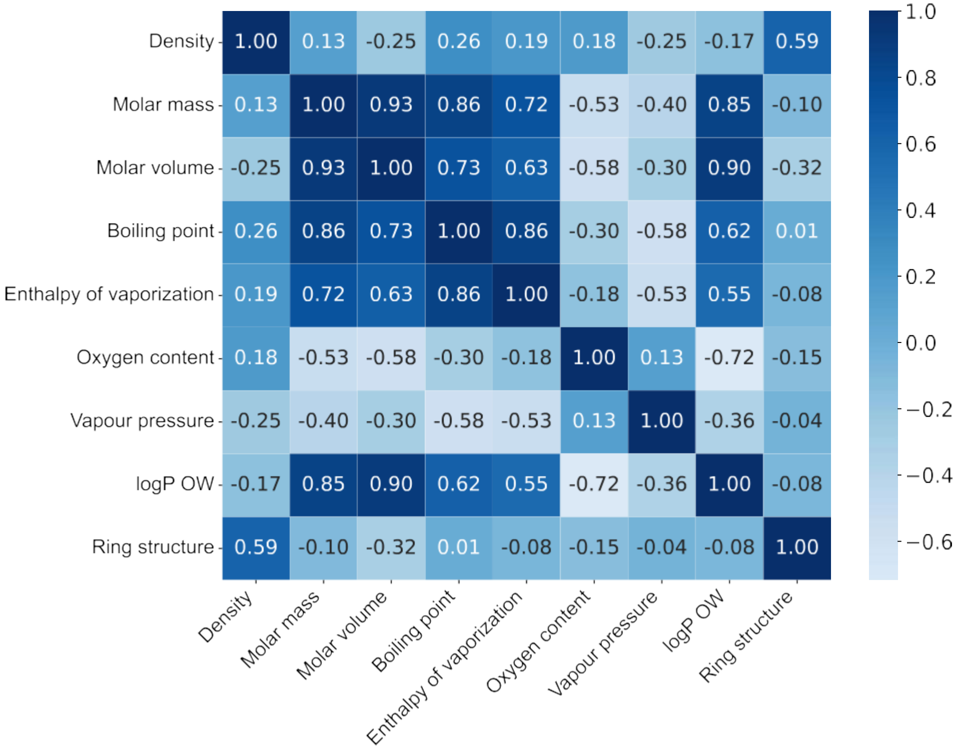

Figure 4: Correlation matrix of input parameters

When investigating the correlation matrix of the input parameters, it becomes apparent that several parameters show a high correlation score (see Figure 4). Applying the same models only on selected parameters with a correlation score lower than 0.80, leads to a small decrease in training accuracy (increase of MSE) while positively affecting the testing accuracy to a greater degree, and thus decreasing the overfitting effect. This is also apparent in the increase in R^2 score during the testing process (see Table 5). Another benefit of reducing the number of input parameters is the accelerated computation time.

Table 5: Results of normalized input data using selected input parameters. With absolute difference to baseline ΔBL

Model	MSE				R^2			
	Train	ΔBL	Test	ΔBL	Train	ΔBL	Test	ΔBL
linear	0.19	0.02	0.33	-0.15	52.58%	-6%	13.06%	36%
poly	0.09	0.09	0.59	-219.42	76.99%	-23%	-51.02%	52835%
lasso	0.32	0.01	0.33	-0.03	20.83%	-3%	16.84%	9%
mlp	0.20	-0.05	0.30	-0.03	51.49%	12%	21.23%	8%
svr	0.23	0.10	0.32	-0.01	42.50%	-24%	19.53%	6%
tree	0.13	0.01	0.39	0.04	67.58%	-1%	-6.27%	-20%

5 Discussion

Although the overall performance of the single methods cannot be evaluated at this time due to the limited number of data samples, the results indicate the potential for a promising framework that addresses common drawbacks in data-based regression tasks and predicts the elastomers volume change based on known fluid parameters. The initial setup of the framework yields baseline performance scores, to which all future investigations and additions can be compared. It is expected that with more data samples the results become more evident. Those data samples are constantly being generated by conducting more experimental immersion tests.

It is shown that the reduction of dimensionality by only selecting uncorrelated input parameters, the effect of overfitting was reduced. Although a loss of input information was introduced, the overall performance was not affected. Since at this point only a first selection of parameters is chosen to indirectly describe the polarity and steric requirement, further, more substantial, parameters could be introduced to describe the underlying effects of elastomer swelling more accurately.

It must be noted that at this stage of development, no special attention was paid to preselecting the most suitable hyperparameter-grid for each model on which the method “hal ing grid search” was applied to determine the best hyperparameters for the given model and data. It is evident, that providing at least a preliminary selection of suitable hyperparameters would enhance each model’s performance.

6 Summary and outlook

In this work, a hands-on application of ML regression models was developed to precisely plan the further experimental investigation of the material compatibility of bio-hybrid fuels and elastomer sealing materials. Based on the results of previously conducted immersion tests and physics related fluid properties as input parameters the elastomers volume change is predicted with several regression models. Within the developed framework common drawbacks of data-based ML methods were addressed.

Due to the limited number of samples available at this stage of development, a baseline score of the different models was computed which builds the foundation in the ongoing development process. The framework allows to be easily extended by means of addition of new samples or input parameters. Therefore, further immersion tests are currently being conducted, firstly focusing solely on SRE-NBR 28/SX and different fuels or liquids. Based on the expanded database the actual performance of the models can be tuned and evaluated. Simultaneously additional fluid properties are considered as input parameters allowing for the use of an iterative selection process of few parameters that describe the underlying physics most accurately. This way, the best performing model and input parameters are selected for SRE-NBR 28/SX, enabling the extension of the investigation to other (standard-reference) elastomeric materials. Given the selected model and understanding of how fluid properties affect the material compatibility, also the influence of additives in technical seals can be investigated in the future.

7 Acknowledgements

Funded by the Deutsche Forschungsgemeinschaft (DFG, German Research Foundation) under Germany´s Excellence Strategy – Exzellenzcluster 86 „The Fuel cience Center” ID: 390919832.

8 References

[1] Hofmeister, M.; Schmitz, K.; Laker, J.; Pischinger, S.; Fischer, M. Neue Herausforderungen an Dichtungswerkstoffe im Hinblick auf bio-hybride Kraftstoffe. *Mobility*, **2022**, *7*.

[2] Hofmeister, M.; Frische, A.; Grunewald, M.; Reddemann, M.; Gütering, C.; Blank, L.M.; Kneer, R.; Schmitz, K. Tribological properties of PTFE sealing materials with regard to bio-hybrid fuels. In: *Sealing technology - old school and cutting edge*: *International Sealing Conference : 21st ISC, Stuttgart, Germany, October 12-13, 2022*; Fachverband Fluidtechnik im VDMA e.V: Frankfurt am Main, **2022**; pp. 89–104.

[3] Makansi, F.; Schmitz, K. Simulation-Based Data Sampling for Condition Monitoring of Fluid Power Drives. *IOP Conf. Ser.: Mater. Sci. Eng.*, **2021**, *1097,* 12018.

[4] Duensing, Y.; Rodas Rivas, A.; Schmitz, K. Machine Learning for failure mode detection in mobile machinery. In: *11. Kolloquium Mobilhydraulik : Karlsruhe, 10. September 2020*. Geimer, M., Synek, P.-M., Eds.; KIT Scientific Publishing, **2020**.

[5] Okolie, J.A. Introduction of Machine Learning and artificial intelligence in biofuel technology. *Current Opinion in Green and Sustainable Chemistry*, **2024,** 100928.

[6] Li, J.; Pan, L.; Suvarna, M.; Tong, Y.W.; Wang, X. Fuel properties of hydrochar and pyrochar: Prediction and exploration with machine learning. *Applied Energy*, **2020**, *269,* 115166.

[7] DIN e.V. *DIN EN 590:2022-05: Kraftstoffe - Dieselkraftstoff - Anforderungen und Prüfverfahren;* Beuth Verlag GmbH: 10772 Berlin, **2022-05-00**.

[8] DIN e.V. *DIN EN 228:2017-08: Kraftstoffe - Unverbleite Ottokraftstoffe - Anforderungen und Prüfverfahren;* Beuth Verlag GmbH: 10772 Berlin, **2017-08**.

[9] Voelker, S.; Deutz, S.; Burre, J.; Bongartz, D.; Omari, A.; Lehrheuer, B.; Mitsos, A.; Pischinger, S.; Bardow, A.; Assen, N. von der. Blend for all or pure for few? Well-to-wheel life cycle assessment of blending electricity-based OME 3–5 with fossil diesel. *Sustainable Energy Fuels*, **2022**, *6,* 1959–1973.

[10] Bardow, A.; Voelker, S.; Groll, N.; Bachmann, M.; Mueller, L.; Neumann, M.; Kossioris, T.; Muthyala, P.; Lehrheuer, B.; Hofmeister, M.; Vorholt, A.; Schmitz, K.; Pischinger, S.; Leitner, W. Towards carbon-neutral and clean combustion with hydroformylated Fischer-Tropsch (HyFiT) fuels, **2023**.

[11] Ackermann, P.; Braun, K.E.; Burkardt, P.; Heger, S.; König, A.; Morsch, P.; Lehrheuer, B.; Surger, M.; Völker, S.; Blank, L.M.; Du, M.; Heufer, K.A.; Roß-Nickoll, M.; Viell, J.; Aßen, N. von der; Mitsos, A.; Pischinger, S.; Dahmen, M. Designed to Be Green, Economic, and Efficient: A Ketone-Ester-Alcohol-Alkane Blend for Future Spark-Ignition Engines. *ChemSusChem*, **2021**, *14,* 5254–5264.

[12] Heitzig, S.; Murrenhoff, H.; Weinebeck, A. Investigation of fluid-seal interaction and their prediction based on the Hansen Parameters. *O + P : Fluidtechnik für den Maschinen- und Anlagenbau*, **2015**, *59*.

[13] Bishop, C.M. *Pattern Recognition and Machine Learning,* 1st ed.; Springer New York: New York, NY, **2016**.

[14] Pedregosa, F.; Varoquaux, G.; Gramfort, A.; Michel, V.; Thirion, B.; Grisel, O.; Blondel, M.; Prettenhofer, P.; Weiss, R.; Dubourg, V.; Vanderplas, J.; Passos, A.; Cournapeau, D.; Brucher, M.; Perrot, M.; Duchesnay, É. Scikit-learn: Machine Learning in Python. *Journal of Machine Learning Research*, **2011**, *12,* 2825–2830.

[15] DIN e.V. *DIN ISO 1817:2016-11: Rubber vulcanized or thermoplastic - Determination of the effect of liquids;* Beuth Verlag GmbH: 10772 Berlin, **2016-11**.

[16] DIN e.V. *DIN ISO 13226:2021-06: Elastomere - Standard-Referenz-Elastomere (SREs) zur Charakterisierung des Verhaltens von Flüssigkeiten auf Elastomere;* Beuth Verlag GmbH: 10772 Berlin, **06.2021**.

[17] DIN e.V. *DIN 53521:1987-11: Prüfung von Kautschuk und Elastomeren - Bestimmung des Verhaltens gegen Flüssigkeiten, Dämpfe und Gase;* Beuth Verlag GmbH: Berlin, **11.1987**.

[18] Kier, L.B. Quantitation of solvent polarity based on molecular structure. *Journal of Pharmaceutical Sciences*, **1981**, *70,* 930–933.
[19] Palomar, J.; Torrecilla, J.S.; Lemus, J.; Ferro, V.R.; Rodríguez, F. A COSMO-RS based guide to analyze/quantify the polarity of ionic liquids and their mixtures with organic cosolvents. *Physical chemistry chemical physics : PCCP*, **2010**, *12,* 1991–2000.
[20] Hansen, C.M. *Hansen solubility parameters: A user's handbook,* 2nd ed.; Taylor & Francis: Boca Raton, **2007**.
[21] Asfour, A.-F.A.; Saleem, M.; Kee, D. de; Harrison, B.H. Diffusion of saturated hydrocarbons in low density polyethylene (LDPE) films. *J of Applied Polymer Sci*, **1989**, *38,* 1503–1514.
[22] Hildebrand, J.H.; Scott, R.L. *The solubility of nonelectrolytes / Joel H. Hildebrand Robert L. Scott,* 3rd ed.; Dover Publ: New York, **1964**.
[23] Cheméo. Chemical and physical properties from Cheméo. https://www.chemeo.com/ (Accessed April 25, 2024).
[24] Linstrom, P. *NIST Chemistry WebBook, NIST Standard Reference Database 69*, **1997**.
[25] Wildman, S.A.; Crippen, G.M. Prediction of Physicochemical Parameters by Atomic Contributions. *J. Chem. Inf. Comput. Sci.*, **1999**, *39,* 868–873.
[26] Raschka, S. *Model Evaluation, Model Selection, and Algorithm Selection in Machine Learning*, **November 13, 2018**.

9 Authors

RWTH Aachen University, Institute for Fluid Power Drives and Systems (ifas)

Campus-Boulevard 30, 52074 Aachen, Germany:

Lukas Boden, M. Sc., ORCID 0009-0003-1282-8032,
lukas.boden@ifas.rwth-aachen.de

Marius Hofmeister, M. Sc., ORCID 0000-0002-6672-5800,
marius.hofmeister@ifas.rwth-aachen.de

Faras Brumand-Poor, M. Sc. M. Sc., ORCID 0009-0006-7442-8706,
faras.brumand@ifas.rwth-aachen.de

Linda Pleninger, B. Eng., ORCID 0009-0003-9085-2572,
linda.pleninger@rwth-aachen.de

Univ.-Prof. Dr.-Ing. Katharina Schmitz, ORCID 0000-0002-1454-8267,
katharina.schmitz@ifas.rwth-aachen.de

https://doi.org/10.61319/A2FETW2F

Poetry and truth, how does the hydrolysis-resistant structure come into the polyurethane ? - New, soft, chemical-resistant TPU for pneumatics with a proportion of biogenic raw materials

Joachim Möschel, Dipl. Ing (FH), Konzelmann GmbH, Löchgau

Pneumatic cylinders convert the compressed air generated by compressors into mechanical energy. The piston rod in the cylinder is moved using compressed air, which means that power is usually transmitted in a linear direction. The elastic seals on the piston and rod play a central role here when it comes to function, tightness, energy efficiency and service life in the case of pneumatic cylinders and valves.

Traditionally, TPUs compete with soft rubber materials, especially when it comes to covering high-quality chemical resistance in this genre. Rubber materials have so far been the first choice when it comes to higher temperature requirements and chemical resistance.

Konzelmann (KKI) is currently working on bringing a platform of high-performance TPU materials for pneumatics, among other things, to market maturity. These should not only have high chemical resistance, but also meet all standard market requirements for cylinders and valves.

In the usual structure of TPU, urethane hard phases are used, which are homogeniously distributed as domains in an ester or ether soft phase. Their characteristics and frequency are the reason for the high-quality physical properties.

The predominantly amorphous soft segment consists of special macrodiols, which are potentially at risk of degradation due to their polar structure. The ester groups present in the soft segment can be attacked by various application-relevant media: e.g.

- Lubricating greases with alkaline soaps
- External cleaners
- Diluted acids, alkalis
- Food media
- CIP media
- Bio-oils
- Tropical humidity in combination with bio-oils or lubricating greases

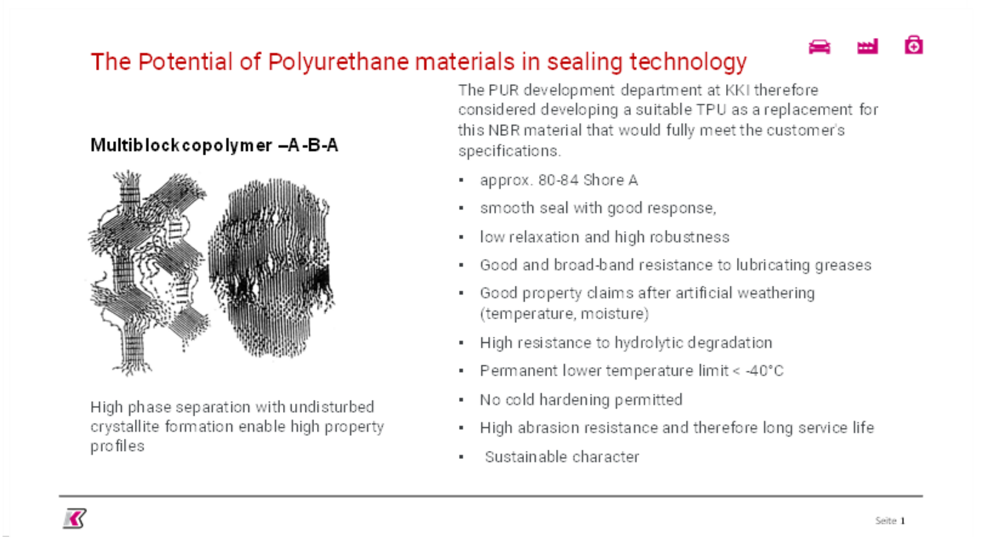

Objective:

The starting point was the requirement to develop a tailor-made sealing lip material for a pneumatically operated pulse generator piston used in a truck brake. This was to be manufactured as a complete piston using a 2K process, with the hard core made of aliphatic polyketone being overmolded with the new polyurethane material.

In the previous generation, the complete piston was made of aromatic polyamide paired with a soft NBR. The problem arose on the one hand from a certain influence of moisture, which caused the piston based on aromatic polyamide to swell, the sealing lip was pressed too tightly and as a result there was severe abrasion. The NBR, which was trimmed to meet the demanding cold requirement of -40°, was initially able to meet this high requirement. After heat exposure at 85°C, the flexibility in the cold area deteriorated significantly, with the piston allowing very high leaks at low temperatures. The analysis showed cold hardening, which was noticeable due to plasticizer migration and increasing post-crosslinking on the butadiene groups of the NBR. This meant that the cold tightness requirement of -40°C could no longer be met.

The PUR development department at KKI therefore considered developing a suitable TPU as a replacement for this NBR material that would fully meet the customer's specifications:

- approx. 80-84 Shore A
- smooth seal with good response, low relaxation and high robustness
- Good and broad-band resistance to lubricating greases
- Good property claims after artificial weathering
- High resistance to hydrolytic degradation
- Permanent lower temperature limit < -40°C

- No cold hardening permitted
- High abrasion resistance and therefore long service life
- Sustainable character

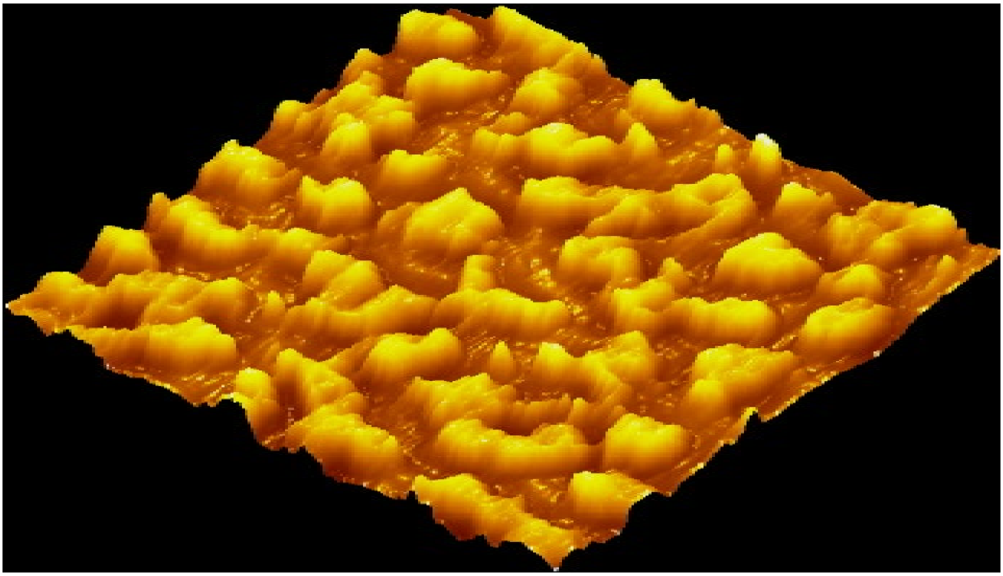

TPU as a high-performance elastomer with a two-phase structure: Atomical force microscopy / submicrometer structure / Picture: Currenta

The protruding areas visualize the hard segment, the valleys the soft segment

Due to the bivalent structure of the TPU chains, the crystallization-capable areas can separate from the amorphous areas. This means that the phase-separated polymer can form ordered areas in the form of hard and soft segments.

Regularly structured, aromatic urethane hard phases are usually used, which are distributed as clusters in a non-crystalline ester or ether soft phase. They cause physical cross-linking points by means of hydrogen bonds on the negatively charged electron pairs of the carbonyl groups (in the urethane functions) and thus ensure high cohesive forces (tear propagation energies). The predominantly amorphous soft segment consists of special macrodiols, which, as mentioned, are based on ester and ether functions. Due to its polarity, it mainly contributes to the material swelling in polar media and the TPU breaking down over time under the influence of temperature.

Based on new modified biogenic raw materials, innovative TPU materials have been developed. Their soft segments also enable significantly lower glass transition ranges and, due to their more hydrophobic nature, higher chemical stability (1).

The following table shows the physical property profiles of the new TPU materials, VP 020 and VP 026, in comparison to a commodity TPU and a low temperature NBR:

These are consistently at a high level: Compared to the referenced NBR material, 3.6 times the tensile strength and 5.8 times the tear resistance as well as 80% lower abrasion values according to DIN ISO 4649.

Eqorctkuqp"qh"rtqrgtv{"rtqdnkgu<"Jkij"rgthqtocpeg"VRW xu0"eqooqfkv{"xu0"PDT

	Hardness Shore A	Tensile-Modulus (Mpa)	Tensile Strength (Mpa)	Elongation at break (%)	Tear Resistance (N / mm)	Rebound Resilience (%)	Abrasion mm³	Content of biogenic Raw material
Norm	DIN ISO 7619-1	Tangenten -modul	DIN 53504	DIN 53504	DIN ISO 34-1	DIN 53517	DIN ISO 4649	
VP 020	84,9	12	51,2	>500%	47	62,9	21,	**26%**
VP 026	84,5	12	51,5	>500%	53	58,5	21,6	**45%**
C-TPU 85 A AU	87	28	33,1	750	58	49,3	30	---
NBR 75	76	8	14	220	8	20	118	---

For the newly developed materials there could be found a much higher level of physical properties in comparison to the C-TPU and the NBR-material.

The values for permanent deformation at higher temperatures are only slightly higher than for NBR. In contrast, C-TPU 85 A falls significantly in this comparison. At a short-term elevated temperature (3h/130°C), relatively low CS values are determined for VP 020 and VP 026.

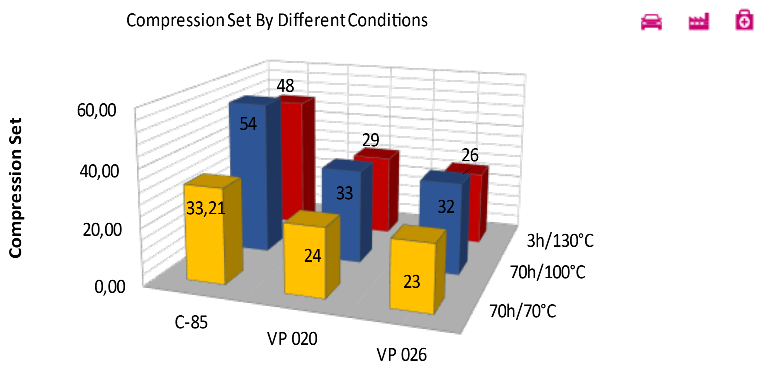

	C-85	VP 020	VP 026
70h/70°C	33,21	24	23
70h/100°C	54	33	32
3h/130°C	48	29	26

Seite 1

The artificial weathering cycle specified by the customer is defined as follows:

1. 400 hours at 85°C at 93% relative humidity

2. Subsequently, 100 hours in 85°C hot air

It was found that the prescribed weathering cycle does not lead to degradation of the materials VP 020 and VP 026. No significant changes are evident in any of the relevant parameters.

The following table shows the long-term hydrolysis behavior at 85°C in hot water:

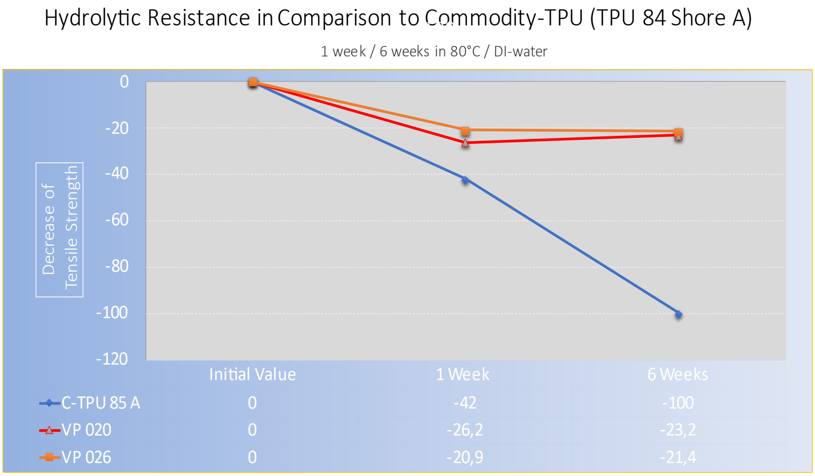

The course of the tensile strength can be linked to the degradation of the average molecular weight (2).

Ultimately, the ester-based commodity TPU is no longer usable after two weeks. In contrast, the two newly developed TPU materials show slight degradation with a loss of tensile strength of around 22% and continue to perform their function without impairment after 1000 hours.

In practice, there are many influences that require stability against hydrolyzing media. Many lubricants, additives or thickeners can generate degradation, especially in conjunction with tropical humidity. Acidic or alkaline cleaning fluids can also break down polyurethanes after a short time. For this reason Hydrolysis-resistant materials can be seen as a high priority in food applications in conjunction with CIP media.

To determine their general suitability for pneumatics, some commercially available types of grease were tested for resistance. Ultimately, the newly developed materials show a very broad range of resistance in commercially available pneumatic greases:

Immersion Testing of VP 020 and VP 026
Testing Conditions: 85°C 168h

		Change in Tensile Strength (MPa)	Volumen Change (%)	Change in Hardness (Shore A)
VP 020	Autol Top 2000 SL	+ 22,3	+5,4	-2,6
VP 026	Autol Top 2000 SL	+6,6	+3,2	-2,3
VP 020	Elkalub GLS 993 H1	+5,9	-0,3	-1,7
VP 026	Elkalub GLS 993 H1	+5,3	-0,7	-1,2
VP 020	Mobilux EP 2 NLG2	+2,0	+2,8	-2,5
VP 026	Mobilux EP 2 NLG2	-1,9	+1,4	-1,9

DMA-Low Temperature Analysis of VP 020

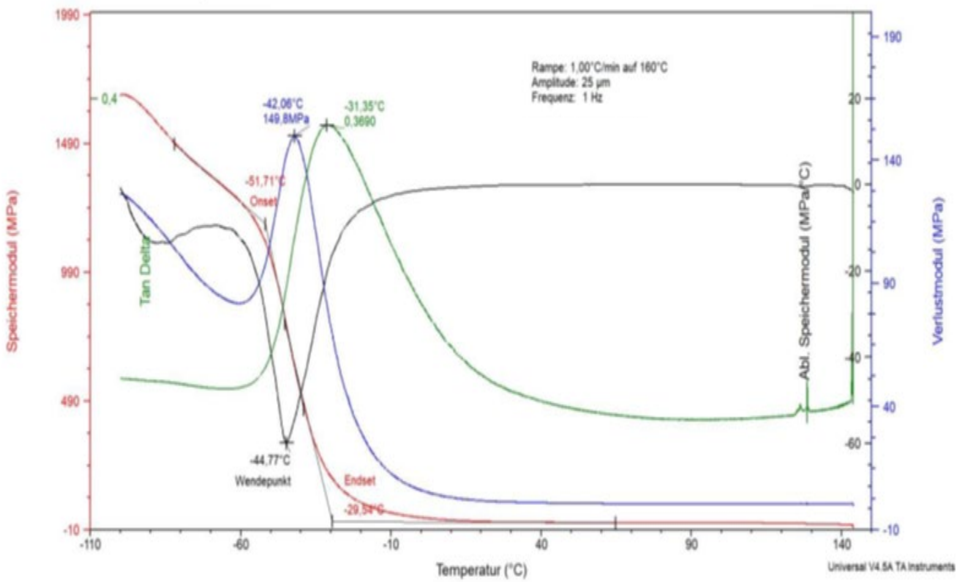

	Onset of the E'-Curve	Turning Point of the E'-Curve
VP 020	-51,7	-44,8
VP 026	-44,7	- 34,9

The low temperature properties of the new TPUs are of crucial importance for the function of the pulse generator piston. The cold behavior of the weathered samples was determined on the basis of a DMA measurement. The heating rate selected was 1K/min at 1 Hz in tension mode. The E' values (red curve) resulting from the DMA measurement describe the elastic behavior of the material.

A turning point of -44.8°C for VP 020 ultimately provides evidence of sufficiently good cold flexibility for the intended application on the pulse generator piston. The soft segment, which is chemically firmly integrated into the PUR matrix, does not allow any negative changes here. Likewise, no post-crosslinking has taken place, triggered by the artificial weathering.

It was therefore obvious that VP 020 would be the preferred choice for the pulse generator piston in the intended series application.

Other target applications for VP 020/VP 026 can be found in pneumatics piston and valve seals as well as flange seals and O-rings (2).

In particular, when standard TPU grades lead to rapid degradation due to chemical influences, these newly developed TPU materials can lead to reliable problem solutions.

The structure of these materials contains relevant proportions of renewable raw materials, which means that with 26% for VP 020 and 45% for VP 026, it has been possible to establish a sustainable sealing product portfolio.

Sources:

[1] “Oleochemical products as building blocks for polymers” Andreas Heidbreder, Rainer Höfer, Roland Grützmacher, Alfred Westfechtel, C. William Blewett Veröffentlichung: Wiley- VCH Verlag GmbH, Weinheim, 1999

[2] „Thermoplastische Polyurethan-Werkstoffe für anspruchsvolle O-Ring Anwendungen in der Fluid-Industrie“ Joachim Möschel Vortrag ISGATEC-Forum 17./18. 11. 2020

https://doi.org/10.61319/CR9CO7U2

μ-Mechanical characterization of tribologically stressed elastomer surfaces with respect to radial shaft sealing systems

Christian Wilbs, Matthias Adler, Daniel Frölich, Alisa Bellon, Nicole Schuster, Jasmin Menzel, Emely Bopp

This paper introduces the new μ-mechanical characterization method and its application for the post-test analysis of radial shaft seals (RSS) used for dynamic lubricant-elastomer compatibility tests. Therefore, the measurement procedure and accuracy will be discussed as well as the features which can be drawn from the measured force-displacement curve. Furthermore, it will be shown, how these features allow a precise evaluation of the seal material condition regarding hard deposits, hardening and softening. This will be summarized by showing the correlation of the visual-haptic elastomer assessment and the results of the newly developed characterization method which will increase the significance of dynamic lubricant-elastomer tests.

1 Introduction

The radial shaft seal (RSS) is a widely used machine element, e.g. in gearboxes to seal lubricants against the environment. For this purpose, the RSS, the shaft surface, and the sealed fluid as well as the operation conditions (sliding speed, temperature, pressure, etc.) form a tribological system - the radial shaft sealing system (Figure 2). In terms of sustainability and cost efficiency, high expectations are set on the reliability and service life of such radial shaft sealing systems.

Figure 1 Worm-gearbox with leakage due to lubricant-elastomer incompatibility

Therefore, downtimes due to maintenance or even leakages (Figure 1) must be avoided. In particular, the complex interactions between the sealed lubricant and the radial shaft seal have a major influence on the long-term reliability and lifetime of a radial shaft sealing system. It is therefore essential to ensure lubricant-elastomer compatibility under dynamic tribological stress.

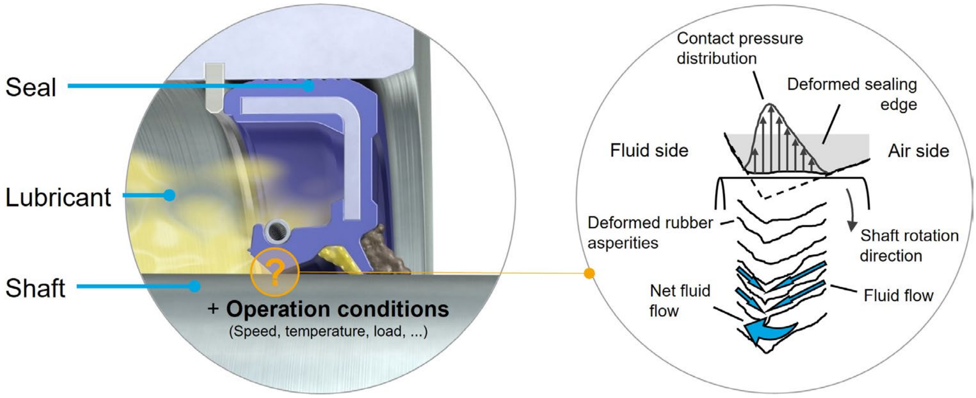

Figure 2 Radial-shaft-sealing System [1] (left side) and reverse pumping effect according to Kammüller [2] (right side)

The lubricant elastomer compatibility can be verified by dynamic tests in accordance with established industry test standards. Due to the tribological stress of the lubricant and seal material within the sealing gap, physical and chemical interactions between lubricant and elastomer take place (see Figure 3) [5].

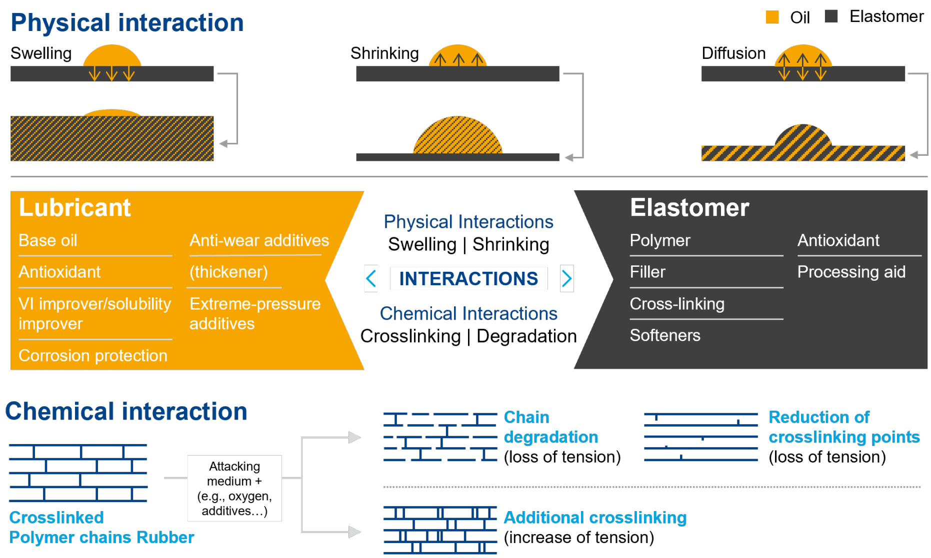

Figure 3 Lubricant-elastomer interaction

Depending on whether the compatibility between lubricant and elastomer is given or not the intensity of interactions is different and has impact on the properties of the lubricant and elastomer. Especially the near surface material properties (µ-mechanical material properties) within the first 60 µm of the sealing edge are crucial for a well performing reverse pumping effect (see Figure 2, right side) and therefore the performance of the radial shaft sealing system.

2 RSS Analysis and Characteristics

The post-test analysis of the RSS is an essential process to determine the material condition and how the lubricant affects the seal under tribological stress. Besides leakage, seal wear width, shaft wear depth, radial load- and interference change it is of great importance to consider the near surface material condition of the sealing edge. While the seal and shaft wear, the radial load and interference are measurable continuous values the seal material condition, is rated based on visual-haptic feedback of the material by seal experts with years of practical experience. The material condition rating scale is not a continuous value but a categorial with five levels: without (= 1), little (= 2), moderate (= 3), heavy (= 4) and severe (= 5). This scale is applied to nine post-test seal characteristics to determine the intensity of the seal condition change, see Table 1.

Table 1 Post-test seal condition characteristics

Characteristic	**Method**
Grooving	Visual
Hollow wear	Visual
Contact discoloration	Visual
Cracking	Visual*
Blistering	Visual*
Soft deposits	Visual-haptic
Hard deposits	Visual-haptic
Hardening	Visual-haptic
Softening	Visual-haptic

*) in some cases, also haptic feedback

While grooving, hollow wear and the wear band width, are describing the geometrical change of the sealing lip, the other characteristics, such as deposits (soft and hard), cracking, blistering, hardening, and softening allow a conclusion regarding the physical and chemical interaction influencing the seal material properties [4].

Even though that all characteristics are important to be considered, hard deposits, hardening and softening are essential for the dynamic sealing function and at the same time the most difficult to rate. Because all three characteristics are evaluated not only through visual inspection, but also by haptic feedback, which indicates whether the sealing edge is harder or softer than before the test or if there is a hard, brittle layer covering the sealing edge.

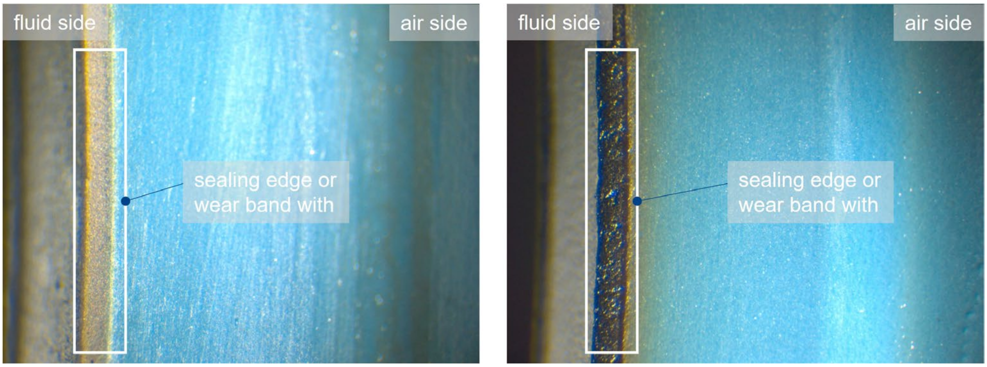

Figure 4 NBR seal after 768h dynamic test showing no damage (test no. 3, left side) and hard deposits covering the sealing edge due to incompatibility (test no. 2, right side)

The left side of Figure 4 shows a post-test sealing edge of a NBR seal without any sign of a significant change of the material property, indicating a good lubricant elastomer compatibility. All other results of the dynamic test have been within the limits too. In comparison, the sealing edge in Figure 4 on the right side is covered by a dark, brittle, hard layer – hard deposits – indication a lubricant incompatibility. The corresponding dynamic test results show that 3 out of 3 seals leaked after only 120 h and the shaft wear is above 10 µm.

This comparison uses two extreme examples – highly compatible (Figure 4, left side) vs. highly incompatible (Figure 4, right side) lubricants which makes it easy to differentiate one from the other. However, for the purpose of development and approval tests, it is crucial to distinguish the condition of the seal material across a range of possibilities, ensuring repeatability and reproducibility even within these extreme variations. Therefore, it is necessary to move from a visual-haptic feedback rating with a categorial scale to an objective measurement method of continuous values.

3 µ-Mechanical Material Characterization of RSS

The new tactile seal characterization method – “µ-mechanical seal characterization” – is realized by using a micro indentation tester named “LNP® nano touch” with a high precision force-displacement sensor (force resolution: 0.6 mN). Due to the very small probe tip radius of R = 40 µm it is possible to measure directly on the wear band, even of narrow wear band widths of 100 - 150 µm (see Figure 5, detailed view).

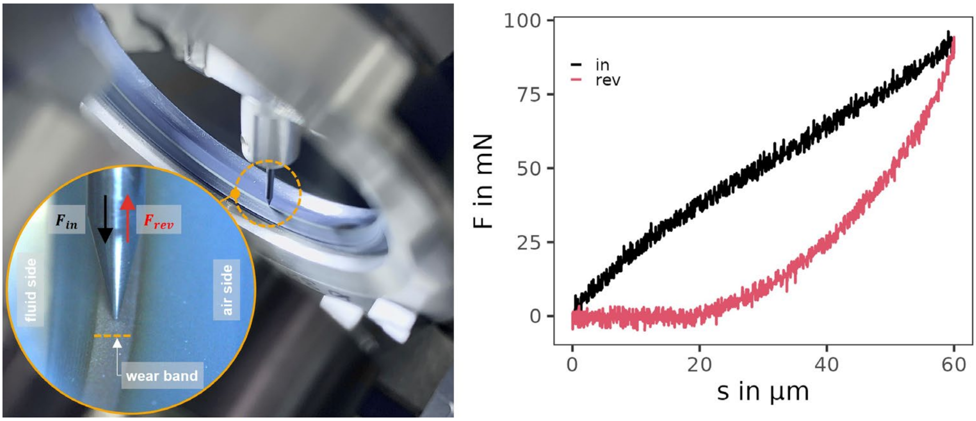

Figure 5 µ-Mechanical measurement setup and force-displacement curve

In Figure 5 (left side) is shown the measurement setup with the mounted seal and a detailed view of the probe tip positioned on top of the wear band. The measurement results in a force-displacement curve (Figure 5, right side) showing the force F on the vertical axis in mN and the penetration depth s on the horizontal axis in µm. The colour differentiates the force when the probe is penetrating the seal F_{in} (black line) and reversing F_{rev} (red line). To ensure comparability of the results it is necessary to use the same measurement parameters (see Table 2).

Table 2 Measurement parameters

Measurement	Value	Unit
Probe-tip type	Sphere (Radius)	-
Probe-tip radius	40	µm
s_M	60	µm
v_M	5	µm/s
t_M	0	s
s_L	0	s
v_L	5	µm/s
t_L	0	s
Type	v-Control Linear	-

However, with the force-displacement curve alone it is not possible to characterize a seal properly. Thus, features need to be calculated from the curve which then allow the characterization of the seal material properties, in particular: hard deposits, hardening and softening.

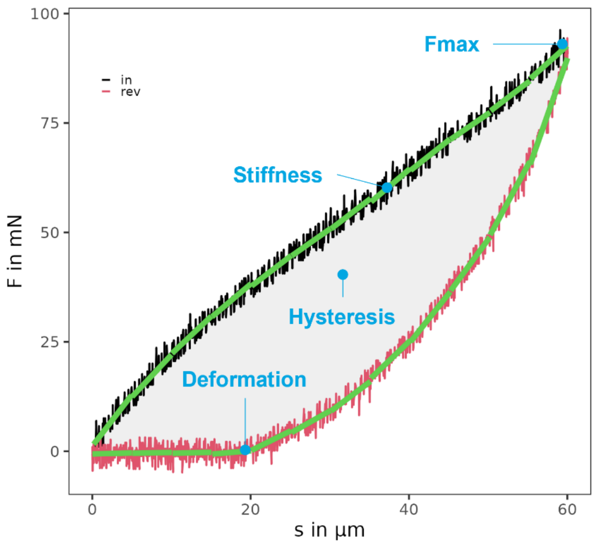

Figure 6 µ-Mechanical characteristics calculated from the force-displacement curve

Figure 6 shows qualitatively the calculated features from the force-displacement curve in blue. F_{max} is the maximum measured force at the maximum penetration depth s_M. The Hysteresis H is the relative area enclosed by the F_{in}- and F_{rev}-curve related to the area under the F_{in}-curve. The slope derived from a linear regression of the force-displacement curve at a discretization length of 5 µm corresponds to the stiffness S of the seal material. Another interesting feature is the homogeneity b which describes the rate between the surface stiffness and the bulk stiffness. The surface stiffness is considered as the mean stiffness of the penetration depth range from 0 to 15 µm and the bulk stiffness as the mean stiffness from 50 to 60 µm. Table 3 summarizes the most important features calculated from the force-displacement curve for a proper post-test µ-mechanical seal material characterization.

Table 3 µ-Mechanical features for seal characterization

Characteristic		**Unit**
F_{max}	Maximum force	mN
H	Hysteresis	-
S	Stiffness	mN/µm
b	Homogeneity	-

4 RSS Characterization Map and Interpretation

Finally, Figure 7 shows the RSS Characterization Map including the maximum force F_{max} in mN on the horizontal axis, the hysteresis H in % on the vertical axis and the homogeneity b as colour code.

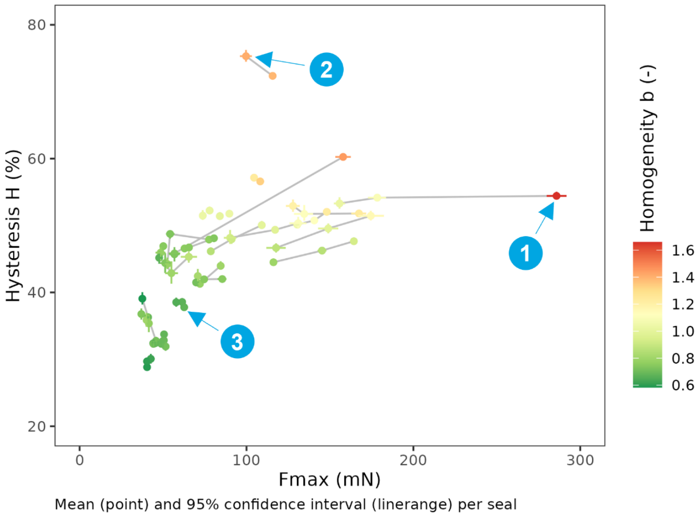

Figure 7 RSS Characterization Map

The Characterization Map includes only results from dynamic tests with seals out of 72 NBR 902, but with different test conditions (e.g. fluid, pressure, duration, sliding speed, etc.). The two examples, test no. 2 and 3, were tested at the same test conditions but with different fluids and test no. 1 additionally at a higher duration time and pressurization. The general trend in data shows with increasing maximal force F_{max} a fast rise of the hysteresis H and the homogeneity b (green to red) before it is levelling out at high F_{max} values. This curve progression correlates with the seal material degradation intensity due to lubricant elastomer incompatibility.

Table 4 shows the post-test material condition rating results of the visual-haptic feedback method and the corresponding results from the micro mechanical characterization.

Table 4 Post-test material condition rating results

No	Damage	Rating (-)	Fmax (mN)	Hysteresis (%)	Stiffness bulk (mN/µm)	Homogeneity (-)
1	Hardening	5	280	54	3.0	1.7
2	Hard deposits Softening	5 4	99	78	1.6	1.3
3	none	1	61	38	0.9	0.7

The test results clearly show the difference between hardening and hard deposits. Since hardening is mainly correlated to high F_{max} values and a bulk stiffness S greater than approx. 1.8 mN/µm while hard deposits correlate with a high hysteresis H, homogeneity b greater than 1.1 and relatively small F_{max} values. Often the seal material underneath hard deposits is softened as well. In Figure 8 the seal condition and stiffness curves of test 1 to 3 are shown.

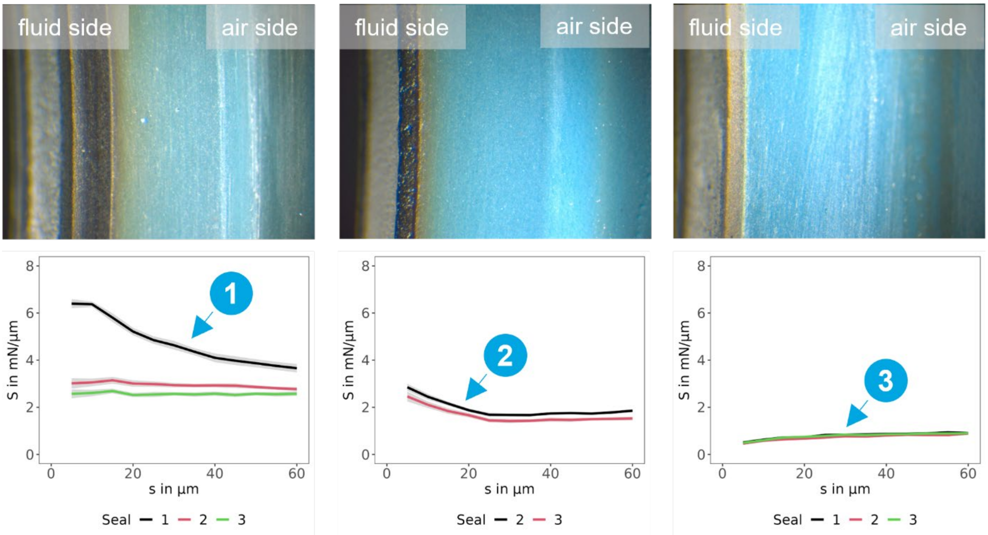

Figure 8 Seal wear band and stiffness curve

Seal 2 and 3 of test 1 show a typical stiffness curve for hardened seals, a constant progression at a high stiffness level (bulk stiffness approx. 3 mN/µm). Sometimes the material at the surface is even more hardened as the stiffness curve of seal 1 reveals. However, the stiffness curve of seals with hard deposits show a significant drop to a lower level of stiffness (bulk stiffness approx. 1.6 mN/µm) after the first 15-20 µm. The penetration depth range where the stiffness is degreasing until it is levelling out corresponds to the layer thickness of the hard deposits. In contrast the stiffness curves of test 3 are slowly rising with increasing penetration depth s and levelling out at a bulk stiffness of approximately 1 mN/µm indicating that no material degradation took place and therefore a good lubricant elastomer compatibility.

5 Summary and Conclusion

The new µ-mechanical seal characterization method realized by using the micro indentation tester from LNP® and the here presented features drawn from the force-displacement curve, are the basis to successively update the state-of-the-art visual-haptic seal assessment method. Features such as the maximum force F_{max}, hysteresis H, homogeneity b and the stiffness curve S allow a characterization of the seal material properties change and thus an evaluation of the lubricant elastomer compatibility. This characterization and evaluation are based on highly precise measurements which will increase the significance of dynamic lubricant elastomer compatibility tests even more. Other interesting outcomes of this analysis are, that it shows:

1. The new µ-mechanical characterization method accurately reflects the results from the visual-haptic feedback method and the dynamic test results.
2. With increasing seal material degradation due to incompatibility, the precise µ-mechanical measurement shows an increased, up to 4 times higher, variation of the results. This suggests that the variation is mainly caused by unstable tribological conditions within the contact due to an incompatibility.

Increasing the experience with the new µ-mechanical characterization method will allow to narrow down the exact feature combinations and limits for a complete characterization. Also, the development of further features [3] will provide the possibility to characterize additional characteristics e.g. in terms of seal wear or permanent deformation. Furthermore, it is necessary to extend the analysis to other elastomer compounds such as FKM's, ACM's and HNBR's.

6 Nomenclature

Variable	***Description***	***Unit***
F	Measured force	[mN]
F_{max}	Maximum force	[mN]
H	Hysteresis	[-]
S	Stiffness	[mN/µm]
b	Homogeneity	[-]
s	Penetration depth	[µm]
s_M	Maximum penetration depth	[µm]
v_M	Penetration velocity	[µm/s]
t_M	Holding time at maximum penetration depth	[s]
s_L	End of test penetration depth	[µm]
v_L	Reverse velocity	[µm/s]
t_L	Holding time at end of test penetration depth	[s]

7 References

[1] Freudenberg FST GmbH, Weinheim, 2024

[2] Kammüller, M.: *Zur Abdichtwirkung von Radial-Wellendichtringen*, Dissertation, Stuttgart, Institut für Maschinenelemente, 1986

[3] Alt K., Hüttinger A., Wöppermann M.: *Automatisierung und Standardisierung der Analyse von tribologisch geschädigten Radialwellendichtringen*, 64. Tribologie-Fachtagung, 2023

[4] Merkle, L., Bauer F.: *Gestaltung von Lastkollektiven zur Prüfung von Radial-Wellendichtungen*, FVA 696 III / 696 IV, Heft 1512, Forschungsvereinigung Antriebstechnik e.V., Frankfurt am Main, 2022

[5] Weiser, G. S.: *Bedeutung instationärer Versuchsbedingungen für die Testung von Radialwellendichtringen am Beispiel der Blasenbildung*, Dissertation, Technische Universität Hamburg, 2023

8 Authors

Freudenberg FST GmbH

Höhnerweg 2-4, 69469 Weinheim, Germany:

Christian Wilbs, M. Sc., christian.wilbs@fst.com

Dr.-Ing. Daniel Frölich, ORCID 0000-0002-2707-948X, daniel.froelich@fst.com

Dr.-Ing. Matthias Adler, matthias.adler@fst.com

Alisa Bellon, M. Sc., alisa.bellon@fst.com

Emely Bopp, B. Sc. emely.bopp@fst.com

Freudenberg Technology Innovation SE & Co. KG

Höhnerweg 2-4, 69469 Weinheim, Germany:

Dr.-Ing. Nicole Schuster, ORCID 0000-0002-9766-5548, nicole.schuster@freudenberg.com

Dr.-Ing. Jasmin Menzel, jasmin.menzel@freudenberg.com

https://doi.org/10.61319/2BMEKGRS

Group B
Session 2

Materials and Surfaces I

B 01

Hiroyoshi Tanaka, Ayako Aoyagi, Hikaru Hashimoto, Yoshinori Sawae, Joichi Sugimura, Kyushu University, Mechanical Engineering, Fukuoka, Japan

Friction and wear properties of several rubber materials for high pressure O-ring

B 02

Margrit Junk, Joachim Germanus, Institut für Luft- und Kältetechnik gemeinnützige Gesellschaft mbH, Applied Materials Engineering, Dresden, Germany

Testing elastomeric materials in liquified gases

B 03

Cem Tanyeri, Mine Unlu, Baris Caylak, Alper Kocamaz, Ozan Devlen, Kastas Sealing Technologies Research and Development, Izmir, Turkey

Enhancing sealing element security: Quantum dot marking Solutions of NBR and TPU sealing elements

Friction and wear properties of several rubber materials for high pressure O-ring

Hiroyoshi Tanaka, Ayako Aoyagi, Hikaru Hashimoto, Yoshinori Sawae, Joichi Sugimura

Friction and wear characteristics of rubber materials were investigated to look for the suitable candidates for O-ring using in hydrogen energy system for renewable energy society. In this study, reciprocating sliding test of rubbers were conducted under hydrogen environment. To understand the sealing performance and durability of rubber O-rings, friction and wear characteristics of hemispherical rubber specimens sliding against stainless steel disk were evaluated. Several rubber materials including silicone rubber, EPDM rubber, fluorinated rubber and natural rubber based elastomer were selected to identify the best fit for the hydrogen facility. Each rubber material exhibited unique friction and wear performance depending on its nature (mechanical properties, chemical composition, type of filler), environment gases and operating conditions. A silicone rubber demonstrated that low wear and high and stable coefficient of friction in hydrogen compare with that in Air. A fluorinated rubber with carbon black filler showed low coefficient of friction in hydrogen. In order to understand the wear process of each rubber, topography measurement and surface analysis were conducted after the sliding test.

1 Introduction

Hydrogen energy system for renewable energy society that handles high pressure hydrogen gas requires high safety performance and high environmental compatibility. Rubber O-ring is usually used in many components as simple, reliable sealing element. Further efforts are requested to improve durability which directly connected to the lifecycle and/or maintenance period of component[1,2,3]. Friction and wear properties of rubber materials were investigated to look for the suitable candidates for O-ring in hydrogen energy system.

In this study, reciprocating rotational sliding test of rubbers are conducted under hydrogen and the other gas environments. Friction and wear properties of rubber specimens slide against stainless steel are evaluated to understand the seal performance and durability of rubber O-ring.

2 Tests and results

A reciprocating sliding tests were carried out using tribo tester with environment control chamber. Hemispherical rubber specimen and stainless steel disk specimens were used as a tribo-pair. Several rubber materials were selected to identify the most suitable materials for hydrogen facilities. In order to understand the progress of wear on each rubber specimen, surface observation and chemical analysis were performed after the sliding test.

2.1 Experimental

In order to obtain the useful information for hydrogen facilities, it is necessary to carefully design the experimental set up[4,5,6].

2.1.1 Test rig

Pin-on-disk sliding tests were conducted in a chamber equipped with a turbo molecular pump and gas impurity control system [7] because impurities such as oxygen and water must be avoided from hydrogen gas environment. Also reciprocating sliding was selected to evaluate the wear on elastomer surface in the compression decompression process of high pressure vessel in hydrogen facilities.

2.1.2 Specimens

The dimensions of the pin and disk specimens are shown in Fig. 1. The disk was made of JIS SUS316L stainless steel. The pin specimens were moulded with hemispherical shape with 5mm diameter as shown in Fig. 1. The pin specimens were wiped with ethanol just before the sliding tests.

2.1.3Test conditions

The disk specimen was mounted on a rotating shaft, while the pin was pressed against the disk specimen by a loading lever in the sealed chamber. After the specimens were set up, the chamber was evacuated to a pressure level of 1x10-4 Pa, and then the test gas was introduced into the chamber at a flow rate of 1.0 L/min. Impurities in the supplied gas were measured at the exhaust line with a moisture sensor and an oxygen sensor. Experiments started after trace water and oxygen in hydrogen were stabilized at 3 ppm and 0.5 ppm, respectively. All the sliding tests were conducted at 296 K in dry contact condition. Test load was 5 N. Test conditions are summarized in Table 1.

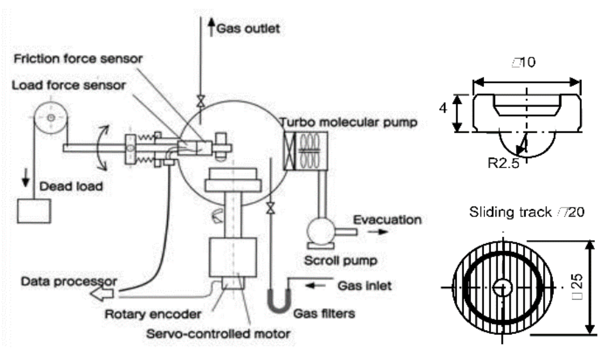

Figure 1: Test rig (a) and specimens (b, c) Roughness of disk surface: Rz=0.045

Table 1: Test conditions

Description	***Values***	***Unit***
Load	5	[N]
Stroke	1, 2, 3	[mm]
Sliding velocity	6	[mm/s]
Temperature	23 (R.T.)	[C]
Environmental gas	Hydrogen, Atmospheric air	[-]

2.2 Materials

In order to find a best candidate for hydrogen energy system, six elastomers were selected as shown below. NR means a natural rubber based material.

Table 2: Rubber test specimens

	A	B	C	D	E	F
	VMQ1	VMQ2	EPDM	FKM1	FKM2	NR
Hardness(IRHD)	81	81	82	93	82	74
Tensile strength(Mpa)	11	6.32	20.4	15.7	17.9	21.4
Elongation(%)	310	170	210	140	290	436

2.3 Surface analyses

During the sliding tests, friction force and normal force were measured. After the tests, the pin specimens were observed with an optical microscope and a confocal laser microscope, and analysed with Raman microscopy.

2.4 Test results

The typical results of reciprocating sliding test were summarized in Fig. 2 to Fig. 5. Basically, COF increased with increasing reciprocating stroke in all rubber samples. Rubber materials exhibited individual friction and wear performance depending on each environment and operating condition. VMQ rubbers showed lower COF than others in both hydrogen and air. VMQ rubbers showed a sharp drop in COF in air at stroke of 2mm and 3mm. In contrast, FKM showed a sharp drop in COF in hydrogen regardless of stroke distances. There were little differences in the changes in COF due to the difference in environmental gas with EPDM and Natural rubber. As the stroke distance increased, the COF also steadily increased. Natural rubber showed stable performance against friction and wear due to its soft and stable mechanical properties at room temperature. In summary, friction and wear properties strongly depended on the type of rubber base resin. On the other hand, rubber materials contained multiple elements included fillers besides of base resin, and the following surface analyses and detailed surface observation were carried out to know the effects of these functions.

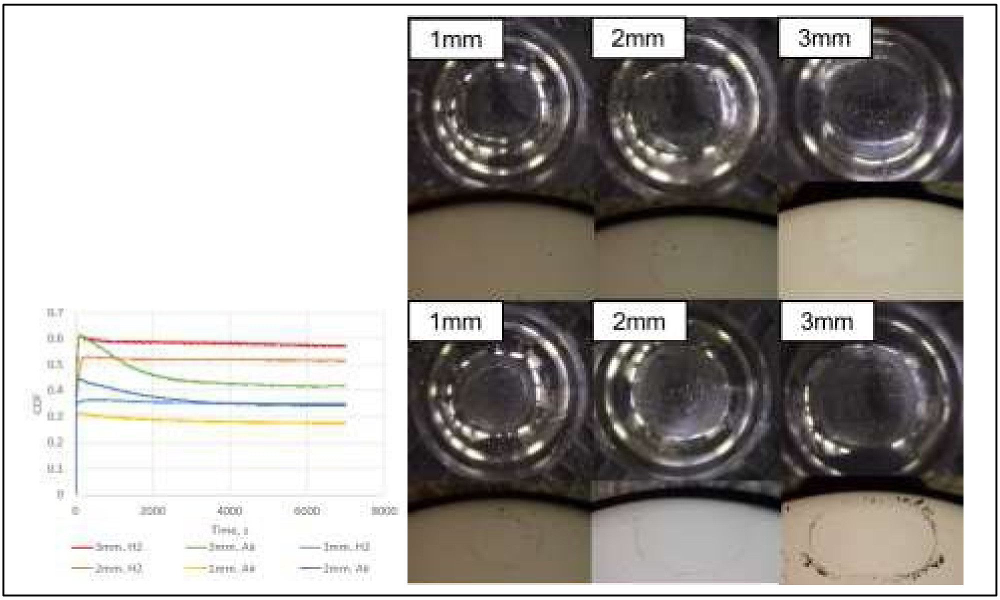

Figure 2: Changes in COF tested with VMQ1 and Photos after the sliding test (a) in hydrogen (b) in air

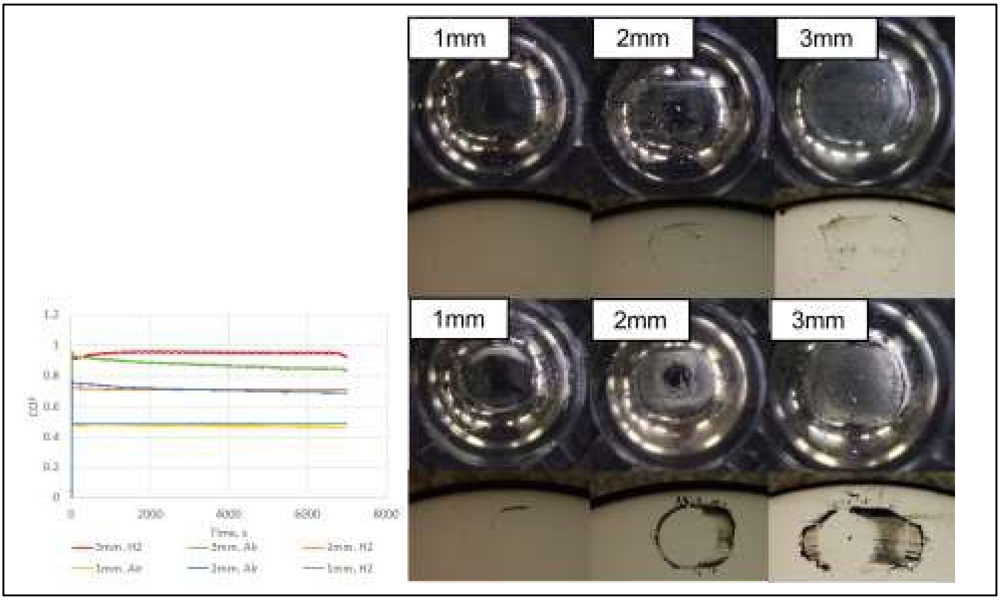

Figure 3: Changes in COF tested with EPDM and Photos after the sliding test (a) in hydrogen (b) in air

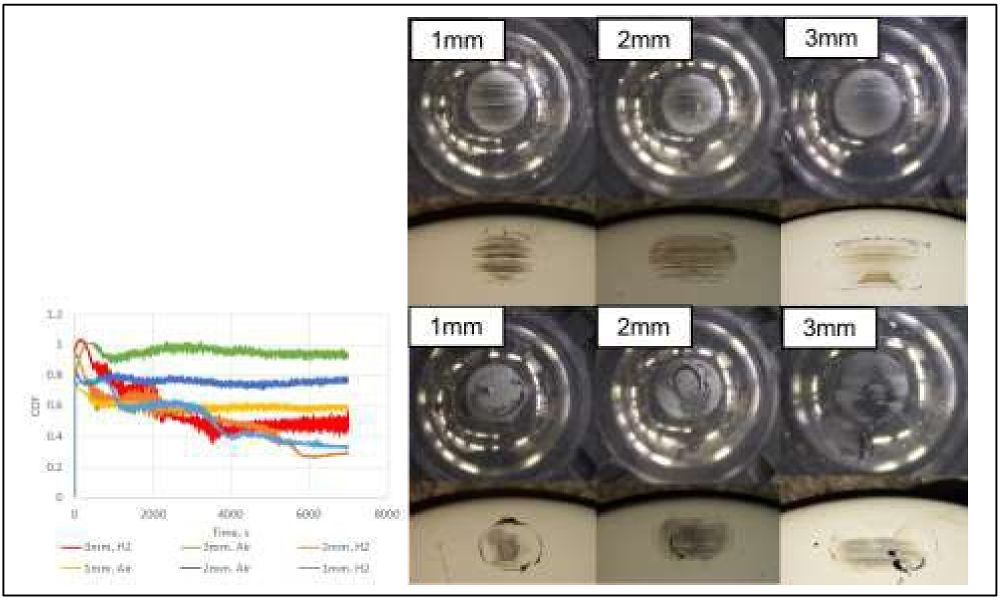

Figure 4: Changes in COF tested with FKM1 and Photos after the sliding test (a) in hydrogen (b) in air

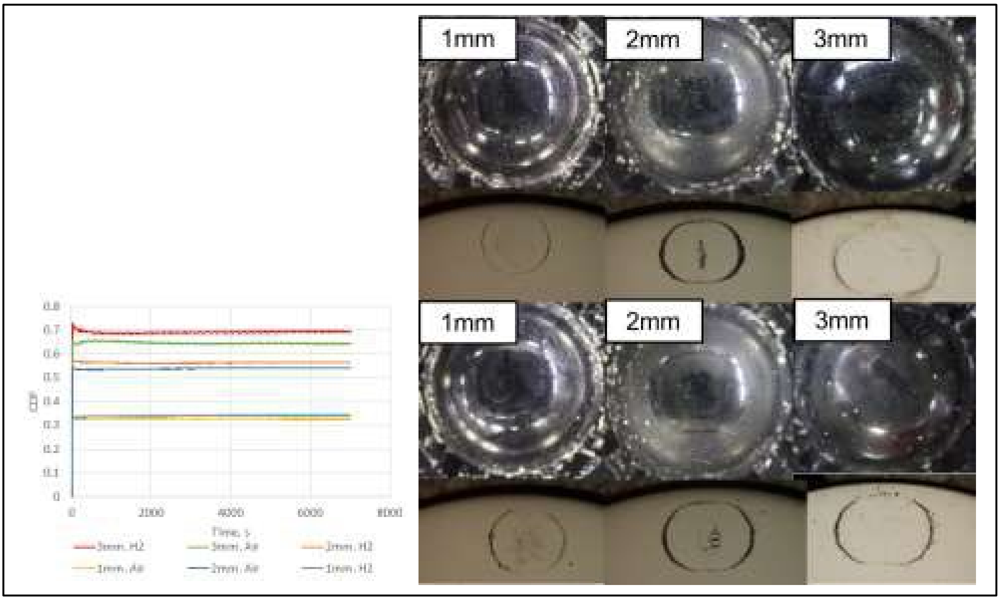

Figure 5: Changes in COF tested with NR and Photos after the sliding test (a) in hydrogen (b) in air

2.4.1 COF and mechanical properties

As the results above, friction and wear properties varied with type of rubbers. Figure 6 showed the changes in COF for each rubber material as a function of reciprocating stroke. Roughly the greater tensile strength exhibited higher COF in reciprocating sliding test. The greater tensile strength maintained the adhesion between the rubber and steel surface even at larger displacements, avoiding local slip and abrasion of rubber surface. Note that FKM1 had the highest hardness and NR the lowest in this series of tests. The softest NR showed elastic behaviour and hardly be worn even with a 3mm stroke. On the other hand, the hardest FKM1 rubber tended to slip and abraded easily in hydrogen. Except for these two cases, the COFs were in the order of tensile strength.

2.4.2 Running in process

When slip started, running-in process also started. Running in process included tearing of rubber, abrasion, transfer of substance and surface film formation. FKM1 had a harder matrix and slip at a small displacement. Slip, both local and entire slip, promoted local wear, which exposed carbon black filler particles. Figure 7 showed the Raman analysis results of rubber surfaces and disk surfaces after the sliding test in hydrogen and air respectively. The Raman results for FKM1 showed the surface film contains a large amount of carbon black in hydrogen, but in the atmosphere, the rubber base resin itself was the main component. The facts suggested that transfer of filler material tended to occur selectively in hydrogen, while transfer of rubber itself tended to occur in air. Initial transfer process as mentioned above drastically changed the following frictional process.

2.4.3 Effects of filler type and content

FKM1 rubber contains a larger amount of carbon black, which tends to transfer to the stainless steel surface and forms a carbon film on the stainless steel surface under hydrogen environment. Amorphous carbon film often reduces friction under hydrogen environment[8]. This may be the reason why FKM1 rubber had lower friction after running-in in hydrogen.

VMQ showed completely opposite trend. A large amount of silica filler was observed on the disk after the test in hydrogen especially with VMQ2, but COF remained high. Detached silica filler was pushed out from the contact area and didn’t involve in friction. Raman analysis supported this hypothesis. Silica was hardly observed in any cases on the contact area of the disk surface slide against VMQ1 and 2, whereas silicone rubber base resin itself was observed in both rubber samples tested in air. This meant that silica couldn’t absorbed effectively on the stainless surface under hydrogen environment. VMQ rubber also degraded in air, making VMQ's friction in air lower than hydrogen.

As mentioned above, it was found that the friction and wear characteristics were complexly and strongly influenced by the type of rubber, the type of filler, and the environmental conditions.

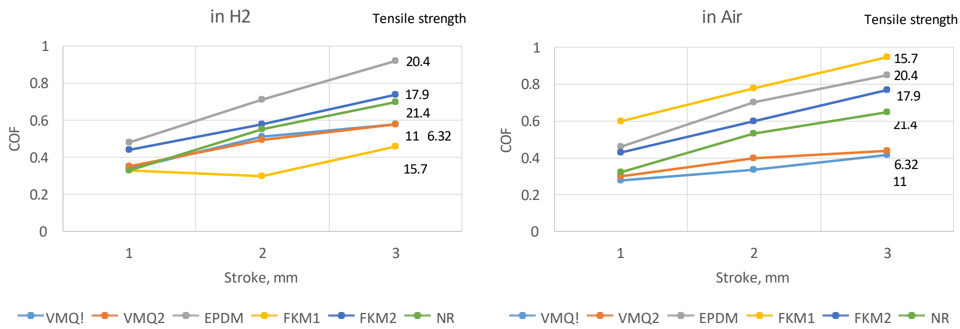

Figure 6: Changes in COF depending on rubber type under different environments

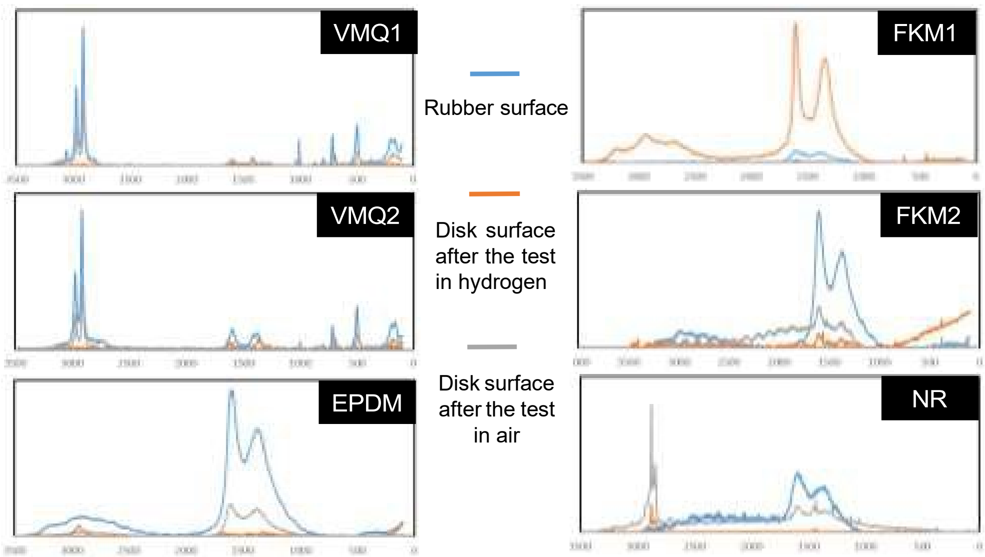

Figure 7: Variety of Raman spectrum for rubber and disk surface after the sliding test

3 Summary and Conclusion

A reciprocating sliding tests were carried out using hemispherical rubber specimen. Friction and wear characteristics were complexly and strongly influenced by the type of rubber, the type of filler, and the environmental conditions. Greater tensile strength of rubber exhibited higher COF in reciprocating sliding test if rubber sample had similar hardness. VMQ showed lower COF than others in hydrogen and air. VMQ showed a sharp drop of COF in air. In contrast, FKM showed a sharp drop of COF in hydrogen.

4 Acknowledgements

This research work was performed within the "Strategic International Collaborate Research Program(SICORP)" (grant number: JPMJSC2121), which was supported by Japan Science and Technology Agency (JST) and Federal Ministry of Education and Research (BMBF)

The authors are grateful to the Bundesanstalt für Materialforschung und -prüfung (BAM), namely Dr. Theiler and Dr. Murillo, to Freudenberg Technology Innovation SE & Co. KG corporate R&D, namely Dr. Dobbelaar, Dr. Schauber and Mr. Christian for informative discussion.

5 References

[1] Yamabe, J., Koga, A., Nishimura, S.; Failure behavior of rubber O-ring under cyclic exposure to high-pressure hydrogen gas, Engineering Failure Analysis, 2013, , https://doi.org/10.1016/j.engfailanal.2013.01.034

[2] Fujiwara, H., Ono, H., Nishimura, S.; Degradation behavior of acrylonitrile butadiene rubber after cyclic high-pressure hydrogen exposure, International Journal of Hydrogen Energy, 2015, http://dx.doi.org/10.1016/j.ijhydene.2014.11.106

[3] Kuang, W., Bennett, W. D., Roosendaal, T. J., Arey, B. W., Dohnalkova, A., Petrossian, G., Simmons, K. L.: In situ friction and wear behavior of rubber materials incorporating various fillers and/or a plasticizer in high-pressure hydrogen, Tribology international, 2020, https://doi.org/10.1016/j.triboint.2020.106627

[4] Johnson, K. L., Kendall, K. and Roberts, A. D., Proc. R. Soc. London, Set. A, 324 (1971) 301

[5] Barquins, M. (1985). Sliding friction of rubber and Schallamach waves - A review. Materials Science and Engineering, 73(C), 45–63.

[6] Barquins M, Courtel R. Rubber friction and the rheology of viscoelastic contact.Wear, 1975, (32):133-150

[7] Fukuda, K., Kurono, Y., Izumi, N., Sugimura, J., "Influence of Trace Water and Oxygen in a Hydrogen Environment on Pure Fe Friction and Wear," Tribology Online, 5, 2010, 280-86.

[8] Sawae, Y., Morita, T., Takeda, K., Onitsuka, S., Kaneuti, J., Yamaguchi, T., Sugimura, J.: Friction and wear of PTFE composites with different filler in high purity hydrogen gas, Tribology international, 2021, https://doi.org/10.1016/j.triboint.2021.106884

6 Authors

NOK corporation

4-3-1 Tsujidoshinmachi Fujisawa-shi, Kanagawa-ken, 251-0042 Japan:

Hikaru Hashimoto, M. Sc., hashimoto.18.hikaru@jp.nokgrp.com

Suguru Norikyo, M. Sc., norikyo.21.suguru@jp.nokgrp.com

Dr.-Eng. Ayako Aoyagi, aoyagi.07.ayako@jp.nokgrp.com

Kyushu University, Faculty of Engineering, Department of Mechanical Engineering

744 Motooka Nishi-ku, Fukuoka-ken, 819-0395 Japan:

Univ.-Asst. Prof. Dr.-Eng. Hiroyoshi Tanaka, ORCID 0000-0002-2392-4789,

tanaka.hiroyoshi.315@m.kyushu-u.ac.jp

Takehiro Morita, M. Sc.,

morita.takehiro.871@m.kyushu-u.ac.jp

Univ.-Prof. Dr.-Eng. Yoshinori Sawae, ORCID 0000-0001-9255-5297,

sawae.yoshinori.134@m.kyushu-u.ac.jp

Dr.-Eng. Joichi Sugimura, ORCID 0000-0001-0002-0003,

sugimura.joichi.666@m.kyushu-u.ac.jp

https://doi.org/10.61319/BCWRTC88

Testing elastomeric materials in liquified gases

Margrit Junk, Joachim Germanus

To ensure safe and reliable products, elastomeric sealing materials in refrigeration systems and heat pumps have to be tested for their compatibility with refrigerants. The test method described in ISO 14903 and ISO 21922 covers aging in liquid refrigerant including a test in "wet" and "dry" condition. As part of a project to investigate the in-situ swelling behaviour of elastomers, the performance of elastomeric materials in liquid refrigerants was studied. The investigation focused on the behaviour of the materials during and after decompression in the autoclave. The data clearly indicate that the test description in the above-mentioned standards does not ensure a comparable test procedure or comparable results.

1 Introduction

Elastomeric materials play an important role as sealing in refrigeration systems and heat pumps. Knowledge of the interaction of these materials with refrigerants is therefore of interest.

The swelling behaviour of elastomers in contact with liquid refrigerants (also mixed with lubricants) is a common indicator of their resistance to the medium and thus an important parameter for the applicability of the polymer seals. Until now, it has only been possible to evaluate changes of the materials which were aged in refrigerants after their removal from the medium, i.e. after the decompression phase. Unfortunately, the data available to date were only of limited significance for the relevant behaviour of the materials during media exposure. Here, a new in-situ measurement method is showing its advantage. The measurement method allows an evaluation of materials under the influence of media (in-situ) and provides a basis for improved test procedures in conventional testing.

2 Compatibility testing of sealings for refrigeration systems and heat pumps

Compatibility tests for sealings used in refrigeration systems and heat pumps are listed in two standards. While ISO 14903 [1] describes the qualification of tightness of components and joints, ISO 21922 [2] covers the requirements, testing and marking of valves.

The general test procedure for elastomers is identical in both standards. The aging resp. exposure is carried out in a pressure vessel (test chamber /autoclave) suitable for safe handling of refrigerants under high pressure. The samples are aged completely submerged in the liquid phase of the refrigerant (which may contain oil). The aging temperature is 50 °C (ISO 14903) or 70 °C (ISO 21922) which is implemented by placing the autoclave in an oven or by direct heating of the autoclave. The minimum duration of exposure is 14 days (two weeks) for rubber seal materials and 42 days (six weeks) for thermoplastic seal materials.

After the aging, the autoclave is cooled down to ambient temperature and the test pieces are taken out from the autoclave. A procedure for removing the refrigerant from the pressure vessel (e.g. depressurization rate) is not described.

For the further testing two material states are specified: “wet” and “dry”. The material is considered to be wet within 30 min of removal from the autoclave. During this time, the hardness, weight and volume of the test pieces are to be determined. For testing in dry state, the samples are subsequently degassed at 50 °C in an oven until a constant mass is reached, and the resulting hardness, weight and volume are determined.

In both standards is noted that “*elastomers tested with CO_2, can accumulate significant amount of CO_2. The CO_2 cannot escape immediately when the test items are exposed to atmospheric pressure (de-gassing). Thus, it can create an immediate volume change larger than 25 %. Provided that no surface damage is made, volume change above 25 % is acceptable for CO_2.”* [1] [2]

3 In-situ testing of elastomeric materials

3.1 Experimental setup

For the in-situ testing, a temperature-controlled autoclave with a sight glass was used, which allows testing at temperatures up to 100 °C and pressures up to 95 bar (Figure 1). To provide the necessary illumination for visual evaluation of the sample, the autoclave was equipped with a pressure-resistant interior light.

The autoclave was heated using a connected thermostat. For measuring the temperature inside the autoclave, a Pt100 resistance thermometer was used. The pressure was monitored with both an analogue manometer and a digital pressure sensor. During the tests, pressure and temperature were recorded with a data acquisition system.

The elastomeric materials were tested as O-rings, which were found to be the most suitable sample geometry for the tests. The rings were placed on an adjustable O-ring holder which allows a defined elongation of the samples (Figure 2). This sample fixture can be rotated when installed in the autoclave so that exact positioning of the O-rings is possible.

The time-dependent swelling behaviour of the samples was recorded with a high-resolution camera system. Depending on the fluid density and the changing refractive index, the camera was focused manually. The recorded single pictures were analysed with image processing software. For each sample, the cross-section width of the O-ring cords as well as the distance between the cords were measured, (Figure 2). To eliminate errors due to different refractive indices of the test fluids, the sample holder was used as a calibration scale.

Figure 1: Autoclave system with camera

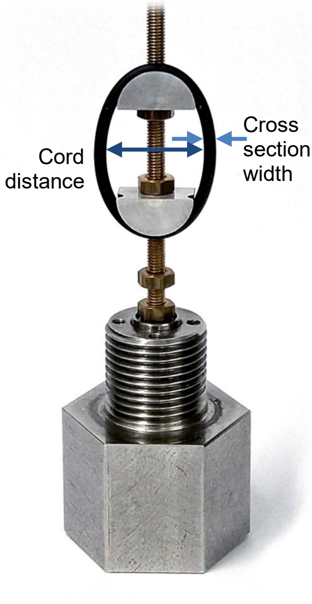

Figure 2: Sample holder

3.2 Samples and test conditions

The tests were performed with 20 x 2 mm O-rings placed on the specimen holder with a preload corresponding to an elongation of the rings of 5 %. The preload was kept the same for all tests in order to guarantee secure positioning of the samples and prevent them from slipping off the holder.

For the investigations, EPDM and HNBR were chosen. All elastomers tested are generally compatible for use with R744 (CO_2) and R1234yf. For clarity, only the investigations of the HNBR with R744 are presented here.

The tests in the liquid refrigerant were carried out at room temperature. The pressure given in the table (Table 1) is the equilibrium pressure of the refrigerant above the liquid phase.

Table 1: Test conditions for in-situ-tests with liquid refrigerants

	R744	R1234yf
Temperature [°C]	25	25
Pressure [bar]	64	7
Fluid density [g/cm³]	0.711	0.109

3.3 Results

In all tests, a short-term reduction in the sample volume occurred during the autoclave filling. This effect is related to the temperature reduction during the filling process.

The pressure reduction from 65 to 1 bar at the end of the test was realized by evaporation of the liquid refrigerant over a period of approximately 15 min. This also resulted in a temperature reduction, which is compensated to a certain extent by a corresponding counter-heating of the autoclave (external temperature control).

In contact with the liquid refrigerant, the samples showed an increase in volume. Depending on the material, a stationary state of swelling was reached after 15 min to 3 h when stored in liquid R744. After this exposure time, the volume of the sample did not increase any further (Figure 3).

During and after removing refrigerant from the autoclave, the samples showed a significant volume increase. Especially in a period of several minutes after reaching the ambient pressure, the liquid refrigerant dissolved in the material evaporates and causes the material to swell (Figure 3 and Figure 4).

The time required for the O-ring to regain a volume corresponding to that of the steady state during storage in liquid R744 was between 20 min and 2 h, depending on the material. After 1.5 to 4 hours, the samples have returned to their initial volume.

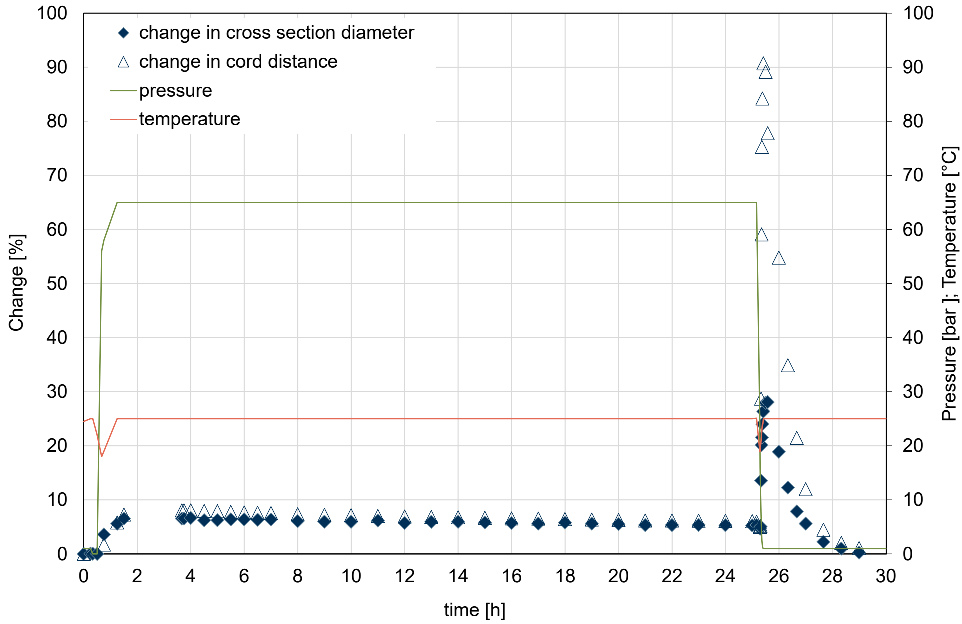

Figure 3: Changes of HNBR O-ring during and after storage in liquid R744

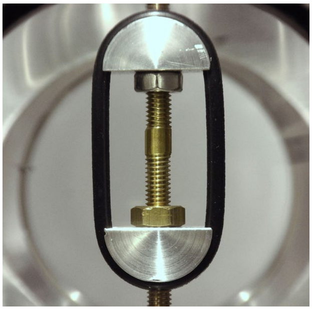

HNBR in air (prior to the test)

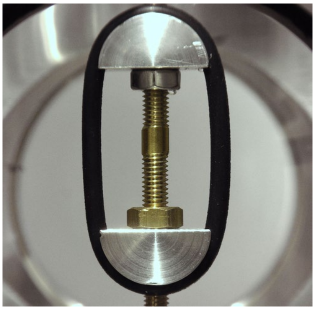

HNBR in R744 (l) at 65 bar after 4 h

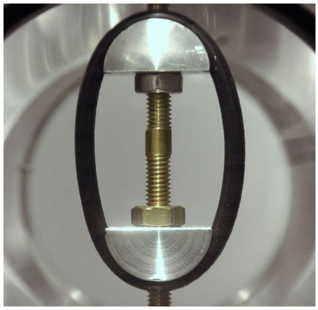

HNBR in R744 (g) at 7 bar; approx. 10 min after starting pressure release

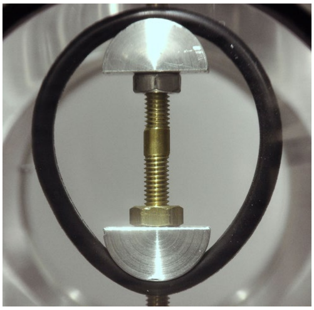

HNBR in R744 (g) at 1 bar; approx. 15 min after starting pressure release

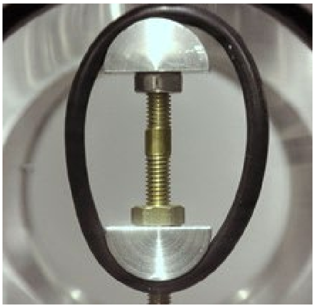

HNBR in R744 (g) at 1 bar; approx. 45 min after starting pressure release

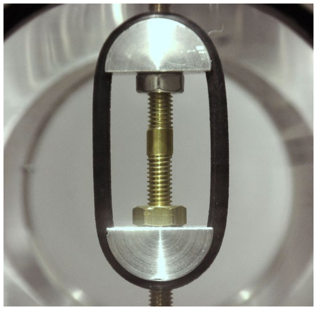

HNBR in R744 (g) at 1 bar; after 28 h

Figure 4: HNBR O-ring during storage in liquid R744 and after pressure release

4 Conventional tests and comparison with in-situ tests

To evaluate and compare the results of the in-situ tests, conventional autoclave tests were performed. The samples were aged in autoclaves under the same test conditions than in the in-situ test (Table 1). In contrast to the in-situ tests, some of the samples were also tested for mechanical properties after aging.

The mass and volume resp. cross section diameter as well as the hardness and tensile properties were determined in defined time intervals after removing samples from autoclave. The measurements were carried out every minute for the first 10 min, then the intervals were increased. Complete depressurisation (reaching 1 bar) in the autoclave was defined as the starting point for the time measurements.

The results clearly show that the major changes in dimensions were found within the first 15 min. The time dependent behaviour of the mechanical properties was similar.

The comparison of the in-situ tests and the conventional autoclave tests show a good correlation regarding changes in cross section diameter of the O-rings (Figure 5).

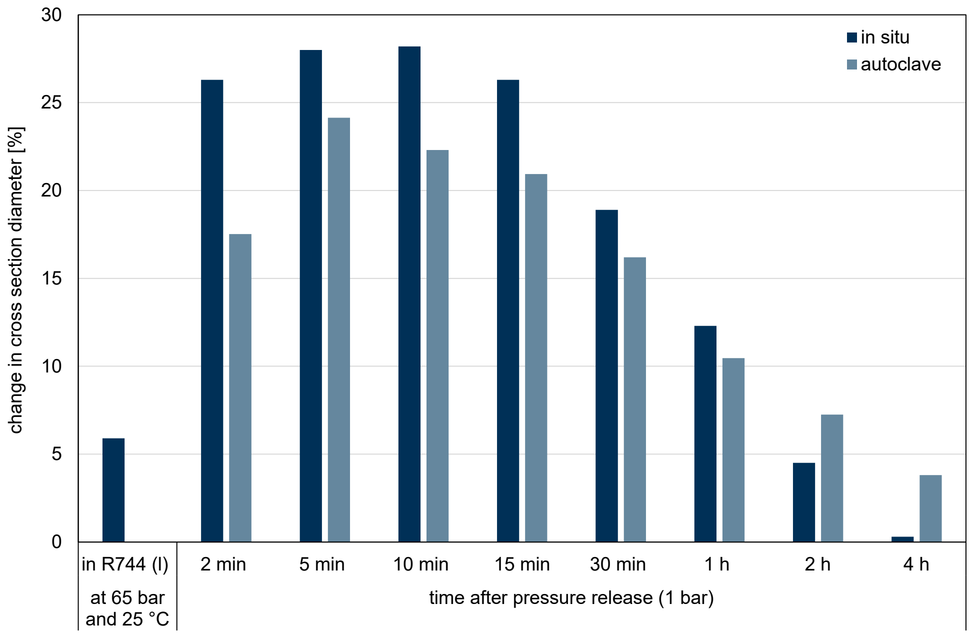

Figure 5: Changes in cross section diameter of HNBR O-rings during and after storage in liquid R744

5 Consequences for compatibility testing in liquid refrigerants

As shown in the previous sections elastomeric materials show a volume increase after removing from a liquid refrigerant. These changes occur with a time delay after the samples are taken from the autoclave and are associated with the outgassing of refrigerant dissolved in the elastomer. The volume change during storage in liquid refrigerant was found to be significantly lower.

The procedure for compatibility testing described in ISO 14903 or ISO 21922 defines a testing in “wet” state within 30 min after removal from the autoclave. Assuming that the autoclave is opened immediately after pressure release, this is exactly the period in which dissolved refrigerant outgasses and the volume change is greatest (Figure 6). For the tested HNBR it was found, that at the end of the 30 min period after pressure release the change in cross section diameter was still significantly higher than during storage in liquid R744.

In reality, the so-called wet state corresponds to a decompression state.

Both the rate of pressure release and the time interval between reaching ambient pressure and opening the autoclave are not defined in the standards. This means that the 30 min time window for the measurement can start immediately after depressurization, but also several hours after the ambient pressure has been reached. Furthermore, rapid gas decompression cannot be excluded. Hence, the results of the measurements extremely depend on the particular timing of the tests in the laboratory.

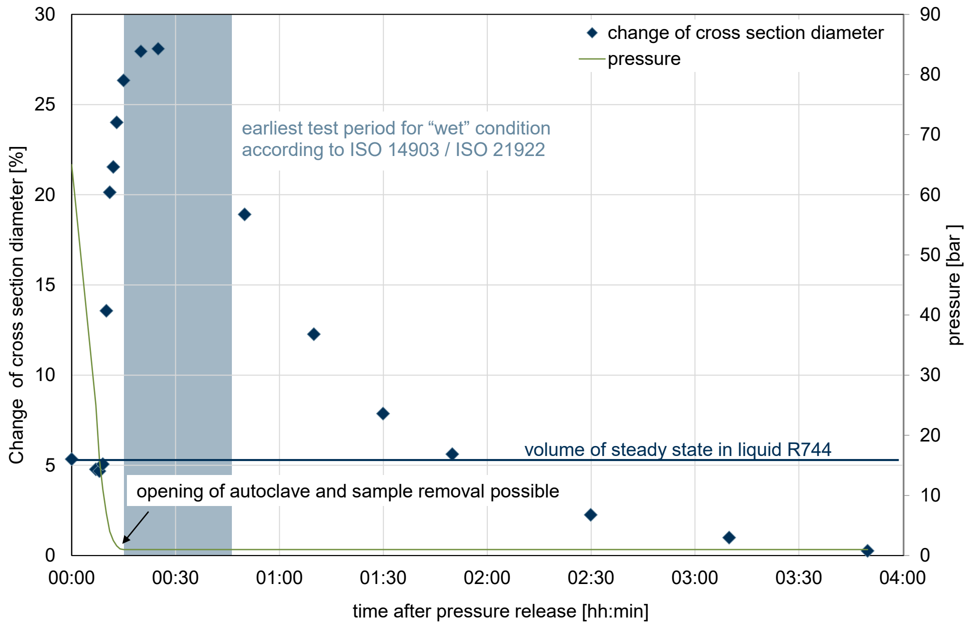

Figure 6: Changes of HNBR O-ring after storage in liquid R744 (detail from Figure 4)

6 Summary and Conclusion

In-situ investigations of elastomeric materials in liquid refrigerants have shown that the volume increase during exposure in liquid R744 is smaller than the swelling after pressure release. The outgassing of the dissolved refrigerant begins as soon as the pressure is reduced and continues even after the ambient pressure has already been reached. Volume changes determined after taking samples from the autoclave will be strongly influenced by this process.

The so-called wet state, as described in ISO 14903 or ISO 21922, is neither a defined condition nor does it represent the state in the liquid refrigerant. As these standards for testing the compatibility of elastomeric materials with refrigerants do not specify an exact test procedure, it is necessary that at least the time between complete depressurization and the measurement is kept the same for all tests and is documented in the test report.

7 Acknowledgements

The authors would like to acknowledge the financial support of this study by the Federal Ministry for Economic Affairs and Climate Action of Germany. FuE-Project-Reg.-No. MF200163 "In-situ-Untersuchungen an Polymerwerkstoffen".

8 Nomenclature

R744	carbon dioxide (refrigerant number ac. to ANSI/ASHRAE 34-2022)
R1234yf	2,3,3,3-tetrafluoro-1-propene (refrigerant number ac. to ANSI/ASHRAE 34-2022)
(l)	liquid state
(g)	gaseous state

9 References

[1] ISO 14903:2017: Refrigerating systems and heat pumps - Qualification of tightness of components and joints

[2] ISO 21922:2021: Refrigerating systems and heat pumps - Valves - Requirements, testing and marking

10 Authors

Institut für Luft- und Kältetechnik gemeinnützige Gesellschaft mbH

Bertolt-Brecht-Allee 20, 01309 Dresden, Germany:

Dr.-Ing. Margrit Junk, margrit.junk@ilkdresden.de

Dr. rer. nat. Joachim Germanus, joachim.germanus@ilkdresden.de

https://doi.org/10.61319/WFG2JRQM

Enhancing sealing element security: Quantum dot marking Solutions of NBR and TPU sealing elements

Tanyeri Cem[1], Unlu Mine[1], Caylak Baris[1], Kocamaz Alper[1], Devlen Ozan[1]

This study addresses the rising need for product security against counterfeiting by utilizing luminescent labels with nanoparticles for marking. Integrating quantum dot (QD) marking solutions into NBR and TPU used in hydraulic and pneumatic sealing elements enhances product safety, traceability, and sustainability while reducing costs. The research examines the optical and mechanical properties of QD-infused elastomers, both post-abrasion and aging. Special sensors and smart algorithms convert optical readings into electronic signals for verification against reference data, ensuring authenticity. The study demonstrates the effectiveness of QD marking in enhancing the security of sealing elements and combating counterfeiting in critical industrial systems.

1 INTRODUCTION

Quantum dots (QDs) are semiconductor crystals with a nanocrystalline structure, a diameter of approximately 2–10 nm, and good optical properties, such as easy wavelength control based on the controllable size and narrow full width at half maximum (FWMH) of the emission wavelength. The optoelectronic properties of QDs are determined by the size of the crystal, which is described as the quantum confinement effect. In bulk semiconductors, the energy levels overlap because of the countless adjacent atoms, thereby forming an almost continuous energy band. Owing to the overlaps, the continuous energy band decreases gradually, and the bandgap increases with decreasing size of the semiconductor material. Therefore, a discrete energy level occurs when the size of the semiconductor material becomes smaller than the exciton Bohr radius, and the electrons inside the semiconductor are confined to this energy level. As a result, the energy gap of QDs and the wavelength of the light emitted can be controlled by changing the particle size [1].

With the increasing development of global commerce, the dangers of counterfeit goods cannot be underestimated. In particular, counterfeit medicines pose a significant threat to patient safety and public health, and counterfeit high-tech products cause significant economic losses. The urgent anticounterfeiting demands in the global economy and human health push people to develop reliable anti-counterfeiting technologies. Currently, the graphical anti-counterfeiting labels that combine easy detection and rich anti-counterfeiting features are one of the best answers to the problems [2].

Counterfeiting and forgery is a global problem that causes significant financial damage and poses security threats to individuals, companies, and society as a whole. Over the past decades, counterfeit products have spread from daily consumer goods to medicines and high-tech products. Although majority of the products are protected by an anti-counterfeiting technique, the global economic loss of counterfeiting has been increasing annually and estimated to reach 1.7 trillion US dollars in 2015 [3].

Quantum dot technology has been widely used in our daily life, including energy, solar cells, displays, biomedical and biological applications.

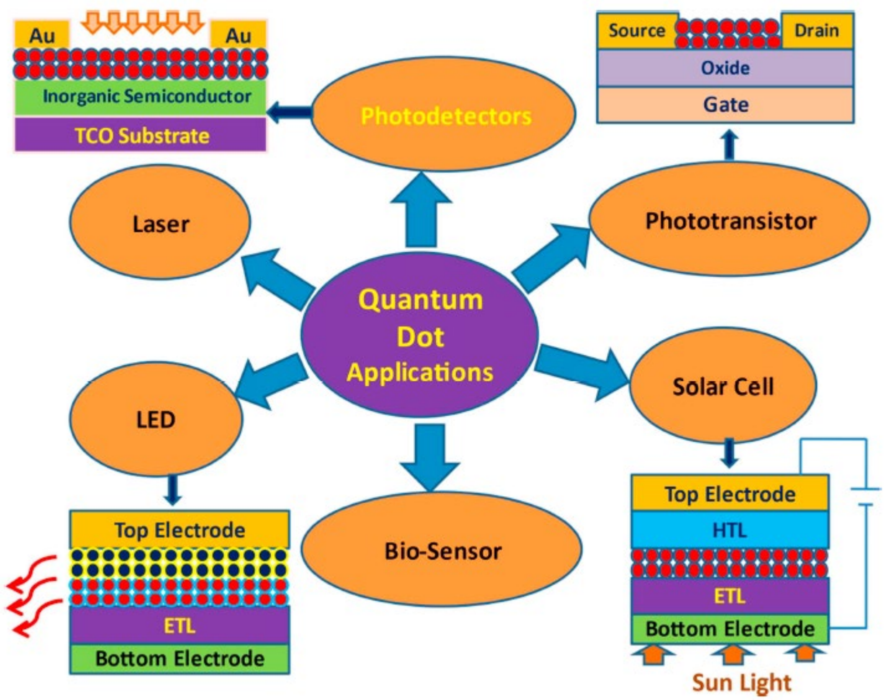

Figure 1.1: Device applications of quantum dots in photodetectors, LED, solar cell, phototransistor, laser and biosensor

Kastaş, integrated product security in mind, has aimed to adopt the Quantum nanodot marking solution to its products through an innovative approach. To ensure end-to-end product tracking and secure product authenticity, a series of R&D studies have been conducted. This work is expected to enable real-time verification of products through previously unseen technology applications, smart sensor systems, and intelligent algorithms, preventing revenue losses caused by counterfeiting. Fundamentally, this study will guarantee product authenticity against potential problems in the field.

To summarize QDots technology: Quantum Labels are produced using different types of QDots, either together or separately. These quantum labels generate a series of codes by utilizing the optical properties of the quantum dots, which are read and converted into signals by specially manufactured sensors and intelligent algorithms. This signal is compared with reference data for verification. In the continuation of the study, the mixing ratios of raw materials with nanoparticles and the comparison of sensor values with reference values will be conducted.

2 MATERIAL AND METHOD

2.1 Application of Qdots on Kastaş Raw Materials

In this study, Qdots applications and measurements were performed on elastomer rubber and thermoplastic raw materials from Kastaş. Experiments were conducted using five different raw materials with water-based, xylene-based, ethylbenzene-based, and benzyl alcohol-based Qdots. Based on the measurement results from these experiments, various studies were conducted concerning the amount of marker used. Mechanical tests were performed on the raw materials at the concentrations where the marker was detected. It was demonstrated that the addition of Qdots to the raw materials did not affect their mechanical properties.

2.2 Labeling Studies

Labeling studies were conducted with markers on rubber elastomer samples, including FKM, NBR, HNBR, VMQ, and thermoplastic polyurethane, which were prepared using Kastas's compound mixtures.

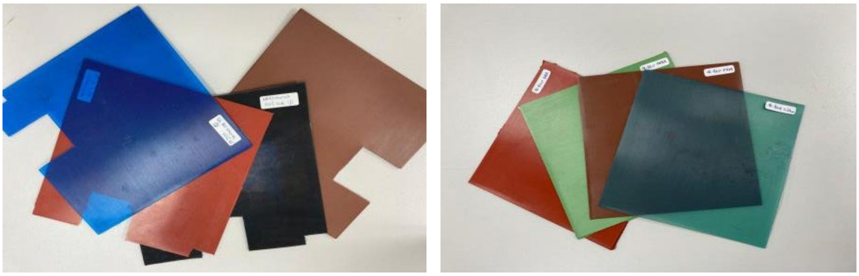

Figure 2.1 : Samples of Raw Materials with Qdots (as plates)

Figure 2.2: Products with Qdots

Classification of Sealing Element Raw Materials and Added Qdots:

- Water-based QDots 1: 150000 ppm
- Water-based Qdots 2: 250,000 ppm

Pu

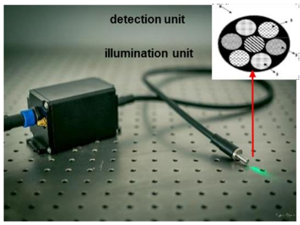

Figure 2.3 Qdots Reading Device

- Xylene-based QDots: 500 ppm
- Ethylbenzene-based QDots: 500 ppm
- Xylene-based QDots: 6450 ppm
- Ethylbenzene-based QDots: 12000 ppm
- Benzyl alcohol-based QDots: 28000 ppm

NBR
HNBR
FKM
VMQ

2.3 Measurement Methods

After preparing the mixture, it is necessary to determine the measurement method.

	Surface Measurements	Liquid (Extraction) Measurements
Advantage	Quick check capability, portable device for fast and on-site measurement	More precise measurement capability with lower doping amounts, independent of sample geometry, contamination, and deformation
Disadvantage	Low measurement sensitivity: • Sample geometry and operator effect • Influence of surface contamination and physical changes (deformation) • High marker concentration requirement due to small area reading Sample holder requirement specific to the product	Additional processing, infrastructure, and time requirements: The product with the customer complaint must be sent to the laboratory for liquid measurements

Based on the above table, the appropriate measurement method for both the thermoplastic product PU and the elastomer group products (FKM, NBR, HNBR, VMQ) has been determined as follows:

- For the PU product, it was decided to use surface measurement.
-
- For the elastomer product group, due to surface and color parameters, effective reading with an optical reader was not possible. Thus, it was decided to dissolve the samples with a suitable solvent before measurement.

2.4 Results of Studies with Water-Based Particles

- Using a special sensor for Qdots emitting in the blue region, surface measurements were performed on the plates.
- Initially, water-based Qdots 1 (150,000 ppm) were added to PU samples at a concentration of 2.5 ml per 1 kg of the compound.

- To minimize the amount of water introduced into the polymer and preserve material properties, a more concentrated product, water-based Qdots 2 (250,000 ppm), was used.
- Other particle concentrations used: 1 kg of material with 1.250 ml marker, 0.625 ml marker, 0.250 ml marker, and 0.125 ml marker.
- Initial quality control test results at Kastaş indicated that a concentration of 0.125 ml marker per 1 kg of material was suitable.
- In summary, it was found that water-based Qdots are appropriate for marking PU samples, and surface measurement methods are effective for their detection.

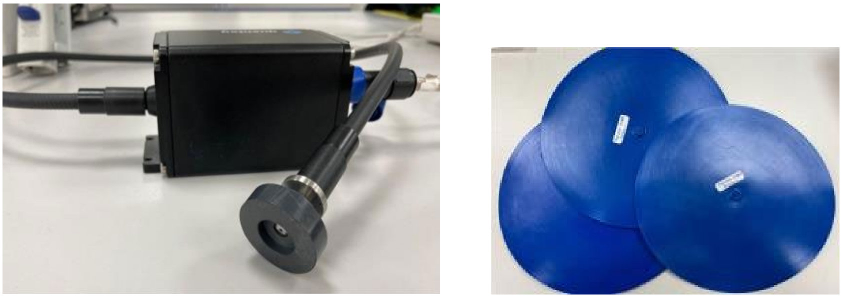

Figure 2.4 Qdots Reading Device and PU Qdots Plate

Due to low precision and high influence of other factors (sample geometry, contamination, etc.) in surface measurements, the labeled product must be at least 2 times the unlabeled reference product.

Thus: $S_{product} \geq 2 \times S_{ref}$

1 kg Material - 0,125 ml Marker Trial
S_{PU}/S_{ref} : 4.7 → Marked Product

2.5 Results of Studies with Solvent-Based Particles

- Experiments were conducted with xylene-based QDots and ethylbenzene-based QDots on four different rubbers (FKM (Brown), NBR (Black), NBR (Brick), VMQ (Blue)). The doping ratio was 2.5 ml per 1 kg of compound. However, due to the active marker concentration in the sample being 500 ppm, readings could not be taken with either method.
- Dosing studies were conducted with benzyl alcohol-based QDots at a ratio of 2.5 ml Marker per 1 kg of compound.
- Surface measurements of samples prepared with solvent-based markers at a ratio of 2.5 ml Marker per 1 kg of compound did not yield reliable results.

- Subsequent liquid measurements with an appropriate solvent showed that the samples were labeled and successfully distinguished from the reference.

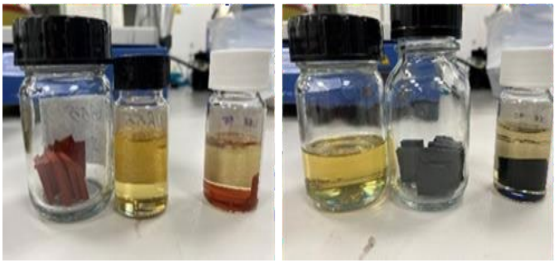

Figure 2.5 NBR 55 (Nitril Butadiene Rubber) and NBR 90 (Nitril Butadiene Rubber)

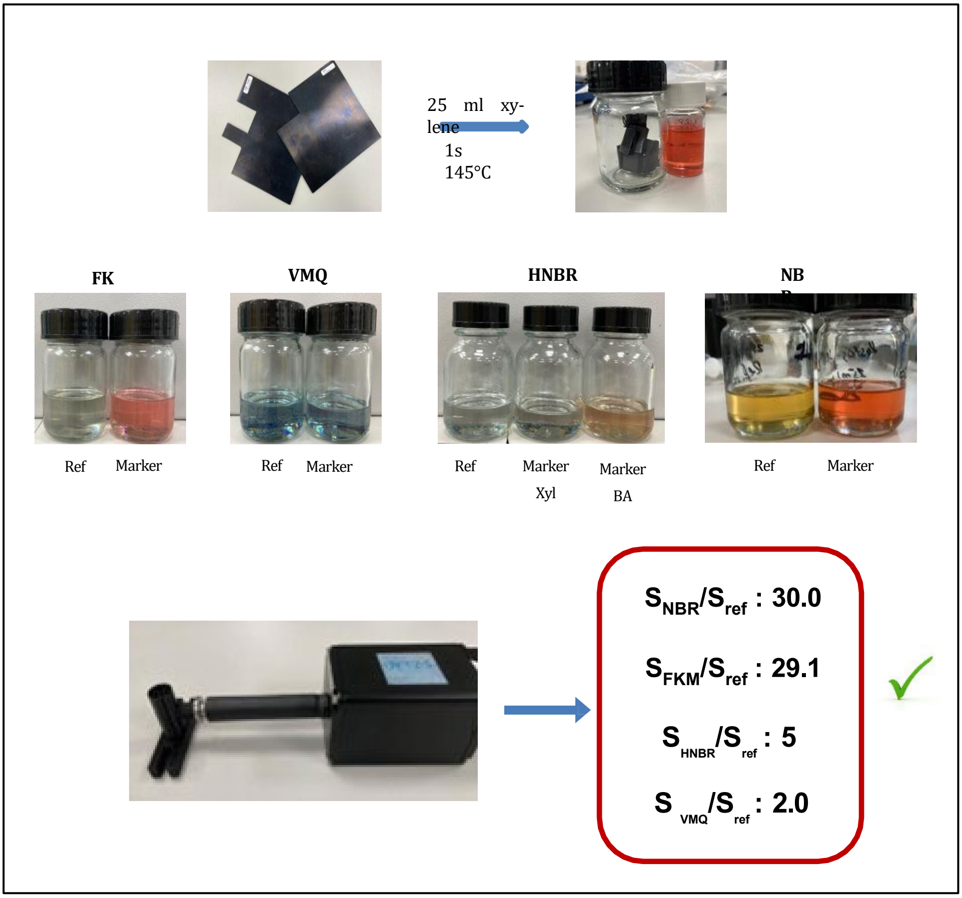

Figure 2.6 Detail of Solvent-Based Particles

3 CONCLUSION

- Quantum Labeling is technically applicable for PU, NBR, FKM, VMQ and HNBR rubber structures.
- Marker concentrations that do not affect the rubber's critical characteristics but are still detectable need to be determined.
- The proof of concept is successful.

After applying QDots to thermoplastic and elastomer raw materials, mechanical tests were carried out to determine whether there was any deterioration in their mechanical properties. Both the previous and next values of the test results are shared in the table.

Table 3.1 PU6006 Test Results

Property	**Before QDots Application PU6006**	**After QDots Application PU6006**
Hardness (Shore D)	63.3	62.09
Tensile Strength (MPa)	48.6	48.11
Elongation at Break (%)	440	439.12
Compression Set % (22 hours at 100°C)	28.53	28.21

Table 3.2 NB9001 Test Results

Property	**Before QDots Application NB9001**	**After QDots Application NB9001**
Hardness (Shore A)	88.13	88.02
Tensile Strength (MPa)	20.8	21
Elongation at Break (%)	166	165.74
Compression Set % (22 hours at 100°C)	19.53	19.03

3.1 Future Work

- Optimization studies specific to product and color should be conducted, and standard methods for each product should be established.
- Used and aged products should also be studied. The effects of deformation, contamination, etc., particularly on surface readings, should be evaluated on used samples.

4 REFERENCES

[1] Myeong, Chon, Kumar, Son, Kang, Seo Quantum dot photolithography using a quantum dot photoresist composed of an organic–inorganic hybrid coating layer. 2022; 4, 1080–1087

[2] Zheng, Zhu, Liu, Inkjet-Printed Quantum Dot Fluorescent Security Labels with Triple- Level Optical Encryption. 2021; 15701

[3] Liu, Han, F. Li, Inkjet-printed unclonable quantum dot fluorescent anti-counterfeiting labels with artificial intelligence authentication. 2019; 2 //doi.org/10.1038/s41467-019-10406-7

5 AUTHORS

Kastas Sealing Technologies,

Atatürk Plastik OSB 3. Street No:5 35660 Menemen / IZMIR / TURKEY:

Cem TANYERI[1], M. Sc., ORCID 0000-0002-1290-2875, ctanyeri@kastas.com

Mine UNLU[1], ORCID 0009-0008-4200-7530 mcebeci@kastas.com

Baris CAYLAK[1], ORCID 0009-0000-9026-0452 bcaylak@kastas.com

Alper KOCAMAZ[1], ORCID 0009-0000-5070-1233 akocamaz@kastas.com

Ozan DEVLEN[1] , M. Sc., ORCID 0000-0002-8079-0553, odevlen@kastas.com

https://doi.org/10.61319/O261V4LO

Group B
Session 3

Additive Manufacturing

B 04

Thomas Ebel, Kathrin Ottink, Hochschule Emden-Leer, Faculty of Technology Mechanical Engineering, Emden, Germany

Functional testing of additively manufactured hydraulic rod seals

B 05

Jacqueline Gerhard, Lothar Hörl, Frank Bauer, University of Stuttgart, Institute of Machine Components Sealing Technology, Stuttgart, Germany

Additive Manufacturing of Sealing rings: Material Selection and Application Development

B 07

Alper Kocamaz, Ozan Devlen, Cem Tanyeri, Barthel Engendahl, Kastas Sealing Technologies, Research and Development, Izmir, Turkey

Innovation in Seal Production: Novel Additive Manufacturing for High-Performance PU Seals

Functional testing of additively manufactured hydraulic rod seals

Thomas Ebel, Kathrin Ottink, Matthias Graf, Tobias Lankenau

Hydraulic rod seals are crucial machine elements in a lot of applications [1]. The malfunction of rod seals can cause, among other things, huge economic loss by long shutdown times for repair. In addition, the last years have shown that geopolitical incidences, such as a war or a pandemic, can have a huge impact on international channels of trade. To avoid or at least minimize machine shutdown times, it seems desirable to have local production solutions for rod seals by using easy-to-handle machinery and a single, simple raw material. A possible solution to circumvent delivery challenges can be the use of an additive manufacturing (AM) method. The research question addressed in this study is whether it is possible to produce functional rod seals using a simple AM method. The functional tests conducted on a rod seal test rig showed that the research question can be answered in an affirmative way for tested pressures up to 15 MPa. Even in a long-term test, the function of the additively manufactured seals met the demands.

1 Introduction

The results of a method screening and the preliminary investigations were presented at the 21st International Sealing Conference in Stuttgart in 2022 [2]. The main results were the choice of Fused Filament Fabrication (FFF) as the AM method for the study, thermoplastic polyurethane (TPU) as the material class to be used, and a choice of TPU filaments for the tests. The latest results, the outcomes of two series of functional tests conducted with these different filaments, will be the core of this paper.

2 Materials and Methods

A reference part was chosen to be able to compare the additively manufactured specimens with an existing conventionally made seal. The chosen seal is a U-cup seal [3] made from TPU as shown in Figure 1.

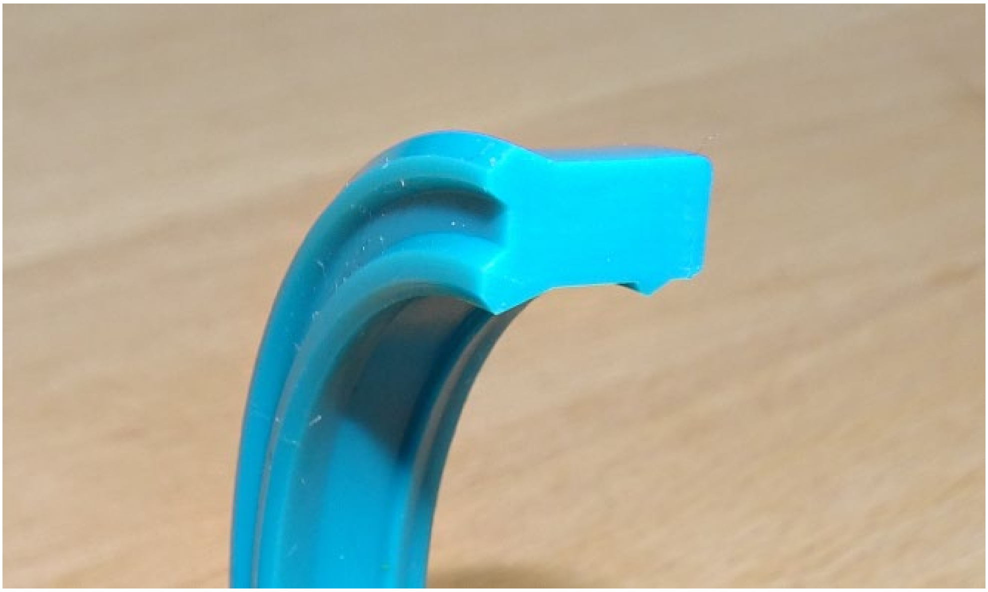

Figure 1: Cut specimen of the reference seal

2.1 Materials

In the preliminary studies, a variety of different commercially available TPU filaments was characterized with the goal of finding the most promising ones for the functional tests. The selection criteria were processability and comparability with the reference seal in terms of radial force, temperature range, friction coefficient, and shore hardness.

The following filaments were examined in the functional tests:

- Extrudr TPU Hard D58
- BASF Ultrafuse TPU 95A
- Extrudr TPU Semisoft A85
- Extrudr TPU Medium A98
- Polymaker Polyflex TPU 95A
- TreeD Flexmark 9

2.2 Production of the test parts

The test parts were produced on a standard FFF 3D printer with a 0.4 mm nozzle. The printing speed was set to a low value of 20 mm/s, which worked with every filament. The other start parameters, bed temperature and nozzle temperature, were set to the values suggested by the filament manufacturer for the first test phase.

2.3 Test rig

The test rig that was used for the functional tests was originally designed for optical investigations and therefore did not comply with the specifications of the ISO 7986:1997 [4] standard, which defines test methods to assess the performance of rod seals. The maximum speed achievable is 0.25 m/s, and the maximum pressure is 15 MPa. The traveling distance is 150 mm. Nevertheless, the functionality of the additively manufactured seals can be assessed with the test rig up to the aforementioned parameters.

Figures 2 and 3 show the test rig.

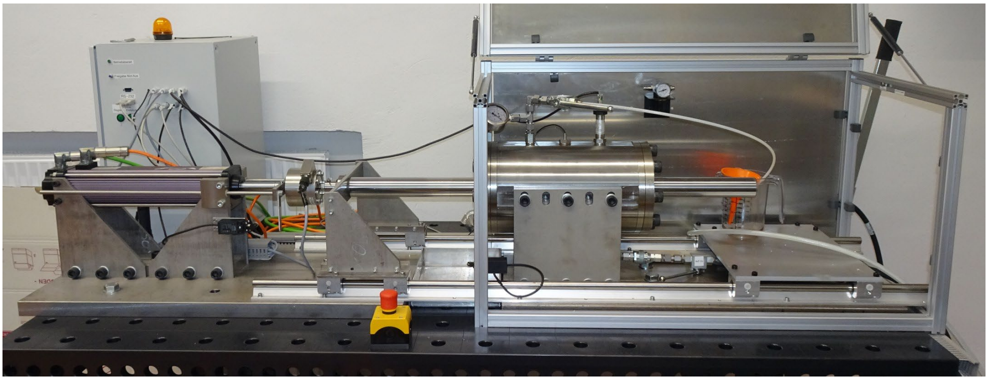

Figure 2: Rod seal test rig

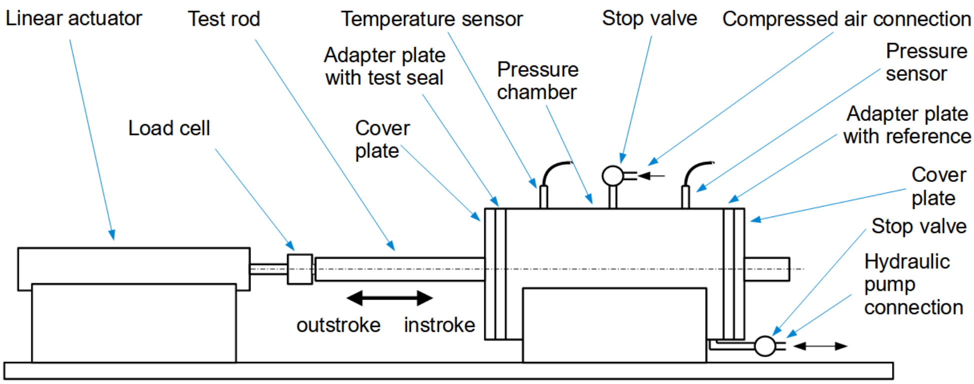

Figure 3: Rod seal test rig — Schematic view

On the left side of the pressure chamber (toward the actuator), a test seal was mounted. On the other side, there was always a reference part. To have force values to compare with, three reference seals were also tested. For these reference tests, reference parts were mounted on both sides of the chamber. The fluid used for the tests was a mineral oil (ISO 32 HLP).

2.4 Test procedures

Before the functional tests were conducted, some preliminary examinations took place. The following functional tests were conducted in two phases. The first one was supposed to determine whether the additively manufactured parts are likely to fulfill the main function: to avoid fluid leakage. The maximum pressure applied and the number of test cycles were moderate in that phase.

In the second phase, tests were conducted up to the maximum pressure the test rig was designed for. The parts tested were manufactured with optimized parameters regarding the outcomes of the first test phase. Also, a long-term test with a total sliding distance of 5,320 m was performed with one test part.

2.4.1 Preliminary examinations

Before and after the tests, the following values were measured and documented: the mass, the inner diameter, and the radial force. The measurement method for the radial force was first described by Debler in [5]. Because of the different mounting methods (no compression of outer diameter), the measured radial force is not the force in the application. Nevertheless, it allows the comparison with reference parts, and it shows possible deviation after the functional tests.

2.4.2 First test phase

In the first phase, ten cycles were performed with an acceleration of 0.8 m/s² and a maximum speed of 0.05 m/s. The stroke length was 100 mm.

This was done with the following system pressures: 0, 1, 2, 3, 4, and 5 MPa. After every pressure change, there was a waiting time of 10 minutes.

Since the test rig does not allow leakage measurement so far, the following distinction was defined to evaluate the tests:

- no visible leakage;
- slight leakage, like single drops on the adapter plate or a fluid film on the rod (as in Figure 4); or
- severe leakage, leading to an abortion of the test—this was done in case fluid dropped down the adapter plate (see Figure 5).

The main goal of the first test phase was to see whether the additively manufactured test parts had the potential to fulfill their main purpose: to avoid leakage.

The tests were performed with three test parts per filament, as listed in Section 2.1.

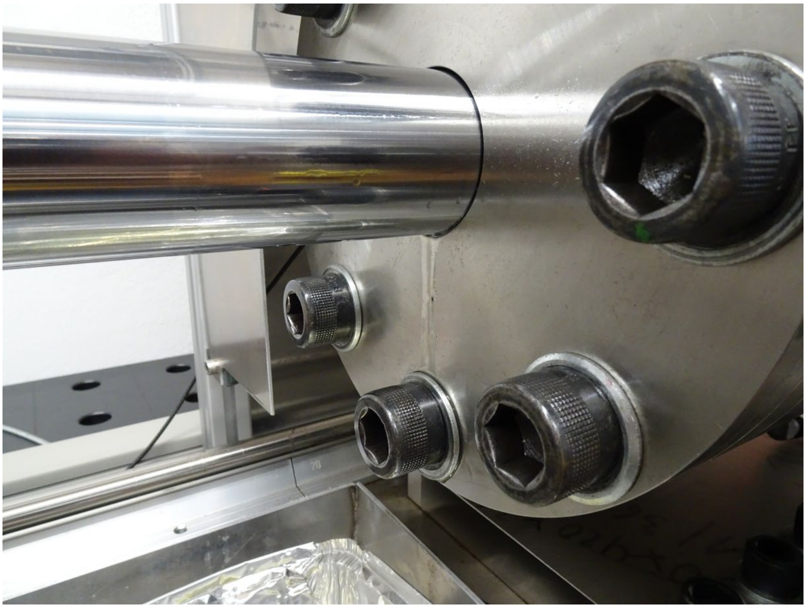

Figure 4: Slight leakage with the assembled test seal 10 at 0 MPa

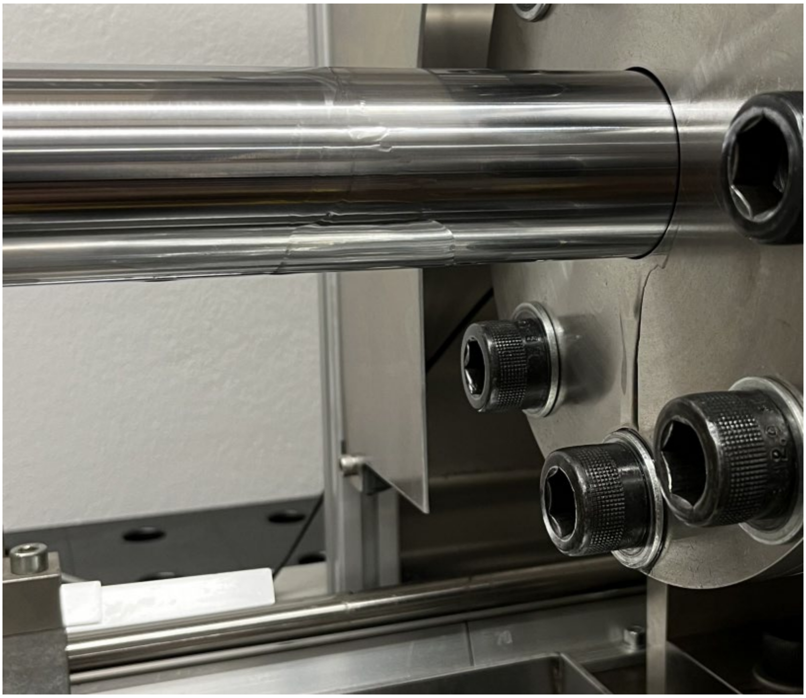

Figure 5: Severe leakage at 5 MPa with the assembled test seal 36

2.4.3 Second test phase

Based on the findings of the first test phase, the manufacturing parameters were optimized to achieve denser parts. The goal was to achieve a theoretical filling degree of 100 %. Therefore, the actual mass of the parts was compared to the theoretical density based on the CAD file and the measured density of the filaments.

Also, one filament (Extrudr Hard D58) was excluded from the second test phase because in the first phase, the parts made from that filament turned out to be too hard, leading to very high radial forces, and in case of different seal references, they were not mountable.

In the second phase, the goal was to test up to the maximum pressure of 15 MPa, which is achievable with the test rig. Also, the number of cycles was changed to 100. The pressure stages were: 2.5, 5, 7.5, 10, 12.5, and 15 MPa. The values for acceleration, speed, and stroke length remained the same. A waiting time of 8 hours after mounting the test parts was implemented to achieve material relaxation before the tests started.

After these tests, a longer test at a pressure of 6.3 MPa was conducted with 1,000 strokes. With one test part, a test with a sliding distance of 5,000 m (25,000 cycles) was added.

3 Summary and Conclusion

The following sections show the general qualitative results of the test phases, the long-term test, and comparisons of axial force measurements with reference parts.

3.1 First test phase

The following list shows the assignment of the test part numbers to the filaments, while Table 1 shows the qualitative results of this first phase:

- TreeD Flexmark 9: 01, 15, 16
- BASF Ultrafuse TPU95: 02, 03, 04
- Extruder Hard D58: 05, 06, 22
- Polymaker TPU95: 07, 08, 17
- Extrudr Semisoft: 09, 10, 18
- Extrudr Medium: 19, 20, 21

Theoretical filling degrees beyond 100 %, as seen in Table 1, can have two reasons.

The actual dimensions can differ from the nominal size because of over-extraction, and the actual density can differ from the one listed in the datasheet. To avoid the latter, the actual density of the filaments was measured before the second test phase.

Table 1: Results of the first test phase

Nr.	Mass before test in g	Mass after test in g	Δm in %	Filling degree in %	Result
01	8.938	9.195	2.88	91.14	Aborted at 1 MPa
02	9.280	9.363	0.89	103.02	Successful
03	9.161	9.220	0.64	101.70	Successful
04	9.214	9.277	0.68	102.29	Successful
05	8.946	9.069	1.37	94.26	Successful
06	8.964	9.156	2.14	94.45	Successful
07	9.034	9.184	1.66	92.12	Successful
08	8.991	9.217	2.51	91.68	Successful
09	8.571	8.808	2.77	91.84	Aborted at 1 MPa
10	8.519	8.846	3.84	91.29	Aborted at 1 MPa
15	9.087	9.366	3.07	92.66	Successful
16	8.936	9.204	3.00	91.12	Aborted at 1 MPa
17	8.948	9.144	2.19	91.24	Successful
18	8.036	8.604	7.07	86.11	Aborted at 1 MPa
19	8.785	8.933	1.68	93.35	Successful
20	8.437	8.933	5.88	89.65	Aborted at 2 MPa
21	8.408	8.920	6.06	89.34	Aborted at 2 MPa
22	8.224	8.920	8.46	86.66	Aborted at ambient pressure

The results of the first phase showed the importance of a high filling degree. Therefore, the manufacturing parameters were optimized to achieve a filling degree near 100%, although given the manufacturing method, there will remain a certain porosity in any case. Figure 1 shows the axial forces of three test parts made from the BASF filament compared to three reference seals. “Left” and “right” refer to the mounting position, as explained in Section 2.3.

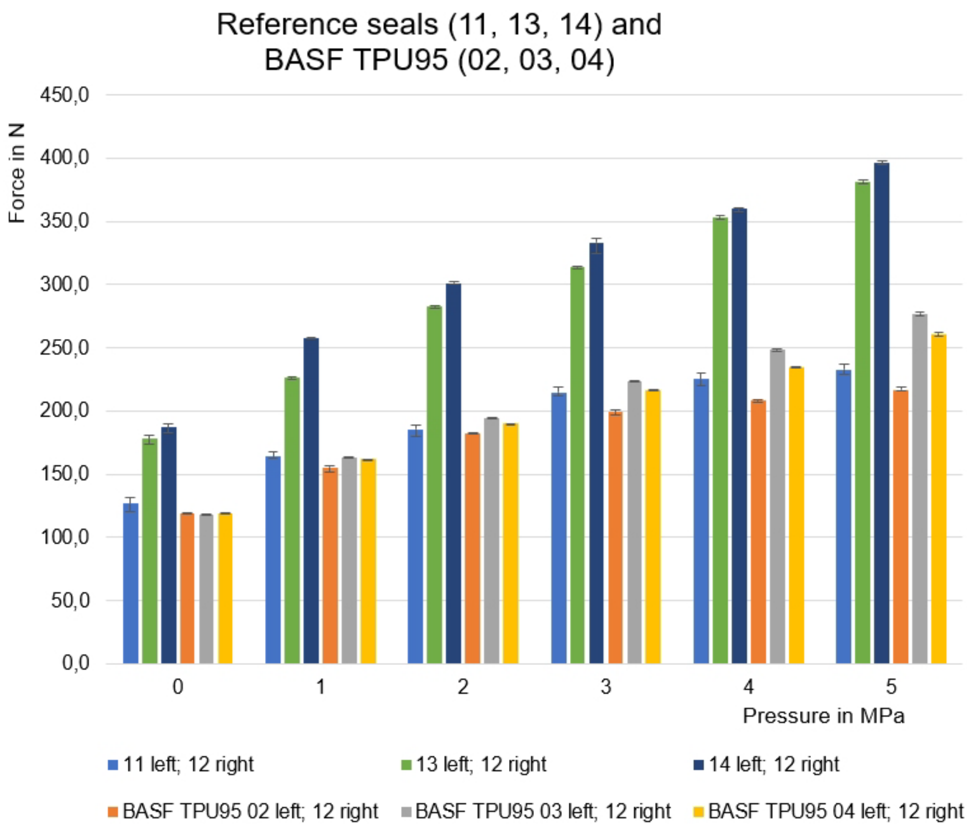

Figure 6: Axial forces (Outstroke) — Reference parts and BASF TPU95 (Phase 1) [6]

The axial forces tend to be lower than with the reference seals, although in various cases, the radial forces were higher. This is due to a higher compressibility of the additively manufactured parts because of their porosity, compared to the conventionally made reference parts.

3.2 Second test phase

The following list shows the assignment of the test part numbers to the filaments for the second phase, while Table 2 shows the qualitative results of the second phase:

- TreeD Flexmark 9: 44, 45, 46
- BASF Ultrafuse TPU95: 32, 33, 34
- Polymaker TPU95: 38, 39, 40
- Extrudr Semisoft: 35, 36, 37
- Extrudr Medium: 29, 30, 31

Table 2: Results of the second test phase [6]

Nr.	Δm in %	Filling degree in %	Result
29	1.00	98.11	Successful, slight leakage
30	0.92	98.97	Successful, slight leakage
31	0.54	98.37	Successful, slight leakage
32	0.69	98.65	Successful, slight leakage
33	0.68	98.73	Successful, no leakage
34	0.68	99.05	Successful, slight leakage
35	1.40	98.86	Successful, slight leakage
36	1.33	99.41	Aborted at 5 MPa
37	1.36	99.94	Successful, slight leakage
38	0.46	102.27	Successful, slight leakage
39	0.34	101.95	Successful, slight leakage
40	0.40	101.62	Successful, slight leakage
44	0.46	99.79	Successful, slight leakage
45	0.62	100.68	Successful, slight leakage
46	0.64	100.67	Aborted at 10 MPa

The axial forces still tend to be lower than with the reference seals. Parameter optimization in the forefront of the second test phase led to a higher filling degree; thus, less porosity decreased that gap.

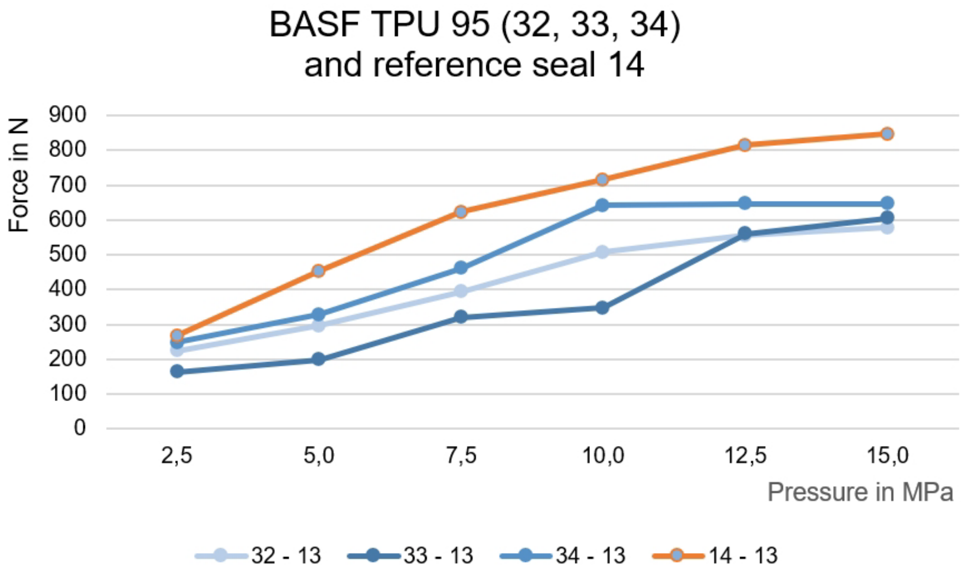

Figure 7: Axial forces (Outstroke) — BASF TPU95 (Phase 2)

It is noticeable that in some cases, the force increase stagnates from 10 MPa on. This can be seen, for example, in Figure 7 with the test part 34. This is supposedly a sign of a forthcoming failure with pressures beyond 15 MPa. Parts made from other filaments such as Extrudr Semisoft or Polymaker showed less tendency of stagnation. Such tendency was more distinctive with the parts made from Extrudr Medium and TreeD Flexmark 9.

The long-term test with one of the BASF parts (33) showed no visible sign of wear after a total sliding distance of 5,320 m.

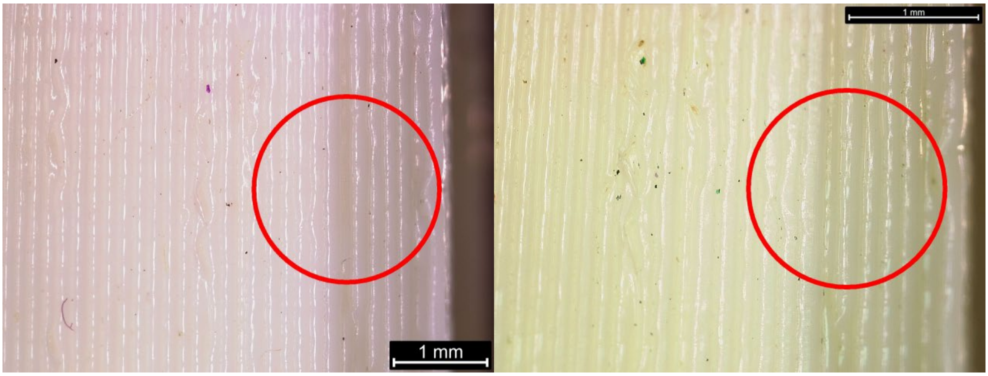

Figure 8: Microscope pictures of part 33 before (left) and after (right) the long-term test

Figure 8 shows pictures of the inside of the seal, taken using a prism. The circles indicate the sealing edge. Apart from discoloration caused by the fluid, no signs of abrasion or surface breakdown are noticeable. Although the loads act normally to the layers, which often leads to delamination, there are no signs of this being visible. The polished cut images in Figure 9 also do not indicate visible signs of wear.

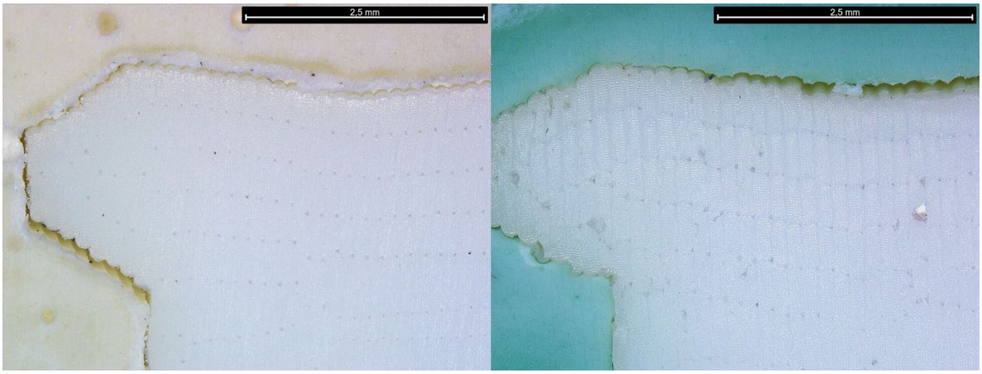

Figure 9: Polished cut images of part 33 (right) and an untested part made from the same material (left)

3.3 Conclusion

The functional tests have shown that at least within the conditions used for the tests, additively manufactured seals can be successfully used. Numerous seal types have delivery times of up to three months, and in recent years, it has become especially evident that supply chains can be vulnerable for geopolitical reasons such as wars or pandemics. This makes it desirable to enable distributors to locally produce spare parts so as to avoid or reduce costly machine shutdown times. The functional tests described in this paper show that such a local production using inexpensive machinery and a single raw material can be a realistic option.

Similar results were achieved by investigating two-component rod seals, consisting of a TPU component and an NBR (acrylonitrile butadiene rubber) component, both additively manufactured [7][8].

In the future, these tests will be continued with higher pressures and sliding distances after a redesign of the test rig. It also seems advantageous to conduct further functional tests with parts made from materials optimized for the application that are already used for the conventional production of rod seals.

4 Acknowledgments

This research has been partially funded by the Deutsche Forschungsgemeinschaft (DFG), Project Number 447009134. The authors would like to express their gratitude to the “Deutsches Institut für Kautschuktechnologie e.V.” for their valuable discussions.

5 References

[1] Müller, H. K., Nau, B. S.: www.fachwissen-dichtungstechnik.de Kapitel 5 Hydraulikdichtungen, visited on April 17, 2024

[2] Graf, M., Ebel, T., Lankenau, T. Ottink, K.: Towards additively manufactured dynamic rod seals, In: 21st International Sealing Conference Stuttgart 2022, Stuttgart, Germany, pp. 47–62, October 12–13, 2022

[3] Seals-Shop GmbH: Technical Information Rod Seals Zurcon® U-Cup RU2, https://www.seals-shop.com/content/medias/technical_datasheets/ TDS_Rod_Zurcon_U-Cup_RU2_01.pdf, visited on June 6, 2024

[4] ISO International Organization for Standardization: ISO 7986:1997 — Hydraulic fluid power — Seal devices — Standard test methods to assess the performance of seals used in oil hydraulic reciprocating applications. 1997.

[5] Debler, C.: Bestimmung und Vorhersage des Verschleisses für die Auslegung von Dichtungen, Dissertation, Gottfried Wilhelm Leibniz Universitaet, 2005, Hanover — Germany

[6] Ebel, T.: Eignung von additiven Fertigungsverfahren für die Herstellung dynamischer Dichtungen, Dissertation, Gottfried Wilhelm Leibniz Universitaet, 2024, Hanover, Germany, https://doi.org/10.15488/16456

[7] SKF: PTB Rod Seals, https://www.skf.com/us/products/industrial-seals/hydraulic-seals/rod-and-buffer-seals/energized-u-cup-rod-seals/ptb, visited on June 6, 2024

[8] Ebel, T., Lankenau, T., Sundermann, L., et al.: Functional testing of entirely additively manufactured two-component hydraulic rod seals made of TPU and NBR, Discover Mechanical Engineering, Vol. 3, article number 4, 2024, https://doi.org/10.1007/s44245-024-00034-x

6 Authors

University of Applied Science Emden-Leer
Constantiaplatz 4, 26723 Emden, Germany:

Dr.-Ing. Thomas Ebel, ORCID 0000-0003-2099-763X,
thomas.ebel@hs-emden-leer.de

Prof. Dr.-Ing. Kathrin Ottink, ORCID 0000-0002-5977-5316,
kathrin.ottink@hs-emden-leer.de

Prof. Dr.-Ing. Matthias Graf, ORCID 0000-0001-9999-7768,
matthias.graf@hs-emden-leer.de

Tobias Lankenau, M. Eng., ORCID 0000-0001-8105-0082,
tobias.lankenau@hs-emden-leer.de

https://doi.org/10.61319/ZMBIHUSV

Additive Manufacturing of Sealing rings: Material Selection and Application Development

Jacqueline Gerhard, Lothar Hörl, Frank Bauer

The use of additive manufacturing, particularly 3D printing, for the production of seal rings is a promising way to speed up the development cycle of new products. In addition, this technology enables the rapid optimization and investigation of seal profiles. In order to guarantee the required sealing function, the sealing material must meet specific requirements. In this study, a comprehensive analysis is performed focusing on the evaluation of elastic 3D printable materials to gain an understanding of the general properties and behaviour of these materials. A liquid crystal display printer was used for all tests. The first prototypes of additive manufactured rod seals for a pneumatic application were tested.

1 Introduction

The use of additive manufacturing in the sealing technology allows for the rapid exploration and implementation of geometric variations in sealing profiles, enabling rapid optimization for individual applications. However, this manufacturing process presents new challenges. In order to guarantee the required sealing function, the sealing material must meet specific requirements and therefore it is important to fully understand the material behaviour.

In the following, the most common 3D printing techniques and the objective of this work will be explained. Chapter 2 will present the most significant results of the material tests, followed by the results of pneumatic rod seals on the test rig in chapter 3.

1.1 3D Printing Technologies

In the **Fused Deposition Modeling** (FDM) process, the material, a solid thermoplastic in the form of filaments, is melted in the extruder and applied through a nozzle onto the printing platform. After printing, the thermoplastic cools and hardens again.

In addition to the FDM process, there are processes in which liquid photosensitive resins are cured using some form of light energy, in the following called “resin printer”. These processes use a resin tank with a transparent film on the bottom and a non-stick surface. The resin tank contains the liquid resin. During the printing process, the printing platform is lowered into the resin tank. Some space is left between the bottom of the printing platform and the non-adhesive surface of the tank bottom. This space corresponds to the layer height. The liquid resin in the gap between the printing platform and the tank bottom is selectively exposed to light through the transparent film to cure the desired areas, leaving the remaining areas liquid. By moving the platform up, the hardened layer is separated from the tank bottom and new resin flows into the gap between the printing platform and the tank bottom. This process is repeated until printing is complete. The most common techniques that utilize UV light to cure photosensitive polymers are presented below.

In the **Stereolithography** (SLA) technique, a laser is used to selectively cure the resin by punctually laser scanning the surface. The **Masked Stereolithography** (mSLA) technique uses LEDs which are projected through a masking screen. The mask prevents light from passing through to create the curing pattern. Because the LCD (Liquid Crystal Display), i.e. the mask, absorbs most of the energy of the LEDs, the mSLA technology has a lower amount of energy per unit area but is generally a faster printing technique than SLA because the projector can expose the entire layer at once rather than curing point by point. **Digital Light Processing** (DLP) is a technique that uses a digital light projector as a light source to cure the resin. The projector shines its light onto the DMD (Digital Micromirror Device), which consists of thousands of small mirrors, each of which is capable of deflecting the light from the projector in a different direction. For each layer, these mirrors are arranged in a specific orientation that reflects the digital light beam from the projector onto the bottom of the tank in the shape of the layer to be printed.

Photopolymers for resin printers are UV-activated synthetic resins. During photopolymerization, the resin consisting of monomers and photo initiators is exposed to UV rays. The initiators are split into free radicals by the exposure. The free radicals cause the monomers to crosslink to form polymer chains. Components produced by photopolymerization exhibit anisotropic behavior, primarily due to inadequate crosslinking during layer formation.

Another process is **Selective Laser Sintering** (SLS), in which small polymer powder particles are sintered into a solid structure. For this process, powder is applied to the printing platform in a thin layer. The printer heats the powder to a temperature slightly below the melting point. The laser then scans the areas, which should be printed, and heats the powder which mechanically fuses the particles and creates a solid part.

In all additive manufacturing processes, layers are added sequentially, resulting in stepped structures on rounded or angled edges of the component. These are generally more pronounced when using FDM printers than when using resin printers. As example, an O-ring with a round cross-sectional geometry was printed with the mSLA printer Mono M5s from Anycubic and then measured with the IMA seal scanner [1]. For comparison, the same O-ring was printed using the FDM printer Sovol S06 with a layer height of 0.1 mm. The contour of the printed O-ring using FDM is shown in Figure 1 (left) and the contour of the printed O-ring using mSLA in Figure 1 (middle). For comparison, an injection-molded O-ring was measured, Figure 1 (right). The contours of the FDM printed O-ring are significantly more stepped than those of the mSLA printed O-ring. An injection-molded O-ring with smooth contours is more similar to an mSLA printed O-ring and the mSLA technique is therefore more suitable for printing seal rings.

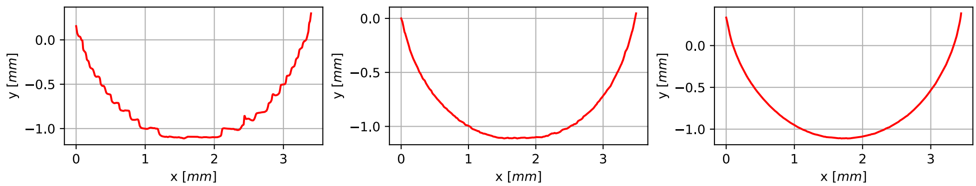

Figure 1: Geometry of printed O-rings: FDM (left), mSLA (middle) and of an injection-molded O-ring (right)

1.2 Objective

There have already been a few attempts to realize the additive manufacture of seal rings [2-7]. One approach is to print injection moulds and use them to produce seals in an injection moulding machine. There are various materials that are advertised for this purpose, for example the ultracure 3D RG 3280 from BASF or the Somos PerFORM material from Stratasys. However, this requires an injection moulding machine to be available. In addition, there exist different modifications of the standard printing processes presented in chapter 1.1. As example, Cubicure developed the Hot Lithography technique which can be used to print temperature-resistant and long-term stable moulds for an injection moulding machine. ViscoTec focuses on cross-linked chemistry and developed an extruder to print cross-linked 2-component materials. The acquisition costs for these systems are higher than those for standard resin printers, but they have already been used to successfully print seals [8].

In this study, the objective is to analyse the most straightforward approach and therefore the direct printing of seal rings. In order to achieve this, the first goal is to understand photopolymers for 3D printing and study how they behave under different conditions. Based on this, it will be possible to determine which type of seal they are suitable for. In the scope of this work, the focus was on one mSLA 3D printing technique and four pre-selected materials from two manufacturers. These materials will be used to investigate the behaviour and possibilities of the materials. A resin printer was chosen as this has significantly better printing accuracy than FDM printers.

2 Material property studies

Two Anycubic models were used as mSLA printers (Mono M5s and M3 Max). Tensile and compression set tests were performed on samples from both printers and no difference was found between the two mSLA printers when using the same resin. The printing parameters were initially set to achieve the most accurate printing of a test geometry. For example, the exposure time, the length of time each layer is exposed, depends on the material and must be adjusted for each material. If the exposure time is too short, either the desired area will not be fully cured, resulting in geometric deviations, or the layers will not adhere to each other and the part will fall off during the printing process. If the exposure time is too long, light scattering will cause areas outside the exposed area to cure. As a result, the parts are usually larger than defined in the Computer Aided Design (CAD) software.

The materials analysed are listed in Table 1. The Shore A hardness of the materials was measured according to DIN ISO 48-4 [10] on the day of printing ($t_{storage}$ = 0 h) and 4 weeks later ($t_{storage}$ = 4 w). These measurements are compared with the hardness specified in the manufacturer's data sheet. In the following, only the abbreviation in the second column is mentioned instead of the entire name of the materials.

Table 1: Materials and their Shore A hardness

		Shore A hardness		
Material	Abbreviation	$t_{storage}$ = 0 h	$t_{storage}$ = 4 w	Data sheet
Loctite 3D 8195	L 8195	59	60	58
Loctite 3D IND475	IND475	60	70	60
Resione F69	F69	73	95	60-75
Resione F80	F80	56	78	50-60

Based on the measured hardness listed in Table 1, changes in the materials over time were determined. Throughout the storage period, the specimens were stored at room temperature and protected from light. Ideally, the sealing material and therefore the sealing function of a seal should not change significantly over time. Therefore, a change of more than 20 Shore A in a 4-week period could render a material unsuitable as sealing material. After a further 4-weeks ($t_{storage}$= 8 w), this change in hardness was no longer detectable, indicating that the material could still be used as sealing material. Tensile tests were carried out for further analysis and the results are presented below.

2.1 Tensile Tests

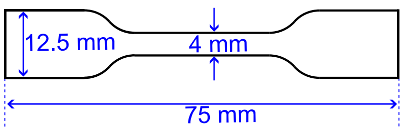

Figure 2: S2 Test specimen

As the materials cure under UV light, the material properties can still change after printing if the printed parts are exposed to sunlight. To analyse these material changes due to post-curing, tensile tests according to DIN 53504 [9] were performed. Figure 2 shows the geometry of the S2 test specimen with a thickness of 2 mm. Firstly, it was investigated how the stress-strain curve changes after the samples have been stored for a certain time at room temperature and protected from light. These changes were then tried to be reproduced by a longer exposure time or curing time. The samples were tested at a speed of 100 mm/min. Each variant was measured five times and then a representative curve, the most central, was selected from the five resulting measurements for further analysis. The technical strain and the technical stress are shown in the following.

To analyse the material changes due to post-curing, specimens made of IND475 were tested after different time intervals. The specimens were all printed at the same time and then stored for the time $t_{storage}$ until they were tested. Figure 3 shows the measured stress-strain curves for different storage times t_{storage} between printing and testing. The stress-strain curve shifts upwards and the material becomes stiffer due to post-curing.

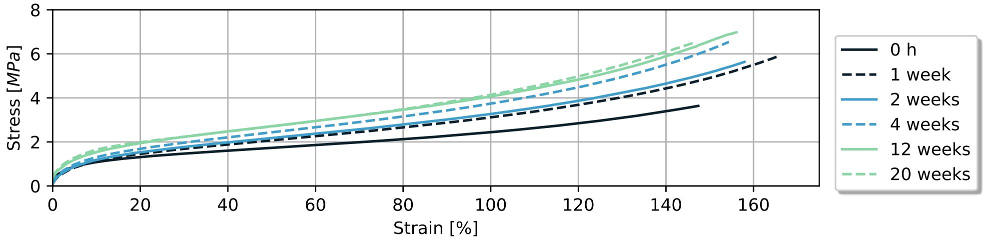

Figure 3: Tensile tests, IND475 Material, varying $t_{storage}$

In a further test, the curing time t_{cure} was increased to achieve a more cured state. The curing time defines how long the specimen is exposed to UV light in the curing station after printing in order to fully cure. The samples were all printed at the same time and then placed in the curing station for different lengths of time. In the curing station, the specimens are placed on a rotating plate and are exposed to UV light at a uniform wavelength of 405 nm from two angles. Afterwards they were immediately tested, the resulting stress-strain curves are presented in Figure 4. The upwards shift of the curve can also be observed with increasing t_{cure}, but is less significant than with increasing t_{storage}. After a longer curing time than 120 min, the samples became too brittle and broke between 80 % and 100 % strain. Therefore, longer times in the curing station were not further analyzed.

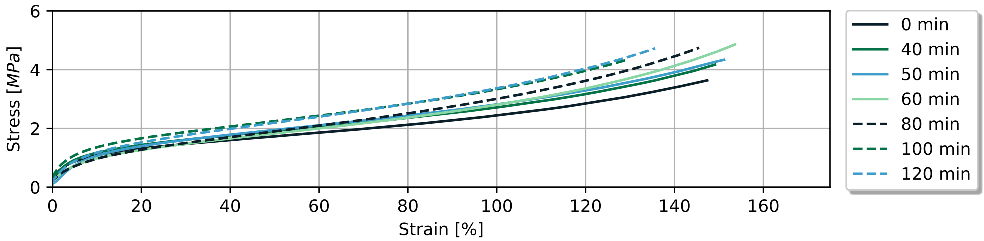

Figure 4: Tensile tests, IND475 Material, varying t_{cure}

As a third approach, the exposure time t_{exposure} with which each layer is exposed during printing was increased. Increasing the exposure time means that the geometry can no longer be reproduced well. Therefore, a sheet was printed and the samples were cut out of the printed sheet material. When increasing the exposure time, the effect of the upward shifted curve could not be observed for the material IND475. The differences in the stress-strain curves were too small to be recognized in the general scattering. The material behavior of F69 changes much faster with the storage time t_{storage} between printing and measurement, Figure 5. The upwards shift of the stress-strain curve is in the case of the F69 material also visible by increasing the exposure time t_{exposure}, Figure 6.

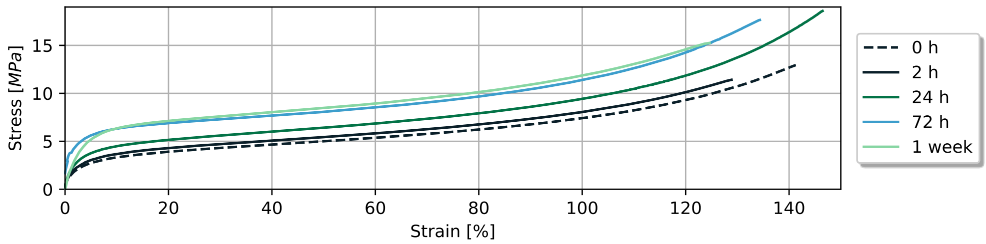

Figure 5: Tensile tests, F69 Material, varying $t_{storage}$

An increase in tensile strength of approximately 35 % was detected after only one week of storage for the F69 material, for which the greatest change over time was observed. For the IND475, the increase in tensile strength of approximately 20 % was measured after one week storage time and about 60 % after 20 weeks. For all tested materials from the resin printer, the change in material behaviour due to the storage time between printing and measurement was noticeable, but to different extents. For example, the upward shift in the stress-strain curve for the IND475 only became apparent after several days or weeks. In the case of the F69, the upward shift of the stress-strain curve was already visible after hours. This upward shift of the curve could also be caused by increasing the curing time. For some of the materials, the upwards shift could be reproduced by increasing the exposure time, but by a much smaller amount than by increasing the curing time. It was therefore not possible to prove that the change in material behaviour over time is only due to post-curing by UV light. Before testing, the tensile samples were weighed. A reduction in weight over time was observed for all materials. This indicates that the change over time is not only due to post-curing by UV light, but due to another effect.

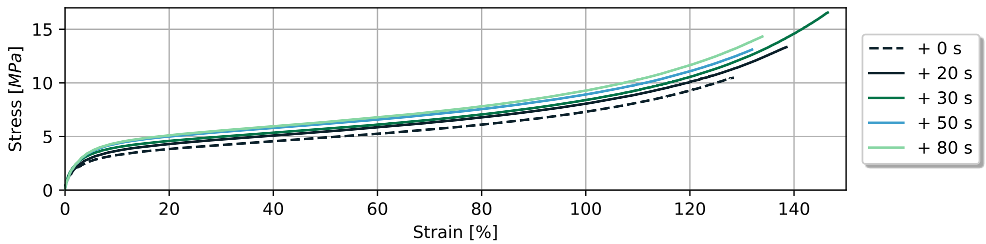

Figure 6: Tensile tests, F69 Material, varying $t_{exposure}$

An upward shift of the stress-strain curve of elastomers, and thus a higher stiffness, can be achieved by a higher loading speed [11]. A downwards shift can be achieved by higher temperatures [11]. At faster loading speeds, the stress-strain curve of the photopolymers is shifted upwards, meaning the behavior of the photopolymers is thus similar to that of elastomers. However, no reduced material stiffness was observed at higher temperatures.

2.2 Compression Set

The compression set (CS) was measured according to DIN 815 [12] at room temperature (RT), 55 °C and 85 °C. Cylindrical specimens with a diameter of 13 mm and a height of 6.3 mm were compressed by 25% for a period of 24 hours or 72 hours. For each variant five specimens were tested, the results shown hereafter are the average of the five measurements. For each material, the curing time t_{cure} was varied to reproduce different curing states. However, no correlation was found between the compression set and the curing times of t_{cure} = {10, 20, 30, 40} minutes. The first significant changes in the CS could only be determined for curing times of 60 minutes or more. In the following only the results of the materials IND475 and F69 are shown, as the CS for the two materials F80 and L 8195 ranged between 0 % and 2 % for all measurements and is therefore insignificantly small. For the F69 material, the CS ranged between 25 % and 30 % for the 24 h and 72 h tests at room temperature. For all tests at higher temperatures, the CS was less than 2 %.

For elastomers, the CS increases at higher temperatures [13]. This was not the case with the printed materials. Figure 7 shows the measured CS for samples cured after printing for curing times t_{cure} = {10, 60, 120} minutes. In each case, one day was waited between printing and measurement (t_{storage} = 1 day). The results of the measurements after t_{storage} = 20 weeks are also shown, in this case the curing time was set to t_{cure} = 10 minutes.

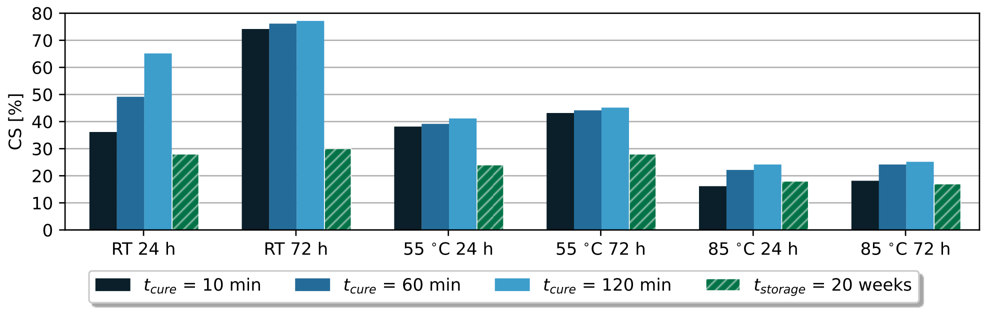

Figure 7: Compression set, IND 475

The CS increases for longer post-curing times t_{cure}. However, it decreases as the storage time t_{storage} between printing and testing increases. These results therefore indicate that the change in material behaviour over time is not just due to post-curing with UV light.

It could be that the materials are not yet fully cross-linked after printing. Testing at higher temperatures could accelerate the cross-linking, which is why the CS is lower at higher temperatures. At room temperature, the material does not fully cross-link during the test. Furthermore, the material behavior is different when it is cross-linked in a compressed state than when it is cross-linked in a relaxed state, which would explain the difference between the CS after longer curing times and after the storage time of 20 weeks.

The compression set at higher temperatures is generally lower for the IND475 material than at room temperature. Figure 8 shows the results for the F69 material at room temperature. At 55°C and 85°C, the CS ranged between 0 % and 2 %. As with the IND475 material, the CS of the F69 material decreases as the storage time t_{storage} increases. However, as the curing time t_{cure} increases, the CS increases.

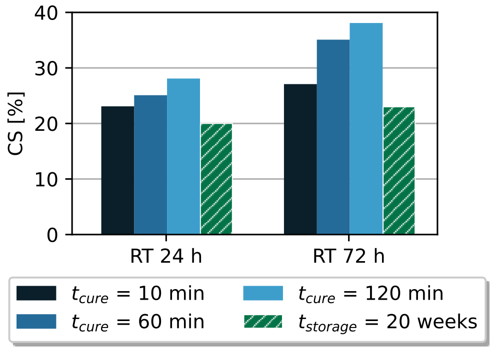

Figure 8: Compression set, F69

After the storage time of 20 weeks, the CS of the IND material decreases by 25 % in the 24-hour tests and by 60 % in the 72-hour tests at room temperature. In the case of the F69 material, the CS decreases about 15 % in both the 24-hour tests and the 72-hour tests at room temperature. In the tensile tests, the change in material behaviour over time was much more apparent for the F69 material than for the IND475 material. In the case of compression set the change over time is greater for the F69 material.

As defined in DIN 815, the CS was measured after 30 minutes. Figure 9 shows the results of the measurement in 5-minute steps from the time the samples were taken out of the steel plates for the 72-hour test at room temperature. The results of two polyurethane compounds from Parker Hannifin GmbH are shown for comparison.

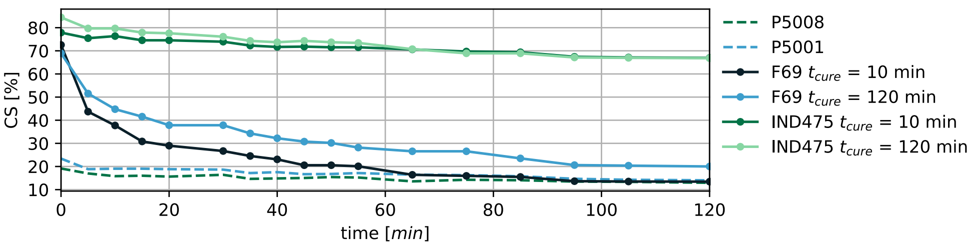

Figure 9: Compression set (72 h, room temperature) over time

The two polyurethane P5008 and P5001 from Parker Hannifin GmbH behave almost ideally. The CS is generally low and does not change much over time. The F69 material changes about 40 % in the first 40 minutes after removing the samples. The CS of the IND475 material decreases almost linearly and therefore similar to the Parker polyurethane. The samples made of IND475 and the samples made of polyurethane have probably deformed significantly within the first few seconds. This decrease within a few seconds was not measured. Thus, the material F69 takes longer to deform back, as the strong decrease of the CS occurs only after minutes. This indicates that the F69 specimens have not yet fully recovered after the 30-minute waiting time specified in DIN 815, which is a disadvantageous characteristic for a sealing material.

3 Additive Manufactured Rod Seals

A pneumatic rod seal design was printed from the four materials and analyzed. The test rig and the results of the reference seal are introduced below. This is followed by an explanation of the challenges encountered when printing the seal and the geometric optimization of the CAD file. The geometric optimization is then validated using the Finite Element Method (FEM).

3.1 Translational Test Rig

The frictional force between a seal ring and rod was measured at ambient pressure during horizontal movement of the rod on the translational test rig at the IMA. For this purpose, the ARUP seal ring [14] from Trelleborg Sealing Solutions for a rod diameter of 20 mm was printed. To obtain the CAD geometry the ARUP seal ring was cast in epoxy resin and the geometry measured. For all of the printed seal rings the same geometry file was used first, but had to be adapted later.

3.1.1 Reference Seal

The original ARUP seal ring from Trelleborg Sealing Solutions (TSS) made from a Polyurethan with 90 Shore A (WU9E1) was tested as reference. The seal rings were installed in a seal ring carrier first and then mounted on the rod. Next to the seal ring 0.1 ml of grease (Klübertemp GR M07 N) was then applied around the circumference of the rod. In a grease distribution run, the seal spreads the grease over the entire rod, after which the measurement was started. The frictional forces measured while moving the seal ring on the rod are shown in Figure 10 (left). For each variant, five seal rings have been tested. The frictional forces from the different seal rings are shown in different colors. During each measurement, the seal ring is moved 10 times with v_{max} = 200 mm/s from position x_{start}= 5 mm to position x_{end}= 70 mm which is why there are 10 curves for each tested seal ring. As the scatter between the five seal rings tested is very small and they all behave very similarly, the curves overlap. Figure 10 (right) shows the average frictional force and the scatter of the five seal rings. This was done by averaging the amount of the measurements taken at x = 35 mm. The minimum and maximum values of the measured force are marked by the grey bar. To analyze the force required at the beginning of the measurement and during the change of direction, the average of the amount of frictional force measured between x = 5 mm and x = 7 mm was calculated. The maximum value of the measured force in the range x = [5,7] mm is marked by the grey bar.

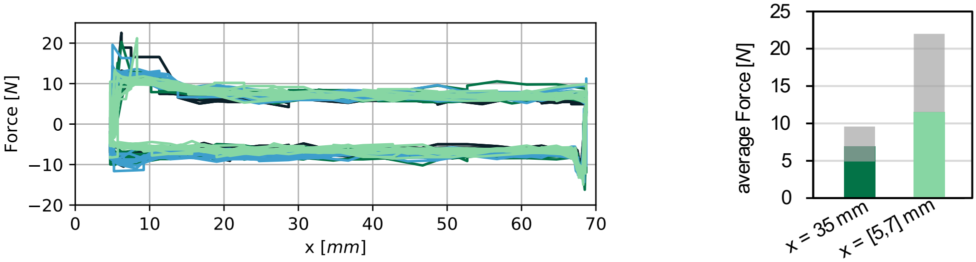

Figure 10: Measured frictional force (left) and average frictional force (right), seal rings from Trelleborg Sealing Solutions

3.1.2 Geometric Optimizations

When using an mSLA printer without optimizing the CAD geometry, printed parts tend to be oversized. In general, the first layers are exposed longer to ensure the components adhere to the printing plate. As a result, the first layers are printed larger, which can be corrected by a respective change in the CAD file. In addition to the oversize of these first layers, it was noted that the inner diameters of the printed seals were too small and the outer diameters too large. Therefore, these had to be adjusted as well. The printed seal rings were measured to determine the true inner diameter and the inner diameter in the CAD file was then adjusted. Figure 11 shows the sectional geometry of the seal ring. As an example, three dimensions are illustrated, which were adjusted in the CAD file in order to print the original geometry as accurately as possible. Using the diameters $d1_{\mathrm{CAD}}$ and $d2_{\mathrm{CAD}}$ listed in Table 2, an inner diameter of $d1_{\mathrm{printed}}$ = 19.5 mm ± 0.05 mm and an outer diameter of $d2_{\mathrm{printed}}$ = 29.5 mm ± 0.1 mm could be achieved for the printed seals. The width b of 3.6 mm could be achieved for all printed seals.

Table 2: Dimensions defined in the CAD file and actual measured dimensions [mm]

	$d1_{\mathrm{CAD}}$	$d1_{\mathrm{printed}}$	$d2_{\mathrm{CAD}}$	$d2_{\mathrm{printed}}$	b_{CAD}	b_{printed}
IND475	20.4	19.45	28.9	29.6	3.2	3.6
L 8195	19.3	19.5	29.4	29.5	3.6	3.6
F69	19.4	19.45	29.4	29.5	3.45	3.6
F80	19.6	19.5	29.3	29.5	3.5	3.6

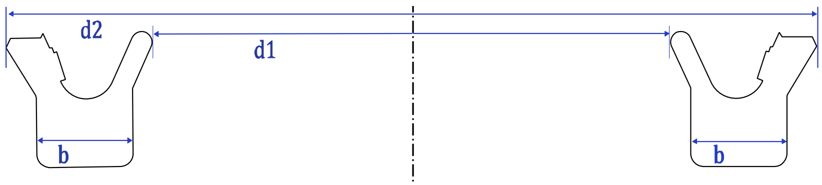

Figure 11: Sectional view of the seal ring

Despite the adjustment of the geometry according to Table 2, the shape of the sealing lip still deviates from the actual shape in the CAD file. Thus, the geometry of the seal ring made of IND475 was further optimized, as this was the geometry that deviated the most from the original geometry. Figure 12 (left) shows the measured frictional forces for the first printed seals with an inner diameter of $d1_{\mathrm{CAD}}$ = 19.5 mm in the CAD file and an average inner diameter of $d1_{\mathrm{printed}}$ = 18.5 mm measured on the printed seals. After adapting the geometry in the CAD file according to Table 2, an average inner diameter of $d1_{\mathrm{printed}}$ = 19.45 mm was measured, which significantly reduced the frictional force, Figure 12 (middle). Casting the printed seal rings in epoxy resin and measuring the printed geometry showed that the printed sealing lip was still too wide. The design of the sealing lip was then adjusted in the CAD file, which led to the frictional forces shown in Figure 12 (right).

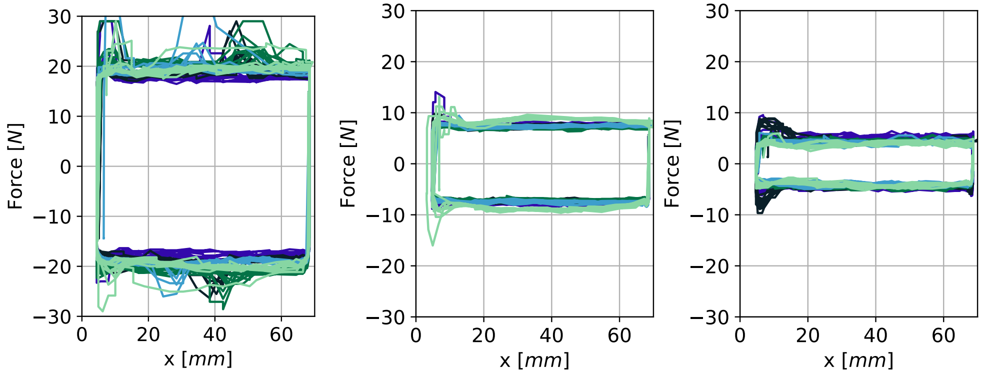

Figure 12: Frictional force, IND475, first printed seal (left), optimization of the diameters (middle) and adjustment of the sealing lip (right)

Thus, depending on the material, the geometry defined in the CAD file must first be adapted before a seal ring can be printed accurately using an mSLA printer.

Figure 12 also shows how quickly a seal geometry can be modified to achieve specific characteristics, such as lower friction. With a 3D printer, these geometry changes can be made fast and without much effort.

3.1.3 Material Comparison

For the 3D-printed seal rings, the printing parameters were selected for which the best accuracy could be achieved in printing tests. In order to test all seals under the same conditions, exactly seven days were waited between printing and testing. Figure 13 compares the frictional forces of the seals made of L 8195, F69 and F80. The diameters of the seal geometries have been adjusted to match the inner diameter of the original ARUP seal.

The individual seal rings made from L 8195 behave very differently, but the measurement results of a single seal ring vary only slightly. In the case of F69, it is the opposite: The five seal rings made of F69 all behave in a similar way, but the dispersion of one seal ring is greater.

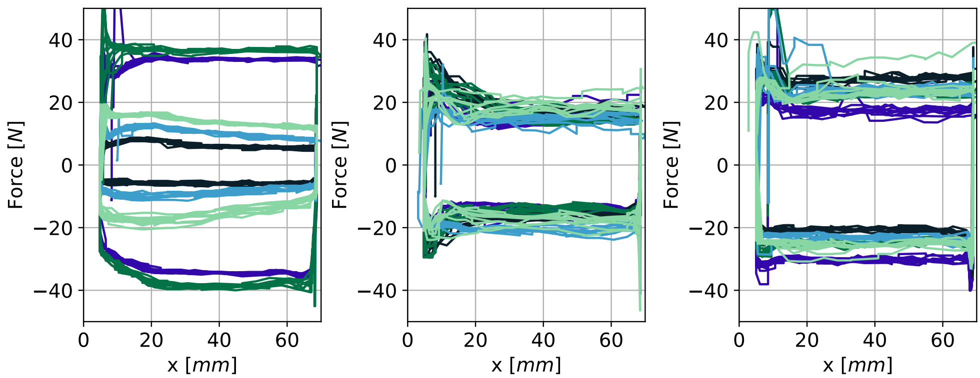

Figure 13: Frictional force, L 8195 (left), F69 (middle) and F80 (right)

In Figure 14, the average frictional force and the scatter is shown for the

- reference seal ring from Trelleborg (TSS),
- seal rings made of Loctite 8195, Resione F69 and Resione F80,
- Loctite IND475 seal rings, without geometric optimizations (IND475_1),
- Loctite IND475 seal rings with the optimization of the diameter (IND475_2),
- Loctite IND475 seal rings with the adjustment of the sealing lip (IND475_3).

The average of the five measurements at position x = 35 mm is displayed by the darker color. The average of the amount of frictional force measured between the positions x = 5 mm and x = 7 mm is displayed in a lighter color. The scattering, marked by the gray bar, is greatest for Loctite 8195. The Loctite IND 475 seals showed the lowest scatter, even without adjusting the geometry. In addition, the difference between the frictional force during movement (at position x = 35 mm) and the frictional force required to change direction (in the range x = [5,7] mm) is lowest for the seal rings made of Loctite IND 475.

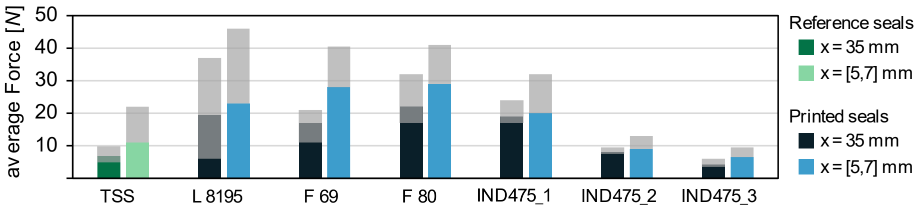

Figure 14: Average frictional force

In order to analyse the impact of the storage time on the frictional force, experiments were run with seal rings after t_{storage} = {0, 1, 4, 16} weeks. No trend in any direction could be recognized for the materials IND475, F69 and F80. The measured frictional forces of the seals made of L 8195 were generally so scattered that no trend could be identified either. The longest test run lasted 24 hours. The only seals that could not withstand this test run were made of the L 8195 material. These have torn after 18-21 hours. None of the other seals broke or showed signs of wear. In addition to the results shown in this chapter, measurements were performed under pressure. With the exception of the seals made of L 8195 material, all seals were able to withstand a pressure of 6 bar.

3.2 Assembly Simulation

The geometric optimizations of the seals made from IND475 were evaluated using the Finite Element Method (FEM). The actual printed geometries were measured and used. The measured frictional forces for these geometries are shown in Figure 12. The frictional force measured on the test rig can be calculated by

$$F_{\text{fric}} = \mu \; F_{\text{N}} \tag{1}$$

with the coefficient of friction μ and the contact normal force F_{N}. In an FEM simulation in the software MSC Marc Mentat, the assembly of the 2-dimensional cross-sectional geometry of the seal ring was simulated to get the contact normal force between seal ring and rod. To do so, the printed geometry was measured in order to ensure the same conditions as in the experiments. The seal ring carrier, in which the seals are installed before they are mounted on the rod, was also measured. In the FEM simulation, as in the experiments, the seal ring was first pushed into the groove, i.e. the seal ring carrier. The installed seal ring is then mounted on the shaft. The used Ogden material model is based on the tensile tests of the IND475 material at room temperature after t_{storage} = 1 week. Relaxation was not considered. The simulation results of the seal rings

- TSS: Reference seal ring, measurements shown in Figure 10
- IND475_1: First printed seal, measurements shown in Figure 12 (left)
- IND475_2: Optimization of the diameters, measurements Figure 12 (middle)
- IND475_3: Adjustment of the sealing lip, measurements Figure 12 (right)

are discussed in the following. Figure 15 shows the simulated installed seal ring IND475_3. The colors represent the first component of stress. Figure 16 shows the simulated contact forces between the sealing lip and shaft. The position x = 0 is defined by the node located left of the first node in contact with the shaft. The maximum values of the simulated normal force $F_{\mathrm{N,max}}$ are listed in Table 3. In addition, the frictional forces F_{fric} measured on the test rig are given. These are the average of all frictional forces measured between the two positions 20 mm and 40 mm.

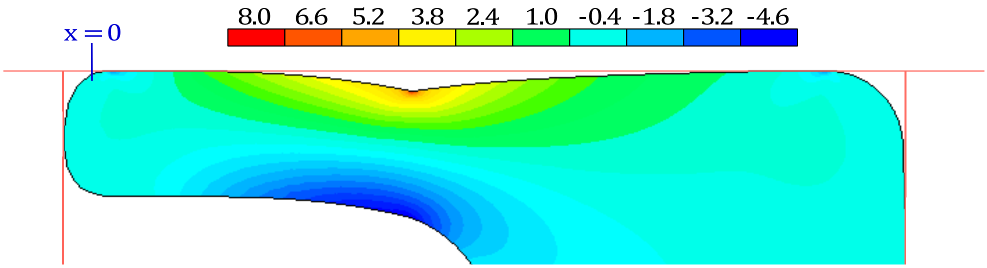

Figure 15: Simulation result, mounted seal IND475_3, 1st Component of Stress [N/mm^2]

The radial force, i.e. the force with which a seal ring is pressed against the shaft over the entire circumference, was measured using a radial force gauge [15] according to DIN 3761-9. Five seal rings were measured in each case, the average radial forces are given in in Table 3. When measuring the radial force, a higher value is measured at the beginning. Due to relaxation, the radial force decreases after only a few seconds. The values given in in Table 3 are the radial forces measured at the beginning, as no relaxation was considered in the simulation.

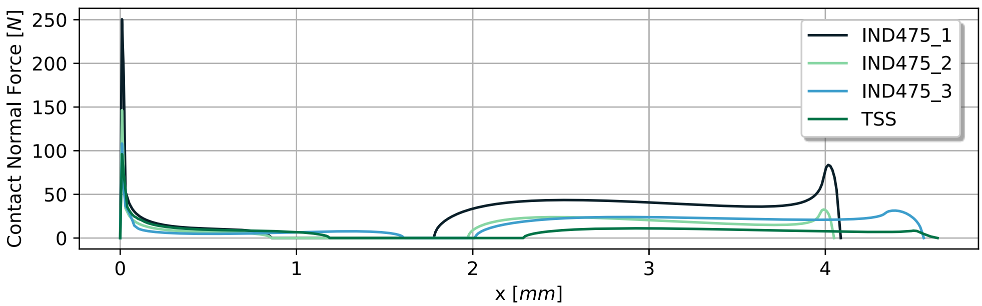

Figure 16: Simulation result, Contact Normal Forces of the sealing lip

Table 3: Frictional Forces measured on the test rig, Contact Normal Force obtained from the simulations and measured radial force

IND475_1	IND475_2	IND475_3	TSS
F_{fric} = 19 N	F_{fric} = 12 N	F_{fric} = 9 N	F_{fric} = 8 N
$F_{\mathrm{N,max}}$ = 251 N	$F_{\mathrm{N,max}}$ = 146 N	$F_{\mathrm{N,max}}$ = 108 N	$F_{\mathrm{N,max}}$ = 96 N
F_{radial} = 241 N	F_{radial} = 138 N	F_{radial} = 102 N	F_{radial} = 94 N

The measured radial forces agree well with the simulation results. Both the radial force and the frictional force could be significantly reduced by adjusting the inside diameter and optimizing the geometry of the sealing lip. Calculating the coefficient of friction from either the measured radial force F_{radial} or the simulated contact force $F_{\mathrm{N,max}}$ according to equation (1), results in a coefficient of friction between 0.076 and 0.088. These values are reasonable for a fully lubricated steel rod. On the test rig the same rod was used for all tests and the same amount of grease was applied. In the simulations, the same conditions were defined, the only change was the geometry of the seal. Therefore, the coefficient should be exactly the same. Small differences may be due to inaccurate measurement of the geometry.

4 Conclusion

The potential of additive manufacturing of seal rings using an mSLA printer was investigated. Additive manufacturing opens up many new possibilities in sealing technology. New and complex geometries can be produced and different geometric variations can be realized quickly. However, in order to fully exploit the potential, some preliminary work must be done first. This includes finding the right material, as there are many different photopolymers for mSLA printers available on the market.

The 3D-printed materials analyzed in this study have a lower elongation at break and a much lower tensile strength than conventional sealing materials. Nevertheless, the elongation at break of the printed materials is still sufficient for seals. In addition, very good Compression Set values were measured for the printed materials. One disadvantage is the change of the material behavior over time. All tested materials show a stiffer behavior in tensile tests after a longer period of time between printing and testing. The compression set is reduced by a longer waiting time, which is generally beneficial, but this still makes the material difficult to evaluate. The material change could not be reproduced by increasing the curing time or the exposure time, indicating that the change in material behavior was not due to post-curing with UV light. Before the materials can be used reliably, it is important to gain an understanding of the reason for their behavior. The change in material behavior could be due to reactions with the surrounding environment. Further tests need to be carried out, for example after storage times in a vacuum chamber, in order to detect evaporation of solvents out of the printed material.

The advantage, on the other hand, is the geometrical flexibility. For example, the sealing lip width can be changed very quickly to achieve the desired contact pressure between the sealing lip and the rod. In order to be able to do this, it is necessary to know how the geometry will be printed. Due to geometric deviations, the geometry file must be adapted depending on the printer and the material. If this is neglected, the geometry of the printed seal will not match the desired geometry which can lead to a poorer sealing performance. The impact of the geometric deviations on the frictional force between the seal and the rod was proven within the scope of this study.

It should be noted that the samples for all material tests were manufactured using an mSLA printer with a 405 nm light source. Printing on a different printer with a different light source may result in different material properties depending on the wavelength for which the material has been optimized by the manufacturer.

5 Acknowledgements

The authors thank the Fluid Power Research Fund of the VDMA for its financial support (grant: FKM No.7058300).

6 Nomenclature

Variable	***Description***	***Unit***
b_{CAD}	Width defined in the CAD file	[mm]
b_{printed}	Width measured on the printed seal	[mm]
$d1_{\mathrm{CAD}}$	Inner diameter defined in the CAD file	[mm]
$d1_{\mathrm{printed}}$	Inner diameter measured on the printed seal	[mm]
$d2_{\mathrm{CAD}}$	Outer diameter defined in the CAD file	[mm]
$d2_{\mathrm{printed}}$	Outer diameter measured on the printed seal	[mm]
F_{fric}	Frictional force	[N]
F_{N}	Contact normal force	[N]
t_{cure}	Curing time	[s]
t_{exposure}	Exposure time	[s]
t_{storage}	Storage time	[s]
v_{max}	Maximum velocity	[mm/s]
x_{start}	Start position of measurement	[mm]
x_{end}	End position of measurement	[mm]
μ	Coefficient of friction	[-]

7 References

[1] University of Stuttgart - Institute of Machine Components, “IMA-Sealscanner® (IMA-TechSheet #102050 V2)“. Accessed: 2. May 2024. [Online]. Available at: https://www.ima.uni-stuttgart.de/dokumente/forschung/dichtungstechnik/einrichtungen/en/102050en.pdf

[2] M. Graf, T. Ebel, T. Lankenau, K. Ottink, “Towards additively manufactured dynamic rod seals” in Proc. 21st Int. Sealing Conference 47-62, October 2022, doi: 10.61319/W7SZ07FJ

[3] T. Ebel, T. Lankenau, L.Sundermann, K. Ottink, et al. „Functional testing of entirely additively manufactured two-component hydraulic rod seals made of TPU and NBR” in *Discover Mechanical Engineering*, February 2024, doi: 10.1007/s44245-024-00034-x

[4] L. Sundermann, et al., “Tailoring the Curing Kinetics of NBR-Based Rubber Compounds for Additive Manufacturing of Rod Seals“, Advances in Polymer Technology, Bd. 2023, S. 1–16, August 2023, doi: 10.1155/2023/7343194

[5] A. Zhong, A. Phan, C. Glaesman, “World’s First 3D Printed Functional Polymeric Sealing Solutions“, in *Day 2 Tue, October 27, 2020*, October. 2020, doi: 10.2118/201573-MS

[6] D. Luning-Prak, B. Baker, und J. Cowart, “Engine O-Rings Produced Using Additive Manufacturing“, presented at the WCX SAE World Congress Experience, Detroit, Michigan, United States, April 2023, S. 2023-01–0893. doi: 10.4271/2023-01-0893

[7] B. Engendahl, C. Leibig, “3D Printing Flexible Materials: From Prototyping to Industrial Manufacturing”, Presentation at the 21st ISC 2022, Stuttgart

[8] ISGATECH GmbH, “Dichtungen drucken? Ja“, Dicht! Dichten.Kleben.Polymer.verstehen, Nr. 4.2023, ISSN: 1863-4699

[9] DIN German Institute for Standardization, “DIN ISO 48-4, Rubber, vulcanized or thermoplastic – Determination of hardness – Part 4: Indentation hardness by durometer method (Shore hardness)“. Beuth publishing DIN, February 2021

[10] DIN German Institute for Standardization, “DIN 53504:2009-10, Testing of rubber - determination of tensile strength at break, tensile stress at yield, elongation at break and stress values in a tensile test“. Beuth publishing DIN, October 2009

[11] F. Bauer, „Federvorgespannte-Elastomer-Radial-Wellendichtungen. Grundlagen der Tribologie & Dichtungstechnik, Funktion und Schadensanalyse“, Springer Vieweg, Wiesbaden, 2021, ISBN 978-3-658-32921-1, doi: 10.1007/978-3-658-32922-8

[12] DIN German Institute for Standardization und International Organization for Standardization, “DIN ISO 815-1:2022-04, Rubber, vulcanized or thermoplastic - Determination of compression set - Part 1: At ambient or elevated temperatures“. Beuth publishing DIN, April 2022

[13] U. Blobner, B. Richter, “Fachwissen Prüfverfahren für Elastomere – Druckverformungsrestprüfung“, O-Ring Prüflabor Richter GmbH, June 2015

[14] Trelleborg Group, “Trelleborg Sealing Solutions - Pneumatic Seals catalog“, 2011.

[15] University of Stuttgart - Institute of Machine Components, “Radialkraftmessgerät Desktopversion (IMA-TechSheet #102100 V2)“. Accessed: 8. May 2024. [Online]. Available at: https://www.ima.uni-stuttgart.de/dokumente/forschung/dichtungstechnik/einrichtungen/102090_102100.pdf

8 Authors

University of Stuttgart, Institute of Machine Components (IMA)

Pfaffenwaldring 9, 70569 Stuttgart, Germany:

Jacqueline Gerhard, M. Sc., ORCID 0000-0002-4879-5653,
Jacqueline.gerhard@ima.uni-stuttgart.de

Dipl.-Ing. Lothar Hörl, ORCID 0000-0002-2851-3364,
lothar.hoerl@ima.uni-stuttgart.de

apl. Prof. Dr.-Ing.Frank Bauer, ORCID 0000-0001-7799-7628,
frank.bauer@ima.uni-stuttgart.de

https://doi.org/10.61319/VC628LDF

Innovation in Seal Production: Novel Additive Manufacturing for High-Performance PU Seals

Ozan Devlen, Cem Tanyeri, Alper Kocamaz, Barthel Engendahl

Our study unveils a groundbreaking additive manufacturing (AM) technology poised to redefine the standards of polyurethane seal production. By meticulously merging the precision of AM with the robustness of injection-molded TPU, this technology not only promises to bridge existing manufacturing gaps but also to set new benchmarks for seal performance and durability. Our rigorous evaluation underscores the technology's superior design flexibility, enabling the creation of custom, high-performance seals that surpass traditional capabilities in both efficiency and environmental sustainability. The results of our comprehensive testing and validation process reveal a significant leap forward, offering not just an alternative but a superior solution in seal manufacturing. We propose this AM technology as a transformative force capable of revolutionizing industry standards and paving the way for innovative applications across sectors. This is not just an advancement; it's a call to reimagine what's possible in seal manufacturing.

1 Introduction

The sealing industry continually seeks advancements to improve the performance and longevity of seals used in diverse applications. This paper explores the utilization of additive manufacturing (AM) techniques for producing high-performance PU seals, offering a detailed analysis of the benefits and challenges associated with this innovative approach.

1.1 Background

Polyurethane seals are widely recognized for their exceptional mechanical properties and resistance to wear and chemicals. Traditional manufacturing processes for PU seals typically involve molding techniques, which may limit design flexibility and increase costs for small series. Additive manufacturing, also known as 3D printing, offers a transformative alternative that can overcome these limitations by enabling complex geometries and material customization. [1]

This paper focuses on polyurethane technology by comparing traditionally produced polyurethane seals with their additively manufactured counterparts. Additive technologies available to produce polyurethane parts include solid extrusion or selective laser sintering (SLS) of TPU resins, utilizing filament extrusion (FDM), pellet extrusion, or SLS processes involving TPU powders. Additionally, reactive extrusion technology is highlighted, where a reactive liquid two-component system consisting of an isocyanate and a polyol component reacts during the printing process to form crosslinked polyurethane resin.

In this paper, we will exclude comparisons to other additive manufacturing technologies that cannot process pure polyurethane materials. Examples include solid extrusion-based methods, where a solid plastic or thermoplastic elastomer is processed into a filament. These filaments are often composed of the same plastic formulations as those used in traditional injection molding processes. The idea behind this process is that using similar polymers with a novel method to build the structure would result in a part with comparable mechanical properties. Unfortunately, while operating at similar temperatures to traditional injection molding, solid extrusion-based processes lack the pressures needed to entangle polymer chains. This results in lower material strength in the build direction of the production process, often up to 50% less, making them unsuitable for high-performance applications.

Even if this drawback can be overcome, solid extrusion-based processes involve placing a heated, flowable, but highly viscous polymer bead on top of an already cooled and solid polymer. Due to the high viscosity of the flowable bead, the contact areas between beads always contain voids, forming channels in the movement direction of the printhead. These voids create two problems: they are starting points for mechanical failure and contribute to crack propagation, and they allow fluids in the form of gases or liquids to travel through the part.

In powder processing technologies similar to solid extrusion, there is no applied pressure to ensure polymer chains entangle to achieve the same tensile strength as traditionally manufactured parts. Additionally, these processes depend on applying melted material onto solidified polymer resin, creating similar channels. While there are methods to post-process or soak surfaces to close voids or channels, these often involve coating with a different material that might not be compatible with the sealing application.

In conclusion, solid extrusion and powder melting processes have the drawbacks of non-isotropic material properties, as well as voids and channels that allow fluids to pass through, which is a significant issue for sealing applications. Reactive extrusion technology, though similar in processing to solid extrusion methods, distinguishes itself by combining the two components needed to make polyurethane during the form-giving process. No heat is applied, and no pre-reacted polymer is melted in the process. The closest comparison to traditional production processes is casting, where polyurethane is made by mixing an isocyanate and a polyol component in liquid form before filling the liquid into a mold. Chemically, the only difference between PU casting and PU reactive extrusion processes is the absence of a mold.

If the reactivity and print parameters are chosen carefully, the material will flow as a liquid bead onto the solidified layer below. The solidified layer and the new bead will have unreacted isocyanate and polyol groups on the surface, allowing for interlayer and interbead adhesion to provide isotropic material properties. High-performance PU materials tailored to the reactive extrusion process will enable the production of high-performance seals.

1.2 Objectives

The primary objective of this study is to evaluate the feasibility and performance of PU seals produced using AM techniques. Specific goals include:

- Assessing the mechanical properties and durability of AM-produced PU seals.
- Comparing the performance of AM seals with traditionally manufactured seals.
- Identifying potential applications and industry benefits

2 Methodology

2.1 Materials and Equipment

Material Development and Selection: Reactive extrusion technology cannot utilized by traditional 2K PU cast systems. These systems are designed to have very low viscosity, fill all mold cavities, and be processable within minutes. However, the material requires a higher viscosity to build structure for reactive extrusion. Therefore, a completely new type of 2K PU system needed to be developed.

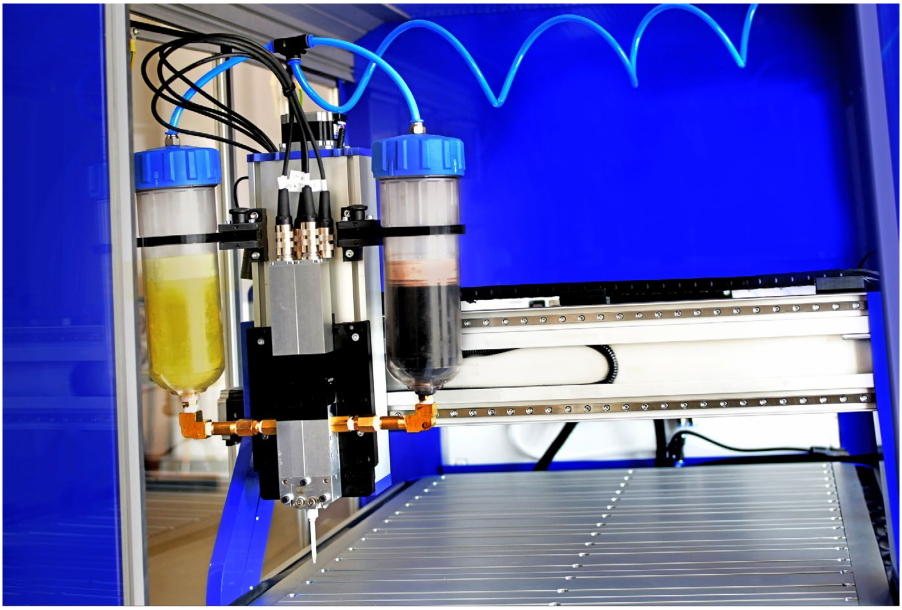

Figure 1: RX-AM 3500 printer from Chromatic 3D Material

This new system had to be created using only commercially available and registered chemicals, as this is a prerequisite for large-scale industrial applications, which are the only type of applications that will provide a payback for such material development endeavors. Several 2K PU systems are commercially available, and for these trials, ChromaLast 90 was chosen. It was developed to have a high tensile strength at a Shore A Hardness of 90, with a compression set below 30% at a temperature of 100˚C

Additive Manufacturing Software and Equipment: To create a shape using additive manufacturing, a design in the form of a CAD file has to be transformed into a machine path for the 3D printer to follow. In solid extrusion technology, commercially available slicing software such as Simplfy3D or Cura will create the tool path with the click of a button. The machine path created does not take into account the changes in viscosity and flow behavior of printing with a liquid 2-component system. Thus, next to standard slicing software, a post-processor, in this case, ChromaWare, was used to alter the tool path so that the deposited liquid could solidify into the desired shape during the printing process.

- The gaskets were printed on a 1st generation RX-AM 3500 printer from Chromatic 3D Materials equipped with a ViproDuo 5/5 printhead by Viscotec. A Sulzer Mixpac MKH 02-16S was used to combine the liquids.
- During the printing process, the print parameters were chosen, and the mixing of the two components was done within a window to allow for optimal material properties as well as inter-layer and inter-bead times that create a solid part with uniform material properties.

2.2 Experimental Setup

A series of tests were conducted to evaluate the performance of the AM-produced PU seals. These tests included:

- **Tensile Strength Test**: To measure the material's resistance to tension.
- **Compression Set Test**: To assess the seal's ability to return to its original thickness after compression.

Table 1: Mechanical Properties of ChromaLast 90

PROPERTY	MEAN	STD. DEVIATION	UNIT	STANDARD
Tensile Strength (XY)	41.4 (6012)	2.5 (361)	MPa (psi)	ASTM 648
Tensile Strength (Z)	34.6 (5020)	2.8 (410)	MPa (psi)	ASTM 648
Elongation at Break (XY)	288	8	%	ASTM 648
Elongation at Break (Z)	264	8	%	ASTM 648
Modulus at 100% Strain (XY)	10.7 (1549)	0.2 (28)	MPa (psi)	ASTM 648
Modulus at 100% Strain (Z)	10.2 (1486)	0.2 (32)	MPa (psi)	ASTM 648
Hardness	91	+/-5	Shore A	ASTM D2240

2.3 Additive Manufacturing Strategies

Alternative trials were conducted to explore the novel additive manufacturing method, testing different printing strategies and employing both 2K and 4K options. In this context, 2K refers to a single material produced by combining two components, while 4K involves using two different materials in one print, each created from two components.

Below is the list of Printing Strategies employed:

- 2 Walls: 2K Material of 90 Shore A PU
- 2 Walls + Base: 2K Material of 90 Shore A PU
- 2 Walls + Base: 4K Material of 90 Shore A Walls and 65 Shore D Base
- 1 Wall + Base: 4K Material of 90 Shore A Walls and 65 Shore D Base
- 1 Wall: 2K Material of 90 Shore A PU – Solid billet

2.3.1 2 Walls Strategy: 2K Material of 90 Shore A PU

The strategy involved printing two walls close to each other and allowing the beads to mix. However, the cross-section of the initial iterations revealed that the walls were not melding together properly. To address this, a filling extrusion (indicated by the red marker) was introduced to ensure the binding of the two walls.

The main challenge with this strategy was printing with over-dimensions to allow for machining afterward. Printing with over-dimensions required the print motions to be further apart, which meant that the beads needed to be thicker to merge properly. Increasing extrusion and speed helped with bead size, but higher speeds resulted in a less viscous extruded mixture that also did not hold its shape.

Figure 2: Cross-Section of First Iteration

To ensure the best concentricity, the print had to be done in a vase mode. Finding the optimal parameters required numerous iterations, balancing extrusion, speed, and bead thickness to achieve the desired results.

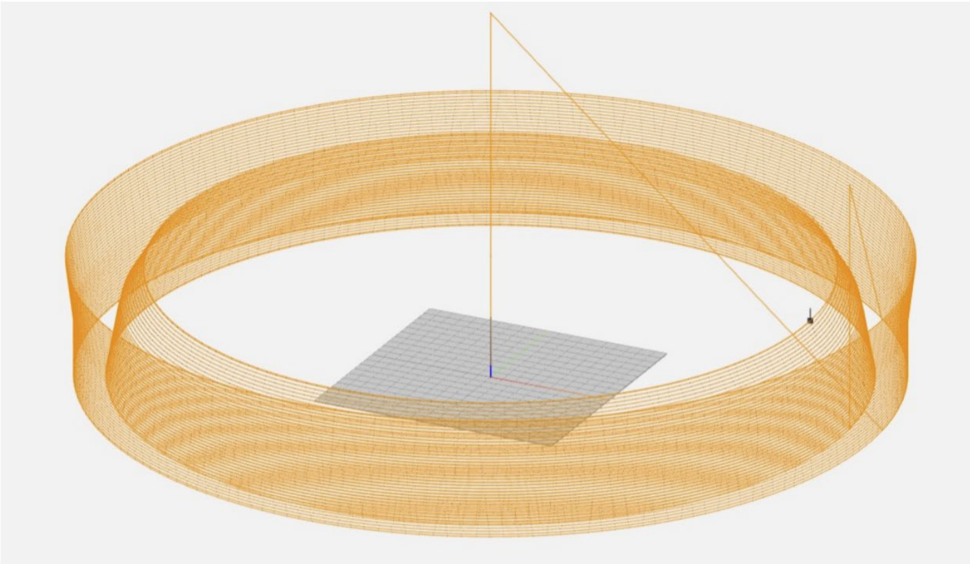

Figure 3: Printing path for 2 Wall strategy

Figure 4: Injection molded XT200 vs 2 Wall Print

2.3.2 2 Walls + Base Strategy: 2K Material of 90 Shore A PU

Printing a base increases the spread of the bead, as the surface properties of the material cause a stronger attraction to itself than to other materials. With a base, the aim is to print thicker and more homogeneous walls.

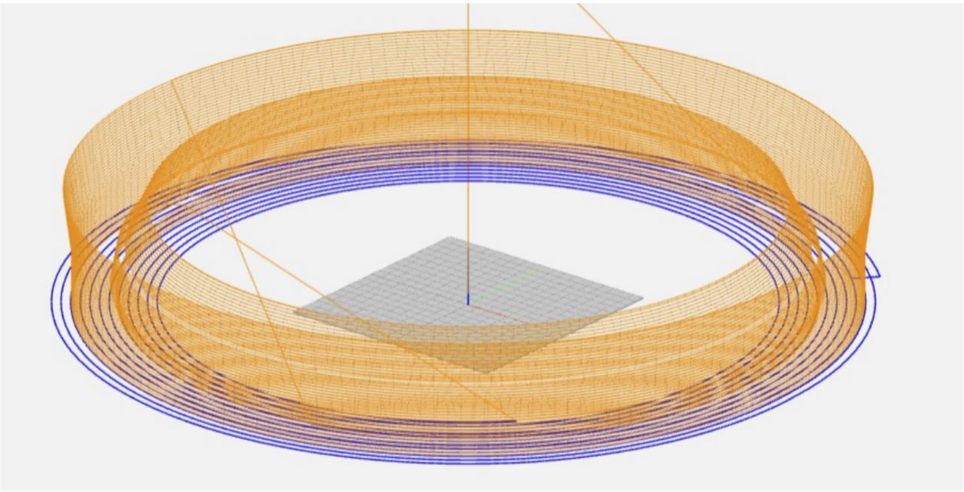

Figure 5: Printing path for 2 Walls + Base

A disc was printed to ensure a good merge at the Base of the print. Printing with more material per mm and at a faster rate increased the bead width. However, this also resulted in decreased stiffness and predictability of the material.

Figure 6: Comparison of Printed seal vs Injection Molded seal

Proper positioning of the walls, along with appropriate extrusion and speed settings, allowed for near-voidness printing. However, as the bead became saggy and easily disturbed, the shape of the cross-sections began to worsen. A suitable combination of parameters was achieved, resulting in a print with machining allowance but an irregular shape for work holding.

2.3.3 2 Walls + Base Strategy: 4K Material of 90 Shore A Walls and 65 Shore D Base

The objective of this project was to print a gasket using two different materials. Initially, the strategy involved printing the Base and the first three layers of inner and outer walls with D65 material, followed by switching to Shore A90 for the remaining walls. However, this approach resulted in a significant cavity between the walls due to the material transition. A second strategy was implemented to address this, which involved a billet-like print method. This method printed consecutive concentric circles with a smaller bead width than the wall thickness, resulting in better control and reduced voids.

Figure 7: Cavity in the base plate of 65 Shore D material

The billet-like print method improved printing by eliminating voids and providing better dimensional control. However, printing numerous layers created a rough axial surface texture, so the Base was printed oversized to compensate. Additionally, the viscous nature of the material caused the corners of the printed parts to round, requiring the Base to be printed oversized for a flatter surface. Despite these adjustments, cross-sections of the prints showed inconsistencies, with varying degrees of sagging and voids. However, samples for testing were created successfully despite the difficulties.

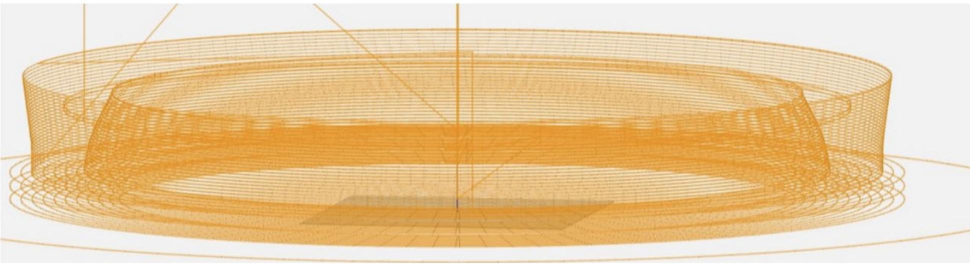

Figure 8: Printing path for 4K material

Using a base material with a Shore D hardness of 65 enabled further machining without the need for clamping rings, thanks to the high hardness of the base material. Additionally, this choice improved the extrusion resistance of the seal during high-pressure testing.

2.3.4 1 Wall + Base: 4K Material of 90 Shore A Walls and 65 Shore D Base

The strategy involved laying concentric beads from the outside to the inside to create a disc of 65 Shore D, then repeating this process to stack discs on top of each other. At a height of 3mm, the Shore A90 material was primed, and the printing continued. This method produced a raw material that could be fully machined to shape the gasket.

Figure 9: 4K material into near-net-shape billet

Cutting the billet revealed a print without voids. However, different materials have different printing properties, so using the same print parameters resulted in varying dimensions. Print speed and extrusion were adjusted for each material section to achieve the desired dimensions. To facilitate further tests of entirely shaped gaskets before developing a near net shape multi-material print and sent for machining.

2.3.5 1 Wall: 2K Material of 90 Shore A PU – Solid Billet

Another strategy we tested involved printing long billets directly to machine seals. This approach allowed us to prepare billets without the need for molds, streamlining the production process. By continuously extruding material to form elongated billets, we were able to produce a uniform and consistent raw material. This method provided greater flexibility in manufacturing and reduced the time and costs associated with mold preparation. The long billets could then be machined to the precise specifications required for high-performance seals, ensuring both efficiency and quality in the final product.

Figure 10: 2K 90 Shore A Billet

3 Results

All the samples were tested on the test rigs of Kastas Sealing Technologies R&D Test Center. Two sets of test runs will be presented on paper from the seals acquired with different print strategies.

3.1 Results of Test Group I

The first group of seals was tested for 10 km at a pressure of 50 bar, followed by another 10 km at 240 bar. The seals failed before completing the second 10 km at the higher pressure due to significant leakage. Upon disassembly, the seals exhibited excessive extrusion and a high level of deformation. These results indicate that the 90 Shore A 2K PU material, combined with the initial set of strategies, was insufficient to meet the demands of standard hydraulic applications.

Tested seals are listed below:

- Sample 1B: 2 Walls: 2K Material of 90 Shore A PU
- Sample 1A: 2 Walls + Base: 2K Material of 90 Shore A PU
- Sample 2A: 2 Walls + Base: 2K Material of 90 Shore A PU

Three samples were tested using the test parameters below in the first test group.

Table 2: Test Group I - Test Parameters

Test Parameter	1st Period	2nd Period
Pressure (Bar) :	50	240
Speed (m/s):	0,3	0,3
Target Distance (km):	10	10
Temperature (°C):	60	60
Range of Extrusion Gap (mm):	0.15	
Media:	Vg 46 Hydraulic Oil	

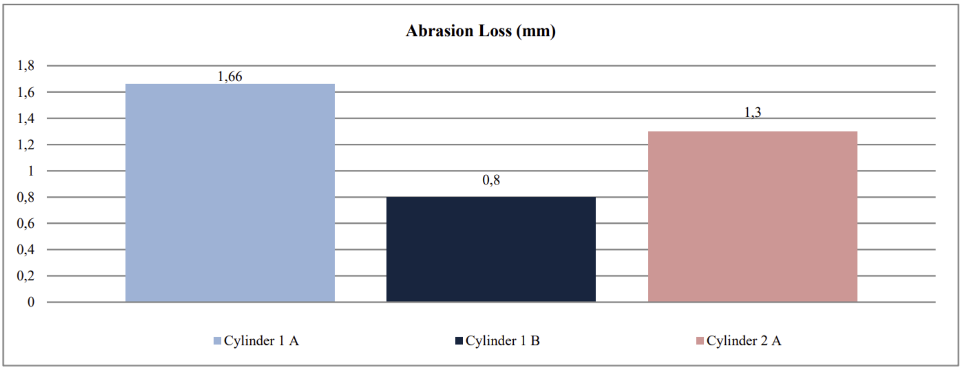

Figure 11: Abrasion loss results for Test Group 1

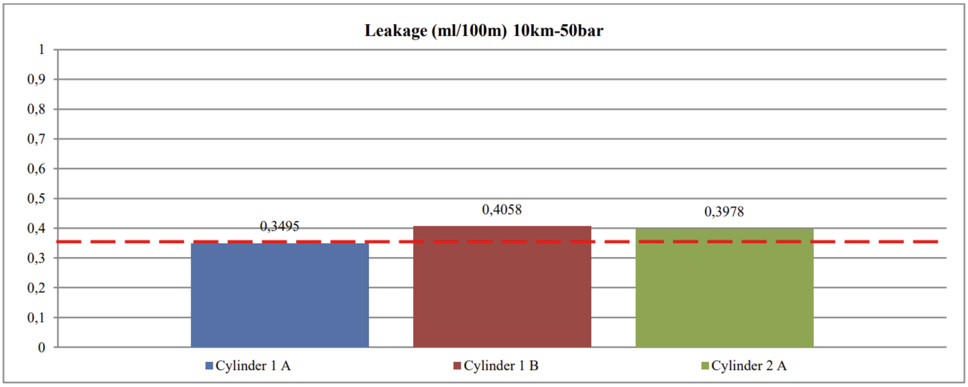

Figure 12: Leakage results for Test Group 1

Sample 1A: 2 Walls + Base: 2K Material of 90 Shore A PU

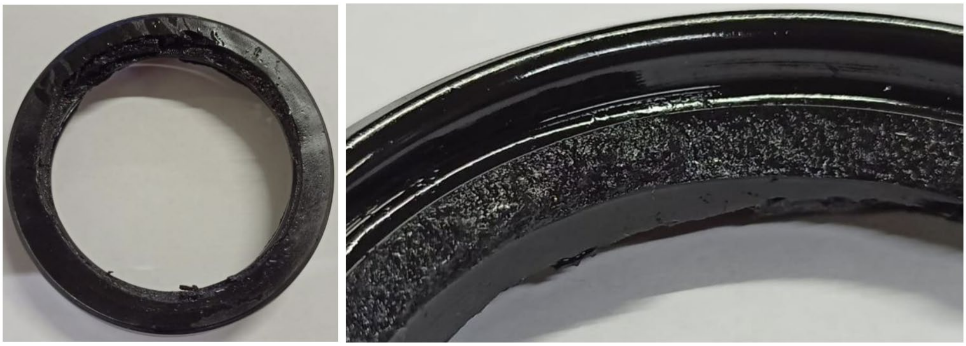

Figure 13: Sample 1A After testing

Sample 1B: 2 Walls: 2K Material of 90 Shore A PU

Figure 14: Sample 1B After Testing

Sample 2A: 2 Walls + Base: 2K Material of 90 Shore A PU

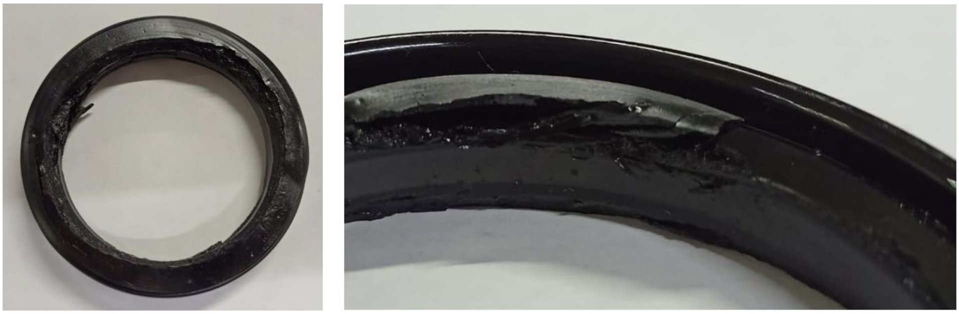

Figure 15: Sample 2A After testing

3.2 Results of Test Group II

Improved printing strategies were employed for the second set of tests, enabling higher pressure testing over a longer duration of 80 km or 220,000 cycles. The seals withstood the testing, although they exhibited higher-than-usual levels of leakage and visible extrusion, except for the 4K material with a 65 Shore D base, which performed more reliably.

Tested seals are listed below:

- Sample 2A: 2 Walls + Base: 2K Material of 90 Shore A PU
- Sample 2B: 2 Walls + Base: 4K Material of 90 Shore A and 65 Shore D PU
- Sample 3A: 1 Wall: 2K Material of 90 Shore A PU – Solid billet

Table 3: Test Group II - Test Parameters

Test Parameter	1st Period	2nd Period
Pressure (Bar) :	50	240
Speed (m/s):	0,3	0,3
Target Distance (km):	10	70
Temperature (°C):	60	60
Range of Extrusion Gap (mm):	0.15	
Media:	Vg 46 Hydraulic Oil	

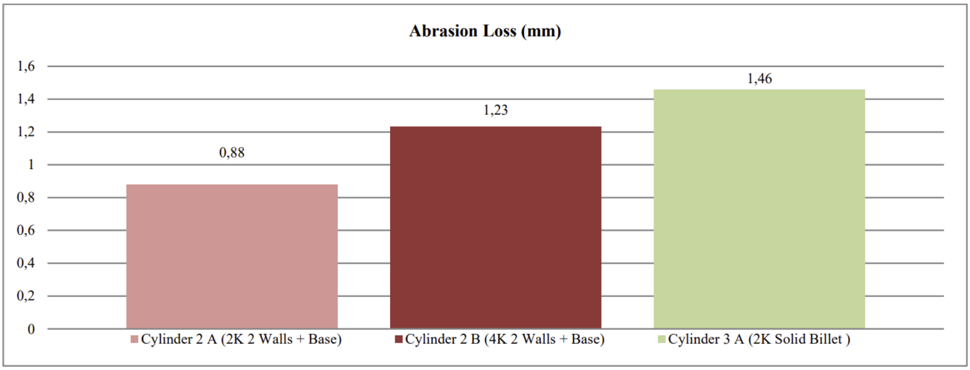

Figure 16: Test Group II – Abrasion Loss

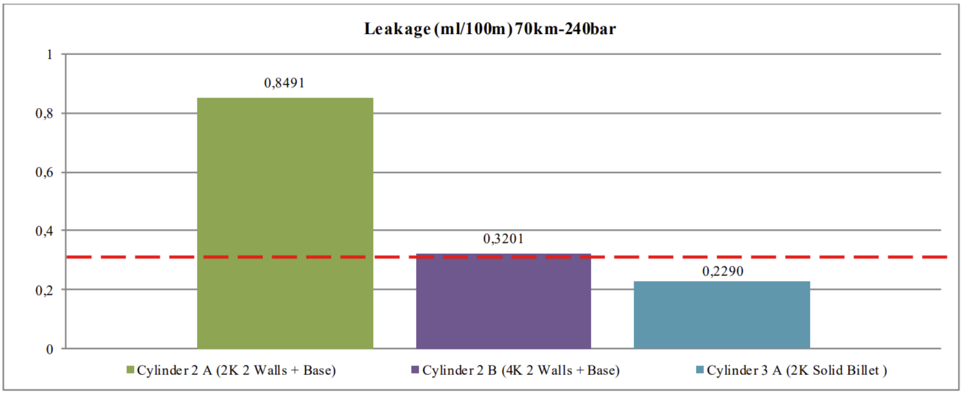

Figure 17: Test Group II – Leakage

Sample 2A: 2 Walls + Base: 2K Material of 90 Shore A PU

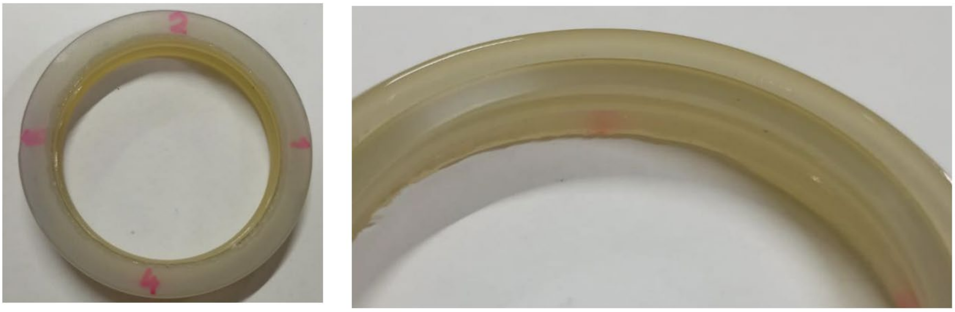

Figure 18: Sample 2A After testing

Sample 2B: 2 Walls + Base: 4K Material of 90 Shore A and 65 Shore D PU

Figure 19: Sample 2B After Testing

Sample 3A: 1 Wall: 2K Material of 90 Shore A PU – Solid billet

Figure 20: Sample 3A After testing

4 Summary and Conclusion

This study explores the innovative use of additive manufacturing (AM) technologies to produce high-performance polyurethane (PU) seals. By merging the precision of AM with the robustness of injection-molded TPU, the research aims to bridge existing manufacturing gaps and set new benchmarks for seal performance and durability. The comprehensive testing and validation results indicate that while the initial strategies using 90 Shore A 2K PU material were insufficient for standard hydraulic applications, subsequent strategies demonstrated improved outcomes.

Introducing a billet-like print method and using 4K materials with a 65 Shore D base showed significant improvements in extrusion resistance and overall seal integrity under high pressure. Despite some challenges with leakage and dimensional consistency, the refined strategies allowed for better control over the final dimensions and reduced void formation.

In conclusion, the novel AM technology presents a transformative solution for the seal manufacturing industry, offering enhanced design flexibility, material customization, and environmental sustainability. The findings underscore the potential for AM technologies to revolutionize industry standards and pave the way for innovative applications across various sectors. Further research and optimization of print parameters and material combinations are recommended to fully realize the benefits of this approach in large-scale industrial applications.

Further printing strategies should be explored to fully exploit the design freedom provided by the AM method, maximizing the potential of this technology. Future trials will include such design instances to bring additional value to the finished seals. By continuously refining and expanding these strategies, we can enhance AM-produced seals' performance, durability, and applicability, ensuring they meet and exceed industry demands.

5 References

[1] Culmone, C. (author). "3D Steering: Additive Manufacturing in Snake-Like Surgical Devices." 2022, https://doi.org/10.4233/uuid:f2b07624-8a6d-41c9-b931-2423849182a7.

6 Authors

Kastas Sealing Technologies,

Atatürk Plastik OSB 3. Street No:5 35660 Menemen / IZMIR / TURKEY:

Cem TANYERI[1], M. Sc., ORCID 0000-0002-1290-2875, ctanyeri@kastas.com

Alper KOCAMAZ[1], ORCID 0009-0000-5070-1233 akocamaz@kastas.com
Ozan DEVLEN[1] , M. Sc., ORCID 0000-0002-8079-0553, odevlen@kastas.com

Chromatic 3D Materials GmbH
Kirchstr. 18, 52538 Selfkant Germany
Barthel Engendahl, bengendahl@c3dm.com

https://doi.org/10.61319/WO3C22H8

Group B
Session 4

Test procedures

B 08

Adrian Heinl, Christian Wilbs, Daniel Frölich, Matthias Adler, Freudenberg FST GmbH, Weinheim, Germany

Performance of the radial shaft sealing system under the influence of shaft lead

B 09

Maximilian Engelfried, Matthias Baumann, Frank Bauer, University of Stuttgart, Institute of Machine Components Sealing Technology,

From Tactile to Optical - Advancements in Shaft Lead Analysis

B 10

Georg Haffner, Matthias Baumann, Frank Bauer, University of Stuttgart, Institute of Machine Components Sealing Technology, Stuttgart, Germany

Insights into the pumping behavior of sealing counterfaces using continuous logging

B 11

Takao Horiuchi, Yohei Sakai, Ayako Aoyagi, NOK corporation, Engineering Research , Fujisawa-shi, Japan

In Situ Observation of a Grease Lubricant Film on a Radial Seal by Fluorescence Induced Microscopy

Performance of the radial shaft sealing system under the influence of shaft lead

Adrian Heinl, Christian Wilbs, Daniel Frölich

1 Introduction

A tribological system fundamentally consists out of the main components: base body, counter body, intermediate substance, and surrounding medium. The applied load spectrum as well as disturbances form the input variables of the tribological system influence the tribological processes and interactions. Applied to the tribological system of a radial shaft seal (Figure 1) the following system components can be derived:

- Base body → Radial shaft seal
- Counter body → Shaft surface as counter surface
- Intermediate substance → Lubricant to be sealed

The radial shaft sealing system for example is used in gearboxes, wind turbines or robots to seal rotating components. It prevents the leakage of lubricant or the exchange of two media. During use, the operating conditions such as speed, pressure, temperature of the fluid etc. as well as the geometric installation situation influence the system components. The latter and the operating conditions are in constant interaction with each other and determine the performance and lifetime of the radial shaft sealing system. The occurrence of disturbances, such as damage or faulty system components, can lead to unfavorable operating conditions of the system, which in turn can result in poor lubrication, thermal or chemical damage to the components, high wear and ultimately leakage.

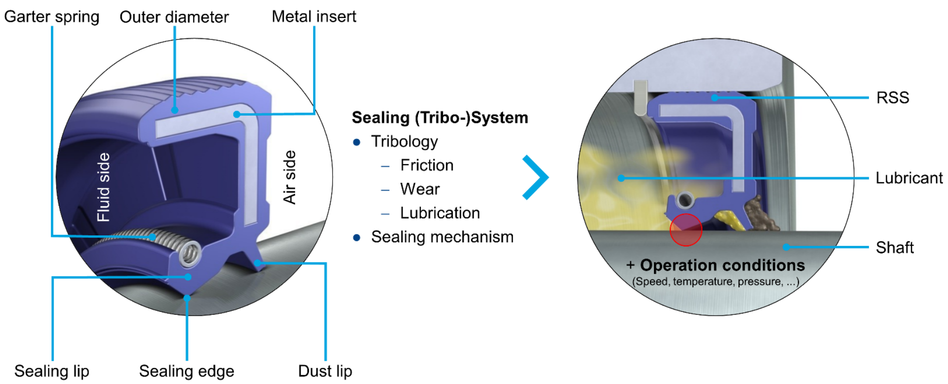

Figure 1: Radial shaft seal (left), complete tribological radial shaft sealing system (right)

In an optimally functioning system, a hydrodynamic fluid film forms between the sealing edge and the shaft surface, i.e. in the sealing gap, under dynamic load. Radial shaft seals (RSS) have a dynamic sealing mechanism that causes the sealed lubricant to be actively pumped in the axial direction, from the air side to the fluid side. This effect is partly responsible for the sealing performance of the radial shaft sealing system. The fluid pumping effect of the sealing system is not only depending on the radial shaft seal but is also significantly influenced by the shaft surface topography. Therefore, the shaft surface roughness parameters must be in an acceptable range. To ensure the performance of the sealing system, in addition to the known roughness parameters, the shaft must be free of fluid pumping structures, so-called shaft lead. Depending on the shaft lead characteristics, lead structures can create an axial pumping effect of the fluid which can lead to either in leakage or poor lubrication conditions and therefore to an increased wear of the sealing system. The effect of shaft lead on the radial shaft sealing system is shown in Figure 2.

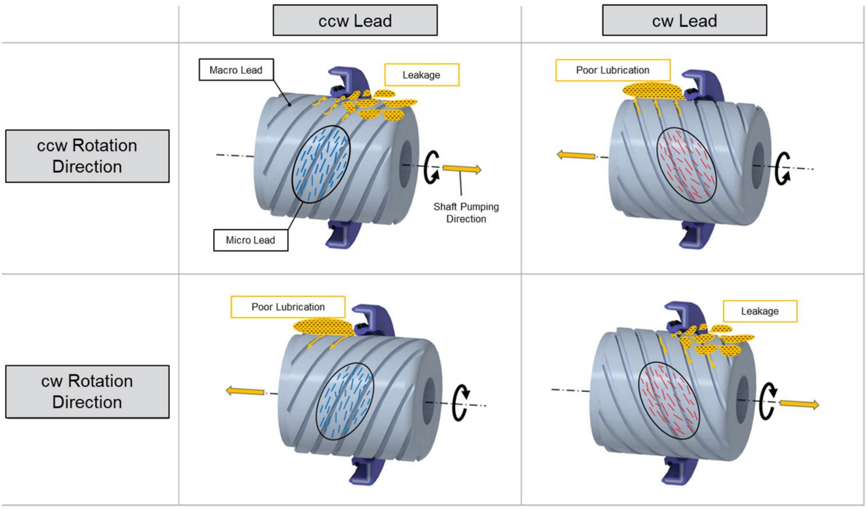

Figure 2: Influence of lead structures on the radial shaft sealing system.

Figure 2 shows how the fluid is pumped in an axial direction depending on orientation of the lead structures and the rotation direction of the shaft, and how this is superimposed on the axial pumping effect of the radial shaft seal, the fluid pumping effect of the radial shaft seal is always from the air side to the fluid side. Regarding to the superimposed fluid pumping effects, two different operating states of the sealing system can be set:

1. The pumping effect of the lead structure is from the fluid side to the air side and thus counteracts the pumping effect of the radial shaft seal. If the shaft pumping effect exceeds that of the radial shaft seal, a net pumping effect towards the air side results, which is expressed in leakage.

2. The pumping effect of the lead structure is from the air side to the fluid side and thus in the same direction as the pumping effect of the radial shaft seal. As a result, the system is subject to poor lubrication, which in turn causes increased wear of the components and increased temperature within the sealing gap.

Both operation conditions can lead to an earlier failure of the sealing system, which in turn can result in significant repair costs and extensive environmental damage.

Due to the variety of manufacturing processes and parameters to produce counter surfaces, shaft lead with different characteristics and scaling can be generated. Shaft lead can be classified into three categories [1], see Figure 3.

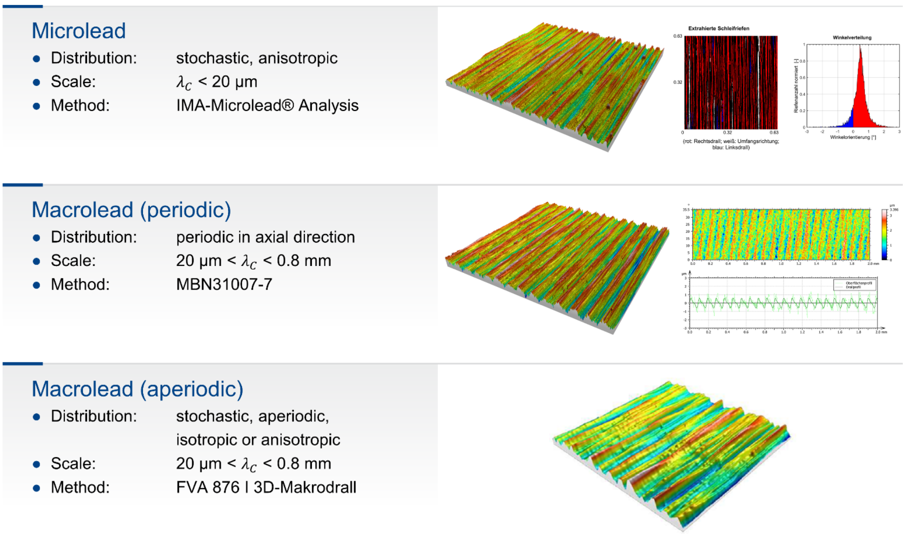

Figure 3: Shaft Lead classification [1]

The longest known characterization method is the CARMEN method according to the Daimler standard MBN31007-7 [2]. This method describes axially and circumferentially periodic lead structures in a scale range of 20 µm to 0.8 mm. The frequency-based analysis method can be used to determine characteristic macrolead parameters such as depth, angle, and period length.

Structures in the same scale range but with an aperiodic and stochastic distribution in axial and circumferential direction, are referred to as aperiodic macrolead or micro waviness [1]. The analysis and evaluation of this shaft lead is not yet available and is part of a research project of the FVA 876 I Research Association for Drive Technology [3].

Individual grooves within the scale range of < 20 µm and are distributed stochastically and anisotropic on the counter surface are referred to as microlead. The IMA-Microlead® Analysis [4] defines the measurement and evaluation of the individual grooves using an optical measurement system and a structure-based algorithm. The algorithm extracts and analysis the geometry characteristics such as angular orientation, length, depth etc. of the grooves.

These different shaft lead categories can be measured and quantified with state-of-the-art measuring and analyzing methods. Using these methods, the correlation between lead parameters and leakage resp. seal wear can be shown. The insights drawn from that analysis, will be applied to unpressurized and pressurized radial shaft sealing systems. Based on the results, limits for an acceptable shaft lead can be set to ensure a reliable sealing system.

2 Measurement methods and test conditions

Chapter 2 describes the used measurement methods and test conditions.

2.1 Shaft lead measurement

To study the performance of the radial shaft sealing system under the influence of shaft lead, plunge ground shafts with different characteristics of microlead and periodic macrolead were examined. The measurement and analysis methods will be explained in more detail in the next chapters.

2.1.1 Microlead measurement acc. IMA-Mikrodrall® Analyse

The microlead measurement uses optical surface measurement instruments to measure the surface topography. The measurement grid consists out of three axial areas and 18 areas in circumferential direction, with a step size of 20 °, around the entire circumference. The measured surface topographies are segmented and the microlead structures are extracted. The corresponding geometric characteristics such as depth, width, length, angle, and volume are then determined for each extracted structure (groove). The determined parameters are evaluated using statistical methods and characteristic distribution curves. The number of all structures and structure volumes with the same angular orientation are added and plotted against the angular orientation. If the median angle of the distribution curve deviates significantly from zero, this means that an increasing number of structures or volumes have an orientation that deviates from the circumferential direction. Figure 4 shows the measurement grid, the geometric groove characteristics, and the distribution curve.

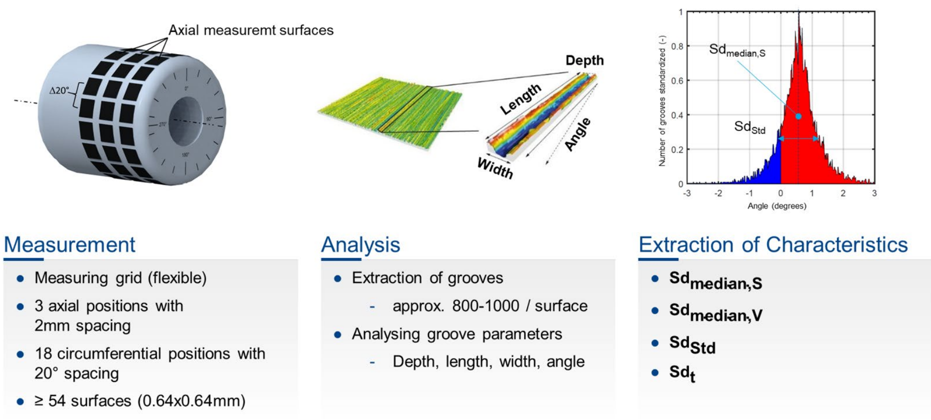

Figure 4: Microlead measurement acc. IMA-Mikrodrall® Analyse [4]

Quantitative microlead parameters can be drawn from the distribution curves by calculating the median angle of the structures $Sd_{\text{median,S}}$ and the median volumes $Sd_{\text{median,V}}$.

2.1.2 Macrolead measurement acc. MBN31007-7

For the analyze of periodic macrolead structures on the counter surface, 72 axial profiles are measured at equal intervals over two measuring grids. Measuring grid 1 extends over a circumferential range of 36 °, with an axial profile spacing of 0.5 °, and measuring grid 2 covers the entire shaft circumference of 360 °, with an axial profile spacing of 5 °. The individual axial profile plots are aligned in the circumferential and axial direction and merge to a 3D pseudo topography. This is followed by a frequency analysis to identify the dominant, periodic macrolead structure. This results in a mathematically approximated lead profile, which is used to determine the macrolead parameters lead depth Dt, lead angle $D\gamma$ and period length DP of the counter surface.

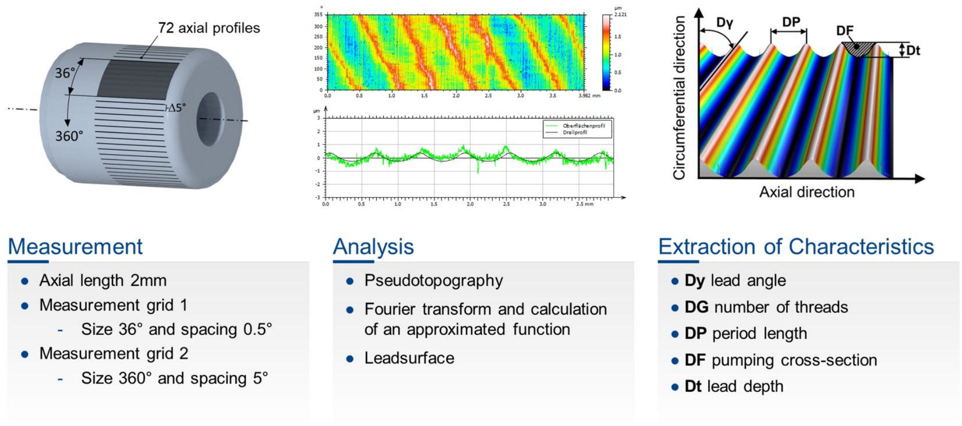

Figure 5: Macrolead measurement acc. MBN31007-7 [2]

2.2 Experimental Test conditions

Certain test conditions were defined and described in the following chapters to measure the shaft pumping rate and to investigate leakage and wear.

2.2.1 Shaft pumping rate measurement

The pumping rate of the sealing system results from the pumping rate of the radial shaft seal and the shaft surface. The pumping rate of the radial shaft seals in usually independent of the shaft rotation direction whereas the pumping rate of the shaft surface can depend on the rotation direction if a shaft lead is present. Depending on the shaft lead orientation and the shaft rotation direction the sealing system pumping rate can be higher or lower compared to a sealing system without shaft lead.

Based on this effect RAAB [5] developed a pumping rate test which make it possible to measure the pumping rate of the counter surface due to shaft lead. The test conditions to carry out the shaft pumping rate measurement are shown in Table 1.

Table 1: Test conditions for shaft pumping rate measurement

Radial Shaft Seal	BAUM3X2, 75 FKM 585
Dimension	35-52-7
Fluid	Mineral gear oil ISO VG 220
Fluid Temperature	80 °C
Shaft sliding speed	5,5 m/s
Test Cycle	1h, 1h, 2h, 2h
Rotation direction	cw, ccw, cw, ccw
Test duration	6 h

2.2.2 Leakage and seal wear tests

The determination of radial shaft sealing system failure due to shaft lead is conducted through a leakage and seal wear tests. Therefore, shafts with and without lead were used. The leakage test was performed by selecting the rotation direction to induce a shaft fluid pumping from the oil to the air side, forcing leakage of the system. The rotation direction for the seal wear tests was selected to induce a fluid pumping from the air to the fluid side, causing poor lubrication conditions and therefore increased wear. Two different sealing system were tested, which are unpressurized, see Table 2, and pressurized, see Table 3.

Table 2: Test conditions for unpressurized sealing system

Investigation	Leakage	Seal wear
Radial Shaft Seal	BAUM3X2	
Dimension	35-52-7	
Material	72 NBR 902 75 FKM 585	
Fluid	Mineral gear oil ISO VG 220	
Fluid Temperature	80 °C	
Shaft sliding speed	5.5 m/s	
Test duration	96 h	504 h
Rotation direction	cw or ccw	

Table 3: Test conditions for pressurized sealing system

Investigation	Leakage	Seal wear
Radial Shaft Seal	BAB, PPS	
Dimension	60-80-7	
Material	75 FKM 595	
Fluid	Hydraulic oil ISO VG 68	
Fluid Temperature	80 °C	
Shaft sliding speed	5.5 m/s	
Pressure	0 bar, 1.5 bar	
Test duration	96 h	240 h
Rotation direction	cw or ccw	

3 Experimental results

The experimental results of the shaft pumping rate measurements as well as the leakage and seal wear tests are shown in the following chapter.

3.1 Results of the shaft pumping rate measurement

In [6] SCHIEFER showed that the influence of periodic macrolead on the fluid pumping rate can be predominantly characterized by the parameters lead depth Dt, lead angle $D\gamma$ and period length DP. The hypothesis which has been formulated is supported by the experimental results of this investigation and state:

1. With an increasing lead depth, the shaft pumping rate increases as well, due to a higher possible pumping volume (Figure 6, A).
2. With an increasing lead angle, the fluid pumping rate increases too, as there are steeper threads for redirecting the fluid below the sealing edge (Figure 6, B).
3. The shaft pumping rate is increasing with decreasing periodic length because there are more lead threads within the sealing contact (Figure 6, C).

The results of the shaft pumping rate measurement are shown in Figure 6. In diagrams the x-axis shows the macrolead parameters and the y-axis the shaft pumping rate PR_{shaft}. Even though, the results show a certain variation the overall trend as described before is obvious.

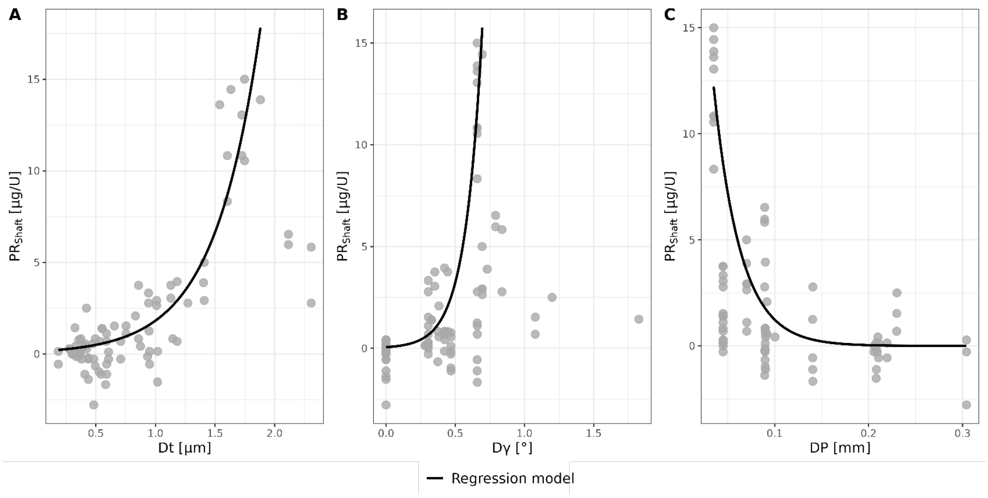

Figure 6: Shaft pumping rate depending on the periodic macrolead parameters

Based on the hypothesis and empirical results, a combination parameter was defined from the three parameters [6]. The combination parameter Km is defined by the following equation:

$$Km = \left|\frac{Dt \ \cdot D\gamma}{DP}\right| \quad (1)$$

Finally, the shaft pumping rate PR_{shaft} shows a significant linear correlation with the combination parameter Km, see Figure 7.

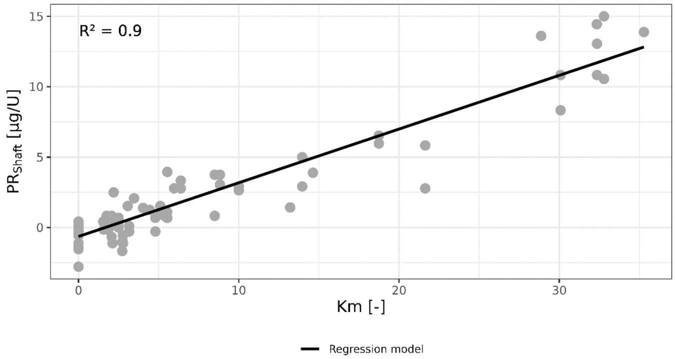

Figure 7: Shaft pumping rate depending on the macrolead combination parameter Km

Microlead shows the same linear correlation as periodic macrolead, but it depends mainly on the microlead parameter $Sd_{\mathrm{median,S}}$, see Figure 8.

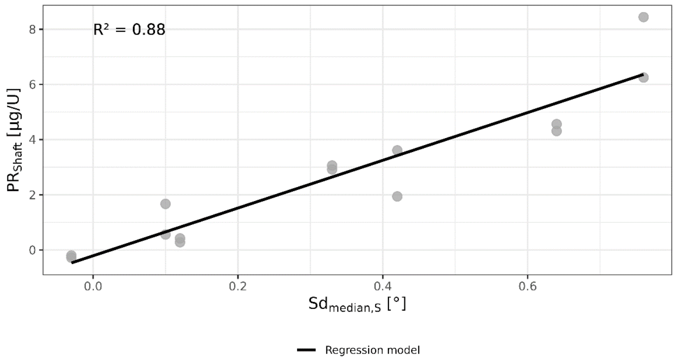

Figure 8: Shaft pumping rate depending on median angle of microlead structures

The shaft pumping rate analysis shows that the lead parameters Km, for periodic macrolead, and $Sd_{\mathrm{median,S}}$, for microlead, provide significant information to characterize and evaluate shaft lead.

3.2 Leakage and seal wear results of the unpressurized sealing system

The following chapter investigates the influence of shaft lead on an unpressurized sealing system. Figure 9 shows the observed leakage rate LR in diagram A and the seal wear band width in diagram B depending on the periodic macrolead characteristics in form of the combination parameter Km. The leakage rate shows an exponential increase with increasing lead characteristic. Concurrently, a noticeable linear increase in the seal wear band width is observed with the increase in macrolead characteristic. The results indicate that periodic macrolead with a Km value greater than 10 affect the analyzed sealing system.

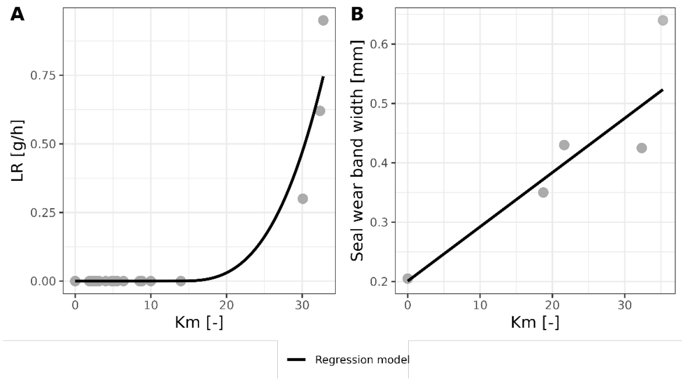

Figure 9: Influence of periodic macrolead structures on unpressurized sealing system

Figure 10 shows the influence of microlead structures on the unpressurized sealing system. Diagram A and B illustrate the relationship between the median angle of the structure distribution $Sd_{\text{median,S}}$ and the leakage rate as well as the seal wear band width. Notably, a median angle of $Sd_{\text{median,S}} > 0.1$ ° results in a significant increase in the seal wear band width. Leakage becomes evident only at a median angle of approximately $Sd_{\text{median,S}} \approx 0.3$ °.

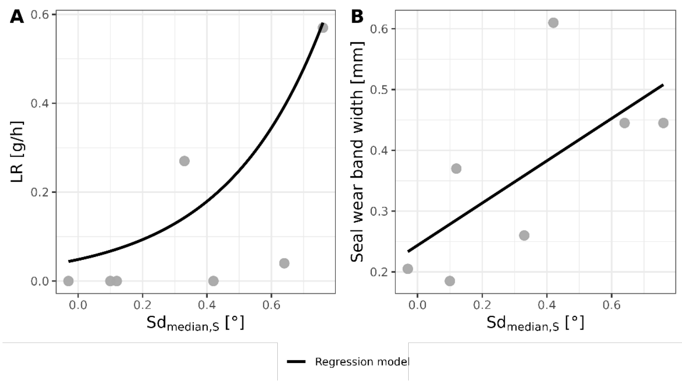

Figure 10: Influence of microlead structures on unpressurized sealing system

3.3 Leakage and seal wear results of the pressurized sealing system

The effects of shaft lead on a pressurized sealing system are shown in the following chapter. Figure 11 shows the correlation between the median angle $Sd_{\mathrm{median,S}}$ and the seal wear as well as the leakage rate of the pressure seals, BAB and PPS, under varying pressure conditions of $0\ bar$ and $1.5\ bar$. The correlation between the median angle (x-axis) and the leakage rate (y-axis) are shown in diagram A. The data indicates that the leakage rate increases exponential with the median angle and elevated pressure levels. Specifically, the unpressurized PPS leaked at a microlead of $Sd_{\mathrm{median,S}} \approx 0.04\,°$. When pressurized, the PPS started leaking at median angle of $Sd_{\mathrm{median,S}} \approx 0.06\,°$. The PPS shows under pressurized operation conditions a higher performance then unpressurized.

Figure 11, diagram A, shows the relationship between the microlead characteristic and seal wear band width. The data show a consistent linear increase in seal wear corresponding to increasing median angles across all tested systems.

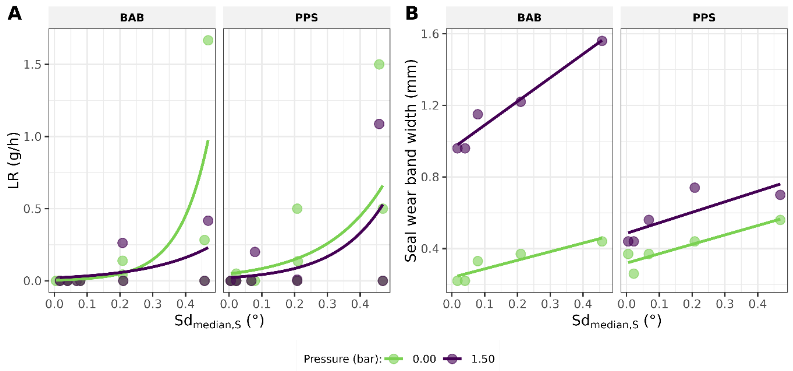

Figure 11: Influence of microlead on a pressurized sealing system

The influence of periodic macrolead on the pressurized sealing system is shown in Figure 12. The leakage test results show slight variations compared to test results with microlead shafts. An increase in the leakage rate with increasing macrolead characteristics is evident for both pressure seals, but this effect is only observable under pressurized conditions. This effect may be attributed to the wider sealing contact induced by pressurize, which increases the number of lead threads within sealing contact and thus can caused a higher fluid pumping of the shaft than that of the seal. The PPS seals leaked at a macrolead characteristic of $Km \approx 2$, whereas the sealing system with the BAB failed at $Km \approx 6$.

Both pressurized and non-pressurized seals show a linear increase in seal wear band width with an increasing macrolead characteristic, shown in diagram B of Figure 12.

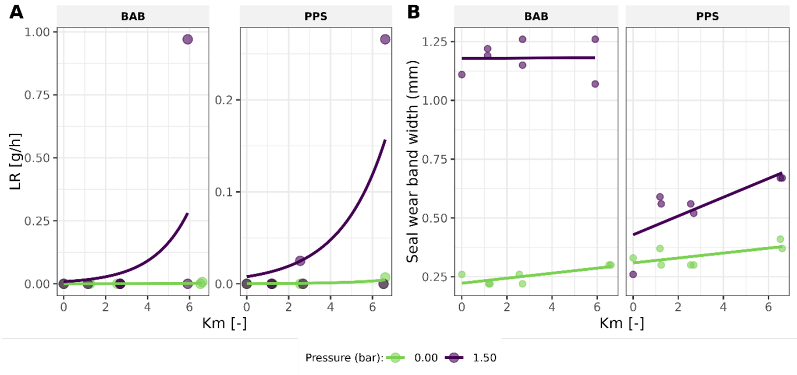

Figure 12: Influence of periodic macrolead on a pressurized sealing system

4 Summary and Conclusion

The performance of a radial shaft sealing system is dependent on the shaft surface. In particular, the sealing system can be disturbed by shaft lead due to the fluid pumping effect. This paper examines the fluid pumping effect of period macrolead as well as microlead, measuring their influence on an unpressurized and pressurized sealing system.

The shaft pumping rate measurement for periodic macrolead indicates that the parameters lead depth Dt, lead angle $D\gamma$ and period length DP significantly influence the shaft pumping effect. This is further corroborated by the combination parameter Km, which shows a significant linear correlation with the shaft pumping rate. Comparable linear relationship was shown by the median angle of microlead structures $Sd_{\mathrm{median,S}}$. These results suggest that both macrolead and microlead parameters can be used to predict shaft pumping rates and assess the performance of radial shaft sealing systems.

Additionally, leakage and seal wear tests in both unpressurized and pressurized sealing systems show a consistent increase in leakage rate and seal wear band width as a function of periodic macrolead and microlead. Microlead with a median angular distribution of approximately $Sd_{\mathrm{median,S}} \approx 0.04\,°$ have been shown to significantly impact on the analyzed radial shaft sealing systems. Regarding to the periodic macrolead, a combination parameter of $Km \approx 2$ has already been shown to be an unsuitable value for a sealing system.

The test results indicates that the influence of the shaft lead depends on the respective radial shaft sealing system with its components and the operating conditions. Further research is needed to determine how variables such as rotation speed, lubricant viscosity or shaft diameter impact the shaft pumping effect thus and, consequently, the overall performance of the sealing system.

5 Nomenclature

Variable	***Description***	***Unit***
λ_c	Gaussian filter	[µm]
Dt	Lead depth	[µm]
DP	Period length	[mm]
$D\gamma$	Lead angle	[°]
DG	Number of threads	[-]
DF	Pumping cross-section	[µm²]
Km	Combination parameter	[-]
$Sd_{\mathrm{median,S}}$	Median angle of the angular structure distribution	[°]
$Sd_{\mathrm{median,v}}$	Median angle of the angular volume distribution	[°]
Sd_{Sdt}	Standard deviation of the angular orientations	[°]
Sd_{t}	Arithmetically averaged structure depths	[µm]
PR_{shaft}	Fluid pumping rate of the shaft	[µg/U]
LR	Leakage rate	[g/h]

6 References

[1] Baumann, M. *Abdichtung drallbehafteter Dichtungsgegenlaufflächen - Messung, Analyse, Bewertung und Grenzen.* Dissertation, Universität Stuttgart: Institut für Maschinenelemente, 2017.

[2] Daimler AG. Teschnische Norm. MBN 31 007-7: *Oberflächenbeschaffenheit. Mess- und Auswerteverfahren zur Bewertung von drallreduzierten dynamischen Dichtflächen.* 2009.

[3] FVA 876 I – 3D-Makrodrall. Research Association for Drive Technology. ger.: Forschungsvereinigung Antriebstechnik e.V.

[4] IMA-Mikrodrall® Analyse. IMA-TechSheet #104140 V1. Universität Stuttgart: Institut für Maschinenelemente.

[5] Raab, H. *Wellenlaufflächen. Einfluss der Wellenlaufflächen auf das Dichtverhalten von Radial-Wellendichtringen.* FKM-Vorhaben. Nr. 211. Universität Stuttgart: Institut für Maschinenelemente. 1998.

[6] Schiefer, F. and Baumann, M. und Bauer, F. *Untersuchung des Förderverhaltens makro-drallbehafteter Dichtungsgegenlaufflächen.* Essen, VDMA Fluidtechnik, 2018. ISBN 978-3-8163-0727.

7 Authors

Freudenberg FST GmbH, Engineering Services

Höhnerweg 2-4, 69469 Weinheim, Germany:

Adrian Heinl, M. Sc., Adrian.Heinl@fst.com

Christian Wilbs, M. Sc., Christian.Wilbs@fst.com

Dr.-Ing. Daniel Frölich, Daniel.Froelich@fst.com

https://doi.org/10.61319/XFODFK5S

From Tactile to Optical - Advancements in Shaft Lead Analysis

Maximilian Engelfried, Matthias Baumann, Frank Bauer

Tactile measuring instruments were used for a long time to measure surface characteristics of sealing counterfaces and are still state of the art today throughout the industry. The data measured are roughness profiles mostly in the axial direction of the shaft. Rapid developments in computer hardware and software have improved optical measurement technology, advancing its application in the analysis of sealing counterfaces. The measurement data are topographies that represent partial areas of the shaft with high resolution in both the axial and circumferential direction. These characteristics are especially useful for the analysis of shaft lead. Lead describes all types of structural features on the shaft surface that axially pump oil in sealing contact during operation. Their pumping effect influences the sealing mechanism depending on the direction of rotation of the shaft and can result in leakage. Lead structures appear in various forms and sizes – micro and macro lead, which are superimposed on the shaft surface. Optical measurements enable the detection of the superimposed structures with a single measurement run. Specially developed segmentation algorithms can be used to separate micro and macro lead and then identify flow channel-like structures as individual elements in surface topographies. The statistical analysis of the segmentation results offers an objective characterization of the sealing counterface. This article presents the benefits of utilizing optical measurement techniques in conjunction with innovative structure-based analysis approaches for lead on shaft counterfaces. The outcome can improve the reliability of sealing systems and associated products.

1 Introduction

Rotary shaft seals, as outlined in [1, 2], prevent fluid leakage from openings in housings through which rotating shafts emerge. Figure 1 illustrates the tribological system “rotary shaft sealing”, consisting of the three main components: the rotary shaft seal (green), the shaft with the sealing counterface (red) and the fluid to be sealed (yellow). Special feature of rotary shaft sealings is the formation of an active sealing mechanism of the rotary shaft seal during operation. In a properly functioning sealing system, the sealing edge floats on a film of fluid, usually an oil for lubricating the machine components in the housing. However, the fluid does not leak through the sealing gap because the rotary shaft seal pumps it back [3]. This phenomenon is based on several operation principles, primarily explained by the distortion principle of the sealing edge. In this context, wear structures on the sealing edge deflect tangentially dragged fluid in the axial direction from its side with the smaller flank angle β to the side with the larger flank angle α [4]. On the one hand, the formation of these hydrodynamically active wear structures is based on the asymmetrical pressure distribution in the sealing contact between the sealing edge and the shaft surface, coupled with the properties of its elastomeric material. On the other hand, the surface properties of the shaft, which is the sealing counterface, are of particular importance in this context.

In literature [5] and standards [6, 7], plunge grinding is typically regarded as the optimal manufacturing method for imparting the desired surface properties to the sealing counterface. However, the grinding process is very complex and requires very precisely set parameters, which are often difficult to monitor. This may result in the unintentional manufacture of sealing counterfaces with surface properties that impair the functionality of the sealing mechanism [8, 9]. Therefore, the surface properties of sealing counterfaces must be measured, tolerated and controlled.

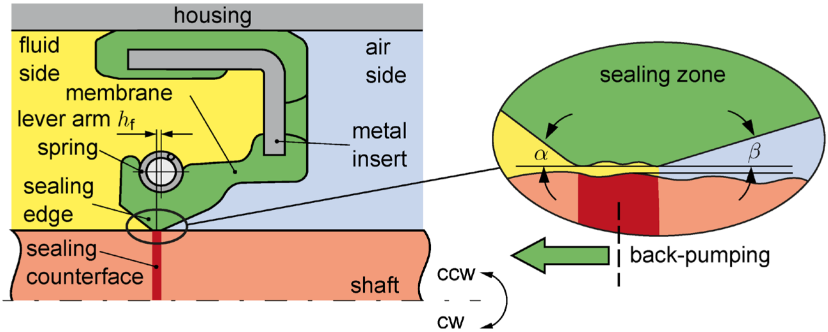

Figure 1: Rotary shaft sealing system

Surface roughness affects the wear of the elastomer sealing edge and the friction in the sealing contact, which in turn affects the sealing gap temperature [10, 11]. But, a certain roughness of the sealing surface is necessary to create the hydrodynamically active wear structures on the sealing edge. Without their formation, there is no lubricating film build-up and no back-pumping effect [12, 13]. Empirical experience led to the specification of a tolerance range of 2D roughness in axial direction of the shaft with lower and upper limit, specified in various standards [1, 2, 6, 7]. The 2D roughness is measured with a tactile measuring device using the profile method according to DIN EN ISO 4287 [14]. The DIN EN ISO 25178 [15] series of standards introduced 3D parameters to describe surface roughness, based on optically measured high-resolution topography measurement data. However, their use in the industry is not yet widespread and tactile measurement technology is still the established method for the measurement of surface roughness. The reasons are the lack of experience in the evaluation of optical measurement data and the lack of availability of the measurement technology in companies. The assessment of surface roughness alone, regardless of whether it is measured and determined in two or three dimensions, is not sufficient to provide a comprehensive description and evaluation of the sealing counterface.

In the early history of the rotary shaft seal, it was already observed that structures can be present on ground shaft surfaces that create themselves an axial pumping effect in the sealing gap during operation [16].The structures are depressions in the shaft surface that deviate in their orientations from the circumferential direction. They act as flow channels when the shaft rotates. In simple terms, the mechanism works like a screw pump, as shown in Figure 2. The term "shaft lead" is established in sealing technology to describe this type of structural elements. Leakage and dry run caused by insufficient lubrication may occur depending on the orientation of lead in combination with the direction of shaft rotation. A distinction of lead is drawn between the coarse and fine structures of lead, which can be superimposed on the ground shaft surface. The Mercedes-Benz Standard (MBN) 31007-7 [17] establishes the terms micro lead and macro lead for these structures on different geometric size levels.

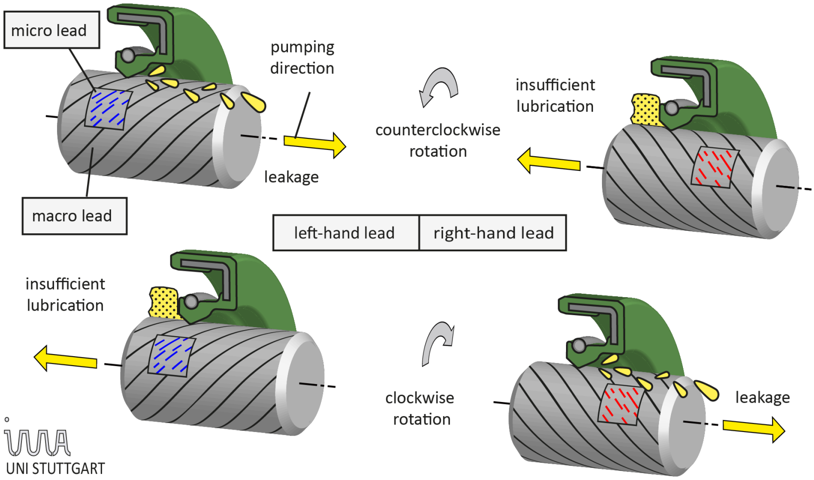

Figure 2: Influence of shaft lead

Micro lead comprises stochastically distributed grinding grooves, which are formed by the engagement of individual abrasive grains on the grinding wheel. These grooves are anisotropic and show a preferred orientation. If this preferred orientation deviates from the circumferential direction of the shaft, axial pumping of fluid is performed. Due to their small size, with widths of approximately 15 µm, micro lead structures can only be detected geometrically using high-resolution optical topography metrology. A structure-based approach for the evaluation of micro lead was developed within the scope of the research of various individuals and research projects [18–23]. In this context, grinding grooves are localized as individual structural elements and statistically evaluated as a whole.

The manufacturing process of macro lead differs from that of micro lead. Grinding wheels are dressed before use and have a helix on the surface. The macroscopic structure of the sealing counterface results from the repetitive transfer of this grinding wheel contour onto the shaft surface. An unfavorable combination of certain grinding and dressing parameters can result in the formation of periodic structures circulating around the shaft, known as macro lead [24]. MBN 31007-7 [17] presents a measurement and evaluation method for the evaluation of macro lead. The measurement strategy provides for several axial profile measurements to be measured at equidistant intervals in the circumferential direction on the shaft. The evaluation process approximates the shaft surface as a kind of screw thread, based on the dominant frequencies as a result of frequency analysis [25]. The lead parameters according to MBN 31007-7 include, among others, the period length *DP*, the lead angle *Dγ* and the lead depth *Dt* to describe macro lead. Its functional principle limits the MBN method to strongly periodic and circumferential structures.

However, research over the past decade has shown that aperiodic structures on ground sealing counterface with structure widths in the order of the periodic lengths of macro lead also have a fluid pumping effect [20, 21]. As part of the FVA funded project “3D Makrodrall” [26], a methodology for measuring and analyzing periodic and aperiodic macro lead structures was developed. It uses a different strategy than the structure-based micro lead analysis, but also follows the approach of separating relevant structures on the surface topography as individual elements. The ability to detect structures with a variety of geometries places higher demands on the lateral resolution and quantity of measurement data than the MBN method. Therefore, only area-measuring optical measuring methods are suitable.

In summary, lead on sealing counterfaces for rotary shaft seals can be classified according to Figure 3. Surface imperfections are included for the comprehensive lead categorization, as e.g. scratches or rust can pump fluid in axis direction. Structures of this type of lead are usually caused by incorrect handling and occur individually on the surface. It is possible to metrologically detect surface imperfections randomly, specifically, or by measuring the entire surface. However, as they are mainly visible to the unaided eye, a visual inspection is more efficient and recommended.

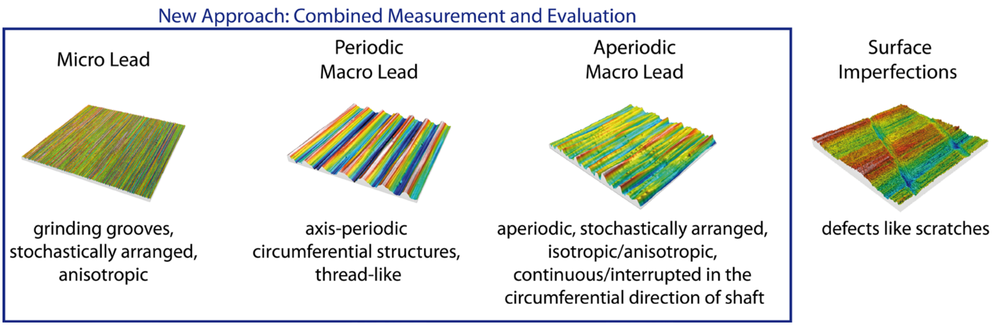

Figure 3: Classification of lead on sealing counterfaces for rotary shaft seals

The focus of metrological detection is therefore on the manufacturing-related lead categories “micro lead”, “periodic macro lead” and “aperiodic macro lead”. The measurement of all three lead categories represents an effort, as they are currently measured in different measurement sequences, even on different measuring devices. This is time-consuming and not economical in industrial applications. Nevertheless, the use of optical measurement data provides the basis for a comprehensive evaluation of all the aforementioned lead categories. In addition, the surface roughness can also be determined on the basis of the topographical data provided. The 3D parameters provide a variety of options here. This article presents a novel approach for measuring sealing counterfaces with respect to lead. The methodology presented comprises a single measurement run and thus enables the data to be analyzed in a single pass. The resulting time advantage and simplified handling represent a significant step towards the industrial applicability of lead measurement.

2 Methods

The following methods are applied to the optical measurement data to analyze micro lead and periodic and aperiodic macro lead of the sealing counter face.

2.1 IMA-Micro Lead Analysis

The IMA micro lead analysis as a measurement and evaluation method for micro lead was developed through the work of several researchers and as part of several funded projects [18–23]. This has led to the development of a commercially available method [27]. The localization of micro lead as individual grinding grooves on high-resolution optically measured topography and their description proceed as illustrated in Figure 4. After the form removal of the cylindrical shaft shape, the high-frequency structural elements of the topography are separated and localized using segmentation algorithms. The segmentation produces a binary image where micro lead structures are distinguished from the background as individual elements. This information is then used to determine lateral and volumetric geometric properties of each individual structural element based on the topographical data.

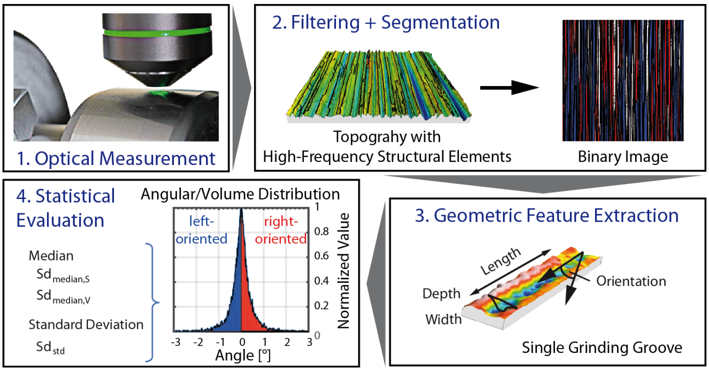

Figure 4: Schematic sequence of the micro lead analysis

The preferred orientation of the abrasive grooves is of particular importance, which is determined by a statistical evaluation of the individual structure orientations. The angular positions of the grinding grooves are normally distributed due to the nature of their formation. This is shown by angular distribution curves, which represent the number of all grinding grooves oriented in a certain angular position. The preferred orientation of the grinding grooves is indicated by the median value $Sd_{median,S}$ of the angular distribution. The distribution width is described by the standard deviation Sd_{std}. Even a slight deviation of the median value $Sd_{median,S}$ from the circumferential direction (0° position) results in a pumping effect of the grinding grooves. In this case, the sealing counterface is micro lead affected.

In order to obtain reliable results, it is necessary to capture a sufficient number of grinding grooves and to examine different positions on the shaft surface. The high level of precision required for the calculation of the angle $Sd_{median,S}$ also requires a precise and user-independent alignment of the shaft within the measuring device. A clamping error of the shaft in the jaw chuck can result in a wobbling movement while rotating. This phenomenon causes circumference-dependent angular misalignments of the shaft axis, which are transferred to the measured grinding groove angles at the respective circumferential position. Incorrectly calculated values of $Sd_{median,S}$ are the result. However, the wobble of the shaft can be identified, quantified, and compensated for with the use of a specific measuring grid and a cylinder-fitting algorithm developed for this purpose. The measuring grid comprises several measurements on the shaft circumference and along the axis.

2.2 3D Macro Lead Analysis

A methodology for the measurement and analysis of macro lead using optical measurement instruments was developed within the FVA-funded project "3D-Makrodrall" [26]. The methodology follows a structure-based approach, with the sequence of operations shown in Figure 5.

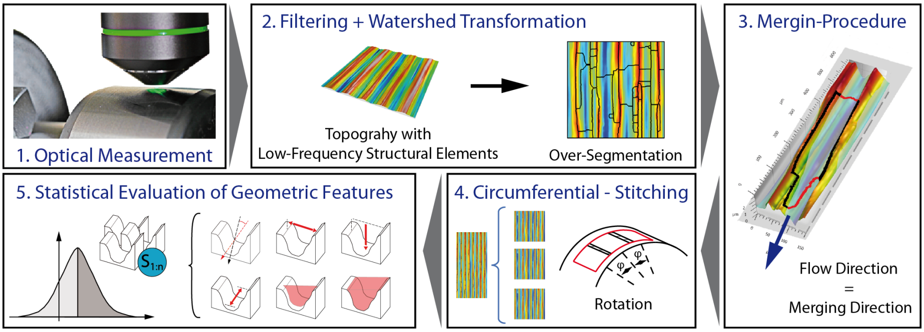

Figure 5: Schematic sequence of the 3D macro lead analysis

In the first step after measurement, the segmentation method "Watershed Transformation" according to DIN EN ISO 25178-2 [15] is applied to the form-removed, low-pass filtered surface topography. In this application, the watershed transformation segments the surface topography into dale-like features. However, the segmentation result is initially over-segmented. Over-segmentation means that the result includes many insignificant features that are only part of relevant structures. Therefore, the over-segmented features must be subsequently merged into evaluation-relevant structures. The merging procedure involves tracing the flow paths of an imaginary fluid that passes through the topography in the circumferential direction. Subsequently, the neighboring over-segmented features are iteratively merged along the flow paths into superior structures.

In order to determine certain structural features, such as the characteristic of a circumferential continuous course or the angular position of the structure, sufficiently large measuring field sizes in the circumferential direction are required. This is achieved by measuring overlapping measuring fields on the shaft surface, whereby the overlapping area is achieved by rotating the shaft. The individual topographies are circumferentially stitched to a large topography based on overlapping structural courses. The stitching itself is also included in the evaluation algorithms.

Subsequently, the shapes of the structures are described in terms of geometric property classes, such as the structure width, depth, and angle with respect to the circumferential direction. This is followed by a statistical evaluation of the values of all structures detected for each geometric property class. The mean value and standard deviation are representative parameters for describing the average structure and dispersion. Furthermore, distribution curves can be derived to illustrate certain characteristics.

It is necessary to examine a number of positions on the shaft surface to obtain statistically reliable results. By distributing the measurement fields around the circumference and in the direction of the shaft, it is possible to compensate for wobble. A special feature of the measurement grid of the 3D macro lead analysis is that overlapping measurement fields must be recorded for each measurement position.

3 Results

A novel procedure for the measurement of all manufacturing-related categories of lead on the sealing counterface was developed with the objective of eliminating the need for multiple measurement sequences or even device changes. First, the combined lead measurement procedure is explained through the use of a special measuring grid on the shaft surface. Subsequently, exemplary results from the combined lead measurement of two different shafts are presented. A confocal measurement instrument and a white light interferometer were used for the measurements. Finally, the suitability of both measurement methods is demonstrated by comparing the results of one of the shafts measured on both devices.

3.1 Procedure for Combined Lead Measurement

The measurement of the combined lead analysis requires an optical topography measurement instrument with a motorized axis of rotation and a motorized axis in the direction of the shaft axis, enabling it to move at various shaft positions. The following presented measurement grid is the result of a systematic measurement grid analysis. A comprehensive measurement grid comprising 180 individual measuring fields at various positions on the shaft surface was subjected to a continuous reduction process. The resulting impacts of measurement field reductions on the accuracy of the lead analysis results were evaluated. Detailed excerpts of this study can be found in [26]. Figure 6 shows a schematic illustration of the final measuring grid, comprising 54 individual measuring fields.

The grid consists of two axial measuring positions at a distance of $\Delta X = 4$ mm each, which are distributed over nine positions on the shaft circumference at $\Delta\Phi = 40°$ intervals. At each of the 18 positions, three overlapping measurements are measured by rotating the shaft by the angle $\Delta\varphi$. This is required for the topography stitching in the circumferential direction for the 3D macro lead analysis. The overlap angle $\Delta\varphi$ is dependent on the shaft diameter and measuring field size. The area of the overlap should be approximately 10% of the total area of the measurement field. For the micro lead analysis, it is sufficient to consider one measuring field per measuring position. A clamping error of the shaft is compensated using all measuring fields as individual ones.

The length *l* and width *w* of the measuring field may vary depending on the measuring device and the lens used. However, they must have a minimum size of 1 mm. The minimum length of the stitched topography must be at least $l_{stit} \geq 3$ mm.

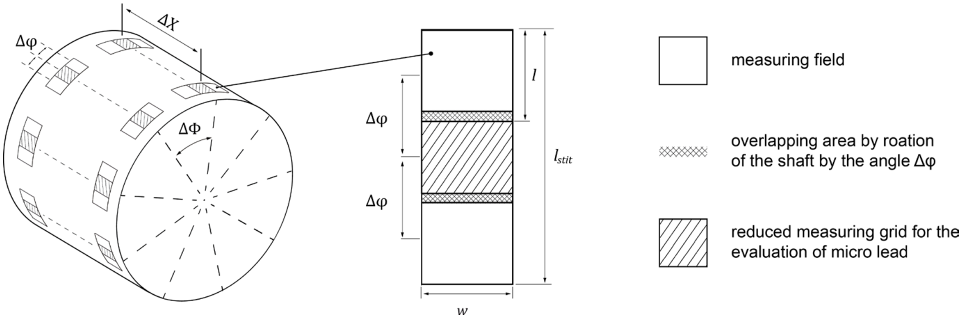

Figure 6: Measuring grid for the combined optical lead measurement

A confocal measurement instrument (CF) from Confovis [28] and a white light interferometer (WL) NPFLEX-LA from Bruker [29] were used in the following investigations. The measuring time for the measuring grid with the confocal measurement instrument is approximately 50 minutes. The combined lead measurement takes about 8 minutes with the white light interferometer. In comparison, the two previously required measurement sequences for the IMA micro lead analysis and the macro lead measurement according to MBN 31007-7 collectively averaged about 75 min for CF and 68 min for WL. Table 1 compares the composition of the measurement times. The profile measurements for the MBN method can generally be measured with both optical measuring instruments. However, the majority of the measurement data remains unused, as only one profile of a topography per circumferential position is evaluated. Apart from the fact that both measurement sequences can be carried out with a single device, there is also no advantage in terms of measurement time of the macro lead measurement according to MBN 31007-7 compared to tactile measurement.

Table 1: Comparison of measurement times

	Previously: Sequential Measurement			**Novel Approach: Combined Measurement**
	IMA Micro Lead Analysis	Macro Lead MBN 31007-7	Total	IMA Micro Lead Analysis + 3D Macro Lead Analysis
CF	~15 min	~60 min	~75 min	~50 min
WL	~8 min	~60 min	~68 min	~8 min
Tactile	/	~60 min	/	/

3.2 Exemplary Results

The following section presents results of the combined lead analysis of two investigated shafts. Shaft (a) shows macro lead on the sealing counterface, while micro lead is not present. The sealing counterface of shaft (b) is affected by a macro lead, which is additionally superimposed by a micro lead. The results of the combined lead analysis for shaft (a) are presented in Figure 7, those for shaft (b) in Figure 8. The figures are structured as follows: the results of the IMA micro lead analysis are shown in the upper part of the figures, including the angular and volume distributions, as well as an exemplary binary image with segmented grinding grooves. Associated and relevant micro lead parameters are listed below the graphs. The lower section of the figures presents the results of the 3D macro lead analysis, including the structure angle distribution and the structure width distribution. The left-hand side shows a stitched topography overlaid with the segmented structural courses. Relevant structure-based macro lead parameters are also listed.

The results of sealing counterface (a), illustrated in Figure 7, were obtained using a white light interferometer.

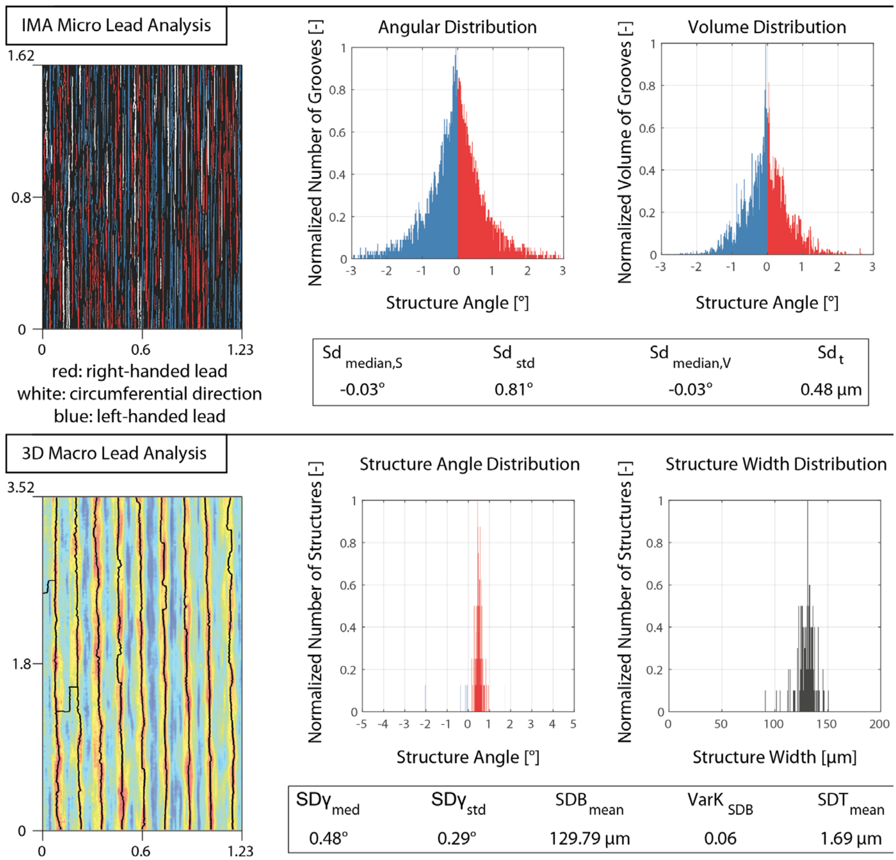

Figure 7: Lead analysis results of sealing counterface (a) measured with WL

The angular distribution as well as the volume distribution are almost symmetrical to the circumferential direction with $Sd_{median,S}$ = - 0.03° or $Sd_{median,V}$ = -0.03°. No axial pumping effect can be predicted based on this information. With a standard deviation of Sd_{std} = 0.81, the width of the angle distribution is also above the minimum specification of 0.3° [30]. The results are inconspicuous and indicate a micro lead-free sealing counterface.

In contrast, the results of the 3D macro lead analysis are unfavorable. The structure angle distribution shows a small distribution width and is almost completely located in the positive angle range. This phenomenon is described by the median structure angle $SD\gamma_{med}$ = 0.48° and the standard deviation of $SD\gamma_{med}$ = 0.29°. It is to be expected that the structures exert an axial pumping effect. The structure width distribution also appears to be normally distributed, with a narrow range of values. The low coefficient of variation CV_{SDB} = 0.06, which is a relative measure of scattering, serves to demonstrate the axial periodicity of the structures. In this context, sealing counterface (a) can be described as a prime example of macro lead.

Figure 8 illustrated the results of shaft (b), measured with the confocal measurement instrument.

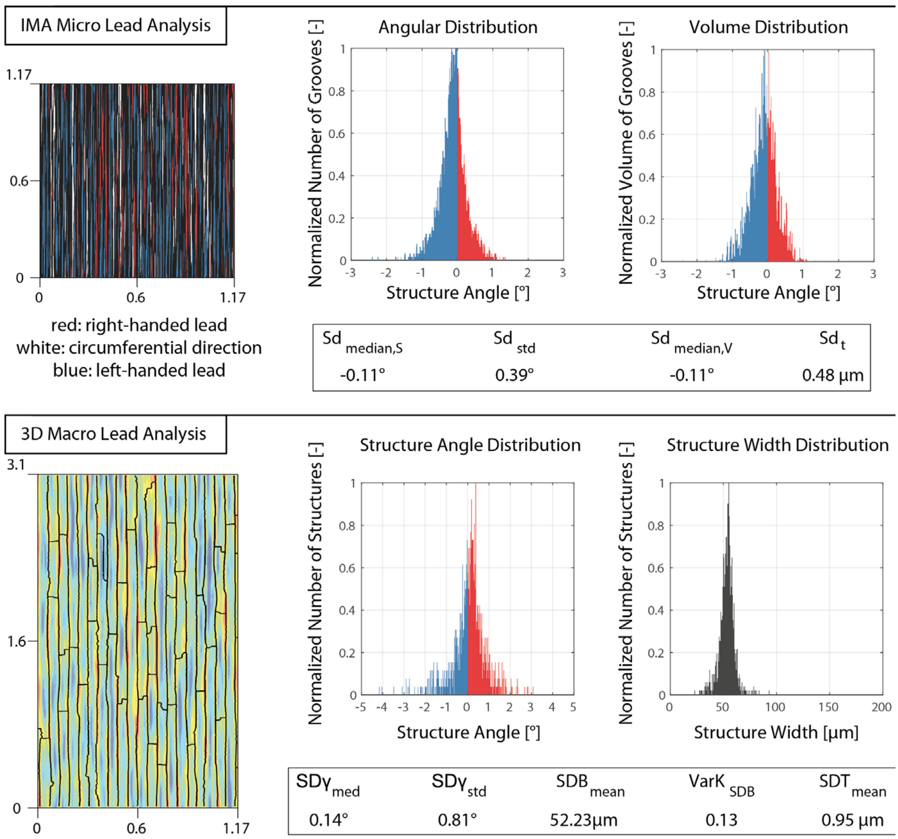

Figure 8: Lead analysis results of sealing counterface (b) measurend with CF

Sealing counterface (b) exhibits a right-handed macro lead superimposed with a left-handed micro lead. This is shown by the respective shifts and associated parameters of the angular distribution, the volume distribution and the structure angle distribution. The structure width distribution demonstrates the presence of axially recurring structures, which identifies a periodic macro lead on the sealing counterface. The average structure width of SDB_{mean} = 53.23 µm is relativly small for macro lead and characterizes a very pumping-active behavior of the structures [31, 32]. The opposing directions of micro lead and macro lead, coupled with the associated opposing pumping effects, make the functional behavior of the sealing couterface particularly difficult to understand. In conclusion, the sealing counterface can be classified as highly critical.

3.3 Comparison of the Results of Confocal Measurement Instrument and White Light Interferometry

In the configurations carried out, the white light interferometer (WL) measures the grid for combined lead analysis over 6 times faster than the confocal measurement instrument (CF) and thus has a great time-advantage. However, the measurement with the white light interferometer is accompanied by a lower lateral measurement resolution (WL: 1,2 µm – CF: 0,25 µm), a generally higher measurement noise, and a higher number of artifacts in the data. Nevertheless, both measurement methods provide valid, reproducible and, with one exception, comparable results in the combined lead analysis. This is shown by the results of the combined lead measurement of shaft (a) with the confocal measurement instrument and the white light interferometer. The measurements were repeated 10 times each to additionally investigate repeatability.

Table 2 shows with $Sd_{median,S}$ and Sd_{std} excerpts of the results of the IMA micro lead analysis. SDy_{med} and SDB_{mean} are representative of the results of the 3D macro lead analysis, shown in Table 3. The parameters not listed show only minor deviations and are inconspicuous.

Table 2: Comparison confocal (CF) – white light (WL) and repeatability within 10 repetitions of the results of the combined lead measurement for micro lead

	$Sd_{median,S}$ [°]				Sd_{std} [°]			
	Mean	**Min**	**Max**	**Std**	**Mean**	**Min**	**Max**	**Std**
CF	-0,03	-0,03	-0,02	0,002	0,41	0,40	0,43	0,006
WL	-0,03	-0,03	-0,02	0,003	0,83	0,81	0,84	0,011

Table 3: Comparison confocal (CF) – white light (WL) and repeatability within 10 repetitions of the results of the combined lead measurement for macro lead

	SDy_{med} [°]				SDB_{mean} [µm]			
	Mean	**Min**	**Max**	**Std**	**Mean**	**Min**	**Max**	**Std**
CF	0,47	0,46	0,48	0,004	131,08	130,67	131,44	0,25
WL	0,48	0,47	0,50	0,007	129,98	129,79	130,27	0,16

For both measurement methods, the minimum and maximum values of the 10 repeat measurements show only slight deviations. Besides, the standard deviation of the values over the 10 measurements is very low for all parameters. This demonstrates the reliability of the measurement results and ensures its repeatability on the same measuring device.

The differences in the parameter values between CF and WL are also insignificant. An exception is the parameter Sd_{std}. This parameter depends on the measurement resolution and must therefore be considered separately depending on the measuring device and measuring configuration. In summary, the results of these investigations demonstrate the compatibility of the combined lead measurement with the confocal measurement technique and the white light interferometer. The most economical method for measurement is the use of the white light interferometer, which is capable of measuring a sealing counterface in less than 10 minutes.

4 Summary and Conclusion

Until now, the use of various sequential measurements and analysis methods was required to comprehensively examine the sealing counterface of rotary shaft seals for shaft lead. This process is time-consuming and generates data whose potential is not fully utilized. However, the data from optical topography measurement instruments in particular offer the great potential to measure and evaluate all categories of lead, including micro lead, periodic macro lead, and aperiodic macro lead, in a single run.

This article shows that the structure-based lead analysis methods “IMA micro lead analysis” [27] and “3D macro lead analysis” [26] can be applied to a common data set, generated from a specially developed measuring grid in a single measuring run. The presentation of the measurement results includes two sealing counterfaces with different lead characteristics, which are described through the use of clear visualizations and parameters. In addition, one of the sealing counterfaces serves to show the compatibility of both the confocal measurement technique and white light interferometry for the purpose of combined lead analysis.

When measuring the shaft for combined lead, both measurement methods prove to be more time efficient, than the case of using several measurement methods in succession. The confocal measuring instrument is characterized by its excellent data quality, while the white light interferometer is particularly characterized by its rapid measurement capabilities. In the configurations carried out, the white light interferometer is approximately six times faster than the confocal measurement instrument, requiring only eight minutes to complete a combined lead measurement compared to 50 minutes for the confocal measurement instrument.

Further steps include the evaluation of the surface roughness based on the topography measurement data of the measuring grid. The 3D parameters according to DIN EN ISO 25178 [15] offer this potential.

In conclusion, the presented combined lead measurement and analysis represents a significant advance in terms of the quality assurance of sealing counterfaces of rotary shaft seals. The reasons for this are that the procedure for lead measurement and evaluation is more time-efficient and straightforward to use. This establishes a foundation for further dissemination of the lead measurement within the industry.

5 Nomenclature

Variable	***Description***	***Unit***
α	Larger flank angle of sealing edge	[°]
β	Smaller flank angle of sealing edge	[°]
CV_{SDB}	Coefficient of variation of the structure widths	[-]
DP	Period length	[mm]
Dt	Lead depth	[µm]
Dγ	Lead angle	[°]
h_f	Spring lever arm	[µm]
$Sd_{median,S}$	Median value of angular distribution	[°]
$Sd_{median,V}$	Median value of volume distribution	[°]
Sd_{std}	Standard deviation of angular distribution	[°]
Sd_t	Micro lead depth	[µm]
SDB_{mean}	Average structure width	[µm]
SDT_{mean}	Average structure depth	[µm]
$SD\gamma_{med}$	Median structure angle	[°]
$SD\gamma_{std}$	Standard deviation of the structure angles	[°]

Abbreviations

2D	Two-dimensional
3D	Three-dimensional
CF	Confocal measurement instrument
DIN	German Institute for Standardization
EN	European standard
FVA	Research Association for Drive Technology
IMA	Institute of Machine Components
ISO	International Standards Organization
MBN	Mercedes-Benz Factory Standard
WL	White light interferometer
WST	Watershed transformation

6 References

[1] **Deutsches Institut für Normung e.V.:** DIN 3760: *Radial-Wellendichtringe*, Berlin. September 1996.

[2] **International Organization for Standardization:** ISO 6194: *Rotary shaft lip-type seals incorporating elastomeric sealing elements.* 15.09.2007.

[3] **Bauer, F.:** *Federvorgespannte-Elastomer-Radial-Wellendichtungen. Grundlagen der Tribologie & Dichtungstechnik, Funktion und Schadensanalyse*, Wiesbaden, Heidelberg: Springer Vieweg, 2021, Springer Fachmedien Wiesbaden, - ISBN 978-3-658-32922-8.

[4] **Kammüller, M.:** *Zum Abdichtverhalten von Radial-Wellendichtringen*. Dissertation, 1986, Universität Stuttgart, Institut für Maschinenelemente, - ISBN 3-921920-19-1.

[5] **Heyn, W. O.:** *Shaft Surface Finish Is an Important Part of the Sealing System*. Journal of Lubrication Technology. 1969, 91 (1), S. 213.

[6] **Deutsches Institut für Normung e.V.:** DIN 3761-1: *Radial-Wellendichtringe für Kraftfahrzeuge - Begriffe; Maßbuchstaben; zulässige Abweichungen; Radialkraft*, Berlin: Beuth. Januar 1984.

[7] **Rubber Manufacturers Association:** Technical Bulletin RMA OS-1-1: *Shaft Finish Requirements for Radial Lip Seals.* 2004.

[8] **Haffner, G.; Baumann, M.; Bauer, F.:** *Formation of Macro Lead Using Plunge Grinding – a Kinematic Approach.* 21st International Sealing Conference (ISC), Stuttgart, 12.-13. Oktober 2022; Frankfurt am Main: Fachverband Fluidtechnik im VDMA e.V, 2022, S. 193–209 - ISBN 978-3-8163-0756-3.

[9] **Röttger, J.; Bergs, T.; Barth, S.; Baumann, M.; Bauer, F.:** *Influence of dressing parameters on the formation of micro lead on shaft sealing counterfaces during external cylindrical plunge grinding*. Advances in Industrial and Manufacturing Engineering. 2022.

[10] **Jagger, E. T.:** *Rotary Shaft Seal Some Effects of Shaft Surface Finish.* 1st International Conference on Fluid Sealing: British Hydromechanics Research Association, 1961.

[11] **Lines, D. J.; O'Donoghue, J. P.:** *The effect of surface roughness and thermal operating conditions on the under-lip temperature of a rotary shaft seal.* 8th International Conference on Fluid Sealing, University of Durham, England, September 11-13, 1978; Cranfield: British Hydromechanics Research Association, 1978 - ISBN 9780900983931.

[12] **Hirano, F.; Ishiwata, H.:** *The Lubricating Condition of a Lip Seal.* Institution of Mechanical Engineers, 1965, S. 187–196.

[13] **Kawahara, Y.; Abe, M.:** *An Analysis of Sealing Characteristics of Oil Seals*. A S L E Transactions. 1980, 23 (1), S. 93–102.

[14] **Deutsches Institut für Normung e.V.:** DIN EN ISO 4287: *Geometrische Produktspezifikation (GPS) - Oberflächenbeschaffenheit: Tastschnittverfahren; Bennenung, Definition und Kenngrößen der Oberflächenbeschaffenheit*: Beuth. Juli 2010.

[15] **Deutsches Institut für Normung e.V.:** DIN EN ISO 25178-2: *Geometrische Produktspezifikation (GPS) - Oberflächenbeschaffenheit: Flächenhaft; Teil 2: Begriffe und Oberflächen-Kenngrößen*: Beuth, 17.040.30. September 2012.

[16] **Lein, J.:** *Mechanische Untersuchungen an Dichtungsringen für rotierende Wellen*, Berlin, Heidelberg: Springer Verlag, 1954, - ISBN 3662253356.

[17] **Mercedes-Benz:** Norm MBN 31007-7: *Geometrische Produktspezifikationen (GPS) - Oberflächenbeschaffenheit Mess- und Auswerteverfahren zur Bewertung von drallreduzierten dynamischen Dichtflächen.* September 2008.

[18] **Kunstfeld, T.:** *Einfluss der Wellenoberfläche auf das Dichtverhalten von Radial-Wellendichtungen*. Dissertation, 2005, Universität Stuttgart, Institut für Maschinenelemente, - ISBN 3-936100-16-0.

[19] **Baitinger, G.:** *Multiskalenansatz mit Mikrostrukturanalyse zur Drallbeurteilung von Dichtungsgegenlaufflächen*. Dissertation, 2011, Universität Stuttgart, Institut für Maschinenelemente, - ISBN 978-3-936100-36-5.

[20] **Baumann, M.:** *Abdichtung drallbehafteter Dichtungsgegenlaufflächen - Messung, Analyse, Bewertung und Grenzen*. Dissertation, 2017, Universität Stuttgart, Institut für Maschinenelemente, - ISBN 978-3-936100-69-3.

[21] **Baitinger, G.; Haas, W.:** *Strukturanalyse. Drall- und Mikrostrukturanalyse zur funktionalen Bewertung von Dichtringgegenlaufflächen*. Abschlussbericht FKM Vorhaben Nr. 285, AiF-Nr. 15628 N/1, Frankfurt am Main: FKM, 2011, Forschungskuratorium Maschinenbau e.V. (FKM).

[22] **Baumann, M.; Bauer, F.; Haas, W.:** *Strukturanalyse II. Ganzheitliche, funktionale Bewertung von Dichtungsgegenlaufflächen mittels Strukturanalyse unter Einbeziehung der Wirkung von Strukturen auf die Förderwirkung der Welle*. Abschlussbericht FKM Vorhaben Nr. 298, IGF-Nr. 17138 N/1, Frankfurt am Main: FKM, 2015, Forschungskuratorium Maschinenbau e.V. (FKM).

[23] **Baumann, M.; Bauer, F.:** *Strukturanalyse III. Anwendung von Strukturanalyse und Festlegung von Qualitätskriterien für die gezielte Bewertung von Dichtungsgegenlaufflächen*. Abschlussbericht FKM Vorhaben Nr. 308, IGF-Nr. 18186 N, Frankfurt am Main: FKM, 2017, Forschungskuratorium Maschinenbau e.V. (FKM).

[24] **Kersten, G.:** *Optische und antastende Prüfung der Gegenlauffläche von Radial-Wellendichtringen*, Düsseldorf: VDI Verlag, 1992, Verein Deutscher Ingenieure e.V. (VDI), - ISBN 3-18-148102-5.

[25] **Seewig, J.; Hercke, T.:** *2nd Generation Lead Measurement.* XIX IMEKO World Congress, Lisbon, Portugal, September 6-11, 2009, 2009 - ISBN 9781615675937.

[26] **Engelfried, M.; Baumann, M.; Bauer, F.:** *3D-Makrodrall - Strukturbasierte 3D-Analyse von Makrodrall*. Forschungsheft 1471, Forschungsvereinigung Antriebstechnik e.V., Abschlussbericht FVA Vorhaben Nr. 876 I, Frankfurt am Main, 2022.

[27] **University of Stuttgart, Institute of Machine Components:** *IMA-Microlead®Analysis.* Universität Stuttgart, Institut für Maschinenelemente (Hrsg.), IMA-TechSheet, V1, #104140, Stuttgart, URL: https://www.ima.uni-stuttgart.de/dokumente/forschung/dichtungstechnik/dienstleistungen/en/104140en.pdf.

[28] **University of Stuttgart, Institute of Machine Components:** *Confovis Surface and Lead Measuring Instrument.* Universität Stuttgart, Institut für Maschinenelemente (Hrsg.), IMA-TechSheet, V1, #102010, Stuttgart, URL: https://www.ima.uni-stuttgart.de/dokumente/forschung/dichtungstechnik/einrichtungen/en/102010__11en.pdf.

[29] **University of Stuttgart, Institute of Machine Components:** *White-Light Interferometer Bruker NPFLEX-LA.* Universität Stuttgart, Institut für Maschinenelemente (Hrsg.), IMA-TechSheet, V1, #102020, Stuttgart, URL: https://www.ima.uni-stuttgart.de/dokumente/forschung/dichtungstechnik/einrichtungen/en/102020en.pdf.

[30] **University of Stuttgart, Institute of Machine Components:** *Optimal Shaft Counterfaces for Radial Shaft Seals – Plunge Grinding.* Universität Stuttgart, Institut für Maschinenelemente (Hrsg.), IMA-TechSheet, V1, #104170, Stuttgart, URL: https://www.ima.uni-stuttgart.de/dokumente/forschung/dichtungstechnik/dienstleistungen/en/104170en.pdf.

[31] **Engelfried, M.; Haffner, G.; Baumann, M.; Bauer, F.:** *Modeling the Pumping Behavior of Macroscopic Lead Structures on Shaft Counterfaces of Rotary Shaft Seals*. Lubricants. 2023, 11 (11), S. 495.

[32] **Schiefer, F.; Baumann, M.; Bauer, F.:** *Untersuchung des Förderverhaltens makrodrall-behafteter Dichtungsgegenlaufflächen.* 20th International Sealing Conference (ISC), Stuttgart, 10.-11. Oktober 2018; Fluidtechnik; Frankfurt am Main: Fachverband Fluidtechnik im VDMA e.V, 2018, S. 301–312 - ISBN 978-3-8163-0727-3.

7 Authors

University of Stuttgart, Institute of Machine Components (IMA)

Pfaffenwaldring 9, 70569 Stuttgart, Germany:

Maximilian Engelfried, M. Sc., ORCID 0000-0002-7280-7589,
maximilian.engelfried@ima.uni-stuttgart.de

Dr.-Ing. Matthias Baumann, ORCID 0000-0002-1962-5153,
matthias.baumann@ima.uni-stuttgart.de

Apl. Prof. Dr.-Ing. Frank Bauer, ORCID 0000-0001-7799-7628,
frank.bauer@ima.uni-stuttgart.de

https://doi.org/10.61319/DLDXU4PE

Insights into the pumping behaviour of sealing counterfaces using continuous logging

Georg Haffner, Matthias Baumann, Frank Bauer

Surface structures of the sealing counterface are called “lead structures” when they have the capability to pump oil rotation dependent through the sealing contact of a rotary shaft seal systems. This feature is called “pumping effect”. The structures interrupt the equilibrium state of the sealing system, which may cause dry run or leakage as failure result. Especially for higher circumferential velocities the pumping effect increases and therefore cannot be neglected.

To assess the functional influence of lead structures on the sealing system, one can measure the pumping rate of the sealing counterface experimentally. The higher the pumping capability of a sealing counterface, the more likely the sealing system will fail. In this paper, the development a new pumping rate evaluation method with the help of a continuously measuring scale, which allows to visualize the course of the pumping rate over time, is described. With this knowledge it is possible to determine the end of the running-in phase of the rotary shaft seal and to determine the minimum duration of the pumping rate tests. The pumping rate evaluation method is demonstrated with different shaft counterfaces to validate the stability of the new method.

1 Introduction

Rotary shaft sealing systems consist of the rotary shaft seal, a fluid to be sealed and the sealing counterface [1]. The components - during operation - form a complex tribological system, which has many different external and internal influences able to affect the life expectancy of the system.

External influences are e.g. temperature, pressure, humidity or the environmental circumstances. Internal influences, on the other hand, are based on the components of the sealing system itself. The material of the rotary shaft seal (e.g. FKM or NBR), the oil (e.g. mineral oil or synthetic oil) and its compatibility with the rotary shaft seal material [2] and the sealing counterface material as well as structures on the counterface are examples of internal influences.

The sealing counterface possesses an important role in the tribological system “rotary shaft seal”. It has direct contact with the sealing lip of the rotary shaft rotary shaft seal, therefore it has to be matched to the rotary shaft seal in order to work properly. Since the sealing counterface is mostly manufactured inhouse in contrast to the rotary shaft seal which is purchase part with mostly the same tolerances and quality [3], there are different guidelines which assist the manufacturing process of the sealing counterface to match with the rotary shaft seal, e.g. [4, 5].

Those guidelines describe the material properties of the sealing counterface as well as the surface properties like roughness, maximum shape divergence and micro and macroscopic structure properties. Micro- and macroscopic structures can apply additional fluid movement through the sealing contact during operation. Such structures are called “lead”. The fluid moving, also called “pumping effect”, is rotation direction and circumferential velocity dependent.

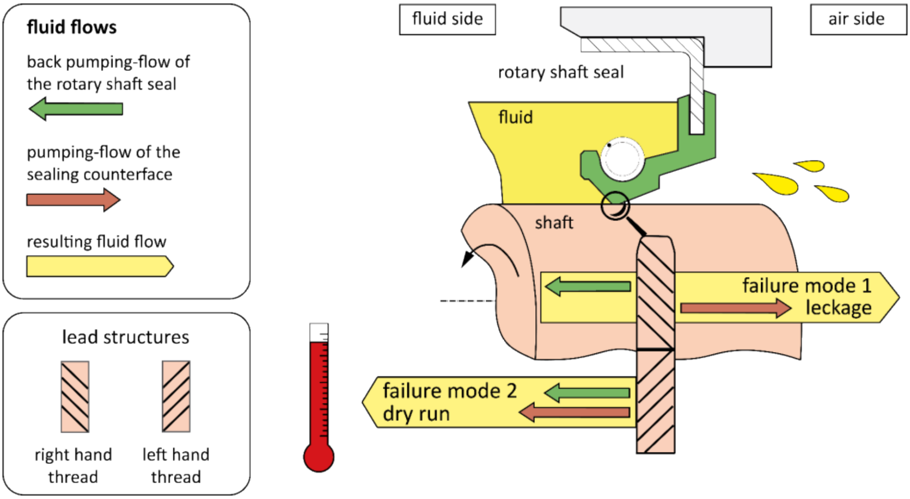

Figure 1: Failure modes due to lead

The pumping effect of the sealing counterface is mostly unwanted as it disturbs the equilibrium state of the rotary shaft seal system. A pumping effect of the sealing counterface can lead to the failure of the sealing system in two different ways, as shown in Figure 1. Either the fluid is pumped into the housing of the sealing system, so direct contact between the sealing edge and the counterface occurs with increased friction and wear which leads to thermal damage of the sealing edge and therefore leakage or the fluid is pumped out of the housing, which results in direct leakage. Both failure mechanisms result in the standstill or failure of the affected devices, expensive repairs and environmental damage.

Table 1: Categories of lead [6]

high-pass →
$\lambda_c = 20\ \mu m$
→ low-pass

	Category	Illustration	Classification
microscopic	micro lead	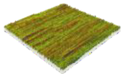	stochastically arranged, anisotropic
macroscopic	micro waviness	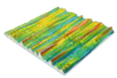	stochastically arranged, aperiodic, isotropic / anisotropic
macroscopic	macro lead	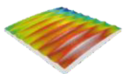	axial periodic, circumferential
any size	scratches	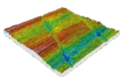	defects, any size

As mentioned before, lead can occur in different scales. Table 1 gives an overview of the lead types, their respective classification and analysis method.

Basically, lead is categorized by its scale. Measuring lead requires special hardware like a microscope with different magnifications. While scratches may appear in every scale from visible by eye to visible by microscope, the evaluation of macro- and micro lead is primarily carried out with the help of a topography measuring device (periodic/aperiodic macro lead and micro lead) or tactile measuring device (periodic macro lead).

A lot of research has been carried out to measure and evaluate lead [4, 6, 7]; it's possible to evaluate if the shaft surface should be used in a rotary shaft sealing system. But the decision is solely based on if lead is present in any of the mentioned methods. The quantitative influence of lead – e.g. how much lead is tolerable for the reliable usage – is mostly unknown.

Lead is a major influence to the equilibrium state of the sealing system; therefore, its effect is examined in pumping rate measurement runs. There are different methods for evaluating the pumping rate of a sealing system, which either check a very short time span of the pumping rate like [8], where oil rise due to pressure difference in a riser pipe is evaluated or one only checks the start and the end of the run [9, 10], which averages out the pumping rate and describes the behaviour less detailed.

The aim of this paper is to give insights in the behaviour of the sealing system during multiple runs of [10] to see the behaviour of the run-in phase of the rotary shaft seal and the development of the pumping rate over time using “lead free” sealing counterfaces and mostly same test circumstances. This is achieved using a continuous measuring scale, which is triggered using a microcontroller.

2 Materials and methods

The next section covers the used test equipment, especially the test-rig as well as the scale, the measurement procedure and the scope of the experiment of this paper.

2.1 Research approach

To investigate the pumping behaviour of a rotary shaft sealing system, a test-rig with precise geometric tolerances as well as precisely adjustable temperature and rotation speed is used. These parameters reduce the influence of clamping errors or errors due to material and fluid property changes. Furthermore, a precise scale adapted to geometric constraints of a test-rig was developed and applied, which can be read out automatically so the generated data can be visualized and evaluated algorithmically.

2.2 Test-rig

For the examinations, the modular 24 chamber test-rig [11] from the institute is used. It offers the advantage of a directly visible sealing contact, easy adjustment of the running track and good clearance underneath the test chamber, as seen in Figure 2, where the scale and a beaker are positioned.

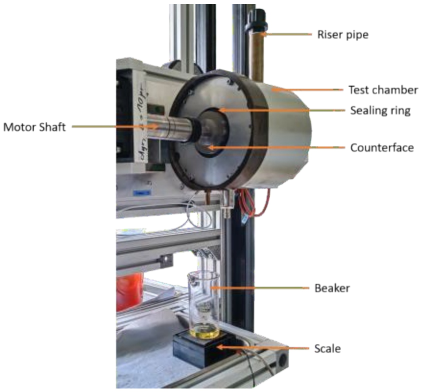

Figure 2: Test setup

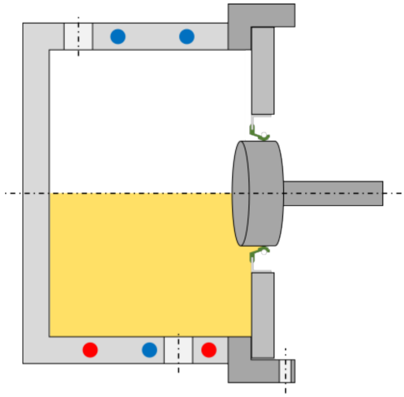

Figure 3: Cross-section of a test chamber

Every test chamber has multiple bores with heating elements (red) and bores for cooling water (blue), Figure 3. The fully assembled test setup consists of the chamber with a filtering riser pipe, so the chamber is vented and has ambience pressure, a mounted sealing counterface, and a holder for the rotary shaft seal. In front of the holder is a small outlet, which allows leakage to be collected and dropped into a beaker. The beaker itself is positioned on a scale.

Velocity, temperature of the oil sump and the load collective of every module can be controlled individually. They can be adjusted in the graphical user interface of the test-rig.

2.3 Pumping rate measurement

The pumping rate measurement is carried out after the method proposed by [9], where the rotary shaft seal is mounted in inverse direction, so the front is constantly in contact with the oil. Therefore, the rotary shaft seal will pump out oil during rotation independently of the rotation direction and the sealing counterface depending on its rotation direction.

The pumping rate of the rotary shaft seal can be calculated as followed:

$$PR_{Sealing} = \frac{1}{\Delta t} \cdot \frac{Leakage_{ccw} + Leakage_{cw}}{2} \tag{1}$$

The pumping rate of the sealing counterface can be calculated as followed:

$$PR_{Counterface} = \frac{1}{\Delta t} \cdot \frac{Leakage_{ccw} - Leakage_{cw}}{2} \tag{2}$$

In this investigation, only the pumping rate of the sealing counterface is considered. The pumping rate is calculated for every clockwise (cw)/counter clockwise (ccw) run under the limitations proposed by [9].

2.4 Continuous measuring scale

A scale was developed to continuously record the pumping behaviour of the sealing system, Figure 4. This was necessary due to the space restrictions under the test rig as well the integration into the test-rig software. The scale was extensively tested and problems such as temperature dependency were compensated for with mathematical models.

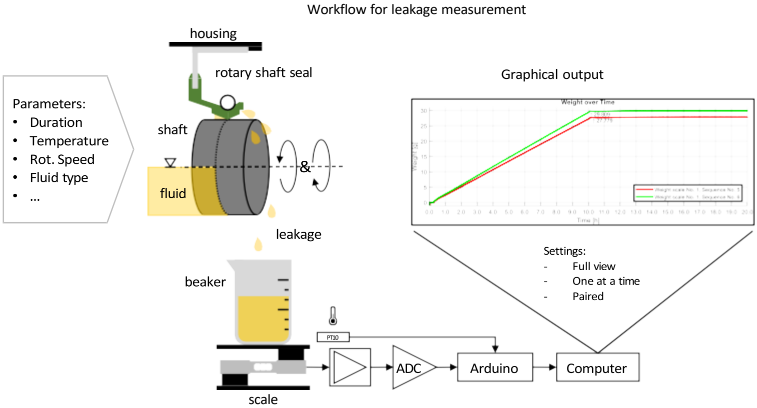

Figure 4: Schematic principle for measurement

The scale is based on a 1kg measuring range bending beam with a strain gauge full bridge. Its analogue signal is interpreted by a 24-bit analogue-digital converter, resulting in approx. 0.1 mg[1] resolution. The digital signal is processed by an Arduino alongside the signal of the device temperature, which is measured using a PT10, which is digitalized with 12-bit. The sensor is needed for the temperature compensation of the scale.

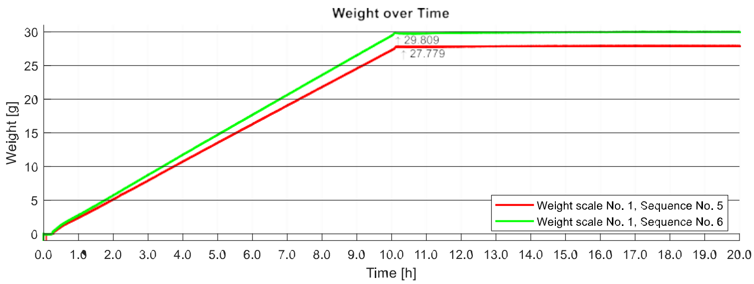

Figure 5: Continuous weight recording (cw and ccw) of a lead-free shaft surface

[1] Assuming 1 bit is quantification noise

Both signals are sent to a computer over the serial interface using Python (Version 3.9). Every temperature and weight signal are saved in a text file with its proper timestamp, the measuring frequency is set to 1 s. The text file is interpreted, processed and visualized using MATLAB (Version R2022a), Figure 5.

The processing includes removal of spikes, the above-mentioned temperature compensation, offset removal to compensate the beaker weight and the division into sequences. The measurement in the upper example was carried out on a lead-free surface. The clockwise run (or odd sequence number) is coloured red, the counter clockwise run is coloured green. On the abscissa the time is applied, on the ordinate the weight. The peak weight at around the 10 h mark is also printed in the graph. The legend on the bottom-right tells which scale is used and which run (or sequence) the graph is currently displayed with its associated colour.

2.5 Scope of experiment

The test runs were carried out on two different chambers of the test-rig. Every chamber had one scale, both scales were connected to the same Arduino which received both weight signals at the same time. Both beakers were measured before and after each test-run. The measured oil was poured back into the test chamber after every test run.

The test run conditions can be taken from the following table:

Table 2: Test run conditions

Rotary shaft seal	*Freudenberg BAUM5X7 FKM*
Oil	*FVA3 mineral oil [12]*
Oil amount	*Centre of shaft*
Oil sump temperature	*80°C*
Rotational speed	*±1000 1/min*
Shaft diameter	*80 mm*
Run duration	*10 h (single direction)*
Pressure	*Ambient pressure (vented test chamber)*

The runs were carried out on different shaft surfaces, two lead-free and two macro lead-afflicted shaft surfaces. In the following overview, the topography measurements of the shaft surfaces can be seen along with their macro lead parameters, measured and evaluated according to [4]:

Table 3: Overview of selected shafts surfaces

Name	***Topography***	***Type***	***Dt [µm]***	***Dy [°]***	***DP [mm]***
LF01	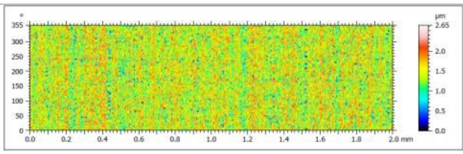	Lead-free	0.18	0.00	0.209
LF02	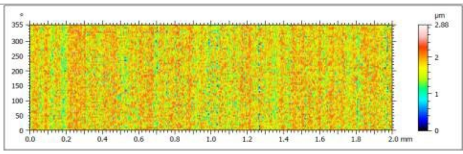	Lead-free	0.15	0.00	0.205
LA01	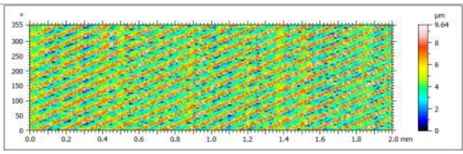	Lead-afflicted	5.10	- 0.316	0.139
LA02	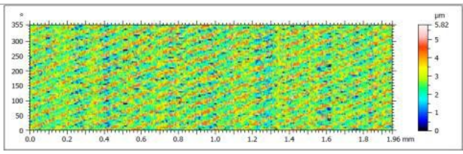	Lead-afflicted	2.34	- 0.327	0.143

The height of the topographies in Table 3 is displayed in false colour representation, where blue represents a low and red a high height value. The scaling of every surface is different to better visualize the different structures on the shaft counterfaces. Both lead-free surfaces are very similar in every mentioned macro lead parameter. A major difference in the lead-afflicted surfaces is the lead depth *Dt*, which differs about 2 times. The other two macro lead parameters, period length *DP* and lead angle *Dy*, differ significantly less. Micro lead measurement and evaluation on all shaft surface has also been carried out according to [13]; all surfaces are micro lead-free.

The test runs were carried out on the same tracks, repetitions on the lead-free shaft surfaces were carried out on a different track. This ensures the same initial condition for every sealing system.

In total, 6 runs over 180 h of test time with two lead-free and two lead afflicted surfaces were carried with continuous measurement.

3 Experimental results

The experimental results are split in two parts. First, a complete test run is evaluated and specific features and occurrences are pointed out. In the second part, the first run of the same lead-free shaft surface is considered in more detail, especially at start and the end of a run.

3.1 Continuous measurements

The continuous measurement displays the whole test period, with every clockwise and counter-clockwise run as well as the standstill time. An example of a continuous test run is seen in the following figure:

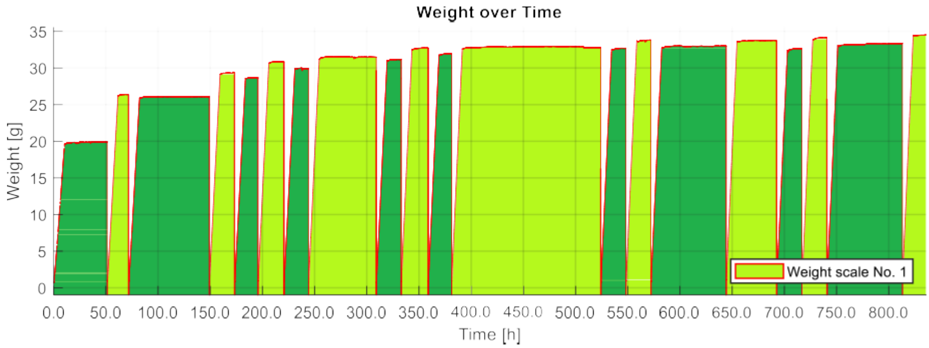

Figure 6: Full test run, LF01

Figure 6 shows 20 runs of the same sealing system using LF01 as sealing counterface; the runs were carried out according to Table 2, clockwise runs are coloured dark green and counter clockwise runs are coloured light green. The scale is continuously acquiring weight data, after 10 hours of continuous weight rising due to rotation of the shaft, the shaft stops rotating and the weight remains at its last value since no more fluid is pumped. The different holding times after every weight rise are due to weekends or holidays. Before changing the rotational direction, the beaker is then emptied back into the test chamber to keep the fluid level at the centre of the shaft. This process is visible in the drop of the weight to below 0 g. When the beaker is put back onto the scale, the weight settles back at approx. 0 g. Afterwards, the test run is started again with the opposite rotation direction.

A clear trend is visible since the difference between the cw weight and associated ccw weight is getting continuously smaller. The difference is more apparent when looking at the fluid pumped of each cw/ccw pair and note the resulting weights, seen in Figure 7:

Figure 7: Weights of the full test run, LF01

The maximum weight value of every run in Figure 6 was evaluated and presented as bars in the figure above and the difference between cw and associated ccw run was positioned between both runs in a diamond shape.

The sum of the pumped fluid rises every cw/ccw run, beginning at 19 g/25 g and ending at about 32 g/33 g. But the difference between cw and ccw decreases from 6.4 g to 1.10 g, Table 4. From pair 5 to pair 10, the difference settles at about 1.15 g ± 0.35 g.

Table 4: Leakage values full test run, LF01

Pair:	1/2	3/4	5/6	7/8	9/10	11/12	13/14	15/16	17/18	19/20
cw [g]:	18,90	24,84	27,78	28,95	30,28	30,92	31,81	31,94	31,58	32,15
ccw [g]:	25,33	28,44	29,81	30,57	31,74	31,73	32,78	32,61	33,02	33,25
Δ [g]:	6,43	3,60	2,03	1,62	1,46	0,81	0,97	0,67	1,44	1,10

When assuming, this result is the final pumping rate of the sealing system in this configuration, a longer testing period for a sealing system is needed to achieve more stable results since the difference in the first cw/ccw run is more than 6 times larger compared against the last pair in the test period. The difference becomes less significant after the second and third test run. The most stable result can be achieved after the fifth cw/ccw pair, since from there on until the end of the investigation, the change pumping rate is less significant, seen in the next figure:

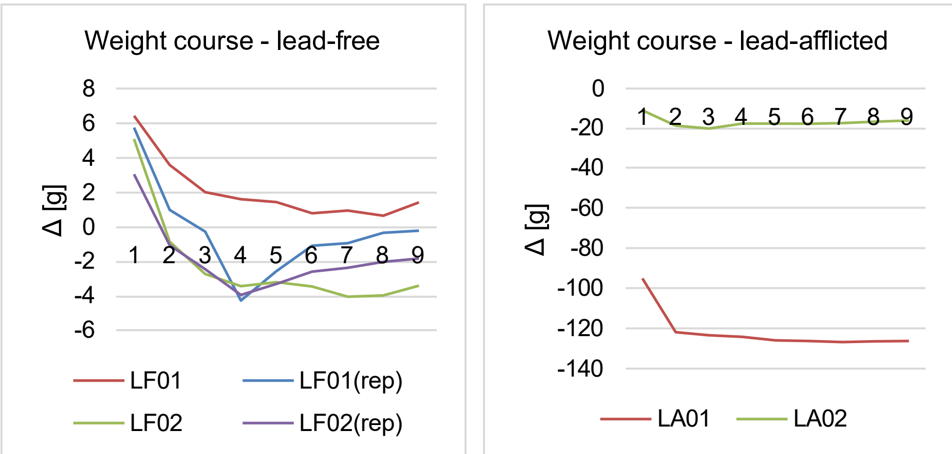

Figure 8: Weight courses

The runs were split into two diagrams since the absolute pumping rate difference between lead-free and lead-afflicted surfaces in the observation is up 60 times. All lead-free surfaces settle at about -4 g to 2 g, where the lead-afflicted surfaces spread between -120 g to -20 g. The drop in *LF01(rep)* during the 4th cw/ccw run occurred when not keeping the minimum of 10h resting time. Interestingly, the sealing system slowly rises back to about 0 g pumping rate difference, which was the last pumping rate difference seen at the 3rd cw/ccw pair.

3.2 Detailed view of a cw/ccw pair

The overview in Figure 6 gives a good insight into the pumping behaviour of a sealing system over time. The change in the difference in the pumped fluid can be observed with lead-free and lead-afflicted shaft surfaces. Next, it is interesting to see, how the sealing system itself behaves in one cw/ccw pair. Therefore, the first pair is observed in more detail since this pair showed the greatest change over the time. The cw/ccw pair is visualized in Figure 9. Both runs were put in the same diagram, with the same time scaling and the same height scaling.

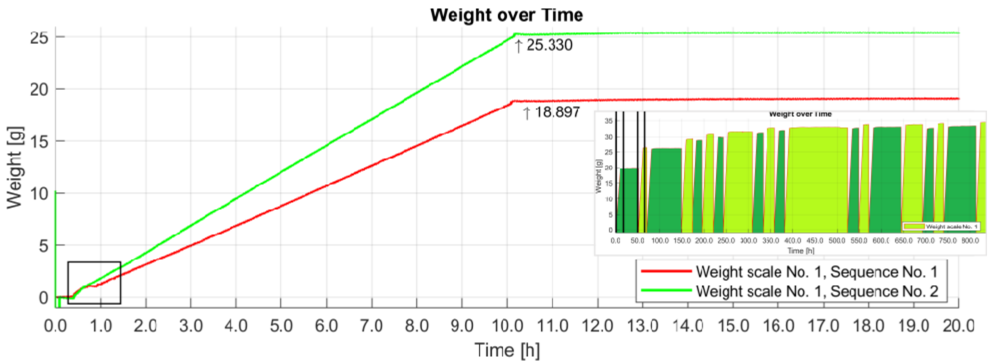

Figure 9: First run LF01, detailed view

The figure shows a section from the test-run LF01, the cw run is coloured red and ccw run is coloured green. The first run appears to have an elevation, highlighted in the grey box which disappears after about 1h of test run time. At similar position, an elevation has appeared on four of the other detailed measurement runs, but the shape of the elevation differs, Figure 10. The exceptions are LF02 and LA01, which do not appear to have an elevation in their first run.

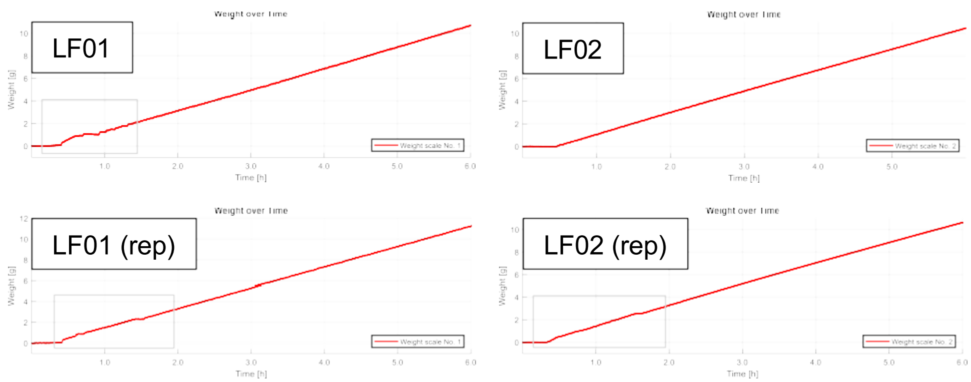

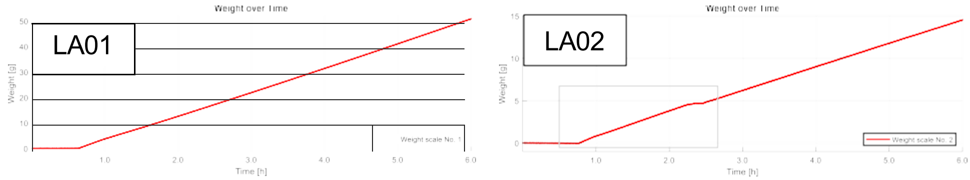

Figure 10: Initial elevation during first run

In the ccw run, an elevation cannot be seen. This might be due to the run-in behaviour of the rotary shaft seal. Based on the test-rig design, in the first minutes of the test run, no leakage is detected because the fluid first collects at the sealing lip before it combines to a droplet and falls into the beaker. The next droplets are more uniform and easier to discover as seen in the magnification view of hour 2 and hour 4.

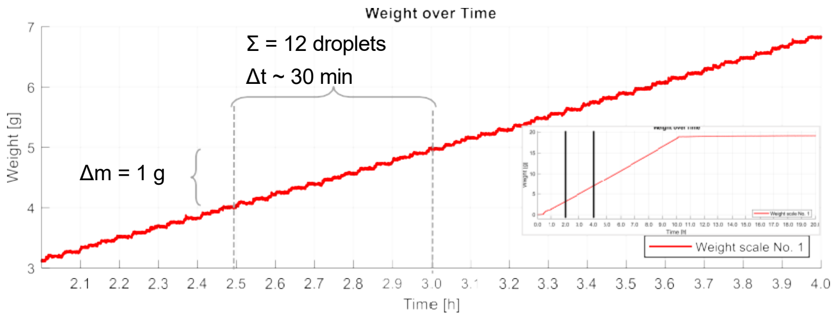

Figure 11: Weight course LF01, 2h-4h

The resolution of the scale is sufficient enough to represent a droplet and approximate weight and the duration between every droplet, which then can be evaluated. In Figure 11, a droplet has the approximate weight of 0.083 g and appears every 2.5 minutes. Accumulated over the test duration, the final weight of the pumped oil is 19.92 g, which matches well with the measured leakage (18.90 g) when not considering the run-in phase. This means after the run-in phase. the pumping rate behaviour remains mostly linear over the testing time of the run.

At the end of each run, no more fluid is pumped and the fluid around the sealing edge is no longer dragged along the circumference of the sealing edge.

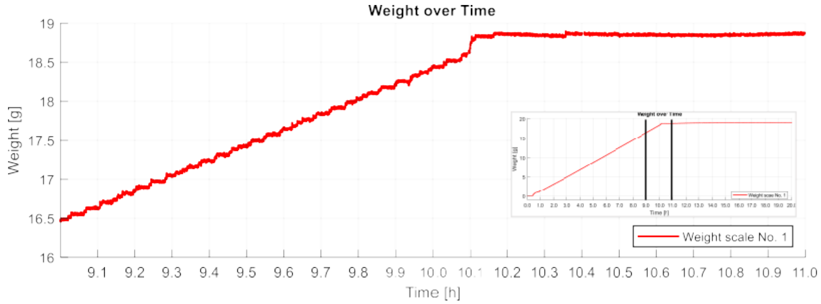

Figure 12: Detailed view of the end of a run, LF01

The fluid collects at the lowest point of the sealing edge, forms into a droplet and runs down into the beaker. This behaviour can be seen in Figure 12. The offset of 0.1 hours to the 10 h mark is the result of the scale being switched on first before the test run is started. At the 10.1 h mark, a bigger than usual droplet with about 0.25 g (compared to ~0.09 g) was formed and dropped into the beaker. Afterwards, at standstill of the test-rig, near 10.2 h and near 10.4 h, a small droplet can also be seen.

3.3 Visual examination of components

A change in the rate of pumped fluid of every sealing system has been determined, Figure 8. Such an effect can appear due to changes in the sealing system components like the rotary shaft seal or the sealing counterface. Both components are visually examined using a digital microscope.

3.3.1 Visual examination of rotary shaft seal

The sealing edge is a highly stressed part of the rotary shaft seal. Wear as well as thermal damage may appear when the sealing system isn't proper designed. To assess the condition of the sealing edge, direct view onto the sealing edge is needed. It was achieved using [14]; the condition of rotary shaft seal of LF01 compared to a new rotary shaft seal is displayed in Figure 13:

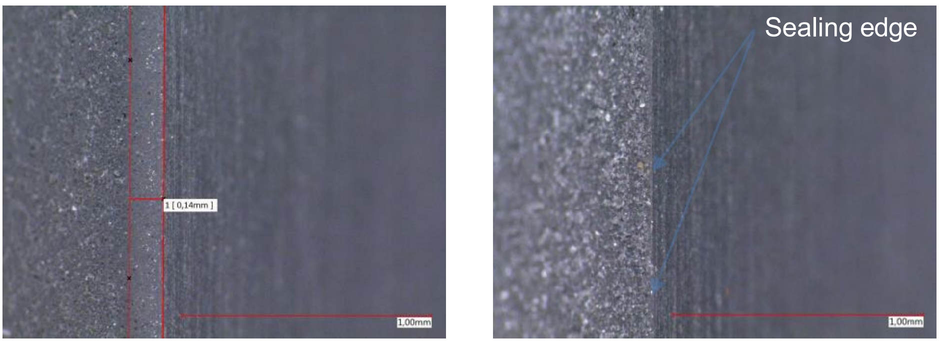

Figure 13: Comparison of used vs. new sealing edge

The sealing edge is not discoloured, so no thermal damage occurred on the sealing edge. The sealing contact was continuously supplied with fresh oil. Compared to a new sealing edge of the same batch (Figure 13, image on the right), wear can definitely be seen. The sealing edge, even though constantly supplied with oil, still wears out, meaning, the contact is not constantly fully lubricated. It has an approximate wear width of about 0.14 mm where the new sealing edge is still “sharp”.

The wear width of the sealing edges of the other (lead-free surface) rotary shaft seals also settle around 0.14 mm to 0.18 mm. Since all rotary shaft seals appear to have wear on the sealing edges, which is similar over the test runs, the formation of wear during the runs can explain the behaviour of the pumped fluid, determined in 3.1. Starting with the first run pair, the difference between cw and ccw run is 6.43 g, the absolute fluid pumped is around 19 g (cw) and 25 g (ccw). The difference in the following run pair (3/4) in fluid pumped is only 3.6 g, so it can be assumed, that wear on the sealing edge was already formed during the first run pair (1/2). With each successive run pair, the rate of change in the difference of the pumped fluid becomes smaller indicating a decrease in wear formation and a stabilisation of the tribological state in the sealing contact. At the fifth run pair of LF01, the change of fluid pumped (30 g/32 g) and the difference between the run is not changing as significantly compared to the first run pair. At this point in this investigation it can be assumed that the sealing edge did not wear significantly further.

3.3.2 Visual examination of sealing counterface

A change in the surface of the sealing counterface can also cause the change of the pumping rate behaviour. In visual microscopy, the deeper a grove, the darker the colour gets. The surfaces do not have a groove with a high wear depth, since only light colour changes can be seen. On the surfaces, it’s only possible to see the running track of the rotary shaft seal, Figure 14:

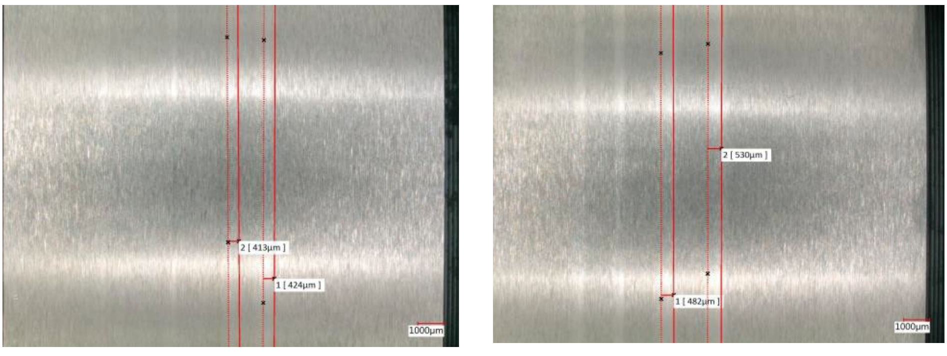

Figure 14: Surface analysis LF01(left) and LF02 (right)

The running tracks are hardly visible in the magnified view on the sealing counterface. Both images were taken with 50x magnification and the same light settings. The peaks of the roughness of the surfaces have been smoothed out but no measurable depth has been created during the test runs. The smoothing of the peaks of the roughness cannot explain the behavior seen in 3.1, since the major macroscopic structures would still be completely intact.

4 Discussion and conclusion

The paper presented a more detailed view into the pumping behaviour of different shaft surfaces with the help of continuous measuring scales during pumping rate measurements according to [9, 10]. The goal was to visualize the running-in phase of the sealing and derive a more stable duration for pumping rate measurements. Using a continuous measuring scale proved to be a convenient way to carry out pumping rate measurements since the weight difference can be calculated automatically and the beaker isn't needed to be weighed before and after each run.

As seen in the overview images in Figure 8, the first pumping rate differs in absolute value and can also differ in sign compared to the following pumping rate measurements. In the scope of this paper, it is recommended to use a at least 6 measurement runs, three clockwise and three counter-clockwise to achieve a more stable result for the pumping rate since the scattering of the leakage is smaller. Longer testing periods result in a more stable pumping rate. The change in pumped fluid can be traced back to the wear of the sealing edge although it was constantly surrounded by oil. A closer examination of the sealing counterfaces hasn't given indication of the change of pumped fluid, since only smoothening of roughness tips was seen.

After 180 hours of testing according to Table 2, the difference between the cw and corresponding ccw run settles at about 1.15 g ± 0.35 g. Since a deviation is still present, a much longer testing time could be used to check, where the sealing system with the corresponding shaft surface settles.

When looking at the first run of a sealing system in more detail, an elevation can be captured, where the pumping rate deviates from a constant increase. This different behaviour finishes after about 2-3 h of continuous running. In two of six runs on two different test chambers, this effect hasn't appeared, which argues against a system-wide effect. The duration and magnitude of the elevation are also not constant. There, more runs with continuous measuring scales could be carried out systematically in order to understand how this elevation appears.

The method allows further applications such as leakage detection or extensive comparison of sealing systems. It's also possible to implement the scales into an existing test rig software to allow more data of the test run to be collected.

5 Nomenclature

Variable	***Description***	***Unit***
cw	clockwise	[-]
ccw	counter clockwise	[-]
Dy	Lead angle	[°]

DP	Period length	[mm]
Dt	Lead depth	[µm]
Δt	Run duration	[h]
$Leakage_{cw}$	Mass of pumped fluid during cw operation	[g]
$Leakage_{ccw}$	Mass of pumped fluid during ccw operation	[g]
$PR_{Sealing}$	Pumping Rate of a radial shaft seal	{g/h]
$PR_{Counterface}$	Pumping Rate of a sealing counterface	[g/h]

6 Authors

University of Stuttgart, Institute of Machine Components (IMA)

Pfaffenwaldring 9, 70569 Stuttgart, Germany:

Georg Haffner, M. Sc., ORCID 0000-0002-6484-235X, georg.haffner@ima.uni-stuttgart.de

Dr.-Ing. Matthias Baumann, ORCID 0000-0002-1962-5153, matthias.baumann@ima.uni-stuttgart.de

Apl. Prof. Dr.-Ing. Frank Bauer, ORCID 0000-0001-7799-7628, frank.bauer@ima.uni-stuttgart.de

7 Literaturverzeichnis:

[1] **Bauer, F.:** *Federvorgespannte-Elastomer-Radial-Wellendichtungen. Grundlagen der Tribologie & Dichtungstechnik, Funktion und Schadensanalyse*, Wiesbaden, Heidelberg: Springer Vieweg, 2021, Springer Fachmedien Wiesbaden, - ISBN 978-3-658-32922-8.

[2] **Florez, A.; Hentschke, C.; Jacobs, G.:** *Elastomerverträglichkeit. Verträglichkeit von Schmierstoffen und Elastomeren*. Abschlussbericht FVA Vorhaben Nr. 683 I, IGF-Nr. 17450 N, Frankfurt am Main: FVA, 2015, Forschungsvereinigung Antriebstechnik e.V. (FVA).

[3] **Deutsches Institut für Normung e.V.:** DIN 3761-1: *Radial-Wellendichtringe für Kraftfahrzeuge - Begriffe; Maßbuchstaben; zulässige Abweichungen; Radialkraft*, Berlin: Beuth. Januar 1984.

[4] **Mercedes-Benz:** Norm MBN 31007-7: *Geometrische Produktspezifikationen (GPS) - Oberflächenbeschaffenheit Mess- und Auswerteverfahren zur Bewertung von drallreduzierten dynamischen Dichtflächen.* September 2008.

[5] **Deutsches Institut für Normung e.V.:** DIN 3760: *Radial-Wellendichtringe*, Berlin. September 1996.

[6] **Baumann, M.:** *Abdichtung drallbehafteter Dichtungsgegenlaufflächen - Messung, Analyse, Bewertung und Grenzen*. Dissertation, 2017, Universität Stuttgart, Institut für Maschinenelemente, - ISBN 978-3-936100-69-3.

[7] **Engelfried, M.; Baumann, M.; Bauer, F.:** *3D-Makrodrall - Strukturbasierte 3D-Analyse von Makrodrall*. Forschungsheft 1471, Forschungsvereinigung Antriebstechnik e.V., Abschlussbericht FVA Vorhaben Nr. 876 I, Frankfurt am Main, 2022.

[8] **Britz, S.:** *Ein Beitrag zur Erfassung der Funktionsprinzipien dynamischer Wellendichtungen unter besonderer Berücksichtigung des Radialwellendichtrings*. Dissertation, 1988, Universität Kaiserslautern.

[9] **Raab, H.:** *Wellenlaufflächen. Einfluß der Wellenlauffläche auf das Dichtverhalten von Radial-Wellendichtringen*. Abschlussbericht FKM Vorhaben Nr. 211, AiF-Nr. 10670, Frankfurt am Main: FKM, 1998, Forschungskuratorium Maschinenbau e.V. (FKM).

[10] **Kawahara, Y.; Hirabayashi, H.:** *A Study of Sealing Phenomena on Oil Seals*. A S L E Transactions. 1979, 22 (1), S. 46–55.

[11] **Universität Stuttgart, Institut für Maschinenelemente:** *Wellendichtungen 24-Zellen-Dauerprüfstand.* Universität Stuttgart, Institut für Maschinenelemente (Hrsg.), IMA-TechSheet, V1, #101010, Stuttgart, URL: https://www.ima.uni-stuttgart.de/dokumente/forschung/dichtungstechnik/einrichtungen/101010.pdf.

[12] *Referenzöle: Referenzöle für Wälz- und Gleitlager-, Zahnrad- und Kupplungsversuche. Datensammlung für Mineralöle*, Frankfurt am Main: FVA, 1985, Forschungsvereinigung Antriebstechnik e.V. (FVA).

[13] **Universität Stuttgart, Institut für Maschinenelemente:** *IMA-Mikrodrall®Analyse.* Universität Stuttgart, Institut für Maschinenelemente (Hrsg.), IMA-TechSheet, V1, #104140, Stuttgart, URL: https://www.ima.uni-stuttgart.de/dokumente/forschung/dichtungstechnik/dienstleistungen/104140.pdf.

[14] **Universität Stuttgart, Institut für Maschinenelemente:** *IMA-Sealobserver.* Universität Stuttgart, Institut für Maschinenelemente (Hrsg.), IMA-TechSheet, V1, #102070, Stuttgart, URL: https://www.ima.uni-stuttgart.de/dokumente/forschung/dichtungstechnik/einrichtungen/102070.pdf.

https://doi.org/10.61319/DI2CJQ5C

In Situ Observation of a Grease Lubricant Film on a Radial Seal by Fluorescence Induced Microscopy

Takao Horiuchi, Yohei Sakai, Ayako Aoyagi

Reduction gears are installed inside the joints of industrial robots and lubricated with grease. In this study, the sealing surfaces of radial seals were observed in grease lubrication with fluorescence microscopy. The sealing performance was tested with oscillating operation. The pump rate tends to increase and sealing performance improves in proportion to the oscillation angle. Changes in oil film thickness and amount of thickener were observed on the sealing surfaces. Our results suggest pumping ability of radial shaft seals in grease lubrication is related to the viscosity of the base oil.

1 Introduction

Industrial robots are operated by servomotors and reduction gears in their joints. Grease lubrication of the reduction gears is important for the delicate movements of the robot, and radial seals prevent grease leakage. These sealing mechanisms in oil lubrication have been studied by various authors and are comparatively well understood [1]. However, many aspects of the sealing mechanism have not been understood, with grease as the sealing target in oscillating operation. Oscillating operation is defined here as an operation pattern that rotates in the forward and reverse circumferential directions, the same as the joints of an industrial robot. Grease generally contains a base oil, thickener and additives. It is a non-Newtonian fluid with frequency dependence. Because thickeners have the ability to retain the base oil and reduce friction. It is necessary to observe the base oil and thickener individually to understand the lubrication condition in grease lubrication. Y. Sato et al observed the lubrication film on the radial seal in oil using LIF (Laser Induced Fluorescence). However, the lubrication film on the radial seal in grease was not observed [2]. It is known that infrared spectroscopy and fluorescence induced microscopy are effective in observing grease behaviour in situ. These methods were used due to their special feasibility of observing film thickness and thickener individually [3,4]. Previous research suggest thickener particles are present in the sealing gap and influence the performance of the sealing system [5]. However, there are no results of individual observations of the film thickness and thickener in the grease lubrication film on the radial seals. In this study, the sealing surfaces of radial seals in grease lubrication were observed individually for film thickness and thickener using a fluorescence induced microscopy.

2 Amount of leakage and pump rate

First, the seal surfaces were observed in grease and oil lubrication to measure the amount of leakage and pump rate. To replicate the motion of an industrial robot joint, a servo motor was used. Three different operations were tested. A hollow glass shaft was used for the shaft and the sealing surface was observed in-situ using a mirror from inside the shaft.

2.1 Sample and test rig

A schematic diagram of the test rig is shown in Figure 1. A hollow glass shaft was used for the shaft. The sealing surface and amount of leakage was observed from the inside of the shaft using a mirror. An observed image is shown in Figure 2. The test conditions and operations are shown in Table 1, movement of the shaft in each operation is shown in Figure 3, and the test program under each operation is shown in Figure 4. To investigate the effects of the oscillating operation, we tested three operations: one with a small oscillation angle (A), one with a one-way rotation stop (B) to investigate the effects of the pause that occurs during the oscillating operation, and one with a large oscillation angle (C). FKM radial seals were used for the test sample. The lubricants used were lithium soap grease, often used to lubricate reduction gears for industrial robots, and PAO (Poly-Alpha-Olefin), which is a base oil component of lithium soap grease. Sample details are shown in Table 2.

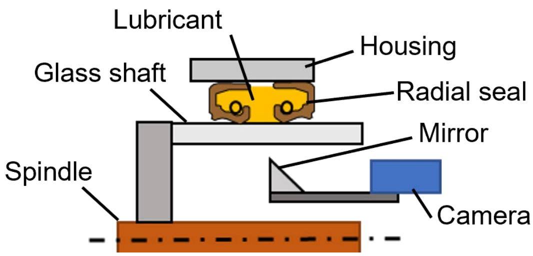

Figure 1 : Schematic diagram of test rig

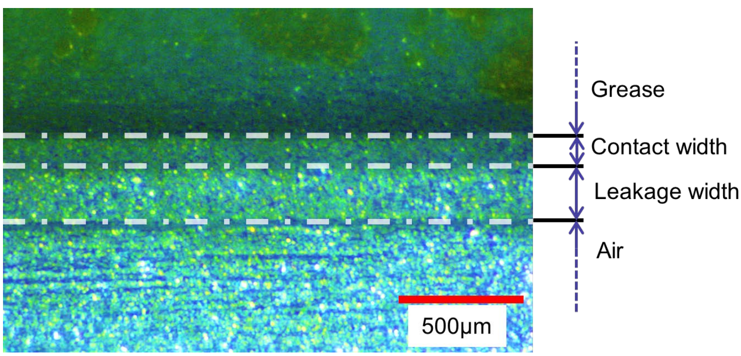

Figure 2 : Observation imager

Table 1 : Test condition

	(A)	(B)	(C)
Shaft eccentricity	T.I.R. aiming for 0mm		
Rotation speed	Max 42mm/s		
Operation	Oscillation	One-way rotary stop	Oscillation
Oscillation angle	17°	45°	90°
Test time	24~48h		

Table 2 : Sample details

Test radial seal			
Material	FKM		
Remarks	Dust lip cut out		
Lubricant			
	Li soap grease1	Li soap grease2	oil
Base oil	PAO		
Base oil viscosity, cSt@40℃	30,191		30,191,400
Thickener	12-Hydroxystearic acid lithium salt		-
Thickener shape	Long fiber	Short fiber	-
Penetration	285		-

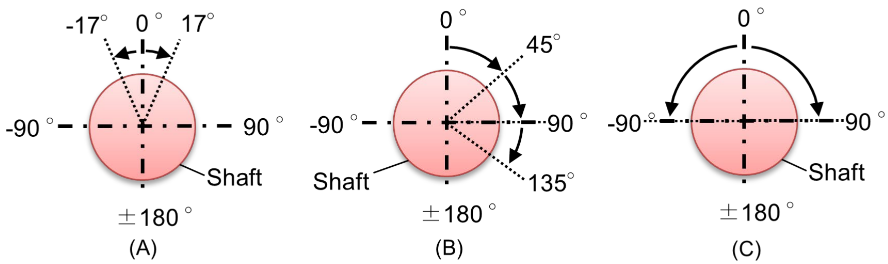

Figure 3: Movement of the axis in each operation

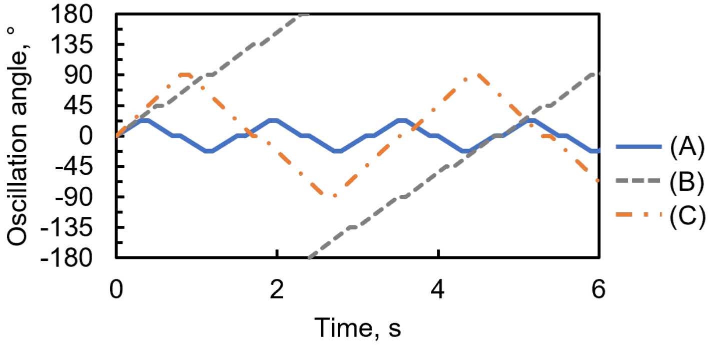

Figure 4: Program of each operation

2.2 Results and discussion

The results of leakage measurements using oil with a viscosity of 30 cSt under (A) operating conditions are shown in Figure 5. These tests were conducted four times with new radial seals under the same conditions and changes in leakage were observed. The amount of leakage increased linearly with the sliding distance. Also, the amount of leakage was different in all four cases despite the same test operations. This is probably due to some other factor than insufficient pump rate during oscillating operation. The results of the seal test for each lubricant under operations (A) and (B) are shown in Table 3. Test results are indicated only as leak or seal. This was because the amount of leakage was different for each test. From those results, the higher the viscosity of the base oil, the less tendency to leak during oscillating operation. In test operation (B), any lubricant would seal. Pump rates were also measured in each operation. Pump rate was calculated from the amount of leakage caused by installing the seals backwards. When measuring with this method, it was necessary to determine whether the leakage volume is due to gap leakage or leakage due to pump effect. Therefore, only the sealed condition of PAO and 400cSt was considered. The results are shown in Table 4. It was found that the pump rate tends to increase in proportion to the oscillation angle. This seemed to show that the pump rate is related to the sliding distance, even during oscillating operation. When the sealing target is oil, the pump rate related to the viscosity, the lubricant with higher viscosity seemed to seal better. When the sealing target is grease, the pump rate is also related to the base oil viscosity and showed a tendency to increase the sealing performance.

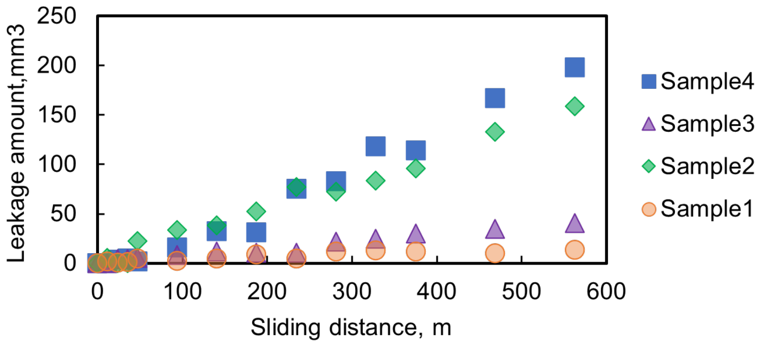

Figure 5: Visualization test result (about leakage amount)

Table 3: Seal test result

Operation	Oscillating							One-way rotary		
Lubricant	PAO			Li soap grease				PAO	Li soap grease	
Thickener shape	-			Long fiber		Short fiber		-	Long fiber	Short fiber
Base oil Viscos-ity(cSt)	30	191	400	30	191	30	191	30	30	30
Condition	Leak	Leak	Seal	Leak	Seal	Leak	Seal	Seal	Seal	Seal

Table 4: Pump rate at each oscillation angle

Operating conditions	Pump rate (mm^3/min)
Oscillating operation at 17°	0.25
One-way rotary stop operation at 45°	1.07
Oscillating operation at 90°	1.29

3 Fluorescence observation

From the measured leakage and pump rate, it was found that the base oil viscosity of the grease is related to the sealing property. To find out how the thickener affects pump rates and leakage, the sealing surfaces of the radial seal were observed individually for film thickness and amount of thickener using the fluorescent method.

3.1 Sample and test rig

A schematic diagram of the test apparatus is shown in Figure 6. A mercury xenon lamp and a line laser were used as light sources. An excitation filter was used to extract light of the wavelength that excites the fluorescent agent from the light source, and an emission filter was used so that only the light that fluoresces can be observed. For the test sample, a FKM radial seal was used, and for the lubricant, fluorescent agents were dissolved in the Li soap grease1 in Table 2. Pyrene was used as the fluorescent agent to observe the film thickness, and Coumarin 6 to observe the amount of thickener. 1 wt.% of Pyrene and 500 ppm of Coumarin6 was dissolved in Li soap grease1. To observe the behaviour of thickener and film thickness of grease during pumping, the lip was pushed with a spatula to make it leak to the air side.

3.2 Results and discussion

Figures 7 and 8 show the distribution of luminance on the sliding surface. Because the luminance is proportional to the film thickness and thickener amount, Figures 7 and 8 represent their respective distribution [4]. The film thickness distribution of the radial seal for grease lubrication was found to be thinner toward the air side. This result is similar to the film thickness distribution during oil lubrication of radial seals [2]. The distribution of thickener was different from that of the film thickness distribution, and the amount of thickener seemed to be almost constant in the contact area. From the results, the base oil in the grease appeared to flow along the contact pressure distribution in the contact area. The thickener remained trapped in the contact area as in the start of the test. It was observed that occasionally agglomerates of the thickener would enter the contact area. However, the base oil basically flowed within the contact area while most of the thickener did not.

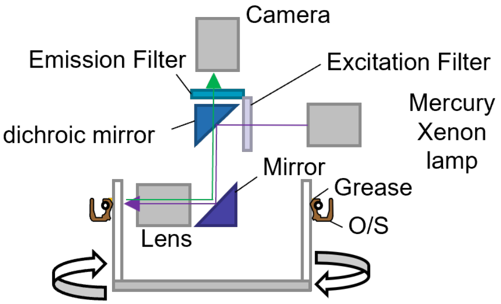

Figure 6: Schematic of Fluorescence observation

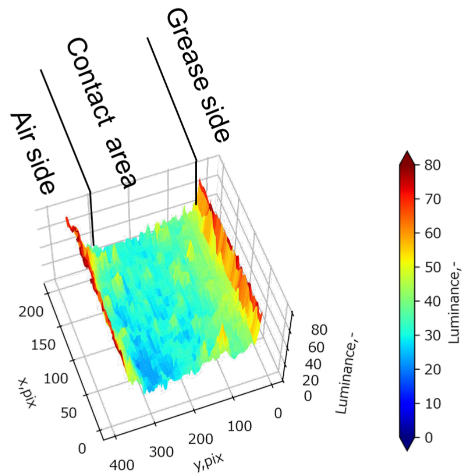

Figure 7: Distribution of film thickness on sealing surface

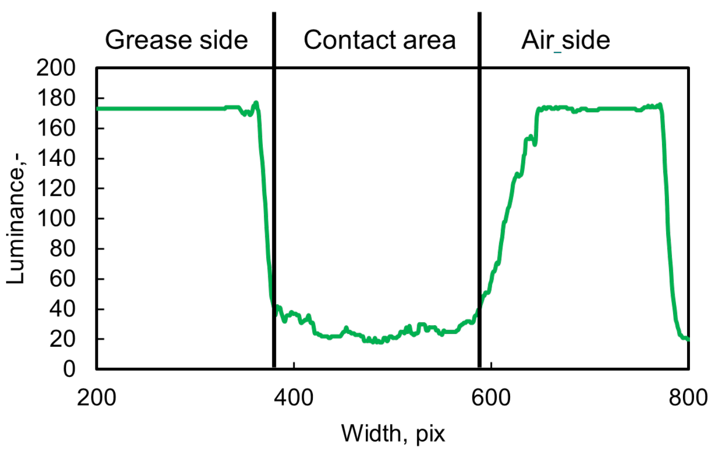

Figure 8: Distribution of thickener amount on sealing surface

4 Summary

To investigate the lubrication and sealing mechanism of radial seals in industrial robots, seal performance tests and sealing surface observation using a fluorescence method in grease lubrication were conducted. The pump rate in grease lubrication seemed to be related to the viscosity of the base oil. The pump rate tends to increase and sealing performance improves in proportion to the oscillation angle. This suggests pump rate required for sealing could differ depending on the oscillation operating conditions. Fluorescence observation might be useful to investigate the state of the lubricant seal in more detail.

5 References

[1] Jagger,E.T. :*Rotary shaft seals: the sealing mechanism of synthetic rubber seals running at atmospheric pressure*, Proceedings of the Institution of Mechanical Engineers, Vol171,Issue1 p.597-616,1957

[2] Sato,Y.: *Study of lubrication mechanism on oil seals*, Kyushu University, 2001

[3] Yasushi, H., Koji, T., Hidetaka, N., Shigeyuki, M., *In situ Observation of Transient Responses in Grease Lubrication by Micro Infrared Spectroscopy*, J. Japanese Soc. Tribol. (Toraiborojisuto), 4, 15, 201, 2020

[4] David, K., Michal, O., Josef, F., Ivan, K., Martin, H., *Novel in-situ observation of the grease constituents in elastohydrodynamic contacts by fluorescence microscopy*, Faculty of Mechanical Engineering, Brno University of Technology, 17, 8, 2022

[5] Max, S., Werner, H., *A new approach on grease tribology in sealing technology: Influence of the thickener particles*, Tribology International, 103, 574-583, 2016

6 Authors

NOK corporation

4-3-1 Tsujidoshinmachi Fujisawa-shi, Kanagawa-ken, 251-0042 Japan:

Takao Horiuchi, M. Sc., horiuchi.22.takao@jp.nokgrp.com

Yohei Sakai, M. Sc., sakai.13.yohei@jp.nokgrp.com

Dr.-ing. Ayako Aoyagi, aoyagi.07.ayako@jp.nokgrp.com

https://doi.org/10.61319/A8RFWQRZ

Group B
Session 5

Applications in practice II

B 12

Serhii Shevchenko, G.E. Pukhov Institute for Modelling in Energy Engineering, Kyiv, Ukraine

Study of the non-contact seals influence on the centrifugal machine's dynamic characteristics

B 13

Thomas White, Aalto-korkeäkoulusäätiö Department of Mechanical Engineering, Helsinki, Finland

Thermal Behaviour of Marine Lip Seals – A Pathway Towards Condition Monitoring

B 14

Omar Morad, Vesa Saikko, Raine Viitala, Aalto University Mechanical Engineering, Espoo, Finland

Frictional behavior of marine lip seals: Sensitivity to operational parameters

B 15

Joseph Kaleshian, Ray Clark, Henri Azibert, Michael Grimanis, A.W. Chesterton Company Innovation Engineering, Groveland, United States

A method of direct thermal conditioning of mechanical seal faces: CFD, empirical analysis and testing

Study of the non-contact seals influence on the centrifugal machine’s dynamic characteristics

Serhii Shevchenko

As the parameters of centrifugal machines increase, it becomes more and more difficult to ensure the effectiveness of sealing. Non-contact seals, in addition to sealing, perform an equally important function – to improve the vibration state of the centrifugal machine. Models of systems "rotor-gap seals", impulse seals, "rotor-hydraulic face" and seals-supports of a shaftless pump have been studied to assess the effect of seal systems on the oscillatory characteristics of the rotor. Analytical dependencies are obtained for calculating the dynamic characteristics and stability limits of seals as hydromechanical systems. The proposed general technique makes it possible to purposefully select the design parameters of seals to adjust work in vibration-safe modes.

Introduction

The rotor sealing system of a high-speed centrifugal machine is one of the most complex and critical units that determine the reliability of the entire unit. This is due to the harsh operating conditions of the seals, combined with high tightness requirements in all operating modes [1, 2].

Non-contact seals, in addition to the function of sealing, perform no less important - they improve the vibration state of the centrifugal machine [3, 4, 5]. Structural measures aimed at increasing the hydraulic resistance of seals, as a rule, increase their hydrostatic stiffness and damping, and thereby improve their dynamic qualities [6, 7]. Dynamic performance is especially important for seals in high-speed rotary machines.

Another important indicator is the resource of the assembly, which is determined by the wear of the sealing surfaces. When designing sealing systems, it is necessary to coordinate their tightness and reliability, on the one hand, and resource indicators, on the other [8, 9].

The creation of highly loaded equipment with sealing systems for non-standard operating conditions is impossible without taking into account the above factors [10]. Examples of such non-standard products are pumping units for nuclear power plants [11] and turbopump units for rocket engines [12].

Pumps for the power industry need an increased resource of sealing units. To do this, it is necessary to use sealing systems with guaranteed controlled leakage in order to provide lubrication and cooling, and, consequently, the required service life [13].

The seals of LRE turbopump units operate under extreme conditions, for which vibration reliability and tightness are the most important requirements [14]. The requirement for a low mass of equipment leads to the creation of units with flexible rotors, which can have significant deflections during transient conditions.

In connection with the transition of aerospace technology to reusable systems, their engines are designed for repeated activation, so the required resources reach tens of hours. All these new increased requirements for engine operation complicate the already difficult work of sealing assemblies.

Modern approaches to the creation of mathematical models of oscillatory systems based on experimental data are presented in [15, 16]. Monograph [17] evaluates the coefficients of mathematical models of oscillatory systems, including rotor systems for multistage centrifugal machines. In works [18, 19] the phenomena of loss of stability of rotation of the rotor in rolling bearings are considered.

Modern approaches in the field of linear and nonlinear dynamics of rotors and their practical applications are presented in the monograph [20]. The works [21, 22] gives an estimate of the rigidity of segment bearings during balancing of flexible rotors of turbine. Modern methods for determining the stiffness of active magnetic bearings and identifying damping from the frequency responses of control systems are presented in [23, 24]. The application of the finite element method for calculating the stiffness and critical speed of the magnetic bearing-rotor system for electrical machines is described in the article [25]. The article [26] presents an analysis of the stability and vibration of a complex flexible rotor-bearing system. In [27], the phenomenon of subharmonic resonance of a symmetric ball-bearing-rotor system was studied. In [28], models are proposed for studying the critical frequencies of the rotor of a centrifugal compressor, taking into account the nonlinear stiffness characteristics of bearings and seals.

As indicated in [29], the energy of volume losses can be converted into useful energy if slot seals are used simultaneously as hydrostatic supports, capable of not only having high radial rigidity, but also effectively damping rotor vibrations to acceptable values, even in the presence of a significant imbalance. This effect is especially significant in the presence of steep velocity and pressure gradients inherent in the small gaps of slotted seals, on which high pressure drops are throttled and one of the surfaces belongs to the rotor, which simultaneously rotates and vibrates [30, 31]. In [32], the dynamic characteristics of slotted seals as intermediate supports were studied.

The hydrodynamic characteristics of slotted seals, taking into account the flow of the sealed liquid in the annular channels, the surfaces of which rotate and simultaneously perform radial-angular oscillations, are considered in [33]. The results of the conducted studies show that when creating sealing systems of modern centrifugal machines, it is necessary to take into account the effect of non-contact seals on the dynamic characteristics of the rotor [34, 35, 36].

Thus, it became necessary to create a methodology for the design and calculation of sealing systems based on the configuration of seal components in order to achieve harmonization between sealing and vibration reliability.

1. Algorithm for constructing dynamic characteristics of non-contact seals

For an analytical description of the processes occurring in sealing units, we will consider them as automatic control systems.

The model of the hydromechanical system "rotor - slotted seals", presented in the paper [29], is shown in fig. 1.

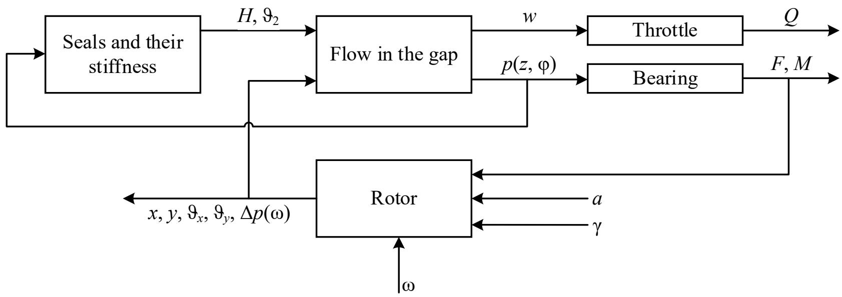

Fig. 1. Hydromechanical system rotor-slotted seals

Hydrodynamic forces and moments arise in the sealing gaps, which depend on the nature of the rotor movement. At the same time, these forces and moments affect the radial and angular oscillations of the rotor.

On the other hand, the pressure distribution in the gap depends on the shape of the gap, and the deformations of the gap walls are determined by the pressure distribution in this gap.

Thus, due to the occurrence of feedbacks, a hydromechanical system is formed.

The model of a non-contact mechanical seal, as a system for automatic control of the mechanical clearance and leakage, on the example of impulse compaction [14] is shown in fig. 2.

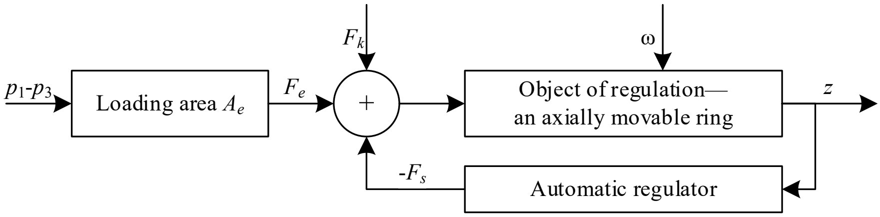

Fig. 2. Impulse seal as the automatic control system

At present, for large high-pressure multistage pumps, the most effective way to balance axial forces is to use automatic balancing devices that simultaneously perform the functions of a radial-face non-contact seal and a journal-thrust hydrostatic bearing.

Automatic balancing devices, despite the many designs, are built according to the general principle: negative feedback is created between the balancing force and the axial position of the rotor, providing only small deviations of the axial position of the rotor from some predetermined position [37].

The model of the automatic balancing device is shown in fig. 3

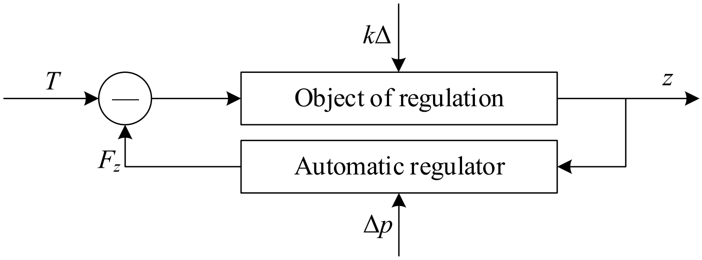

Fig. 3. The balancing device

Non-contact rotor seals have gaps of the same order as in journal bearings. Therefore, the seal is a full-circle bearing, the bearing capacity of which is ensured not only by the rotation of the eccentrically located shaft, but also, first of all, by a significant axial pressure drop throttled on the seal.

An example of the use of non-contact seals as supports is the so-called shaftless pumps [38] (Fig. 4), in the design of which the functions of the supports are already deliberately shifted to the seals.

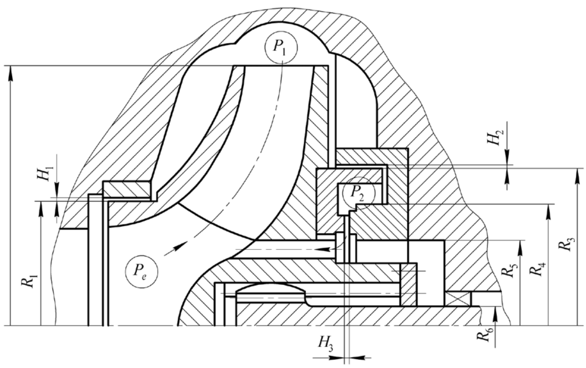

Fig. 4. Scheme of a shaftless pump

The non-contact mode of operation of the impeller of such a pump is determined by the hydrodynamic characteristics of the system of automatic offloading of axial forces and slotted seals.

The impeller of a shaftless pump with a support-seal assembly is a system of automatic control of a variable end clearance, which creates negative feedback [39]. Therefore, for its study, one can jointly use the above models of slotted seals and automatic balancing device.

2. Frequency characteristics and evaluation of dynamic stability

Forced joint radial-angular oscillations of the rotor at a constant pressure drop across slotted seals are described by the equations [31]

$$\begin{aligned}
&a_1\ddot{u}+a_2\dot{u}+a_3u\mp i\left(a_4'\dot{u}+a_5'u\right)\omega-\left(\alpha_2'\dot{\theta}+\alpha_3'\theta\right)\omega\mp\\
&\mp i\left(\alpha_4\dot{\theta}+\alpha_5\theta-\alpha_0\theta\right)=\omega^2a^*=\omega^2\left|a^*\right|e^{\pm i\omega t},\\
&b_1\ddot{\theta}+b_2\dot{\theta}+b_3\theta\mp i\left(b_4'\dot{\theta}+b_5'\theta\right)\omega+\left(\beta_2'\dot{u}-\beta_3'u\right)\omega\mp\\
&\mp i\left(\beta_4\dot{u}+\beta_5u+\beta_0u\right)=\left(1-j_0\right)\omega^2\gamma^*=\left(1-j_0\right)\omega^2\left|\gamma^*\right|e^{\pm i\omega t}.
\end{aligned}\qquad(1)$$

Substituting the solution of equations (1) in the form

$$u=u_ae^{i(\omega t+\varphi_u)}=\tilde{u}e^{i\omega t},\;\;\theta=\theta_ae^{i(\omega t+\varphi_\vartheta)}=\tilde{\theta}e^{i\omega t},$$

we obtain a system of algebraic equations for the complex amplitudes A and Γ:

$$\begin{aligned}
&\left[-a_1\omega^2+a_3+a_4\omega^2+i\left(a_2-a_5\right)\omega\right]\tilde{u}-\left[\left(\alpha_3-\alpha_4\right)\omega+i\left(\alpha_2\omega^2+\alpha_5-\alpha_0\right)\right]\tilde{\theta}=\mathrm{A}\omega^2\\
&\left[-\left(\beta_3-\beta_4\right)\omega+i\left(\beta_2\omega^2-\beta_5-\beta_0\right)\right]\tilde{u}+\left[-b_1\omega^2+b_3+b_4\omega^2+i\left(b_2-b_5\right)\omega\right]\tilde{\theta}=\Gamma\omega^2.
\end{aligned}\qquad(2)$$

From the system of inhomogeneous algebraic equations (2), after a series of transformations, we obtain the amplitudes and phases expressed in terms of external perturbations:

$$\begin{aligned}
&u_a=\overline{\omega}^2\sqrt{\frac{\left(\mathrm{A}U_{22}-\Gamma U_{12}\right)^2+\left(\mathrm{A}V_{22}-\Gamma V_{12}\right)^2}{U_0^2+V_0^2}},\\
&\theta_a=\overline{\omega}^2\sqrt{\frac{\left(\Gamma U_{11}-\mathrm{A}U_{21}\right)^2+\left(\Gamma V_{11}-\mathrm{A}V_{21}\right)^2}{U_0^2+V_0^2}},\\
&\varphi_u=-\operatorname{arctg}\frac{\left(\mathrm{A}U_{22}-\Gamma U_{12}\right)V_0-\left(\mathrm{A}V_{22}-\Gamma V_{12}\right)U_0}{\left(\mathrm{A}U_{22}-\Gamma U_{12}\right)U_0+\left(\mathrm{A}V_{22}-\Gamma V_{12}\right)V_0},\\
&\varphi_\vartheta=-\operatorname{arctg}\frac{\left(\Gamma U_{11}-\mathrm{A}U_{21}\right)V_0-\left(\Gamma V_{11}-\mathrm{A}V_{21}\right)U_0}{\left(\Gamma U_{11}-\mathrm{A}U_{21}\right)U_0+\left(\Gamma V_{11}-\mathrm{A}V_{21}\right)V_0}.
\end{aligned}\qquad(3)$$

Using a similar algorithm, it is possible to obtain expressions for amplitudes and phases for other types of non-contact seals.

For impulse seals [14]:

$$A\left(\omega\right)=\sqrt{\frac{b_1^2+\omega^2b_0^2}{U^2+\omega^2V^2}},\varphi=-\operatorname{arctg}\omega\frac{b_0U-b_1V}{b_1U+\omega^2b_0V}.\qquad(4)$$

The amplitude and phase frequency characteristics of the auto-balancing system according to the corresponding external influences have the form:

$$A_{\tau}(\omega)=\sqrt{U_{\tau}^{2}+\omega^{2}V_{\tau}^{2}}=\sqrt{\frac{U_{p}^{2}+\omega^{2}V_{p}^{2}}{U^{2}+\omega^{2}V^{2}}},\quad \varphi=\operatorname{arctg}\omega\frac{UV_{p}-VU_{p}}{UU_{p}+\omega^{2}VV_{p}} \qquad (5)$$

and for shaftless pumps [39]:

$$A\ (\omega)=\sqrt{\frac{U_{e}^{2}+\omega^{2}V_{e}^{2}}{U_{0}^{2}+\omega^{2}V_{0}^{2}}},\qquad \varphi\ (\omega)=\operatorname{arctg}\omega\frac{U_{0}V_{e}-U_{e}V_{0}}{U_{0}U_{e}+\omega^{2}V_{0}V_{e}}; \qquad (6)$$

As can be seen, expressions (3-6) for the amplitudes and phases of various non-contact sealing systems have a similar form.

The stability is determined using the Routh-Hurwitz criterion for a system of 4th order [40]

$$a_2\left(a_2a_3+a_4a_5\right)-a_1a_5^2>0,$$

which reduces to the form [37]:

$$\omega_u^2<\frac{a_{21}^2\Omega_{u0}^2}{a_1a_5^2-a_{21}^2a_{31}-a_{21}a_4a_5}. \quad (7)$$

It can be seen from inequality (7) that the main destabilizing factor is the circulation force characterized by the coefficient a_5. Damping a_{21}, gyroscopic force a_4 and shaft flexural stiffness Ω_{u0} stabilize the rotor in seals.

For impulse seals, the stability criterion is reduced to the inequality [2]:

$$V_0<\frac{A_sEz_0g_{s0}}{3(1+n_i)(k_1g_{30}-k_3g_{10})(p_{10}-p_{30})}. \qquad (8)$$

from which it is possible to determine the stability-admissible volume of impulse seal chambers V_0. Where $g_{s0}=g_i+g_{10}+g_{30}=g_{sn}z_0^3$, $k_1=\frac{g_i'+g_{10}}{g_{s0}}$, $k_3=\frac{g_{30}}{g_{s0}}$.

It can be seen from inequality (8) that the stability region of the seal expands due to a decrease in the volume of the chambers and in the coefficient of hydrostatic stiffness.

For a balancing device

$$V<\frac{A_ehEg_s^2z_0}{3Q_0^2}, \qquad (9)$$

Inequality (9) limits the volume of the balancing face chamber, at which the stability of independent axial oscillations of the rotor is maintained.

For the seals-bearings, the axial stability condition is reduced to the inequality

$$h<\frac{Ez_0}{3p_n}\cdot\frac{\Delta\psi_{s0}}{\Delta\psi_{20}\Delta\psi_{c0}}. \quad (10)$$

Since the chamber depth *h* is an independent parameter that can be easily modified by design, condition (10) can be used when designing a pump to ensure its stability.

As can be seen from inequalities (7-10), the dynamic stability conditions for various types of non-contact seals also have a similar form. By adjusting the design parameters of the seals, which are included in these inequalities, it is possible to expand the boundaries of stable operation.

3. Results

On fig. 5 shows the frequency responses built for three values of the taper parameter. For a diffuser channel $(\theta_0 = -0.3)$, the total resistance is negative. For cylindrical $(\theta_0 = 0)$ and confusor $(\theta_0 = 0.3)$ channels, the stability condition is satisfied at all speeds.

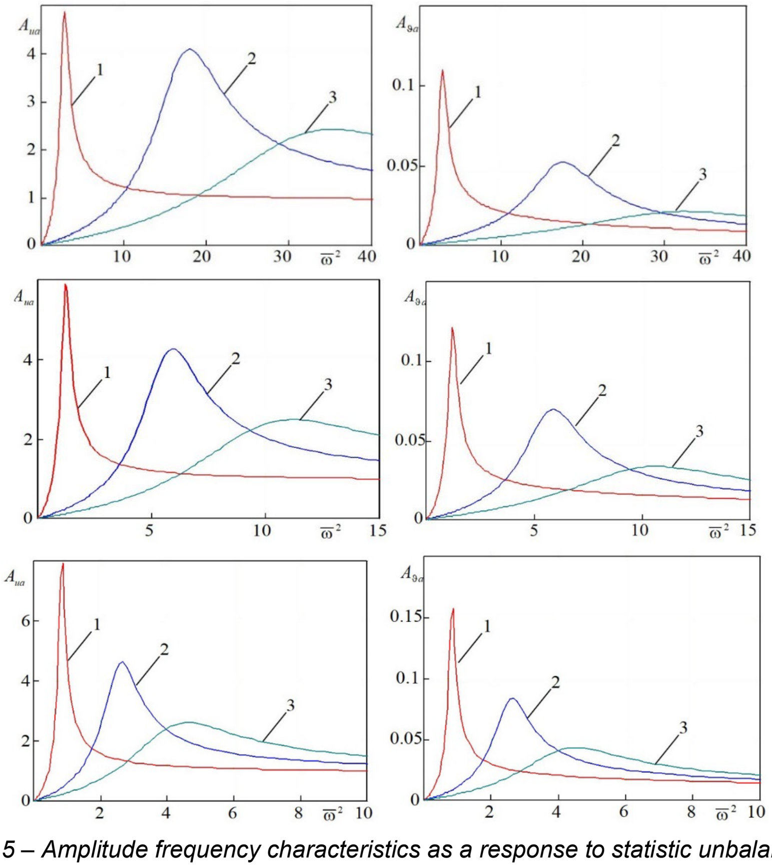

Fig. 5 – Amplitude frequency characteristics as a response to statistic unbalance:

$a-\Delta p_0 = 1.5$ MPa $=$ const, $b-\Delta p_0 = 4$ MPa $=$ const, $c-$ $\Delta p_0 = 13.3$ MPa $=$ const

$1-\theta_0 = -0.3;\ 2-\theta_0 = 0;\ 3-\theta_0 = 0.3$

In seals with a diffuser gap $(\theta_0 = -0.3)$, the rotor is unstable even in the absence of rotation. The research results showed that the critical value of the diffuser is $\theta_{0*} = -0.27$. In a cylindrical gap at $\Delta p_0 = 1.5$ MPa, the limiting stability dimensionless speed is $\overline{\omega}_* \approx 6.5$. With an increase in the pressure drop to 4 MPa, an instability region appears in the range $\overline{\omega} \approx 3-4$. Confusor seals ensure the stability of the rotor at all investigated speeds.

4. Discussion

An analysis of the gap seals' dynamic characteristics showed that the force coefficients of slotted seals are determined by geometric (clearance, radius, length, taper, shape of the leading edges) and operational (pressure drop, operating speed range, physical properties of the pumped medium) parameters. With a purposeful choice of these parameters, it is possible to influence the vibrational state of the rotor and the machine itself.

An important feature of centrifugal machines is that the pressure drops throttled at the gap seals are proportional to the rotor speed. This is due to the self-tightening effect of the rotor, which leads to a positive shift of the critical frequencies.

The operation of non-contact mechanical seals is accompanied by complex non-stationary, high-frequency hydrodynamic processes determined by micron end gaps. For the analytical description of the processes, a model for a sealing in the form of an automatic control system is proposed.

Automatic compensation systems for axial forces acting on the rotor of a multistage centrifugal pump simultaneously perform the functions of a self-adjusting non-contact mechanical seal and a heavily loaded radial-axial hydrostatic bearing. Such systems largely determine the oscillatory state of the rotor.

Axial and radial hydrodynamic forces arising in the throttling gaps of the balancing device are interconnected. As a result, the "rotor-auto-offloading" system, under the influence of the inevitable radial static imbalance, discharge pressure pulsations and harmonic changes in the axial force acting on the rotor perform interconnected forced radial-axial oscillations. At rotational frequencies coinciding with any natural frequency, the resonant amplitudes of these oscillations can exceed the permissible limits, therefore, the determination of resonant rotational frequencies and detuning from them is of great practical importance.

The wheel of a shaftless pump performs independent axial oscillations under the action of kinematic excitation in the form of given radial oscillations due to the static imbalance of the impeller. In this case, the adjustable end throttle creates negative feedback, so the impeller with the support-seal assembly is an automatic control of the end clearance system.

When designing a shaftless pump, it is necessary to compute the axial and angular vibrations of the impeller freely floating in the slotted seals. This will allow to ensure self-tightening of the rotor relative to its oscillations and avoid destabilizing factors by selection of design parameters.

Similar support-balancing devices can also be successfully used in multistage centrifugal pumps.

Using the proposed general approach to the analysis of non-contact seals as automatic control systems, and the algorithm for constructing their dynamic characteristics at the design stage, it is possible, by changing the geometric parameters of the seals, to ensure their vibration resistance margin.

5. Examples of building a complex sealing system

Fig. 6 shows the sealing system of the Nuclear Power Plant (NPP) main circulation pump [6]. The operating pressure and water temperature in the primary circuit are 12.5 MPa and 270°C, respectively. The seal operates on blocking water, which is taken from the primary circuit, cooled to 40°C and cleaned by passing through the cooler and ion-exchange filter. Automatic regulators maintain a predetermined (0.5–0.6 MPa) excess of the blocking water pressure over the pressure in the pump cavity, as a result of which about 50% of the input water (0.3–0.5 m^3/h) enters the pump, excluding the exit from it of a hot radioactive coolant.

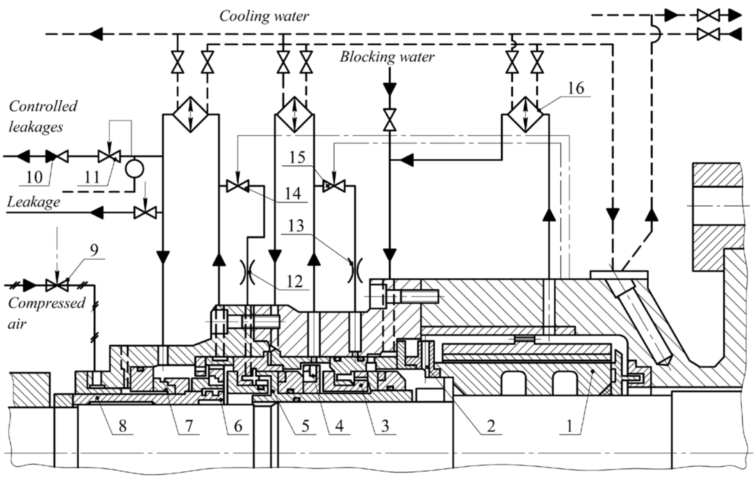

Fig. 6. Diagram of RCP shaft seal [6]

On fig. 7 shows [41] a design diagram of the separation unit of the TPU seals between the oxygen pump and the TPU turbine of the Space Shuttle engine, driven by hot gas with excess hydrogen (“sweet” gas). With an “acidic” fuel environment in the pump and “sweet” gas in the turbine adjacent to the pump, leakage from the pump to the turbine and mixing of these leaks with turbine gas is unacceptable, since this mixture is explosive.

The separating block of the sealing system in this case is a very important element of the pump and consists of several sealing units: a bellows mechanical seal with a friction pair 1, 2 on the side of the cavity 3 with liquid oxygen, a block of floating rings 4, 5 and a block of floating rings 6, 7 with sides of the cavity 8 with gaseous hydrogen, between which there is a chamber for supplying 9 helium barrier gas. Spiral grooves are made on the contact surface of the rotating ring 1. Drainage channels 10 serve to drain the helium mixture and oxygen leaks, and channels 11, 12 - to drain the helium mixture and the hydrogen-enriched gas mixture overboard the engine.

Compressed helium on board the ship is stored in a cylinder, and its consumption can determine the number of engines starts and the total duration of the ship's flight.

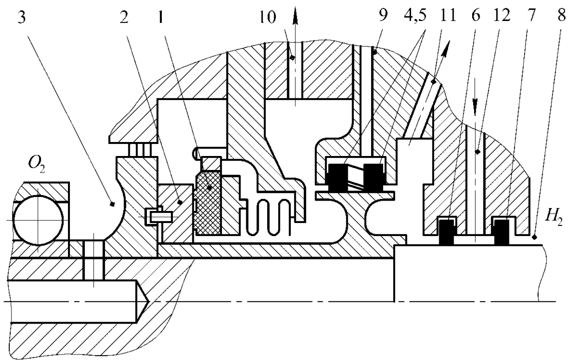

Fig. 7. Sealing system between oxygen pump and turbine with reducing media:

1, 2 - rotating and non-rotating rings of a friction pair; 3 - cavity of liquid oxygen; 4, 5 - block of floating rings from the side of the oxygen cavity; 6, 7 - a block of floating rings from the side of the cavity with gaseous hydrogen; 8 - cavity with gaseous hydrogen; 9 - chamber for supplying helium barrier gas; 10 - drainage channels for removing helium mixture and oxygen leaks; 11, 12 - drainage channels for removing a mixture of helium and gas enriched with hydrogen

The operating parameters of such a mechanical parking seal TPU LRE: sealing pressure drop 3.1 MPa, sliding speed 180 m/s; the required resource is 10 h with the number of inclusions of TPU on the order of 300.

Summary and Conclusion

The development of complex sealing systems must be carried out based on the configuration of the constituent seals in order to achieve harmonization between sealing and vibration reliability, taking into account oscillatory processes due to hydrodynamic sealing characteristics.

The studies carried out have shown that all sealing units with throttling gaps or sealing paths filled with a high-pressure medium to be sealed should be considered as dynamic systems. The medium to be sealed, acting on the walls of the sealing paths, affects the dynamic state of the rotor.

It is shown that the purposeful choice of the design parameters of the seals makes it possible to improve the vibrational state of the rotor. In this case, the initially "flexible" dynamically rotor, in combination with properly designed seals, becomes "rigid". The proposed general technique makes it possible to evaluate this effect depending on the design characteristics of the seals and, by changing them at the design stage, to rebuild the “rotor-seals-auto-unloading” system from resonant operating modes.

Nomenclature

LRE	Liquid Rocket Engine
MPC	Main circulation pump
NPP	Nuclear power plant
TPU	Turbo pump unit

Variable	***Description***	***Unit***
a	eccentricity of mass center	m
a_{ij}	the coefficients of the equations of motion, which depend on the parameters of the gap seals	-
A_e	the effective area of the balancing face disk	m^2
A_s	is the area of the end surface of the impulse seal chamber sector	m^2
E	isothermal volumetric module of the sealed medium elasticity	Pa, N/m^2
F	hydrodynamic forces arising in sealing gap	N
F_e	external force (regulating influence) of the impulse seal	N
F_k	force of elastic elements of the impulse seal	N
F_s	pressure force opening the butt joint of the impulse seal	N
F_z	pressure force in the end gap of the impulse seal	N
g_{10}, g_{30}	conductivities of the corresponding end throttles for a steady value of the impulse seal gap z_0	$(m^7/kg)^{0.5}$
g_i	conductivity of the impulse seal feeders	$(m^7/kg)^{0.5}$

g_s	the total conductivity of the radial and end chokes of the unloading device	$(m^7/kg)^{0.5}$
h	is the chamber depth of the unloading device	m
H	mean radial clearance of gap seal	m
k	compression ratio of the pressing device	-
M	hydrodynamic moments arising in sealing gap	Nm
n_i	number of feeders for impulse seal	-
$p(z, \varphi)$	gap pressure	Pa, N/m^2
p_1	sealing pressure of the impulse seal	Pa, N/m^2
p_3	back pressure of the impulse seal	Pa, N/m^2
p_{10}, p_{30}	sealing pressure and counterpressure for a steady value of the impulse seal gap z_0	Pa, N/m^2
p_n	nominal discharge pressure	Pa, N/m^2
Q	seal leakage	m^3/h
Q_0	seal leakage in steady state	m^3/h
T	axial force	N
V	volume of balancing face chamber	m^3
V_0	volume of impulse seal chamber	m^3
w	gap fluid flow rate	m/s
x, y	radial vibrations of the rotor	m
z	end gap (adjustable)	m
z_0	clearance in steady state of the unloading device	m
γ	angle of deviation of the inertia axis	rad
Δ	deformation of the pressing device	m
Δp	sealing pressure	Pa, N/m^2
$\Delta\psi_{s0}$, $\Delta\psi_{20}$, $\Delta\psi_{c0}$	dimensionless pressure drops in the chambers of the shaftless pump	-
ϑ_2	mean radial taper	rad
ϑ_x, ϑ_y	rotor angular oscillations	rad
ω	rotor speed	s^{-1}
Ω_{u0}	the bending stiffness of a shaft	N/m

References

[1] Martsinkovsky, V. Hermomechanics, its role in ensuring the efficiency and environmental friendliness of pumping and compressor equipment. Bulletin of the Sumy State University. Series of technical sciences. 2005. 1 (73). 5—10.

[2] Bondarenko, G. On the Influence of Seals on the Dynamics of the Rotor of a High-Pressure Centrifugal Compressor. In Proceedings of the 10th International Scientific and Technical Conference, Sumy, Ukraine, 10–13 September 2002; Volume 3, pp. 250–251.

[3] Martsynovsky V. Radial-Angular Oscillations of the Centrifugal Machine Rotor in the Groove Bearings-Seals. Proceedings of the Mechanics. Kielce, 1995. 54. 247—259.

[4] Marzinkovski, V. Dynamic characteristics of gap seals. Investigation and application of sealing elements. XI. Dichtungskollokuium. Essen, Vulkan-Verlag, 1999. 251—261.

[5] Marcinkowski, W., Kundera, C. Theory of Non-Contact Seal Design. Wydawnictwo Politechniki Świętokrzyskiej: Kielce, Poland, 2008. 443 p.

[6] Kundera, C.; Marcinkowski, W. The Effect of the Annular Seal Parameters on the Dynamics of the Rotor System. Int. J. Appl. Mech. Eng. 2010, 15, 719–730.

[7] Shevchenko, S.S.; Shevchenko, O.S.; Vynnychuk, S. Mathematical Modelling of Dynamic System Rotor-Groove Seals for the Purposes of Increasing the Vibration Reliability of NPP Pumps. Nuclear and Radiation Safety. 2021, 1(89) 80–87. https://doi.org/10.32918/NRS.2021.1(89).09

[8] Mueller H., Nau B. Fluid sealing technology. New York, Marcel Dekker Inc., 1998. 485 p.

[9] Martsynovskyi, V.A. Groove Seals: Theory and Practice; Sumy State University: Sumy, Ukraine, 2005. 416 p.

[10] Bai C., Zhang H., Xu Q. Subharmonic resonance of a symmetric ball bearing-rotor system. International Journal of Non-Linear Mechanics. 2013, 50, 1—10. https://doi.org/10.1016/j.ijnonlinmec.2012.11.002

[11] Shevchenko S., Shevchenko O. Improvement of Reliability and Ecological Safety of NPP Reactor Coolant Pump Seals. Nuclear and Radiation Safety. 2020. 4(88). 47—55. https://doi.org/10.32918/nrs.2020.4(88).06

[12] Martsynkovskyy V., Gaft Y., Gromyko B., Chernov O. Development and application of double pulse gas-liquid seals. Proc. of 16th International Conference on Fluid Sealing. Brugge, Belgium, 2000, pp. 255–260.

[13] Kim, S.H.; Ha, T.W. Prediction of Leakage and Rotordynamic Coefficients for the Circumferential-Groove-Pump Seal Using CFD Analysis. J. Mech. Sci. Technol. 2016, 30, 2037–2043.

[14] Shevchenko, S., Chernov, A. Development of pulse mechanical seal calculation methods on the basis of its physical model construction. Eastern-European

Journal of Enterprise Technologies, 2020, 3, 2 (105), 58–69. https://doi.org/10.15587/1729-4061.2020.206721

[15] Pavlenko, I.; Simonovskiy, V.; Pite', J.; Demianenko, M. Dynamic Analysis of Centrifugal Machines Rotors with Combined Using 3D and 2D Finite Element Models; RAM-VERLAG: Lüdenscheid, Germany, 2018; ISBN 978-3-942303-64-4

[16] Simonovskiy, V. Refinement of Mathematical Models of Oscillatory Systems according to Experimental Data: Monograph; Sumy State University: Sumy, Ukraine, 2010.

[17] Simonovskiy, V.I. Evaluation of Coefficients of Mathematical Models for Oscillatory Systems; Lambert Academic Publishing: Saarbrücken, Germany, 2015. 100 p.

[18] Pavlenko, I.; Simonovskiy, V.I.; Demianenko, M.M. Dynamic Analysis of Centrifugal Machines Rotors Supported on Ball Bearings by Combined Application of 3D and Beam Finite Element Models. IOP Conf. Ser. Mater. Sci. Eng. 2017, 233, paper ID 012053. https://doi.org/10.1088/1757-899X/233/1/012053

[19] Villa, C.; Sinou, J.-J.; Thouverez, F. Stability and Vibration Analysis of a Complex Flexible Rotor Bearing System. Commun. Nonlinear Sci. Numer. Simul. 2008, 13, 804–821.

[20] Ishida, Y.; Yamamoto, T. Linear and Nonlinear Rotordynamics: A Modern Treatment with Applications, 2nd ed.; Wiley Online Library: Hoboken, NJ, USA, 2012. 355 p. https://doi.org/10.1002/9783527651894

[21] Yashchenko, A.S.; Rudenko, A.A.; Simonovskiy, V.I.; Kozlov, O.M. Effect of Bearing Housings on Centrifugal Pump Rotor Dynamics. IOP Conf. Ser. Mater. Sci. Eng. 2017, 233, paper ID 012054. https://doi.org/10.1088/1757-899X/233/1/012054

[22] Gadyaka, V.; Leikykh, D.; Simonovskiy, V. Phenomena of Stability Loss of Rotor Rotation at Tilting Pad Bearings. Procedia Eng. 2012, 39, 244–253.

[23] Jin, C., Xu, Y., Zhou, J., & Cheng, C. Active magnetic bearings stiffness and damping identification from frequency characteristics of control system. Shock and Vibration, 2016, article ID 1067506. https://doi.org/10.1155/2016/1067506

[24] Wang, T.; Wang, F.; Bai, H.; Cui, H. Stiffness and Critical Speed Calculation of Magnetic Bearing-Rotor System Based on FEA. In Proceedings of the 2008 International Conference on Electrical Machines and Systems, Wuhan, China, 17–20 October 2008; pp. 575–578.

[25] Zhang, K.; Yang, Z. Identification of Load Categories in Rotor System Based on Vibration Analysis. Sensors 2017, 17, article ID 1676. https://doi.org/10.3390/s17071676.

[26] Pozovnyi, O.; Deineka, A.; Lisovenko, D. Calculation of Hydrostatic Forces of Multi-Gap Seals and Its Dependence on Shaft Displacement. Lect. Notes Mech. Eng. 2020, 10, 661–670. https://doi.org/10.1007/978-3-030-22365-6_66

[27] Pozovnyi, O.; Zahorulko, A.; Krmela, J.; Artyukhov, A.; Krmelová, V. Calculation of the Characteristics of the Multi-Gap Seal of the Centrifugal Pump, in Dependence on the Chambers' Sizes. Manuf. Technol. 2020, 20, 361–367. https://doi.org/10.21062/mft.2020.048

[28] Pavlenko, I.; Simonovsky, V.I.; Pitel', J.; Verbovyi, A.E.; Demianenko, M.M. Investigation of Critical Frequencies of the Centrifugal Compressor Rotor with Taking into Account Stiffness of Bearings and Seals. J. Eng. Sci. 2017, 4, C1–C6. https://doi.org/10.21272/jes.2017.4(1).c1

[29] Shevchenko S. Mathematical modeling of centrifugal machines rotors seals for the purpose of assessing their influence on dynamic characteristics. Mathematical Modeling and Computing. 2021. 8(3).422—431. https://doi.org/10.23939/mmc2021.03.422.

[30] Djaidir, B.; Hafaifa, A.; Kouzou, A. Faults Detection in Gas Turbine Rotor Using Vibration Analysis under Varying Conditions. J. Theor. Appl. Mech. 2017, 55, 393–406. https://doi.org/10.15632/jtam-pl.55.2.393

[31] Martsynovskyi, V.A. Dynamics of the Centrifugal Machine Rotors: Monograph; Sumy State University: Sumy, Ukraine, 2012. 562 p.

[32] Korczak, A.; Marcinkowski, W.; Peczkis, G. The influence of sealing gaps on the dynamics of the rotating assembly of a centrifugal pump. Politech. Śląska Pr. Nauk. 2007, 18, 161–170.

[33] Gudkow S., Marcinkowski W., Korczak A., Kundera Cz. Centrifugal pump with an impeller mounted in sealing slots. Proc.XIII Int. ScientificTechnical Conference. Seals and Sealing Technology of Machines and Dewices. Wroclaw, SIMP, 2013, 178-187.

[34] Davidenko, A.; Boyarko, N.; Katsov, S. Improvement of Pumps of the CNS Type with the Use of Built-in Journal Bearings Operating on the Pumped Medium. In Proceedings of the XI International Scientific and Technical Conference, Sumy, Ukraine, 6–9 September 2005; pp. 59–69.

[35] Pavlenko I., Trojanowska J., Ivanov V., Liaposhchenko O. Scientific and methodological approach for the identification of mathematical models of mechanical systems by using artificial neural networks. 3rd Conference on Innovation, Engineering and Entrepreneurship. Regional HELIX 2018. Lecture Notes in Electrical Engineering. 2019, 505, 299—306. https://doi.org/10.1007/978-3-319-91334-6_41

[36] Marcinkowski W., Korczak A., Peczkis G. Dynamics of the rotating assembly of a multistage centrifugal pump with a relief disc. Kielce University of Technology. Terotechnology. 2009. 10. 245—263.

[37] Martsinkovsky, V. A., Zhulyov, A., Kundera, C. Static and dynamics of a pump impeller with a balancing device Part II: Dynamic analysis. International Journal of Applied Mechanics and Engineering, 2014, 19, 3, 621–631. https://doi.org/10.2478/ijame-2014-0043

[38] Gorovoy, S. A. Experimental studies of the pump with self-aligning impeller. Oil and Gas Mechanical Engineering, no. 2, pp. 36–40. 2019.

[39] Shevchenko, S. S., Shevchenko, O. S. Mathematical Model and Calculation Method of a Shaftless Pump with Seals-Bearings. Electronic modeling, 2021, 43(1), 03–16. https://doi.org/10.15407/emodel.43.01.003

[40] Vasylenko M., Alekseychuk, O. Theory of oscillations and stability of motion. Kyiv, Higher School, 2004. 525 p.

[41] Melnyk, V. End seals of shafts. Reference book. Moscow: Mashinostroenie, 2008, 320 p.

Author

Pukhov Institute for Modelling in Energy Engineering (IPME)

General Naumov Str. 15, 03164 Kyiv, Ukraine:

Serhii Shevchenko, Dr.-Ing., ORCID 0000-0002-5425-9259,

shevchenkoss@nas.gov.ua

https://doi.org/10.61319/FKOE7DJ9

Thermal Behaviour of Marine Lip Seals: A Pathway Towards Condition Monitoring

Thomas White, Omar Morad, Vesa Saikko, Raine Viitala

This paper examines the behaviour of marine thruster lip seals in a full-scale, fully flooded environment with a view to developing a condition monitoring system. Lip contact temperature was identified as a suitable variable to characterise the condition of the seal. A custom test device was built to measure the sub-surface contact temperature of a commercial thruster seal package operating fully submerged. The seal package consisted of three seals of 300 mm nominal diameter. A tungsten carbide coated stainless steel shaft liner was used as the counter-face. Results validated the viability of the proposed concept and highlighted the inter-dependent nature of seal thermal behaviour in a package configuration.

1 Introduction

Marine propulsion is the mainstay of modern maritime transport, which has been estimated to account for over 80 percent of all global goods transportation by volume [1] and is essential to many facets of modern industry. It is known, however, that oil leakage to the oceans because of sub-optimal sealing in marine propulsion systems is significant; some estimates suggest upwards of 75 million litres per year [2]. Leakage is, therefore of great concern, and many jurisdictions have moved to limit the environmental impact of the marine sector in terms of operational oil spillage to the oceans [3]. Radial lip seals are commonly used in a variety of marine propulsion systems and are responsible for preventing the discharge of lubricating oils into the marine environment: a well-designed lip seal should not leak [4]. Predicting their behaviour, however, is difficult: the harsh conditions in which the seals operate greatly increase the likelihood of malfunction, increased wear and/or failure. Factors such as exposure to sea water and its contaminants, variations in pressure and water temperature, as well as large sliding speeds precipitated by the large seal diameters can all severely compromise sealing performance [5]. Moreover, literature pertaining to the matter is exceedingly scarce [5].

Condition monitoring provides a pathway to addressing the main shortcomings associated with the use of marine lip seals:

- Lip seals can perform almost flawlessly; however, they are known to also leak, sometimes significantly [2, 4, 6].
- Leakage impacts the marine environment detrimentally.
- Unnecessary seal maintenance can be very costly, as it can often require the use of a dry dock [7].

Published literature pertaining to lip seals operating in non-submerged conditions has identified three main mechanisms that govern lip seal functions: lubrication, sealing and pumping [8]. Also, it has been identified that temperature can have an influence on all three of these mechanisms [9]. According to Salant [9], elastomer aging, swelling and lubricant coking are all failure modes that are linked to lip temperature. Furthermore, temperature strongly influences the characteristics of the lubricating oil that forms the basis of the film responsible for the dynamic sealing ability of the lip seal-shaft tribological system, in particular the viscosity of said fluid [6].

The main research problems that were addressed in the present work are:

1) How temperature at the contact between a large diameter marine lip seal and its counter-face can be measured more optimally during all phases of operation.
2) How lip contact temperature influences the wear characteristics of large diameter marine lip seals.
3) How contact temperature can be applied to develop a condition monitoring system for marine lip seals.

The main aim of the present work is to broaden the foundation of empirical knowledge regarding the influence of lip contact temperature on the behaviour of large diameter marine lip seals. The secondary aim is to apply the knowledge obtained from this study with a view to identifying a viable mechanism upon which a condition monitoring system for thruster lip seal packages could be based. To these ends, the behaviour of the sub-surface contact temperatures of the three rotary lip seals contained within a commercial lip seal package designed for azimuth thrusters was investigated and analysed. This seal package can be seen in figure 1. Seals within a seal package are typically denoted in ascending order from the propeller side to the gearbox side. Sub-surface temperature measurements were performed during multi-stage experiments using a custom, full-scale test apparatus designed and manufactured to operate fully submerged and in conjunction with the industrial partner's test apparatus. Temperatures were measured during a series of tests designed to simulate normal running, and during a series of destructive tests. The analysis of experimental results was performed with respect to published literature on the matter, in particular, the work of Morad et. al. [5] and Borras et. al. [3, 7, 10-12], in addition to assessing the applicability of the observed behaviour to a condition monitoring system. An attempt was made to identify any relationships between lip seal sub-surface contact temperature and wear. To the author's best knowledge, no published material specific to investigating the role temperature plays in the operation of a full-scale marine lip seal package designed for use in azimuth thrusters exists.

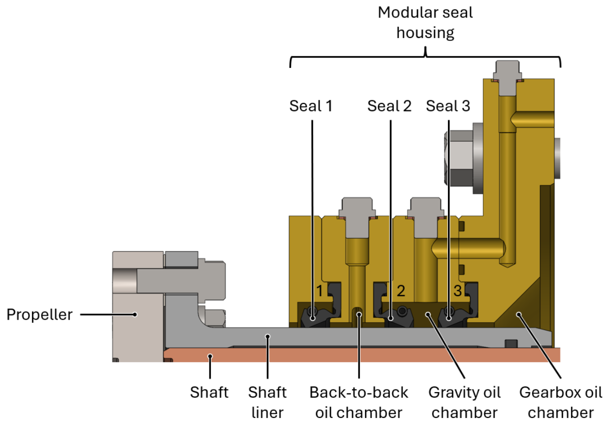

Figure 1: Commercial lip seal package for marine thrusters used for the present study.

2 Materials and Methods

2.1 Test Apparatus Design

An experimental device was built to measure the sub-surface contact temperature of the three lip seals contained within the commercial thruster lip seal package. The device was designed to operate in conjunction with the industrial partner's test rig, pictured below in figure 2. The primary function of the test rig is to facilitate the testing of full-scale, large diameter lip and face seal packages.

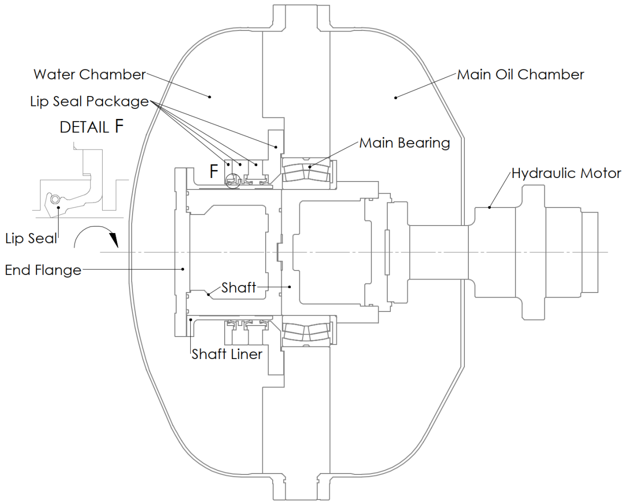

Figure 2: Sectioned and simplified schematic of industrial partner's test apparatus. Scale is not accurate, and some components have been omitted for clarity.

The main features of the test rig are as follows:

- Two main chambers: a water chamber and a main oil chamber.
    - The water chamber replicates the water side of the thruster when in operation.
    - The main oil chamber replicates the oil filled pod used to house the mechanical drive of a typical azimuth thruster. It serves to lubricate the main shaft bearings, the bearings of the hydraulic motor, and the back side of seal 3.
- A hydraulic motor acting as the prime mover for the rotation of the shaft.
- A two-piece hollow shaft.

The thruster seal package in the configuration tested consisted of a tungsten-carbide coated stainless-steel liner, three lip seals and a modular housing. The nominal outer diameter of the liner was 300 mm, while its surface roughness was determined using a Mahr MarSurf PS 10 portable surface roughness measurement device. Roughness measurements were taken at 6 different locations on the liner surface in the axial direction. The shaft liner is designed to be fitted to the shaft by the propeller of the thruster, or, in the case of the industrial partner's test apparatus, an end flange, as pictured in figure 2.

All lip seals tested were manufactured from 80 NBR 94207, with a nominal inner diameter of 300 mm, an interference fit of 4.5 mm, and a hardness of 80 Shore A. The four-piece seal housing was made from bronze. The three oil chambers formed by the fully assembled seal housing were between seals 1 and 2, named the back-to-back oil chamber, between seals 2 and 3, named the gravity oil chamber, and on the back side of seal 3, named the gearbox oil chamber. These are pictured in figure 1.1. The capacity of the back-to-back oil chamber was 0.25 l, while the capacity of the gravity oil chamber was 0.5 l. Mobil MOBILGEAR 600 XP ISO grade 150 gear oil was used as the lubricating oil for this study. It has a kinematic viscosity of 150 mm^2/s at 40 °C and 14.7 mm^2/s at 100 °C.

The back-to-back and gravity oil chambers were filled with lubricating oil before the commencement of tests. They were then resupplied oil lost to operational discharges with remotely located, pneumatically pressurised reservoirs. The gearbox oil chamber was supplied oil directly from the gearbox oil chamber of the test rig via its main shaft bearing. Back-to-back and gravity oil chamber pressures were regulated pneumatically with manually adjustable pneumatic pressure regulators. The gearbox oil chamber was pressurised by the oil pressure of the main oil chamber of the test rig. Its pressure was regulated by manually adjusting the pressure control valve of the main oil chamber. Measurement of the oil pressure and temperature of both the back-to-back and gravity oil chambers was realised by mounting pressure transducers and K-type thermocouples to the respective oil supply ports. This can be seen in figure 3.

The measurement apparatus constructed for this study was designed to be compatible with and fitted to the industrial partner's test rig. A novel method previously employed by Morad et. al. [5] and Saikko et. al. [13] was adapted to estimate the contact temperature of the lip seals of the studied seal package. The contact temperature was measured at five points across each seal by fitting K-type thermocouple probes

1.5 mm in diameter 0.5 mm beneath the contact surface. This can be seen in figure 3. The thermocouple probes were calibrated by the manufacturer and their accuracy was ± 0.5 °C. Five measurement points spaced 1 mm apart axially were allocated to each seal. Such axial spacing was chosen to minimise information loss by overlapping measurement points (owing to the 1.5 mm probe diameter vs 1 mm axial spacing) and ensure the actual contact location of the measured seal was captured. In total, 81 holes were drilled for the fitment of thermocouple probes. Hole locations were designed to follow a helical path around the inner surface of the shaft liner included with the seal package. Compression fitting fasteners were used to securely mount the thermocouple probes to the shaft liner via the inner surface of the hollow shaft. Here, threaded through holes in the shaft following the same pattern used to locate the probes were designed to make provision for the attachment of the fasteners.

The 15 thermocouple probes were powered by four Nokeval FTR 264 wireless 4 channel thermocouple transmitters. The FTR 264 was chosen based on its transmission frequency, 433.92 MHz. According to the results of Maher et. al. [14], at distances of 40 cm, data transmission through water at radio frequency signals of 433 MHz produces less end-to-end delay, is more reliable, and is less susceptible to signal attenuation than at signals of 2.4 GHz. Thermoplastic housings were designed and manufactured for the wireless transmitters and receiver to minimise the effect of a Faraday's cage created by the steel water chamber of the test rig. Water chamber pressure and temperature, gearbox oil chamber pressure and shaft rotational speed were measured using sensors integrated into the test rig. The main features of the water side of the test rig with the custom measurement apparatus fitted can be seen in figure 3.

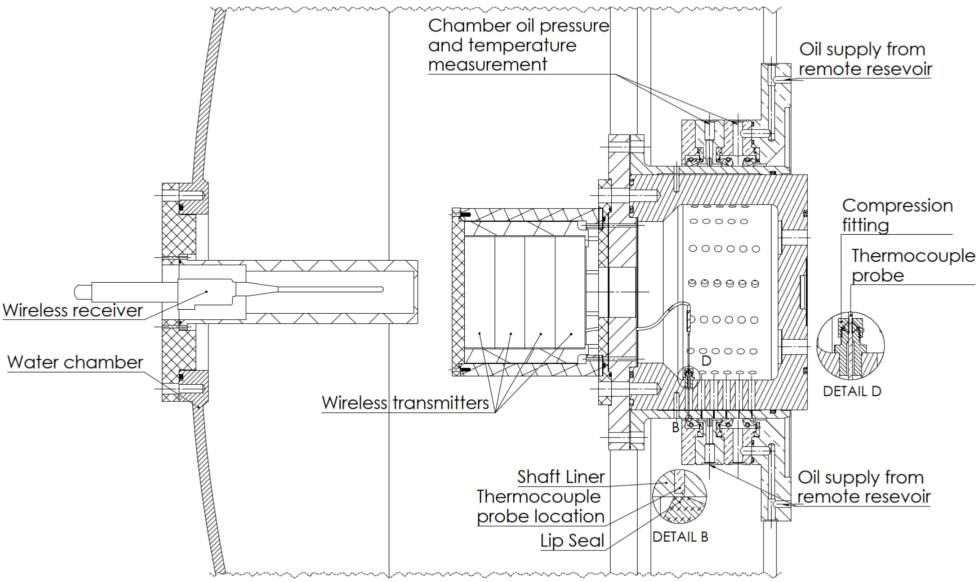

Figure 3: Schematic of the complete water side of the test apparatus used for the present study, with main features labelled.

2.2 Experimental Procedure

Before the commencement of sub-surface temperature measurements under test conditions, the optimal thermocouple locations relative to the actual axial contact locations of the seals on the shaft liner were first calibrated. This was achieved by installing the thermocouples according to the expected axial contact locations of the seals and running the test apparatus without the water chamber fitted. The measurement point exhibiting the highest sub-surface temperature of the five allocated to each seal during running was deemed to be closest to the actual contact location of the respective seal. Thermocouples were relocated as necessary to fit the actual contact location of each seal. Seals were concurrently run in during this process, which was carried out in three stages. The stages were run at shaft rotational speeds of 100 rpm for the first two stages, and 200 rpm for the final stage. The pressure differential set point across all seals was 0.1 bar for the first and last stages and 0.3 bar for the second stage. The stages were run for 46.3, 49.6 and 92.2 hours, respectively. The seal housing shaft-to-bore misalignment was found to be only 0.08 mm; thus, it was not altered.

Measurements were performed according to a test program consisting of six tests. The first three tests were designed to simulate normal running, while the last three were designed to simulate extreme conditions that bring about a loss of seal function and likely seal destruction. Shaft speed was controlled. For the three tests simulating normal running, shaft speed was varied in 100 rpm increments from 100–300 rpm from the first test to the last. During these tests, pressure differentials across all seals were designed to be set to 0.3 bar, however, after an initial running of the second test they were reduced to 0.1 bar due to excessively high sub-surface temperatures observed at seals 2 and 3. The second and third tests were then performed with pressure differentials of 0.1 bar across all seals. For the three tests simulating extreme conditions, the pressure differentials across seals 1 and 2 were varied in 0.2 bar increments from 0.6–1 bar from the first test to the last. The pressure differential across seal 3 was fixed at 0.5 bar during the destructive tests. These pressure differentials were chosen based on previous observations made by the industrial partner. Pressure differentials were always applied from the spring side to the back side of the seal. Pressure differentials were set before each test but not controlled during the tests.

Test durations were not controlled. Where possible, they were determined based on the test system obtaining a steady state. The steady state condition definitions were adapted from the work of Borras et. al. [7]. The sub-surface temperature of all seals, in addition to the oil temperatures of the back-to-back and gravity chambers, had to show variation of less than 5 % for at least 2 h. The steady state condition of the water chamber was defined as a variation of not less or more than ± 3 °C for at least 2 h. For the system to achieve a steady state, both the seal package system and water chamber had to concurrently fulfil their respective steady state condition criteria. The test program can be seen in table 1.

Table 1: Sub-surface temperature measurement test program. Variable names are based on the names of the inputs, e.g., Pgo = Pressure, gearbox oil. All given pressures are absolute. The 'Range' column pertains to the maximum range of the input, abbreviation 'unt. s.s.' = until steady state.

INPUTS	Variable	Unit	Range	Test 1.1	Test 1.2	Test 1.3	Test 2.1 D	Test 2.2 D	Test 2.3 D
Gearbox oil chamber pressure	*Pgo*	bar	1.4…1.9	1.9	2.1	2.1	1.7	1.7	1.7
Gravity chamber pressure	*Pg*	bar	Pb-b<Pg>Po	2.2	2.2	2.2	2.2	2.2	2.2
Back-to-back chamber pressure	*Pb-b*	bar	1.1…Pws	1.9	2.1	2.1	1.6	1.4	1.2
Water static pressure	*Pws*	bar	1.25…2.25	2.2	2.2	2.2	2.2	2.2	2.2
Shaft rotational speed	*n*	rpm	0…300	100	200	300	200	200	200
Test phase duration	*t*	h	1…250	≥30 (unt. s.s.)	≥30 (unt. s.s.)	≥30 (unt. s.s)	≥30 (unt. s.s.)	≥30 (unt. s.s.)	≥30 (unt. s.s.)

3 Results

For all test program tests (section 3.1–3.6), the sub-surface temperatures of all seals and the oil temperatures of all oil chambers are presented together on the same plot (plot (a)). This is to highlight any observable relationships between the sub-surface and oil chamber temperatures. Also, the pressure differentials across all seals are presented together on a secondary plot (plot (b)).

3.1 Test 1.1

Shaft rotational speed was set to 100 rpm and pressure differentials across all seals were set to 0.3 bar. No steady state condition was observed. The test was run for a duration of 73.2 hours. Test results are presented in figure 4.

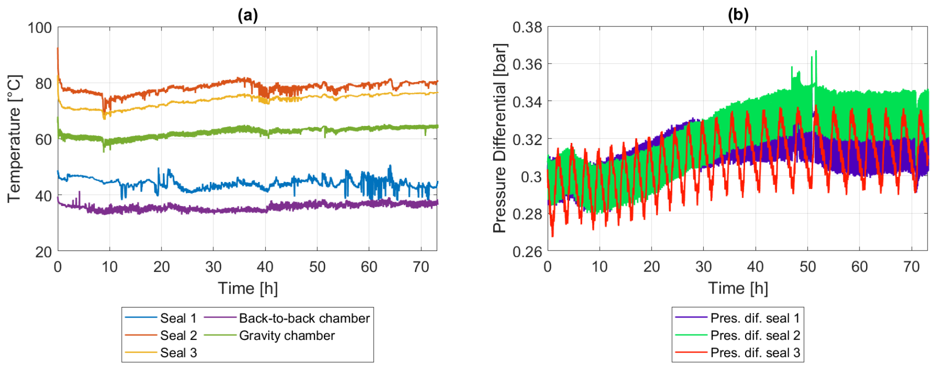

Figure 4: (a) sub surface temperature of lip seals 1, 2, 3, and oil temperature of gravity and

back-to-back chambers; (b) pressure differentials across seals 1, 2, and 3. Shaft rotational speed was 100 rpm.

3.2 Test 1.2

Shaft rotational speed was set to 200 rpm and pressure differentials across all seals were set to 0.1 bar. No steady state condition was observed. The test was run for a duration of 89.2 hours. The results are presented in figure 5.

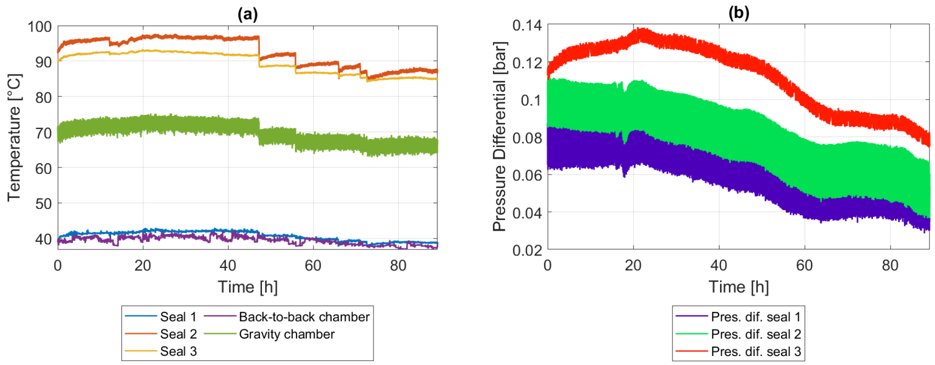

Figure 5: (a) sub surface temperature of lip seals 1, 2, 3, and oil temperature of gravity and back-to-back chambers; (b) pressure differentials across seals 1, 2, and 3. Shaft rotational speed was 200 rpm.

3.3 Test 1.3

The shaft rotational speed was set to 300 rpm, while pressure differentials across all seals remained set at 0.1 bar. No steady state condition for the system was observed. The test was run for a duration of 94.8 hours.

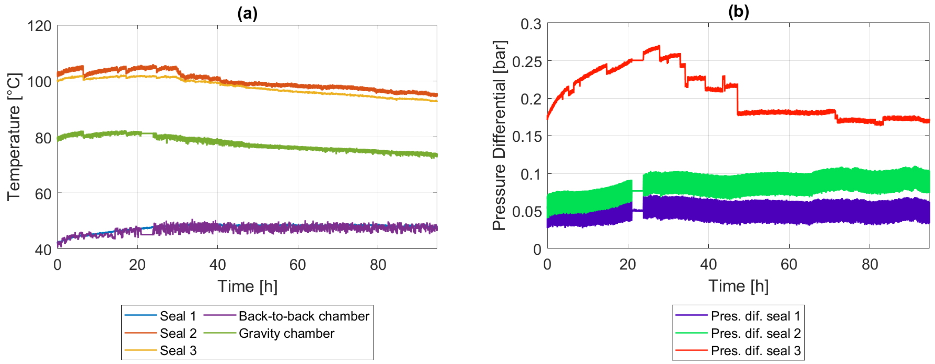

Figure 6: (a) sub surface temperature of lip seals 1, 2, 3, and oil temperature of gravity and back-to-back chambers; (b) pressure differentials across seals 1, 2, and 3. Shaft rotational speed was 300 rpm.

3.4 Test 2.1 D

For the first destructive test, the shaft rotational speed was set to 200 rpm, while the pressure differentials across seals 1 and 2 were set to 0.6 bar. The pressure differential across seal 3 was set to 0.5 bar. No steady state condition was observed. The test was run for a duration of 73.9 hours. The results are presented in figure 7.

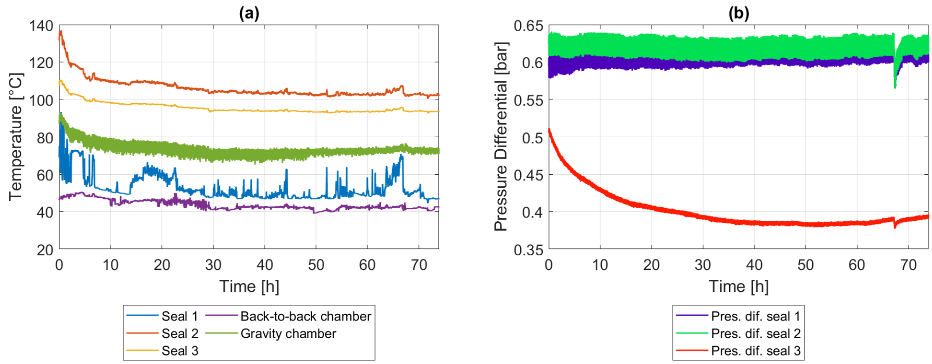

Figure 7: (a) sub surface temperature of lip seals 1, 2, 3, and oil temperature of gravity and back-to-back chambers; (b) pressure differentials across seals 1, 2, and 3. Shaft rotational speed was 200 rpm.

3.5 Test 2.2 D

The shaft rotational speed remained unchanged at 200 rpm, while the pressure differentials across seals 1 and 2 were set to 0.8 bar. The pressure differential across seal 3 remained set at 0.5 bar. No steady state condition was observed. The test was run for a duration of 38.6 hours. The results are presented in figure 8.

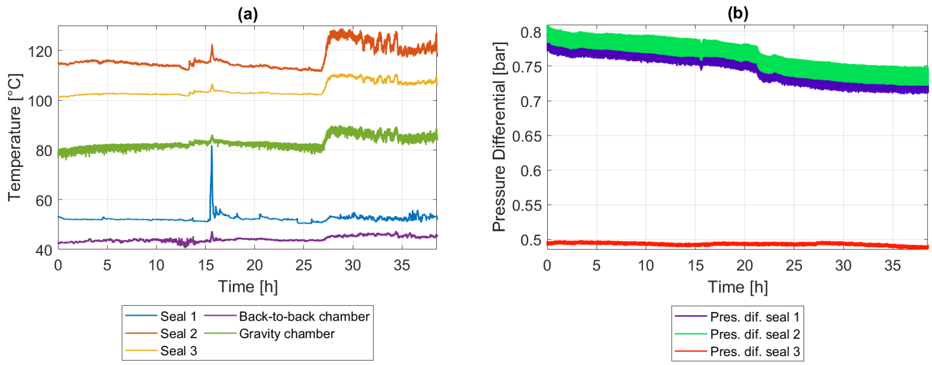

Figure 8: (a) sub surface temperature of lip seals 1, 2, 3, and oil temperature of gravity and back-to-back chambers; (b) pressure differentials across seals 1, 2, and 3. Shaft rotational speed was 200 rpm.

3.6 Test 2.3 D

The shaft rotational speed remained set at 200 rpm, while the pressure differentials across seals 1 and 2 were set to 0.8 bar. The pressure differential across seal 3 remained set at 0.5 bar. No steady state condition was observed. The test was run for a duration of 76.3 hours.

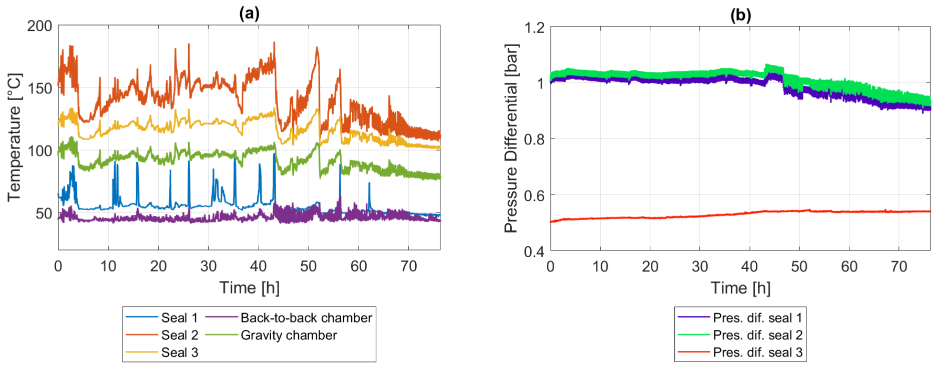

Figure 9: (a) sub surface temperature of lip seals 1, 2, 3, and oil temperature of gravity and back-to-back chambers; (b) pressure differentials across seals 1, 2, and 3. Shaft rotational speed was 200 rpm.

4 Discussion

Throughout the test program, the sub-surface temperature of seal 2 was consistently the highest, whilst the sub-surface temperature of seal 1 was consistently the lowest, likely owing in part to the influence of the water as a heatsink on the spring side of seal 1. During the first destructive test, 2.1 D, seal 2 operated for the whole test above 100 °C, while seal 3 ran above 100 °C for over 5 hours. Furthermore, during the second destructive test both seals 2 and 3 ran at over 100 °C for the entirety of the test, while seal 2 ran at over 120 °C for more than 7 hours of the test. Finally, during the third and final destructive test, seal 2 ran at over 120 °C for more than 70 % of the test duration, while seal 3 ran at over 120 °C for more than 40 % of the test duration. According to Flitney [15], seals made from nitrile butadiene rubber (NBR) can operate at a maximum temperature of 100 °C and as much as 120 °C for short periods, thus seals 2 and 3 exceeded both maximum temperatures for NBR for long periods of the test program.

The subsurface temperature appeared to be sensitive to changes in shaft rotational speed. The average sub-surface temperature of all seals increased significantly from the first to last test simulating normal running, tests 1.1 to 1.3. This was despite the change in pressure differentials across all seals, from 0.3 to 0.1 bar, implemented after the first attempt at completing test 1.2 was unsuccessful. This is illustrated in figures 4, 5, and 6. Here, the average sub-surface temperature of seals 1, 2 and 3 increased by 3.5 °C, 21.8 °C and 21.8 °C respectively. These limited results agree with the experimental findings of Morad et. al. [5] and Borras et. al. [7]. Also, larger pressure differentials across the seals precipitated higher sub-surface temperatures. This is evident in figures 7–9. Moreover, all maximum sub-surface temperatures were recorded at the maximum, uncontrolled pressure differential set points for seals 1–3 during the test program: 1.0 bar, 1.0 bar and 0.5 bar respectively. These results are thus consistent with the work of Morad et. al. [5]. Ultimately, as only the shaft rotational speed of the test apparatus was controlled in the present study, the influence of pressure cannot be ascertained based on the obtained experimental results. Hence, further investigation is required.

The results demonstrate the sensitivity and interdependence of the system. As can be seen in figures 4–9, any significant changes in the sub-surface temperature of a seal were reflected almost simultaneously in the sub-surface temperature of another seal or seals and usually also the oil temperature of the back-to-back chamber and the gravity chamber. Variation in the rotational speed of the shaft and pressure differentials across the seals did not appear to influence the phenomenon. It is likely the insignificant capacity of both the back-to-back and the gravity oil chambers (approximately 0.25 and 0.5 L respectively), the lack of active oil circulation in the oil chambers, the material construction of the seal package, and particularly the proximity of the contacts of seals 2 and 3 to each other (approximately 17.13 mm) facilitate the rapid transfer of heat within the system. In general, some uncertainty in the absolute values of the sub-surface temperature measurements existed. The results, however, remain valid, as fundamentally we are interested in the changes of the sub-surface temperatures measured under different operating conditions, not the absolute values.

Inspection of the seal package after the conclusion of the test program revealed significant damage to seal 1. The wear track present on the seal was very wide and the seal showed signs of extreme wear. Significant material build-up was visible on the seal and on both edges of the wear track of the seal, and throughout the back-to-back chamber. Furthermore, deposits were found bordering the running track made by the seal on the shaft liner. Similarly, deposits were also found on the shaft liner bordering the running tracks made by seals 2 and 3. The deposits suggest that some adhesive wear may have taken place and thus the lubrication regimes were likely starved, boundary, or mixed at some point during the test program. The cause of the extreme wear to seal 1 was determined to be oil starvation resulting from a faulty oil reservoir supplying the gravity oil chamber. The cause, therefore, of the sudden, approximately 30 °C change in the sub-surface temperature of lip seal 1 recorded during destructive test 2 and presented in figure 8 is likely a very significant wear event, in this case indicating starved lubrication. The initiator of the relatively large and rapid sub-surface and chamber oil temperature changes reflected throughout the seal package system appeared to be the sudden and very significant change in the sub-surface temperature of seal 1. Hence, in general, the cause of sudden and significant sub-surface temperature changes could be seal wear. Depending on the magnitude of the change in sub-surface contact temperature resulting from wear, therefore, a heat transfer process may bring about observable temperature changes to other areas of the seal package. This hypothesis can be correlated with results from all tests, but particularly with the results from the destructive tests, as can be seen in figures 6–8.

If a very significant wear event occurred as described during test 2.2 D, the recorded sub-surface temperature of lip seal 1 during test 2.3 D indicates the precipitation of increased wear. The results from test 2.3 D, however, highlight again the interdependence of the system, where sudden changes in temperature are quickly reflected throughout the system, as can be seen in figure 9. Here, further investigation is required to determine which sub-surface temperature peaks may be directly associated with wear events and which are induced.

5 Summary and Conclusions

The sub-surface temperature of the studied thruster lip seals contained within the investigated commercial seal package appeared to be sensitive to changes in shaft rotational speed and large changes in the pressure differentials across the seals. Moreover, the sub-surface temperature of each of the seals and the oil temperature of two of the oil chambers, the back-to-back and gravity oil chambers, appeared to be interdependent. Also, large, and comparatively sudden changes in the sub-surface temperature appeared to signify the incidence of wear events. The exact mechanism or mechanisms precipitating the wear and thus sudden changes in sub-surface temperature are unknown and must be investigated further.

The sub-surface temperature measurement method investigated herewith could be used in a condition monitoring implementation for large diameter marine lip seal packages. Sub-surface temperature can be measured without interfering with the tribological interactions taking place at the sealing interface. Furthermore, the sub-surface temperature of the seal was shown to have great promise as an indicator of seal condition. If it is assumed that sudden sub-surface temperature changes greater than a certain magnitude represent wear events based on the results obtained from the present study, then the magnitude, number, and frequency of such events could be used to evaluate seal condition using a statistical model. Such a model could be derived from larger datasets obtained from tests designed to measure the wear rate of the seal and the magnitude, number, and frequency of wear events attributed to the described sub-surface temperature changes under different operating conditions.

6 Acknowledgements

The research was funded by Business Finland (PowerBeyond, grant number 2534/31/2022), Kongsberg Maritime Finland Oy, and the Finnish Maritime Foundation.

7 References

1. Simcock, A., O.K. Kamara, and L. Inniss, *Shipping*. 2016.
2. Lundberg, J., *Undocumented oil leakages: A study about stern tube seals and leakages*. 2021.
3. Borras, E.X., M.B. de Rooij, and D.J. Schipper, *Rheological and Wetting Properties of Environmentally Acceptable Lubricants (EALs) for Application in Stern Tube Seals.* Lubricants, 2018. **6**(4).
4. Salant, R.F., *Soft elastohydrodynamic analysis of rotary lip seals.* Proceedings of the Institution of Mechanical Engineers Part C-Journal of Mechanical Engineering Science, 2010. **224**(C12): p. 2637-2647.
5. Morad, O., V. Saikko, and R. Viitala, *Performance characterization of marine lip seals: Contact temperature and frictional torque.* Wear, 2023. **523**.
6. Muller, H., *Fluid sealing technology: principles and applications*. 2019: Routledge.
7. Borras, F.X., et al., *Stern tube seals operation: A practical approach.* Advances in Mechanical Engineering, 2021. **13**(2).
8. Baart, P., P.M. Lugt, and B. Prakash, *Review of the lubrication, sealing, and pumping mechanisms in oil- and grease-lubricated radial lip seals.* Proceedings of the Institution of Mechanical Engineers Part J-Journal of Engineering Tribology, 2009. **223**(J3): p. 347-358.
9. Salant, R.F., *Theory of lubrication of elastomeric rotary shaft seals.* Proceedings of the Institution of Mechanical Engineers Part J-Journal of Engineering Tribology, 1999. **213**(J3): p. 189-201.
10. Borras, F.X., et al., *Stern tube seals under static condition: A multi-scale contact modeling approach.* Proceedings of the Institution of Mechanical Engineers Part J-Journal of Engineering Tribology, 2021. **235**(1): p. 181-195.
11. Borras, F.X., M.B. de Rooij, and D.J. Schipper, *Misalignment-Induced Micro-Elastohydrodynamic Lubrication in Rotary Lip Seals.* Lubricants, 2020. **8**(2).
12. Borras, F.X., M.B. de Rooij, and D.J. Schipper, *Misalignment-induced macro-elastohydrodynamic lubrication in rotary lip seals.* Tribology International, 2020. **151**.
13. Saikko, V., O. Morad, and R. Viitala, *Effect of type and temperature of serum lubricant on VEXLPE wear and friction.* Wear, 2021. **470**.
14. Maher, S.M., et al., *Performance of RF underwater communications operating at 433 MHz and 2.4 GHz.* Proceedings of 2019 International Conference on Innovative Trends in Computer Engineering (Itce 2019), 2019: p. 334-339.
15. Flitney, R.K., *Seals and sealing handbook*. 2011: Elsevier.

8 Authors

Aalto University, Department of Mechanical Engineering, Aalto ARotor Lab

Sähkömiehentie 4P, 02150 Espoo, Finland:

Thomas White, B. Sc., ORCID 0000-0001-0002-0003, thomas.white@aalto.fi

Omar Morad, M. Sc., ORCID 0000-0001-0002-0003, omar.morad@aalto.fi

Vesa Saikko, D. Sc., ORCID 0000-0001-0002-0003, vesa.saikko@aalto.fi

Asst. Prof. D. Sc. Raine Viitala, ORCID 0000-0001-0002-0003 raine.viitala@aalto.fi

https://doi.org/10.61319/UVUUHHQM

Frictional behaviour of marine lip seals: Sensitivity to operational parameters

Omar Morad, Raine Viitala, Vesa Saikko

Marine lip seals are a seldom studied topic in published literature. They are unique in their harder material compound, large diameters, and higher sealed pressures. This paper evaluated the behaviour of a 300 mm NBR marine lip seal (n = 3) under typical operating conditions. The lip seals were tested under three oil pressures, three oil temperatures, and three rotational speeds, for a total of 27 combinations. The frictional torque and subsurface temperature were measured at each operating point. The frictional torque increased significantly with increasing oil pressure. The subsurface temperature increased significantly with increasing speed. The subsurface temperature increased and the frictional torque decreased with increasing oil temperature.

1 Introduction

Lip seals are a commonly used type of seals in many fields, one of which is the marine field. It is typically placed on the propeller shaft, which is either connected to an azimuth thruster or a stern tube. The former is a thruster which has the gearbox outside the ship body, fully immersed in seawater, while the latter is a tube that connects the propeller to the gearbox which is placed inside the ship body. In both scenarios, it is imperative to keep the lubricating oil and seawater separate. This is typically done by placing three or more lip seals on the propeller shaft in varying orientations, such as the example shown in Figure 1. The lip seals are separated by pressurized chambers, where each chamber has a designated pressure. The chambers are pressurized in a way that allows for the middle chamber to collect any leaks, so it has the lowest pressure. The chamber closest to the gearbox typically has the highest pressure to prevent seawater ingress in case of leakage. The seawater facing chamber typically has a lower pressure, but not the lowest. While conventionally, the spring side of lip seals is usually pressurized higher, some systems are designed so that the backside of the lip seal has higher pressure. While many other systems exist to address the issue of sealing a marine thruster, the overall leakage rate is quite high, since it can be 1–10 Liters per day for one thruster, which totals more than 20 million Liters per year from operational marine vessels [1].

Besides leakage, premature failure can also occur. A sudden and premature failure can cause mechanical damage to the gearbox of the thruster and typically necessitates a dry docking to change the seals. This has both a negative impact on the operator, in terms of increased cost, and on the environment since synthetic gear oils negatively affect marine microorganisms. While Environmentally Acceptable Lubricants (EAL) are available and can be used with no issues, they are avoided due to their lower lubricating performance and higher cost. They can also have a negative effect on NBR lip seals, which may necessitate a change to FKM lip seals, which are more expensive but have better chemical and thermal resistance.

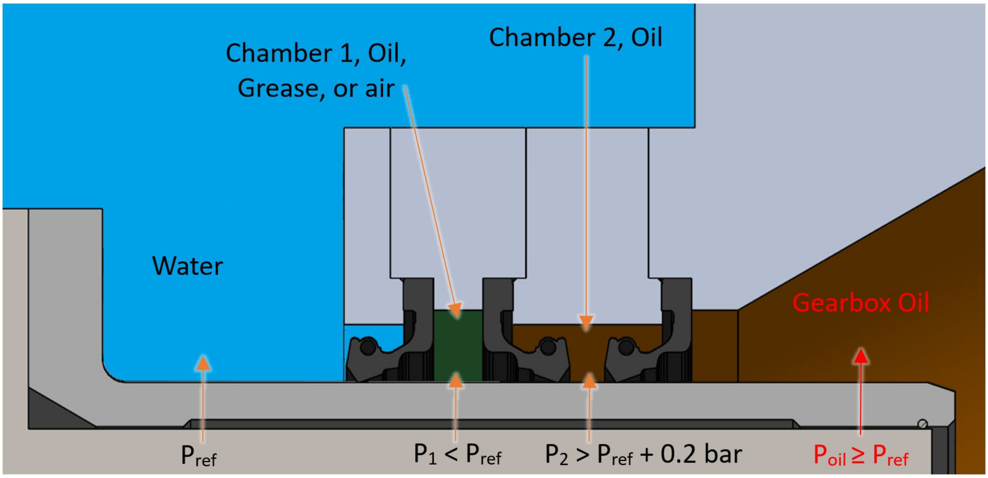

Figure 1: Schematic of typical marine lip seal package.

The sealing mechanism of elastomeric lip seals is best explained by the theory of reverse pumping, introduced by Müller [2] and Qian [3]. Under static conditions, the seal prevents leakage due to its interference fit with the shaft. When the shaft rotates, the seal deforms tangentially due to this rotation. The tangential deformation of the lip seals distorts the asperities at the contact area to resemble an uneven V-shape. This causes the lip seal to act as two helical or vane pumps, where the net flow of the oil goes towards the spring side of the seal, in a successful seal. Concurrently, the shaft drags oil within the cavities of the rough contact area, and as it approaches an asperity peak, a hydrodynamic pressure is generated within the oil due to the forming wedge. This causes the oil to go between the lip seal and the shaft, lubricates the contact, and results in an oil film between the lip seal and the oil. The presence of the oil film was discovered by Jagger [4], but the theory that explained the presence of a film and the lack of leakage was presented almost 30 years later.

Many numerical models have been published, which predict the behaviour of lip seals. The models combine fluid dynamics, solid mechanics, and contact theory. They are typically solved iteratively since the physics is coupled and for instance, solving for the fluid film thickness requires calculation of the deformation, and vice versa. Some models make simplifications, such as assuming constant film thickness, constant lip seal deformation, smooth counterface, axisymmetric conditions, and uniformly distributed asperities. From those assumptions, the one that has the most significant effect on the outcome is the distribution of the asperities [5, 6]. While the numerical models are powerful, they typically require experimental verification, and their applicability is typically limited to the studied seal. There is yet to be an analytical model of lip seal behaviour. Therefore, an experimental approach was chosen to study the behaviour of marine lip seals.

A thruster lip seal package has many interconnected variables that affect its performance, so it is difficult to study them in a scientific manner. Borras et. al. [7-10] studied marine lip seals of 200 mm diameter, made from FKM, and the tests ran with EAL lubricants. Apart from their research, little has been published on marine lip seals. In this paper, individual thruster lip seals were studied in a single-station test device. The tested lip seals are part of a commonly used thruster lip seal system. They were tested under various typical operating conditions.

2 Methods

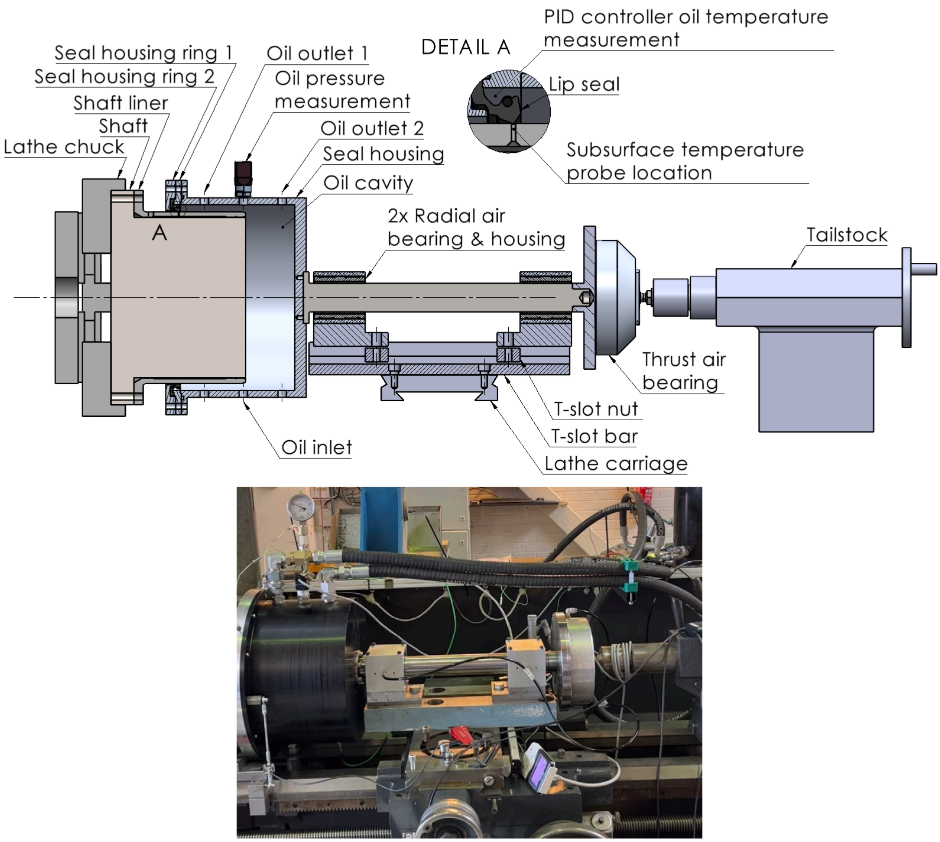

Figure 2: Cross section and picture of the test device.

To test the large diameter lip seals, a test device was constructed, which was introduced in [11]. A cross-section of the test device is shown in Figure 2. It is explained here for convenience. The basis of the test device was a lathe with sufficiently large dimensions to fit the seal, the liner, the seal housing, and the bearings. The lathe was aligned to be horizontal within ±0.05°. The lathe had a 5.6 kW motor connected to a gearbox with various speeds. The lathe was connected to a Variable Frequency

Drive (VFD), which controlled the rotating speed of the motor, and allowed for precise speed control. The rotational speed was measured using a laser tachometer. A solid shaft, made from Fe60, was fixed to the chuck. The shaft had a diameter of 280 mm and resembled the propeller shaft section where the seals are fixed. A shaft liner was placed onto the shaft, which was made from AISI 316 stainless steel and hard coated with tungsten carbide. The liner was aligned to the rotation axis within ±0.06 mm. All seals ran at the same axial location on the liner, and the measurement of the surface roughness R_a showed no change before, during, and after the tests.

At the other end of the shaft, the lip seal and its housing were assembled and fixed to the tool carriage. The tool carriage was used to support and align a static shaft that carried the seal and its housing. The static shaft had a diameter of 50 mm and was radially supported by two radial air bearings. A ground disk was placed at one end of the static shaft, which was the counterface for a thrust air bearing that countered the axial load from the oil pressure. The axial bearing was locked in place by the tailstock. The air bearings had minimal friction which ensured precise measurement of the frictional torque. At the other end of the shaft, the seal housing, the housing rings, and the lip seal were fixed. The seal housing resembled an empty bucket, which mainly contained the circulated lubricant. The housing rings were used to fix the lip seal to the seal housing. The housing rings had grooves that provided a preload for the seal and allowed for static sealing. The housing rings were assembled by 12 bolts, which allowed for fine alignment. The seal was aligned from the metal edge of seal housing ring 1, and the axial and radial alignments were within ±0.2 mm. Three samples of an NBR seal were tested, which had a hardness of 80 Shore A, and a garter spring. The rotation of the seal housing was prevented by a load cell with a 200 N maximum load. The frictional torque was calculated by multiplying the measured load by the lever arm (0.19 m). The load cell was vertical within ±0.15°, as shown in Figure 2.

The lubricant was an ISO VG 100 grade synthetic oil that is commonly used in azimuth thrusters and contained some additives for this specific usage, such as antifoam additives. The oil had a viscosity of 100 mm^2/s at 40 °C and 11.2 mm^2/s at 100 °C. The oil was filled to the main reservoir, a vertical tank, using a diaphragm pump without any filters. The tank was filled with approximately 80 Liters of oil. The oil was circulated through the system via two helical gear pumps. One pump circulated the oil within the tank itself to maintain a uniform oil temperature, while the other pump circulated the oil through the seal housing to maintain the oil temperature. The seal housing was fully flooded with oil. The oil was circulated from the bottom of the housing to the top to remove any air bubbles. The seal housing was placed on the discharge side of the pump to prevent cavitation pressure development in case of pneumatic pressure failure. The oil was circulated through filters with a mesh size of 10 µm on both pump lines, to filter out any contamination. The pumping rates were 10–20 Liters per minute. The oil was heated by adhesive heating pads which were placed on the outer wall of the tank. The heaters had a power of 2.1 kW and were controlled via a PID controller, which took the temperature measurement from the oil near the lip seal. The oil was pressurized via a pneumatic regulator connected to the oil tank, which was controlled by a PID controller that took the oil pressure measurement at the seal housing.

The subsurface temperature was measured by a thermocouple that was embedded into the shaft liner, 0.5 mm beneath the liner surface. The thermocouple was connected to a wireless transmitter that rotated with the shaft, and transmitted to a receiver every 5 seconds. To ensure that the lip seal was located at the location of the thermocouple, it was moved forwards and backwards on the liner by the tailstock while the shaft rotated, until the subsurface temperature reached a maximum value. The location of the maximum temperature was fixed for the entirety of the test. The load cell was realigned after this step.

The test sequence started by running-in. In the running-in process, the seals ran for at least 100 hours at a rotation speed of 200 RPM, an oil temperature of 40 °C, and an oil pressure of 0.03–0.08 bar. The test started with room temperature oil, which reached a temperature of 40 °C within 2–3 hours due to the frictional heating of the seal and the electric heater. After the running-in was completed, the test sequence started. At each test point, the oil temperature was 40, 50, or 60 °C, the oil pressure was 0.1, 0.2, or 0.3 bar, and the rotational speed was 100, 200, or 300 RPM, which correspond to sliding speeds of 1.57, 3.14, and 4.71 m/s, respectively. At each point, the parameters were allowed to settle to a steady state, then the measurements were taken for at least one hour of steady state running.

3 Results and Discussion

In this section, the performance results are shown as average values for all three seals. The surface roughness of the shaft liner was 0.41 µm R_a and remained unchanged throughout the tests. The standard deviations of the mean of the steady state measurements seldom exceeded 1%, which demonstrates the stability at steady state conditions.

The results of the tests are shown in Figure 3. From the figure, it can be seen that an increase in the rotating speed increases the subsurface temperature significantly. This can be explained by the increased frictional heating generated due to the increase in speed. The higher contact temperature indicates that asperity contact may be higher. This was not always accompanied by an increase in frictional torque. An increase in frictional torque would indicate that the lubrication regime is hydrodynamic. In this case, however, it is most likely that the lip seals operated in the mixed lubrication regime. An increase in rotational speed did not produce a clear effect on the frictional torque; while it decreased in some cases, it remained constant or increased slightly in others.

In contrast, an increase in oil pressure significantly increased the frictional torque, while it caused a less significant increase in the subsurface temperature. As known from the literature [12], an increase in oil pressure, or rather the pressure differential over the seal, leads to an increase in contact width and an increase in contact pressure. The magnitude of increase can be different for either and depends on the seal geometry, material, and pressure level. In this case, the increase in pressure can be considered moderate. Therefore, the increase in contact width can be assumed small relative to the increase in contact pressure [10, 12]. The combined effect is an increase in contact pressure with a minor increase in contact width, which results in an increase in radial load, which leads to an increase in frictional torque. The minor increase in the contact width may explain the minor increase in subsurface temperature, since the frictional heating is distributed over a larger contact area, so the heat generation does not significantly increase.

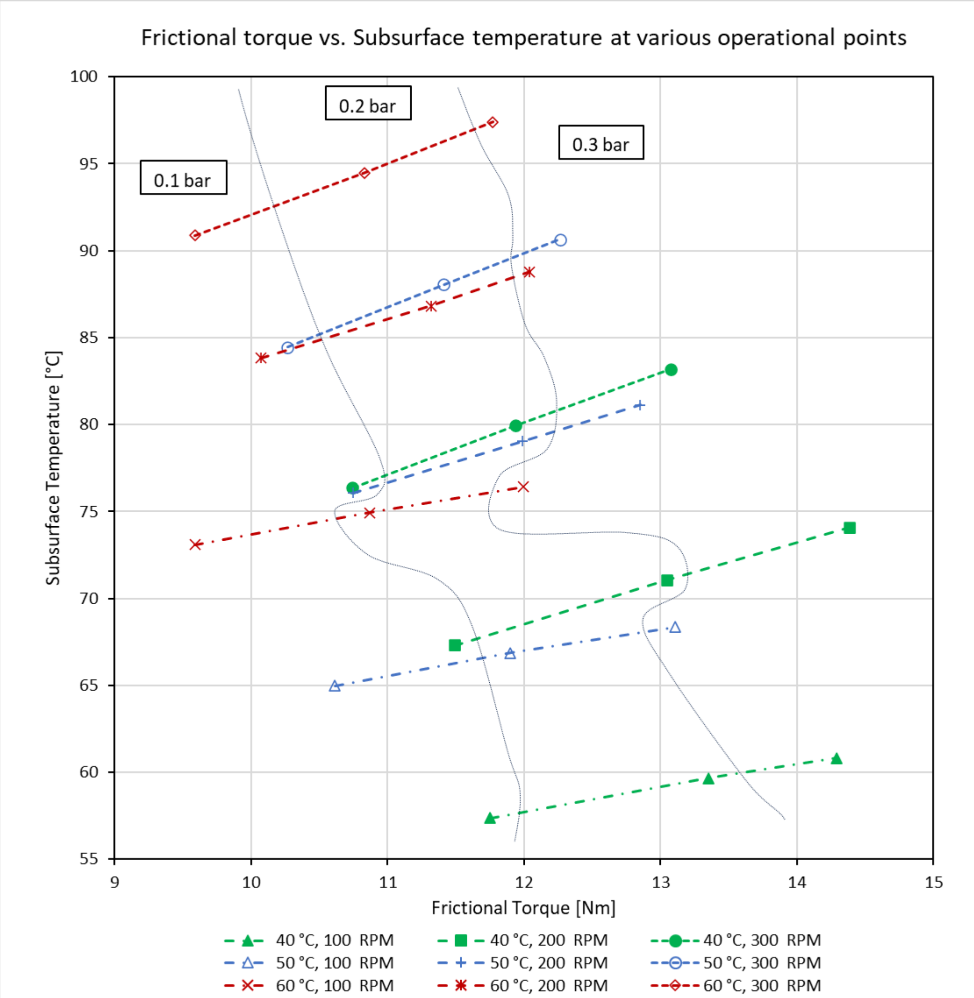

Figure 3: Average performance results of all three seals under various conditions. The solid splines separate the points by oil pressure.

An increase in the oil temperature increased the subsurface temperature and decreased the frictional torque. The increase in the subsurface temperature can be explained by the lower film thickness, which occurs due to the decrease in oil viscosity at higher temperatures [13]. A thinner oil film may increase the asperity contact, which can increase the frictional heating. While an increase in asperity contact should increase the frictional torque, a higher oil temperature may result in a decrease in the elastic modulus of the elastomer [13], which results in a lower contact pressure and a lower frictional torque. Furthermore, the frictional torque is a combination of the dry friction resulting from the asperity contact and the viscous friction from the viscous shear of the oil film. The latter part decreases with increasing temperature due to the lower viscous shear resulting from a lower oil viscosity.

The subsurface temperature reached its highest values in the tests with an oil temperature of 60 °C and a rotation speed of 300 RPM. The highest temperature occurred at a pressure of 0.3 bar and reached an average of 97.4 °C. While this is the measured temperature 0.5 mm beneath the contact, it is also the average temperature on the surface of the probe, which is a circle with a diameter of 1.5 mm. Thus, it is certain that the contact temperature is higher than this value, and may be higher than 100 °C. If an NBR lip seal is exposed to such high temperatures for a prolonged period, glazing may occur at the contact surface. A glazed surface usually results in a smooth wear surface and increases the contact temperature, which in turn results in more glazing, an increase in the smooth worn surface, and a higher contact temperature again. A seal that undergoes this cycle usually fails, prematurely in many cases. The current tests were conducted in a lab environment, under conditions that may be considered favourable for the seals relative to the conditions in a marine thruster. Therefore, lip seals in thrusters may be exposed to consistently high contact temperatures due to the harsher operating conditions, thus they require careful design to avoid unfavourable conditions, especially with NBR seals.

4 Summary and Conclusion

In this paper, the performance of three samples of a large diameter lip seal was evaluated using measurements of frictional torque and subsurface temperature at 27 combinations of typical operating conditions, consisting of oil pressure, oil temperature, and rotational speed. The results shed light on the behaviour of marine lip seals. The results showed that the subsurface temperature increased with increasing oil temperature and rotational speed, and that the frictional torque increased with increasing oil pressure and decreased with increasing oil temperature. The relation between frictional torque and subsurface temperature was not clear in the present study.

5 Acknowledgements

The research was funded by Academy of Finland (AI-ROT, grant number 335717), Business Finland (Power Beyond, grant number 2534/31/2022), and Kongsberg Maritime Finland Oy.

6 References

[1] Lundberg, J., *Undocumented oil leakages: A study about stern tube seals and leakages*. 2021.

[2] Müller, H.K. and Ott, G.W. *Dynamic sealing of rubber rotary shaft seals*. in *10th International Conference on Fluid Sealing*. 1984.

[3] Qian, D., *The sealing mechanism and design factors of radial lip seals for crankshafts.* Neiranji Gongsheng/Chinese Internal Combustion Engine Engineering, 1984. **5**: p. 10-13.

[4] Jagger, E.T. *Study of the lubrication of synthetic rubber rotary shaft seals*. in *Proc. Conf. on Lubrication and Wear, Institute of Mechanical Engineers*. 1957.

[5] Salant, R.F. and Flaherty, A.L., *Elastohydrodynamic Analysis of Reverse Pumping in Rotary Lip Seals With Microasperities.* Journal of Tribology, 1995. **117**(1): p. 53-59.

[6] El Gadari, M.h., Fatu, A., and Hajjam, M., *Shaft roughness effect on elasto-hydrodynamic lubrication of rotary lip seals: Experimentation and numerical simulation.* Tribology International, 2015. **88**: p. 218-227.

[7] Borras, F.X., de Rooij, M.B., and Schipper, D.J., *Misalignment-Induced Micro-Elastohydrodynamic Lubrication in Rotary Lip Seals.* Lubricants, 2020. **8**(2): p. 19.

[8] Borras, F.X., de Rooij, M.B., and Schipper, D.J., *Misalignment-induced macro-elastohydrodynamic lubrication in rotary lip seals.* Tribology International, 2020. **151**: p. 106479.

[9] Borras, F.X., Bazrafshan, M., et al., *Stern tube seals under static condition: A multi-scale contact modeling approach.* Proceedings of the Institution of Mechanical Engineers, Part J: Journal of Engineering Tribology, 2020. **235**(1): p. 181-195.

[10] Borras, F.X., van den Nieuwendijk, R., et al., *Stern tube seals operation: A practical approach.* Advances in Mechanical Engineering, 2021. **13**(2): p. 1-14.

[11] Morad, O., Saikko, V., and Viitala, R., *Performance characterization of marine lip seals: Contact temperature and frictional torque.* Wear, 2023. **523**.

[12] Lee, C.-Y., Lin, C.-S., et al., *Simulation and experimentation on the contact width and pressure distribution of lip seals.* Tribology International, 2006. **39**(9): p. 915-920.

[13] Yan, C., Jia, X., et al., *Influence of Oil Temperature on the Lip Seal's Performance.* Tribology Transactions, 2019. **62**(5): p. 739-746.

7 Authors

Aalto University, School of Engineering

Otakaari 24, 02150 Espoo, Finland:

Omar Morad, M.Sc., ORCID 0000-0001-9330-4086, omar.morad@aalto.fi

Asst.-Prof. Dr Raine Viitala, ORCID 0000-0003-1672-1921, raine.viitala@aalto.fi

Dr. Vesa Saikko, ORCID 0000-0002-0196-0033, vesa.saikko@aalto.fi

https://doi.org/10.61319/BABRUXJU

A method of direct thermal conditioning of mechanical seal faces: CFD, analytical analysis and testing

Joseph Kaleshian, Ray Clark, Henri Azibert, and Michael Grimanis

Direct and indirect cooling of contacting mechanical seals are fundamentally known practices to enhance durability and improve machinery performance. A new alternate stationary seal face design with a modified seal gland provides direct thermal conditioning of the mechanical seal face by circulating cooling or heating fluid directly through an isolated flow channel. The pressure-velocity capability increased significantly as a result of highly effective heat removal ability and the utilization of a wider face materials range. Simulation showed the generation of turbulence in the circumferential flow direction significantly improving heat transfer in agreement with the experimental and analytical results. In addition dry nitrogen gas was investigated for the dry running condition.

1 Introduction

Mechanical seals are used to contain fluid where a rotating shaft enters a housing as in pumps, mixers, compressors, and other equipment. They prevent leakage of high-pressure fluid into the environment. In many applications the heat soak and or heat generation must be mitigated to obtain extended seal life. In standard practice mechanical seals are cooled using heat exchangers, flush plans and quenching methods. These methods require extensive hardware set up and associated periodic maintenance. Localized thermal conditioning of the mechanical seal faces allow for cooling or heating of the faces independent from the process fluid based on process requirements.

2 Mechanical Seals

2.1 Overview

In general, contacting mechanical seals have a set of primary seal faces, rotary and stationary, and a set of secondary static or semi-dynamic seals such as o-rings and gaskets. Both primary seal faces are pushed against each other using a combination of spring force and hydraulic force from the sealed fluid. The primary sealing interface is between the rotary and the stationary, where the rotary face is rotating with the shaft and the stationary face is secured inside the equipment housing. In operation, mechanical seal faces are designed to utilize lubrication from the sealed fluid and the seal face material combination to minimize frictional heat generation and prevent damage. Common mechanical seal design types are pressure balanced and unbalanced, pusher and non-pusher, single spring and multi-spring configurations [25].

2.2 Mechanical Seal Failure Causes

Several factors can contribute to mechanical seal inadequate life and/or failure; the most common causes of failure [25] can be divided into two groups:

2.2.1 Mechanical or Material Issues

There can be a number of mechanical failure considerations with mechanical seals such as improper installation, misalignment, excessive vibration, and process fluid contamination. Material related failures can stem from improper material selection to resist corrosion or temperature conditions. Seals can also be subject to abrasive wear eroding and damaging components, and clogging that can restrict necessary components motion and proper seal face tracking. Furthermore, excessive heat from high fluid temperatures can cause elastomers to swell or age restricting their effectiveness leading to leakage [25].

2.2.2 Lack of Adequate Lubrication

Process liquid can vaporize within the seal interface due to localized heat generation caused by heat soak or frictional heat. The combination of pressure and velocity may exceed the seal design or face material capabilities. Insufficient pressure margin above the liquid flash temperature can also lead to vaporization. The process liquid can solidify due to low temperature (freezing), or too high a temperature (crystallization). Dry running conditions, where the sealed process is a gas, either incidental or intentional can also lead to seal failure. Some unloader pumps are sometimes operated after the feed tank has been emptied; some vertical multistage pumps can be started without liquid in the seal chamber. Top entry mixers will typically have gas over the mixed liquids, and the pressure and velocity conditions could exceed the face material capabilities.

2.3 Flush Plans and Methods of Temperature Control

In this paper the primary focus is on the lack of lubrication at the seal faces due to temperature conditions, so it is useful to review the typical solutions that are routinely applied to prevent this problem.

The American Petroleum Institute (API), Standard 682 4th edition [24], piping plans are widely used in the industry to control seal chamber fluid temperature. One strategy is to introduce a flush liquid inside the seal chamber in close proximity to the seal faces to maintain proper lubrication, pressure, and temperature conditions.

API Flush Plan 11 (API 682 Appendix G section G.6): Recirculation from the pump discharge to the seal chamber through an orifice. It provides cooling and can be used to increase seal chamber pressure.

API Piping Plan 21 (API 682 Appendix G section G.10): Recirculation from the pump discharge to the seal chamber through a heat exchanger. It provides cooled liquid to the seal chamber and improves fluid vapor temperature margin. However, it is extremely energy inefficient as the cooled liquid must be reheated to process temperature. The heat exchanger must be able to handle pump discharge pressure.

API Piping Plan 23 (API 682 Appendix G section G.12): Recirculation of the seal chamber liquid using a pumping ring through a heat exchanger and back into the seal. It is energy efficient as it only cools the seal chamber fluid. The heat exchanger must be able to handle seal chamber pressure.

API Piping plan 32 (API 682 Appendix G section G.14): It introduces clean cool liquid to the seal chamber from an external source. The purpose is to provide cooling and/or increase pressure. It is commonly used in the industry and is relatively simple. The flush fluid supply pressure must be reliable and higher than seal chamber pressure. If used for cooling the flush fluid must often be reheated to process temperature. This external liquid may also need to be removed from the process at a later point, which can be highly energy intensive if evaporation is required. Another strategy is to introduce a fluid on the outside of a primary seal. It is separated from the process and does not need to be pressurized above seal chamber pressure.

API Piping Plan 55 (API 682 Appendix G section G.22): A dual seal arrangement is used, and an external liquid is introduced to cool or heat the primary seal. It is simple but requires a dual seal.

API Piping Plan 62 (API 682 Appendix G section G.24): A quench stream is brought from an external source to the atmospheric side of the seal faces. The quench stream can be low-pressure steam or clean water to heat or cool the seal. This quench stream is not sealed from the environment.

3 Direct Thermal Conditioning of Mechanical Seal Faces

The direct thermal conditioning concept of mechanical seal faces uses a nonconventional approach to cool or heat mechanical seal components without the use of standard piping plans. This alternate design provides a mechanical seal assembly which can adapt to variable process liquid temperature requirements including the absence of liquid process for dry running, (gas), conditions. The assembly includes a rotary seal face and a modified stationary face with two profiles, as shown in Figure 1(a) for wet, (liquid), process fluid conditions, and Figure (b) for dry process conditions (for example, dry nitrogen gas as the process fluid). In addition, a stationary seal elastomeric boot with inlet and outlet ports is used as shown in Figure 2(a) for wet conditions, and figure 2(b) for dry conditions. Finally, a modified seal gland with corresponding inlet and outlet ports completes the assembly as shown in Figure 3(a). Thus, an independent heat transfer flow channel isolated from the process fluid is radially positioned in close proximity to the rotating interface at the static seal outside diameter, as shown in Figure 3(b). The elastomeric boot and gland ports thereby allow for an independent flow of a circulating heat transfer fluid through the stationary seal face. As the circulating liquid flows through the isolated channel, the static and rotary interface temperature is altered based on the circulating fluid temperature required to thermally condition the seal assembly, shown in Figure 3(b).

(a)Two sided (b) Three sided

Figure 1: Modified Stationary Face (a) For wet evaluation, (b) For dry evaluation

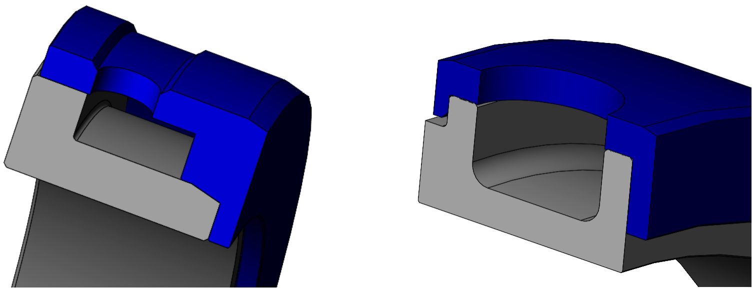

(a) Two sided flow channel (wet) (b) Three sided flow channel (dry)

Figure 2: Modified Stationary Seal Ring Secured Inside Elastomeric Boot

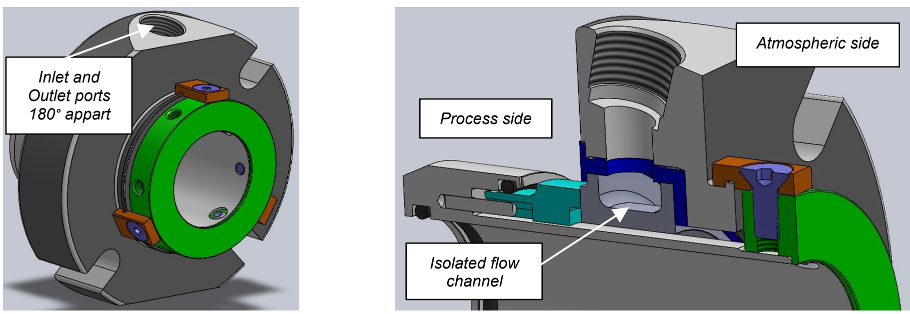

(a) (b)

Figure 3: (a) Modified static housing, (b) Independent flow channel for heat transfer

In dry running condition both mating surfaces can often retain the frictional heat generated due to limited thermal dissipation. In such cases the cooler heat transfer liquid is flowing through the static face channel can cool both mating surfaces and prevent damage to the seal assembly. In process conditions requiring elevated temperatures, a warmer fluid can be introduced through the flow channel to heat the mating surface to a desired process temperature. In addition, the isolated heat transfer channel eliminates dilution of process fluid and the associated hardware maintenance. The piping plans related to this concept are plans 11, 21, 23, 32, 55 and 62 [24]. Thus, in comparison to conventional piping plans, direct cooling can reduce life cycle costs associated with external flush dilution, external flush removal, and flush system pressurization maintenance. Another benefit for dry operation is the dramatic increase in pressure-velocity (PV) limit due to improved thermal conditioning. Thermal deformation of the mechanical seal faces and degradation of the secondary seal materials may also be reduced. Standard single cartridge mechanical seal assembly can be modified to fit in standard dimensional envelopes. Optional standalone modular cooling or steam generating units can be used for circulating heat transfer fluids depending on application requirements. This concept is a part of thermal conditioning of mechanical seals effort that has been investigated in earlier technical publications [10].

4 Design Validation

Thermally conditioned faces can fulfil various process operating temperature requirements using suitable heating or cooling fluid temperatures. Effective heat removal reduces the seal face temperature by dissipating frictional heat generation and minimizing wear. The direct thermal conditioning concept was verified for wet and dry process fluids. Comparative results were obtained and evaluated analytically, through Computational Fluid Dynamics (CFD) simulation, and experimentally through physical laboratory tests.

4.1 Analytical

Analytical study was conducted to investigate the potential heat transfer and heat flow within the concept. The following correlation shown in equation (1) was used in developing the analytical heat transfer model [11]. The correlation for Nusselt number, Nu, is used when calculating convective heat transfer coefficients for internal laminar flow in channels, shown in Equation (1). The correlation was derived from experimental data and theoretical analysis and adjusted for a rectangular channel using a hydraulic diameter, Dh, relationship.

$$Nu = 3.66 + \frac{0.0668\left(Re*Pr*(\frac{Dh}{L})\right)}{1+0.04\left(Re*Pr*\left(\frac{Dh}{L}\right)\right)^{2/3}} \tag{1}$$

This correlation therefore represents the laminar flow conditions (Re< 2100) in non-circular channels with constant wall temperature. The 3.66 constant represents the laminar flow regime (Re < 2100), and is derived from the Sieder-Tate correlation [23]. The additional constant in the correlation adjusts for the effects of buoyancy and thermal boundary layer development. The PV factor for mechanical seals [12] refers to the product of pressure and velocity experienced by the seal interface during operation. It is a critical parameter in determining the suitability and face material combination of a mechanical seal for a specific application. The frictional heat generated from the mechanical seal faces in the analytical heat transfer model was derived from the product of PV shown in Equation (2), along with the face area, Af, and coefficient of friction, μ, shown in Equation (3).

$$PV = \left(Psp + Pp(b - k)\right) * Vm \tag{2}$$

$$H = Pm * Vm * Af * \mu \tag{3}$$

Results obtained from this analytical method are in close agreement with the CFD analysis and the experimental results that are given in detail in the Summary and Results section. The analytical model takes average values of parameters (e.g. velocity, heat transfer coefficient, wall temperatures) through the flow channel. As indicated in the CFD model, localized values are calculated, possibly accounting for certain minor discrepancies between the analytical and computational models.

4.2 Computational Fluid Dynamics (CFD) Simulation Analysis

4.2.1 Analysis for Wet Condition

Flow models consistent with laboratory test conditions were developed, meshed, and computationally prepared to simulate the fluid flow and conjugate heat transfer performance of the direct cooling device for mechanical seals under both wet and dry running conditions. CFD analyses were then carried out using Ansys Fluent with a k-ω turbulence model [26] which included viscous heating and curvature correction. A cutaway view of the flow model used for wet running analysis is shown in Figure 4(a). This model consists of a self-sintered silicon carbide (SSC) stationary seal ring (SSR) paired with a carbon graphite (CB) rotary seal ring (RSR) driven by an 89,0 mm (3.5 in) shaft at 3600 rpm. The process fluid was water at gage pressure of 1.379 MPa (200 psi) and 71 C (160 F) with zero through flow. The rectangular flow channel bounded by the SSR and Buna boot had an axial width of 9,65 mm (0.380 in) and a radial height of 4,29 mm (0.169 in) forming a cross-sectional flow area of 41,4 mm^2 (0.064 in^2) and a hydraulic diameter of 5,94 mm (0.234 in). The coolant fluid was also water having an inlet temperature of 21,7 C (71 F) and flow rate of 7,51 l/min (2 gpm), or 3,79 l/min(1 gpm) per channel side. The outlet pressure of the coolant was set to 0.028 MPa (4 psi) matching the experimental data. The frictional heat generation at the sliding interface of the RSR and SSR was calculated to be 0,859 kW (2932 Btu/h) using Equation (2) and (3) shown above. Finally, based on previous internal data for this seal face material combination 80% of the frictional heat generated was assumed to enter the higher thermally conductive SSR, while 20% entered the (RSR) material. The 80-20% proportion was determined internally in previous work.

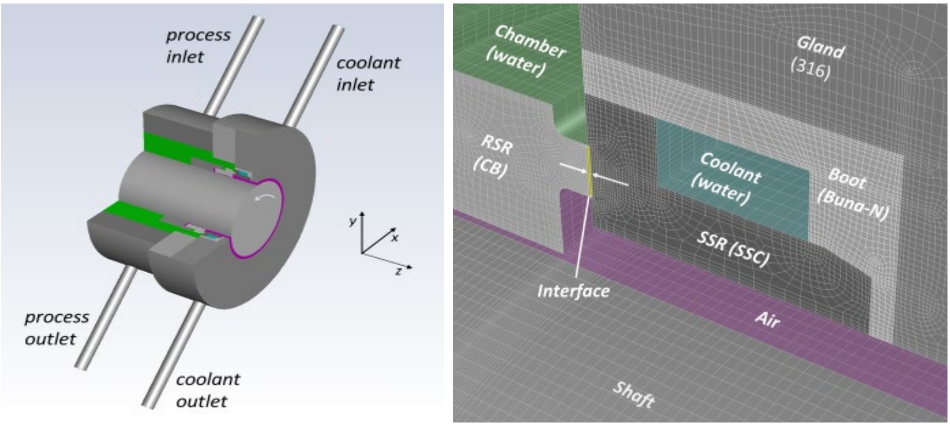

(a) (b)

Figure 4: CFD Wet Model Configuration (a) Full model view, (b) Sectional view

Figure 4(b) shows a cross-section of the flow channel region, including both solid and fluid material components along with associated meshing of the various zones. Axially thin 0,127 mm (0.005 in) by 3,175 mm (0.125 in) radial interface regions represent the heat-sources, one for each seal ring. The frictional generated heat was distributed uniformly within these regions.

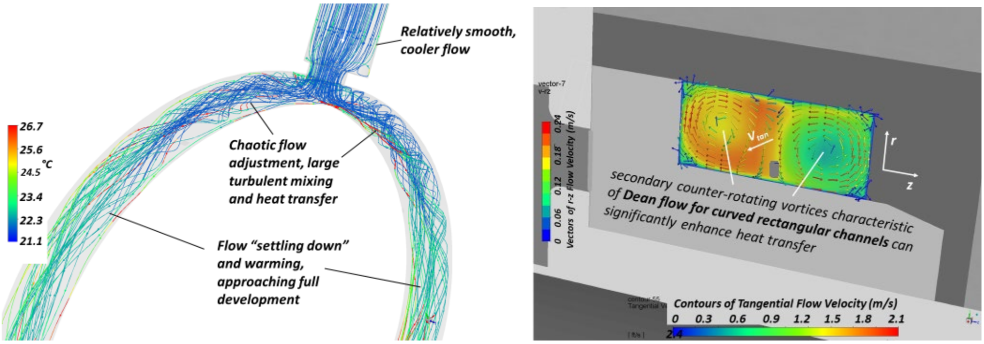

(a) (b)

Figure 5: CFD Wet Flow Channel Patterns (a) Flow pathlines, (b) Dean flow vortecies

Figure 5(a) shows a close view of temperature-colored pathlines of flow near the entrance region of the cooling channel. Here, the effects of abrupt change in flow boundary shape from the circular cross-section of the inlet port to the rectangular cross-sections of the channel branches is evident. The nature of the flow in the circular sections is seen to be developed and regularly organized, especially when compared with the more chaotic, highly turbulent regions immediately downstream of the channel inlets. Note also that within a relatively small distance further downstream from the flow channel inlets the turbulent flow becomes more organized as it approaches full development.

Figure 5 (b) shows an interesting pattern of both tangential and rotational flow within the flow channel. The secondary *r-z* flows called Dean vortex pairs [13, 14] are characteristic of flow in curved rectangular channels. The Dean Number, De, is a dimensionless parameter representative of the ratio of inertial and centrifugal forces to viscous forces, and is defined in Equation (4) as:

$$De = Cr^{\frac{1}{2}} * Re \tag{4}$$

Here, the Curvature Ratio, Cr, is defined as Dh/R (hydraulic diameter/mean radius of flow channel). Flows with De > 400 can typically be considered fully turbulent, although strong curvature has been found to delay complete transition to De = 800, or higher. For the case described, the Reynolds Number was 9,234 corresponding to a Dean Number of 3,015, well within the turbulent regime. In addition, it should be noted that reduction of heat removal efficiency by the coolant as it travels through the flow channel can be attributed to warming of the wall-adjacent flow as well as moderation of local turbulence intensity. The Dean Number which determines the regime of flow does not vary with position along the channel. The presence of secondary rotational flow patterns (Dean vortices) within the curved rectangular channel act to promote heat transfer [13,15]. One author has reported that selective combination of channel curvature and aspect ratio can enhance heat transfer up to 2 or 3 times that of a straight channel [16]. By contrast, the analytical model assumed a simplified straight channel utilizing a hydraulic diameter to compensate for the rectangular geometry.

Based on the above, the CFD analysis yielded an outlet coolant flow temperature of 24.5 C (76.1 F), amounting to a temperature rise of 2.83 C (5.1 F). This rise in fluid temperature corresponds to a heat removal rate of 0.74 KW (2,539 Btu/h), or 86.6 % of the frictional heat generated at the sliding interface of the seal rings.

4.2.2 Analysis for Dry Condition

Figure 6 (a) shows the fluid zones used for the dry operating conditions. These zones consisted of the N_2 process gas, ambient air, and water inside the flow channel. The Nitrogen gas had a gauge pressure at 0.69 MPa (100 psi), and temperature of 34,4 C (94 F), again with zero throughflow. The total flow through the cooling channel was set to 1,89 l/min (0.5 gpm), or 0,95 l/min (0.25 gpm) per channel side, with inlet temperature of 23,6 C (74.4 F). The corresponding Reynolds Number per channel side was 1934, with a Dean Number of 807. The flow regime throughout the cooling channel was therefore considered to be turbulent. Finally, the rotational speed of the shaft was set to 750 rpm. For this set of operating conditions the simulated temperature rise through the flow channel was found to be 2,7 C (4.5 F), corresponding to a heat removal rate of 0,328 KW (1119 Btu/h), amounting to 84.9% of the calculated generation rate of frictional heat at the seal ring interface. The temperature rise measured in the laboratory was found to be 1,4 C (2.5 F) corresponding to a heat removal rate of 0,184 KW (624 Btu/h) amounting to 46.2% of the frictional heat generation rate based of a coeficient of friction estimate of 0,3, same as that used for the CFD calculations. The simulation was then repeated assuming a friction coefficient of 0.15. The new rise in predicted temperature was 1,5 C (2.7 F), and a heat removal rate of (669 Btu/h), both within 7% of the measured values. Figure 6(b) shows the evolution of temperature and turbulence colored flow vectors at various angular positions along the channel.

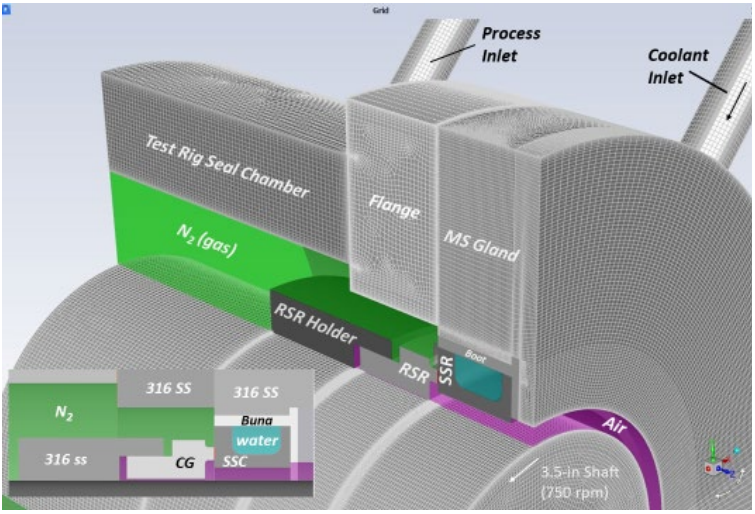

(a)

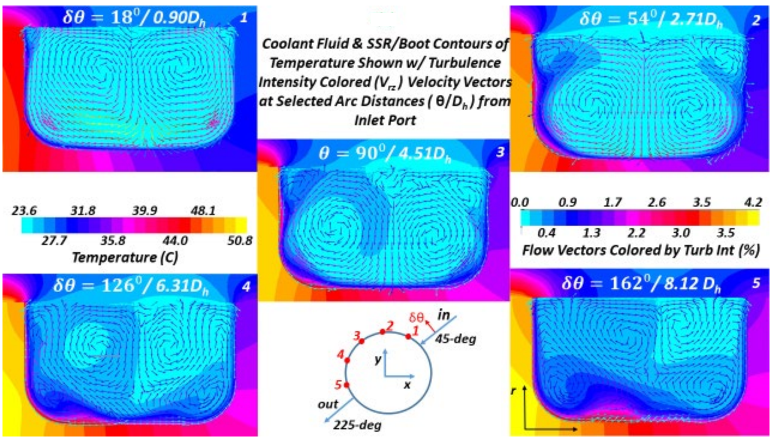

(b)

Figure 6: CFD dry running conditions (a) mesh, (b) flow patterns

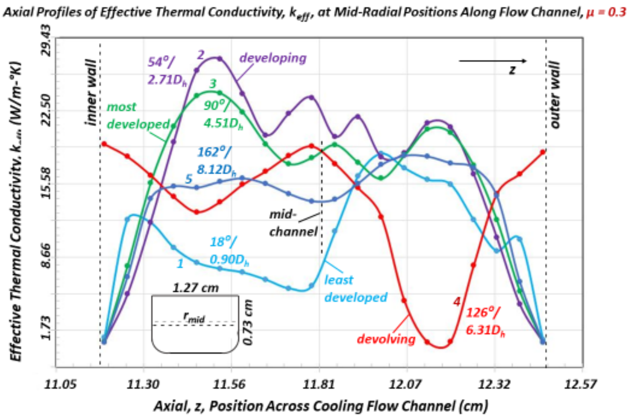

(a)

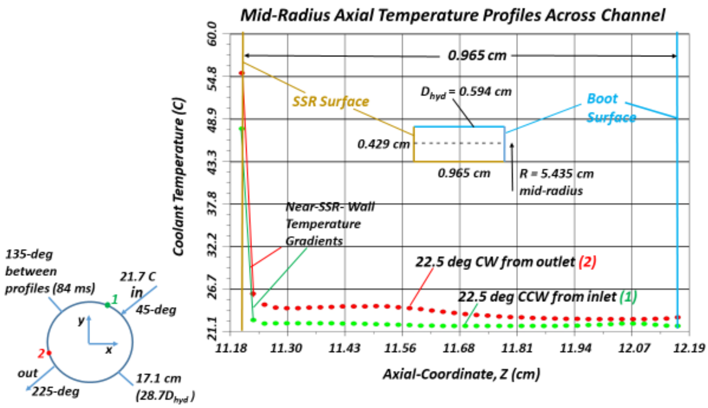

(b)

Figure 7: CFD dry running conditions (a) Thermal conductivity, (b) Temperature profiles

Shown in Figure 7(a) are axial profiles of effective thermal conductivity, again at the same various angular positions along the flow channel. The behaviour of these curves is related to the local flow vorticity within the channel. Finally, Figure 7(b) shows axial temperature profiles near the channel inlet and outlet positions.

It should be noted that the coefficient of friction was adjusted to the experimental data. The subject of friction can be expanded upon in a separate paper. Any accompanying non-axisymmetric face deformation is minimal due to the low temperature gradient across the faces < 2 C (3.6 F) and was not considered in this study.

4.3 Experimental Tests and Results

The concept of direct thermal conditioning of the mechanical seal faces was tested under two main operating conditions; first wet running in the presence of process liquid city water, and second dry running with dry nitrogen gas replacing the process liquid. The experimental test rig, Figures 8(a,c), was designed to examine the flow through the process isolated channel, with focus on seal ring cooling via heat transfer to the coolant. In both test configurations a rotating shaft passing through a fluid reservoir was used and sealed by a companion seal on one end of the reservoir and the concept seal on the other. A thermocouple shown in Figure 8(b) was located in close proximity to the mating interface primarily attached to the modified stationary face; other thermocouples were located at the inlet and outlet of the flow channel ports. A flow meter depicted in Figure 8(a) connected to the inlet port to control and measure the circulating water flow. In the same Figure, pressure and temperature gauges on both inlet and outlet ports were installed to measure the pressure and temperature differentials.

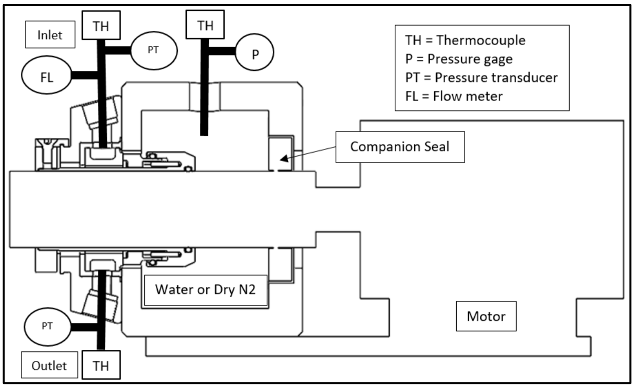

(a)

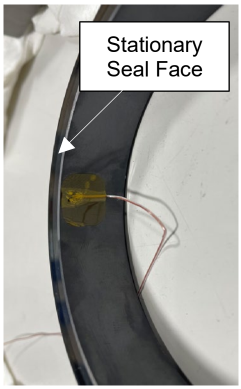

(b)

(c)

Figure 8: (a) Test rig set up, (b) Stationary face thermocouple location (c) Test apparatus

4.3.1 Wet Running

Test conditions: shaft diameter 89,0 mm (3.5 in) at 3,600 rpm, 1.379 MPa (200 psi) process pressure, 1,89 l/min (0.5 gpm), 3,79 l/min (1.0 gpm), 5,68 l/min (1.5 gpm), and 7,57 l/min (2 gpm) flow rate of city water through the stationary flow channel. Test duration was 10 hours. Seal assembly face combination was carbon graphite for the rotary against self-sintered silicon carbide for the modified stationary. Temperature measurements of process, stationary face, and flow channel inlet and outlet were made. Inlet and outlet pressures were measured and found to be negligible. As mentioned, a thermocouple was attached inside the stationary face at 1,27 mm (0.050 in) axial proximity to the mating interface with the rotary. The heat removed by the flow channel was calculated in relation to various flow rates at two process temperatures, as shown in Figure (9). As expected, the heat removal rate rises with increasing rate of flow circulation through the modified stationary face. Note also that the heat removal for the 93 C (200 F) process case exceeds that of the 38 C (100 F) process, for example at 5,68 l/min (1.5 gpm) flow rate.

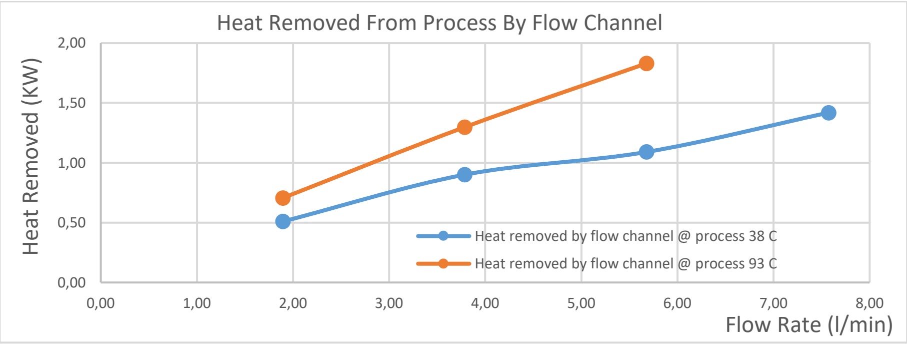

Figure 9: Heat Removed by Flow Channel at Various Flow Rates

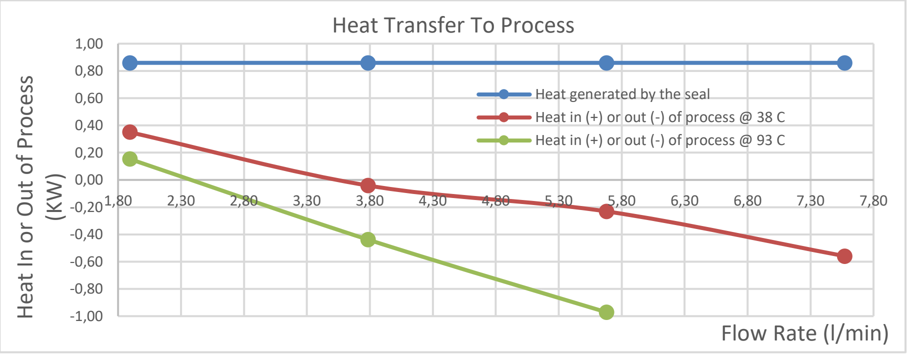

Figure 10: Heat Transfer to the Process in Relation to Flow Rate

The heat transfer to the process fluid is shown in Figure (10), as the flow rate increases the heat removed from the mating surface increases surpassing the constant heat generated by the seal. The excess heat removal is then taken out of the process as an additional source of process fluid thermal conditioning. Comparison of wet running results obtained for the heat transfer, Q, from the analytical, CFD, and experimental analyses are presented in Table (1). Reasonable agreement can be seen between the corresponding results, thereby offering an acceptable degree of validation for this investigation of the direct cooling design concept.

Table 1: Comparative Results for wet at 1.379 MPa, 3600 rpm, and 7,57 l/min

Coolant Variable	***Experimental***	***Analytical Calculation***	***CFD analysis***
Tin (C)	*22*	*21,6*	*21,7*
Tout (C)	*25*	*24,0*	*24,5*
ΔT (C)	*+3*	*+2,4*	*+2,8*
Q (KW)	*1,6*	*1,3*	*1,5*

Wear for wet running conditions was negligible.

4.3.2 Dry Running

Additional tests were conducted using dry nitrogen gas as the process fluid and water circulating through the flow channel to determine the effect of process pressure and shaft speed on the effectiveness of heat transfer in dry running conditions. first at 0.345 MPa (50 psi) and 500 rpm, and second at 0.689 MPa (100 psi) and 750 rpm respectively; in both tests the flow rate of circulating water through the stationary face was at 1,89 l/min (0.5 gpm). Seal assembly face combination was carbon for the rotary against self-sintered silicon carbide for the modified stationary. Inlet and outlet flow channel circulating water pressures were again found to be negligible. At 0.345 MPa (50 psi) and 500 rpm the process temperature exceeded the face temperature while at 0.689 MPa (100 psi) and 750 rpm the face temperature increased in relation to the process temperature, shown in Figure (11). As pressure and speed increase the mating interface temperature at the faces increases. As Figure (11) shows, due to the effectiveness of the flow channel the face temperature remains close to process temperature.

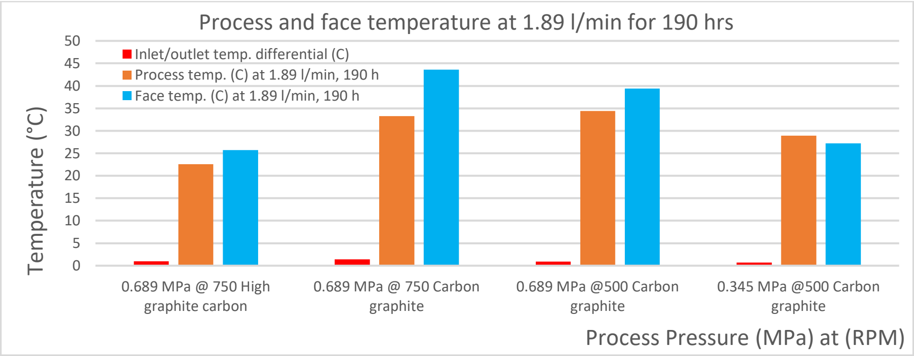

Figure 11: Comparative Experimental Temperature Results

A comparable test was conducted at 0.689 MPa (100 psi) process pressure and 750 rpm to determine the change in carbon material grade effect on the heat generation and removal and PV factor capability; a high graphite content carbon rotary face material was used to compare against carbon graphite material at the same conditions. As a result the high graphite content carbon face temperature was measured significantly lower compared to the carbon graphite face.

To determine comparable wear characteristics both face materials were measured before and after the test. The measurements were taken at six locations along the rotary face wear track and an average wear was calculated. As shown in Table (1), minimal average wear 0,023 mm (0.0009 in) for the carbon graphite and 0,021 mm (0.0008 in) for the high graphite content carbon were calculated.

Table 2: Average wear measurenment for dry running at 0.689 MPa over 190 hrs

Rotary face material	***Wear Measurement locations (mm)***						***Average wear (mm)***
	1	*2*	*3*	*4*	*5*	*6*	
Carbon graphite at 750 rpm	*0,025*	*0,013*	*0,013*	*0,025*	*0,025*	*0,038*	*0,023*
High graphite content carbon at 750 rpm	*0,025*	*0,013*	*0,013*	*0,025*	*0,038*	*0,013*	*0,021*

Comparison of dry running results obtained for the heat transfer, Q, from the analytical, CFD, and experimental analyses are presented in Table (3). Reasonable agreement can be seen between the corresponding results, thereby offering an acceptable degree of validation for this investigation of the direct cooling design concept.

Table 3: Comparative Results for dry N2 gas at 0.689 MPa, 750 rpm, and 1.89 l/min

Coolant Variable	***Experimental***	***Analytical Calculation***	***CFD analysis***
InT (C)	*23,5*	*23,8*	*23,6*
OutT (C)	*24,9*	*25,2*	*25,1*
ΔT (C)	*+1,4*	*+1,4*	*+1,5*
Q (KW)	*0,184*	*0,181*	*0,196*

5 Summary of Results

The PV capability of the mechanical seal face combinations was increased nine fold. Figure (12) shows the heat transfer to the mechanical seal face cooling channel versus the PV factor for the experimental data and the values derived with the heat transfer model.

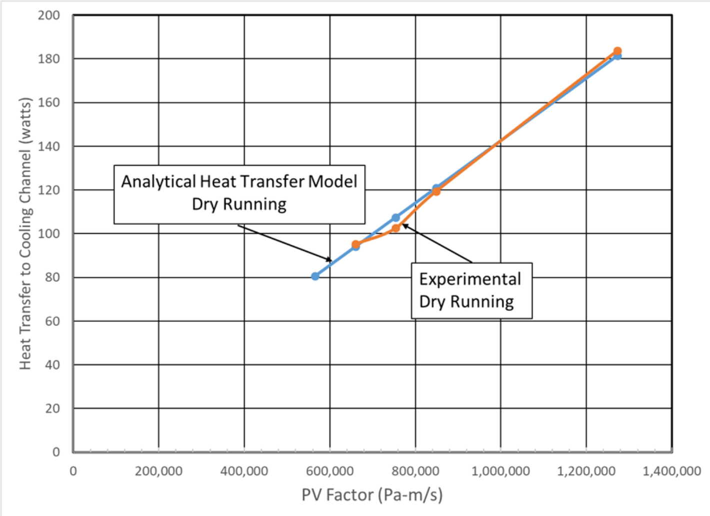

Figure 12: Heat Transfer to Flow Channel vs. PV From Experimental and Analytical Results

CFD model development and associated meshing involved both solid and fluid zones representative of the hardware used for testing. Highlights related to the CFD analysis:

- In curved rectangular channels, secondary flow pairs of rotating *Dean* vortices are created by centrifugal forces acting on the fluid.
- The presence of such vortices have been shown to enhance heat transfer in curved rectangular channels [2,6,14,15].
- The strength and thermal effectiveness of Dean Flows are characterized by the Dean number, De, a modified Reynolds number based on the ratio of the hydraulic diameter to the mid-radius of the channel, the so-called *curvature ratio, Cr*.
- For the wet flow case simulated, channel conditions were found to be, Re = 9234 and De = 3015, both considered to be well within in the turbulent flow regime. For the dry flow channel conditions, Re = 1934 and De = 807.
- Due to the positioning of the heat sources (chamber fluid and sealing interface) relative to the flow channel, as well as the large difference in thermal properties of the flow surface materials, the temperatures of SSC surfaces were found to be much higher and more conductive than those of the Buna surfaces.
- For the cases examined, more than 99% of the total heat absorbed by the flow channel occurred through the (SSC) surface boundaries.
- Thus, for purposes of heat transfer analysis, the Buna surface boundaries of the flow channel were treated as adiabatic.

- High levels of turbulence intensity within the channel were found to locally enhance the transfer of heat into and within the fluid by means of chaotic fluctuations and mixing of the wall adjacent fluid film and bulk flow stream.
- Potential may exist for improving the heat removal capacity of rectangular channel designs by implementing surface features which can sustain higher levels of turbulence intensity throughout the flow.

6 Conclusion

Uncontrolled temperature variations during operation of a mechanical seal can present grave challenges to the proper performance and life of the seal. An isolated thermal conditioning modification of the stationary seal ring has been shown to potentially offer a valuable degree of thermal control over the performance flexibility and adaptability, and thus life of the seal. These advantages can be achieved using standard seal materials, without affecting process thermal requirements or dilution of the process.

Compared to traditional thermal management piping plans, direct cooling can be significantly more energy efficient. Several factors that often plague conventional thermal management methods such as direct impact on process temperature, the need to remove an external fluid from the process, and the requirement to pressurize cooling or heating liquids to or above process pressure can all add significant contributions to energy consumption. The isolated thermal conditioning system offers elimination or reduction of such power consuming constraints.

7 References

[1] Tilak T. Chandratilleke, Nima Nadim, and Ramesh Narayanaswamy, “Vortex structure-based analysis of laminar flow behaviour and thermal characteristics in curved ducts”, International Journal of Thermal Sciences, Volume 59, September 2012., pp 75-86, https://www.sciencedirect.com/science/article/abs/pii/S1290072912001317 1/7.

[2] Tilak T. Chandratilleke, Nima Nadim, and Ramesh Narayanaswamy, “Analysis of secondary flow instability and forced convection in fluid flow through rectangular and elliptical curved ducts”, Volume 34, 2013 - Issue 14: Selected Papers Presented at the Eighth International Conference on Heat Transfer, Fluid Mechanics, and Thermodynamics (HEFAT2011), July 11-13, 2011.

[3] Xueling Liu, Yuguo Fu, Jiansheng Wang, Huipeng Zhang, and Jianxiao Zhu, “Investigation on flow and heat transfer in rectangular cross-section sinusoidal channels”, International Journal of Thermal Sciences, Volume 176, June 2022.

[4] Xueling Liu, Yuguo Fu, Jiansheng Wang, and Gianan Ge, “Dean instability and thermal characteristic in sinusoidal structure”, International Journal of Heat and Mass Transfer, Volume 206, June 2023.

[5] H. K. Moffatt, “Helicity in laminar and turbulent flow”, Annual Review of Fluid Mechanics 1992.24, pp 281-312.

[6] S. Yanase, R.N. Mondal, and Y. Kaga, “Numerical study of non-isothermal flow with convective heat transfer in a curved rectangular duct”, International Journal of Thermal Sciences, November 2005, pp 1047-1060.

[7] K. C. Cheng, Ran-Chau-Lin, and Jenn-Wuu-Ou, “Fully Developed Laminar Flow in Curved Rectangular Channels”, Journal of Fluids Engineering, March, 1976.

[8] Habchi, Charbel & Lemenand, Thierry & della Valle, Dominique & Peerhossaini, Hassan, “On the Correlation Between Vorticity Strength and Convective Heat Transfer”, 14th International Heat Transfer Conference, 2010.

[9] “This page contains Frequently Asked Questions (FAQ) about mechanical seals”, https://www.sealfaqs.com/?page_id=192#HeatGen.

[10] Xiao, Nian, Khonsari, M. M. “A Review of Mechanical Seals Heat Transfer Augmentation Techniques,” Department of Mechanical Engineering, Louisiana State University, Baton Rouge, LA 70803, USA, January 01, 2013.

[11] McCabe, Warren L., Julian C. Smith and Peter Harriot, “Unit Operations of Chemical Engineering, 5th ed., New York, McGraw-Hill Book Company, 1993.

[12] Buck, Gordon S., “Pressure Ratings of Mechanical Seals“, Proceedings of the 14th International Pump Users Symposium, Houston, Texas, 1997.

[13] Bo Zhou and Shougi Yuan, Soon Keat Tanb, “Dean Instability and Secondary Flow Structure in Curved Rectangular Ducts”, Yalin Li, Xikun Wang, International Journal of Heat and Fluid Flow, 68, 189-202, Dec 2017.

[14] P. M. Ligrani, S. Choi, A. R. Shallert, P. Skogerboe, “Effects of Dean Vortex Pairs on Surface Heat Transfer in Curved Channel Flow”, International Journal of Heat and Mass Transfer, 39, 27-37, Jan 1996.

[15] J. Christopher Sturgis and Issam Mudawar, “Single-phase Heat Transfer Enhancement in a Curved Rectangular Channel Subjected to Concave Heating”, International Journal of Heat and Mass Transfer, 42, 1255-1272, Apr 1999.

[16] Paisarn Naphon and Somchai Wongwises, “A Review of Flow and Heat Transfer Characteristics in Curved Tubes”, Renewable and Sustainable Energy Reviews, 10, 463-490, Oct 2006.

[17] D. D. Joye,“Optimum Aspect Ratio for Heat Transfer Enhancement in Curved Rectangular Channels”, Journal of Heat Transfer Engineering, 15, 32-38, Aug, 2007.

[18] Fluid Mechanics: Fundamental and Applications, Yungus A Cengal and John M Cengel, McGraw-Hill Higher Education, 2006, ISBN 978-0072472363.

[19] Y M Zhang, W Z Gu, and J C Han, “Heat Transfer and Friction in Rectangular Channels with Ribbed or Ribbed Grooved Walls, Journal of Heat Transfer”, 116 (1), 58 -65, Feb 1994, https://doi.org/10.1115/1.2910884.

[20] Nian Xiao and M M Khonsari,“A Review of Mechanical Seals Heat Transfer Augmentation Techniques”, Recent Patents on Mechanical Engineering, May, 2013.

[21] Nian Xiao, “Innovative Heat Transfer Augmentation Techniques in Mechanical Face Seals”, LSU Doctoral Dissertation, 2014.

[22] Heat Transfer, Frank M. White, Addison Wesley, 1984, ISBN 0201083248.

[23] E.N. Sieder and G.E. Tate, “Heat Transfer and Pressure Drop of Liquids in Tubes”, Industrial and Engineering Chemistry, 28, 1429-1435, 1936.

[24] American Petroleum Institute Standard 682, 4th edition.

[25] Fluid Sealing Association. https://fsaknowledgebase.org/. 10th April, 2024.

[26] ANSYS Fluent 2019R3 Users Guide, p 1404. 10th April, 2024.

8 Nomenclature

Nu	Nusselt number	
Re	Reynolds number	
Pr	Prandtl number	
De	Dean Number	
D	Cylindrical inner diameter	[m]
Dh	Hydraulic diameter	[m]
Cr	Curvature ratio, Dh/R	
SSR	Stationary Seal Ring	
RSR	Rotary Seal Ring	
SSC	Self-sintered silicon carbide	
CB	Carbon graphite	
R	Mid radius of the flow channel	[m]
L	Cylinder length	[m]
PV	Pressure_Velocity Factor	[Pa-m/sec]
Psp	Spring pressure	[MPa]
Pp	Process pressure	[MPa]
b	Seal balance	
k	Pressure drop factor	
Vm	Velocity at mean diameter	[m/sec]

Pm	Pressure at mean diameter	[MPa]
H	Frictional heat generation	[KW]
Af	Seal face area	[m²]
μ	Coefficient of friction	
Q	Heat transfer	[KW)
Tin	Inlet port temperature	[° C]
Tout	Outlet port temperature	[° C]

9 Lists

9.1 List of figures:

Figure 1: Modified Stationary Face (a) For wet evaluation, (b) For dry evaluation

Figure 2: Modified Stationary Seal Ring Secured Inside Elastomeric Boot

Figure 3: (a) Modified static housing, (b) Independent flow channel for heat transfer

Figure 4: CFD Wet Model Configuration (a) Full model view, (b) Sectional view

Figure 5: CFD Wet Flow Channel Patterns (a) Flow pathlines, (b) Dean flow vortecies

Figure 6: CFD dry running conditions (a) mesh, (b) flow patterns

Figure 7: CFD dry running conditions (a) Thermal conductivity, (b) Temperature profiles

Figure 8: (a) Test rig set up, (b) Stationary face thermocouple location (c) Test apparatus

Figure 9: Heat Removed by Flow Channel at Various Flow Rates

Figure 10: Heat Transfer to the Process in Relation to Flow Rate

Figure 11: Comparative Experimental Temperature Results

9.2 Figure 12: Heat Transfer to Flow Channel vs. PV From Experimental and Analytical Results List of equations:

$$Nu = 3.66 + \frac{0.0668\left(Re*Pr*(\frac{Dh}{L})\right)}{1+0.04\left(Re*Pr*\left(\frac{Dh}{L}\right)\right)^{2/3}} \quad (1)$$

$$PV = \left(Psp + Pp(b-k)\right)*Vm \quad (2)$$

$$H = Pm*Vm*Af*\mu \quad (3)$$

$$De = Cr^{\frac{1}{2}}*Re \quad (4)$$

9.3 List of tables:

Table 1: Comparative Results for wet at 1.379 MPa, 3600 rpm, and 7,57 l/min

Table 2: Average wear measurenment for dry running at 0.689 MPa over 190 hrs

Table 3: Comparative Results for dry N2 gas at 0.689 MPa, 750 rpm, and 1.89 l/min

10 Acknowledgements

The authors extend a special appreciation to A.W. Chesterton Company to encourage and support the work that has been allocated to innovate and engineer the concept.

11 Authors

Company Name: A. W. Chesterton Company

Address: 860 Salem Street, Groveland Massachusetts USA

Principle Engineer: Joseph Kaleshian, Joseph.Kaleshian@chesterton.com

Research and Development Engineer: Ray Clark, Ray.Clark@chesterton.com

Technology and Innovation Consultant: Henri Azibert, camtrackllc@aol.com

Director Innovation Engineering: Michael Grimanis,
Michael.Grimanis@chesterton.com

https://doi.org/10.61319/AW0UCDTV

Group B
Session 5

Reciprocating Seals

B 16

Gonzalo A. Barillas, Andreas Gropp, Freudenberg Sealing Technologies GmbH, Schwalmstadt, Germany

Further Observations in Wiper design and Particle Transport Simulation in the Sealing Gap

B 17

Faras Brumand-Poor, Florian Barlog, Nils Plückhahn, Matteo Thebelt, Katharina Schmitz, RWTH Aachen University, Institute for Fluid Power Drives and Systems (ifas) Faculty of Mechanical Engineering, Aachen, Germany

Advancing Lubrication Calculation: A Physics-Informed Neural Network Framework for Transient Effects and Cavitation Phenomena in Reciprocating Seals

B 19

Anja Dobrinsky, Sebastian Betz, Christoph Schüle, Boris Brodmann, Trelleborg Sealing Solutions R&D, Stuttgart, Germany

Advanced characterization of counter surfaces in linear applications

Further Observations in Wiper design and Particle Transport Simulation in the Sealing Gap

Gonzalo A. Barillas, Andreas Gropp

In the last ISC results with several wiper designs with regards to dirt insert rate into a sealing system was presented. Also, the simulation of the motion of such particles in the sealing gap was shown. Material wear resistance and fluid streamlines before the lip seems to have an influence on particle's ability to pass the gap between seal and rod.In this paper, starting from a standard wiper, lip design alterations were tested. By changing the wiper's lip design a change in the flow lines of the fluid and therefore the particle insert was intended. Among the lip design changes furthermore the improvement in simulation of particle flow in the wiper-rod interaction area is presented. The effects of the lip variation on the particle insert test results will be discussed and compared with simulation results.

1 Introduction

Debris particles in any machine are the main source for premature wear and failure. The costs of damage and reduced lifetime are impressive, as 70% of industrial equipment fail previously due to abrasive particles in the system [1]. Filters help strongly to avoid such damage, nevertheless, understanding the process of particle insert into systems is necessary to design elements that will avoid the contamination of machine systems. In hydraulic systems, one main source of insert is the rod of cylinders in motion. And here for, the wipers are the sealing elements responsible to keep particles outside the system and maintaining sufficient lubrication for the whole rod sealing system endurance. In past works, such particle ingress has been presented [3,4,5]. In previous studies, the mechanics of ingress mechanism based on friction between particle and rod and wiper material was presented [7]. Also, the filtering effects and change of particle size distribution of hydraulic wipers has been observed [5]. At the last ISC in 2022, results showing the potential lip design on particle ingress was presented [8]. Further studies to corroborate these first findings will be presented here: Variation of lip angles on insert behaviour has been done experimentally and analytically with the implementation of particle flow in the Reynold's equation.

2 Test Set Up and Test Procedure

2.1 Test Set Up

In the above-mentioned studies [3,4,5,8] different testing rigs have been used. Repeatability and reproducibility (R&R rate) shown that a simple test rig as shown in **Fig. 1** offers the best rate of approx. 30% which, considering multiple effects like rod surface, wiper variation (tolerances on material and design), particle concentration and distribution, etc., is a quite acceptable value. Additionaly, this setup represents a quite close field application depiction compared to other test rigs.

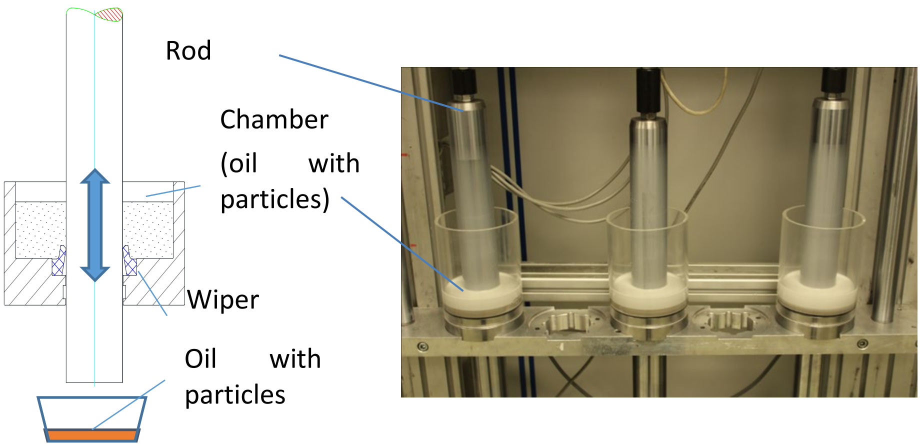

Figure 1: Wiper test arrangement with vertical rod

In this testing set-up, a vertically driven, chrome hard plated, Ø50 mm rod was reciprocating moved up and down (stroke 200 mm) through a wiper holding a defined amount of contaminated fluid, both part of a single fixture. For each tests, three rods were used parallel to have identically motion cycles on wipers. The chamber with contaminated fluid contained a mixture of 1:2 weight ratio (1 part HLP hydraulic oil and 2 parts Arizona sand class 2).

To avoid effects of wiper rocking in the housing detected in previous works [5,8] and so allowing wiper ingress through the outer diameter of the wiper and the housing, TPU wipers with metal cage were chosen. Using standard TPU wipers, the sealing lip was removed and the face angle towards the oil chamber was cut in different angles (110°, 80° and 60°), while the wiper contact zone to the rod was unchanged and is net-moulded with a radius (**Fig.2**). Wiper material: 94 AU 30000, a high performance TPU. The wipers were produced under series conditions and the lip angle alteration was done by mechanical trimming without altering the wiper lip edge.

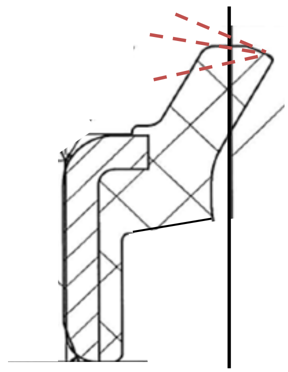

Figure 2: Wiper lip design variation

2.2 Test Procedure

Like previous work on wipers [5,8] three rods were used to test parallel three wipers of each type. The test consisted of two following steps or phases:

First step:

- 20.000 cycles
- Stroke: 200 mm
- Upstroke speed: 0.3 m/s
- Downstroke speed: 0.3 m/s
- Medium: HLP oil and Arizona Sand class 2 mixed in a 1:2 weight ratio
- Room temperature
- Atmospheric pressure

Second step (following to first step):

- Upstroke speed: 0.1 m/s
- Downstroke speed: 0.3 m/s
- Other conditions as in first step

This second step with slower upstroke speed was intended to show effects of stroke velocity on dirt ingress.

Rod surfaces roughness was measured before and after each test, using for every test new rods.

Also, the radial load of the wiper lips was measured before and after each test. The real wiper geometry was measured with a 3D microscope, these data was used to generate the FEM models for the FEA analysis.

The amount of contaminated oil that passes through the wiper was weighed every 5,000 strokes.

3 Test Results

The results show a high spreading of insert rate for each wiper. From three wipers of each variation, only one wiper showed insert rate, while the others showed no measurable insert rate.

As expected, the ingress rate increased at higher downstroke velocities (after 20,000 cycles). And also as seen in [8], a sedimentation effect lead to a decrease in the insert rate with longer operation time.

Wipers with 80° face angle did not show any insert at all. But considering, that each two wipers with 60° and 110° did also not show any insert at all, this cannot be taken as a better result. So, the data basis for a conclusion is still not sufficient at this point.

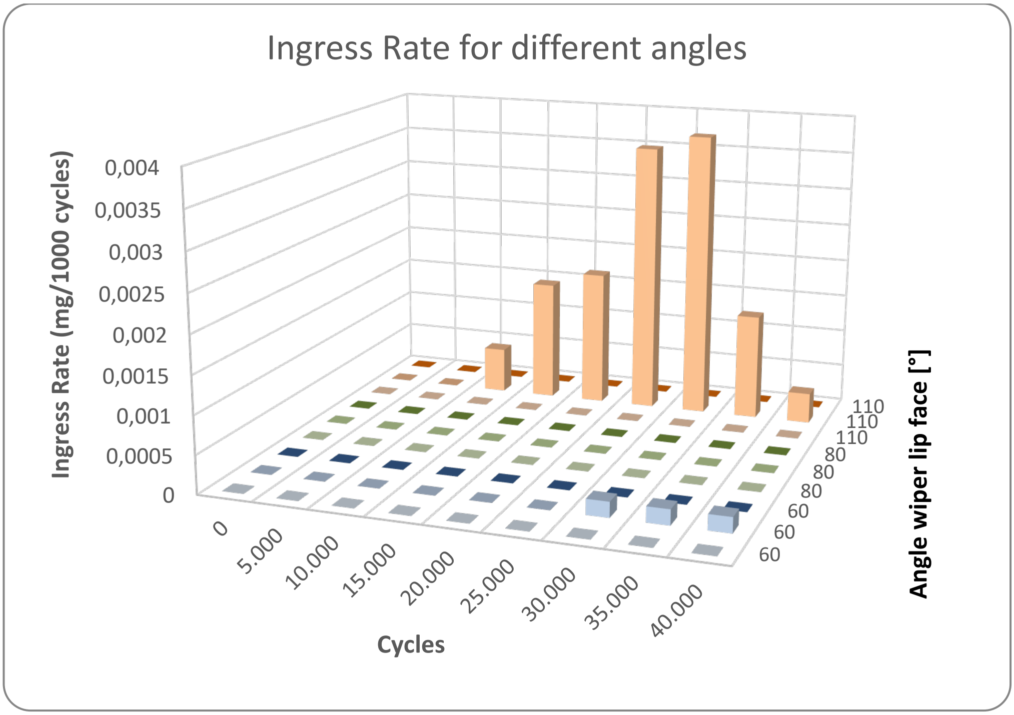

Figure 3: Ingress rate for different wiper lip face angles

It is also remarkable that only the middle rod showed ingress.

Looking at the rod surfaces roughness before the test, we see also some differences: for 60°, all three rods were very similar:

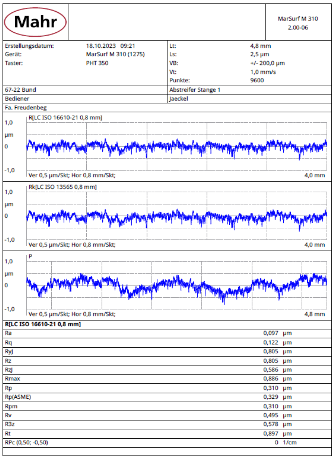
Mahr — MarSurf M 310 2.00-06

Erstellungsdatum: 18.10.2023 09:21 | Gerät: MarSurf M 310 (1275) | Taster: PHT 350 | Lt: 4,8 mm | Ls: 2,5 µm | VB: +/- 200,0 µm | Vt: 1,0 mm/s | Punkte: 9600

67-22 Bund | Abstreifer Stange 1 | Bediener | Jaeckel | Fa. Freudenbeg

R[LC ISO 16610-21 0,8 mm]	
Ra	0,097 µm
Rq	0,122 µm
RyJ	0,805 µm
Rz	0,805 µm
RzJ	0,586 µm
Rmax	0,886 µm
Rp	0,310 µm
Rp(ASME)	0,329 µm
Rpm	0,310 µm
Rv	0,495 µm
R3z	0,578 µm
Rt	0,897 µm
RPc (0,50; -0,50)	0 1/cm

Rod 1 60°

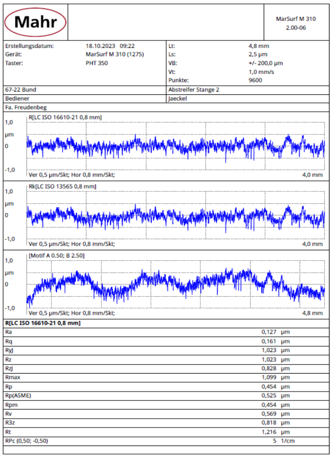
Mahr — MarSurf M 310 2.00-06

Erstellungsdatum: 18.10.2023 09:22 | Gerät: MarSurf M 310 (1275) | Taster: PHT 350 | Lt: 4,8 mm | Ls: 2,5 µm | VB: +/- 200,0 µm | Vt: 1,0 mm/s | Punkte: 9600

67-22 Bund | Abstreifer Stange 2 | Bediener | Jaeckel | Fa. Freudenbeg

R[LC ISO 16610-21 0,8 mm]	
Ra	0,127 µm
Rq	0,161 µm
RyJ	1,023 µm
Rz	1,023 µm
RzJ	0,828 µm
Rmax	1,099 µm
Rp	0,454 µm
Rp(ASME)	0,525 µm
Rpm	0,454 µm
Rv	0,569 µm
R3z	0,818 µm
Rt	1,216 µm
RPc (0,50; -0,50)	5 1/cm

Rod 2 60°

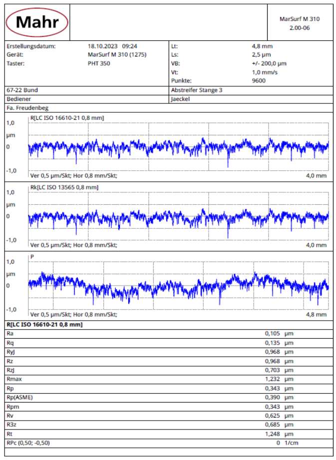
Mahr — MarSurf M 310 2.00-06

Erstellungsdatum: 18.10.2023 09:24 | Gerät: MarSurf M 310 (1275) | Taster: PHT 350 | Lt: 4,8 mm | Ls: 2,5 µm | VB: +/- 200,0 µm | Vt: 1,0 mm/s | Punkte: 9600

67-22 Bund | Abstreifer Stange 3 | Bediener | Jaeckel | Fa. Freudenbeg

R[LC ISO 16610-21 0,8 mm]	
Ra	0,105 µm
Rq	0,135 µm
RyJ	0,968 µm
Rz	0,968 µm
RzJ	0,703 µm
Rmax	1,232 µm
Rp	0,343 µm
Rp(ASME)	0,390 µm
Rpm	0,343 µm
Rv	0,625 µm
R3z	0,685 µm
Rt	1,248 µm
RPc (0,50; -0,50)	0 1/cm

Rod 3 60°

The rods used for the 80° face angle wipers:

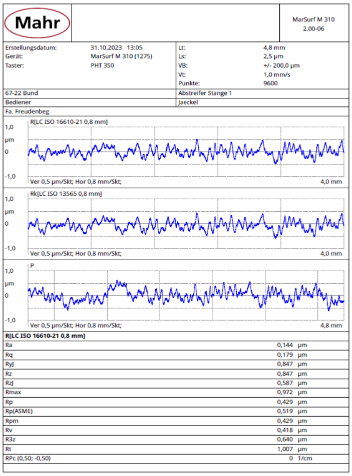
Mahr — MarSurf M 310 2.00-06

Erstellungsdatum: 31.10.2023 13:05 | Gerät: MarSurf M 310 (1275) | Taster: PHT 350 | Lt: 4,8 mm | Ls: 2,5 µm | VB: +/- 200,0 µm | Vt: 1,0 mm/s | Punkte: 9600

67-22 Bund | Abstreifer Stange 1 | Bediener | Jaeckel | Fa. Freudenbeg

R[LC ISO 16610-21 0,8 mm]	
Ra	0,144 µm
Rq	0,179 µm
RyJ	0,847 µm
Rz	0,847 µm
RzJ	0,587 µm
Rmax	0,972 µm
Rp	0,429 µm
Rp(ASME)	0,519 µm
Rpm	0,429 µm
Rv	0,418 µm
R3z	0,640 µm
Rt	1,007 µm
RPc (0,50; -0,50)	0 1/cm

Rod 1 80°

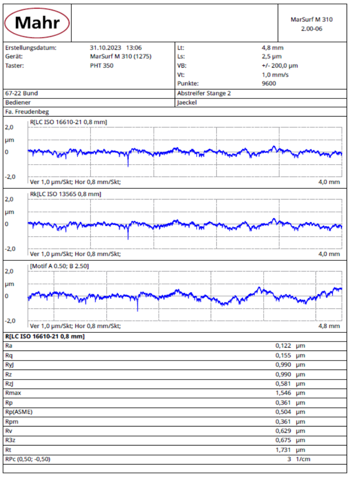
Mahr — MarSurf M 310 2.00-06

Erstellungsdatum: 31.10.2023 13:06 | Gerät: MarSurf M 310 (1275) | Taster: PHT 350 | Lt: 4,8 mm | Ls: 2,5 µm | VB: +/- 200,0 µm | Vt: 1,0 mm/s | Punkte: 9600

67-22 Bund | Abstreifer Stange 2 | Bediener | Jaeckel | Fa. Freudenbeg

R[LC ISO 16610-21 0,8 mm]	
Ra	0,122 µm
Rq	0,155 µm
RyJ	0,990 µm
Rz	0,990 µm
RzJ	0,581 µm
Rmax	1,546 µm
Rp	0,361 µm
Rp(ASME)	0,504 µm
Rpm	0,361 µm
Rv	0,629 µm
R3z	0,675 µm
Rt	1,731 µm
RPc (0,50; -0,50)	3 1/cm

Rod 2 80°

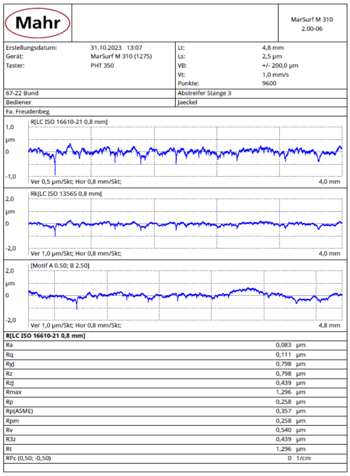
Mahr — MarSurf M 310 2.00-06

Erstellungsdatum: 31.10.2023 13:07 | Gerät: MarSurf M 310 (1275) | Taster: PHT 350 | Lt: 4,8 mm | Ls: 2,5 µm | VB: +/- 200,0 µm | Vt: 1,0 mm/s | Punkte: 9600

67-22 Bund | Abstreifer Stange 3 | Bediener | Jaeckel | Fa. Freudenbeg

R[LC ISO 16610-21 0,8 mm]	
Ra	0,083 µm
Rq	0,111 µm
RyJ	0,798 µm
Rz	0,798 µm
RzJ	0,439 µm
Rmax	1,296 µm
Rp	0,258 µm
Rp(ASME)	0,357 µm
Rpm	0,258 µm
Rv	0,540 µm
R3z	0,439 µm
Rt	1,296 µm
RPc (0,50; -0,50)	0 1/cm

Rod 3 80°

And the rods used for the 110° face angle wipers:

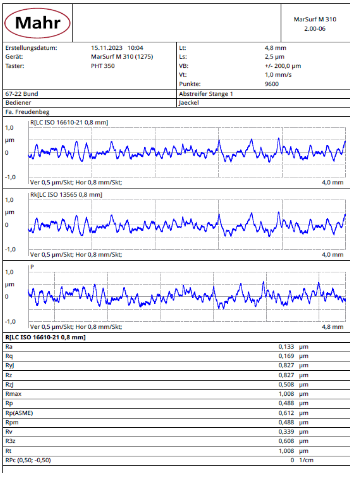

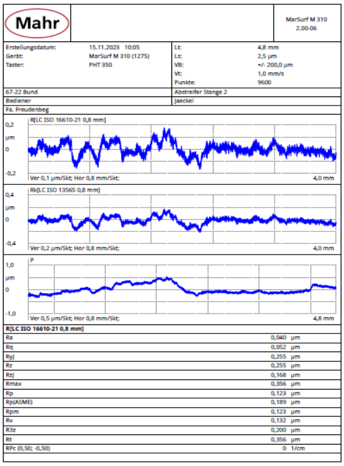

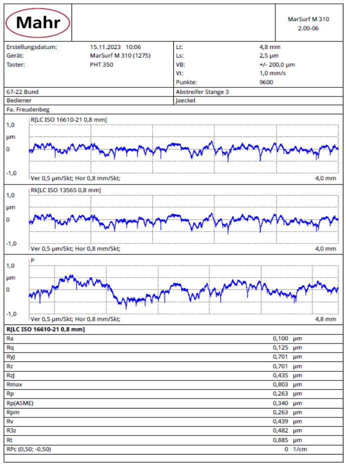

Rod 1 110° Rod 2 110° Rod 3 110°

Summarizing some roughness values for all rods (***Table 1***), we see that the rod with the highest insert rate had at the beginning of the test the smoothest surface:

	Ra	Rmax	Rp	Rv
Rod 1 for wiper 60°	0,097	0,886	0,310	0,495
Rod 2 for wiper 60°	0,127	1,099	0,454	0,569
Rod 3 for wiper 60°	0,105	1,232	0,343	0,625
Rod 1 for wiper 80°	0,144	0,972	0,429	0,418
Rod 2 for wiper 80°	0,122	1,546	0,361	0,629
Rod 3 for wiper 80°	0,083	1,296	0,258	0,540
Rod 1 for wiper 110°	0,133	1,008	0,488	0,339
Rod 2 for wiper 110°	0,040	0,356	0,123	0,132
Rod 3 for wiper 110°	0,100	0,803	0,263	0,439

Table 1: Surface roughness of tested rods before test

This result leads to the need of further testing to statistically corroborate the correlation between surface and particle insert. A possible explanation for this behaviour could be obstacles that surface roughness represents for a particle trying to pass the gap between wiper lip and rod.

4 FEA on Particles in Sealing Gap

The simulation of a particle in a sealing gap was presented in [8]. There, a possible effect of flow lines in a fluid on the particle migration through the sealing gap, was postulated. To corroborate this hypothesis, a deeper understanding of the fluid flow in the gap and around the particles is provided.

But here, the initial assumption, that the Reynolds differential equation would deliver sufficient basis for solving the problem, faces its limitations: The fluid flows around the -assumed as a spherical body- particle not in a 2-dimension field anymore but from all sides.

Additionally, it makes a difference if the fluid is stationary flowing around a fixed particle or if the particle itself is in motion in the instationary fluid (**Fig. 4**)

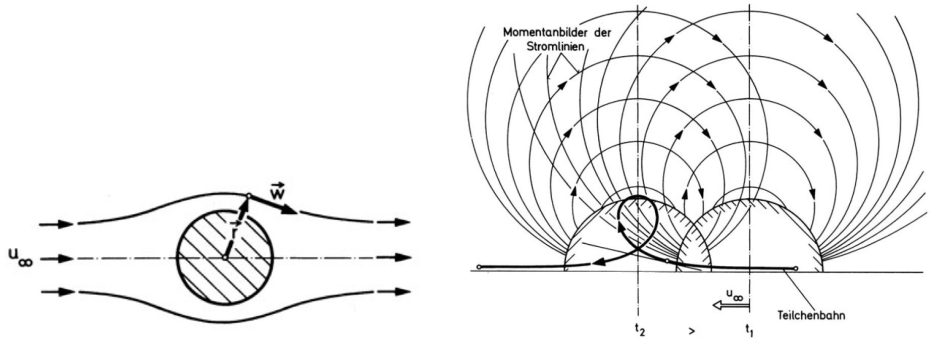

Figure 4: Flow lines around bodies [10]: Left: fixed spherical body being passed by a stationary flowing medium. Right: a cylinder body in motion in a not stationary flowing surrounding

So, the solving of this problem requires adaptions on the Reynolds differential equation which delivers a 2-dimension pressure field around the particle to be able to generate results.

Having x as the rod axis, y as the circumferential axis and z as the radial axis, the particles will be flowing in a pressure field, which is in radial direction (z-axis) constant. Around the particle, we will have four areas in which the pressure field will be constant in radial direction: before, after, below and above the particle. These need to be analyzed individually.

In [8] the particle motion in the gap was described: Particles do not only move in x and z direction, but they also rotate in their y- axis due to different pressure distribution around the particles, especially on the upper and lower side of the particle.

To generate the flow lines or the velocity vector field, we need to use the 2-dimensional results from the Reynolds differential equation to generate a 3-dimensional field with the velocities u, v and w corresponding to the coordinates x, y and z.

The approach to gain results for the velocities u and v consists in using the pressure distribution in x and y direction and the velocity boundary conditions which are the rod velocity, the particle's velocity and its rotation (Fig. 5 and 6).

Furthermore, the continuity equation with the velocity boundary conditions of the particle's velocity and rotation in the field will help us to obtain the velocity w in z direction.

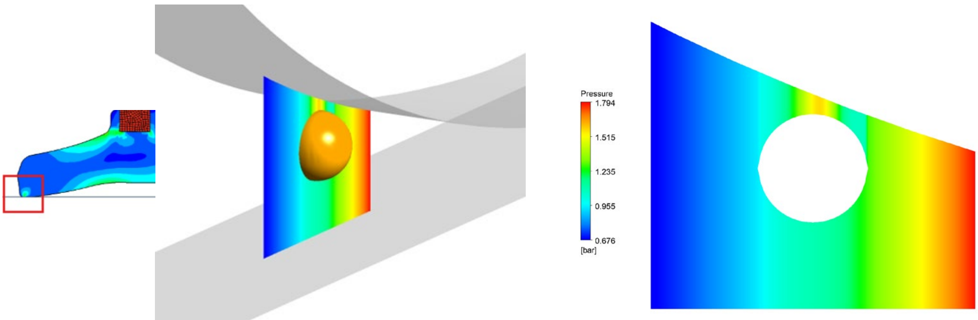

Figure 5: Lip detail and pressure distribution in the x-z field around a particle in the gap

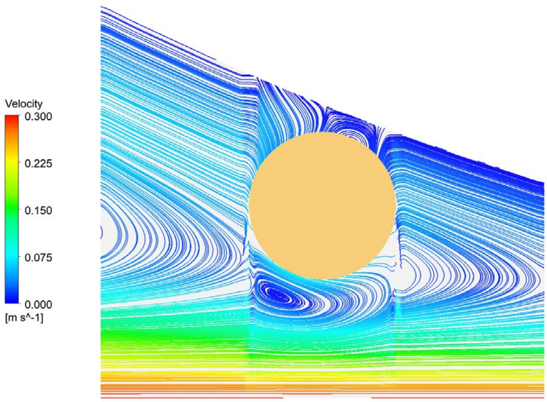

Figure 6: velocity field around the particle in the gap in the x-z field

Fig.6 shows how the strong discontinuity of the oil film thickness generated by the particle in the gap causes dramatical changes on velocity vector field near to the particle. There is a strong influence of the numerical accuracy in the velocity vector field calculation results. This leads to a quite high amount of simulation time and care of the numerical deviations (i.e. gradients calculation) to avoid wrong results.

This calculation must be done for every time step and areas around the particle to generate a full 3-dimensional field.

This is quite time-consuming, and a simplification of the process is being investigated. Nevertheless, the results lead to a 3-dimensional vector field. The effects on wiper lip design on particle ingress are still in the simulation works.

5 Summary and Conclusion

The continuation of the work regarding particle transportation in a gap between an hydraulic wiper lip and a rod in motion reveals still some questions regarding the reproducibility of results in the testing area. Data gathered is not sufficient to postulate relationships between design variables and particle insert. Further testing is still necessary to confirm the relationship between wiper lip geometry and flow line generation and particle insert into the hydraulic system.

Also, the FEA of the velocity field vector around the particle has shown that numerical problems arise around the particle, as the pressure distribution and the particle rotation during the motion in the gap deliver a highly gradient sensibility leading to numerical related inaccurate results. High awareness during the calculation is needed to gather useful results.

The momentaneous 2-dimensional results are the basis to develop a 3-dimensional velocity field around the particle in motion.

6 References

[1] NoriaCorporation. www.machinerylubrication.com. [Online] 16.03.2020. https://www.machinerylubrication.com/Read/29331/machine-failure-causes.

[2] Woydt, Mathias, et al. *Tribologie in Deutschland Querschnittstechnologie zur Minderung von CO2-Emissionen und zur Ressourcenschonung*. Aachen : Gesellschaft für Tribologie e.V., 2019.

[3] Lawrence, Michael David. *Experimentelle und analytische Untersuchung der Verschmutzungsempfindlichkeit hydraulischer Komponenten.* Aachen : Rheinisch-Westflische Technische Hochschule, 1989

[4] Will, Florian and Weber, Jürgen*. Analysis of Particle Currents of a Wiper Seal at a Cylinder Rod.* Stuttgart : in 20th ISC – International Sealing Conference, 2018.

[5] Barillas, Gropp, Rininsland, Will. *Dirt ingress behavior of wipers: Analysis approach.* Dresden: 12th International Fluid Conference, October 12th.-14th., 2020

[6] Müller, H. K. *Abdichtung bewegter Maschinenteile.* Medienverlag, Waiblingen, 1990, ISBN 3-920484-00-2

[7] Nikas, G.K. *Theoretical Modelling of the Entrainment and thermomechanical effects of contamination particles in elastohydrodynamic contacts.* London : Diss. University of London, April 1999

[8] Barillas, Gropp, van Dawen. Observations on Particle Wiping Bahaviour of Hydraulic Wipers. Stuttgart: in 21st. ISC – International Sealing Conference 2022

[9] Freudenberg Sealing Technologies, *Technical Handbook*. fst_technisches_handbuch_2015_kap02_hydraulikkomponenten.pdf, visited im April 2022

[10] Zierip, Bühler: Grundzüge der Strömungslehre, Grundlagen, Statik und Dynamik der Fluide, 12. Aufage, Springer Verlag, Wiesbaden 2023

[11] Schade, Kunz, Kameier, Paschereit: Strömungslehre, 5. Auflage, De Gruyter Studium, Berlin 2022

7 Authors

Freudenberg Sealing Technologies GmbH

Ascheröder Str. 57, 34613 Schwalmstadt, Germany:

Gonzalo Barillas, Dipl. Ing. (FH) Gonzalo.Barillas@fst.com

Freudenberg Technology Innovation SE & Co. KG

Höhnerweg 2-4, 69465 Weinheim, Germany:

Andreas Gropp, Dipl. Ing. andreas.gropp@freudenberg.com

https://doi.org/10.61319/12WIRG4Y

Advancing Lubrication Calculation: A Physics-Informed Neural Network Framework for Transient Effects and Cavitation Phenomena in Reciprocating Seals

Faras Brumand-Poor, Florian Barlog, Nils Plückhahn, Matteo Thebelt, Katharina Schmitz

In numerous technical applications, gaining insights into the behavior of tribological systems is crucial for optimizing efficiency and prolonging operational lifespans. Experimentally investigating these systems, such as reciprocating seals in fluid power systems, is expensive and time-consuming. An alternative is using elastohydrodynamic lubrication (EHL) simulation models, which however require extensive computational time. Physics-informed machine learning (PIML), particularly physics-informed neural networks (PINNs), offers an accelerated solution by integrating data-driven and physics-based methods into the training process to solve EHL's governing equations. This study demonstrates PINNs' capability to efficiently model tribological systems and accurately predict pressure dynamics and cavitation, showcasing their potential to enhance computational efficiency.

1 Introduction

The performance, efficiency, and durability of components in technical systems are significantly affected by their lubricated tribological contacts, such as those found in seals. Due to the complexity of the occurring phenomena in lubricated contacts, grasping a deeper understanding has proven to be a challenge. Especially, the dynamic friction, mainly described by fluid dynamics, is crucial for the accurate modeling of these contacts. Analytical model approaches are often not feasible without further simplification and neglect of certain phenomena, resulting in inaccurate models. Experimental measurements to obtain an understanding of the tribological behavior, are typically time-consuming and expensive. A commonly applied approach is modeling the system with an elastohydrodynamic lubrication (EHL) simulation, which employs the Reynolds equation to compute pressure distribution and the deformation of the contact surfaces.

An EHL simulation model for reciprocating seals, the ifas-DDS, was developed at the Institute for Fluid Power Drives and Systems of the RWTH Aachen (ifas). This model computes the friction by solving the hydrodynamics within the sealing contact, described by the Reynolds equation, and considering the contact mechanics and the seal deformation. In prior studies, the EHL model was validated with experimental data [1]. A major limitation of this approach is the extensive computation time necessary to solve the underlying equations with numerical methods. Increasing computational resources might improve this issue, but is not always viable, particularly as simulation complexity grows and real-time computation for applications like control systems or digital twins is required.

Machine learning algorithms, like neural networks, represent a promising alternative to classical EHL simulations due to their fast computation ability after an initial training session. However, traditional neural networks are typically not implemented in such a manner that the underlying physical principles are integrated into the network. The main goal of the utilization of a neural network, typically in regression tasks, is to minimize the deviation of the network's prediction to a desired value. This purely data-based approach might result in a good prediction for the provided data but may lead to overfitting, which means that new data points inside the training domain and especially outside of it are predicted with a high error. An advancement in the field of neural networks is physics-informed neural networks (PINNs) tackling this challenge by incorporating physical laws into the network's training, thereby enhancing the networks' predictive accuracy and generalizability across unfamiliar data regimes. PINNs are a class of machine learning solvers for partial differential equations (PDEs). Their main distinguishment from the traditional neural network is, that their training process is not purely data-driven. The optimal parameter configuration of a given network structure is determined by the so-called loss, which is computed by data in the case of a conventional neural network. In the case of PINNs, the loss also incorporates physical laws underlying the investigated problem. The physical laws are described by initial and boundary conditions and the residuals of the PDEs. Several research has been conducted on the hydrodynamic part of EHL simulations, neglecting deformation and friction. Recent developments in this area like the studies by Almqvist [2] and others, showcase the potential of PINNs to combine the preciseness of distributed simulation models with the computational efficiency of neural networks, ensuring robust, accurate, and faster computations.

This contribution demonstrates the capability of PINNs to solve the Reynolds equation with dynamic contact geometry changes and cavitation modeling applied to sealing contact with housing. For this investigation, a hydrodynamic-PINN (HD-PINN) framework, which has previously been validated for stationary scenarios without cavitation [3], is applied. This framework is extended and applied to two scenarios. Firstly, a dynamic change of the investigated gap height and secondly a divergent gap with cavitation. Like the prior mentioned studies, this work focuses on the hydrodynamic part of the EHL. It focuses on computing the pressure and cavitation distribution while neglecting friction and contact mechanics. Deformation is artificially modeled by a constant movement of the seal, neglecting any pressure dependencies. The following section presents the considered model for hydrodynamic lubrication. In section 3, PINNs are described in general. The subsequent section 4 presents the HD-PINN framework, the extensions applied to it, the two investigated scenarios, and the physics-based losses. Subsequently, the results of the PINNs are shown and validated by a modified version of the ifas-DDS, referred to as the rigid DDS, neglecting the prior mentioned factors of the EHL. Eventually, a summary and conclusion are provided in section 6.

2 Hydrodynamic Lubrication

Modeling tribological systems by EHL simulations is a common approach to obtaining a detailed description of friction, leakage, and wear within lubricated mechanical interfaces. EHL models assess the dynamic relationship between surfaces in contact with lubricants, resolving the surface deformation and the hydrodynamic pressure within the contact area. These simulations are essential tools for designing and optimizing tribological contacts in various technical applications.

The ifas-DDS is a distributed parameter simulation model, which simulates complex interactions between a reciprocating seal and its mating countersurface. One essential aspect of this simulation is the consideration of a lubricant, which separates the sealing and the housing and allows a characterization of the sealing behavior. The model consists of two main parts, first the deformation determined by the finite element software Abaqus and second the hydrodynamic part described by the Reynolds equation, which is integrated into Abaqus via user subroutines.

The focus of this research lies in solving the Reynolds equation, therefore simplifying the model by neglecting the deformation of the contacting surfaces, the contact mechanics, and the friction. Within the scope of this research, the investigation focuses on hydrodynamic lubrication. Therefore, the rigid DDS is employed instead of the ifas-DDS.

In this study, the PINN is validated by the rigid DDS. This comparison focuses on the solution process of two solvers for the same set of equations, namely the Reynolds equation and the Fischer-Burmeister equation. The DDS extends the Reynolds equation by the flow factors Φ^{τ} and Φ^{p} as described by Patir and Cheng [4], thus allowing the consideration of surface topography effects on the hydrodynamic lubrication. Furthermore, the cavitation is modeled by integrating the Jakobsson-Floberg-Olsson equation, which introduces the cavitation fraction θ to consider the formation of the gaseous phase, e.g., due to vaporization of solved air in the lubricant due to localized pressure drops [5]. The cavitation fraction describes the gaseous phase's local volume fraction between 0 at no cavitation to 1 for full cavitation.

The original Reynolds equation, as stated by Osborne Reynolds in 1886 is extended to model the cavitation. It is implemented into the DDS and is detailed as follows [6]:

$$\frac{v}{2}\frac{\partial}{\partial x}\Big((1-\theta)\rho h R_q \Phi^{\tau}\Big) - \frac{1}{12\eta}\frac{\partial}{\partial x}\left(\Phi^{p}\rho h^{3}\frac{\partial p}{\partial x}\right) + \frac{\partial}{\partial t}\big((1-\theta)\rho h\big) = 0 \tag{1}$$

Cavitation occurs when the pressure drops below the vaporization pressure which is assumably zero in this work [7]. To describe the relation between pressure and cavitation, the Fischer-Burmeister equation is used:

$$p + \theta - \sqrt{p^2 + \theta^2} = 0 \tag{2}$$

The Jakobsson-Floberg-Olsson cavitation model can be used to track the lubrication distribution in tribological contacts with a limited amount of lubrication supply (starved lubrication), namely grease lubricated sealing contacts in pneumatic spool valves. Due to this modeling, a cavity fraction unequal zero does not necessarily describe the occurrence of cavitation but a partial filled sealing gap at the corresponding position. A better interpretation is obtained by introducing the lubricant film height h_{lub}, which is calculated from h and θ:

$$h_{lub} = (1-\theta)\, h \tag{3}$$

3 Physics-Informed Neural Networks

The previously introduced Reynolds equation describes the pressure distribution in lubricated contacts. When an analytical solution is not available, methods such as finite volume, elements, or differences are often used to solve tribological problems. As these methods are often computationally intensive and time-consuming, machine learning methods have shown promise in the past and are becoming increasingly important in the field of tribology [8, 9].

Machine learning models, often referred to as black-box models, are typically data-driven and advantageous due to their simplicity and adaptability. However, since their inception, hybrid models, which combine ideas from physics with data-driven methodologies, have become increasingly important. These models benefit from the common lack of adequate measurement data and a thorough mathematical description of the system, which makes data-driven and solely physics-based (white-box) modeling approaches unfeasible [10]. Over time, several different hybrid model configurations have been investigated, including sequential, parallel, and structured forms [11–13].

The development of hybrid models represents a promising advancement in the field of tribology, which is physics-informed machine learning (PIML). PIML is employed in tribology for a multitude of purposes, including the estimation of wear or damage and the evaluation of lubrication conditions in hydrodynamic interfaces. In contrast to traditional machine learning techniques, which predominantly utilize data-driven approaches (black-box models), PIML, particularly when utilizing PINNs, integrates physical principles to direct the learning procedure. Consequently, the outputs generated by these models are frequently both more accurate and dependable than those obtained by data-driven methods [14]. A PINN can be conceptualized as a hybrid model in contrast to the previously discussed models. It employs a neural network as the prediction model and incorporates residual terms into the loss function during training to integrate information from physical laws [15].

Hyuk [16] and Lagaris [17] did the fundamental work in physics-based regularization of neural networks after Cybenko [18] and Hornik [19] provided the necessary evidence that neural networks can be used as universal function approximators. Although Hyuk and Lagaris did not specifically use the term "physics-informed" in their study, their goals are similar to the ideas that are now recognized as the foundation of PINNs. Hyuk's method laid the foundation for the later field of PINNs by extending the loss function of the neural network to include the governing differential equation. Because computer resources were limited and computational algebra techniques were still in their infancy, the idea of combining physical rules with neural network training initially received little attention. However, with the advancement in hardware capabilities and the emergence of effective gradient computation methodologies, such as automatic differentiation, this theory has experienced a resurgence.

In 2014, Owhadi was the first to reintroduce PIML, integrating past knowledge into the problem-solving process. He proposed that algorithms be enhanced by incorporating prior information and formulating PDE solutions as Bayesian inference problems [20]. Building upon these premises, Raissi and colleagues employed a probabilistic machine learning technique to solve general linear equations using Gaussian processes, tailoring it particularly for integro-differential or partial differential equations [21, 22]. To address the challenge of solving nonlinear partial differential equations, this technique was subsequently expanded [23, 24]. Moreover, a noteworthy development was the creation of the PINN, which are mesh-free models that restructure the solution of PDEs into a loss function optimization problem [25]. To handle forward and inverse problems given by PDEs, Raissi presented PINNs, a new class of hybrid solvers [26–28]. In Figure 1 an exemplary PINN is shown.

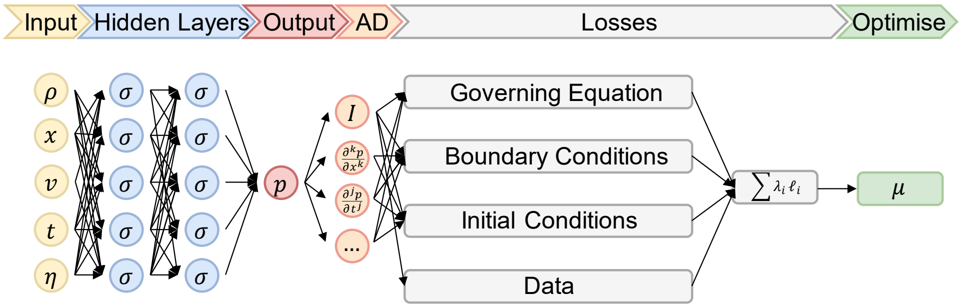

Figure 1: An exemplary PINN.

PINNs process their inputs (such as case-dependent parameters or position x and time t) the same way as traditional neural networks. The values are processed by a multitude of layers to get the network's output. In each layer, multiple neurons are connected to the ones of the previous and next layer. Each neuron executes mathematical operations like multiplying its inputs by a weight, adding a bias, and passing the result to an activation function to calculate its individual output. The sum of all these operations leads to the neural network's ability to predict complex functions as its total output.

The residual losses correspond to the residuals of the governing (physic) equations and thus is an unsupervised loss [14]. This loss is evaluated for specific spatial and, depending on the problem, time points, which are the so-called collocation points in position n_x and time n_t. To integrate complex differential equations, the implementation of automatic differentiation in neural networks is exploited. This method efficiently computes gradients of any order [29] with machine accuracy by applying differential rules such as chain and product rules. In traditional neural networks, automatic differentiation is used to calculate gradients for the update of the parameters, while in PINNs it can additionally be used to calculate derivatives for differential equations.

The boundary condition (BC) and initial condition (IC) losses are used to ensure that the boundary and initial conditions are compliant with given targets. Hence, these two losses are supervised losses. It can be seen in Figure 1 that additional losses can occur. The example in that figure is a so-called hybrid PINN, which uses existing data for the given equations to contribute to a faster or more accurate solution. Therefore, a data loss, which corresponds to the classical data-driven loss, is added.

Before introducing the methods and loss function used in this work in detail, the next section gives a brief overview of the use of PINNs in hydrodynamics.

The first publication to use PINNs for solving a simplified Reynolds equation was released by Almqvist in 2021 [2]. Over the next years, these ideas were expanded by Zhao et al., Li et al., and Yadav et al. who further developed a method to solve the 2D Reynolds equation for more complex problems [30–32]. Notable further progress was made by Rom who first used PINNs for solving the stationary Reynolds equation with the Jakobsson-Floberg-Olsson (JFO) cavitation model. He also introduced soft constraints and collocation point updates to improve cavitation distributions in general but especially in areas with high gradients [33].

Additional advancements were made by Cheng et al., who used PINNs to solve the Reynolds equation for the JFO and Swift-Stieber (SS) cavitation models [34]. Xi et al. further enhanced the solution of PINNs by using hard and soft constraints [35].

Brumand et al. established that one PINN is sufficient to learn the solution of the stationary Reynolds equation for a multitude of different parameters, such as boundary conditions [36].

A step towards using PINNs for a complete EHL simulation was done by Rimon et al. who used a simplified Reynolds equation as well as the Lamé equation for the description of the seal deformation [37].

Although the previously mentioned contributions show immanent progress in solving the complete Reynolds equation, it must be noted that most of these publications were focused on the implementation of PINNs themselves rather than on developing a hydrodynamic lubrication PINN framework. Thus, a significant amount of research and work must be done to solve the complete Reynolds equation in a way that can be used for the replacement of an EHL simulation.

4 HD-PINN Framework

4.1 Test Cases: Physics-Informed Loss and Conditions

In this work, two special cases are investigated. Both scenarios are listed in Table 1. Firstly, the sealing movement and secondly the stationary cavitation are presented, afterwards the training procedure and the framework are briefly described.

Table 1: Investigated test scenarios.

<table>
<tr><td>Scenario</td><td>$\theta \neq 0$</td><td>$\frac{\partial ..}{\partial t}$</td><td>$v$</td><td>BCs</td><td>Gap Geometry</td></tr>
<tr><td>Sealing Movement</td><td>✗</td><td>$\frac{\partial \theta}{\partial t} = 0$
$\frac{\partial h}{\partial t} = -0.1$</td><td>0.1</td><td>$p_{left} = 0.3$
$p_{right} = 0.2$
$\theta_{left} = 0$
$\theta_{right} = 0$</td><td>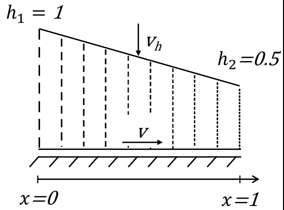
</td></tr>
<tr><td>Stationary Cavitation</td><td>✓</td><td>$\frac{\partial \theta}{\partial t} = 0$
$\frac{\partial h}{\partial t} = 0$</td><td>1</td><td>$p_{left} = 0.7$
$p_{right} = 0.2$
$\theta_{left} = 0$
$\theta_{right} = 0$</td><td>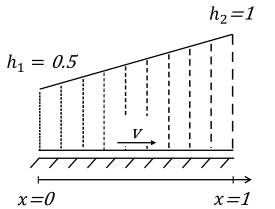
</td></tr>
</table>

4.1.1 Sealing Movement

For the first test case, a converging gap is analyzed. The housing, as the bottom part, moves horizontally in a shearing motion relative to the top part which represents the seal. In addition, the seal is moved vertically towards the housing with the idea in mind to model a simple way of deformation without any interaction with the actual pressure distribution. In this converging setup, no cavitation is modeled.

The Reynolds equation for this specific case is shown in Equation (4). For both scenarios, smooth surfaces and incompressible fluids are assumed, which leads to the neglection of the roughness R_q, the flow factors Φ^{τ} and Φ^{τ} and the density ρ.

$$\frac{v}{2}\frac{\partial h}{\partial x} - \frac{1}{12\eta}\frac{\partial}{\partial x}\left(h^3 \frac{\partial p}{\partial x}\right) + \frac{\partial h}{\partial t} = 0 \tag{4}$$

To solve the Reynolds equation for this specific case, pressure boundary conditions are required. Since the lubricant is incompressible and the seal is moved with a constant velocity, no transient effects are present. Hence the PINN's losses consist of the residual and boundary condition loss being implemented as Mean Squared Error (MSE) terms, which is a common choice for PINNs. Simulation parameters are shown in and the PINN with an exemplary network structure is depicted in Figure 2.

Table 2: Simulation parameters for the sealing movement scenario.

Variable	Value	Variable	Value
n_x	100	v_{rel}	0.1
n_t	10	v_h	-0.1
p_{left}, p_{right}	0.3, 0.2	h	[1, 0.5, 0, 0]

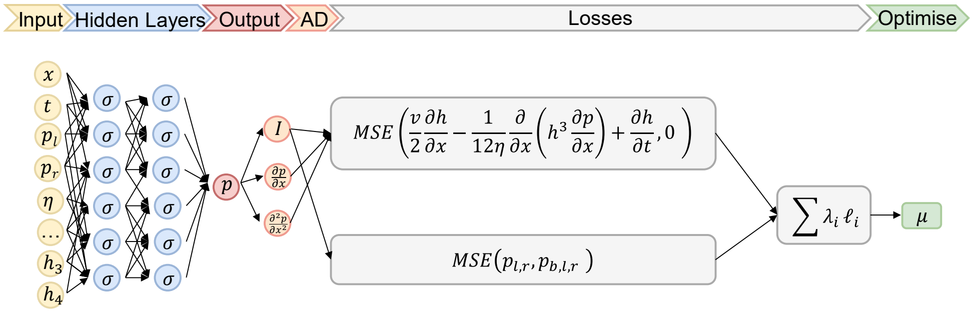

Figure 2: PINN for the sealing movement scenario.

4.1.2 Stationary Cavitation

In the second test case, cavitation is modelled and therefore a diverging gap is chosen. Similar to the first case, the housing is moved horizontally but the seal is fixed.

Since cavitation is modelled, the losses consist of the already introduced residual loss and boundary conditions loss but need further extension by the Fischer-Burmeister loss. Rom demonstrated that the Fischer-Burmeister loss itself is insufficient to model transitions between cavitated and non-cavitated areas adequately and therefore introduced soft constraints [33]. These are implemented as a fourth condition to train the PINN. The set simulation parameters and the PINN are shown in Table 3 and Figure 3, respectively.

Table 3: Simulation parameters for the stationary cavitation scenario

Variable	Value	Variable	
n_x	400	h	[0.5, 1, 0, 0]
n_t	1	p_{thresh}	0.005
p_{left}, p_{right}	0.7, 0.2	θ_{thresh}	0.1
$\theta_{left}, \theta_{right}$	0, 0	$\left(\frac{\partial \theta}{\partial x}\right)_{thresh}$	15
v_{rel}	1	n_{CP_added}	15
v_h	0		

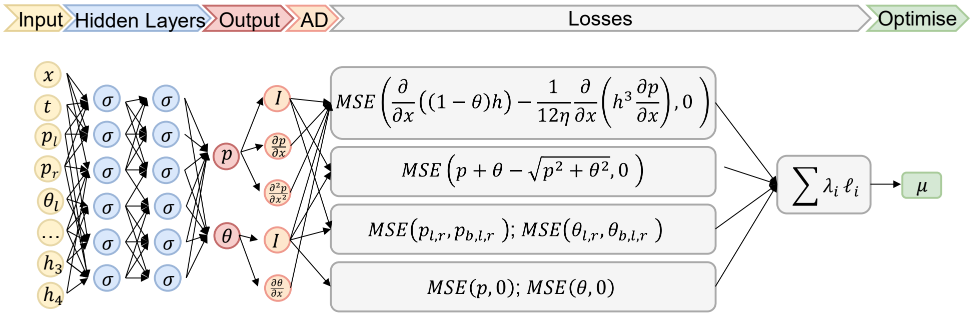

Figure 3: PINN Architecture in case of Cavitation.

Since a stationary model is built, transient effects are neglected. Therefore, the Reynolds equation is as follows:

$$\frac{\partial}{\partial x}\big((1-\theta)h\big) - \frac{1}{12\eta}\frac{\partial}{\partial x}\left(h^3\frac{\partial p}{\partial x}\right) = 0 \tag{5}$$

To enforce the Fischer-Burmeister equation being fulfilled in transition areas especially, the soft constraints loss is implemented in the following two equations:

$$\theta = 0, \qquad if\ p > p_{thresh} \tag{6}$$

$$p = 0, \qquad if\ \theta > \theta_{thersh} \tag{7}$$

Pressure and cavitation should never be non-zero at the same position. Therefore, thresholds are introduced: Whenever one threshold is exceeded, values of the corresponding pressure or cavitation are returned as a loss. Since these transition areas usually make up for a small portion of the whole domain, these areas are considered when normalizing the loss.

4.2 Training Procedure

The framework consists of three main parts, shown in Figure 4: The PINN itself and two optimizers. While the Bayesian optimizer improves the fundamental hyperparameters, initializing a new network each iteration of an outer loop, the Adam optimizer updates the weights and biases of all neurons and therefore improves losses in an inner training loop. In each training iteration, the PINN is evaluated for returning pressure (and cavitation) predictions, and the corresponding losses are calculated. When the final epoch is finished, the Bayesian optimization computes new hyperparameters for the next trial.

Once promising hyperparameters are found, training without Bayesian optimization and a higher number of epochs is started. The final model is saved for evaluation.

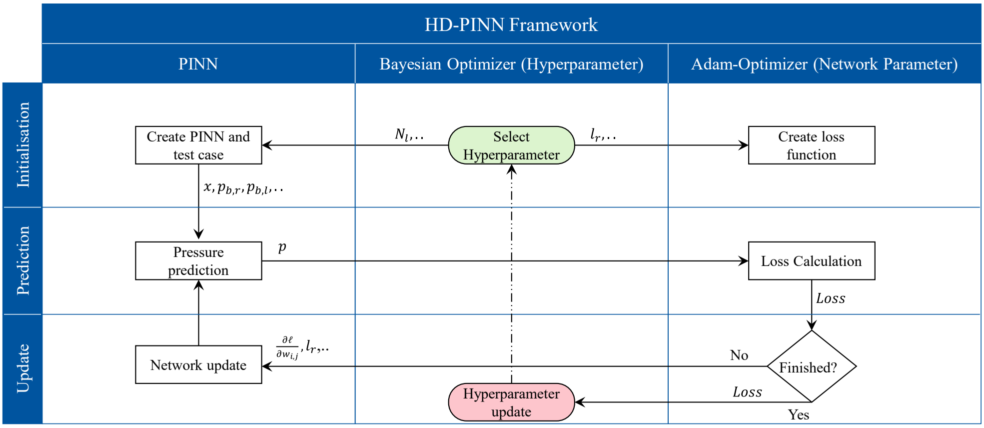

Figure 4: HD-PINN framework for the training procedure. Adapted from [36].

4.3 Adaptive Collocation Points

Areas with high θ-gradients have shown to be hard to predict and therefore need special refinement [33]: After training the neural network for 50000 epochs, new collocation points n_x are added in desired areas. Gradients are checked whether they exceed a certain threshold, and if so a predefined number of 15 collocation points is added to their left. This process is repeated every 5000 epochs until a total of four updates is reached. This ensures that a region with high gradients is sufficiently sampled to obtain an adequate resolution of these areas.

5 Results

5.1 Sealing Movement

The pressure distribution of PINN and DDS for three different time steps, $t = (0, 0.5, 1)$ of the first scenario and the initial seal geometry are shown in Figure 5. The PINN shows good agreement with the DDS for the pressure trajectory for each time step. The pressure increase over time is accurately captured by the PINN.

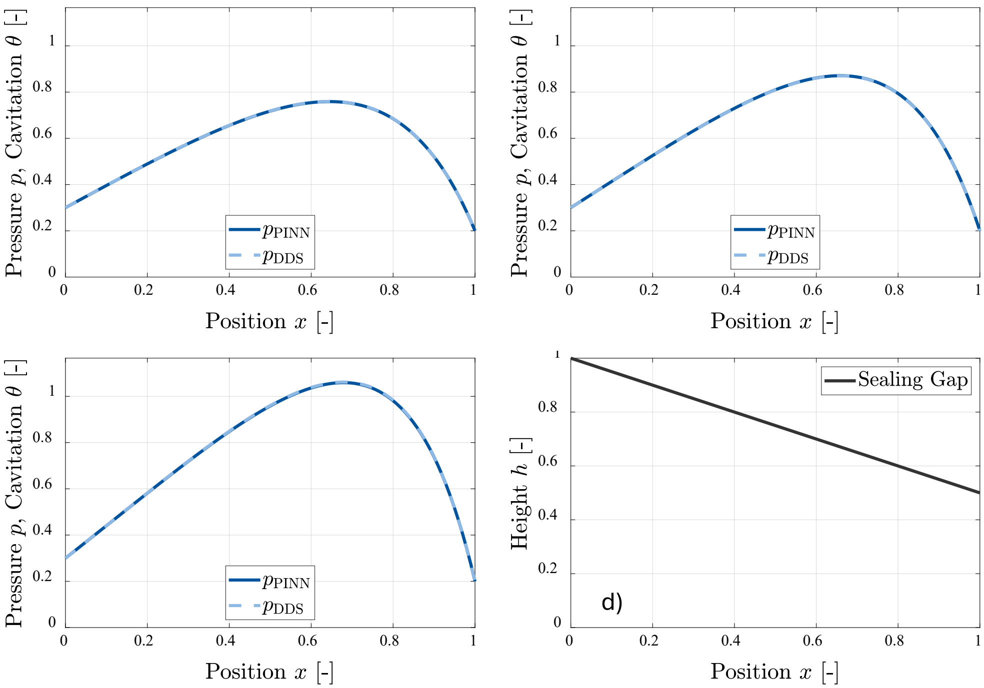

Figure 5: Pressure distribution for the sealing movement scenario for a) $t = 0$, b) $t = 0.5$, c) $t = 1$ and d) the sealing geometry at $t = 0$.

5.2 Stationary Cavitation

The results of the second scenario, the stationary cavitation, are depicted in Figure 6. The results show the pressure distribution and the cavitation fraction in one plot and the lubrication film height in another plot.

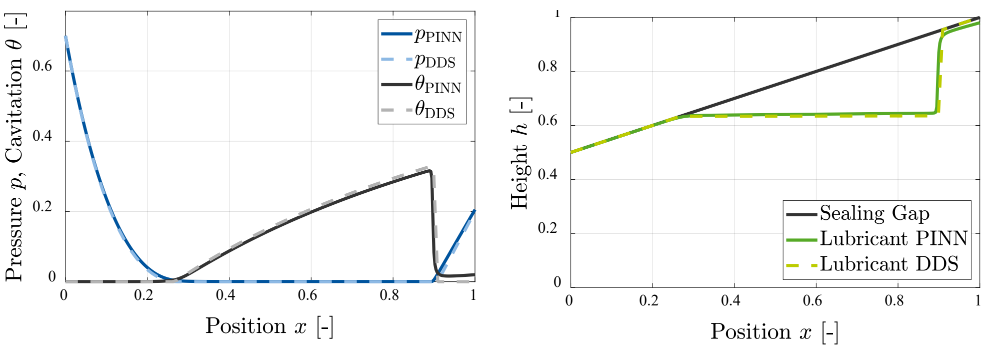

Figure 6: Pressure distribution and cavitation for the stationary cavitation scenario and the lubrication height.

In the second scenario, the PINN also performs well for the pressure distribution and the cavitation area. The right transition regime shows some deviation between PINN and DDS. The soft constraints enhance the location of the switch between pressure and cavitation area. Further tuning of the constraints in combination with new hyperparameters could increase the accuracy even more.

6 Summary and Conclusion

This contribution demonstrates the capability of PINNs to solve dynamic height changes and cavitation modeling tasks, governed by the Reynolds equation. They do so, by computing the pressure distribution and cavitation fraction within sealing contacts in a housing. In the beginning, an introduction to hydrodynamic lubrication was given, followed by a description of PINNs and their application-solving variants of the Reynolds equation. After that, the investigated scenarios of sealing movement and stationary cavitation as well as the applied training procedure for the PINNs were presented in detail.

Regarding the pressure, the PINN can accurately compute the distribution and the boundaries, validated with the DDS. The cavitation determination in the second scenario demonstrates good agreement inside the cavitation region. For the regime where pressure and cavitation area switch, the PINN can locate them and sufficiently compute the desired values. The PINN showed the possibility of computing high gradients, and the introduced soft constraints represent a further possibility for increasing accuracy in these areas. The results of this work represent an advancement in the domain of lubricated contact simulations, depicting a PIML approach to accelerate hydrodynamic lubrication computation with no to less accuracy loss.

Further work will be done by integrating transient behavior for the cavitation fraction of the Reynolds equation and solving this scenario with the framework. Additionally, the soft constraints will be investigated to obtain more accuracy for high-gradient regions.

7 Acknowledgements

The authors thank the Research Association for Fluid Power of the German Engineering Federation VDMA for its financial support. Special gratitude is expressed to the participating companies and their representatives in the accompanying industrial committee for their advisory and technical support.

8 Nomenclature

Variable	***Description***	***Unit***
h	Gap height	[-]
h_{lub}	Lubrication height	[-]
h_1	Height at left end	[-]
h_2	Height at right end	[-]
h_3	Curvature of sealing	[-]
h_4	Position for sealing bend	[-]
n_t	Time collocation points	[-]
n_x	Position collocation points	[-]
p	Hydrodynamic pressure	[-]
$p_{b,l,r}$	Pressure boundary condition for left and right boundary	[-]
$p_{l,r}$	Pressure at the left and right boundary	[-]
p_{thersh}	Pressure threshold for soft constraints	[-]
R_q	Root mean squared contact surface roughness	[-]
t	Time	[-]
v	Velocity of counter surface	[-]
v_h	Velocity of sealing	[-]
x	Axial coordinate	[-]
x_b	Position of sealing bend	[-]
x_l	Left end of the geometry	[-]
x_r	Right end of the geometry	[-]
η	Fluid viscosity	[-]
θ	Cavity friction	[-]
θ_{thersh}	Cavitation threshold for soft constraints	[-]
ρ	Fluid density	[-]
Φ^p	Pressure flow factors	[-]
Φ^τ	Shear flow factors	[-]
$\frac{\partial ..}{\partial x,t}$	Partial differentiation regarding time and position	[-]

9 REFERENCES

[1] Bauer, N.; Sumbat, B.; Feldmeth, S.; Bauer, F.; Schmitz, K. Experimental determination and EHL simulation of transient friction of pneumatic seals in spool valves. *Sealing technology - old school and cutting edge : International Sealing Conference : 21st ISC*, **2022,** 503–522.

[2] Almqvist, A. Fundamentals of Physics-Informed Neural Networks Applied to Solve the Reynolds Boundary Value Problem. *Lubricants*, **2021**, *9,* 82.

[3] Brumand-Poor, F.; Bauer, N.; Plückhahn, N.; Schmitz, K. *Fast Computation of Lubricated Contacts: A Physics-Informed Deep Learning Approach:* Dresden, Germany, **March 19-21**.

[4] Bauer, N.; Baumann, M.; Feldmeth, S.; Bauer, F.; Schmitz, K. Elastohydrodynamic Simulation of Pneumatic Sealing Friction Considering 3D Surface Topography. *Chem Eng & Technol*, **2023**, *46,* 167–174.

[5] Bauer, N.; Rambaks, A.; Müller, C.; Murrenhoff, H.; Schmitz, K. Strategies for Implementing the Jakobsson-Floberg-Olsson Cavitation Model in EHL Simulations of Translational Seals. *TJFP*, **2021**.

[6] Angerhausen, J.; Woyciniuk, M.; Murrenhoff, H.; Schmitz, K. Simulation and experimental validation of translational hydraulic seal wear. *Tribology International*, **2019**, *134,* 296–307.

[7] Liu, X.; Wu, Z.; Li, B.; Zhao, J.; He, J.; Li, W.; Zhang, C.; Xie, F. Influence of inlet pressure on cavitation characteristics in regulating valve. *Engineering Applications of Computational Fluid Mechanics*, **2020**, *14,* 299–310.

[8] Marian, M.; Tremmel, S. Current Trends and Applications of Machine Learning in Tribology—A Review. *Lubricants*, **2021**, *9,* 86.

[9] Paturi, U.M.R.; Palakurthy, S.T.; Reddy, N.S. The Role of Machine Learning in Tribology: A Systematic Review. *Arch Computat Methods Eng*, **2023**, *30,* 1345–1397.

[10] Velioglu, M.; Mitsos, A.; Dahmen, M. Physics-Informed Neural Networks (PINNs) for Modeling Dynamic Processes Based on Limited Physical Knowledge and Data. *2023 AIChE Annual Meeting*, **2023**.

[11] Psichogios, D.C.; Ungar, L.H. A hybrid neural network-first principles approach to process modeling. *AIChE Journal*, **1992**, *38,* 1499–1511.

[12] Su, H.-T.; Bhat, N.; Minderman, P.A.; McAvoy, T.J. Integrating Neural Networks with First Principles Models for Dynamic Modeling. *IFAC Proceedings Volumes*, **1992**, *25,* 327–332.

[13] Kahrs, O.; Marquardt, W. The validity domain of hybrid models and its application in process optimization. *Chemical Engineering and Processing: Process Intensification*, **2007**, *46,* 1054–1066.

[14] Cai, S.; Mao, Z.; Wang, Z.; Yin, M.; Karniadakis, G.E. Physics-informed neural networks (PINNs) for fluid mechanics: a review. *Acta Mech. Sin.*, **2021**, *37,* 1727–1738.
[15] Nabian, M.A.; Meidani, H. Physics-Driven Regularization of Deep Neural Networks for Enhanced Engineering Design and Analysis. *Journal of Computing and Information Science in Engineering*, **2020**, *20,* 436.
[16] Lee, H.; Kang, I.S. Neural algorithm for solving differential equations. *Journal of Computational Physics*, **1990**, *91,* 110–131.
[17] Lagaris, I.E.; Likas, A.; Fotiadis, D.I. Artificial Neural Networks for Solving Ordinary and Partial Differential Equations. *IEEE Trans. Neural Netw.*, **1998**, *9,* 987–1000.
[18] Cybenko, G. Approximation by superpositions of a sigmoidal function. *Math. Control Signal Systems*, **1989**, *2,* 303–314.
[19] Hornik, K.; Stinchcombe, M.; White, H. Multilayer feedforward networks are universal approximators. *Neural Networks*, **1989**, *2,* 359–366.
[20] Owhadi, H. *Bayesian Numerical Homogenization*, **June 25, 2014**.
[21] Raissi, M.; Perdikaris, P.; Karniadakis, G.E. *Inferring solutions of differential equations using noisy multi-fidelity data*, **2016**.
[22] Raissi, M.; Perdikaris, P.; Karniadakis, G.E. *Machine learning of linear differential equations using Gaussian processes*, **2017**.
[23] Raissi, M.; Perdikaris, P.; Karniadakis, G.E. *Numerical Gaussian Processes for Time-dependent and Non-linear Partial Differential Equations*, **March 29, 2017**.
[24] Raissi, M.; Karniadakis, G.E. Hidden physics models: Machine learning of nonlinear partial differential equations. *Journal of Computational Physics*, **2018**, *357,* 125–141.
[25] Cuomo, S.; Di Cola, V.S.; Giampaolo, F.; Rozza, G.; Raissi, M.; Piccialli, F. Scientific Machine Learning Through Physics-Informed Neural Networks: Where we are and What's Next. *J Sci Comput*, **2022**, *92*.
[26] Raissi, M.; Perdikaris, P.; Karniadakis, G.E. *Physics Informed Deep Learning (Part I): Data-driven Solutions of Nonlinear Partial Differential Equations*, **November 28, 2017**.
[27] Raissi, M.; Perdikaris, P.; Karniadakis, G.E. *Physics Informed Deep Learning (Part II): Data-driven Discovery of Nonlinear Partial Differential Equations*, **November 28, 2017**.
[28] Raissi, M.; Perdikaris, P.; Karniadakis, G.E. Physics-informed neural networks: A deep learning framework for solving forward and inverse problems involving nonlinear partial differential equations. *Journal of Computational Physics*, **2019**, *378,* 686–707.

[29] Baydin, A.G.; Pearlmutter, B.A.; Radul, A.A.; Siskind, J.M. Automatic differentiation in machine learning: a survey. *Atilim Gunes Baydin*.

[30] Zhao, Y.; Guo, L.; Wong, P.P.L. Application of physics-informed neural network in the analysis of hydrodynamic lubrication. *Friction*, **2023**, *11,* 1253–1264.

[31] Li, L.; Li, Y.; Du, Q.; Liu, T.; Xie, Y. ReF-nets: Physics-informed neural network for Reynolds equation of gas bearing. *Computer Methods in Applied Mechanics and Engineering*, **2022**, *391,* 114524.

[32] Yadav, S.K.; Thakre, G. Solution of Lubrication Problems with Deep Neural Network. In: *Advances in Manufacturing Engineering*. Dikshit, M.K., Soni, A., Davim, J.P., Eds.; Springer Nature Singapore: Singapore, **2023**; pp. 471–477.

[33] Rom, M. Physics-informed neural networks for the Reynolds equation with cavitation modeling. *Tribology International*, **2023**, *179,* 108141.

[34] Cheng, Y.; He, Q.; Huang, W.; Liu, Y.; Li, Y.; Li, D. HL-nets: Physics-informed neural networks for hydrodynamic lubrication with cavitation. *Tribology International*, **2023**, *188,* 108871.

[35] Xi, Y.; Deng, J.; Li, Y. A new method to solve the Reynolds equation including mass-conserving cavitation by physics informed neural networks (PINNs) with both soft and hard constraints. *Friction*, **2024**.

[36] Brumand-Poor, F.; Bauer, N.; Plückhahn, N.; Thebelt, M.; Woyda, S.; Schmitz, K. Extrapolation of Hydrodynamic Pressure in Lubricated Contacts: A Novel Multi-Case Physics-Informed Neural Network Framework. *Lubricants*, **2024**, *12,* 122.

[37] Rimon, M.T.I.; Hassan, M.F.; Lyathakula, K.R.; Cesmeci, S.; Xu, H.; Tang, J. In: *ASME Power Applied R&D 2023*, ASME Power Applied R&D 2023, Long Beach, California, USA, 06.08.2023 - 08.08.2023; American Society of Mechanical Engineers, **2023**.

10 Authors

RWTH Aachen University, Institute for Fluid Power Drives and Systems (ifas)

Campus-Boulevard 30, 52074 Aachen, Germany:

Faras Brumand-Poor M. Sc., M. Sc., ORCID 0009-0006-7442-8706, faras.brumand@ifas.rwth-aachen.de

Florian Barlog B. Sc., ORCID 0009-0006-4275-5825, florian.barlog@ifas.rwth-aachen.de

Nils Plückhahn B. Sc., ORCID 0009-0000-0789-6194, nils.plueckhahn@ifas.rwth-aachen.de

Matteo Thebelt B. Sc., ORCID 0009-0005-8262-3053, matteo.thebelt@ifas.rwth-aachen.de

Univ.-Prof. Dr.-Ing. Katharina Schmitz, ORCID 0000-0002-1454-8267, katharina.schmitz@ifas.rwth-aachen.de

https://doi.org/10.61319/J7I2HNKR

Advanced characterization of sealing counter surfaces in linear applications

Anja Dobrinsky, Boris Brodmann, Christoph Schuele, Sebastian Betz

Counter surfaces are an important aspect for every sealing application and have a direct influence on the sealing performance of the system. Historically, the counter surface is described with multiple roughness parameters based on 2D profile or 3D topography measurements. In addition to the standard parameters, light scattering can be used to describe the counter surface. Compared to the common profile roughness parameters, light scattering measures the angle distribution of a profile and is therefore more robust against external influences. In addition, light scattering measurements are faster at characterizing a complete running surface. In this study, the effect of one rod seal geometry made from PTFE and PU materials on the surface characteristics of the rod is investigated. A deeper understanding of the tribological system is achieved by analyzing for the first time the light scattering roughness parameters of a tested rod surface in addition to the standard profile roughness parameters.

1 Introduction

A linear rod sealing system is a tribological system with the seal and the rod as the tribological surfaces and the hydraulic fluid as intermediate media. The friction and wear of tribological systems is greatly influenced by the surface roughness characteristics of the rod or counter surface of the seal. Classical surface roughness parameters are determined from a surface profile or topography which is measured mechanically via the tactile sectioning method or optical profilometry, e.g. interferometry or confocal microscopy as shown in Figure 1. The tactile method falls under the contact-based measurement techniques, while the optical measurement methods are non-contact measurements. Roughness parameters based on the surface trace acquired by these types of methods are described in DIN EN ISO 21920-2:2022-12.

An alternative to conventional measurement methods is the non-contact optical measurement methods based on scattered light described in VDA2009 [1]. In contrast to classical roughness parameters, which are based on the roughness profile, light scattering parameters are based on the reflectance properties of the rough surface. In previous studies, light scattering has been adopted to analyze roughness and shaft lead effects in rotary sealing systems [2] [3]. No previous work is known on the influence of light scattering parameters in linear sealing systems. Especially for linear sealing systems, where tactile measurements are often restricted to only a small portion of the rod surface, light scattering measurements are hypothesized to offer a considerable advantage in terms of cost and efficiency of characterizing the complete rod surface. For the first time, this research demonstrates the use of light scattering methods for the characterization of the surface roughness of the rod in hydraulic sealing systems.

Table 1: Comparison of different surface measurement methods

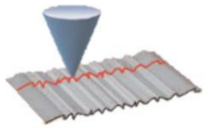	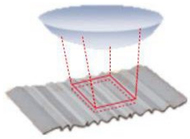	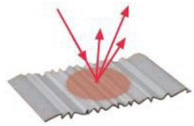
Stylus method	Confocal microscopy	Angle-resolved scattered light measurement technology
Profile parameters: Ra, Rz, Rk, etc.	Surface parameters: Sa, Sz, Sk, etc.	Scattered light parameters: Aq, Aqm, Aqmax, etc.

2 Scattered light measurement

2.1 Roughness parameters

The scattered light parameters capture both the roughness and the reflectance of finely processed surfaces by measuring the distribution curve of the scattered light.

The following study focuses on the parameter Aq, which denotes the variance of the scattered light distribution. Aq describes the second statistical moment of the angular distribution and is an integral measure for the micro-geometry or the extent of roughness within the light spot, respectively [1].

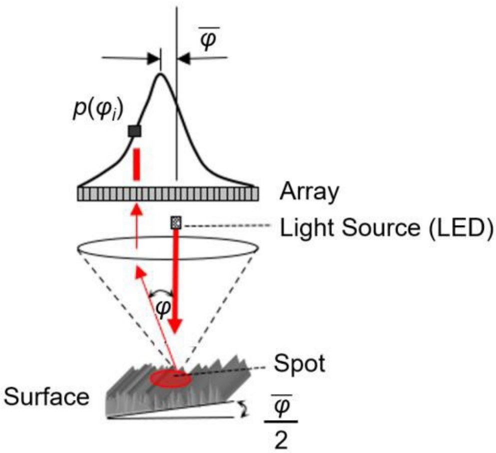

Figure 1: Principle of the angle-resolved scattered light measurement

$$\mathrm{Aq} = k\sum_{i=1}^{n}(\varphi_i - \bar{\varphi})^2\, p(\varphi_i) \tag{1}$$

In Equation (1), k is a normalization factor, φ is the scattering angle, $p(\varphi)$ is the normalized intensity distribution, n is the total number of angle classes, and the bar denotes an average value.

Aq is corresponding to the second statistical moment of the surface power spectrum and reacts very sensitively to changes in surface properties. It is directly proportional to the ISO21920 parameter Rdq [4] and is traceable according to ISO17025 [5]. Its contact mechanical significance is emphasized by Popov [6].

2.2 Sensor principle

In the current study, the Optosurf OS500 scattered light system was used. The measurement spot on the surface is generated by an illumination beam path which, depending on the design, projects measurement spots of various sizes onto the surface. The light scattered back from the surface is transmitted onto a linear detector array by means of Fourier optics. This array converts the incident intensity distribution into electrical currents, which are then digitized and passed on to a microprocessor for further processing. For the standard sensor, the captured angular range is 32°. The scattered light optics are angle-corrected, achieving insensitivity to distance variations. The measurement distance can vary by up to +/- 1 mm for flat samples without changing the distribution curve and thus the roughness characteristic Aq [7]. A full description of the transfer function given by Seewig [8].

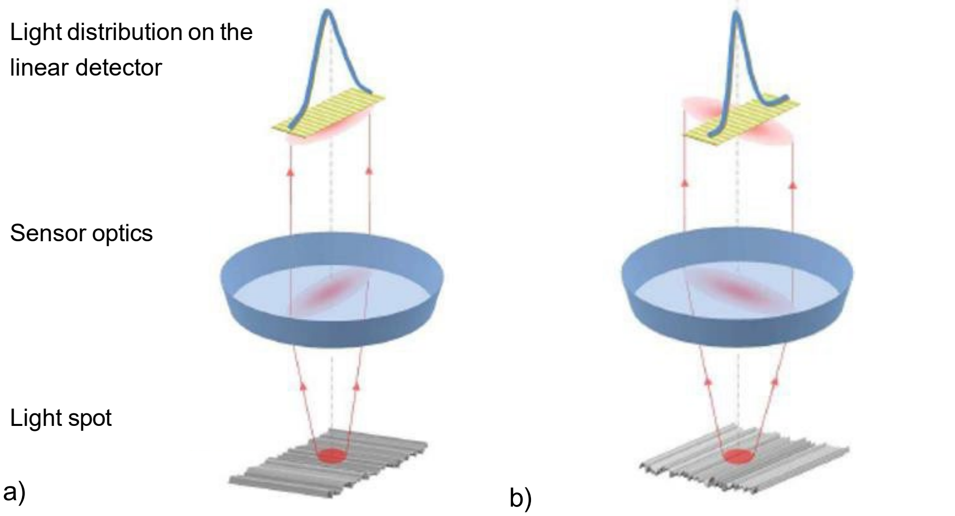

Figure 2: a) Crosswise roughness measurement per definition: diode array oriented across machining direction; b) Longwise roughness measurement per definition: diode array oriented parallel to the machining direction

Depending on the orientation of the sensor or the surface, the roughness is measured transverse to the machining grooves or parallel to them, as illustrated in Figure 2. By default, the two measurement directions are defined as follows:

- Crosswise roughness measurement: diode array oriented across (perpendicular) machining direction.
- Longwise roughness measurement: diode array oriented parallel to the machining direction.

In the following study, the two sensor orientations are defined as

- Crosswise roughness measurement: perpendicular to rod moving direction
- Longwise roughness measurement: perpendicular to processing direction

3 Test rig and test procedure

The linear rod test rig is equipped with two equal test cells arranged symmetrically, see Figure 3. Each hydraulic cylinder is driven linearly by a drive motor via a deflection pulley. The resulting position time signal can be approximated as a sinus. Due to the conversion of the circular to linear movement the speed is not constant. Due to inconstant speed over movement the seal experiences different friction states like static friction, mixed friction and hydrodynamic friction. A test chamber is installed on each test rod. Each test chamber is each equipped with two rod seals in a face-to-face arrangement.

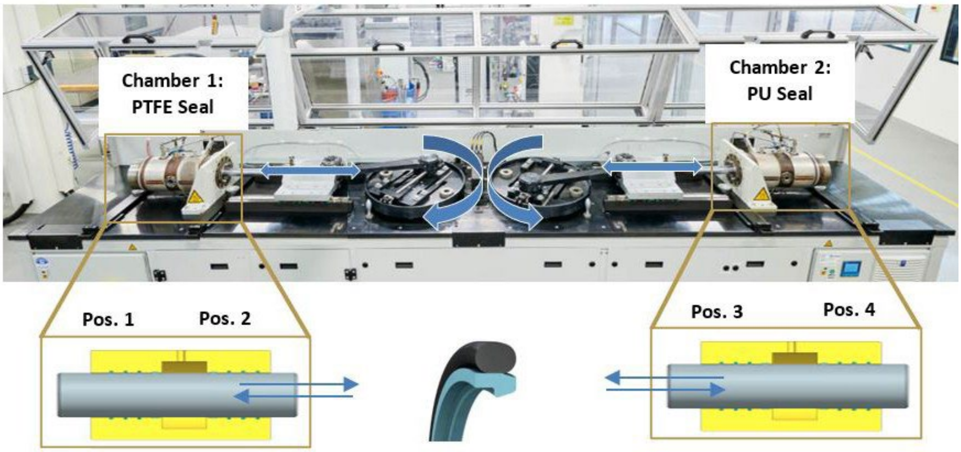

Figure 3: Linear rod test rig

The tested seal configuration consists of a Stepseal® 2K with an O-Ring acting as an energizer. The seal materials used are PTFE (T46) and PU (Z53). T46 is a bronze-filled PTFE, while Z53 is a polyurethane (PU) material. The test was conducted using HLP 46 hydraulic oil as the lubricant. The operating conditions included a constant pressure of 400 bar, an oil temperature of 60 °C, an average rod velocity of 0.2 m/s, and a total number of 600,000 rod double strokes.

4 Test results

4.1 Tactile roughness measurement

The tactile roughness measurement was carried out with the Hommel Etamic T8000 device. The mean Rz values before and after the test are shown in Figure 4. The initial quality of counter surface is measured at three locations along the rod. The initial value in terms of Rz is around 0.6 µm.

After the test the counter surface is measured at twelve locations. As shown in **Fehler! Verweisquelle konnte nicht gefunden werden.**4,**Fehler! Verweisquelle konnte nicht gefunden werden.** the mean Rz value after the test is similar to the value before the test. As a conclusion, the change of the widely used Rz is not indicating a change of the counter surface during the test. In addition, the Average Aq (Aqm) was estimated based on the running area. It already shows the bigger change of the Aqm. In the following chapter the Aq will be explained in detail and in addition the distribution over the surface.

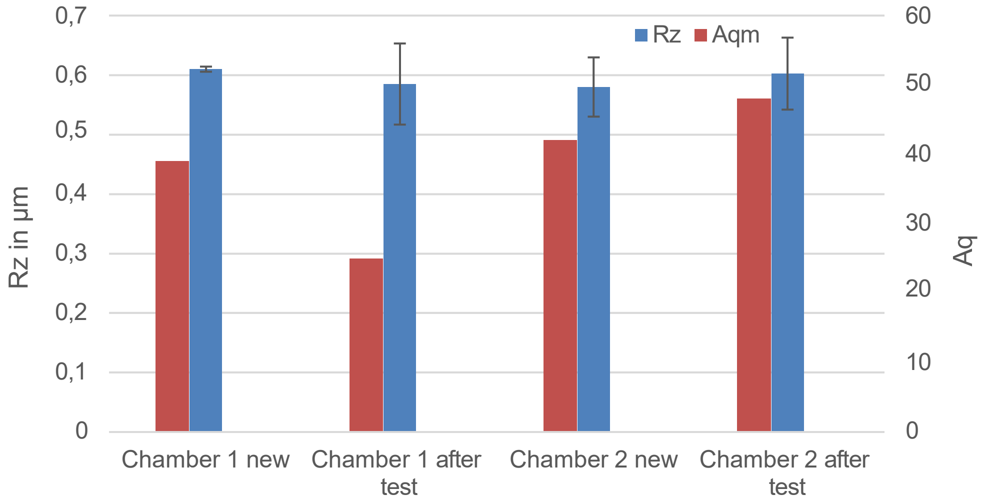

Figure 4: tactile and scattered light measurement before and after test; chamber 1 and chamber 2

4.2 Scattered light analysis before test

As stated above, Aq [1] is seen as a supplementary value to describe the surface roughness. For the conducted tests, new rods were used for each measurement. They were measured using the scattered light sensor before and after the test. Each measurement was performed with the sensor oriented crosswise (i.e. perpendicular to the rod movement) and longwise (i.e. perpendicular to the processing direction). Figure 5 shows a scan of the entire lateral surface of rod 1 before the test with the sensor oriented crosswise. Figure 5 reveals a uniform distribution of Aq. The Aq mean value in the crosswise direction is 5.57 and the Aqmax [1] value is 18.26.

The measurement with the sensor orientation longwise clearly reveals the machining traces, Figure 6. A possible last polishing step could be feed marks of centerless grinding. The Aq mean value in the longwise direction is 45.75, and the Aqmax value is 66.20.

Exemplary, only the scans of rod 1 were depicted, as rod 2 shows a similar image. For rod 2, the Aq mean (Aqm) value in the crosswise direction is 5.56, and Aqmax is 20.37. The Aq mean value in the longwise direction is 45.25, and Aqmax is 68.33.

Table 2: statistic to chamber 1, new; sensor orientation perpendicular to rod moving direction

Aqm	5.57
Aqmax	18.26
Aqs	0.76

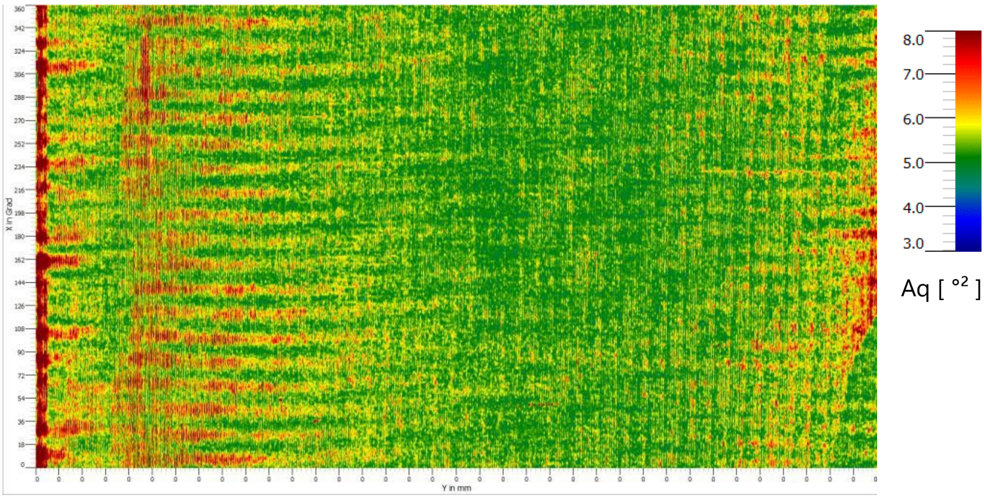

Figure 5: Aq, chamber 1, new; sensor orientation perpendicular to rod moving direction

Table 3: statistics chamber 1, new; sensor orientation perpendicular to processing direction

Aqm	45.75
Aqmax	66.20
Aqs	3.31

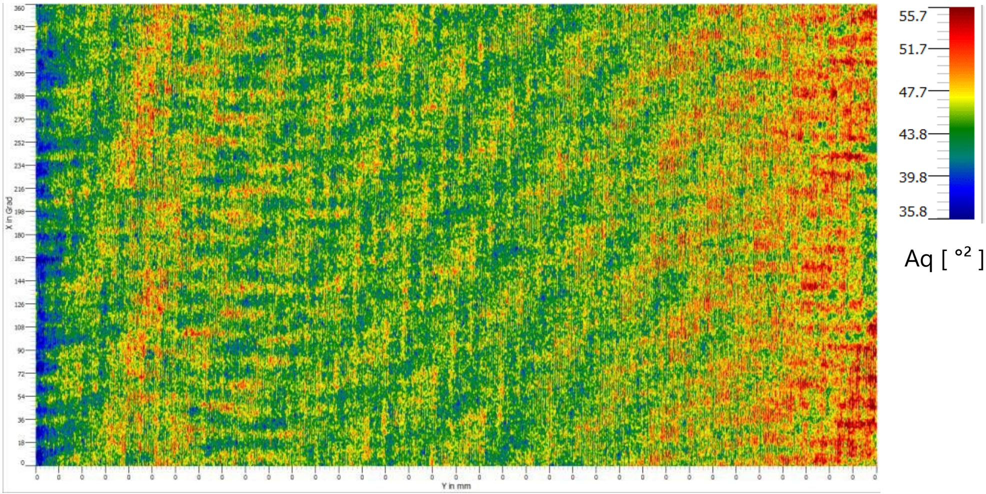

Figure 6: Aq, chamber 1, new; sensor orientation perpendicular to processing direction

4.3 Scattered light analysis after test

The following Figure 7 shows the Aq distribution after testing on rod 1. In the running areas at positions 1 and 2 marked as region 1 and region 2, the Aq values have partially increased from 5.57 to 9. This indicates surface roughening. The measurement with the sensor oriented crosswise (perpendicular to the machining direction) clearly reveals the running tracks of the seals. In the red areas equate with higher Aq values, grooves are visible in the running direction.

Table 4: statistics chamber 1, PTFE, after test; sensor orientation perpendicular

Aqm	6.35
Aqmax	16.41
Aqs	0.89

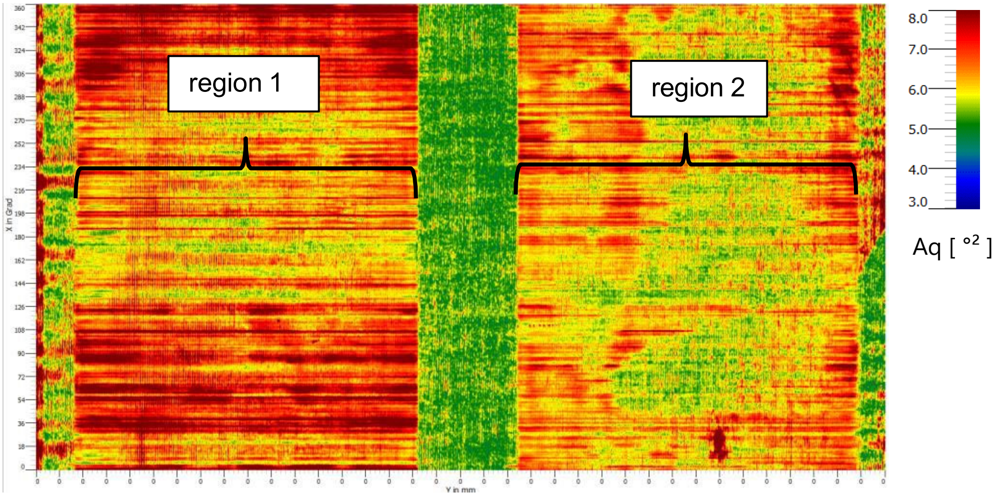

Figure 7: Aq, chamber 1, PTFE, after test; sensor orientation perpendicular to rod moving direction

Figure 8 illustrates the examination of the rod surface of rod 1 (PTFE) with a sensor alignment in the longwise direction. The figure can be divided into five regions. Regions 1 and 2 denote the section of the seal's running surface. Here it is evident that the influence of the seal overlays the machining marks. The machining marks are visible in the unworn area (region 4) at an Aq value of approximately 40 (orange areas). In regions 1 and 2, significant smoothing of the rod surface is observed within the seal's running areas. The Aq values decrease to between 30 and 20 in region 5. Further reduction in Aq values occurs in region 3. These areas correspond to the reversal points in the seal's motion cycle. These regions belong to the upper and lower dead points, where the velocity drops to zero. Lubrication ceases, and the seal comes into direct contact with the opposing surface, resulting in localized surface smoothing. As the velocity increases, the seal enters the hydrodynamic regime and is well-lubricated again. Due to this lubrication state, region 5 exhibits less surface smoothing.

Table 5: statistics chamber 1, PTFE, after test; sensor orientation perpendicular to processing direction

Aqm	28.84
Aqmax	59.51
Aqs	10.43

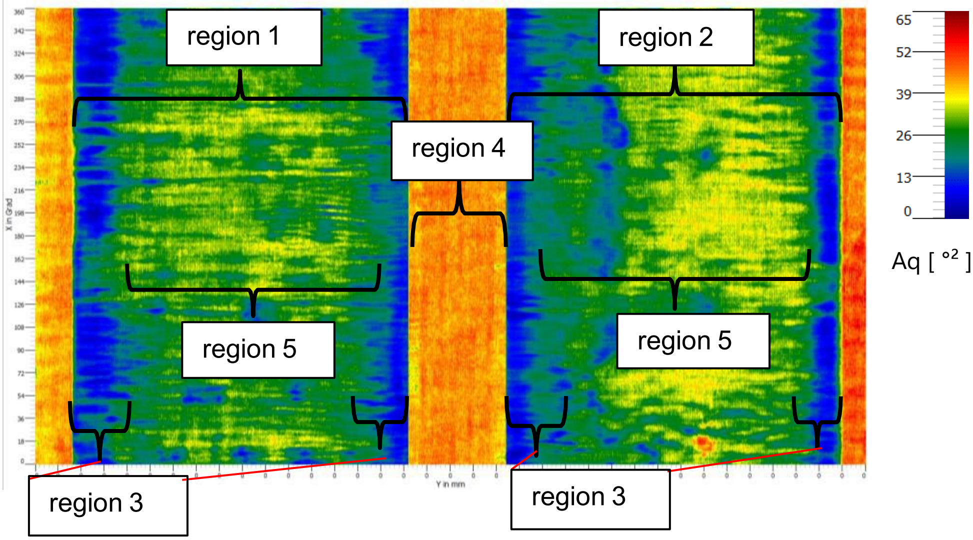

Figure 8: Aq, chamber 1, PTFE, after test; sensor orientation perpendicular to processing direction

Table 6: statistics chamber 2, PU, after test; sensor orientation perpendicular

Aqm	5.66
Aqmax	17.52
Aqs	0.79

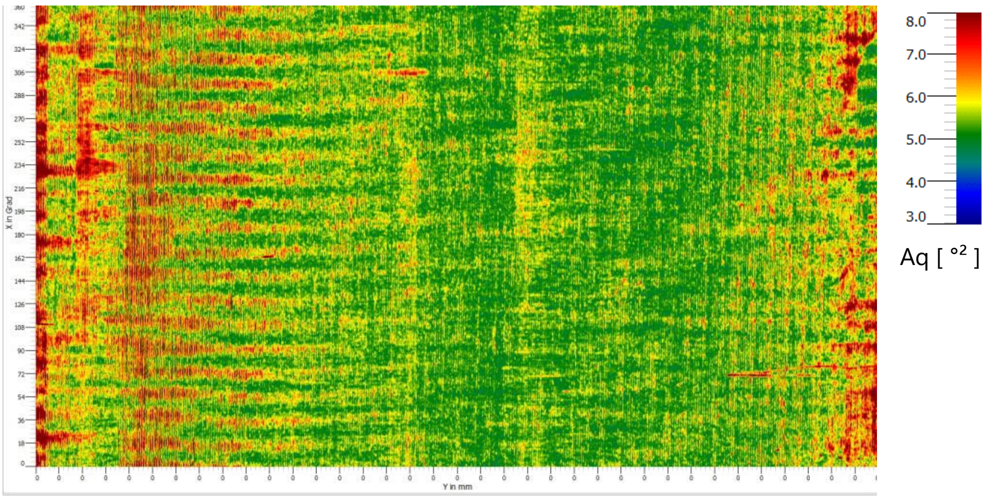

Figure 9: Aq, chamber 2, PU, after test; sensor orientation perpendicular to rod moving direction

Table 7: statistics chamber 2, PU, after test; sensor orientation perpendicular

Aqm	44.98
Aqmax	74.80
Aqs	3.40

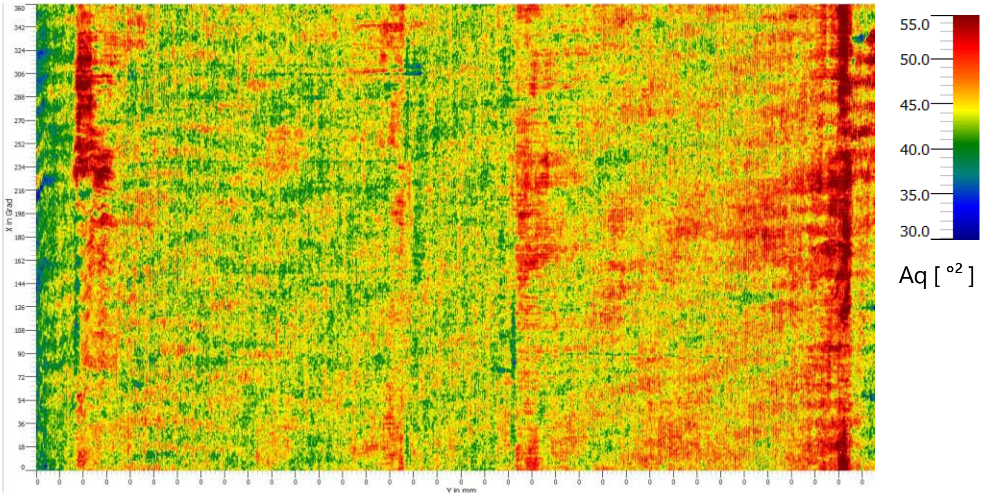

Figure 10: Aq, chamber 2, PU, after test; sensor orientation perpendicular to processing direction

It should be noted that for the evaluation of chamber 1 a scaling of the Aq value over a larger range was used, because PTFE has a stronger impact on the rod surface than PU, refer to region 3 in Figure 8. Aqs corresponds to the standard deviation of the measured values and is 10.55 for rod 1 (PTFE) and 3.4 for rod 2.

The PU seal has significantly less impact on the rod surface. As shown in Figure 9, there are minimal changes in the surface.

The longwise measurement in Figure 10 shows as well hardly any changes in the surface. This confirms the previous experience that PU, when compared to PTFE filled with bronze, exhibits only minimal abrasiveness.

4.4 Friction force analysis

In the test, the friction of each chamber is recorded. The friction was analyzed with an average over 10 hours steps for each angular position. These 10-hour steps can be used to analyze the friction behavior over time. To ensure a good comparison between surface measurement and friction curve the last step was chosen and displayed in Figure 11.

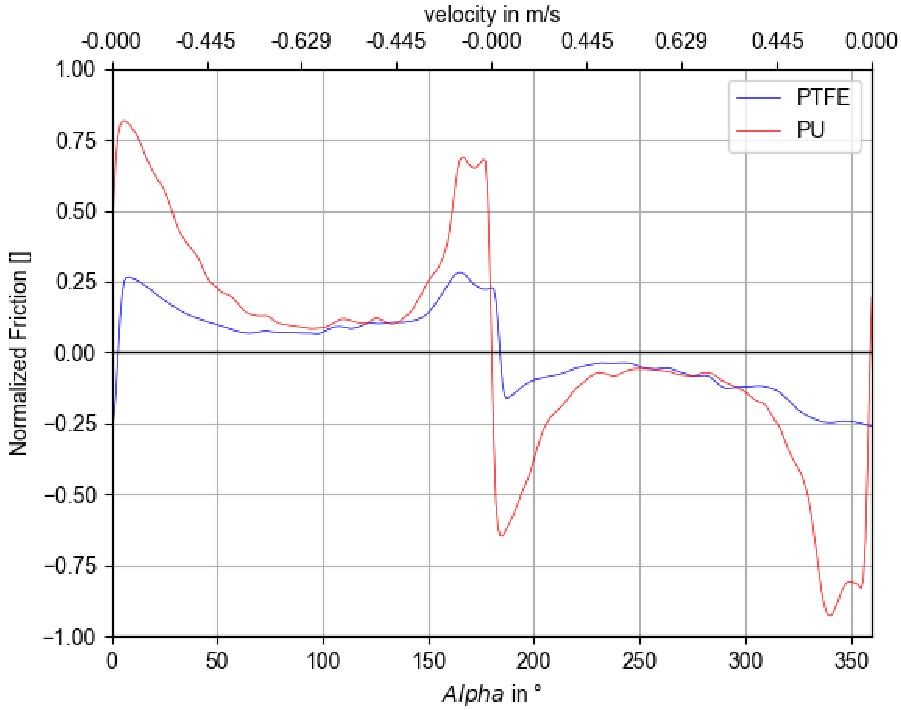

Figure 11: Friction force at end of test

The angular position is corresponding to a speed with a maximum speed at 90° and 270°. In this area, the friction of both materials is in a comparable range and indicating a lubricated contact area. This is corresponding to the scattered light measurements that shows less change in Aq compared to the region 3 at the stroke end. The turning points with less speed and change of direction are visible at 0° and 180° in the friction force plot. This corresponds to the areas with most change detected by the optical measurement. Based on friction and surface characterization the conclusion is a minimal fluid film close to dry running when the direction of movement is changing. In addition, the sliding properties of the general material classes are shown. The PU seal tends to have a higher friction in the areas of low/zero speed. This explains the stick-slip tendency of this material class compared to PTFE-based materials.

5 Summary and Conclusion

In summary, the use of a scattered light sensor ensures a more comprehensive image of a surface structure. Unlike conventional tactile measurements, which only provide information about the surface texture based on a very short measurement distance, this method presents a detailed picture of the distribution of roughness peak angles as well as the overall shape. When combined with traditional measurement techniques, it allows for a holistic view of the mating surface of a seal. The insights gained from these experiments are essential for making reliable statements about our requirements for a sealing mating surface.

In the future, the consideration of FFT (Fast Fourier Transformation) will be another area of focus, which is beyond the scope of this paper. Through Fourier transformation over the entire length of the rod, the shape and texture of the rod surface can be visualized. This will help exclude any unfavorable influences on the sealing function caused by surface waves, ensuring consistent and reliable quality control of the surface - a critical factor for effective sealing. Therefore, the goal is to incorporate both conventional and scatter light measurement values into surface finish specifications.

6 Nomenclature

Variable	***Description***	***Unit***
α	tilt angle of the light spot on the surface	[°]
φ	scattering angle	[°]
k	correction factor	[-]
$p(\varphi)$	normalized intensity distribution	[-]
Aq	variance of the scattered light distribution	[°^{2}]
n	total number of angle classes	[-]

7 References

[1] VDA 2009: *Geometrische Produktspezifikation – Oberflächenbeschaffenheit, winkelaufgelöste Streulichtmesstechnik*, (guideline in German) 2009.

[2] Prokent AG: *DRAVI 3.0 Handsensor zur Dralldetektion*. In: Qualität und Zuverlässigkeit (Dezember 2012)

[3] Hertzsch, A, Großmann, M., Kröger, K.: *Optische Drallerkennung für die fertigungsnahe Qualitätskontrolle*, In: ATZ Produktion, 3, 2010, No. 6, pp. 40-44.

[4] Feidenhans, N. A., Hansen, P. E., Pilný, L., Madsen, M. H., Bissacco, G., Petersen, J. C., & Taboryski, R.: *Comparison of optical methods for surface roughness characterization*. In: Measurement Science and Technology, 26(8), 2015.

[5] Eifler, M., Brodmann, B., Hansen, P. E., Seewig, J.: *Traceable functional characterization of surface topography with angular-resolved scattering light measurement*. In: Surface Topography: Metrology and Properties, 9(3), 2021.

[6] Popov, V. L.: *What does friction really depend on? Robust governing parameters in contact mechanics and friction*. In: Physical Mesomechanics, 19, pp. 115-122, 2016.

[7] Optosurf GmbH: https://www.optosurf.de, visited on June 14, 2024.

[8] Seewig, J., Beichert, G., Brodmann, R., Bodschwinna, H., Wendel, M.: *Extraction of shape and roughness using scattering light*. In: *Optical Measurement Systems for Industrial Inspection VI*, pp. 223-233, 2009.

8 Authors

Trelleborg Sealing Solutions Germany
Schockenriedstr. 1, 70565 Stuttgart, Germany

Anja Dobrinsky,
0009-0002-0300-0535, anja.dobrinsky@trelleborg.com

Christoph Schüle,
0000-0002-2762-4409, christoph.schuele@trelleborg.com

Sebastian Betz,
0009-0007-5686-0762, sebastian.betz@trelleborg.com

OptoSurf GmbH
Nobelstr. 9-13, 76275 Ettlingen, Germany
Boris Brodmann,
0000-0002-1529-5708, boris.brodmann@optosurf.de

https://doi.org/10.61319/OPZY3WCU

Group B
Session 6

Static Seals

B 21

Hariolf Kurz, Michael Hübner Hecker, Hochschule Weihenstephan Triesdorf, Agrartechnik, Weidenbach, Germany

Optimized rubber gasket with internal force shunt

B 22

Finn Bartmann, Alexander Riedl, Elmar Moritzer, FH Münster / University Paderborn Center of Sealing Technologies, Steinfurt, Germany

Development of an analytical calculation method for the design of thermoplastic flange systems

Optimized rubber gasket with internal force shunt

Hariolf Kurz, Michael Hübner-Hecker

With the introduction of TA Luft 2021, plant manufacturers and operators have to carry out flange connection calculations according to DIN EN 1591-1, including gasket parameters DIN EN 13555. This will lead to enhanced plant safety and less emissions, however, it implies the development of optimized gasket materials and design. According to the design rule "for every functionality, implement a specific feature", a well known gasket principle is to put the sealing material in force shunt. This way, the load transfer element and the sealing element are in separate locations, leading to the possibility to optimize them independently. This works already very well for O-Ring seals, spiral-wound gaskets and as well, rubber gaskets with an external force shunt. Due to high manufacturing cost and high effort for assembly, these solutions are not widespread in use in the field. In this paper, a new, efficiently to produce design is proposed, implementing a spiral wound metal spiral with indentations, that creates an internal force shunt. Gasket tests according to DIN EN 13555 show excellent behaviour in every relevant aspect, leading to a reduced effort for flange connection calculations, an easy and reliable assembly process, a high plant safety and minimized fugitive emissions.

1 Introduction

Of nearly every item, product or commodity in our daily life, a plurality of its raw materials are sourced, processed and transported via pressure vessels and pip-ings either in gaseous or in liquid state. Therefore, designing and maintaining a suitable infrastructure is key to enhance plant safety and costs as well as reduce fugitive emissions of environmentally hazardous substances.

With its amended version in 2002, the German government issued TA Luft (referencing to VDI 2440 [1], DIN EN 1591-1 [2], DIN EN 1591-3 [3] and DIN EN 13555 [4]) with the incentive, to provide a comprehensive standard, that enables plant operators and manufacturers to find suitable components as well as enabling gasket manufacturers to determine and optimize their product and also setting limits for allowable emissions. Within this framework, plant operators have to conduct an analytical proof of every flange connection. In 2021, the German government replaced the former version of TA Luft [5] with increased requirements, leading to increasing effort and the need for suitable components.

However, according to researches there are still significant fugitive emissions caused by diffusive leaks in pressure vessels and pipings. Overall water losses in Europe due to leakage ranges between 6 and 14 % and about 40% in Asia, Latin America and Africa [6]. An investigation in the chemical plants of BASF shows, that 17% of the total emissions are a result of leakages, where leaking flange connections account for 28% [7]. These figures show that there is still need for improvements and a huge potential to increase plant reliability and reduce economic losses and environmental impact.

2 Working principle of bolted flange connections – gasket design

The mechanical behaviour of a bolted flange connection is a complex interaction of bolts, flanges and gaskets and has to meet multiple functionalities under various loads. Firstly, a flange connection has to bear and transfer the loads, applied from attached components. Usually, pipings and pressure vessels are subjected to axial loads as well as bending and torsion moments. Additionally, the internal pressure creates an axial load. These loads have to be transferred through a flange connection, resulting in stresses, strain and therefore deflections of the connections. Beside the load bearing capacity, a flange connection also has to prevent fugitive emissions due to leakage.

2.1 Challenges for flat face gaskets

In one of the most commonly used flange connection, flanges with flat faces and a gasket inside the bolt circle (ibc-type), all the requirements also have to be met by the gasket. Therefore, gasket materials have to be capable of transferring the external loads but also have to be soft and flexible, in order to close microscopic gaps and surface irregularities to achieve a high level of leak thightness. This fact leads to a contradiction for the gasket material, having to be a compromise between sufficiently in its load-bearing capacity and as well, it has to ensure a high level of leak tightness. Because of this, it is impossible, to optimize the design and material behaviour of flat-face gaskets for both criteria simultaneously. Typical gasket materials are graphite or fibre seals.

2.2 Patented invention [8]: rubber gasket with internal force shunt

A well-known solution to the discussed aspects is the design of a rubber gasket with force shunt [9]. The patented design applies this principle in a uniquely and efficiently to produce design as shown in figure 1 via an implemented spiral wound metal-wire with indentations. The metal spiral is placed inside the injection mold and during the injection process, the rubber material flows radially from the inside through the indentations to the outside, creating a form fit. This leads to a very efficient and economic manufacturing process, since no scrap metal is left over and no adhesive has to be applied.

figure 1: design of rubber gasket with implemented spiral wound metal-wire with indentations

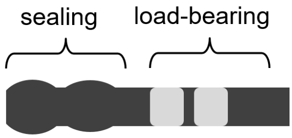

figure 2: cross-section of the gasket, separated area for tightening and area of load bearing

As shown in figure 2, the cross section of the gasket consists of two different areas. The sealing area at the inner diameter contains two circumferential rubber rings with an axial elevation of 1mm with respect to the axial thickness of the metal spiral. The geometry of the sealing area is optimized via finite element simulation, in order to achieve an optimal tightness at minimal radial deflection to the inside. The thickness of the sealing area is compressed from 4 to 3mm during the assembly process. This ensures optimal sealing performance and complies with recommendations for o-ring applications.

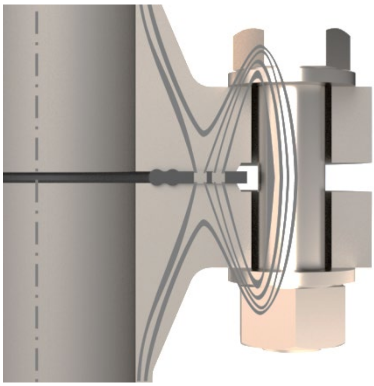

Figure 3: Cross section of a bolted flange connection: optimised load transfer at metal spiral (grey lines indicade effectiv direction of the loads - bolt load and external loads)

At the outer diameter, the enclosed spiral wound metal wire creates a so called force-shunt, and therefore transfers the bolt loads and the external forces. As soon as the gasket is mounted, the sealing area is decoupled from the load transfer, as shown in figure 3. Because of this, the sealing area is not influenced by external loads and the bolt force, the gasket material can be optimized for tightness. The metal spiral covers at least 20% of the overall sealing area. Therefore, it is ensured, that the surface pressure between at the flange faces does not exceed values, that lead to serious plastic deformations and thus to imprints.

3 Proof of concept

Since the gasket is applied like a standard ibc-gasket between flanges with flat faces, it can be tested, calculated and used accordingly. Therefore, the behaviour is measured and described via the gasket parameters according to DIN EN 13555. The test procedure leads to the following gasket parameters [10] that allow a full description of the overall behaviour of gaskets during all load cases:

3.1 Maximum gasket pressure during assembly and operation – Q_{Smax}

In order to prevent the gasket from mechanical damage due to overloading, the load limit is determined in the compression test that provides the gasket parameter Q_{Smax}. The gasket is subjected to increasing gasket pressure and the resulting gasket thickness is monitored continuously. In the case of material failure, the gasket thickness decreases drastically and indicates mechanical failure. The result in figure 4 shows, that at room temperature, even up to the maximum gasket stress up to 190 MPa, there is no mechanical failure detectable. The decrease in gasket thickness results due to plastic deformation of the metal spiral non-critical. In the typical range of use between 10 and 30 MPa , there is no risk of overstressing and destroying the gasket either during assembly or in service. In comparison, standard flat face rubber gaskets fail at gasket stresses as low as 20 MPa (dependent of the service temperature) and thus are prone to failure in typical service conditions due to overstressing.

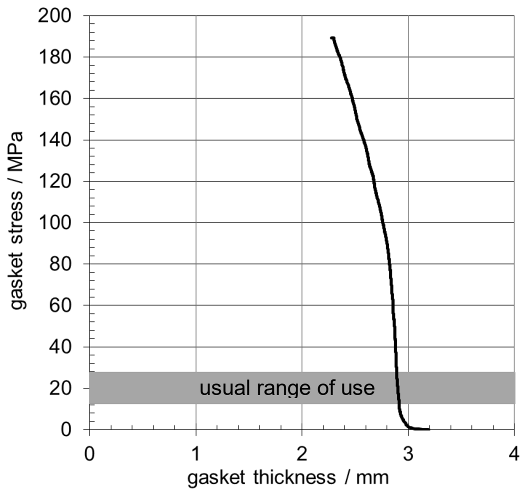

Figure 4: compression test to 190 MPa ⇒ no destruction of the gasket due to overstressing possible (maximum value of test rig reached)

3.2 Leakage test, $Q_{min(L)}$ and $Q_{Smin(L)}$

The leakage test according to DIN EN 13555 subjects the gasket to a specific pattern of gasket stress levels, that simulate the typical service conditions of flat face gaskets, beginning with the stress level at assembly and decreasing stress levels due to creep relaxation. The result of the test procedure are the values $Q_{min(L)}$ and $Q_{Smin(L)}$. $Q_{min(L)}$ indicates, how high the stress level at assembly has to be the least, in order to meet the required tightness level L. According to TA Luft, the leakage level of the gasket has to be below 0,01 mg/sm (determined with helium and at operating pressure). Figure 5 shows, that using soft rubber material leads to an leakage level below 0,0001 mg/(sm) even at very low gasket stress levels of 2,5 MPa. This means, that the gasket meets the leakage requirements in all situations easily. In comparison, typical fibre seals or graphite gaskets need between 20 to 30 MPa gasket stress, in order to achieve the tightness level of 0,01 mg/(sm). This leads to the need for high bolt loads and stresses in the flanges and leaves very little room for errors.

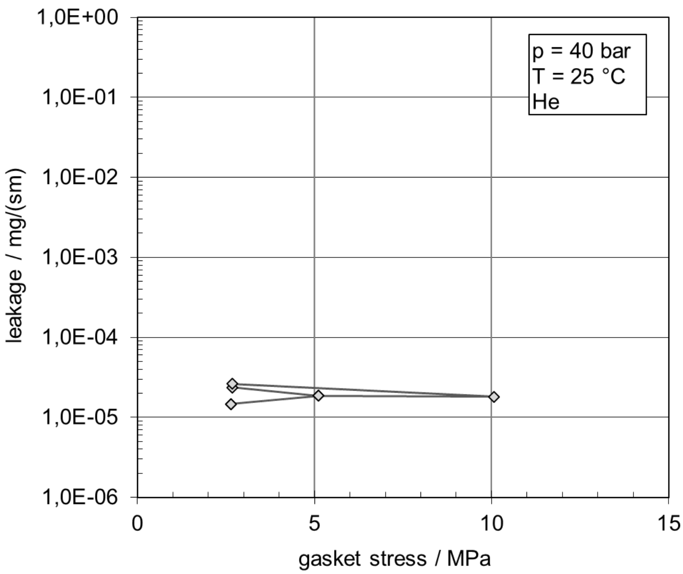

Figure 5: result of leakage test shows a very high level of leak tightness even at very low gasket stresses of 2,5 MPa

3.3 Creep-relaxation - P_{QR}

In order to achieve high levels of tightness, gasket material have to be soft and flexible. Especially, if rubber is part of the gasket, such as in rubber bound fibre gaskets, creep relaxation leads to decreasing gasket stress levels during service. As a concequence, the leakage increases. This has to be adressed via higher gasket stress levels at assembly. To determine the relative decrease of gasket stress, the gasket is subjected to the desired stress at assembly and heated up to the nominal service temperature. As soon as this temperature is reached, the test rig applies a typical stiffness of 500 kN/mm, simulating the elastic behaviour of a bolted flange connection. In figure 6, the results for the rubber gasket with internal force shunt is shown. Since the gasket stress is almost fully applied at the metal spiral, there is no effect due to creep relaxation measurable. The gasket stress level after heating up to 150°C remains constant at 30 MPa. The value for P_{QR} is calculated to 0,98, meaning, 98% of the stress level at assembly remains during service. In comparison, standard rubber gaskets typically lose up to 50% (P_{QR}=0,5) and fibre gasket up to 30% (P_{QR}=0,7) of the gasket stress during service. This effect has to be compensated via higher bolt loads, further increasing stresses in the flange connection, making it difficult, to find solutions in the flange connection calculation.

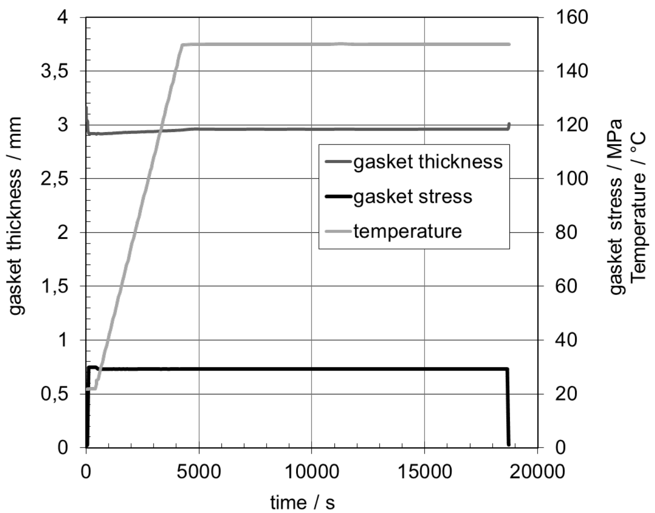

Figure 6: result of the creep relaxation test at 30 MPa initial gasket stress and 150 °C shows no significant loss of gasket stress during service

4 Conclusions

The design of a rubber gasket with an internal force shunt solves the problem of contradicting requirements of gasket materials. The solution implements a spiral wound metal-wire with indentations, that creates a force shunt. It lies inside the rubber material and thus is enclosed, held by the rubber and is easily and efficiently to produce. The design leads to a unique sealing performance with a very high tightness ($L < 10^{-4}$ mg/(sm)) even at very low gasket pressures of 2,5 MPa, no creep relaxation (P_{QR} > 0.98) and a very high load bearing capacity (Q_{max} > 190 MPa). This enables plant manufacturers and operators to effortlessly:

- meet the tightness-requirements according to TA-Luft
- successfully carry out flange connection calculations for almost any flange type
- find suitable torques for the assembly process
- minimize leakage due to errors during assembly
- choose the right gasket material (according to temperature and medium specs)
- generally enhance plant safety
- and reduce overall in-situ emissions of the plant

5 References

[1] VDI 2440: Emissionsminderung – Mineralölraffinerien; Verein Deutscher Ingenieure; Beuth Verlag, Berlin Juni 2021

[2] DIN EN 1591-1: Flansche und ihre Verbindungen - Regeln für die Auslegung von Flanschverbindungen mit runden Flanschen und Dichtung - Teil 1: Berechnung; Deutsche Fassung EN 1591-1:2013

[3] DIN EN 1591-3: Flansche und ihre Verbindungen - Regeln für die Auslegung von Flanschverbindungen mit runden Flanschen und Dichtung - Teil 3: Berechnungsmethode für Flanschverbindungen mit Dichtungen im Kraft-Nebenschluss; Deutsche Fassung CEN/TS 1591-3:2007

[4] DIN EN 13555: Flansche und ihre Verbindungen - Dichtungskennwerte und Prüfverfahren für die Anwendung der Regeln für die Auslegung von Flanschverbindungen mit runden Flanschen und Dichtung, Deutsche Fassung 02/2005.

[5] TA Luft Technische Anleitung zur Reinhaltung der Luft vom 18. August 2021; GMBl 2021 Nr. 48-54, S. 1050,

[6] P. Suchorab, D. Kowalski: Water Resources Protection by vontolling water suppy network leakages, International Journal of Conservation Science, Volume 12, Special Issue 1, 09 2021: pp 745-754.

[7] K.-E. Köppke, C. Cuhls: Untersuchungen und Abschätzung von diffusen Emissionen aus Anlagen der Chemieindustrie, Immissionsschutz, Zeitschrift für Luftreinhaltung, Lärmschutz, Anlagensicherheit, Abfallverwertung und Energienutzung, Erich Schmidt Verlag, 2004, Heft 1, pp 12.

[8] Hariolf Kurz, Michael Hübner-Hecker, 2018, EP3198175B1, seal for sealing flange connections, European Patent Office, url:https://patentimages.storage.googleapis.com/b8/63/02/84d45b19752c3e/EP3198175B1.pdf (05.2024)

[9] Werner Haas, Grundlehrgang Dichtungstechnik, Vorlesungsskript, frei abrufbar unter https://www.ima.uni-stuttgart.de/dokumente/forschung/dichtungstechnik/flyer/skript_dichtungstechnik.pdf (05 2024)

[10] H. Kurz: Auslegung und Optimierung von Flanschverbindungen mit SMC-Losflanschen und PTFE-Dichtungen, Dissertation, Universität Stuttgart, 2014

6 Authors

Hochschule Weihenstephan Triesdorf

Markgrafenstraße 16, 91746 Weidenbach, Germany:

Hariolf, Kurz, Prof. Dr.-Ing., ORCID 0009-0009-7139-6122, hariolf.kurz@hswt.de

Hecker Werke GmbH

Arthur Hecker Straße 1, 71093 Weil im Schönbuch, Germany:

Michael, Hübner-Hecker, Dipl. Ing., ORCID 0000-0001-0002-0003, mhh@heckerwerke.de

https://doi.org/10.61319/A2681WXI

Development of an analytical calculation method for the design of thermoplastic flange systems

Finn Bartmann M.Sc., Prof. Dr. -Ing. Alexander Riedl,
Prof. Dr. -Ing. Elmar Moritzer

In the course of environmental protection and the amendment of TA Luft, emissions from flange connections must be reduced (to L0.01). The design and calculation of steel flanges is easy to handle with the help of EN 1591-1 [3] and EN 13555 [4]. However, the standards mentioned are not suitable in their current form for thermoplastic sealing joints, such as those used in natural gas supply. For this reason, lengthy and cost-intensive tests must currently be carried out to verify tightness and strength.
The aim is therefore to develop a time-efficient and cost-effective analytical calculation method based on the existing standards. For this purpose, the energy-elastic material parameters of the steel must be replaced by viscoelastic material parameters of the thermoplastics and the calculation algorithm adapted accordingly. The problem is to be investigated with the aid of numerical structural simulations (FEM) and experimental investigations. This is an innovative contribution presenting a research project with high practical relevance for industry.

1 Presentation of the research gap

Protecting the environment and using fewer resources is more important than ever. Sealed joints in pipeline and tank construction produce relatively high emissions, which must be reduced as far as possible for the reasons mentioned above. These connections can be critical, especially in the chemical industry. Since 01.12.2021, for example, the new "Technical Instructions on Air Quality Control (TA Luft)" [2] have come into force and must be implemented. As a result, sealing connections made of thermoplastics, which are used in natural gas pipes, for example, are becoming more important, as proof of tightness must be provided. At present, it is only possible to verify the tightness of thermoplastic sealing joints by experimental means to a very limited extent, see [6]. Experimental proofs are both cost-intensive and can only be transferred to other sizes of sealing elements to a limited extent.

2 Target definition

The aim is to develop a cost-effective, quick analytical calculation method for verifying the tightness and strength of thermoplastic flange systems. Based on an existing set of rules for metallic sealing joints (EN1591-1) and taking into account the special viscoelastic and thermal material properties of thermoplastics, the energy-elastic material parameters of steel must be replaced by the viscoelastic material parameters of thermoplastics and the calculation algorithm adapted accordingly. In order to adapt the analytical calculation method to the special features of the mechanical and thermal behavior of thermoplastics, both extensive experimental investigations and FEM analyses are required for the ultimately necessary modification of the calculation algorithm and the validation of the algorithm.

3 Methodological considerations

The following diagram provides an overview of the planned methodology and the interrelationships between them:

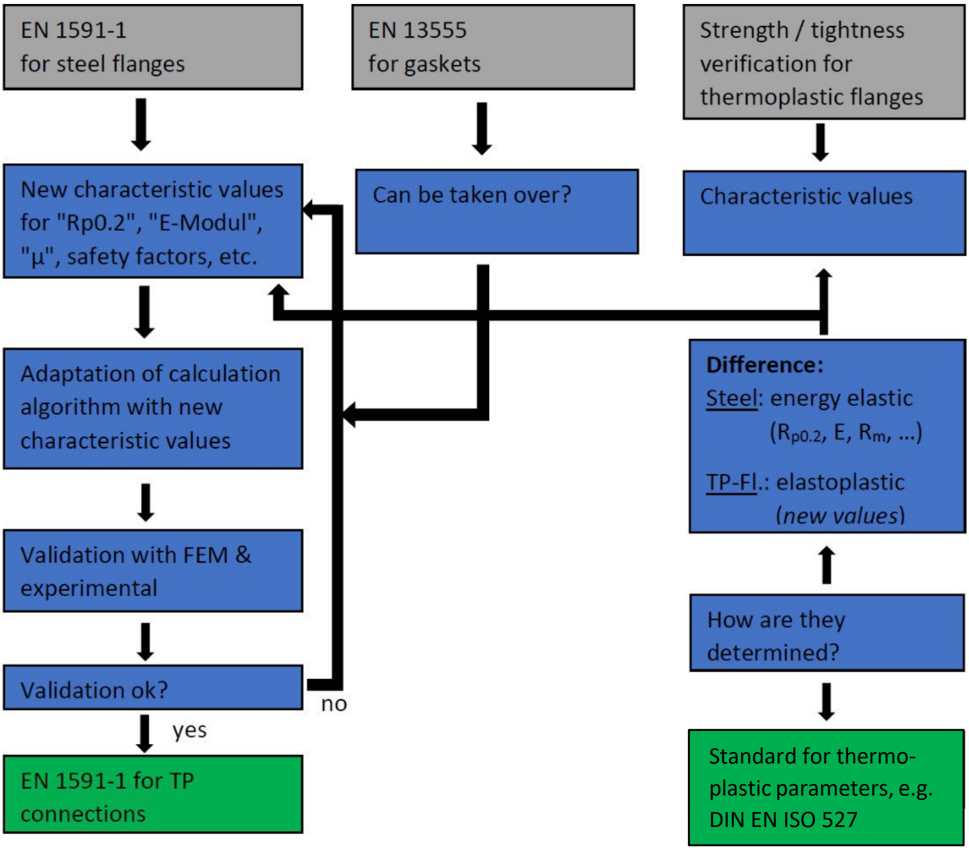

Figure 1: Diagram of the planned procedure

This is based on the standards for the design of steel flanges, marked in gray in Figure 1. In addition, research work was carried out to model the demanding material behavior in the FEM software. An elementary component of this is to model the creep behavior. The phenomenon in flange-connections is usually referred to “creep-relaxation". This is responsible for the decrease in surface pressure on the seal. The analytical calculation algorithm is to be adapted with the help of the simulation results and on the basis of the experimental findings. In the course of the experimental tests, the focus will be placed on investigating the thermoplastic material and its characteristic values.

After adapting the calculation method, the investigations and simulations can be reused to validate the analytical approach. This allows the possibilities and limits of the developed method to be demonstrated and evaluated.

In addition to the simple and cost-efficient design method, optimization potentials for the future can also be better identified and exploited.

4 Current status

For the numerical consideration of the problem, it is necessary to define the creep in the material properties separately using a creep model. Isochronous stress-strain curves can be used as a database for this purpose. Literature values can be found for selected materials. If this is not the case, time-consuming tensile creep tests must be carried out. This involves applying a constant stress to a tensile specimen and documenting the strain at regular intervals. By repeating the measurement at different loads, an isochronous stress-strain diagram can be created, just like in figure 2.

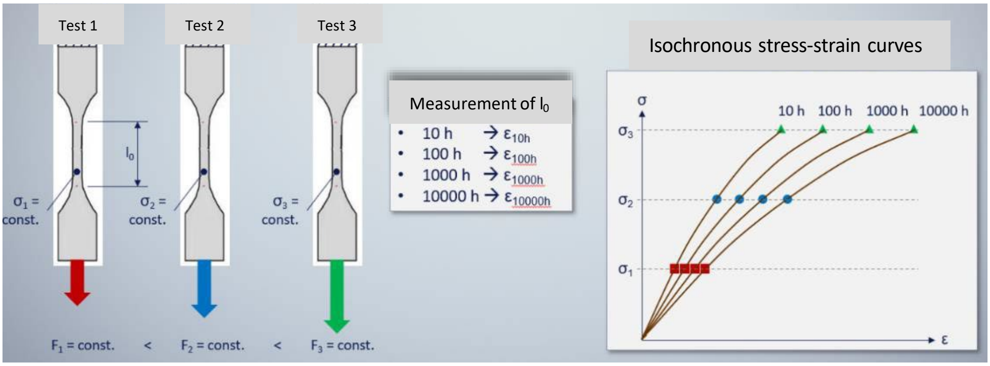

Figure 2: Illustration of creep tensile tests to create isochronous stress-strain curves [5]

As can be seen from [5], it is important to note that the test includes all strain components, which are composed as follows:

$$\varepsilon_{ges} = \varepsilon_{el} + \varepsilon_{pl} + \varepsilon_{cr} \tag{1}$$

Elastic and plastic, time-**in**dependent strains

Time-dependent creep strain

To determine the creep strain, it is therefore necessary to subtract the elastic and plastic strain. The proportions can be determined experimentally using the tensile test in accordance with DIN EN ISO 527.

The creep strain can now be calculated using the **Norton-Bailey** model, for example:

const. Parameter A, n, m

$$\varepsilon_{cr} = A \cdot \sigma^n \cdot t^m \tag{2}$$

Tension

Load time

According to [5], the elastic and plastic components of the strain can be modeled using the **Ramberg-Osgood model**, for example:

$$\varepsilon_{el,pl} = \frac{\sigma}{E} + K \left(\frac{\sigma}{E}\right)^p \tag{3}$$

The complete mathematical description of the isochronous stress-strain curves is thus carried out via:

$$\varepsilon = \underbrace{A \cdot \sigma^n \cdot t^m}_{\varepsilon_{cr}} + \underbrace{\frac{\sigma}{E} + K \left(\frac{\sigma}{E}\right)^p}_{\varepsilon_{el} + \varepsilon_{pl}} \tag{4}$$

<u>Time-dependent</u> creep strain

<u>Time-independent</u> strains

σ, t: freely selectable, e.g.

σ = 10, 20, … , 60 MPa

t = 10, 100, …, 100 000 h

$$\varepsilon = A \cdot \sigma^n \cdot t^m + \frac{\sigma}{E} + K \left(\frac{\sigma}{E}\right)^p$$

A, m, n:

Unknown parameters

E, K, p:

Previously calibrated (known) parameters

Using the model calibrated in this way, the bolt force relaxation due to creep of the thermoplastic material could be determined as follows:

First, the stresses in the component are determined, e.g. with the help of an FEM simulation. Figure 3 shows the von Mises comparative tension in the collar.

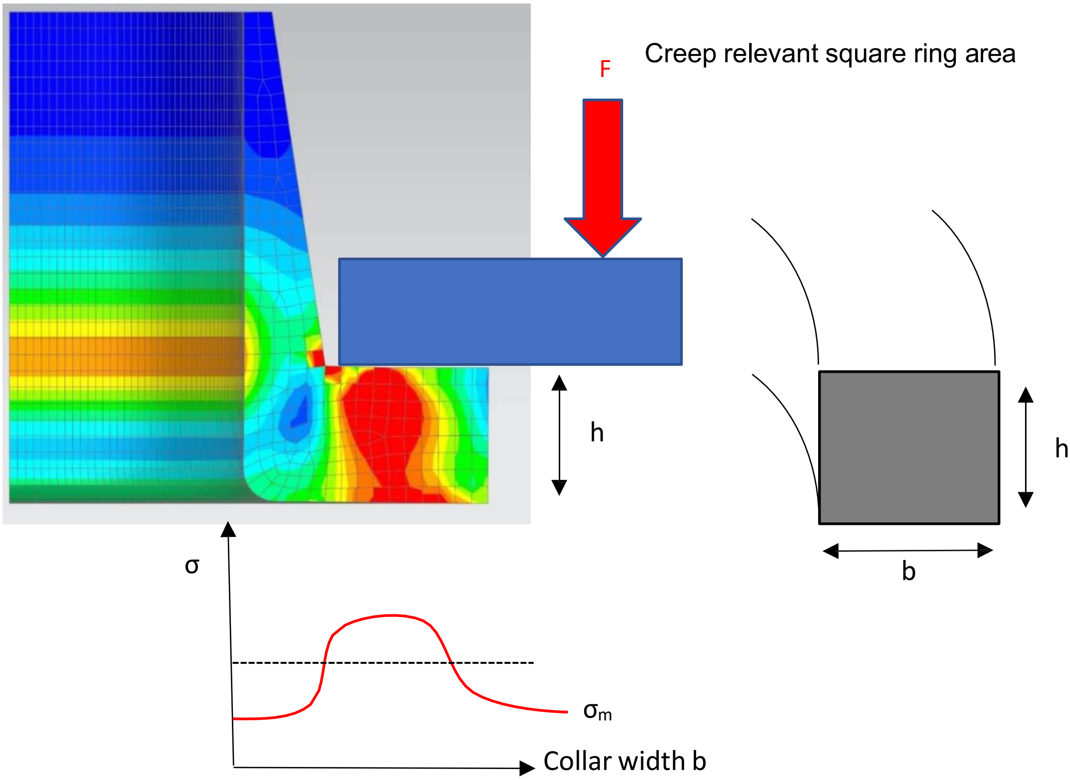

Figure 3: Simulative stress distribution in the flange collar

The change in length due to creep then results in:

$$\Delta l = \varepsilon_{cr} \cdot h \quad (5)$$

Notice that the influence of the circumferential rotation of the loose flange on the mechanical behavior is not considered in this first calculation approach.

The creep strain can then be determined using the Norton-Bailey model:

$$\varepsilon_{cr} = A \cdot \sigma^n \cdot t^m$$

with calibration of A, n, m via isochronus stress- strain diagrams (parameter fitting)

$$\varepsilon_{cr} = f(\sigma, t, T)$$

The resulting bolt force relaxation can then be read approximately from the tension diagram as shown in Figure 4, when rotation is again disregarded.

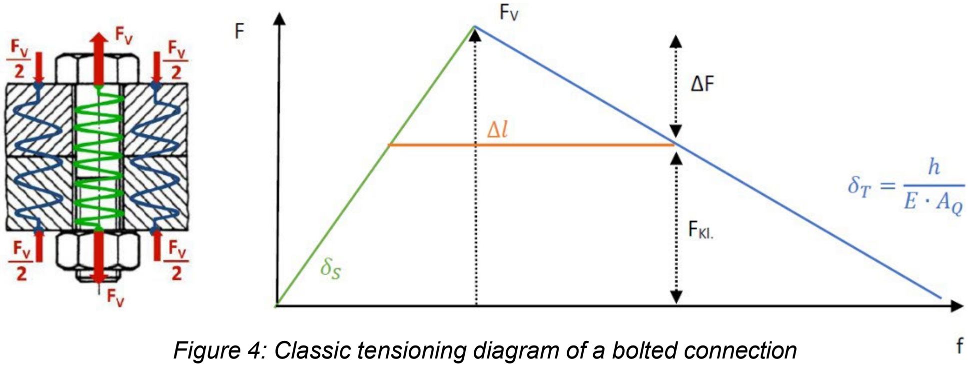

Figure 4: Classic tensioning diagram of a bolted connection

The residual surface pressure of the gasket results in: $P_{Rest} = \frac{F_{Kl.}}{A_G}$ (6)

In order to test the transferability of tensile tests (according to DIN EN ISO 527) to the real application in the flange, compression tests in the AMTEC test bench [1], as shown in Figure 6 and 7, are also planned. The schematic test setup is shown in figure 5. The AMTEC test bench is a leakage test rig that can usually also be used to determine the gasket characteristics in accordance with DIN EN 13555. In addition to the hydraulic cylinder and the heatable test plates, the test bench offers integrated force and displacement transducers as well as the option of leakage measurement using the pressure drop method or a helium mass spectrometer.

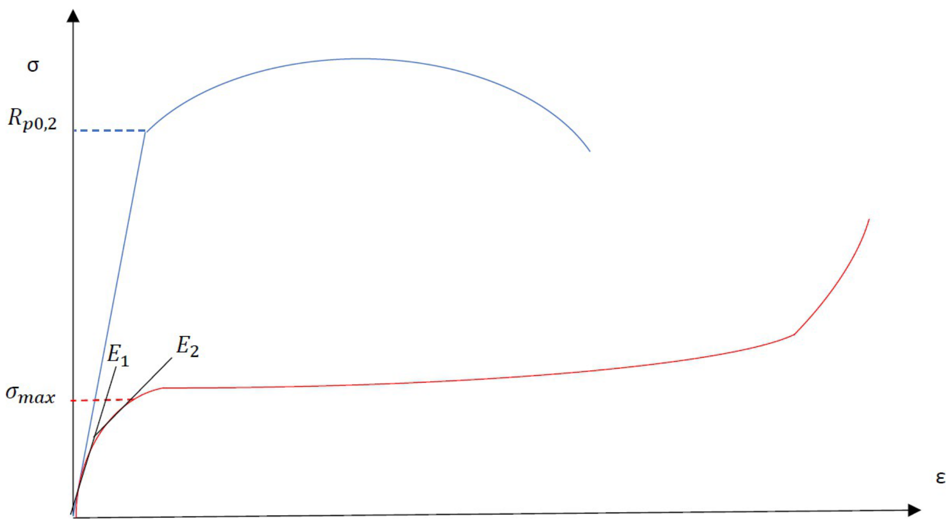

$\sigma_{max} = f\ (T, t, \varepsilon)$

$E_n = f\ (T, t, \varepsilon)$

$\alpha = f\ (T)$

on the flange

$\sigma_{Fl.} = \sigma_{Pressure,Fl.} + \sigma_{Bending,Fl.}$

<u>Equivalent stress</u>

Tensile test on specimen bar

$\sigma_{Equ.} = \sigma_{Tension,Specimen} = \sigma_{Fl.}$

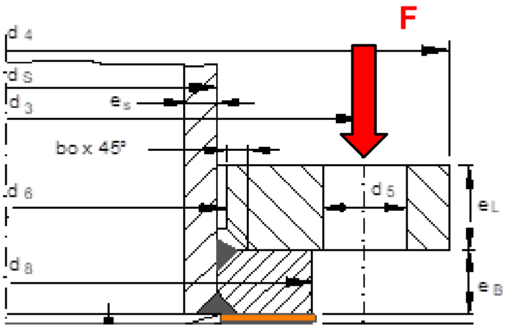

Figure 5: Schematic test setup for determining compressive stresses to check transferability to standard experiments [1]

The long-term goal is to determine the required material parameters using simple standard tests where possible and to convert them to real-life conditions. Whether and how such a conversion is possible is checked with the compression test. Table 1 below clearly shows the pairings for the first tests.

Table 1: Test plan for the compression tests in the AMTEC test rig

	Flange collar	Gasket	Temperature	Load
1	Polypropylen	NBR	21 °C	Short term
2	Polypropylen	EPDM	21 °C	Short term
3	Polypropylen	NBR	80 °C	Short term
4	Polypropylen	NBR	21 °C	Long term (100 h)
5	Polypropylen	NBR	80 °C	Long term (100 h)
6	Polyethylen	NBR	21 °C	Short term
7	Polyethylen	EPDM	21 °C	Short term
8	Polyethylen	NBR	60 °C	Short term
9	Polyethylen	NBR	21 °C	Long term (100 h)
10	Polyethylen	NBR	60 °C	Long term (100 h)

According to the current state of knowledge, the sandwich structure can be treated very similarly to a test specimen in DIN EN 13555 and the results can be applied in DIN EN 1591-1.

Figure 6: Experimental setup for carrying out the compression tests

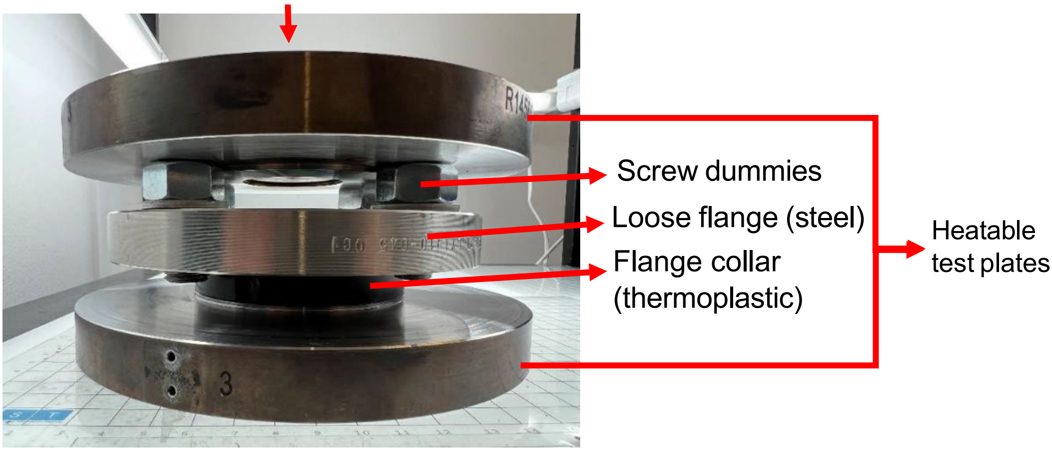

Figure 7: Sandwich structure of the test specimens, in accordance to [7]

5 Summary and Conclusion

In conclusion, it can be said that the investigation of thermoplastic flange systems is long overdue due to their increasing use and is now also gaining economic significance with the amendment of the TA Luft. The same applies to the increasing demands of climate protection. This conference paper is part of a larger research project and therefore initially reflects the current status of this project. In the long term, a draft standard based on EN 1591-1 and EN 13555 for the analytical calculation of thermoplastic flange systems is to be developed in order to reduce time-consuming and cost-intensive tests. The main difficulty lies in the consideration of the viscoelastic material behavior, which requires different material inputs than the implemented linear material behavior of steel materials. The creep of thermoplastic materials in particular ensures that the bolt forces applied are massively reduced and the surface pressure on the seal is significantly reduced. This effect is exacerbated at higher temperatures. The Norton-Bailey approach is used here to predict the creep strain as a function of the applied stresses and time. The model is based on calibration using isochronous stress-strain curves. The reduction in thickness of the flange collars can be calculated using the geometric variables. This is the reason for the bolt force relaxation. The stiffness of the structure represents the relationship between the two variables. The bolt forces in turn are decisive for the surface pressure of the gasket and this is required to determine the leakage class with the corresponding gasket parameters (in accordance with EN 13555). This promising approach is to be validated with the aid of numerical simulations and experimental investigations. Concrete approaches and the test plan will be presented. The AMTEC test rig, which can also be used to determine the gasket characteristics, is suitable. A sandwich structure consisting of a flange collar, loose flange and bolt dummies can be tested there in an upsetting test.

6 Nomenclature

Variable	***Description***	***Unit***
ε_{el}	Elastic strain	[-]
ε_{pl}	Plastic strain	[-]
ε_{cr}	Creep strain	[-]
ε_{ges}	Total strain	[-]
$R_{p0,2}$	Yield strength	[MPa]
Δl	Length change	[mm]
t	Time	[s]
σ_m	Medium stress	[MPa]
σ	Stress	[MPa]
A, n, m	Norton-Bailey parameters	[-]
E	E-Modulus	[MPa]
K, p	Ramberg-Osgood parameters	[-]
F	Force	[N]
$F_{Kl.}$	Remaining clamping force	[N]
F_V	Clamping force	[N]
h	Flange collar thickness	[mm]
b	Flange collar width	[mm]
T	Temperature	[°C]
P_{Rest}	Remaining surface pressure	[MPa]
A_G	Gasket surface	[mm^2]
A_Q	Square ring area	[mm^2]
δ_S	Stiffness screw	[mm/N]
δ_T	Stiffness of thermoplast	[mm/N]
α	Coefficient of thermal expansion	[1/K]

7 Literature references

[1] Amtec Berechnungssoftware: TEMES fl.cal. Lauffen am Neckar. 2023.

[2] Bundesministerium für Umwelt: Technische Anleitung zur Reinhaltung der Luft-TA Luft. 2002.

[3] Deutsche Industrie Norm 1591: Flansche und ihre Verbindung - Regeln für die Auslegung von Flanschverbindungen mit runden Flanschen und Dichtungen. 2014.

[4] Deutsche Industrie Norm 13555: Flansche und ihre Verbindungen – Dichtungskennwerte und Prüfverfahren für die Anwendung der Regeln für die Auslegung von Flanschverbindungen mit runden Flanschen und Dichtungen. 2021.

[5] Funke, D.: Kalibrierung isotroper Materialmodelle für FE-Analysen von thermoplastischen Kunststoffteilen. Präsentation Firma Hengst SE. 2023.

[6] Riedl, A. und Wilming, H.: Harmonisierung der Anforderungen an dichte Verbindungselemente wie Flanschverbindungen zur Begrenzung von diffusen leichtflüchtigen organischen Emissionen (VOC). Umweltbundesamt. 2019.

[7] Kurz, H.: Auslegung und Optimierung vpn Flanschverbindungen mit SMC-Losflanschen und PTFE-Dichtungen. Dissertation. 2014.

8 Authors

University of Applied Sciences Münster, Center of Sealing Technologies (CST)

Bürgerkamp 3, 48565 Steinfurt, Germany:

Finn Bartmann, M. Sc., f.bartmann@fh-muenster.de

Prof. Dr.-Ing. Alexander Riedl, riedl@fh-muenster.de

funded by

University of Paderborn, Kunststofftechnik Paderborn (KTP)

Warburger Straße 100, 33098 Paderborn, Germany:

Univ.-Prof. Dr.-Ing. Elmar Moritzer, elmar.moritzer@ktp.uni-paderborn.de

https://doi.org/10.61319/PQDSDEU6

Fluid Power Association

22nd ISC

International Sealing Conference

See you again

23rd ISC

Stuttgart, Germany
Sept. 30 – Oct. 01, 2026

www.sealing-conference.com

IMA UNI STUTTGART

VDMA Fluidtechnik